[redacted]

ORNL-2221, Part 1–5
C-84 – Reactors-Special Features of Aircraft Reactor

AEC RESEARCH AND DEVELOPMENT REPORT

This document has been reviewed and is determined to be
APPROVED FOR PUBLIC RELEASE
Name/Title: Leesa Laymance, ORNL TIO
Date: December 21, 2015

AIRCRAFT NUCLEAR PROPULSION PROJECT

QUARTERLY PROGRESS REPORT

FOR PERIOD ENDING DECEMBER 31, 1956

DOE 1979 REVIEW OF
DECLASSIFIED REPORTS

This Document is Properly Declassified.

Reviewed by P. S. Baker OCT 17 1979
ORNL Classification Officer PSB

This document has been reviewed and is determined to be
APPROVED FOR PUBLIC RELEASE.
Name/Title: Leesa Laymance/TIO
Date: 9-1-15

OAK RIDGE NATIONAL LABORATORY
OPERATED BY
UNION CARBIDE NUCLEAR COMPANY
A Division of Union Carbide and Carbon Corporation
UCC
POST OFFICE BOX X · OAK RIDGE, TENNESSEE

[redacted]

[redacted]

[redacted]

ORNL-2221, Part 1–5
C-84 – Reactors-Special Features of Aircraft Reactor

This document consists of 394 pages.
Copy 132 of 257 copies. Series A.

Contract No. W-7405-eng-26

AIRCRAFT NUCLEAR PROPULSION PROJECT

QUARTERLY PROGRESS REPORT

For Period Ending December 31, 1956

W. H. Jordan, Director
S. J. Cromer, Co-Director
A. J. Miller, Assistant Director

DATE ISSUED

MAR 12 1957

CLASSIFICATION CANCELLED
DATE MAY 28 1969
For the Atomic Energy Commission
TED REDMON for the
Chief, Declassification Branch

OAK RIDGE NATIONAL LABORATORY
Operated by
UNION CARBIDE NUCLEAR COMPANY
A Division of Union Carbide and Carbon Corporation
Post Office Box X
Oak Ridge, Tennessee

[redacted]

[redacted]

[redacted]

Reports previously issued in this series are as follows:

ORNL-528	Period Ending November 30, 1949
ORNL-629	Period Ending February 28, 1950
ORNL-768	Period Ending May 31, 1950
ORNL-858	Period Ending August 31, 1950
ORNL-919	Period Ending December 10, 1950
ANP-60	Period Ending March 10, 1951
ANP-65	Period Ending June 10, 1951
ORNL-1154	Period Ending September 10, 1951
ORNL-1170	Period Ending December 10, 1951
ORNL-1227	Period Ending March 10, 1952
ORNL-1294	Period Ending June 10, 1952
ORNL-1375	Period Ending September 10, 1952
ORNL-1439	Period Ending December 10, 1952
ORNL-1515	Period Ending March 10, 1953
ORNL-1556	Period Ending June 10, 1953
ORNL-1609	Period Ending September 10, 1953
ORNL-1649	Period Ending December 10, 1953
ORNL-1692	Period Ending March 10, 1954
ORNL-1729	Period Ending June 10, 1954
ORNL-1771	Period Ending September 10, 1954
ORNL-1816	Period Ending December 10, 1954
ORNL-1864	Period Ending March 10, 1955
ORNL-1896	Period Ending June 10, 1955
ORNL-1947	Period Ending September 10, 1955
ORNL-2012	Period Ending December 10, 1955
ORNL-2061	Period Ending March 10, 1956
ORNL-2106	Period Ending June 10, 1956
ORNL-2157	Period Ending September 10, 1956

INTERNAL DISTRIBUTION

1. R. G. Affel
2. C. J. Barton
3. M. Bender
4. D. S. Billington
5. F. F. Blankenship
6. E. P. Blizard
7. C. J. Borkowski
8. W. F. Boudreau
9. G. E. Boyd
10. M. A. Bredig
11. E. J. Breeding
12. W. E. Browning
13. F. R. Bruce
14. A. D. Callihan
15. D. W. Cardwell
16. C. E. Center (K-25)
17. R. A. Charpie
18. R. L. Clarke
19. C. E. Clifford
20. J. H. Coobs
21. W. B. Cottrell
22. D. D. Cowen
23. S. Cromer
24. R. S. Crouse
25. F. L. Culler
26. D. R. Cuneo
27. J. H. DeVan
28. L. M. Doney
29. D. A. Douglas
30. E. R. Dytko
31. W. K. Eister
32. L. B. Emlet (K-25)
33. D. E. Ferguson
34. A. P. Fraas
35. J. H. Frye
36. W. T. Furgerson
37. R. J. Gray
38. A. T. Gresky
39. W. R. Grimes
40. A. G. Grindell
41. E. Guth
42. C. S. Harrill
43. E. E. Hoffman
44. H. W. Hoffman
45. A. Hollaender
46. A. S. Householder
47. J. T. Howe
48. W. H. Jordan
49. G. W. Keilholtz
50. C. P. Keim
51. F. L. Keller
52. M. T. Kelley
53. F. Kertesz
54. J. J. Keyes
55. E. M. King

56–57. J. A. Lane

58. R. B. Lindauer
59. R. S. Livingston
60. R. N. Lyon
61. H. G. MacPherson
62. R. E. MacPherson
63. F. C. Maienschein
64. W. D. Manly
65. E. R. Mann
66. L. A. Mann
67. W. B. McDonald
68. J. R. McNally
69. F. R. McQuilkin
70. R. V. Meghreblian
71. R. P. Milford
72. A. J. Miller
73. R. E. Moore
74. J. G. Morgan
75. K. Z. Morgan
76. E. J. Murphy
77. J. P. Murray (Y-12)
78. M. L. Nelson
79. G. J. Nessle
80. R. B. Oliver
81. L. G. Overholser
82. P. Patriarca
83. R. W. Peelle
84. S. K. Penny
85. A. M. Perry
86. J. C. Pigg
87. P. M. Reyling
88. A. E. Richt
89. M. T. Robinson
90. H. W. Savage
91. A. W. Savolainen
92. R. D. Schultheiss
93. D. Scott
94. J. L. Scott
95. E. D. Shipley

96. A. Simon
97. O. Sisman
98. J. Sites
99. M. J. Skinner
100. A. H. Snell
101. C. D. Susano
102. J. A. Swartout
103. E. H. Taylor
104. R. E. Thoma
105. D. B. Trauger
106. D. K. Trubey
107. G. M. Watson
108. A. M. Weinberg
109. J. C. White
110. G. D. Whitman
111. E. P. Wigner (consultant)
112. G. C. Williams
113. J. C. Wilson
114. C. E. Winters
115–124. ORNL – Y-12 Technical Library Document Reference Section
125–131. Laboratory Records Department
132. Laboratory Records, ORNL R.C.
133–135. Central Research Library

EXTERNAL DISTRIBUTION

136. Aerojet-General Corporation
137. AF Plant Representative, Baltimore
138. AF Plant Representative, Burbank
139. AF Plant Representative, Clifton
140. AF Plant Representative, Longbeach
141. AF Plant Representative, Marietta
142–144. AF Plant Representative, Santa Monica
145–146. AF Plant Representative, Seattle
147. AF Plant Representative, Wichita
148. Air Materiel Command
149. Air Research and Development Command (RDGN)
150. Air Technical Intelligence Center
151–153. ANP Project Office, Fort Worth
154. Albuquerque Operations Office
155. Argonne National Laboratory
156. Armed Forces Special Weapons Project, Sandia
157. Armed Forces Special Weapons Project, Washington
158. Assistant Secretary of the Air Force, R&D
159–164. Atomic Energy Commission, Washington
165. Atomics International
166. Battelle Memorial Institute
167–168. Bettis Plant (WAPD)
169. Bureau of Aeronautics
170. Bureau of Aeronautics (Code 24)
171. Bureau of Aeronautics General Representative
172. Chicago Operations Office
173. Chicago Patent Group
174. Chief of Naval Research
175. Convair-General Dynamics Corporation
176. Curtiss-Wright Corporation
177. Engineer Research and Development Laboratories
178–181. General Electric Company (ANPD)
182. Glenn L. Martin Company
183. Hartford Area Office
184–185. Headquarters, Air Force Special Weapons Center

186. Idaho Operations Office
187. Knolls Atomic Power Laboratory
188. Lockland Area Office
189. Los Alamos Scientific Laboratory
190. Marquardt Aircraft Company
191. National Advisory Committee for Aeronautics, Cleveland
192. National Advisory Committee for Aeronautics, Washington
193–195. Naval Air Development and Material Center
196. Naval Research Laboratory
197. New York Operations Office
198. North American Aviation, Inc. (Missile Development Division)
199. Nuclear Development Corporation of America
200. Office of the Chief of Naval Operations (OP-361)
201. Patent Branch, Washington
202–205. Pratt & Whitney Aircraft Division (Fox Project)
206. San Francisco Operations Office
207. Sandia Corporation
208. School of Aviation Medicine
209. Sylvania Electric Products, Inc.
210. Technical Research Group, New York
211. USAF Headquarters
212. USAF Project RAND
213. University of California Radiation Laboratory, Livermore
214–231. Wright Air Development Center (WCOSI-3)
232–256. Technical Information Service Extension, Oak Ridge
257. Division of Research and Development, AEC, ORO

FOREWORD

This quarterly progress report of the Aircraft Nuclear Propulsion Project at ORNL records the technical progress of the research on circulating-fuel reactors and other ANP research at the Laboratory under its Contract W-7405-eng-26. The report is divided into five major parts: 1. Aircraft Reactor Engineering, 2. Chemistry, 3. Metallurgy, 4. Heat Transfer and Physical Properties, Radiation Damage, and Fuel Recovery and Reprocessing, and 5. Reactor Shielding.

The ANP Project is comprised of about 550 technical and scientific personnel engaged in many phases of research directed toward the achievement of nuclear propulsion of aircraft. A considerable portion of this research is performed in support of the work of other organizations participating in the national ANP effort. However, the bulk of the ANP research at ORNL is directed toward the development of a circulating-fuel type of reactor.

The design, construction, and operation of the Aircraft Reactor Test (ART), with the cooperation of the Pratt & Whitney Aircraft Division, are the current objectives of the project. The ART is to be a power plant system that will include a 60-Mw circulating-fuel reflector-moderator reactor and adequate means for heat disposal. Operation of the system will be for the purpose of determining feasibility and for studying the problems associated with the design, construction, and operation of a high-power circulating-fuel reflector-moderated aircraft reactor system.

CONTENTS

FOREWORD

SUMMARY

PART 1. AIRCRAFT REACTOR ENGINEERING

1.1. AIRCRAFT REACTOR TEST DESIGN 3
- Status of ART Design 3
- Applied Mechanics and Stress Analysis 3
  - Creep Buckling of Shells with Double Curvature 3
  - Tube-to-Shell Connections 6
  - Thermal Expansions of Shells and Reflector 7
  - High-Frequency Temperature-Oscillation Studies 11
- Radioactivity in the Fuel-Pump Oil System 13
- Heat Exchanger Thermal Stresses 14

1.2. ART PHYSICS 15
- Neutron Heating in the ART 15
- Total Radiation Heating in the ART 16

1.3. ART INSTRUMENTS AND CONTROLS 20
- Liquid-Metal-Level Transducers 20
- Magnetic Flowmeters 23
- High-Temperature Turbine-Type Flowmeters 25
- Spark-Plug Liquid-Level Probes 29
- Fuel-Expansion-Tank Level Indicator 29
  - Static-Level Tests 29
  - Dynamic-Level Tests 29
- High-Temperature Pressure Transmitters 30

1.4. COMPONENT DEVELOPMENT AND TESTING 32
- Pump Development Tests 32
  - Bearing, Seal, and Lubricant Tests 32
  - Analysis of Hydraulic Drive Failures 33
  - Fuel Pump Development Water Tests 33
  - Fuel Pump High-Temperature Performance Tests 37
  - Fuel Pump Endurance Tests 38
  - Sodium Pump Tests with Water 38
  - Sodium Pump Tests with Sodium 39
  - Primary NaK Pump Development Tests 41
- Water Flow Tests of Aluminum North-Head Mockup 42
- Reactor Component Development Tests 43
  - Heat Exchanger and Radiator Tests 43
  - Valve Development Tests 45
  - Zirconium Fluoride Vapor Traps 51
  - Liquid-Metal-Vapor Condensers 54

Auxiliary Component Development Tests 54
High-Frequency Thermal-Cycling Test 54
ART Sodium Circuit Water Flow Tests 58
ETU Component Water Flow Tests 60
Cold-Trap Evaluation Tests 61
Water Flow Studies of NaK Systems for Cooling Fuel Fill-and-Drain Tank 63

1.5. PROCUREMENT AND CONSTRUCTION 65

ART Facility 65

ART-ETU Reactor Construction 70
Reactor Assembly 70
ETU Facility 75
Cell Components 75

ART-ETU Reactor Component Procurement 77
Fuel-to-NaK Heat Exchangers 77
Sodium-to-NaK Heat Exchangers 77
Brazing Problems 77
Inconel Stock 78

1.6. ART, ETU, AND IN-PILE OPERATIONS 79

ART and ETU Operation 79
Operating Procedures 79
Process Flow Diagrams 81
Electrical Systems 82
Leak Testing of the ART 83

ART Disassembly 84
Disassembly Procedures in ART Cell 84
After-Shutdown Dose from the Reactor 85
Contamination in ART Cell from Off-Gas Leak 85
Particle-Size Distribution from Cutting Operations 88

In-Pile Experimentation 89
In-Pile Loop No. 6 89
In-Pile Loop Heat Exchanger 90
Prototype In-Pile Loop Pump 90
In-Pile Lubricant and Seal Test 91
In-Pile Tests of Reactor Moderator Materials 91

1.7. ADVANCED REACTOR DESIGN 92

Design Considerations 92

Reactor Configurations 93

Material Problems 97
In-Pile Tests of Moderator Materials 99
Thermal Stresses and Temperature Gradients in ZrH Cylinders 101

Reactor Calculations 102
Curtiss-Wright Corporation 102
Nuclear Development Corporation of America 103

PART 2. CHEMISTRY

2.1. PHASE EQUILIBRIUM STUDIES 109

The System $NaF-RbF-UF_4$ 109

The System $RbF-CaF_2$ 109

The System $7NaF \cdot 6ZrF_4-7NaF \cdot 6UF_4$ 112

The System $RbF-BeF_2$ 112

The System $NaF-RbF-BeF_2-UF_4$ 114

The System $KF-BeF_2$ 115

The System $CsF-BeF_2$ 117

The System $NaCl-ZrCl_4$ 118

Oxides and Oxyfluorides in Molten Salts 119

2.2. CHEMICAL REACTIONS IN MOLTEN SALTS 120

Equilibrium Reduction of NiF_2 by H_2 in $NaF-ZrF_4$ 120

Solubility and Stability of Structural Metal Fluorides in Various Fluoride Mixtures 120

Reduction of UF_4 by Structural Metals 123

Solubility of BaF_2 in $NaF-ZrF_4$ 125

Solubility of LaF_3 and of CeF_3 in Molten Fluoride Mixtures 125

CeF_3 in $NaF-ZrF_4-UF_4$ 125

LaF_3 in $NaF-KF-LiF-UF_4$ and in $NaF-ZrF_4-UF_4$ 126

Partition of CeF_3 Between $NaF-ZrF_4-UF_4$ and $LaF_3(CeF_3)$ Solid Solution 126

Solubility of Helium in $NaF-ZrF_4-UF_4$ 130

Nickel Mass Transfer in $NaF-ZrF_4$ 134

Colors of Corrosion Products in Fused Fluoride Salts 136

Solubility Determinations by Measurement of Electromotive Forces of Concentration Cells 139

Activities Determined from Freezing Points of Binary Fluoride Mixtures 140

2.3. PHYSICAL PROPERTIES OF MOLTEN MATERIALS 145

Vapor Pressures and Activities in the $NaF-ZrF_4$ System 145

Effect of Partial Substitution of UF_4 for ZrF_4 on the Vapor Pressure of ZrF_4 in Fuel Mixtures 146

Vapor Pressures of the $LiCl-FeCl_2$ and $KCl-FeCl_2$ Systems 149

Surface Tensions of Molten Salts 152

2.4. PRODUCTION OF PURIFIED FLUORIDE MIXTURES 153

Preparation of Various Fluorides 153

Pilot-Scale Purification Operations 153

Production-Scale Operations 153

Batching and Dispensing Operations 154

Preparation of ZrF_4 from $ZrCl_4$ 155

Special Services 155
Filling, Draining, and Sampling Operations 155
Shield Mockup Core Materials 155
Fuel Mixture for Pratt & Whitney Aircraft High-Temperature Critical Experiment 156
Preparation and Identification of the Oxides of Sodium and Potassium 156

2.5. COMPATIBILITY OF MATERIALS AT HIGH TEMPERATURES 158
Penetration of Graphite by Molten Fluorides 158
Hydrogen Pressure of the NaOH-Ni Reaction 159
Electrolysis of the NaOH-Ni System 160
Physical Properties of Elastomers Exposed to Attack by Liquid Metals 161

2.6. ANALYTICAL CHEMISTRY 162
Determination of Carbon and Nitrogen in Metallic Lithium 162
Determination of Oxygen in Metallic Lithium 163
Detection of Traces of NaK in Air 164
Spectrophotometric Determination of Nickel in Alkali Metals 165
Determination of Trace Amounts of Zirconium with Pyrocatechol Violet 165
Spectrophotometric Determination of Cerium in Mixtures of Fluoride Salts 166
Preparation of Rare-Earth Fluoride Tracers 166
Determination of Boron in Gases from the Reaction of Boron and $NaF-ZrF_4-UF_4$ 167
Determination of Metallic Boron in Mixtures of Fluoride Salts 167
Compatibility of Lubricants with Molten Alkali Metals and Fused Fluoride Salts 167
Extraction of ART Fuel Components with Organo-Phosphorus Compounds 167
Service Laboratory 168
Analyses for Contaminants in Very Pure Argon 168

PART 3. METALLURGY

3.1. DYNAMIC CORROSION STUDIES 173
Forced-Circulation Loop Tests 173
Fuel Mixtures in Inconel 173
Sodium in Various Structural Materials 175
Heat Exchanger Test Equipment 178
Thermal-Convection Loop Tests 179
Special Nickel-Molybdenum Alloy Loops 179
Special Fuel Mixtures in Inconel 182

3.2. GENERAL CORROSION STUDIES 184
Tests of Inconel Tube-to-Header Joints with Recrystallized Welds 184
Tests of Coast Metals Brazing Alloys 184
Tests of Special Nickel-Molybdenum Alloys 186
Inconel–Graphite–Fused Salt Systems 187
Fused Chloride Corrosion of Nickel and Inconel 188

Porous Rare-Earth Oxides Exposed to Molten Sodium in Inconel Capsules 189
Beryllium-Inconel-Sodium Compatibility 190
Inconel-Sodium-Zirconium Compatibility 192
NaK-Li Mixtures in Inconel 192
Molybdenum and Zirconium in Sodium and in Lithium 192
Molybdenum and Hastelloy B in Rubidium 193
Properties of Lead-Lithium Alloys 194

3.3. FABRICATION RESEARCH 199

Nickel-Molybdenum Alloy Development 199
- Alloy Evaluation Norms 199
- Status of Development Program 199
- Fabrication of Battelle Alloys 203
- Fabrication of ORNL Alloys 204
- Production of Commercial-Size Heats of Nickel-Molybdenum Alloys 205

Shield Plugs for ART Pumps 207

Neutron Shield Material 209
- ART Neutron Shield Plates 209
- Copper-B_4C Parts for Pratt & Whitney High-Temperature Critical Experiment 209

Tubular Control Rods 210

Niobium Fabrication Studies 211
- Evaluation of Arc-Melted Niobium 211
- Nb-UO_2 Compacts 214
- Niobium-Uranium Alloys 214

Fabrication of Hydrides 218

3.4. WELDING AND BRAZING INVESTIGATIONS 221

Weldability Studies of Nickel-Molybdenum Alloys 221
- Tensile Tests 221
- Hardness Tests 221
- Fabrication of Thermal-Convection Loops 223

Brazing Studies of Nickel-Molybdenum Alloys 223

NaK-to-Air Radiator Fabrication 224
- Effect of Temperature Rate-of-Rise on Brazing 225
- Influence of Fin Materials on Brazing 228
- Influence of Atmosphere on Brazing 230

Brazing Alloy Development 232

Studies of Grain Growth in Inconel Tubing 233

Welding of Boron-Containing Stainless Steel 239

Examination of a NaK-to-Air Radiator 241

Fabrication of Valve Components 241

3.5. MECHANICAL PROPERTY STUDIES 244

Creep-Rupture Properties of Inconel 244
- Effect of Section Thickness 244
- Effect of Cold Work 244

Strain Cycling of Inconel 246
Stress-Rupture Properties of Nickel-Molybdenum Alloys 249

3.6. CERAMIC RESEARCH 258
Production of Metal Hydrides 258
Investigations of Moderating Materials 258
Beryllium Carbide 258
Beryllium Oxide 258
Preparation of Rare-Earth-Oxide Cermets 258
Petrographic and X-Ray Examinations 259
Fluoride Fuel Mixtures 259
Optical Properties of Na_2O and K_2O 259

3.7. NONDESTRUCTIVE TESTING AND INSPECTION OF MATERIALS AND COMPONENTS 260
Eddy-Current Inspection Techniques 260
Fluorescent-Penetrant Inspection Techniques 260
Radiographic Techniques for Tubing Inspection 262
Tubing Defect Analysis 263
Materials Inspection 263
Tubing 263
Pipe 269
Plate 269

PART 4. HEAT TRANSFER AND PHYSICAL PROPERTIES, RADIATION DAMAGE, FUEL RECOVERY AND REPROCESSING

4.1. HEAT TRANSFER AND PHYSICAL PROPERTIES 277
ART Fuel-to-NaK Heat Exchanger 277
ART Hydrodynamics 278
Core Hydrodynamics 278
Instantaneous Velocity-Profile Measurements 279
Heat Transfer in Reflector-Moderated Reactor Cores 280
ART Core 280
A New Reflector-Moderated Reactor Core 281
Thermal-Cycling Experiments 282
Heat Capacity 286
Viscosity 288
Thermal Conductivity 288

4.2. RADIATION DAMAGE 290
Examination of Disassembled MTR In-Pile Loops 290
Chemical Problems Encountered in Etching Inconel 293
Creep and Stress-Corrosion Tests of Inconel 299
LITR Vertical In-Pile Loop 299

Effect of Radiation on Static Corrosion of Structural Materials by Fused Salts 300
Inconel Capsules Containing $NaF-ZrF_4-UF_4$ 300
Hastelloy B Capsules Containing $NaF-KF-LiF-UF_4$ 305
Investigation of Reproducibility of Chemical Analyses of Loop and Capsule Fuels 305
Comparison of Analytical Results 305
Effect of Radiation on Analyses 306
Fast-Neutron Detectors 308
Effects of Radiation on Electronic Components 309
Effect of Irradiation on Minority Carrier Lifetime 309
Effect of Barrier Field on Annealing 311
Effect of Radiation on Barrier Properties 311
Effects of Radiation on Thermal-Neutron Shield Materials 313
Effects of Radiation on Polymers 315

4.3. FUEL RECOVERY AND REPROCESSING 323
Pilot Plant Design and Construction 323
Process Development 323

PART 5. REACTOR SHIELDING

5.1. LID TANK SHIELDING FACILITY 331
Attenuation by Water of Radiation from the New LTSF Fission Source Plate (SP-2) 331
Attenuation of Fast Neutrons from a Fission Source by Water: Comparison of Experiment with Theory 331
Recalculation of Point Kernel for SP-1 333
Calculation of Point Kernel for SP-2 334
Comparison of Calculated and Experimental Dose Rate for SP-2 335
Study of Advanced Shielding Materials 335

5.2. BULK SHIELDING FACILITY 343
Calculation of the Gamma-Ray Spectrum at the Surface of a BSF Reactor Containing UO_2–Stainless Steel Fuel Elements 343
Method of Calculation 343
Results of the Calculations 345
Conclusions 347
The Energy and Angular Distribution of Gamma Radiation from a Co^{60} Source After Diffusion Through Many Mean Free Paths of Water 347
Program of Shielding Measurements at the ART 348

5.3. THE TOWER SHIELDING REACTOR II 352
Reactor Mechanical Design 352
Experimental Shield Configurations 354
Nuclear Calculations 355
Development Experiments 355

Effect of Radiation on Static Corrosion of Structural Materials by Fused Salts 300
Inconel Capsules Containing $NaF-ZrF_4-UF_4$ 300
Hastelloy B Capsules Containing $NaF-KF-LiF-UF_4$ 305
Investigation of Reproducibility of Chemical Analyses of Loop and Capsule Fuels 305
Comparison of Analytical Results 305
Effect of Radiation on Analyses 306
Fast-Neutron Detectors 308
Effects of Radiation on Electronic Components 309
Effect of Irradiation on Minority Carrier Lifetime 309
Effect of Barrier Field on Annealing 311
Effect of Radiation on Barrier Properties 311
Effects of Radiation on Thermal-Neutron Shield Materials 313
Effects of Radiation on Polymers 315

4.3. FUEL RECOVERY AND REPROCESSING 323
Pilot Plant Design and Construction 323
Process Development 323

PART 5. REACTOR SHIELDING

5.1. LID TANK SHIELDING FACILITY 331
Attenuation by Water of Radiation from the New LTSF Fission Source Plate (SP-2) 331
Attenuation of Fast Neutrons from a Fission Source by Water: Comparison of Experiment with Theory 331
Recalculation of Point Kernel for SP-1 333
Calculation of Point Kernel for SP-2 334
Comparison of Calculated and Experimental Dose Rate for SP-2 335
Study of Advanced Shielding Materials 335

5.2. BULK SHIELDING FACILITY 343
Calculation of the Gamma-Ray Spectrum at the Surface of a BSF Reactor Containing UO_2–Stainless Steel Fuel Elements 343
Method of Calculation 343
Results of the Calculations 345
Conclusions 347
The Energy and Angular Distribution of Gamma Radiation from a Co^{60} Source After Diffusion Through Many Mean Free Paths of Water 347
Program of Shielding Measurements at the ART 348

5.3. THE TOWER SHIELDING REACTOR II 352
Reactor Mechanical Design 352
Experimental Shield Configurations 354
Nuclear Calculations 355
Development Experiments 355

ANP PROJECT QUARTERLY PROGRESS REPORT

SUMMARY

1.1. Aircraft Reactor Test Design

An experimental study of the creep buckling of shells with double curvature was undertaken in order to evaluate the possible effects of the pressure differentials to which the various shells in the ART will be exposed. Strains computed from experimentally determined buckling patterns will be used to predict the number of cycles to which a shell may be subjected. All tube-to-shell connections, such as the joins of the pump barrels to the pressure shell in the region of the north head and the connection of the NaK lines from the north- and south-head manifolds to the pressure shell, are being analyzed to determine whether they can withstand certain mechanical loads and deformations and whether they can survive a specified number of temperature cycles arising from differences in thermal response of the pipe and the shell.

An over-all thermal analysis of the reactor is being made in order to determine the average operating temperatures of major structural members, to establish fabrication and assembly tolerances, to reveal possible interferences between components, and to determine which areas of the structure would be subjected to excessive thermal distortions.

A series of tests is under way to determine the fatigue life of Inconel tubing and sheet subjected to rapid strain cycling at the surface. The information obtained will be used to evaluate the effects of high-temperature high-frequency local "surface" strain-cycling of the Inconel core shells and heat exchanger tubes.

The transfer of radioactive gases from the fuel expansion tank region of the ART to the pump lubricating oil system was investigated. The results of the calculations indicated a gamma-ray dose rate of about 30 mr/hr at a distance of 1 meter from the oil reservoir and a 500-hr dose from beta emitters of 10^4 rads, which is trivial compared with the 10^8 rads the oil can absorb without serious damage.

Heat exchanger test experience was reviewed, and, in order to evaluate the conclusion that the difficulties experienced thus far have been caused by conditions peculiar to the rig-test design, a circular-arc-tube-bundle rig-test heat exchanger that simulates more closely the ART conditions is to be tested. A similar study of radiators is under way.

1.2. ART Physics

The neutron heating in the reflector, island, and fuel regions of the ART was computed. The results of two-dimensional multigroup calculations made at the Curtiss-Wright Corp. were used in the calculations. The total radiation heating in the ART, excluding that from the fission products and the fission-product beta rays in the core, was calculated by using the previously obtained values for the gamma-ray heating and the values obtained for neutron heating. An integration was also performed over the radiation heating contours to find the total heat load in each region of the ART.

1.3. ART Instruments and Controls

Two types of liquid-metal-level transducers are being tested for service in the main, auxiliary, and special ART NaK pumps. The units consist of a resistance type, manufactured by the General Electric Company, and a variable-permeance type, manufactured by the Crescent Engineering & Research Co. The G-E units have thus far operated quite satisfactorily, but the Crescent devices have been found to be very temperature-sensitive. The tests, which are to continue for 3000 hr, are designed to investigate accuracy, linearity, temperature effects, reliability, lead length effects, probe wetting effects, and time response.

Complete magnetic flowmeter units have been purchased from the General Electric Co. in the two sizes, 2 and $3\frac{1}{2}$ in., required for the ART and ETU NaK circuits. A $\frac{3}{8}$-in. flowmeter has been designed for use in the ART and ETU cold-trap and plug-indicator systems.

An evaluation study was made of the available design, fabrication, and test information on the newly developed ORNL high-temperature turbine-type flowmeter. It was concluded that the operational principle of the unit is sound and that the unit is practical for use with liquid metals and fused salts at temperatures up to 1500°F and

probably higher. Some reduction in the pressure drop through the unit is to be obtained by streamlining. The results of tests of the 1-in. units will be compared with the results of tests of a $3\frac{1}{2}$-in. unit now being installed in a NaK pump test loop.

Work is under way on an on-off type of liquid-level indicator probe that will operate reliably at NaK system temperatures for a minimum of 1000 hr, but no spark plugs tested thus far have met these specifications. A resistance type of probe is being developed which consists of a low-resistance center wire inside a thin-walled Inconel tube. This probe has the advantages that all surfaces exposed to the liquid-metal vapor are Inconel and that it can be welded into the system by replacing the threaded fitting with a welding flange.

Additional static and dynamic tests were made of the helium-bubbler type of level indicator being considered for use on the fuel expansion tank. Careful control is to be maintained over the moisture and oxygen content of the helium purge gas used in future static tests in an effort to prevent clogging of the bubbler tubes. Attempts are being made to improve the accuracy of calibration of the dynamic test rig.

High-temperature pressure transmitters of various types are being tested – a 1:1 pneumatic force-balance type with a fabricated Inconel bellows, a strain-gage type, a unit in which a differential transformer is used to detect the motion of a fabricated-bellows sensor, and a unit which employs a variable-permeance transducer to detect the motion of a formed-bellows sensor. The tests have shown the two-legged strain-gage type of transmitter to be unsatisfactory, but the four-legged strain-gage transmitters have the desired accuracy.

1.4. Component Development and Testing

Tests have shown the lubricants being considered for use in the ART pumps to be inert to the ART process fluids. In-pile tests of dynamic systems are planned for radiation-damage evaluation of the lubricants, and a critical assembly that includes a mockup of the north-head assembly is being measured in order to determine the radiation exposure to be expected in the ART. Tests of elastomers of interest for seal application were continued. Buna-N O-rings were found to be satisfactory in Gulfcrest-34. The journal bearings of the ART sodium pumps were re-evaluated because of an increase in the developed head requirement, and no effects of the increased journal bearing load were noted. Preliminary tests of modified Durametallic seals, which utilize a ceramic-faced steel rotor and a carbon stator, have indicated that these seals will probably be satisfactory for use in the ART NaK pumps.

Thorough water testing and evaluation of a fuel pump with an acceptable impeller has continued, and a similar pump is operating with the fuel mixture (No. 30) $NaF\text{-}ZrF_4\text{-}UF_4$ (50-46-4 mole %). In the developmental water testing of the fuel pump it has been possible to reduce the pressure fluctuations to acceptable limits, to establish a decreasing gas-pressure gradient, and to regulate the fluid flow into the expansion tank to the desired range. Through modifications in the impeller it was also possible to achieve the desired lowering of the loop liquid pressures relative to the gas pressure in the expansion tank in order to reduce the stress loads on the north-head assembly.

Water tests of the sodium pump were also continued. The maximum head required for ART operation was increased, and tests at the new operating conditions revealed ingassing of the pumped fluid. Therefore a re-evaluation of the impeller-volute configuration is under way. Tests of the pump with sodium at 1200 to 1350°F revealed the need for increasing the bearing clearance and decreasing the cold shrinkage tolerance.

Water tests of Inconel primary NaK pumps were completed and high-temperature tests were started. The pump primed satisfactorily on startup, and the oil seal leakage rates have remained within acceptable limits.

The newly modified and now acceptable model 32 impellers were installed in the fuel pumps of the aluminum north-head mockup. Preliminary results indicate that fluid no longer rises up the pump shaft of a stopped pump or a running pump if helium flow is maintained to both pumps and that substantial improvement of the flow characteristics in the xenon-removal expansion tank has been achieved.

Additional heat exchanger and radiator tests were run. The present series of tests are designed for studying the effects of temperature, temperature gradient, and time on mass transfer in the NaK system.

Additional tests of ART prototype dump valves and seat and plug materials have indicated that a satisfactory valve has been achieved. A valve in

which the spherical molybdenum poppet is fixed rigidly to the stem and the copper seating ring is conical has operated satisfactorily for 200 hr through 14 operating cycles. This test is continuing.

Several types of condensation traps for removing zirconium fluoride vapor from the reactor off-gas have been designed and tested. A trap that is being considered for the ART is described, as well as traps of other designs for use on test rigs. Developmental work is also under way on condensers for removing liquid metal vapor from the purge gases bled from the ART sodium and NaK pumps.

Developmental work was completed on a pulse generator for producing temperature oscillations in a fused-salt stream of 150 to 200°F at a frequency of up to 10 cps, and the generator has been built but not yet tested. The loop in which the generator will operate is being fabricated, and an investigation of techniques for measuring rapid temperature oscillations in the liquid stream and at the tube walls is under way.

The total pressure loss in the ART sodium circuit is being determined by calculations and by measuring the loss across mockups of those regions of the circuit which are difficult to analyze and to calculate. Design work was completed and fabrication was begun on the facility for water flow tests of the ETU sodium circuits through and around the reflector-moderator region. Facilities for three other flow tests are being designed.

Cold-trap evaluation tests were continued. The results of these tests will be used to establish ART cold-trap operating conditions. Flow tests are being conducted on mockups of part of the dual cooling system for the ART fuel fill-and-drain tank.

1.5. Procurement and Construction

The initial contract work on the construction of the ART facility, which included the building alterations, the building addition, the cell installation, and the installation of auxiliary services piping, has been completed. Work on the second contract, which included the installation of the diesel-generators and facility, electrical control centers, and spectrometer room electrical and air conditioning equipment, has been completed, except for installation of three diesel control panels, performance testing of diesel-generator sets, and installation of penthouse anchor bolts.

Design work on the process piping and process equipment continued, and a small portion of the work was contracted to the Rentenbach Engineering Co. They will provide a distribution center for supplying electrical power to the pipe and equipment heaters, a dry-air plant, and a building to house the air plant and wound-rotor-motor controllers. In addition, they will install government-furnished wound-rotor-motor controllers and induction regulators.

Preliminary planning work continued on the program of reactor disassembly. Building sites for the hot-cell facility were investigated, and three possible sites were selected.

The preparation of reactor assembly and inspection procedures continued, and component procurement is under way. One set of contoured beryllium parts for the ETU reactor has been received and inspected, and the cooling holes are being drilled. Progress on the fabrication of the thin Inconel core shells that form the fuel annulus indicates that acceptable shells can be produced by the Hydrospinning technique. Samples of fabricated stainless-steel-clad boron-copper cermet parts have been received, and the metallurgical and dimensional checks made thus far indicate that these items are acceptable.

Construction of the ETU facility is under way. Most of the work accomplished during the quarter was in connection with the main NaK system, the control room, and auxiliary services piping. Layout drawings were completed for mockups of most of the ART cell components that will be duplicated in the ETU assembly but not used in its operation, such as the reactor lead shield, the dual cooling system for the fill-and-drain tank, the fuel dump valves and actuators, etc. Design details for these items are to be provided by outside vendors. Some design changes necessitated by disassembly planning were made.

Progress is being made on the fabrication of the fuel-to-NaK and sodium-to-NaK heat exchangers. Assistance has been given to vendors in connection with the close control required on the variables of the brazing operations used in the construction of the radiators. Frequent discussions have been necessary on the problem of obtaining adequate quantities of acceptable Inconel stock.

1.6. ART, ETU, and In-Pile Operations

The critical review of ART operating problems that has been under way for some time is serving not only for the preparation of operating procedures and operator training manuals but also as an analysis of the reactor design. Process flowsheets and control circuitry have been analyzed, and revisions are being made where necessary.

The ETU system will be as similar as possible to the ART, within the limited objectives of the ETU, and thus the ETU will serve as a training facility for ART operating personnel, as well as a test of the reactor system. Revisions are being made in the ETU flowsheets that reflect the revisions being made in ART flowsheets. Because the ETU will not require nuclear controls, it will have only one principal control center rather than the two to be provided for the ART.

Techniques and procedures are being devised for removing the reactor from the ART facility and for transporting it to the disassembly facility. The designs of features which must be built into the system to effect the disassembly were established, and the necessary changes are being made in ART designs. As a basis for preparation of the disassembly procedures, the after-shutdown dose from the reactor was calculated for various reactor shield conditions. Calculations were also made of the contamination that could occur in the ART cell as a result of a leak in the fuel-pump expansion-chamber seal or in the fission-gas purge line.

Four proposed disassembly methods – saw cutting, grinding, Heliarc-torch cutting, and shearing – were studied in order to determine the yields and sizes of the air-borne particles that would be produced. It was found that small piping and thin-walled sections can be sheared without producing air-borne particles. For larger sections, sawing with large blades and slow cutting speeds will be satisfactory.

In-pile loop No. 6 was removed from the MTR on September 15, after a very short operating period, because of pump malfunctioning and apparent breakage of a heat exchanger sniffer tube. Of the total operating time of 224 hr, only 70 hr was at full reactor power. The loop is to be sectioned and shipped to ORNL. Higher power densities and higher loop temperatures, of the order of 1600°F, are being considered in the planning of the future in-pile loop program. A higher capacity heat exchanger is being developed to handle the increased power, and an improved pump and pump purge system are being developed to ensure satisfactory operation of the loop at higher temperatures for more than one reactor cycle.

A radiation test of an operating ART reactor pump bearing housing is being planned. The test will serve to determine the adequacy of the present seal under radiation and to evaluate various lubricants for use in high flux regions. Gamma radiation will be satisfactory for this test, and a special gamma irradiation facility will be set up in the MTR canal.

In-pile tests of moderator materials are being programed. For the first test, four beryllium oxide cermets were inserted in a close-fitting Inconel capsule that was then installed on the forward end of an in-pile plug and inserted in the HB-3 beam hole of the MTR. Other materials to be tested are graphite and metal hydrides.

1.7. Advanced Reactor Design

Preliminary design work has continued on an advanced reactor based on the concept that the circulating fuel cools the moderator. The objective of the advanced design work is a reactor that is simpler than the ART and will operate at a higher temperature. Since the choice of materials and the optimum distribution of materials for a core-moderated, one-fluid reactor of the type being considered depend largely on heat deposition rates and thermal stresses in the core-moderator elements and in the reflector, a study was made of these factors. The reflector of the reactor being studied will serve the normal function of reducing the core size and critical mass, and, in addition, it will serve both as a part of the shield and as a neutron barrier to reduce activation in the heat exchanger.

Two reactor configurations are being studied. One is comprised of rods of a metal hydride placed in the core on uniform equilateral centers. A fused-salt fuel would circulate through the core. The rod diameter increases with radial distance from the center of the core in order to obtain a uniform power density in the fuel and to reduce the gamma-ray heating density near the core boundary so that relatively large-diameter rods can be used in the reflector.

The second configuration resembles the first, except that the reflector would consist of a thick

inner layer of copper surrounded by an outer layer of heavily poisoned hydride. Preliminary design specifications have been prepared for this configuration.

The principal materials that must be tested and evaluated for use in advanced reactors are beryllium oxide, several forms of high-density graphite, zirconium hydride, and yttrium hydride. It appears that, except perhaps for graphite, cladding will be required to isolate the moderator from the circulating fuel in order to minimize corrosion and to provide the strength needed to resist moderate fluid dynamic forces.

The effects of thermal stress and radiation on the moderator materials are to be investigated in in-pile tests. A beryllium oxide specimen has been irradiated and will be examined soon, and a second set of specimens is being prepared for irradiation. The thermal stresses and temperature gradients that would exist in zirconium hydride cylinders in an operating reactor were estimated. Differences in thermal expansion between zirconium hydride and two possible cladding materials, Inconel and molybdenum, indicate that it might be difficult to maintain a solid bond between the hydride and its cladding and that, if a bond did exist, the differences in thermal expansion might cause the can to buckle.

Some preliminary reactor calculations have been run on the computing facility at the Curtiss-Wright Corp. and on the Datatron at the Nuclear Development Corporation of America. The accuracy of the numerical values obtained in the Curtiss-Wright calculations is in doubt because the high-energy cross-section data used were not correct. Comparisons of the code data used for zirconium and yttrium hydride with other computed and experimental data are presented.

2.1. Phase Equilibrium Studies

A study of the system NaF-RbF-UF_4 was completed, and the boundary curves, compatibility triangles, and isotherm characteristics of the system are illustrated. The eutectic and peritectic compositions and their temperatures are listed.

A new furnace was constructed and used for visual observation of fused salts in the system RbF-CaF_2. With the new furnace a temperature of 1200°C can be obtained; the upper temperature limit of the furnace used previously was about 850°C. It was found that $RbCaF_3$ melts congruently at 1110 ± 10°C and that the eutectic between $RbCaF_3$ and CaF_2 melts at about 1090°C.

The equilibrium relations in the solid solution $7NaF{\cdot}6ZrF_4$-$7NaF{\cdot}6UF_4$ were established, and a phase diagram is presented. Quenching studies of the system RbF-BeF_2 were completed, and a phase diagram was prepared on the basis of thermal analysis data previously obtained and the quenching data. Studies of the NaF-RbF-BeF_2-UF_4 systems revealed mixtures with liquidus temperatures and UF_4 concentrations of interest as aircraft reactor fuels. The vapor pressures for these mixtures are not yet available, but they are expected to be much lower than those of the ZrF_4-base fuels.

Additional data for the system KF-BeF_2 are presented, and a thermal analysis investigation of the CsF-BeF_2 system was completed. A tentative phase diagram of the system $NaCl$-$ZrCl_4$ is presented that is based on thermal analysis data and petrographic examination of fused salts.

Tests were performed which indicate that fused salts shown by petrographic examination to be oxide free contain less than 0.1% oxyfluoride compounds. It is concluded that, in cases where such oxide-free fuel has been used and trouble has developed because of precipitation of oxides, the trouble must have been the consequence of improper cleaning of the equipment, exposure of the fused salt to atmospheric contamination, or other mishandling of the system or the fused salt after the petrographic examination.

2.2. Chemical Reactions in Molten Salts

Refinements of the experimental techniques used in the investigation of the equilibrium reduction of NiF_2 by H_2 in NaF-ZrF_4 have resulted in data for concentration constants that are about 30% lower than the average of the results published previously. The new data correlate very satisfactorily with changes of temperature.

The studies of solubility and stability of structural metal fluorides in fluoride mixtures were extended to include investigations of CrF_2, FeF_2, and NiF_2 in RbF-ZrF_4 (60-40 mole %) at 600 and 800°C. Also the studies of the reduction of UF_4 by chromium that have been carried out in various fluoride mixtures were extended to include the reaction medium RbF-ZrF_4 (60-40 mole %) and LiF-BeF_2 (48-52 mole %).

The solubility of BaF_2 in molten $NaF-ZrF_4$ (50-50 mole %) was found to be sufficiently high to assure that there would be no deposition of fission-product barium in a practical circulating-fuel reactor system. The possibility of the formation of much less soluble complex compounds of BaF_2 with other fission-product fluorides is being investigated. A systematic investigation of the solubilities of LaF_3 and CeF_3 in fluoride fuels was continued with the use of radioactive cerium and lanthanum and other radioactive tracers. The solubility of CeF_3 in $NaF-ZrF_4-UF_4$ was shown to be low and to be independent of the quantity added, and it was demonstrated conclusively that CeF_3 crystallizes from such melts as the simple fluoride. It was found that the solubility of LaF_3 (and presumably of all the rare-earth fluorides) is very high in $NaF-KF-LiF-UF_4$. In $NaF-ZrF_4-UF_4$, the solubility of LaF_3 is low and independent of the quantity added, and, as in the case of CeF_3, the saturating phase is the simple trifluoride.

The similarity in the solubility of CeF_3 and of LaF_3 in $NaF-ZrF_4-UF_4$ (50-46-4 mole %) and the observation that CeF_3 and LaF_3 apparently form a continuous series of solid solutions prompted experiments to determine the possibility of removing fission-product rare-earth fluorides from a contaminated $NaF-ZrF_4-UF_4$ mixture to any desired degree by repeated additions of CeF_3, for example. Experiments have conclusively demonstrated that the concentration of labeled CeF_3 in $NaF-ZrF_4-UF_4$ solution can be effectively lowered by the addition of LaF_3.

A new experimental system was set up for studying the solubilities of gases (in particular, xenon) in molten salts. Preliminary calibration tests with helium show good correlation of the results.

Experiments were performed which demonstrated that NiF_2 is a necessary intermediate in the mass transfer of nickel in molten $NaF-ZrF_4$ (53-47 mole %) in a nickel container. The mass transfer mechanism may be explained by the postulation of a subfluoride which forms in the cooler regions and disproportionates in the hotter regions. It is realized, of course, that there are a number of alternate explanations that may be just as plausible.

Observations have been made of the colors displayed by various fused fluoride salts in the half cells used for emf measurements. The results of this survey indicate that the prospects for a spectrophotometric study of the corrosion reaction participants are promising.

Work on the determination of the solubilities of metal fluorides in molten salts by measuring the emf's of appropriate cells was continued. Cells with CuF_2 in $NaF-ZrF_4$ (53-47 mole %) contained in copper crucibles with copper electrodes were investigated. The equation for the effect of temperature on the apparent solubility of CuF_2 in the fused salt was formulated.

Thermodynamic analyses were initiated of the effect of changes in composition of a fused salt mixture on the deviations from ideality of the melting points. Efforts are also being made to develop theories and models which will account for the thermodynamic behavior and to make correlations and predictions on the basis of these models and theories. This information will be useful in adjusting the composition of a fused salt mixture in order to obtain the optimized physical properties.

2.3. Physical Properties of Molten Materials

Measurements were made of the vapor pressures of the $NaF-ZrF_4$ system to check existing data and to examine some compositions for which species other than ZrF_4 must be present in the vapor. The existence of an azeotrope at 75 mole % NaF–25 mole % ZrF_4 was confirmed. Activities of ZrF_4 in $NaF-ZrF_4$ solutions were obtained at several temperatures.

The effect on ZrF_4 vapor pressure of the partial substitution of UF_4 for ZrF_4 in the $NaF-ZrF_4$ system was investigated. The substitution of UF_4 for ZrF_4 diminished the vapor pressure of the ZrF_4 in the salt mixture but was not nearly so effective as increasing the amount of alkali fluoride.

Measurements are being made of the activities of structural metal halides as a function of alkali cation size as an aid in predicting the extent of corrosion reactions in fused salts. The total vapor pressures in the $FeCl_2$-KCl and $FeCl_2$-LiCl systems were measured over the entire range of compositions, and the apparent heats of vaporization were calculated.

Additional measurements of the surface tensions of $NaF-ZrF_4$ (53-47 mole %) were made by the sessile-drop technique. Approximate values are

given for the surface tension of pure, liquid UF_4 that are based on a calculated density of 5.30 g/cm^3.

2.4. Production of Purified Fluoride Mixtures

Many small batches of pure structural metal fluorides were prepared for special studies, and rare-earth fluorides were prepared for use in fission-product removal studies. Requests for the mixture NaF-KF-LiF-UF_4 (11.2-41-45.3-2.5 mole %) have increased sharply, and 600 lb or more will be prepared per month. Investigations are being made to determine why many containers filled with this mixture rupture when the material is remelted after freezing.

Two copper-lined stainless steel reactors used in the production-scale facility failed recently because of faulty temperature controllers. In each case the temperature reached or exceeded the melting point of the copper, and therefore the stainless steel shell was attacked by the molten fluorides. An alarm system has been installed to preclude this type of failure.

In the preparation of the fuel solvent NaF-ZrF_4 for the Pratt & Whitney Aircraft high-temperature critical experiment it was found that the NaF used contained 3.5% water rather than the specified 0.05%. The solvent is being reprocessed to remove the oxides and oxyfluorides.

Satisfactory, good-quality $NaZrF_5$ was obtained from a commercial vendor. This material was of especial interest because the establishment of a reliable commercial source of raw material will be of great value in maintaining product quality. The 250-lb production facility started continuous operation on November 5 in order to fill projected requirements for fluoride mixtures in calendar year 1957.

Difficulties encountered in the conversion of low-hafnium $ZrCl_4$ to ZrF_4 were resolved, and 1850 lb of material was converted. In recent runs the dust loss was only about 3%. The indices of refraction of sodium monoxide and potassium monoxide were determined because of interest in identifying the oxides of NaK collected in cold traps in circulating NaK systems.

2.5. Compatibility of Materials at High Temperatures

Studies of the penetration of high-density graphite by molten fluorides were continued. Several special experimental samples exposed to NaF-ZrF_4-UF_4 at 800°C for 24 hr were found to be penetration resistant, and one sample (density, 2 g/cm^3) showed no penetration. Samples of APC graphite impregnated with NaF-ZrF_4 (53-47 mole %) were also tested. Impregnation alone reduced the penetration by a factor of 2, and an additional pretreatment that consisted of heating the impregnated material in vacuum reduced the diffusion still further.

A series of tests was made to investigate the rate of hydrogen diffusion through quartz at 800°C. The data obtained will be correlated with data obtained in a study of the NaOH-Ni reaction. In electrolysis experiments on the NaOH-Ni system, no mass transfer occurred when hydrogen was being bubbled through the melt, even when there was a temperature gradient across the system. However, when a helium atmosphere was used along with a temperature gradient of 100 to 150°C, nickel deposits were found on the cold (~600°C) cathode. After tests with carbon monoxide bubbling through the system, carbon was found to have deposited inside the crucible, and the NaOH melt contained Na_2CO_3.

Additional studies were made of the effect of hot NaK on elastomers. After tests under simulated valve operating conditions, G-E silicone 81576 showed promise as a valve seat material.

2.6. Analytical Chemistry

A method for the direct spectrophotometric determination of microgram amounts of lithium carbide in lithium was developed. Acetylene, which is formed when the lithium carbide is dissolved in water, is absorbed in a solution of silver perchlorate. The absorbance of this solution, which is measured at 297 and 313 mμ, is a function of the amount of lithium carbide present. The range of the method is from 10 to 200 ppm of carbon at 297 mμ and from 50 to 1100 ppm at 313 mμ. Nitrogen, as lithium nitride, can be determined in the same sample.

In connection with the determination of oxygen in metallic lithium by reaction of lithium with an ethereal solution of *n*-butyl iodide, it was found that lithium nitride reacted with the *n*-butyl iodide to form lithium iodide and nitrogen. These reaction products do not interfere with the proposed method for the determination of oxygen.

A small test facility was constructed to simulate a leak of NaK in a NaK-to-air radiator. In the apparatus NaK at a temperature of 1200°F was

injected at 1000 psi, through a small orifice, into a stream of room-temperature air which was moving at a velocity of 2400 lin ft/min. A concentration of alkali-metal oxides in air in excess of 2200 ppm was delivered to the scrubbers of the detector with less than 25% loss by deposition on the walls of the apparatus.

The use of the new reagent 4-isopropyl-1,2-cyclohexanedionedioxime was studied for the determination of nickel in solutions of alkali metals. .The nickel-dioxime complex is extractable with chloroform. With this reagent, nickel can be determined in concentrations of the order of 0.5 ppm. Another new reagent, pyrocatechol violet, was applied to the spectrophotometric determination of zirconium in sulfate solutions of fluoride salts.

Developmental work was completed on the spectrophotometric method for the determination of cerium in mixtures of fluoride salts. The interference of uranium, zirconium, and iron was effectively eliminated by extracting these three metals with trioctyl phosphine oxide.

Methods were studied for the preparation of radioactive, tagged fluoride salts for use as tracers in studies of equilibria at high temperatures. Cerium fluoride tagged with Ce^{141} and lanthanum fluoride tagged with La^{140} have been prepared.

The method for the determination of boron as the fluoride complex in mixtures of fluoride salts was extended to include the determination of metallic boron in such mixtures. The metallic boron is filtered after dissolution of the fluoride salt in $AlCl_3 \cdot HCl$ and then rendered soluble by fusion with sodium carbonate.

The compatibility of pump lubricants with molten alkali metals and fused fluoride salts was studied in a special apparatus in which small quantities of high-temperature (1100°F) molten metal or salt are dropped into a reservoir of lower-temperature (200°F) lubricant. Of the lubricants tested, only Cellulube was found to react, and it reacted only with sodium.

Studies were continued on the analytical application of trioctyl phosphine oxide (TOPO) as a reagent for the concentration, separation, and determination of components of ART fuels, corrosion products, and fission products. It was demonstrated that chromium can be concentrated by a factor of 100 by a single extraction from solutions of HCl or H_2SO_4.

3.1. Dynamic Corrosion Studies

Inconel forced-circulation loops were operated with the fuel mixture (No. 30) $NaF-ZrF_4-UF_4$ (50-46-4 mole %) to study the effects of flow rate, temperature drop, and operating time on corrosion of the Inconel. Loops operated for 1000 hr at various flow rates showed no significant differences in attack. Results of tests with temperature gradients of 145, 200, and 300°F indicated that a temperature gradient above 200°F noticeably increased the attack and that temperature gradients of below 200°F did not correspondingly reduce the attack. The comparison of corrosion results of the loops operated for various times under similar conditions showed a rapid increase in attack within the first 15 hr followed by a gradual increase in attack at a rate of 1 mil in 280 hr.

Inconel forced-circulation loops were also operated with sodium to study the effect of temperature drop on corrosion and mass transfer. A definite increase in the amount of mass transfer with increased temperature drop was found. There is an approximately linear relationship between temperature drop and weight of mass-transferred deposit. Similar loops operated with sodium to which magnesium chips had been added showed no difference in the amount of mass transfer as compared with the mass transfer in standard Inconel-sodium loops.

A zirconium hot-leg insert in a standard Inconel-sodium forced-circulation loop reduced the mass-transferred deposit slightly compared with the deposit in a standard Inconel-sodium loop. A titanium hot-leg insert had no apparent effect on mass transfer.

A forced-circulation loop constructed of Incoloy (34% Ni–20% Cr–bal Fe) was operated for 1000 hr with sodium at a maximum fluid temperature of 1500°F. The mass-transferred deposits and the maximum depth of attack were similar to those observed in Inconel loops. The deposits, however, in contrast to those in Inconel loops, did not adhere to the loop walls. Mass-transferred deposits were also found in a Hastelloy B loop operated for 1000 hr with sodium. The deposits were predominantly nickel and were similar in appearance to deposits found in Inconel-sodium loops.

A gas-fired heater coil constructed of Inconel was examined metallographically to determine the extent of corrosion during operation as a heater coil in an intermediate heat exchanger test stand.

The heater had been exposed to NaK at temperatures of 1200 to 1600°F for approximately 2700 hr, the exposure being in the temperature range of 1400 to 1500°F. Intergranular attack to a depth of 1.5 mils was found.

Several thermal-convection loops constructed from experimental nickel-molybdenum alloys were tested with the fuel mixture (No. 107) NaF-KF-LiF-UF_4 (11.2-41-45.3-2.5 mole %) at 1500°F. The hot-leg attack in these loops was relatively light, being 1 to 2 mils for 500 and 1000 hr of exposure to the fuel mixture. The fuel in loops fabricated from an alloy containing 2% aluminum showed a high aluminum pickup. Loops constructed of alloys in which the chromium content was varied from 3 to 10 wt % indicated similar depths of hot-leg attack, but the concentration of the attack was highest in the alloy containing 10% chromium. Also, an increase in the operating time from 500 to 1000 hr in a loop constructed of an alloy containing 5 wt % chromium did not increase the depth of attack, although again the concentration of the attack was increased. Nickel-molybdenum loops operated for 1000 hr with sodium at 1500°F revealed hot-leg attack to a depth of 1 mil and a small amount of mass transfer in the cold leg sections.

A series of Inconel thermal-convection loops was operated for 500 hr with special fluoride fuel mixtures at 1500°F. Results from the loops operated with LiF-ZrF_4-UF_4 (50-46-4 mole %) indicate greater depths of attack than those found with related alkali-metal fluoride systems. Loops operated with NaF-ZrF_4-UF_4 (58-32-10 mole %) showed the same type and amount of attack as that found with a similar fuel mixture containing only 5 mole % UF_4, that is, NaF-ZrF_4-UF_4 (60-35-5 mole %).

3.2. General Corrosion Studies

Fusion welds on recrystallized tube-to-header joints were found to have good corrosion resistance to NaK (56-44 wt %) and to the fuel mixture NaF-ZrF_4-UF_4 (50-46-4 mole %) when tested in seesaw apparatus at a hot-zone temperature of 1500°F for 100 hr. These specimens, supplied by the Glenn L. Martin Co., had an additional fusion weld on the tube-to-header joints fabricated by the standard "flange-during-welding" method.

Metallographic results indicate that boron is leached from Coast Metals brazing alloy No. 52 (89% Ni–5% Si–4% B–2% Fe) to a depth of 4 mils in 1000 hr by NaF-ZrF_4-UF_4 (53.5-40-6.5 mole %) at 1500°F in seesaw apparatus. This depth of leaching is approximately the same as that found previously after similar tests of 500-hr duration. In all the tests with Coast Metals brazing alloys Nos. 52 and 53, both containing 4 wt % boron, the depth of depletion of boron increased as the test temperature was increased and became more severe when the exposure time was increased from 100 to 500 hr. In another test in which the surface area-to-volume ratio proposed for the ART was used, the larger amount of test fluid did not affect the depth of boron depletion.

A special nickel-molybdenum (17% Mo–3% Cr–0.075% C–bal Ni) alloy specimen exposed in seesaw apparatus to NaF-KF-LiF-UF_4 (11.2-41-45.3-2.5 mole %) for 1000 hr at a hot-zone temperature of 1600°F showed a weight loss of 0.13%. After the test the fuel mixture was found to contain 0.1% Mo, 0.089% Ni, and 0.12% Cr. A specimen of the same material was attacked to a depth of 1 mil in a thermal-convection loop, and therefore it was concluded that the seesaw apparatus cannot be used for screening tests of nickel-molybdenum alloys.

Tests were performed in seesaw apparatus to determine whether graphite in an Inconel–NaF-ZrF_4-UF_4 (50-46-4 mole %) system at 1500°F would "tie up" the chromium in the Inconel as carbides and thus affect the depth of corrosion attack. The test results indicated that the graphite had no effect on the depth of corrosion of the Inconel and that the graphite was not attacked by the fused salt.

Nickel and Inconel capsules were exposed to NaCl-$MgCl_2$-UCl_3 (50-33.3-16.7 mole %) in seesaw apparatus at a hot-zone temperature of 1800°F for 100 hr. Both capsules had mass-transferred crystals after the test, with the nickel capsule having the greater amount. After 500-hr tests at a hot-zone temperature of 1350°F, both nickel and Inconel revealed slight attack to a depth of 0.5 mil, and there was no mass transfer of the nickel capsule. A slight deposit of metallic crystals was found in the cold zone of the Inconel capsule.

Four rare-earth oxide samples fabricated in the shapes to be used for the ART control rod were tested in molten sodium for 500-, 1000-, 2000-, and 3000-hr periods. These specimens had average densities of 4.10 g/cm^3 and apparent porosities of 46.3%. Chemical analysis of a sodium sample

taken from the bottom of the test capsule used for the 2000-hr test showed a total of 129 ppm of rare earths in the alcohol insoluble residue. The other samples from the 2000-hr test and the samples from the 500- and 1000-hr tests showed no rare earths. The samples from the 3000-hr test have not yet been analyzed.

A compatibility test has been conducted on Inconel staples inserted in Inconel sleeves in beryllium blocks and immersed in sodium for 1000 hr. The temperature was cycled between 1300 and 500°F ten times during this test. Examination revealed 25 mils of intermetallic compound formation near the bottom of the Inconel sleeve. It is therefore thought that in the ART the unalloyed Inconel near the surface will act as a barrier to prevent the brittle compound from spalling into the sodium stream.

An Inconel-sodium thermal-convection loop with a zirconium sleeve inserted in the hot leg was operated for 1000 hr at a hot-leg temperature of 1500°F. Although the oxygen content of the sodium was reduced by the formation of zirconium oxide, no change in the usual sodium attack on the Inconel could be observed.

Since a lithium-rich phase in a lithium-sodium mixture might alter the corrosion resistance of nickel-base alloys to such a mixture, an Inconel thermal-convection loop was operated with NaK containing 5 wt % Li for 1000 hr at a hot-leg temperature of 1050°F. The lithium-rich phase would not be present at higher temperatures. No mass transfer was found in any section of the loop, and it is concluded that if a lithium-rich phase developed it did not affect the corrosion resistance of the Inconel. The effect of larger additions of lithium is to be studied.

Molybdenum and zirconium capsules were exposed to sodium and to lithium in seesaw apparatus for 100 hr at hot-zone temperatures of 1535°F. No evidence of attack by either sodium or lithium was found.

A preliminary investigation of the corrosion resistance of molybdenum and Hastelloy B to rubidium in a dynamic system was completed. No mass transfer occurred in either the molybdenum-rubidium or the Hastelloy B–rubidium systems. No attack occurred in a molybdenum capsule exposed to rubidium for 500 hr in seesaw apparatus at a hot-zone temperature of 1900°F, while a Hastelloy B capsule exposed for 500 hr at 1600°F was attacked to a depth of 1 mil. Hastelloy B–rubidium standpipe tests showed attack of the Hastelloy B after 500 hr at 1400°F of 1.5 mil and after 500 hr at 1500°F of 2 mils.

A lead-lithium alloy containing 0.7-wt % Li is being investigated for possible use as a neutron and gamma-ray shielding material. The alloy containing 0.7 wt % Li was found to have far better mechanical properties than those of pure lead and the lead–0.06% copper alloy being considered for ART shielding applications.

3.3. Fabrication Research

In the development of nickel-molybdenum alloys, a system of evaluation has become necessary. Optimum criteria for the acceptability of an alloy in terms of oxidation resistance, creep strength and rupture life, corrosion resistance, fabricability, joining characteristics, aging characteristics, and nuclear properties have therefore been established. A review of the data compiled to date on experimental alloys has indicated that many of the new alloys being investigated are quite adequate in some respects. Many compositions can be fabricated without difficulty; they possess sufficient oxidation and corrosion resistance; and they are not susceptible to aging.

The effects of carbon and chromium additions to the experimental alloys are sufficiently well known to permit generalizations. The addition of carbon in excess of the amount required for deoxidation seriously reduces the fabricability of an alloy in the tube-reducing operation and also reduces the ductility. Chromium is a dominant factor in determining the oxidation rate and the corrosion resistance of an alloy, and data have been obtained which show that the minimum chromium content for oxidation resistance may be about 7%.

Tubing from four special alloys extruded for Battelle Memorial Institute has been received. Reduction of the tube blanks was only partly successful in that longitudinal cracks developed in the tube walls. Again it was noted that failures occurred only in alloys with high carbon content. Sixteen additional extrusions were prepared from four other alloys selected by Battelle Memorial Institute for studies of fabricability, ductility, strength, and weldability. Sufficient tubing is being prepared from a 17% Mo–10% Cr–7% Fe–bal Ni alloy for fabrication of a forced-circulation loop for a more severe test of this

promising chromium-bearing alloy than can be obtained with a thermal-convection loop.

Welding wire and stress-rupture specimens have been prepared from laboratory melts of the INOR compositions for preliminary evaluation prior to completion of a commercial order for these alloys. An inventory of the material recovery from the commercial-size INOR alloy heats has been received, and a request has been forwarded for the fabrication of the recovered material into tubing, plate, sheet, wire, and rod. Fabrication of rods from some of these alloys is complete, and the stock has been delivered to the New England Materials Testing Laboratory and to Rensselaer Polytechnic Institute for stress-rupture and weldability studies.

A contract proposal for the preparation of large heats of two additional alloys has been received and reviewed. This contract is to include the forging of extrusion billets for processing at the International Nickel Company and the preparation of plate, wire, and rod on a commercial scale.

The shield plugs for the ART pumps are being fabricated. The thin copper-B_4C neutron shield plate is being prepared by hot rolling, and the zirconia thermal shields have been fabricated and finished by grinding to size. The high-density gamma-ray portions of the plugs, which consist of tungsten carbide and Hastelloy C, are being prepared by hot pressing in a large furnace.

Four batches of copper-B_4C cermets roll-clad with type 430 stainless steel that were prepared by the Allegheny Ludlum Steel Corp. were evaluated for distribution of the B_4C, bend radius, tensile strength and ductility, and thickness. All batches were found to be acceptable except for variations in thickness.

A 14-in.-OD, 1.5-in.-wide ring of stainless-steel-clad copper-B_4C cermet was prepared for use in the Pratt & Whitney Aircraft high-temperature critical experiment. A similar 19-in.-OD ring is being fabricated.

The strength of the 30% Lindsay oxide–70% nickel control rod material was determined at 1500°F for various particle sizes of oxide. None of the samples showed ductility, primarily because of stringering and agglomeration of the oxide particles. Several 3-ply extrusions of the Lindsay oxide–nickel control rod with Inconel cladding were made. In all cases the core of the extruded rod cracked during cooling because of thermal stresses and lack of ductility.

Techniques are being developed for the grain refinement by recrystallization of as-received coarse-grained niobium that was arc-melted at Battelle Memorial Institute. Evaluation of the material will be based on its properties after recrystallization.

Several plates of Nb-UO_2 compacts clad with niobium were prepared by roll cladding. An attempt to extrude a billet with a core of 60% Nb–40% UO_2 was unsuccessful, however. The Nb-UO_2 core was not reduced appreciably.

Fabricability and tensile properties of an 80% Nb–20% U alloy were investigated. Attempts to selectively oxidize the uranium in the alloy were partly successful.

A high-temperature controlled-atmosphere tensile rig is being modified to accommodate small specimens for use in the testing of hydride moderators. A retort is also being constructed for the preparation of yttrium metal by calcium reduction.

3.4. Welding and Brazing Investigations

A detailed investigation is being made of the weldability and brazability of commercial and experimental nickel-molybdenum alloys. Preliminary data on the mechanical properties of Hastelloy B joints indicate that as-welded joints fail in the weld metal, with good ductility, when tested at room temperature and in the base metal, with reduced ductility, when tested at 1500°F. Hardness measurements were made on Hastelloy B plate welded with Hastelloy B filler metal and aged at various temperatures. Aging at 1300°F produced the highest hardness values. Nickel-molybdenum alloys of various compositions are being fabricated into thermal-convection loops in order to study the effect of corrosion on the weld zones. The brazing characteristics of the nickel-molybdenum alloys are also being studied in order to determine whether these alloys can be used in heat exchanger and radiator applications. Some results have been obtained in tests of the flowability of Coast Metals brazing alloy No. 52 on the various alloys.

An extensive investigation was made of the effect of temperature rate of rise on brazing because of difficulties encountered at the York Corp. in attempts to braze stainless-steel-clad high-conductivity-fin NaK-to-air radiators. When brought to brazing temperature in the York furnace at a maximum rate of rise from room temperature of approximately 100°F/hr, the brazing alloy rings

retained their original shape and therefore did not provide a satisfactory tube-to-fin joint. Experiments indicate that a minimum heating rate of 300° F/hr should be used.

The effect of the fin material on the flow of the brazing alloy was also studied. Stainless-steel-clad fins were readily wet by the brazing alloy, whereas the brazing alloy rings melted completely on Inconel-clad fins and adequate adherence and fin-collar protection were achieved. In further experiments it was found that stainless-steel-clad fin-to-tube joints brazed in a dry-helium atmosphere showed excellent braze adherence and fin-collar protection, in contrast to the results being obtained by brazing in a hydrogen atmosphere.

The coefficients of thermal expansion of several high-temperature brazing alloys were determined in the range from room temperature to 900°C. The curve for Coast Metals brazing alloy No. 52 was found to be nearly linear over the temperature range investigated, and the curve obtained for a second heating and cooling cycle was slightly lower.

Studies of the effects of various stress-relief heat treatments on grain growth in Inconel tubing were initiated. No oxide films were noted after any of the stress-relief treatments. Heating to the brazing temperature of 1922° F caused significant grain growth on the exterior wall, but the interior wall of the tube retained its fine-grained structure. Further study of the effects of temperature, time at temperature, and type of atmosphere is under way.

Experiments were conducted in order to determine the properties of welded joints of the boron-containing stainless steel being considered for shielding. The welded joints of type 304 stainless steel containing 1% boron were brittle and clearly indicated that this material should not be used for load-carrying components.

A 500-kw high-conductivity-fin NaK-to-air radiator, designated York HCF Radiator No. 9, was examined after test service for 1283 hr in the temperature range of 1000 to 1600° F, including 695 hr of service with a temperature drop across the system. No cracks were found in tube-to-sump plate joint areas and no evidence of incipient cracking was noted.

Developmental work on the fabrication of valve components was continued. Techniques have been developed for attaching the following materials to Inconel: nickel-bonded cermets, tungsten carbide–nickel cermets, copper, molybdenum, tungsten, and Thermenol. Techniques are being developed for attaching cobalt-bonded cermets.

3.5. Mechanical Property Studies

The effect of section thickness on the creep-rupture properties of Inconel in the fuel mixture (No. 30) $NaF-ZrF_4-UF_4$ (50-46-4 mole %) at 1500° F is being studied experimentally. Data have been obtained which show that the strength and ductility of Inconel in sections less than 0.060 in. thick is very dependent upon the specimen thickness, being lower for the thinner sections, but for sections more than 0.060 in. thick the strength is not so sensitive to section thickness. Further, the strength properties of the thinner sheet are somewhat less sensitive to stress and more sensitive to time in the fuel than are the strength properties of the thicker sheet material.

Data have also been obtained which indicate that the creep-rupture strength of Inconel at 1500° F in fuel No. 30 is decreased by previous cold working, whereas the corrosion resistance of Inconel to fuel No. 30 at the same temperature is unaffected by previous cold working. The reduction in strength is attributed to recrystallization during the test.

Experimental investigations are being made to determine the effect of strain cycling on the properties of Inconel. Equipment which may be used to strain-cycle a specimen at elevated temperatures in controlled environments was developed and constructed. In the initial test, as-received fine-grained Inconel was cycled to failure in an argon environment at 1500°F with a total strain per full cycle of 1% and a plastic strain per full cycle of 0.12%. The cycle rate per full cycle was 80 sec. The number of cycles to failure was 3390 and the time to failure was 77 hr. The failure was intergranular, and metallographic examination disclosed no cracks in the gage length other than the single crack which propagated to failure. No grain growth or recrystallization appeared to have occurred during testing.

Creep-rupture testing of the various experimental nickel-molybdenum alloys now available is under way. The results of some tests with an argon environment and some tests with the fuel mixture (No. 107) $NaF-KF-LiF-UF_4$ (11.2-41-45.3-2.5 mole %) are reported. The strengths of some of these alloys at 1500° F in fuel No. 107 have been shown to be adequate for reactor application,

but further testing will be required to establish the optimum composition for high-temperature strength and corrosion resistance.

3.6. Ceramics Research

Equipment for the hydriding of yttrium and zirconium metals is being assembled. With this system it will be possible to heat 4 × 12 in. billets up to 2300°F in an atmosphere of purified hydrogen at constant pressures.

Several beryllium-containing materials were prepared for evaluation as moderating material. A Be_2C-SiC cermet was made that may be more oxidation resistant than Be_2C alone. A large hot-pressed block of beryllium oxide fabricated in France was received for sampling and testing. Also, specimens of beryllium oxide were hot-pressed for testing in the MTR.

Sufficient rings of 70% Ni–30% rare-earth oxide were prepared for the Pratt & Whitney Aircraft high-temperature critical experiment. Studies are being made of methods for fabricating rare-earth oxide hemispheres to be used for cross-section measurements.

3.7. Nondestructive Testing and Inspection of Materials and Components

An instrument is being developed for the inspection of small-diameter tubing which offers the advantages of both impedance analysis and variable frequency. The device has the high sensitivity of the cyclograph and may be operated over a range of frequencies from about 15 to 600 kc. Directly coupled signals are obtained both from the resistance and the reactance changes in the impedance of the coil.

An evaluation of the available penetrant methods for the inspection of tubing resulted in the replacement of dye-penetrant techniques with the postemulsification fluorescent-penetrant method known as "Zyglo." Radiographic inspection techniques have been developed whereby flaws of less than 2% of the wall thickness can be located.

An attempt to correlate the types of defects being found in tubing with the methods used to find them has resulted in the establishment of categories of defects. Sizes of defects are still being investigated.

Materials for ETU, ART, and test components are being routinely inspected with their intended uses as the criteria for acceptability. Tubing and pipe inspection methods have been standardized, but developmental work on plate and sheet inspection methods has not yet been completed.

4.1. Heat Transfer and Physical Properties

The fluid friction characteristics of the fuel side of a 260-tube full-scale model of the present ART fuel-to-NaK heat exchanger were obtained. The data obtained fall 9% below those for a similar 100-tube model. The over-all heat transfer performance of a new compact heat exchanger having a delta-array tube spacing was experimentally determined to be superior to the performance of a square-array heat exchanger having the same hydraulic diameter, the same number of tubes, and the same spacer density.

Additional research was conducted on the technique of stabilizing flow in reactor cores by using screen packing. The phosphorescent-particle technique, which was used previously to observe visually instantaneous fluid-flow phenomena in transparent ducts, was converted to a quantitative method; the velocity profiles are now being recorded photographically.

A mathematical analysis of the temperature structure within the fuel, Inconel core shells, and sodium coolant streams of an idealized ART core was carried out; sodium flow rates and cooling requirements were also established. A conceptual design for a new core configuration for a reflector-moderated circulating-fuel reactor was developed. The core is composed of a cluster of circular pipes, and the axial velocity structures in the fluid flowing in the pipes are controlled so that nearly uniform radial fuel temperature distributions are obtained.

Further research on the influence of thermal cycling on the strength and corrosion characteristics of Inconel in a fluoride fuel environment was conducted. Deeper subsurface void formation than was expected was observed in Inconel test sections under both low- and high-frequency cycling.

The enthalpies and heat capacities of three salts were measured: ZrF_4, $NaNO_2$-KNO_3-$NaNO_3$ (40-53-7 mole %), and NaCl-LiCl (28-72 mole %). Viscosity determinations were made for the molten chloride eutectic KCl-LiCl (41.2-58.8 mole %); the viscosities ranged from 5.4 centipoises at 375°C to 1.8 centipoises at 600°C. A preliminary thermal conductivity value of 1.5 Btu/hr·ft^2(°F/ft) was obtained for NaF-ZrF_4-UF_4 (56-39-5 mole %). A study was initiated to investigate the effect of

subsurface voids formed by corrosion on the effective thermal conductivities of metal walls.

4.2. Radiation Damage

Examination of the remaining portion of in-pile loop No. 3, the impeller, was completed. No evidence of attack on the impeller was found by metallographic examination. In-pile loop No. 4, operated under conditions similar to those used for loop No. 3, was disassembled and partly examined. The only difference from the loop No. 3 results that has been observed in the examination of loop No. 4 is that the attack in the hot zones was 1.5 mils as compared with 3 mils in loop No. 3. The cold zones of both loops showed less than 1 mil of attack. It has been noted that the original grain size of the tubing used for loop No. 3 was larger than the grain size of the tubing used for loop No. 4.

In an attempt to determine the causes of the difficulties encountered in etching Inconel samples for metallographic analysis, the rates of attack of chromic, oxalic, and sulfuric acids on Inconel surfaces prepared by various methods are being studied. Variations in attack associated with the prior history of the Inconel appear to occur, but no final conclusions can be drawn until more data are collected.

Tube-burst experiments were continued in the LITR with specimens of carefully inspected Inconel tubing of the type to be used for ART radiator fabrication. The three inspected specimens that have been in the LITR in a helium atmosphere at a stress of 2000 psi and a temperature of 1500°F for more than 1000 hr have not yet ruptured. These specimens indicate a stress-rupture life that is considerably in excess of the 260-hr arithmetic-mean rupture life reported previously for substandard tubing tested under the same conditions.

The effect of temperature on the electrical resistivity of Inconel was studied to obtain data needed in the design of electromagnetic flowmeters. A resistivity maximum was observed at approximately 900°F, and holding the specimen in the temperature range of 600 to 900°F resulted in a maximum resistivity increase of about 2% in a 24-hr period. Above 900°F, the resistivity was not dependent on time or on rates of heating or cooling.

The modified pump for circulating fused-salt fuel in the LITR vertical in-pile loop has operated satisfactorily for over 1700 hr in a bench test of a loop mockup. The successful operation of this pump indicates that there has been no significant condensation of ZrF_4 in critical areas. Loop No. 8, which will include a pump of the modified design, is now being assembled for operation in the LITR.

Irradiations of Inconel capsules filled with fused-salt fuel mixtures were continued, and three irradiated and four control capsules that had been tested at approximately 1500°F for 200 to 900 hr were opened and examined. The four control capsules and one irradiated capsule that had normal test histories showed attack to a depth of 1 mil or less. The irradiated capsule which had a temperature excursion to 1600°F that lasted for 5 min, in addition to other unusual short temperature excursions, was found to have been attacked to a depth of 4 mils. The other irradiated capsule was attacked to a depth of 8 mils, but this result must be discounted because the capsule was bent during specimen preparation. Two Hastelloy B capsules filled with the fuel mixture $NaF\text{-}KF\text{-}LiF\text{-}UF_4$ were prepared for irradiation in the MTR.

The sampling techniques and the methods used for chemical analysis of radioactive and nonradioactive samples of fused salt fuel mixtures are being investigated in order to improve the reproducibility of the determinations. It has been established that radiation causes the analysis for chromium by the diphenylcarbazide method to be significantly low.

The neutron flux of hole 51 of the ORNL Graphite Reactor was measured both in and out of the donut with boron-covered Pu^{239}, Np^{237}, and U^{238} detectors. These detectors measure the flux greater than about 1 kev, 600 kev, and 1.5 Mev, respectively. The n-to-p transition in n-type germanium was also measured in the two positions and correlated with the flux greater than 600 kev.

Equipment for studying hole lifetime in n-type bulk material was designed and constructed. Preliminary measurements show that the lifetime of injected holes is extremely sensitive to neutron irradiation. An exposure of 10^{10} nvt decreased the lifetime of holes in one sample from 1010 μsec to 404 μsec. A subsequent exposure of 10^{10} nvt also reduced the lifetime by a factor of 2.

The continued studies of electric field effects on annealing rates of irradiated 1N 38-A rectifiers have led to contradictory data. Further investigations will be required, with emphasis on differentiation between surface and bulk effects.

Junction germanium power rectifiers have been exposed to reactor irradiation. The changes observed were qualitatively the same as those observed in point-contact rectifiers. The rectification of the unit was not completely destroyed after 2×10^{17} nvt.

Metallographic examinations were made of irradiated samples of the stainless-steel-clad CaB_6-Fe and BN-Ni cermets being considered for use as thermal-neutron shielding. Measurements show a slight increase in hardness of the irradiated CaB_6-Fe specimens. The BN-Ni samples retained dimensional stability and continuity of the core-to-cladding interface; however, an increase in hardness of both the core and the cladding was observed. Additional B_4C-Cu cermet samples were prepared for irradiation in the MTR.

As part of the study of chemical and physical changes induced in polymeric materials by radiation, infrared spectral measurements were continued on irradiated specimens after protracted exposure to air. Measurements were also begun to obtain quantitative absorption coefficients from the earlier spectral data. Molecular weights of stocks of commercial polystyrene and polymethyl methacrylate were determined by viscosity measurements. Samples of these materials were separated into various molecular-weight fractions by a precipitation technique. Specimens of these molecular-weight fractions have been prepared for irradiation, and specimens of unfractionated material have been irradiated to establish the doses suitable for viscometry samples. Low pressure (linear) and ordinary polyethylene samples have been irradiated to study the influence of molecular shape on radiation effects. Engineering evaluation tests have been carried out on several materials being considered for gasket applications and on impregnated-asbestos sheets for electrical usage.

4.3. Fuel Recovery and Reprocessing

All major equipment for initial runs in the fused salt–fluoride volatility pilot plant is installed and is being tested. In further process development work, Hanford-irradiated uranium, 600 Mwd/ton, was processed by the fused salt–fluoride volatility process. Gross fission-product decontamination factors of greater than 10^6 and uranium losses of 0.2% were obtained on a laboratory scale. There was a tendency for ruthenium and niobium activity to break through the NaF beds with the UF_6 product upon repeated re-use of the NaF. Uranium which was inadvertently fixed on the NaF in one run as U(V) was successfully recovered by raising the bed temperatures while sweeping fluorine through the beds. With the exception of the ruthenium and niobium break-through upon repeated re-use of the NaF bed, which will require further chemical study, the process exceeded expectations in all respects in these high-activity-level tests.

5.1. Lid Tank Shielding Facility

Experiments at the Lid Tank Shielding Facility (LTSF) are performed in a large tank of water in which shield mockups are placed adjacent to a fission source and measurements of the intensity of radiation are made beyond the mockup. The LTSF fission source consists of a "plate" containing U^{235} which absorbs thermal neutrons that issue from a hole in the ORNL Graphite Reactor shield. In September, 1955, a new source plate (SP-2) that has several advantages over the old one (SP-1) was installed. The average source strength of SP-2 has been determined to be 1.62×10^{11} (fissions/sec) $\pm$ 5%. This can be interpreted as 5.18 ± 0.26 w of power based on the assumption of an average reactor energy dissipation of 200 Mev/fission. Since the installation of the new source plate, measurements of the thermal-neutron flux and the gamma-ray and fast-neutron dose rates in plain water have been made at various distances from the source plate. Plots of the results are presented.

Several calculations of the attenuation kernel for the fast-neutron dose rate from a point, isotropic, fission source in water have been performed. One such calculation, which was based on LTSF experiments in which the old source plate (SP-1) was used, did not agree with a calculation performed later with the "moments" method. At the time, the discrepancy could not be resolved, but the installation of the new source plate (SP-2) has allowed some differences to be explained. A new calculation based entirely on experimental data obtained with SP-2 has resulted in agreement with the moments-method calculation.

The latest tests in the new series of experiments on advanced shielding materials have included mockups containing stainless steel and tungsten as the gamma-ray shield. Thermal-neutron flux, gamma-ray dose rate, and fast-neutron dose rate measurements beyond these mockups are presented. In addition, fast-neutron dose rate measurements

for most of the configurations tested earlier in the series are presented. Each mockup in the series consisted of a beryllium moderator region followed by a gamma-ray shield, which was varied, and a lithium hydride and oil neutron shield. In addition to the stainless steel and tungsten, zirconium, lead, and depleted uranium were used for the gamma-ray shield.

5.2. Bulk Shielding Facility

In order to obtain some information as to how the substitution of stainless steel for aluminum in the fuel elements of the BSF reactor would affect the gamma-ray flux spectrum at the surface of the core, a calculation of the flux at the surface of a reactor containing UO_2–stainless steel fuel elements was performed. In order to check the method used, a parallel calculation was performed for the BSF reactor containing uranium-aluminum fuel elements, and the results were compared with existing experimental data. The general shape of a plot of the calculated results corresponds with the plot of the experimental results, although the magnitudes of the two curves were not in complete agreement. The disagreement is not yet explained. The calculation does show that the substitution of stainless steel for aluminum will increase the relative amount of the high-energy flux at the surface of the reactor.

Measurements have been made of the energy and angle spectra of the photon energy flux resulting from 1.17- and 1.33-Mev gamma rays from a point source after diffusion in an infinite water medium. The two sources used had strengths of 100 curies and 195 mc, respectively. Spectral measurements were made with a Compton spectrometer having a peak-to-total ratio of 0.7 and a resolution of 14% (full width of half maximum) for 1.12-Mev photons. The resulting energy and angle spectra of the energy flux are compared, after integration over the solid angle, with calculated results which have been obtained by the "moments" method.

Provisions have been made at the ART facility for a limited number of gamma-ray and fast-neutron dose rate and spectral measurements. Most of these measurements will be made within five collimator tubes which will extend radially from the shield in its horizontal midplane. In addition, dose rate measurements will be made in a region at the north head of the reactor. The design for the collimator tubes has been completed.

5.3. The Tower Shield Reactor II

A change in the concept of the utility of the new reactor being designed for the Tower Shielding Facility has brought about revisions of the design that will provide a facility for general use rather than a mockup of a specific reactor. A spherical arrangement of light-water-cooled and -moderated MTR-type fuel plates was chosen for the reactor. The reactor will be controlled by boron-loaded umbrella-shaped grids that will be located in a spherical water volume enclosed by the core so as to cause a minimum perturbation of the leakage flux. The mechanical design and nuclear calculations are in progress, and a few development experiments have been performed.

Part 1

AIRCRAFT REACTOR ENGINEERING

S. J. Cromer

1.1. AIRCRAFT REACTOR TEST DESIGN

A. P. Fraas

STATUS OF ART DESIGN

The detailed analytical study of the temperature and stress distributions throughout the reactor was continued, and design modifications indicated by the study were made. Many detail design changes have been requested by the procurement staff to facilitate fabrication. These requests have been studied, and the desired changes have been made if they would not have a substantially adverse effect on the integrity of the system. Contamination of the fuel pump lube oil by fission products was studied carefully in the light of new data, and the acceptability of the ART lube oil system was established. Heat-exchanger and radiator-component test experience was carefully examined to determine its significance and implications.

APPLIED MECHANICS AND STRESS ANALYSIS

R. V. Meghreblian

Creep Buckling of Shells with Double Curvature

It was pointed out in a previous report[1] that the various shells within the reactor will be exposed to pressure differentials which can cause creep buckling. The three most critical shells from this standpoint are the island core shell (I), the outer core shell (II), and the reflector shell (IV). The core shells are to be fabricated from $\frac{1}{8}$-in.-thick Inconel sheet, and the reflector shell is to be fabricated from $\frac{1}{16}$-in.-thick Inconel sheet. The general proportions and the locations of these shells are shown in Fig. 1.1.1. There are at present two separate experimental programs under way in which the buckling characteristics of these shells are being studied. One of these programs is concerned with the buckling of the core shells. Although some preliminary information is available on the properties of these shells, most of the data were obtained from low-temperature tests on full-size lead shells and tubes.[2] In the test program presently under way both full-size shells and $\frac{1}{4}$-scale models of half-shells made from Inconel will be used. These tests are being conducted at reactor operating temperatures of 1200 to 1600°F. The first of the tests was carried out on the $\frac{1}{4}$-scale model of one-half of shell II that was used in the power cycling experiment.[3] For this test the two ends of the shell were capped off with heavy plates, and the shell was exposed to an external atmosphere of argon at 52 psi at 1500°F. Failure occurred after

[1] A. P. Fraas and A. W. Savolainen, *Design Report on the Aircraft Reactor Test*, ORNL-2095, p 57 (Dec. 7, 1956).

[2] Experiments carried out by Pratt & Whitney Aircraft personnel on the Fox Project.

[3] R. V. Meghreblian, *ANP Quar. Prog. Rep. Sept. 10, 1956*, ORNL-2157, p 23.

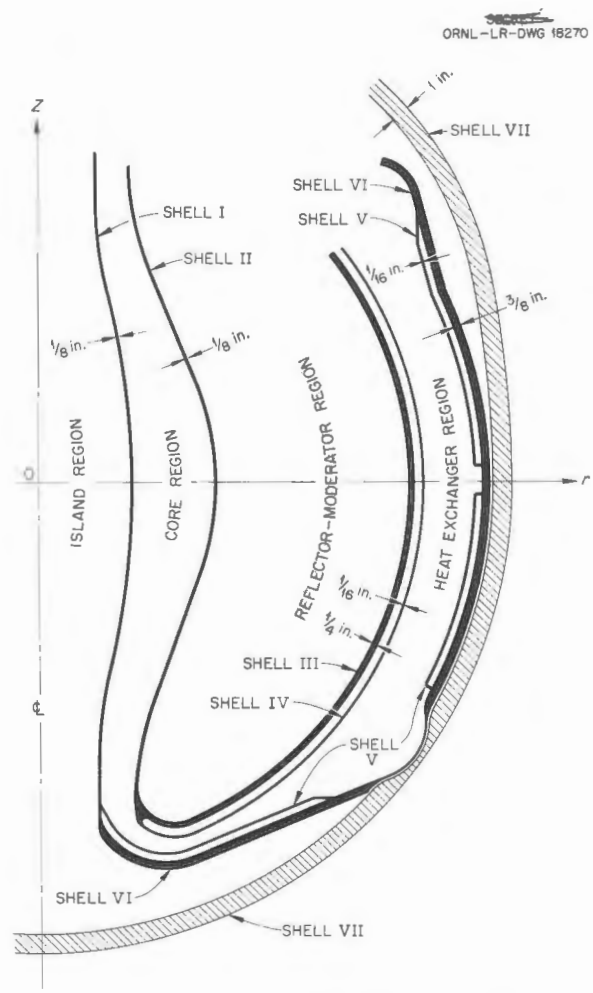

Fig. 1.1.1. Shell Structure of the ART.

275 hr. The collapsed shell is shown in Fig. 1.1.2. It is recognized that the actual end conditions in the reactor were not simulated in this test, since only one-half of a shell was used and each end was supported by a stiff plate. It is expected, however, that results obtained with these models will be useful in correlating data obtained with the complete full-size Inconel shells now being fabricated.

The second portion of the creep-buckling program is concerned with the buckling characteristics of shell IV. This study is under way at the Syracuse University Research Institute. Since shell IV has a spherical shape over most of its surface, preliminary studies are being conducted on lead hemispherical shells of the proper thickness-to-radius ratio. Another important feature of shell IV which has been simulated in the lead model test is the gap which will be between it and a layer of boron tiles. These tiles, which will serve as a thermal-neutron curtain for the outer surface of the reflector, will be in a sodium vapor atmosphere between shells III and IV. At room temperature the gap will be 0.020 in. wide; when the reactor is isothermal at 1200°F the gap will be 0.027 in.; and at full power the gap will be 0.052 in. Under normal operating conditions, the external pressure over some portions of this $\frac{1}{16}$-in. shell will be of the order of 60 psi for prolonged periods of time. Since this pressure is well above the critical pressure for buckling, it is to be expected that shell IV will collapse against the boron tiles. The determination of the time required at various pressures to cause collapse and the precise pattern of dimples, or ripples, which will appear in the shell are the two principal objectives of the Syracuse study. Preliminary tests performed at room temperature on lead hemispherical shells indicate that a regular pattern of dimples will appear in the shell if it is prevented from achieving complete collapse by the presence of a fixed spherical surface placed at a short distance beneath the shell. The buckling pattern obtained on $\frac{1}{16}$-in.-thick 11-in.-radius lead shells when a $\frac{1}{16}$-in. gap is allowed between the under surface of the shell and the supporting surface beneath is shown in Fig. 1.1.3. The shell illustrated was subjected to an external pressure of 1 atm. The pattern which developed after one week of the test is shown in Fig. 1.1.3*a*, and the pattern 34 days later is shown in Fig. 1.1.3*b*. It was found after 34 days that no new dimples had been created, but the ridges between dimples appeared to have become sharper and more clearly defined. A sequence of highly idealized drawings of this buckling process is shown in Fig. 1.1.4. It is of interest to note that no dimples appear at the top of the shell, since the buckling of the lower portions causes the top to be drawn down tightly over the supporting surface underneath the shell.

It is expected that a buckling pattern similar to that obtained on the hemispherical shells will occur in shell IV after prolonged operation with the fuel pumps running at full speed. However, it is also

Fig. 1.1.2. The $\frac{1}{4}$-Scale Model of One-Half of Shell II After Creep-Buckling Collapse. (Confidential with caption)

expected that when the pump speeds are reduced or the power output of the reactor is changed (so that there is a change in the internal temperature profiles) the dimples will disappear, at least in part. Evidently, an important consideration in the design analysis of shell IV is the determination of the plastic deformation that will be developed around the ridges between dimples each time the system is cycled. It will be possible to compute these strains once the general shape and size of the dimples have been determined from experiments. This is the next step to be undertaken in the study. For this purpose it is planned to use one-half-scale copper shells at 300 to 400°F and one-half-scale Inconel shells at 1500 to 1600°F. The strains computed from the experimentally determined buckling pattern will be used to predict the number of cycles to which shell IV may be subjected.

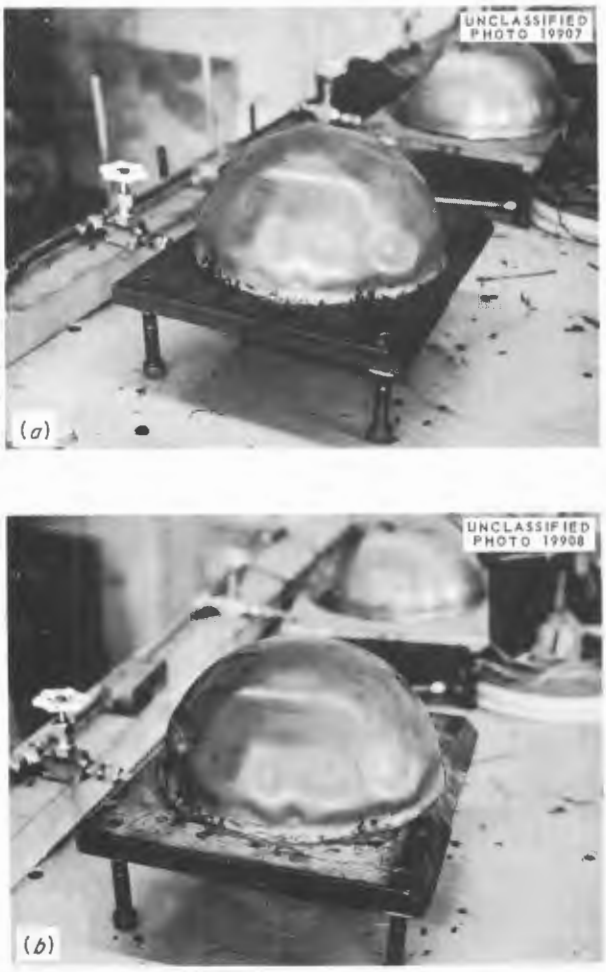

Fig. 1.1.3. Full-Size Lead Mockup of Shell IV After (*a*) One Week at an External Pressure of 1 atm and (*b*) 34 Days Later Under the Same External Pressure. This $\frac{1}{16}$-in.-thick 11-in.-radius shell is separated from a supporting shell by a gap of $\frac{1}{16}$ in. [redacted]

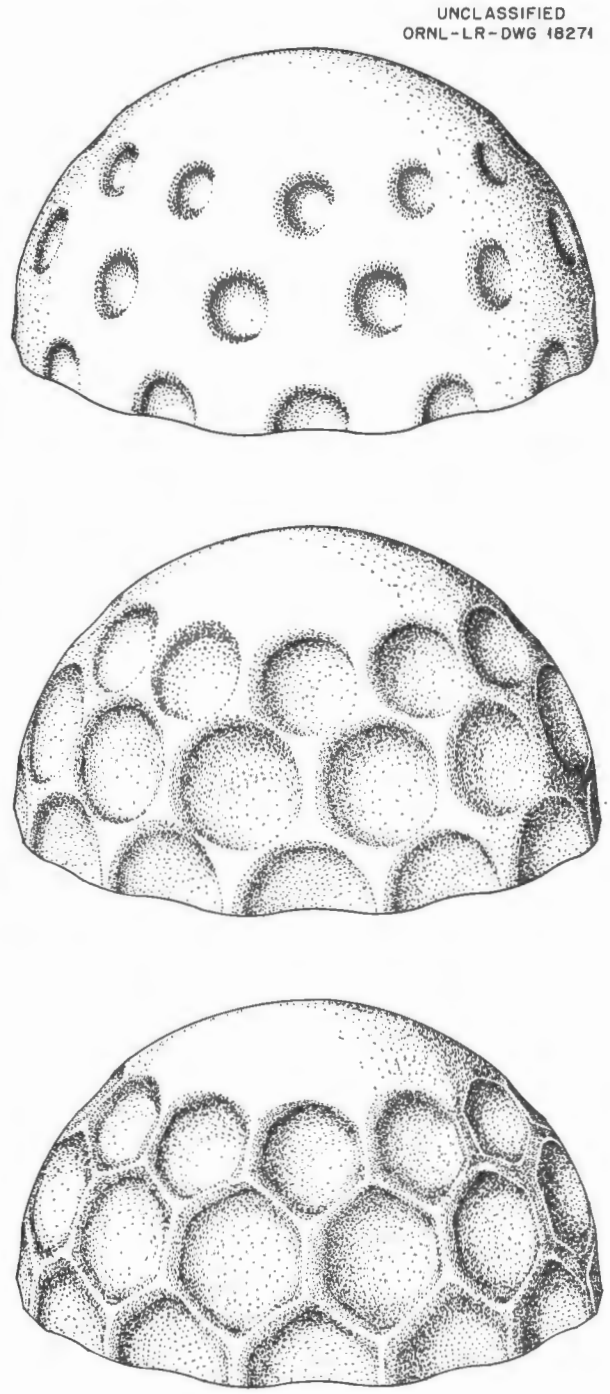

Fig. 1.1.4. Idealization of Buckling Sequence.

Tube-to-Shell Connections

A design feature which appears frequently in the ART configuration is the connection of a pipe to a shell of double curvature. The two most important applications are the connections of the pump barrels to the pressure shell in the region of the north head and the connection of the NaK lines from the north and south head manifolds to the pressure shell. Other similar connections of lesser importance from a structural standpoint are the attachments of the fuel dump lines, the various instrument line tubes, and the thermal sleeves to the pressure shell. For each of these applications the design must be analyzed on the basis of a double criterion, namely, that the connection must withstand certain mechanical loads and deformations (usually transmitted from the pipe to the shell) and that it must survive a specified number of temperature cycles arising from differences in thermal response (and/or boundary conditions) of the pipe and the shell. The analysis has been completed only for the first of these considerations.

The mechanical stresses that will appear at the junctions of the pump barrels and the pressure shell will be due to the combined action of weight and balance loads distributed between the reactor and its support structure.[4] The mechanical stresses at the NaK-pipe–pressure-shell intersections will be due to the balancing loads applied to the reactor by the pipes during off-design conditions.

In most of the cases mentioned above, the general shape of the doubly curved surface is well represented by a spherical shell. Thus the tube-shell intersection stress analyses that have been undertaken were based on the simplified model of a circular tube joined radially to the surface of a spherical shell, as shown in Fig. 1.1.5. Three basic loading conditions were considered in these calculations, namely, a tube with axial load, with side load (pure shear), and with pure moment (axis of the moment perpendicular to axis of tube). More general loading conditions may be obtained by superposition. The first of these analyses, tube-with-axial-load, has been completed.[5] The method used in this study consisted in analyzing separately both the tube and the shell and then coupling the two results with the requirement that the deformations at the

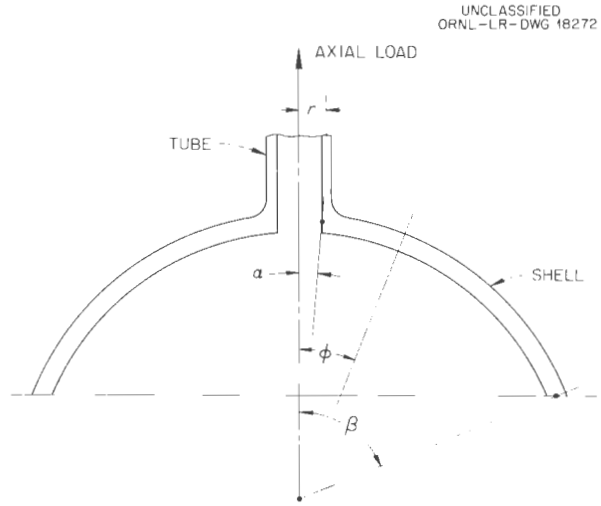

Fig. 1.1.5. Connection of Tube to Spherical Shell Segment.

connection be compatible. Since the solution for the tube, that is, a cylinder, is well known, attention was directed to the analysis of the spherical shell with a circular hole. Although various facets of this problem have been studied at some length,[6] most of these calculations involve simplifying assumptions in the original differential equations (usually in the equilibrium equations). The shell analysis performed for the present case[5] follows the general treatment given by Timoshenko.[6] The results obtained by this approach are limited only by the assumptions of the classical small-deflection theory of thin shells. The method, in short, involves the reduction of the equilibrium and stress-strain relations to a single fourth-order ordinary differential equation for the radial shear in the shell. The solution is given in terms of four hypergeometric series. The convergence of the series solution is dependent upon the value of ϕ (the colatitude angle measured from the center of the hole) and the ratio of the thickness of the shell to its radius (h/a). For example, for $a/h = 25$, and Poisson's ratio $= 0.3$, it was found that 17

[4] R. V. Meghreblian, *ANP Quar. Prog. Rep. Sept. 10, 1956*, ORNL-2157, p 18–21.

[5] F. J. Stanek, *Spherical Segment with Circular Hole at Vertex Loaded Axisymmetrically Along the Edges*, ORNL-2207 (Dec. 19, 1956).

[6] A. E. Love, *The Mathematical Theory of Elasticity*, 4th ed., p 587–589, Dover, New York, 1944; S. Timoshenko, *Theory of Plates and Shells*, McGraw-Hill, New York, 1940, p 454–469; E. Reissner, *J. Math. Phys.* 25, 80–85, 279–300 (1946); M. Esslinger, *Statische Berechnung von Kesselboden*, p 1–20, Springer, Berlin, 1952.

terms were required in each series in order to obtain an accuracy of five significant figures.

The general results obtained for the shell-with-hole and for the cylinder have been combined to determine the stress distribution in the vicinity of a tube-shell intersection. The computed results for the case of an axially loaded tube are shown in Figs. 1.1.6 and 1.1.7. In this calculation the shell parameters, indicated in Fig. 1.1.5, are: $\alpha = 5$ deg, $\beta = 45$ deg, and $a/h = 25$. For a rough comparison, these results have been combined with some experimentally determined data obtained from a test conducted at the University of Tennessee on a tube-shell intersection model of approximately the same geometric proportions, that is, $\alpha = 3.4$ deg, $\beta = 68.4$ deg, and $a/h = 26.51$. It is of interest to note that the meridional stresses appear to be in quite good agreement even though the diameter of the hole for the calculated system differs markedly from that of the test model. This difference is evidently most important in connection with the circumferential stresses, as shown in Fig. 1.1.7.

Thermal Expansions of Shells and Reflector

As an initial step in the over-all thermal stress analysis of the reactor, a detailed calculation has been carried out to determine the temperature structure and thermal growth of the various shells and of the beryllium. The purpose of this study was to determine the average operating temperatures of major structural members, to establish fabrication and assembly tolerances, to reveal possible interferences between components, and to determine which areas of the structure would be subjected to excessive thermal distortions. Although some of

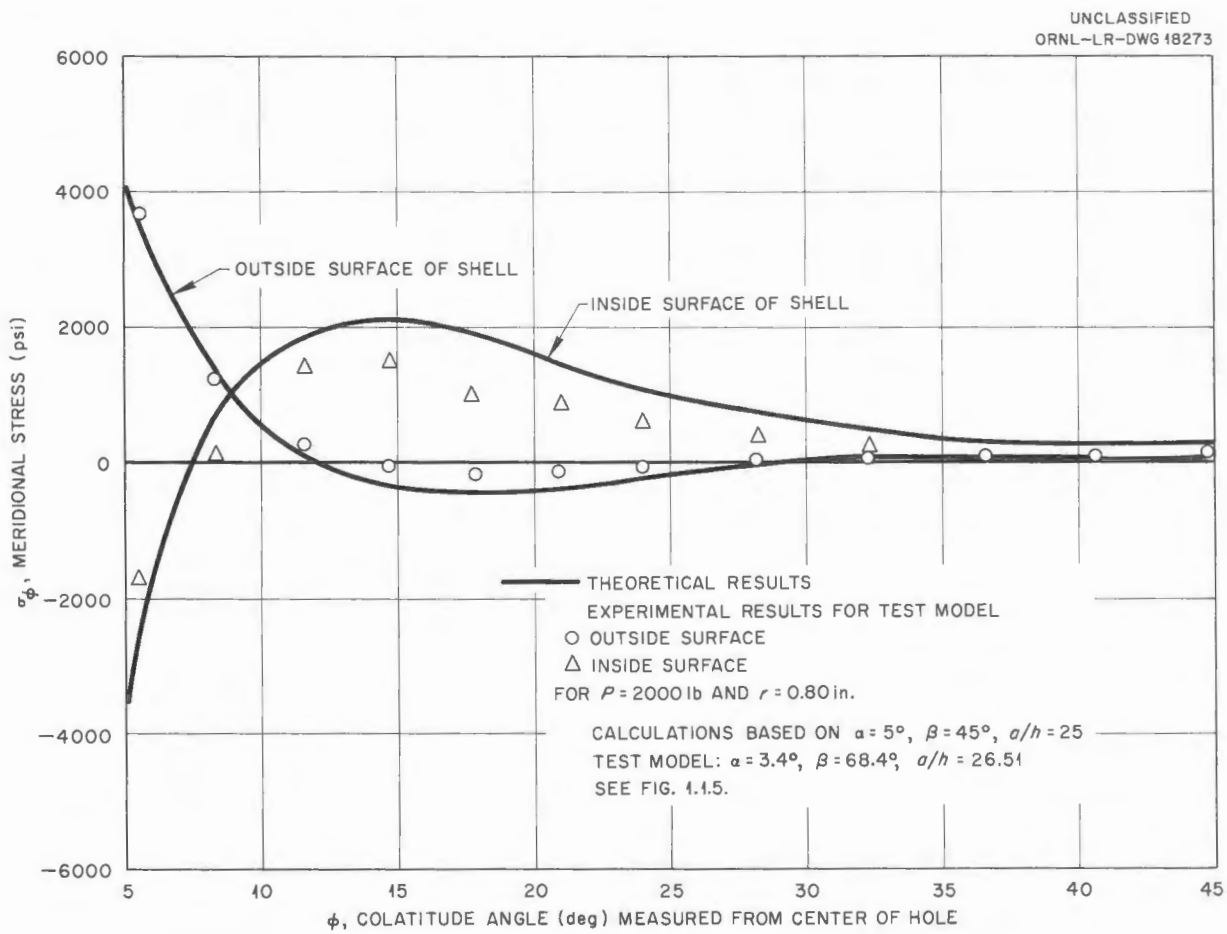

Fig. 1.1.6. Meridional Stresses on Shell at a Tube-to-Shell Intersection.

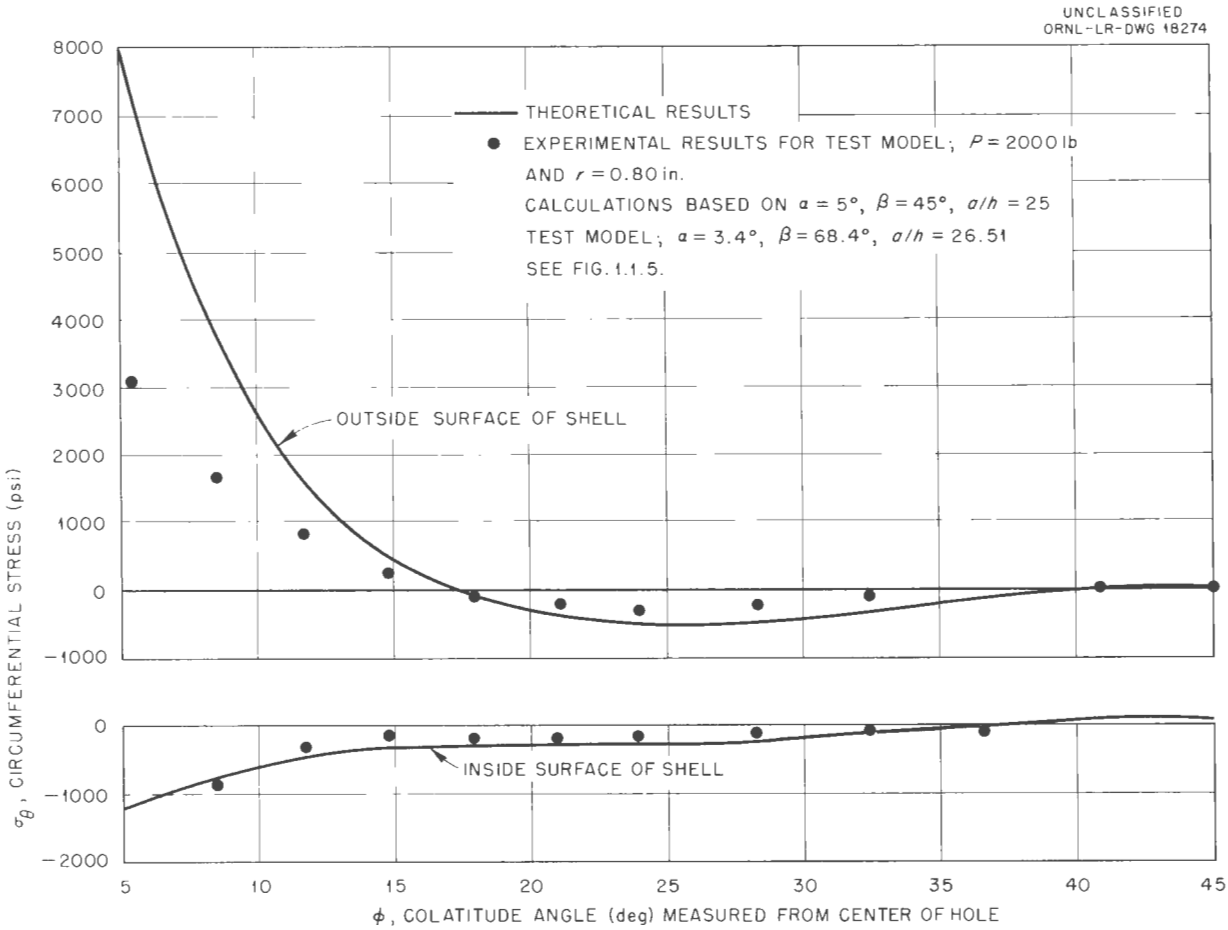

Fig. 1.1.7. Circumferential Stresses on Shell at a Tube-to-Shell Intersection.

the temperature data selected for the fuel and sodium circuits are known to be preliminary estimates, it is believed that the thermal growth analysis gives a reasonably accurate picture of the gross dimensional changes in the system, and these data should be adequate for establishing clearances between adjacent members. However, it should be pointed out that the estimates are based on free-body analyses. Further, since some of the shells cannot expand freely in the full-power condition, local corrections have been introduced in the thermal-growth calculations to account for edge constraints. (For example, shells IV and V operate at average temperatures significantly greater than the temperature of the structure to which they are attached; thus, the edges of the shells must deform to accomodate the colder structure.)

The temperature structure in the core region, which was used as the basis for the thermal-growth analysis, is given in Table 1.1.1. The temperature profiles for shells III and IV were based on the detailed heat balances[7] that have been obtained for the multilayer structure of shells, boron tiles, and sodium annuli which comprise the inner boundary of the heat exchanger region. The average temperature distribution in the island beryllium and in the reflector moderator at full power is given in Table 1.1.2 for the stations indicated in Fig. 1.1.8. The average temperatures at full power for shells I, V,

[7]H. W. Hoffman, C. M. Copenhaver, and J. L. Wantland, *Thermal Structures for the Region Beyond the ART Reflector*, ORNL CF-56-3-23 and Supplement CF-56-4-129 (April 17, 1956); *ANP Quar. Prog. Rep. March 10, 1956*, ORNL-2061, p 174.

TABLE 1.1.1. TEMPERATURE STRUCTURE IN IDEALIZED ART CORE

Distance from Equator, Z (in.)	Core-Wall–Fuel Interface Temperature (°F)	Core-Wall–Sodium Interface Temperature (°F)	Sodium Stream Temperature (°F)
18	1250	1050	1050
12	1325	1096	1076
6	1375	1126	1104
0	1420	1155	1132
–6	1460	1184	1162
–12	1500	1215	1192
–18	1540	1252	1225

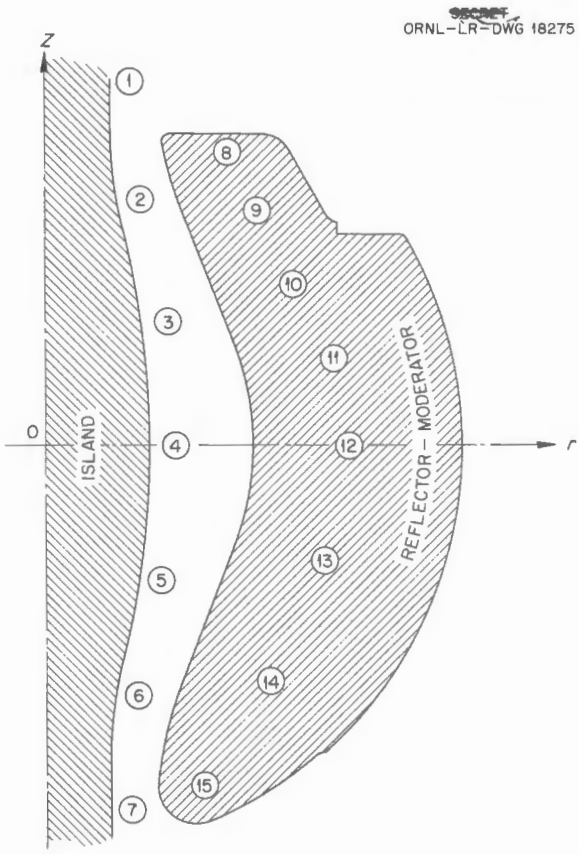

Fig. 1.1.8. Reference Stations on Island and in Reflector-Moderator for Temperature Calculations.

TABLE 1.1.2. ISLAND AND REFLECTOR-MODERATOR MEAN TEMPERATURES AT FULL POWER

Station Indicated in Fig. 1.1.8	Distance from Equator, Z (in.)	Temperature at Station (°F)
1	18	1060
2	12	1105
3	6	1150
4	0	1190
5	–6	1210
6	–12	1225
7	–18	1230
8	16	1070
9	12	1105
10	10	1120
11	6	1150
12	0	1190
13	–6	1210
14	–12	1220
15	–18	1225

VI, and VII are given in Table 1.1.3 for the stations indicated in Fig. 1.1.9, and the average temperatures for shells II, III, and IV are given in Table 1.1.4 for the stations indicated in Fig. 1.1.10.

The temperature data summarized in Tables 1.1.2, 1.1.3, and 1.1.4 have been used to compute the dimensions of the various structural members at full power and under isothermal conditions at 1200°F. The application of these data to the determination of the clearances required between adjacent components is well illustrated by the case of the sodium annulus around the outside of the reflector. In the cold (assembly) condition this gap will be 0.125 in. At full power it will open up to 0.130 in., but at 1200°F (isothermal), it will close up to 0.110 in. (These changes are due to the difference in the coefficient of thermal expansion between beryllium and Inconel.) In order to accomodate these variations in annulus thickness, it will be necessary to provide a cold clearance of 0.015 in. between the shell and the spacers.

The estimates of the temperature distributions and the corresponding thermal expansions are being used to determine the thermal-stress distributions in critical areas. Areas presently being studied include the junction of shells II, III, and IV (Fig. 1.1.1); the junction of shells V and VI; and the blowout patch[8] area of shell VI (the region of

[8] The purpose of the blowout patch is to provide a pressure relief (for an extreme nuclear accident) which will direct the expelled gases and fluids from the reactor down into the bottom of the test cell.

TABLE 1.1.3. AVERAGE TEMPERATURES FOR SHELLS I, V, VI, AND VII AT FULL POWER

Station Indicated in Fig. 1.1.9	Distance from Equator, Z (in.)	Temperature at Station (°F)
	Shell I	
1	18	1160
2	12	1220
3	6	1261
4	0	1297
5	−6	1332
6	−12	1369
7	−18	1406
	Shell VI	
8	−21	1281
9	−22.5	1281
10	−21.5	1281
11	−18	1281
12	−16	1362
13	−12	1265
14	−8	1262
15	−4	1259
16	−1	1257
17	1	1259
18	4	1255
19	8	1253
20	12	1251
21	16	1250
	Shell V	
22	16	1250
	Shell V	
23	12	1290
24	8	1329
25	4	1369
26	1	1408
27	−1	1461
28	−4	1514
29	−8	1566
30	−12	1582
31	−17.4	1582
32	−21	1582
33	−22	1582
34	−20.6	1582
	Shell VII	
35		1230
36	−24	1234
37	−16	1237
38	−12	1239
39	−8	1241
40	−4	1243
41	0	1245
42	4	1247
43	8	1248
44	12	1249
45	16	1250

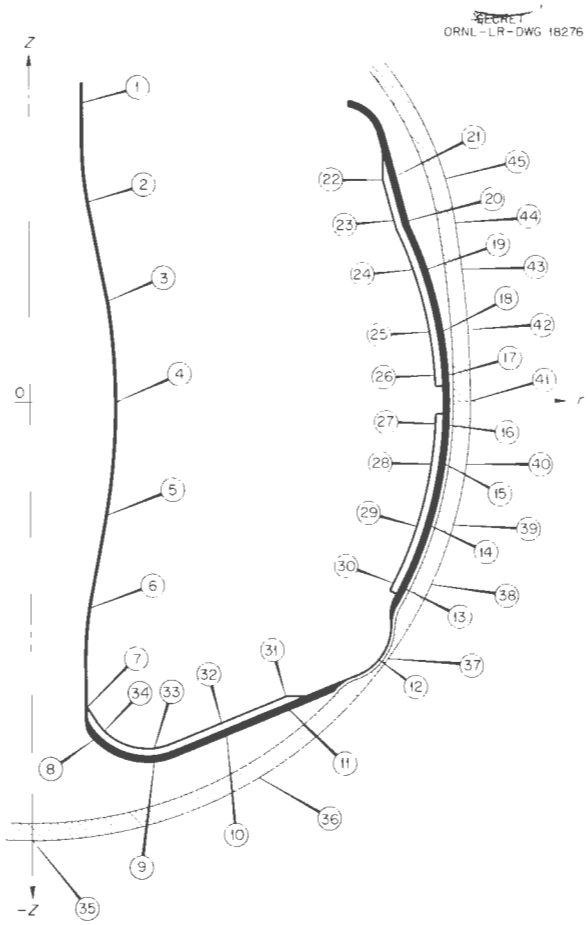

Fig. 1.1.9. Reference Stations on Shells I, V, VI, and VII.

station 12 in Fig. 1.1.9). These analyses will serve as the basis for the design of the critical areas; however, the design of all three regions will be checked by test. The actual thermal distortions of shells II, III, and IV will be determined at the NACA Lewis Flight Propulsion Laboratory. The temperature distributions listed in Table 1.1.4 will be imposed on these shells by the combined action of radiant heaters and cold-air jets. Although the facilities are inadequate for reaching the indicated maximum temperature of 1600°F, the correct temperature differences will be achieved. The highest test temperature will be about 600°F, the lowest, 200°F. The test of the blowout patch areas of shells VI and VII will be conducted on ¼-scale steel models. The test assembly is being prepared at the University of Tennessee.

TABLE 1.1.4. AVERAGE TEMPERATURES OF SHELLS II, III, AND IV AT FULL POWER

Station Indicated in Fig. 1.1.10	Distance from Equator, Z (in.)	Temperature at Station (°F)
	Shell II	
1	18	1160
2	12	1220
3	6	1261
4	0	1297
5	−6	1332
6	−12	1369
7	−18	1406
	Shell III	
8	−19.9	1287
9	−18	1287
10	−12	1291
11	−6	1296
12	0	1300
13	6	1303
14	13	1303
	Shell IV	
15	13	1336
16	6	1382
17	0	1427
18	−6	1427
19	−12	1518
20	−18	1594
21	−20.7	1550

High-Frequency Temperature-Oscillation Studies

A series of heat transfer experiments[9] performed on an idealized model[10] of the ART core indicated that relatively high-frequency (1 to 10 cps) temperature oscillations could appear in the fluid for the two flow configurations tested (swirl entrance and vaned entrance). The extrapolation of these results to the conditions in the ART indicate that in some regions of the core (depending upon the entrance configuration) the fluid temperature oscillations

[9] G. W. Greene *et al.*, *ANP Quar. Prog. Rep. Sept. 10, 1956*, ORNL-2157, p 227.

[10] A one-half-scale test model with uncooled walls and uniform power distribution.

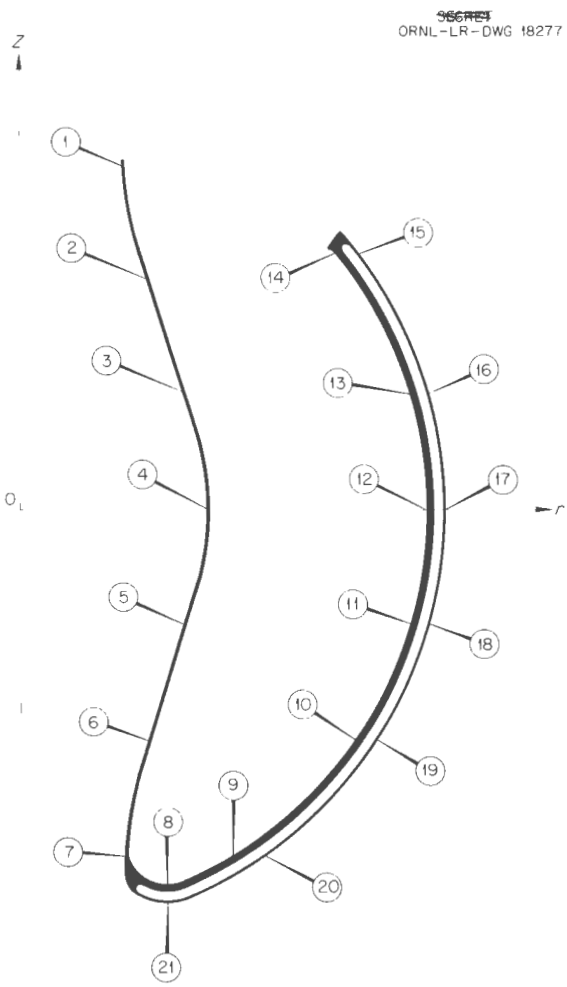

Fig. 1.1.10. Reference Stations on Shells II, III, and IV.

will be of the order of ±60°F. The presence of these oscillations in the fluid stream can cause similar temperature variations on the exposed surface of the core walls. Calculations[9,11] based on various idealized models of the flow conditions at the wall-fluid interface have shown that the amplitude of the oscillations in the exposed surface can range from 20 to 95% of the amplitudes in the fluid. The appearance of these temperature variations at the surface of the metal results in the rapid strain cycling of the outer fibers. At the frequencies (1 to 10 cps) which have been encountered, only the surface layers are exposed to significant amplitudes, since the relaxation length for these disturbances in Inconel is of the order of 15 to 50 mils.

The only information presently available on high-temperature high-frequency strain cycling is based on conventional fatigue tests. These tests, however, do not simulate well the conditions which may arise in the walls of the core because of the rapid decay mentioned above. For this reason a program of tests and experimental studies has been undertaken to determine the fatigue life of Inconel tubing (and sheet) subjected to rapid strain cycling at the surface. Some preliminary results from the first of these tests have been reported.[12] A second series of tests, for which a pulse-valve mechanism[13] has been designed, is presently being prepared. These two studies are being further augmented by a conventional hot-fatigue test, which is now in progress at the Battelle Memorial Institute.[14] Finally, a localized-heat-source test is being prepared at the University of Tennessee. In this test a sheet of Inconel (at high temperature) will be exposed to a cyclic radiant heat source which will be focused on a small area of the sheet, away from the boundaries. It is expected that the information gained from the various tests in this program will suffice to determine the effects of high-frequency local "surface" strain-cycling of the Inconel core shells and heat exchanger tubes.

For the preliminary tests performed with the pulse-valve rig,[13] streams of hot and cold water at moderate temperature levels were used (see Chap. 1.4, "Component Development and Testing," this report). The purpose of these tests has been to develop suitable detection devices and to provide familiarity with the system. Also, an attempt is being made to predict the thermal response of the tube walls in the experiment (to a given temperature oscillation from the valves) by direct analytical methods. This approach will be especially

[11] D. H. Platus and R. V. Meghreblian, *Conduction of Heat in a Finite Plate in Contact with an Environment in Which the Temperature Varies as a Prescribed Function of Time*, ORNL CF-56-9-60 (Sept. 12, 1956).

[12] H. W. Hoffman and D. P. Gregory, *ANP Quar. Prog. Rep. Sept. 10, 1956*, ORNL-2157, p 228.

[13] W. J. Stelzman and J. M. Trummel, *ANP Quar. Prog. Rep. Sept. 10, 1956*, ORNL-2157, p 56.

[14] The comparison of fatigue data from conventional tests with that obtained from surface-strain tests may be of value in correlating the various data.

important when the apparatus is used for tests with high-temperature fused salts, since it may not be possible to obtain reliable temperature measurements of the fluid and of the tube walls. A study has been made[11] therefore of the response of a thin plate to a specified variation in fluid temperature. For these calculations it was assumed that one side of the plate was at bath conditions and that the other side was exposed to an established flow field in which the bulk temperature varied sinusoidally. Some of the results obtained from this study are shown in Fig. 1.1.11. The symbol η denotes the ratio of the amplitude of temperature oscillation at the exposed surface of the plate to the amplitude in the fluid stream, ω is the frequency of the fluid oscillations, h is the average heat transfer coefficient of the fluid, k is the thermal conductivity of the wall, and α is the thermal diffusivity. Evidently, there exists (for a given value of h and ω) a plate thickness, a, which will result in a maximum amplitude of oscillation at the surface. Also, for $am \gtrsim 1$, where $m = (\omega/2\alpha)^{1/2}$, the plate behaves as if it were infinitely thick. For example, a material having a thermal diffusivity equal to 0.2 ft^2/hr if subjected to a frequency of 1 cps would respond as an infinite plate for thicknesses greater than about 50 mils (m = 20 in.$^{-1}$). Also, for a thermal conductivity of 12 Btu/hr·ft·°F and a heat transfer coefficient of 2000 Btu/hr·ft^2, the amplitude at the surface would be about 37% of the amplitude in the fluid. At higher frequencies the surface amplitude is further reduced; for example, at ω = 5 cps, $\eta \simeq$ 19%.

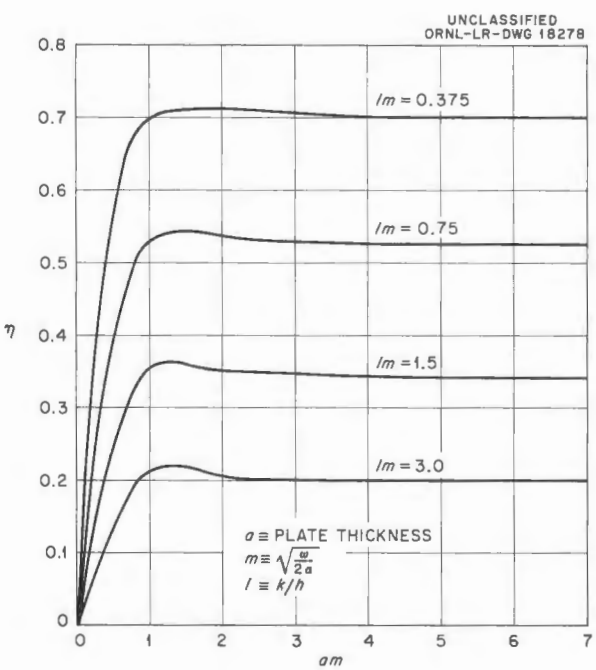

Fig. 1.1.11. Ratio of Amplitude of Temperature Oscillation at Surface of Plate to Amplitude of Environment Oscillation.

It is expected that these calculations will be useful in interpreting the results from the fused-salt experiments. Also, this model should give reasonably good estimates of the thermal response of the core shells and of the heat-exchanger tubes for the case of an established flow field. However, since there appear to be hydrodynamic instabilities in the core region, some care should be exercised in applying this model to the reactor problem. In any event, a conservative approach would be to assume that the metal is subjected to the full amplitude of the fluid oscillations. The material tests are being conducted on this basis.

RADIOACTIVITY IN THE FUEL-PUMP OIL SYSTEM

G. Samuels, Jr.

Until recently there has been a complete lack of data regarding the transfer of radioactive gases from the expansion-tank region of the ART reactor to the pump lubricating oil system. The previous report,[15] however, described results of tests on the back transfer of helium against argon in the fuel pump. These tests were designed to give some indication of the back transfer of xenon and krypton against helium that can be expected during reactor operation. An attenuation of at least 10^4 between the concentration of radioactive gases in the expansion-tank region and the concentration in the oil catch basin and a leakage rate of gas from the oil catch basin to the oil reservoir of 0.8 in.^{3}/day were estimated on the basis of the test results. In determining the leakage rate of 0.8 in.^{3}/day it was assumed that, since the pump had been in operation for some time prior to the test, the oil was completely saturated with argon at the beginning of the test run, and that all leakage across the seal was collected in the oil reservoir. The value of 10^4 for the attenuation in concentration between the fuel expansion tank and the pump seal is a minimum.

[15] S. M. DeCamp, Jr., and W. K. Stair, *ANP Quar. Prog. Rep. Sept. 10, 1956*, ORNL-2157, p 39.

The helium concentration in the argon buffer gas used in the experiment reported previously was 10^{-4}, and hence the actual attenuation in concentration between the tank and the seal may have been greater.

Because of the short half lives of the fission-product gases the attenuation in the amount of activity between the fuel-expansion tank and the oil reservoir will be greater than the attenuation in gas concentration. Thus the rate at which the fission-product gases enter the oil system will be of significant importance. A study was therefore made to estimate the level of the activity in the oil on the basis of these data.

In the ART, as well as in the above-mentioned test, 500 liters per day of buffer gas will flow down through the clearance around the pump shaft into the expansion tank and 50 liters per day will be bled directly from the oil catch basin. The attenuation of 10^4 represents the back transfer of helium against the 500 liters per day of argon. This back leakage was determined from analysis of the 50 liters per day bled from the catch basin.

The equation representing the number of nuclei, N, of any nuclide in the catch basin as a function of time t may be written:

$$\frac{dN}{dt} = S - (\lambda_p + \lambda_d)N,$$

where

S = source strength of leakage rate into basin,

λ_p = reciprocal of average dwell time, or purge rate per unit volume,

λ_d = decay constant of the radioactive nuclide.

After the fission gases are separated from the fuel, their decay products can be treated as gases. This assumption is conservative, but the actual behavior of these nuclides is not known. To calculate the dose rate near the oil reservoirs, all the radioactive nuclides were assumed to be concentrated as a point source in the oil reservoirs. It was also assumed that the ⅜-in.-thick steel wall of the reservoir will give no attenuation for gamma-ray energies above 0.03 Mev, an attenuation of 10 in the energy range of 0.01 to 0.03 Mev, and an attenuation of 75 for energies below 0.01 Mev. In cases where the exact percentages of the gamma-ray energies were not known, the maximum possible percentages were used. The data for yields, energies, and percentage of gamma rays were taken from a report by Blomeke.[16] The data for dosages were taken from Rockwell.[17] The results of the calculations indicate a gamma-ray dose rate of about 30 mr/hr at a distance of 1 m from the oil reservoir.

The approximate volume of oil in each pump lubricant system is 30 gal. If the total beta emitters in the oil are assumed to be equally dispersed throughout the system, the dose to the oil is found to be about 20 rads/hr. This dose for 500 hr of operation amounts to 10^4 rads, which is trivial compared with the 10^8 rads which the oil is capable of absorbing without serious damage. If a distinction is made between the fission gases and their daughter products, it is found that the fission gases account for about 70 to 75% of the total activity in the oil system, but only 25% of the gamma-ray dose calculated.

HEAT EXCHANGER THERMAL STRESSES

Heat exchanger test experience has been carefully reviewed in light of analytical studies and metallurgical examination. The leaks that have been experienced appear to have resulted from severe thermal-strain-cycling conditions peculiar to the rig-test heat exchanger design. These conditions had been recognized as likely to cause trouble, and great care was exercised to avoid them in the design of the spiral tube bundle heat exchanger for the ART. A circular-arc-tube-bundle rig-test heat exchanger has been designed to simulate ART conditions very closely, and fabrication of the first test unit is being expedited.

A similar study of radiators is under way. The more complex geometry and the wider variety of conditions that must be satisfied make this a much more formidable analytical task. It is particularly difficult to arrive at a radiator core matrix sufficiently strong to withstand air and gravity loads and at the same time sufficiently flexible to accommodate the thermal stresses associated with differential thermal expansion of the fins and header drums and/or nearby tubes under temperature or load transients or under oxide-plugging conditions. Several means of reducing the stiffness of the fin matrix by slitting the fins appear to be promising and are being studied carefully to determine which can be incorporated in the ART fin matrix with the least trouble.

[16] J. O. Blomeke, *Nuclear Properties of U^{235} Fission Products*, ORNL CF-54-12-52 (Dec. 20, 1954).

[17] T. Rockwell, III, (ed.), *Reactor Shielding Design Manual*, TID-7004, Fig. 2.1, p 19 (March 1956).

1.2. ART PHYSICS

A. M. Perry

NEUTRON HEATING IN THE ART

C. M. Copenhaver

The neutron heating in the reflector, island, and fuel regions of the ART was computed by using the following equation in conjunction with two-dimensional multigroup calculations made at the Curtiss-Wright Corp.:

$$H_n \text{ (w/cm}^3) = K \sum_i \left(\sum_j N_j \sigma_{ij} \delta_{ij} \right) \bar{E}_i \phi_i \Delta u_i \ ,$$

where

$K = 1.6 \times 10^{13}$ w·sec/Mev,

N_j = the nuclear density of the jth species present at the point under consideration, atoms/cm^3,

σ_{ij} = the elastic scattering cross section of the jth nuclear species in the ith lethargy group, cm^2,

δ_{ij} = the average fractional energy loss of a neutron in the ith group which is scattered by the jth nuclear species,

$\bar{E}_i$ = average energy of neutrons in the ith group, Mev,

ϕ_i = neutron flux in ith lethargy group,

Δu_i = width of ith lethargy group.

Since the lethargy intervals under consideration are small,

$$\phi_i(E)\, \Delta E_i \cong \phi_i(u)\, \Delta u_i \ .$$

For isotropic scattering in the center-of-mass system the average fractional neutron energy loss in an elastic collision is

$$\delta_0 = \frac{1 - \alpha}{2} \ ,$$

where

$$\alpha = \left(\frac{A - 1}{A + 1} \right)^2 ,$$

and A is the atomic weight of the scattering nucleus. However, for the materials of interest in the ART (beryllium, fluorine, etc.) the scattering is not isotropic in the center-of-mass system at the higher energies, and both the average fractional energy loss, $\delta(E)$, and the average logarithmic energy loss, $\xi(e)$, for neutrons having elastic collisions become functions of the differential cross section. As the $\xi(E)$'s used in the multigroup calculations considered anisotropic scattering, neglecting the scattering correction would result in a considerable overestimate in the neutron heating. After integration the average fractional energy loss becomes

$$\delta(E) = \delta_0 [f_0(E) - f_1(E)] \ ,$$

where $f_0(E) \equiv 1$ and $f_1(E)$ can be generated from the neutron cross section angular distributions given in BNL-400.[1] The $f_1(E)$ function for beryllium has an average value of about 0.5 in the 2- to 10-Mev energy range, while the corresponding value for fluorine is about 0.15. Since the fluorine is the main constituent in the fuel and since it has a high $\delta_0(\delta_0 = 0.095)$, about 70% of the neutron heating in the fuel was found to be due to fluorine, and, thus, only the $f_1(E)$ function for fluorine was considered. The elastic scattering cross sections as a function of energy were obtained by using data from BNL-325[2] and ORNL-2113.[3]

The heat generation resulting from elastic collisions of neutrons were integrated over the reflector, island, and fuel regions. The $(n,2n)$ reaction in beryllium apparently results in the reaction $Be^9 + n \longrightarrow 2n + 2\alpha$, with the two alpha particles having a combined energy of about 1.57 Mev for both modes of formation. By using the available $(n,2n)$ cross section for beryllium[3] and assuming the fractional energy loss from inelastic collision to be $1.57/E$, the heating resulting from the $(n,2n)$ reaction was integrated over the reflector and island regions. The contribution to the heating from the additional neutrons is negligible. The inelastic gamma-ray source strength in the fuel, obtained by summing all the individual volume source strengths,[4] was then added to the combined

[1] D. J. Hughes and R. S. Carter, *Neutron Cross Sections Angular Distributions*, BNL-400 (June 1956).

[2] D. J. Hughes and J. A. Harvey, *Neutron Cross Sections*, BNL-325 (July 1955).

[3] H. W. Bertini *et al.*, *Basic Gamma-Ray Data for ART Heat Deposition Calculations*, ORNL-2113 (July 5, 1956).

[4] R. B. Stevenson, private communication to C. M. Copenhaver.

total of the elastic and inelastic neutron heating contributions to give a total source strength of 1879 kw (Table 1.2.1). Recent experimental data[5,6] on the energy spectrum of neutrons from thermal-neutron fission of U^{235} indicate an average fission-neutron energy of 1.963 Mev or 4.91 Mev/fission. Since inelastic scattering of neutrons in the fuel was not considered in the multigroup calculations, it was not possible to normalize correctly the total energy obtained from elastic and inelastic scattering of neutrons to the kinetic energy of the fission neutrons (1487 kw corresponding to 5 Mev/fission). It was realized, however, that it was better to underestimate the fuel inelastic contribution rather than to overestimate it when normalizing, since the neutron heating in the beryllium was much more sensitive to this contribution than was the corresponding gamma-ray heating. Since the inelastic gamma-ray source strength of the fuel used in the gamma-ray heating calculations was 665.3 kw, the normalization procedure used would indicate a possible 3% overestimate of the total heating at the surfaces of the reflector and island regions near the fuel, while keeping the fuel inelastic contribution at 665.3 kw when normalizing would lead to a possible 10% underestimate. The normalized neutron heating rates obtained for the island, fuel, and reflector regions are shown in Fig. 1.2.1. A conservative estimate of the neutron heating in the Inconel core shells resulting from elastic scattering of neutrons is about 2 w/cm^3 at the equator. Since this value is insignificant compared with the corresponding gamma-ray heating, neutron heating in the core shells was neglected in the calculations.

[5] L. Rosen, G. Frye, Jr., and J. Gammel, *Energy Spectrum of Neutrons from Thermal Neutron Fission of U^{235} and from an Untamped Multiplying Assembly of U^{235}*, LA-1670 (May 1954).

[6] L. Cranberg and N. G. Nereson, *Fission Neutron Spectrum of U^{235} from 0.2 to 3 Mev*, LA-1916 (May 1955).

TOTAL RADIATION HEATING IN THE ART

R. B. Stevenson[7]

The total radiation heating (excluding that from the fission products and the fission-product beta rays in the core) was calculated by using the previously reported values for the gamma-ray heating[8] and the values for the neutron heating given above. The result of the combination of these heating values is shown in Fig. 1.2.2.

The heating arising from the capture gamma rays in the control rod was included in these results. This source of gamma rays substantially increases the heating in the island. For the calculation of the heating caused by these gamma rays, it was assumed that the control rod was inserted to the reactor midplane. In this position, the fraction of the total number of neutrons in the reactor absorbed by the control rod will be about 1.5%

[7] On assignment from Pratt & Whitney Aircraft.

[8] R. B. Stevenson, *ANP Quar. Prog. Rep. Sept. 10, 1956*, ORNL-2157, p 33.

TABLE 1.2.1. ELASTIC AND INELASTIC NEUTRON AND GAMMA-RAY HEATING CONTRIBUTIONS IN ART

Contributions	Unnormalized Heating (kw)	Normalized* Heating (kw)		
Fuel inelastic gamma rays	665.3	526		
Island elastic neutrons	236.1	187	= 209	= 961**
Island inelastic neutrons	27.4	22		
Fuel elastic neutrons	182.9	145	= 145	
Reflector elastic neutrons	687.7	544	= 607	
Reflector inelastic neutrons	80.0	63		
Total	1879.4	1487		

*Normalization factor = 0.7917.

**Total neutron heating.

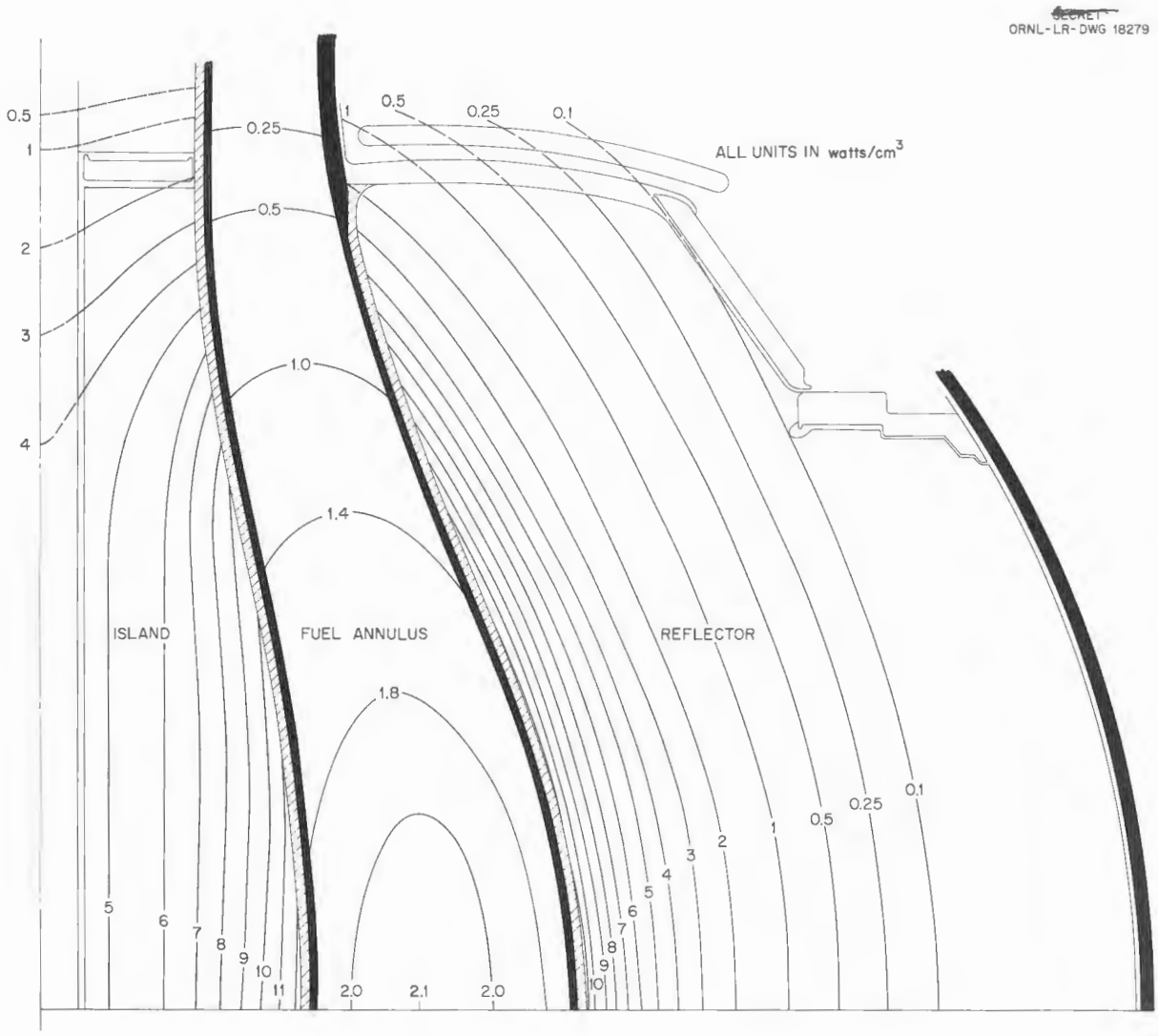

Fig. 1.2.1. Neutron Heating in the ART.

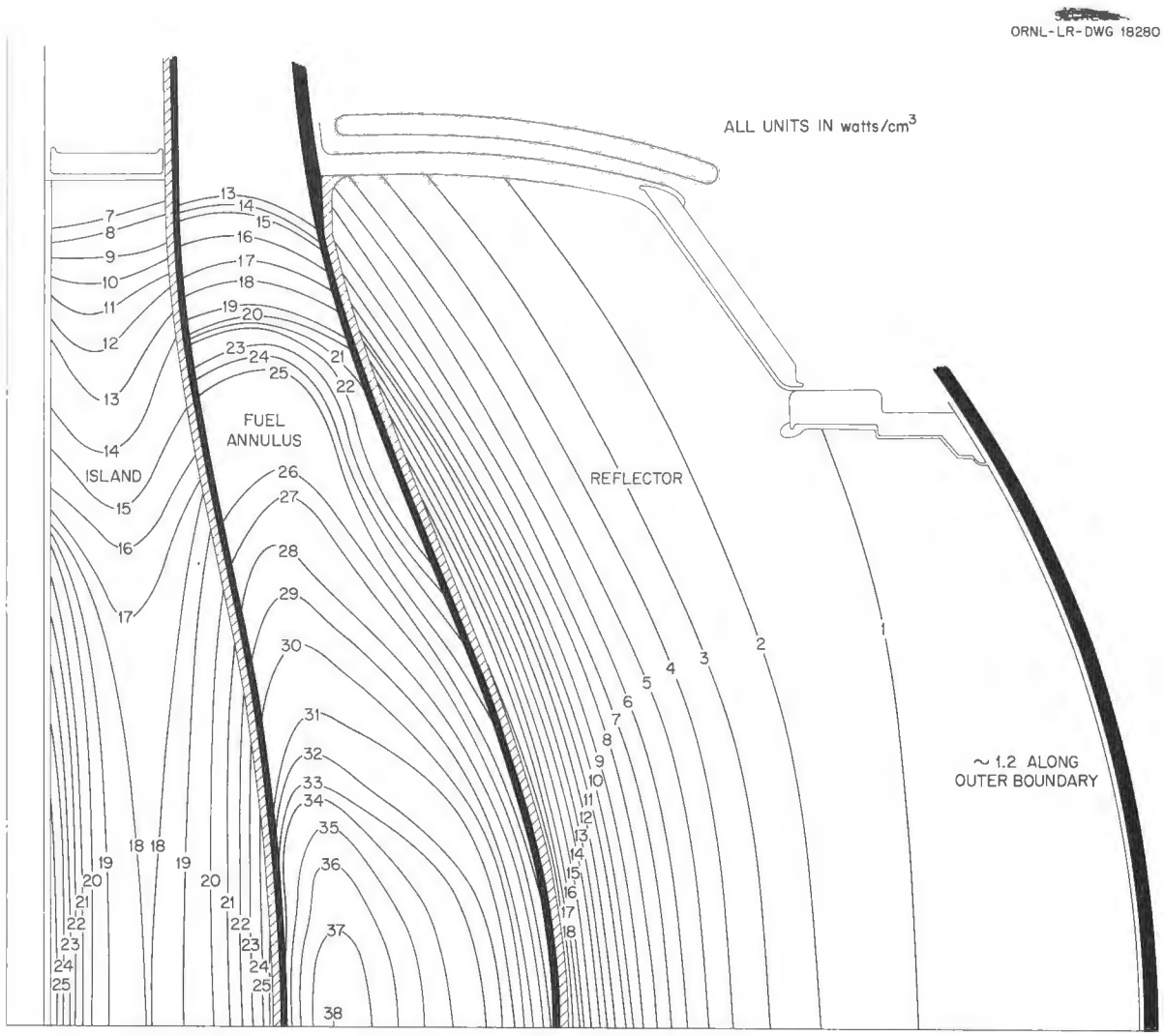

Fig. 1.2.2. Total Radiation Heating in the ART.

($\delta k \sim 2.5\%$), and therefore the total gamma-ray source in the control rod will be about 90 kw. Of this 90 kw, about 24 kw will be absorbed by the control rod and the Inconel thimble, the rest being absorbed by the surrounding regions.

A summary of the total-volume gamma-ray source strengths in the ART (excluding the contributions from the north-head area) is given in Table 1.2.2. The total gamma-ray source strength thus represents about 9.6% of the total available energy (60 Mw). An integration was also performed over the radiation heating contours to find the total heat load in each region of the ART, and the results are given in Table 1.2.3.

TABLE 1.2.2. VOLUME GAMMA-RAY SOURCE STRENGTHS IN ART

Region	Gamma-Ray Source	Heating (kw)	Energy (Mev/fission)
Control rod	Capture	90	0.30
Island	Capture	14	0.05
Core shells	Capture	280	0.93
	Inelastic	60	0.20
Fuel in core	U^{235} capture	598	1.99
	Prompt	2261	7.54
	Decay	622	2.07
	Inelastic	665	2.22
Reflector	Capture	158	0.54
Heat exchanger region	Capture	431	1.44
	Decay	551	1.84
Total		5730	19.12

TABLE 1.2.3. TOTAL RADIATION HEATING IN THE ART

Region	Gamma-Ray Heating (kw)	Neutron Heating (kw)	Total (kw)
Control rod region	24		24
Island	354	209	563
Core shells			
Inner	106		106
Outer	168		168
Core	2488	145	2633
Reflector	764	607	1371
Heat exchanger region	1222		1222
Total	5126	961	6087

1.3. ART INSTRUMENTS AND CONTROLS

R. G. Affel

LIQUID-METAL-LEVEL TRANSDUCERS

R. E. Pidgeon, Jr.[1] G. H. Burger

Level probes or transducers are needed for providing continuous measurement of the NaK level in the main, auxiliary, and special NaK pumps of the ART. The measurement of the level must be accurate to 5% over the temperature range of 72 to 1500°F. A total of approximately 42 transducers will be needed for the ETU and ART pumps, including units for pumps which are being tested or are installed in test rigs. Two types of transducers have been tested, to date, in NaK systems: a resistance type manufactured by the General Electric Company and a variable-permeance type manufactured by the Crescent Engineering & Research Co.

[1] On loan from Radio Corp. of America.

The resistance type of transducer consists of Inconel tubing welded in the shape of a "J". Two current leads and two voltage leads, all made of Inconel wire insulated with magnesium oxide, are inside the tubing. A transformer supplies 3-v, 60-cycle power at approximately 10 amp to the current leads. Sketches of the resistance type of transducer and its equivalent circuit are shown in Fig. 1.3.1, and a photograph of an actual unit is presented in Fig. 1.3.2.

The resistances R_2 and R_3 are the lead resistances of the input current leads, and R_1 is the resistance of the Inconel tubing in the sensing leg. As the NaK level rises on the sensing leg the resistance of the sensing leg will decrease. Since the conductivity of the NaK is high, the resistance of the sensing leg, R_1, and therefore the output voltage, is inversely proportional to the NaK level. The output voltage can vary from

UNCLASSIFIED
ORNL-LR-DWG 18281

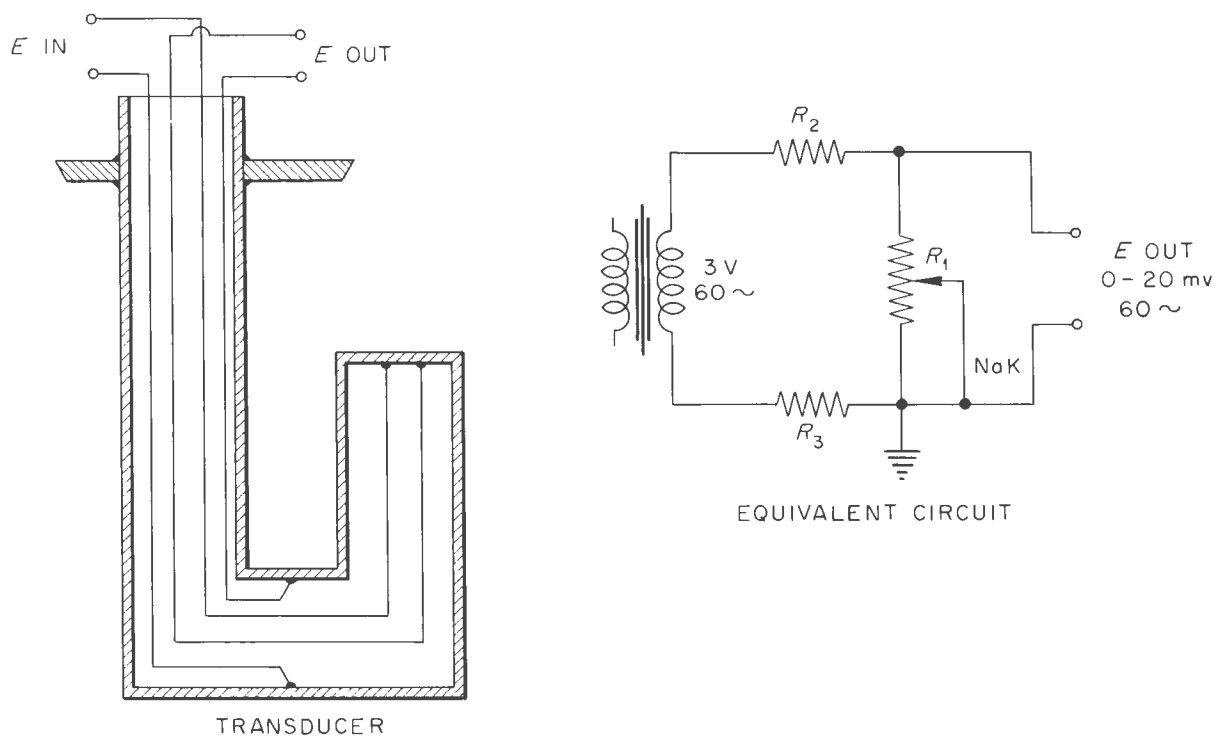

Fig. 1.3.1. Schematic Diagram of the Resistance Type of Transducer and Its Equivalent Circuit.

UNCLASSIFIED
PHOTO 27506

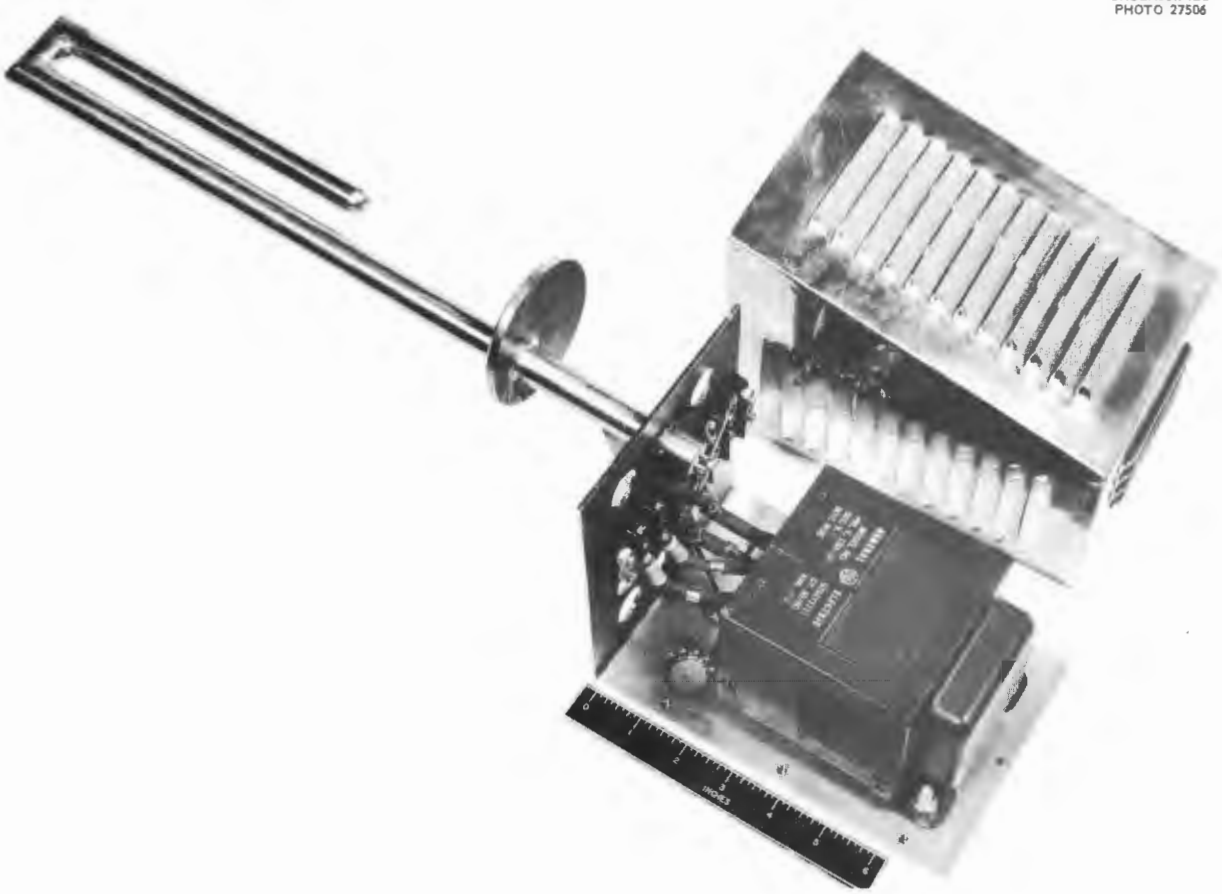

Fig. 1.3.2. A General Electric Co. Resistance Type of Liquid-Metal-Level Transducer.

0 to 20 mv, and it is given by the equation

$$E\ (\text{out}) = 3\,\frac{R_1}{R_1 + R_2 + R_3}\,,$$

which is approximately

$$E\ (\text{out}) = 3\,\frac{R_1}{R_2 + R_3}\,,$$

since $R_1 \ll R_2 + R_3$.

If the sensing leg and current leads are at the same temperature throughout and the temperature coefficients of resistivity of R_1, R_2, and R_3 are the same, the output voltage is independent of the probe temperature. Ideally, when the temperature changes, the numerator and denominator of the equation for the output voltage change by the same factor and the output voltage remains constant. In reality, a small temperature error exists because all parts of the resistance probe are not at the same temperature and the temperature coefficients of resistivity of the Inconel wire and the Inconel pipe used may not be the same.

A vacuum-tube voltmeter can be used to measure the output voltage. For recording, a Foxboro circular chart recorder Model 9650 or a d-c strip-chart recorder modified for 60-cycle operation can be used. The strip-chart recorder is to be used in the ART and the ETU.

The resistance level unit and its measuring system are very simple, and the reliability of the system and the primary element is expected to be extremely good. The temperature compensation of the unit seems to be good, the error introduced by a change of NaK temperature from room temperature to 1200°F (after wetting of the element)

being about 3%. It is expected that after calibration of the units they can measure NaK level to 1% or $\frac{1}{16}$ in. out of the 7-in. range.

The Crescent transducer, shown in Fig. 1.3.3, consists of a coil sealed inside Inconel tubing. The coil forms one leg of a bridge circuit. The bridge is supplied with a 26-kc, low-voltage signal from the measuring and control unit, Fig. 1.3.4. Some of the 26-kc field from the coil penetrates the Inconel tubing and sets up eddy currents in the surrounding NaK. The eddy-current loading causes the effective resistance and inductance of the transducer to vary with the NaK level and therefore the bridge balance varies with the level. The change in NaK level is given by the change in output voltage of the bridge circuit. For small changes in the bridge balance the output voltage is a linear function of NaK level. The first units tested in NaK were extremely temperature sensitive. The effective resistance and inductance of the probe, and therefore the bridge balance, varied drastically as a function of temperature. Since the units were not satisfactory for liquid-metal service, the vendor redesigned them, and they are now believed to be acceptable.

The facility for testing liquid-level-indicating devices, described previously,[2] has been in operation since September. Two G-E and two Crescent elements were installed in the facility. One G-E and one Crescent unit failed shortly after startup. The cause of these failures has not yet been determined because the units are still in the test system. The other Crescent and G-E elements

[2]H. J. Metz, *ANP Quar. Prog. Rep. Sept. 10, 1956*, ORNL-2157, p 36.

UNCLASSIFIED
PHOTO 27508

Fig. 1.3.3. Sensing Leg of Crescent Variable-Permeance Liquid-Metal-Level Transducer.

UNCLASSIFIED
PHOTO 27509

Fig. 1.3.4. Control Unit for Variable-Permeance Liquid-Metal-Level Transducer.

have operated in the system for 1800 hr through 40,000 cycles. The G-E units have operated very satisfactorily, and the operation of the Crescent unit was as described above. It is planned to continue the tests on the units for 3000 hr in order to investigate accuracy, linearity, temperature effects, reliability, lead length effects, probe wetting effects, and time response. All future elements will be calibrated and tested in the existing test facility.

In addition to the G-E level elements installed in the test facility, one was installed in a primary NaK pump test system and has operated very satisfactorily since September. It is planned, as noted above, to install one in each of the NaK pumps being tested.

In addition to the NaK level elements, a total of nine sodium elements will be needed for tests, for use in the sodium expansion tanks of the ART and the ETU, and for spares. These units are to be designed, built, and tested in the near future. Again, all these units will be tested and calibrated in the existing facilities.

MAGNETIC FLOWMETERS

G. H. Burger C. L. Pearce, Jr.[1]

Complete magnetic flowmeter assemblies for the ART and ETU have been purchased from the General Electric Company in the two sizes, 2 and 3½ in., required for the main, auxiliary, and special NaK circuits (Figs. 1.3.5, 1.3.6, and 1.3.7). The specifications for the 3½-in. units

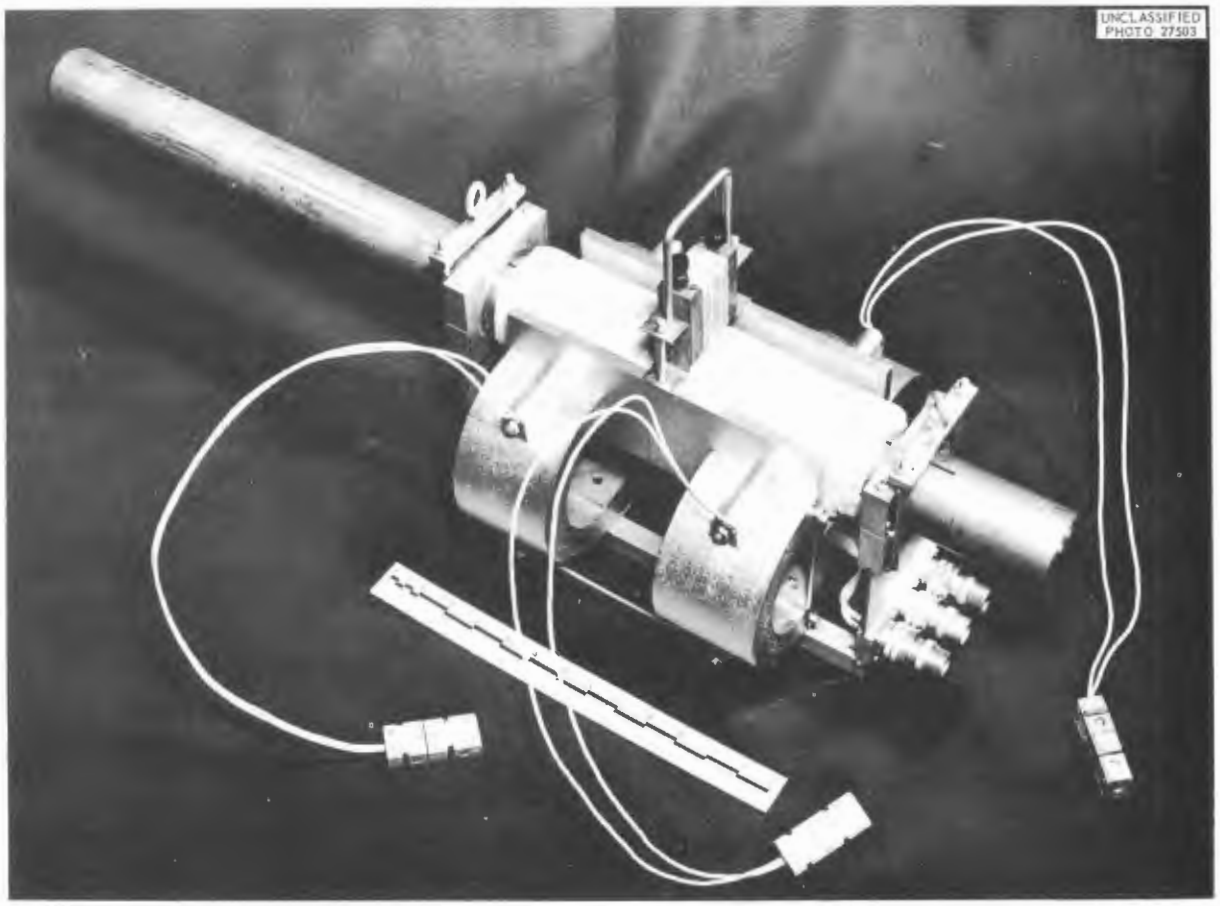

Fig. 1.3.5. G-E Magnetic Flowmeter Assembly for Use on 2-in. NaK Lines.

required an accuracy of within 3.5% for 3000 hr over a flow range of from 45 to 1400 gpm at NaK temperatures from 750 to 1600°F. The 2-in. units are required to have an accuracy of within 1% for 3000 hr at flow rates of 45 to 200 gpm and of within 5% at flow rates above 200 gpm at NaK temperatures from 750 to 1600°F. The specified magnet ambient range for both units is from 100 to 560°F.

A $\frac{3}{8}$-in. flowmeter has been designed for the ART and ETU cold-trap and plug-indicator systems. The $\frac{3}{8}$-in. unit will be required to have an accuracy of within ±15% over the flow and temperature ranges involved. Because of the relaxed accuracy requirement, these units will not be calibrated, but rather the output will be computed by use of the standard magnetic flowmeter equations. These units are now being fabricated in the required number, and it is hoped that the ETU units will be available by February 1.

It is planned to calibrate the 2- and $3\frac{1}{2}$-in. G-E flowmeters on the NaK pump test loops. The calibration of the units in the loops will, in addition to determining the accuracy (calibrated against a venturi accurate to 0.25%), serve to show the effects of temperature and handling and to provide information on the general operation of the units. The purchase specifications required that G.E. supply the instructions and information needed for calculation of the correct flowmeter output. The instructions and data which they supplied include air-gap-flux density values and leakage-flux density values at various temperatures of the magnet and fluid. The leakage-flux density is used to indicate changes in the air-gap-flux density while the units are in operation. This is done by measuring the air-gap-flux density and the leakage-flux density and correlating the two by a given factor for each flowmeter. In checking the air-gap and leakage fluxes of the magnets

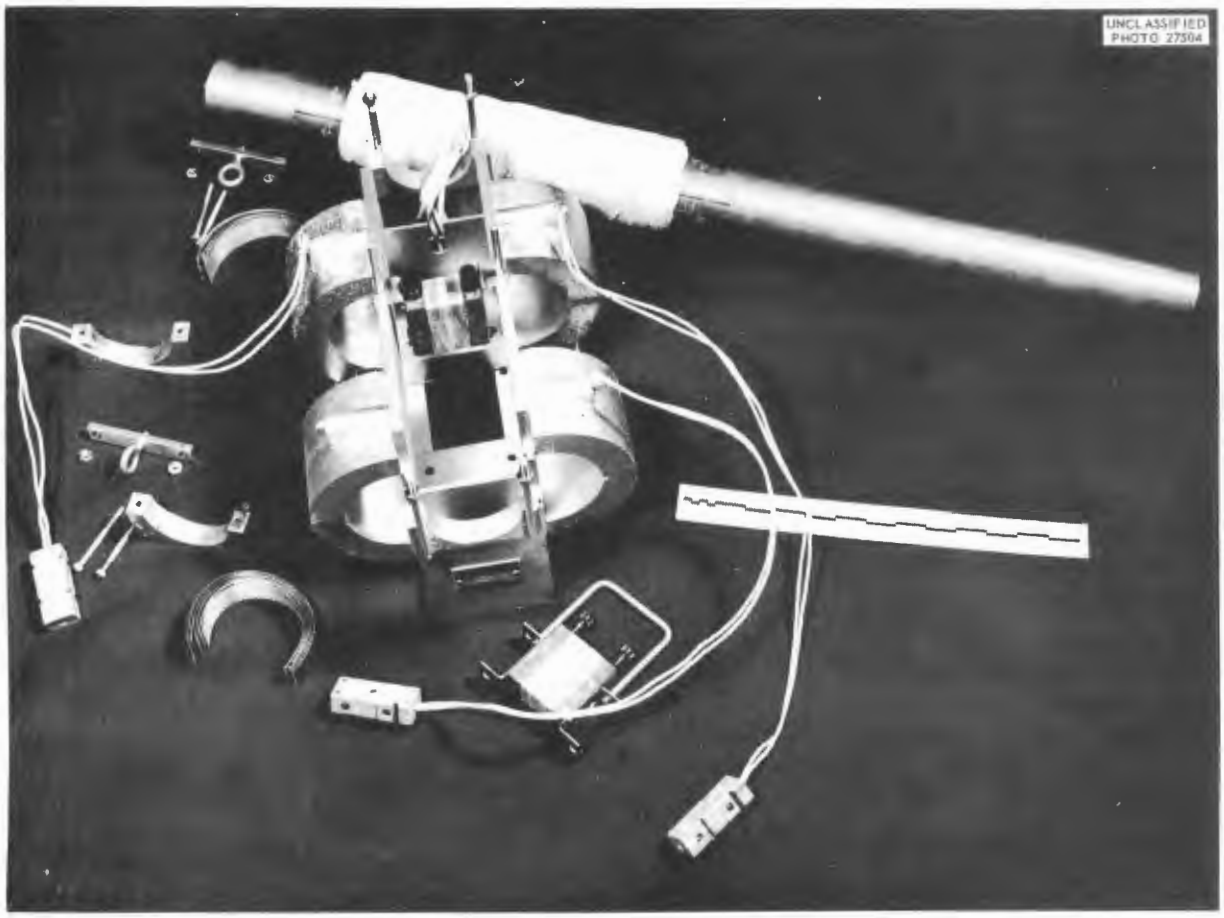

Fig. 1.3.6. Disassembled G-E Magnetic Flowmeter for Use on 2-in. NaK Lines.

prior to installing them into the NaK pump test loop, it was found that they were not in agreement with the G-E supplied data and, in some cases, that the variations were more than allowable under the accuracy specifications. The G-E representatives were notified of these discrepancies, and they are now in the process of checking the magnet flux in order to determine the source of error. The final results of these tests are not yet available, but it appears, on the basis of the tests made thus far, that the required specification has not been met in a number of cases. It is therefore felt that the final accuracy of the flowmeters can be determined only by actual loop operation and calibration. The calibration of the first six 3½-in. units should be completed in February, at which time the accuracy figures will be released to the appropriate personnel. All 3½- and 2-in. units will be calibrated, and the data will be made available to the ETU and ART operating personnel.

HIGH-TEMPERATURE TURBINE-TYPE FLOWMETERS

G. H. Burger

An evaluation study has been made of the available design, fabrication, and test information on the newly developed high-temperature turbine-type flowmeter which is illustrated in Figs. 1.3.8 and 1.3.9 and was described in previous reports.[3] A review of the test conditions and results is presented in Table 1.3.1.

As indicated in the table only three complete units have been fabricated. The other tests were

[3] G. H. Burger, *ANP Quar. Prog. Rep. June 10, 1956*, ORNL-2106, p 43, and *ANP Quar. Prog. Rep. Sept. 10, 1956*, ORNL-2157, p 36.

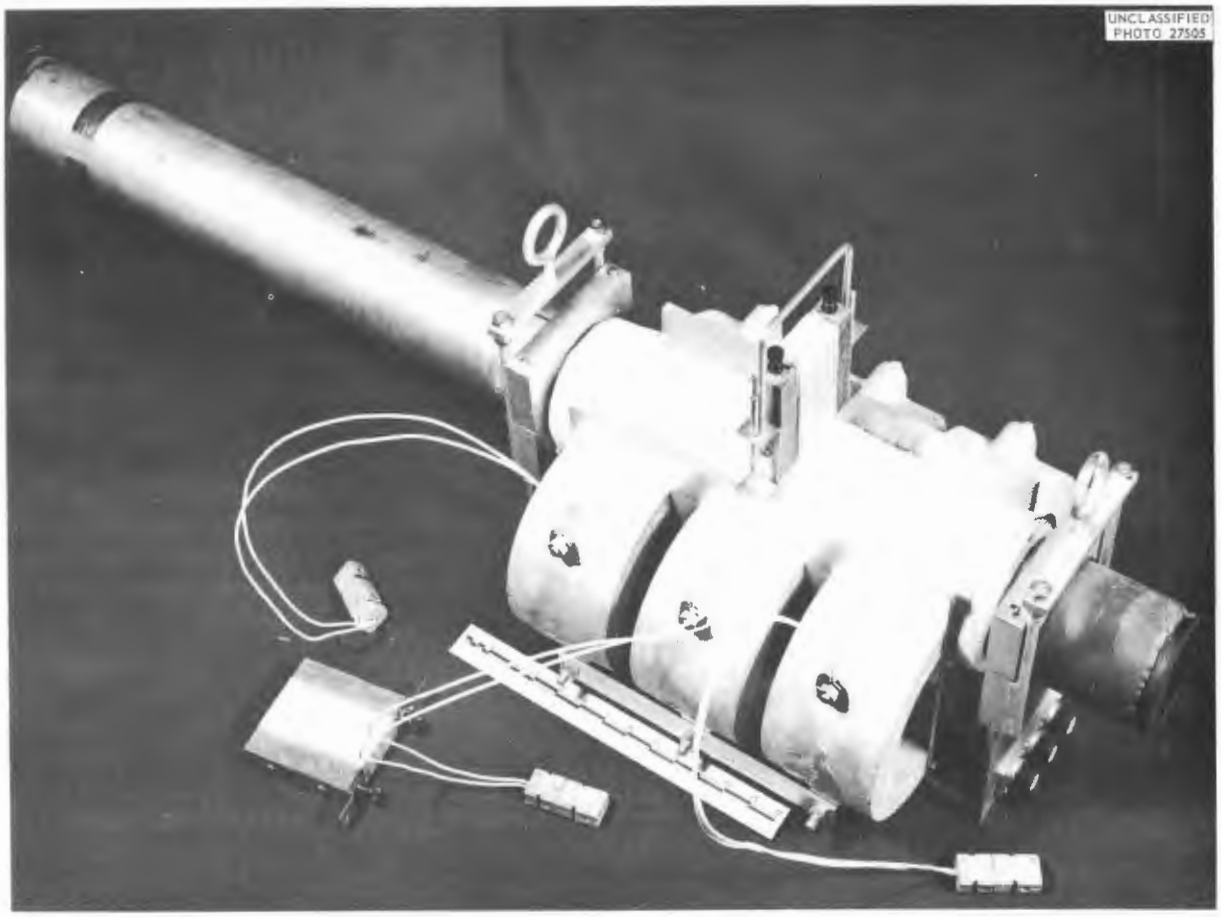

Fig. 1.3.7. G-E Magnetic Flowmeter Assembly for Use on 3-in. NaK Lines.

made with modified or repaired units, since none of the units which failed, except unit No. 1-Rev 1, were damaged to the extent that they had to be completely replaced. Unit No. 1-Rev 1 was damaged beyond repair, because excessive overheating while it was stationary caused the blades to collapse. The results of the tests which have been run thus far are inconclusive with respect to long-term operational reliability of the turbine flowmeters; however, the following conclusions can be drawn from the test results.

The operational principle of the unit is sound, and the unit is practical for use with liquid metals and fused salts at temperatures up to 1500°F and probably higher. The cobalt vane proved to be highly satisfactory for operation over the temperature ranges of interest. The general design of the unit appears to be satisfactory, but some improvement in pressure drop can be obtained by streamlining.

The bearing material (Kentanium) is the only uncertainty, and it appears to be satisfactory for the temperatures and fluids of interest on the basis of the rather short-term tests made to date. There has been no evidence of bearing self-welding in any of the units. Unit No. 1-Rev 1 was analyzed metallurgically, and no evidence of wear or sticking was noted. However, it was noted on unit No. 2-Rev 3 that the outside of the bearing was very soft to a depth of approximately 0.030 in. This soft material was found to be nickel, which was used as a binder and which presumably remained after the unit oxidized. Oxidation of the bearing material was the direct cause of the failure of unit No. 3-Rev 0. This unit was overheated in an oven during an attempt to

UNCLASSIFIED
PHOTO 27501

Fig. 1.3.8. ORNL High-Temperature Turbine-Type Flowmeter.

dry it after water calibration runs. The oxidation of the bearing material indicates that units with titanium carbide (Kentanium) bearings should be used only in systems relatively free from oxygen if they are to operate for the required 3000 hr.

A serious fault of the titanium carbide bearings is that because of their extreme brittleness a sudden shock can cause them to break, and this has happened with the bearings of every unit, except one, which has been removed from the system. This problem can be solved by redesign of the bearing shafts both in size and in construction.

The permanent magnet and pickup coil assembly appears to be satisfactory from the temperature standpoint, but 60-cycle pickup seems to be a considerable problem with the present units. This problem is alleviated somewhat by using 60-cycle rejection filters and by improving the shielding around the pickup coil.

The output signal from the units is fairly small (less than 1 mv) at low rotational speeds and thus increases the 60-cycle pickup problem. This problem can be resolved by redesign of the cobalt vane, the magnets, and the pickup coil to generate larger output signals.

TABLE 1.3.1. RESULTS OF TESTS OF ORNL 1-in. HIGH-TEMPERATURE TURBINE FLOWMETER

Turbine Unit Designation	Test Medium	Test Temperature (°F)	Turbine Running Time (hr)	Reason for Test Termination
1-Rev 0*	Fuel No. 30	1200	0	Jammed flowmeter bearing
1-Rev 1	Fuel No. 30	1000–1500	365	Broken turbine shaft and bad pump seal
2-Rev 0	NaK	72–1200	126.8	NaK pipe leak
2-Rev 1	NaK	72–1400	143.4	NaK pipe leak
2-Rev 2	NaK		0	Bad pump seal
2-Rev 3	NaK**			
3-Rev 0	NaK		2	Oxidation of flowmeter bearings because of excessive preheating without an inert atmosphere

*"Rev" indicates revised or repaired unit.

**Not yet operating.

Fig. 1.3.9. Disassembled ORNL High-Temperature Turbine-Type Flowmeter.

In order to determine the feasibility and reliability of the turbine flowmeter for its intended long-term operation, tests are to be performed with a number of improved units in one test loop. For comparison with the results of these tests of the small (1-in.) units, it is hoped that results of tests of a $3\frac{1}{2}$-in. flowmeter now being installed in the NaK pump test loop for operational tests and calibration with NaK will be available. The large unit will operate at flow rates of up to 1400 gpm at temperatures up to 1500°F. This unit has been calibrated with water at flow rates of up to 1100 gpm. The output signal vs flow rate correlation is extremely good except at high flow rates, where the curve becomes nonlinear, as shown in Fig. 1.3.10. The cause of this deviation from linearity has not been determined, but it could be either the venturi or the turbine.

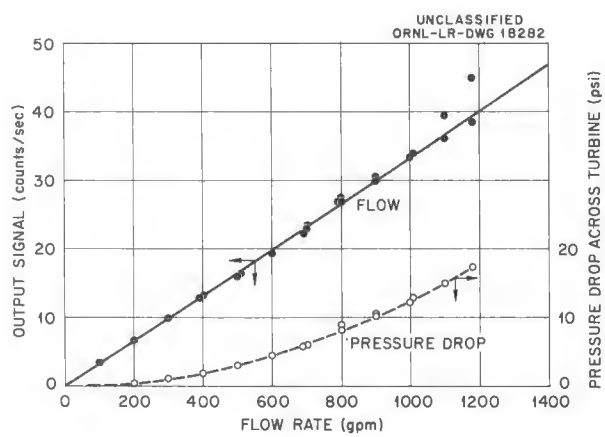

Fig. 1.3.10. Results of Water Calibration Tests of $3\frac{1}{2}$-in. Turbine Flowmeter (Unit No. 2, Rev 1).

SPARK-PLUG LIQUID-LEVEL PROBES

A. M. Leppert

Work is under way on the development of an on-off type of liquid-level-indicator probe that will operate reliably at NaK system temperatures for a minimum of 1000 hr. To date, no spark plug tested has met these specifications.

The Auburn Spark Plug Co. high-temperature liquid-level probe, designated WCC-121, failed completely during tests. With the plug shell at approximately 600°F, the plug shorted out in 36 hr. At 72 hr the insulation split and allowed NaK to escape to the atmosphere. Test units operating at 450°F were still functioning at 72 hr, but they were removed to reduce the hazard involved.

Several Champion Spark Plug Co. liquid-level probes, designated 344-X1, have been operating successfully for one month at temperatures below 500°F. When the Champion plugs were operated at temperatures between 600 and 750°F, they failed within 24 to 48 hr.

Some of these plugs were left in the test rig for six days in an attempt to reduce shorting by using a higher temperature. At the end of six days, the plugs were leaking NaK around the shell and center wire. Upon removal and examination, it was found that all the lower insulation had been dissolved by the liquid-metal vapor. The conclusions from these data are that the Auburn probes are completely unsuitable, that the Champion 344-X1 probes are satisfactory for periods of up to 750 hr if the probe shells are below 450°F, and that further tests are necessary.

A resistance type of probe is now being developed. This probe consists of an insulated low-resistance center wire inside a thin-walled Inconel tube. At one end the tube is welded shut and encloses the center wire. The tube is welded into a threaded fitting and placed in the test pot with the closed end exposed to the liquid metal. An a-c voltage is placed across the center wire and the pot, which is grounded. The load on the transformer is the combined resistance of the wire and tube when the probe is out of the liquid. When the probe contacts the liquid metal, the resistance of the tube shorts out. The accompanying change in current trips a relay to the control panel. This probe has the advantages that all surfaces exposed to the liquid-metal vapor are Inconel and that it can be welded into the system by replacing the threaded fitting with a welding flange.

In cooperation with Champion Spark Plug Co., a BeO insulator is being developed for use in the Champion N-7 special plug. As yet, none of these insulators are available. Champion is also working on the development of high-alumina-content insulation that may be more satisfactory than the insulation now used.

FUEL-EXPANSION-TANK LEVEL INDICATOR

R. F. Hyland

Static-Level Tests

Two tests of the helium-bubbler type of level indicator, described previously,[4] in static level systems were terminated. In one of the test systems one bubbler tube clogged after 1800 hr and the other remained open during 3000 hr of operation at 1500°F. In the other test system one bubbler tube clogged after 2460 hr and the other after 2950 hr at 1500°F. All the bubbler tubes were 0.25-in.-OD, 0.035-in.-wall Inconel tubing, and, as in previous tests, the plugging was apparently due to ZrO_2 deposits in the tube.

Two additional 3000-hr static-level tests are planned. For these tests there will be careful control of the moisture and oxygen content of the helium purge gas. The helium will first be passed over copper turnings maintained at 1000°F and will then be scrubbed with NaK. Dew-point and oxygen analysis tests will be made on the vent gas before the rig is filled and on the supply header periodically thereafter. As a further control measure, it is planned to have a sample of the fuel fill analyzed for oxide content, if it is practical to do so. This is not now being done on a routine basis.

Dynamic-Level Tests

A dynamic-level test rig which mechanically varies the fuel level in two vessels on an adjustable cycle has completed 4000 cycles at 1500°F in 500 hr of operation. Moisture and oxygen control features, as described above, were added to this test rig before it was filled, in order to reduce the bubbler plugging problem. The vent gas from the rig before it was filled had a dew point of −160°F, which was equal to

[4] R. F. Hyland, *ANP Quar. Prog. Rep. June 10, 1956*, ORNL-2106, p 43.

the supply header dew point, and the oxygen content was reduced from 1.5 ppm at the header to 0.6 ppm at the rig.

The apparatus was calibrated by filling it in approximately 1-in. increments and by using an accurately positioned variable probe as a reference. In spite of the improved calibration technique, in comparison with that used on the static-level rigs, errors in measurement ranged from 3 to 7.5% of the total level. Considerable trouble with ZrF_4 vapor was encountered while attempting to fill in small increments, and consequently the reproducibility of the measurements could not be checked at the time of filling; however, it will be checked later.

The large error that still exists in these measurements can probably be accounted for, in part, by the inaccuracy (±5%) in the measured density of the fuel mixture (No. 30) NaF-ZrF_4-UF_4 (50-46-4 mole %). However, since this error is constant for a given batch of fuel, other errors must exist. Probes and bubbler tube lengths change with temperature, exact probe placement is somewhat uncertain, and temperature gradients in the mass of the fuel might produce a density error at the measuring point. In addition, the level sensors now being used are differential pressure cells with metal diaphragms and all-welded construction of the type required for reactor installation. They have an inherent inaccuracy of ±1% and are ambient-temperature sensitive. Similarly, the recorder being used as a readout device has an inherent error of ± ½%.

It is planned to use a differential manometer for the next series of calibrations to eliminate the differential pressure cell and recorder as sources of error. A separate differential-pressure cell test and an evaluation program are also planned.

HIGH-TEMPERATURE PRESSURE TRANSMITTERS

W. R. Miller

The high-temperature pressure-transmitter test and evaluation program was continued. Six units were tested which feature a fabricated (rather than formed) Inconel bellows in a 1:1 pneumatic force-balance type of transmitter. The desirable feature of the fabricated bellows in comparison with the formed bellows is that it can withstand greater differential pressures. Tests have revealed that these units have an average zero shift of ±1.58% of full scale from room temperature to 1400°F, with an average accuracy of ±0.4% of full scale at a constant temperature. Two of the six units tested, as well as one unit of the strain-gage type (mentioned in the previous report[5]), have successfully completed 2430 hr of a 3000-hr life test.

Six transmitters have been received which employ a differential transformer to detect the motion of a fabricated-bellows sensor. Two of these units are being readied for testing as an alternate method of electrical transmission for high-temperature pressure measurement. The large size of these units eliminates them as a first consideration.

One transmitter has been received and is being readied for a test in which a variable-permeance transducer will be employed to detect the motion of a formed bellows sensor. If the tests indicate satisfactory performance, the housing of this unit will be modified to make it practical for production use.

The tests on the two-legged strain-gage type of transmitters described previously[5] proved thses units to be unsatisfactory. Thermal instability was encountered because of the high resistances required to produce a usable resistance change over a narrow pressure span. Since a solution to this problem would require considerable time and no distinct advantages can be foreseen for this unit in comparison with the four-legged strain-gage bridge, it was decided to forego further investigation.

Additional four-legged strain-gage transmitters were tested, and the results were very satisfactory. These units have accuracy and zero shift averages equal to those of the units tested previously,[5] that is, average accuracy, ±0.25% full scale; zero shift, ±1.7% of full scale between room temperature and 1400°F. Through close cooperation with the manufacturer, it has been possible to arrange for compensating changes of the housing which will diminish the effect of ambient changes by a factor of 2.

[5]W. R. Miller, *ANP Quar. Prog. Rep. Sept. 10, 1956*, ORNL-2157, p 37.

An experimental model of a differential-pressure transmitter for high-temperature operation is being prepared for testing. Fabrication of the unit has been completed, but the unit will require annealing before satisfactory data can be obtained.

Stress-analysis studies have been made on the Taylor and Moore sensing unit housings. The analysis indicates that a housing thickness increase will be required to make these units satisfactory for operation at 1500°F.

1.4. COMPONENT DEVELOPMENT AND TESTING

H. W. Savage

PUMP DEVELOPMENT TESTS

E. R. Dytko[1] A. G. Grindell

Bearing, Seal, and Lubricant Tests

W. L. Snapp[1] W. K. Stair[2]

Further results have been obtained from tests of the compatibility of proposed ART pump lubricating-cooling fluids and the ART process fluids (see Chap. 2.6, "Analytical Chemistry," this report and ref. 3). The tests revealed that all the lubricating-cooling fluids being considered for use in the ART pumps are inert both to sodium and to the fuel mixtures of interest. The lubricants tested were Dowtherm-A, OS-45, Gulfspin-60, and Gulfcrest-34. More information concerning lubricant behavior in dynamic systems exposed to radiation and on the radiation exposure to be expected in the ART is needed before the final fluid selection is made. Therefore a series of dynamic tests is to be run in the LITR, and a critical assembly is being measured that includes a mockup of the ART north head.

Tests of the compatibility of elastomers of interest for seal application with the lubricating-cooling fluids being considered were continued. Buna-N O-rings were exposed to Gulfcrest-34 (a paraffinic-base mineral oil) for about 700 hr, during which time the temperature was varied periodically from 90 to 210°F in ½-hr intervals. The exposure periods at 210°F were approximately twice as long as the periods at 90°F. The hardness and strength of the buna-N O-ring were found to have been only slightly affected by the exposure to Gulfcrest-34. Buna-N O-rings are now being tested in the lubricating-cooling fluid UCON LB-140X (polyalkylene glycol).

Further studies were made of the journal bearings of the ART sodium pumps because of an increase in the developed head required. Several tests were conducted on rotary elements operating at 4400 rpm with an equivalent journal bearing load of greater than 600 lb. The rotary elements operated satisfactorily in all these tests, and no deleterious effects of increased journal bearing load were noted. For all the tests, bronze bearings were used which had an initial cold-shrink fit to their steel housings of 0.0005 to 0.0015 in. The bearing rubbing previously noted[4] was found to have been caused by the inadequacy of the original cold shrink (0.003 to 0.004 in.). At the operating temperature of about 200°F, a bronze-steel interface pressure was created that was greater than the yield strength of the bronze for 0.5% elongation. The reduced cold shrinkage tolerance given above has been established for all rotary elements, and no further evidence of bearing rub has been noted.

Further testing of the Cartiseals proposed by a vendor for use in the NaK pumps indicated that the elastomer used in the seal is unsatisfactory and as a result the seal leakage rate increases with continued operation, as previously noted.[4] The elastomer O-rings were replaced by the vendor and the tests have been resumed. Since the O-rings in the Cartiseal are enclosed in a formed cup, they are difficult to change. In addition, the light unit face loading makes the seal balance critical, and the balance could be a problem in vacuum filling operations. Therefore, it is doubtful that this seal can be used for the ART NaK pumps.

Continuously acceptable leakage rates have been obtained in 4000 hr of testing of modified Duramettallic seals. These seals utilize a ceramic-faced steel rotor and a carbon stator. The seal is loaded by multiple springs behind the rotor, and the secondary O-ring seals are readily accessible. Differential pressures as high as 12 psi have been applied in both directions (process fluid to oil and oil to process fluid) without affecting the leakage rate. These tests indicate that the modified Duramettallic seals will be satisfactory for use in the ART NaK pumps unless more extensive tests reveal further problems.

[1] On assignment from Pratt & Whitney Aircraft.

[2] Consultant from the University of Tennessee.

[3] G. Goldberg, A. S. Meyer, Jr., and J. C. White, *Compatibility of Pump Lubricants with Alkali Metals and Molten Fluoride Salts*, ORNL-2168 (Dec. 28, 1956).

[4] W. L. Snapp and W. K. Stair, *ANP Quar. Prog. Rep. Sept. 10, 1956*, ORNL-2157, p 39.

Analysis of Hydraulic Drive Failures

P. G. Smith

Several hydraulic pump drive units obtained from The Dension Engineering Co. have failed in service on fuel and sodium pump test stands. The operating histories of these hydraulic units are given in Table 1.4.1.

Motor No. 5971 failed after 1929 hr of operation at speeds from 2400 to 2700 rpm because one of the seven piston shoes broke up into small parts. The other six shoes were found to be severely worn. Motor No. 5969 failed in a similar manner after 2500 hr of operation, but the wear on the shoes was less severe. Motor No. 7652 failed in a similar manner when it was placed in operation at ORNL. This motor was run by the manufacturer for 40 hr prior to shipment.

The 700 series pump failed after 4400 hr of operation because the bolt-clevis portion of the wobble-plate positioning mechanism broke. It is believed that this failure had its inception in the use of mechanical stops in conjunction with the motor-driven wobble-plate positioner.

The manufacturer is working on the piston shoe problem. Recent developments indicate that the poor reliability of these drive units can probably be overcome by using an available motor which has been proved to be durable at speeds up to 4000 rpm.

Fuel Pump Development Water Tests

M. E. Lackey G. Samuels
J. J. W. Simon[1]

Thorough water testing and evaluation of a fuel pump with an acceptable impeller has continued in one of the two high-temperature performance-test loops. A similar pump is operating in the other loop with the fuel mixture (No. 30) $NaF-ZrF_4-UF_4$ (50-46-4 mole %).

The primary items being investigated are, as previously reported,[5] (1) the possibility of reducing the magnitude of the loop liquid-pressure fluctuations, (2) means for establishing a decreasing gas pressure gradient in the direction of gas flow from the oil catch basin down the shaft annulus into the expansion tank and out through the off-gas line, as shown in Fig. 1.4.1, (3) means for regulating the liquid flow rate through the hollow pump shaft, expansion tank, and centrifuge cup flow path, also shown in Fig. 1.4.1, (4) the possibility of reducing the level of the loop pressures relative to the expansion tank gas pressure to reduce the stress loads on the north-head assembly, and (5) cavitation effects. Satisfactory results can be reported for the first three investigations. The magnitude of the pressure fluctuations was reduced to within acceptable limits, the decreasing gas pressure gradient was established, and the fluid

[5] J. J. W. Simon, M. E. Lackey, and G. Samuels, *ANP Quar. Prog. Rep. Sept. 10, 1956*, ORNL-2157, p 40.

TABLE 1.4.1. OPERATING HISTORIES OF HYDRAULIC PUMP DRIVE UNITS THAT FAILED IN SERVICE

Hydraulic Unit	Operating Time (hr)	Maximum Speed (rpm)	Maximum Power (hp)	Maximum Pressure (psi)
600 series motor, serial No. 5971	1929	2700	27	3000
600 series motor, serial No. 5969	2500	4600	45	4000
600 series motor, serial No. 7652	40*	4600**		5000**
700 series pump	4400	1200		3000

*Operated at factory.

**Reported by manufacturer.

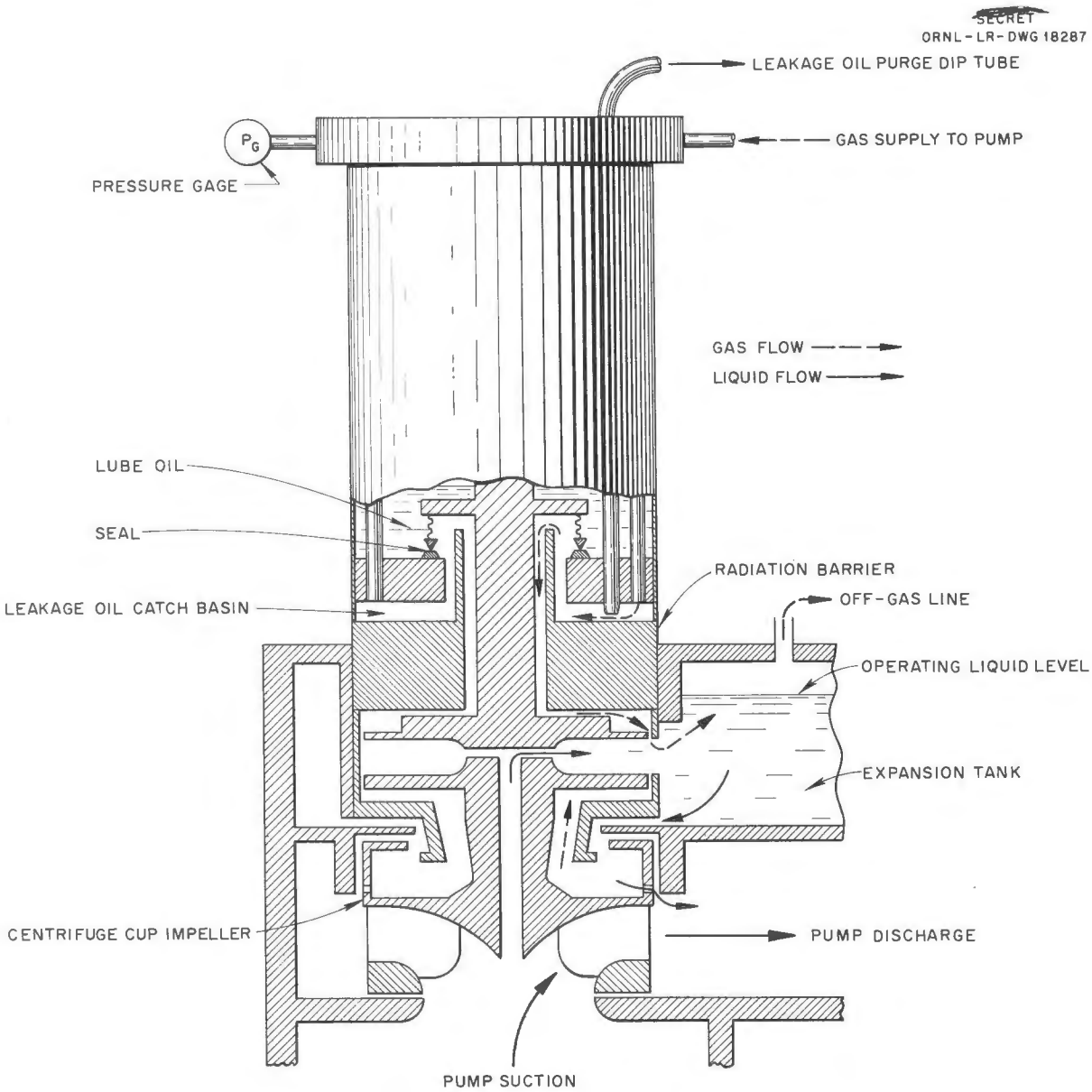

Fig. 1.4.1. Schematic Diagram of Impeller Region of ART Fuel Pump.

flow into the expansion tank was regulated to the desired range. The study of the problems involved in lowering of the loop liquid pressures relative to the gas pressure in the expansion tank to meet stress limitations imposed upon the deck plates in the north-head assembly is described below.

Plots of the suction pressure minus the gas pressure in the expansion tank for several combinations of impeller speed and liquid depth in the expansion tank, based on data obtained with the original pump impeller, are shown in Fig. 1.4.2. Two modifications were considered for reducing the loop pressures, and initial investigations were made of both types. Method A consisted in reducing the diameter and number of the centrifuge cup discharge holes. A blank centrifuge cup (that is, no discharge holes) was fabricated for the main impeller. This modification was tested and was

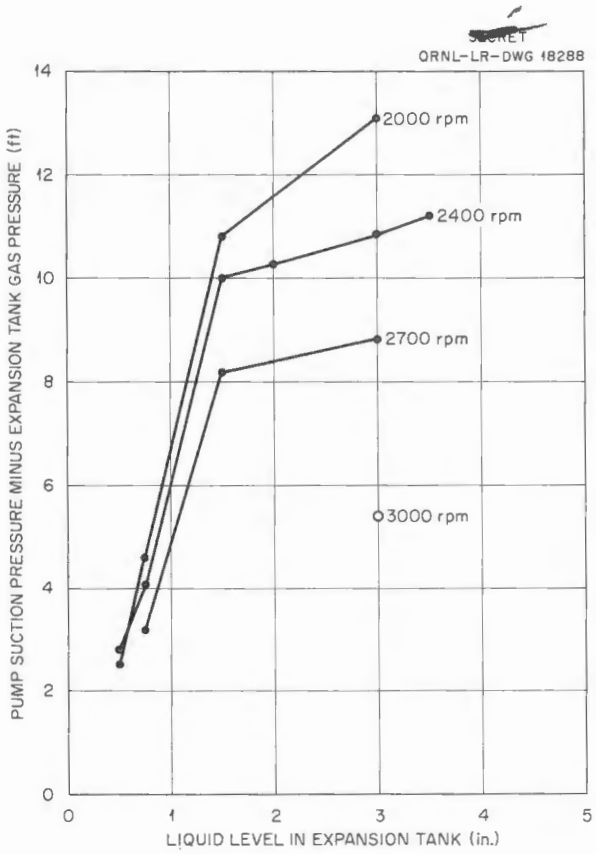

Fig. 1.4.2. Suction Pressure Minus Gas Pressure in Expansion Tank of Fuel Pump with Original Impeller As a Function of Liquid Level in Expansion Tank for Various Pump Speeds and a Flow Rate of 645 gpm.

found to be unsatisfactory. There was no degassing because the fluid from the expansion tank flowed over the top of the cup without being centrifuged. This configuration was modified, progressively, by increasing the size and the number of the cup discharge holes until the point of acceptable operation was reached. It was found that degassing of the system fluid was possible with twenty-two $\frac{1}{8}$-in.-dia holes. An additional modification was made that involved tapering the cup discharge ports from the inside to the outside. A 30-deg included angle was cut that left a sharp-edged $\frac{1}{8}$-in.-dia hole on the outer surface of the cup. This modification lowered the differential between the suction pressure and expansion-tank gas pressure by about 1 ft for normal operating conditions, and it was found that this pressure difference was quite insensitive to operating liquid level changes. The suction pressure differentials measured for selected pump speeds and liquid levels are plotted in Fig. 1.4.3.

It is believed that the centrifuge cup with the fewer and smaller holes would be of advantage under one-pump-stopped conditions during operation of a twin-pump configuration. The fewer and smaller centrifuge holes would increase the resistance to flow up through the stopped impeller into the expansion tank. Such a reduction of the upflow would lower the degree of overload on the centrifuge of the operating pump and thereby reduce the violence of ingassing that would occur when one pump stopped.

Method B consisted in increasing the inside diameter of the centrifuge cup top surface and leaving the thirty-three $\frac{1}{4}$-in.-dia holes of the original impeller unchanged. This modification allows the use of the present impellers by removing

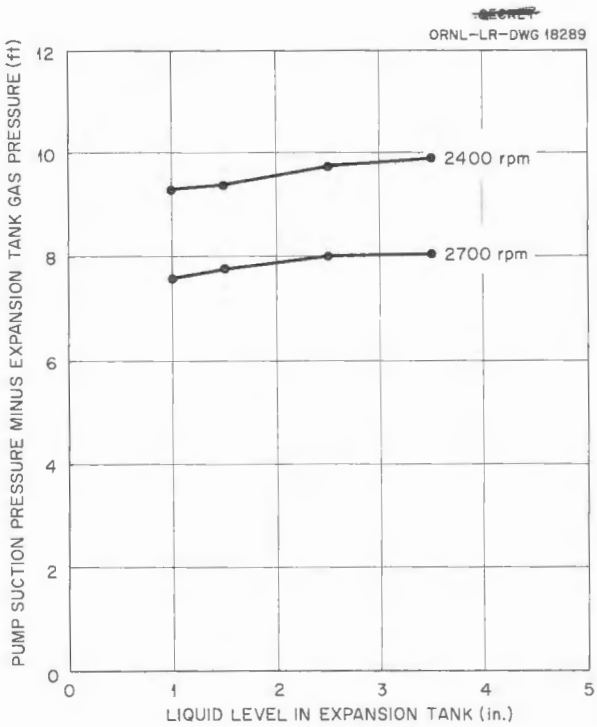

Fig. 1.4.3. Pressure Differential in Fuel Pump with Centrifuge Cup Containing Twenty-Two $\frac{1}{8}$-in.-dia Tapered Holes Operating at a Flow Rate of 645 gpm.

a small amount of metal from the inner surface of the top cover of the centrifuge cup assembly. Tests of this modification show about 1½-ft greater reduction, compared with method A, of the differential between pump suction pressure and the expansion-tank gas pressure under design operating conditions. The pressure differentials obtained with this modification for various liquid levels and selected pump speeds are shown in Fig. 1.4.4. For this configuration, the pressure difference is somewhat more sensitive to liquid levels than it is for method A. The suction pressure level shows a tendency to decrease more sharply when the liquid level is below about 1½ in. However, this configuration does not exhibit as much variation of pressure difference as was found to accompany liquid level changes in the original configuration. A schematic diagram of the impeller region of the ART pump modified according to method B is shown in Fig. 1.4.5. The impeller of this design is designated model 32.

The developmental work on both methods A and B was carried on simultaneously. Method B was found to give very satisfactory results with only minor changes to the original design, and these

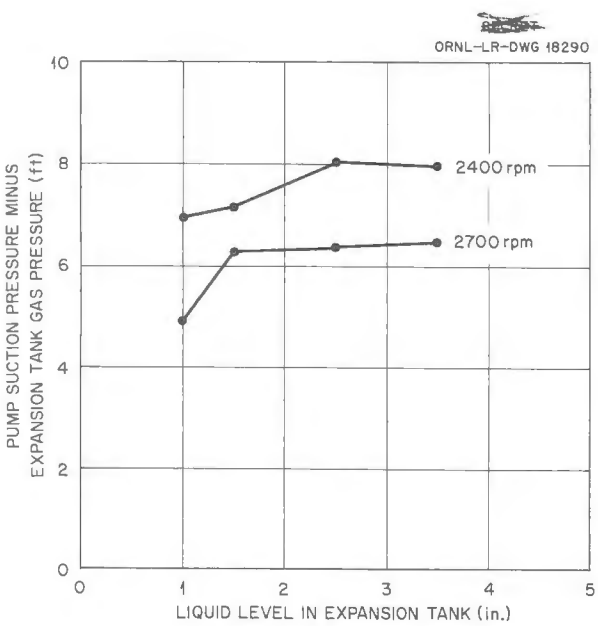

Fig. 1.4.4. Pressure Differential at a Flow Rate of 645 gpm in Fuel Pump with Centrifuge Cup Modified According to Method B.

changes could be made to the existing pump and centrifuge assembly without additional welding. At the time that method B was found to give the desired results, the developmental work on method A was not complete in that the difference between the pump suction pressure and the helium pressure had not been reduced to that required for stress considerations. It was felt that the possible advantages of method A were not sufficient to justify the additional time required to properly size the centrifuge and the increased cost of this method. In addition, the changing of the existing pump and centrifuge assembly to method A would require welding of the finished pieces to the assembly and would probably require the procurement of new pumps.

Subsequent tests with the model 32 impeller indicated that the flow through the shaft feed holes, the xenon-removal expansion tank, and the centrifuge cup was insufficient for proper ART northhead cooling. The suction pressure decrease had caused the flow through the pump shaft to the expansion tank to decrease appreciably. Determination of this flow rate and resizing of the shaft feed holes was accomplished by the method previously described.[5] The effect of increasing the diameter of the shaft feed holes on the pressure differential for selected pump speeds and various liquid levels in the xenon-removal expansion tank is illustrated in Fig. 1.4.6.

The model 32 impeller is currently being subjected to extensive evaluation tests. The pump suction pressure characteristics as a function of liquid levels in the expansion tank for a pump with the model 32 impeller are shown in Fig. 1.4.7. The performance data taken on six constant-resistance lines with a 3-in. depth of liquid in the expansion tank are plotted in Fig. 1.4.8, and Figs. 1.4.9, 1.4.10, and 1.4.11 show the cavitation parameter σ for three flow rates at three constant pump speeds. The data indicate that σ increases with increasing flow at constant speed and decreases with increasing speed at constant flow. The minimum allowable differential between the gas pressure in the expansion tank and the vapor pressure of the working fluid at the suction temperature in order to prevent cavitation is shown in Fig. 1.4.12 as a function of the pump speed, flow rate, and expansion tank liquid level.

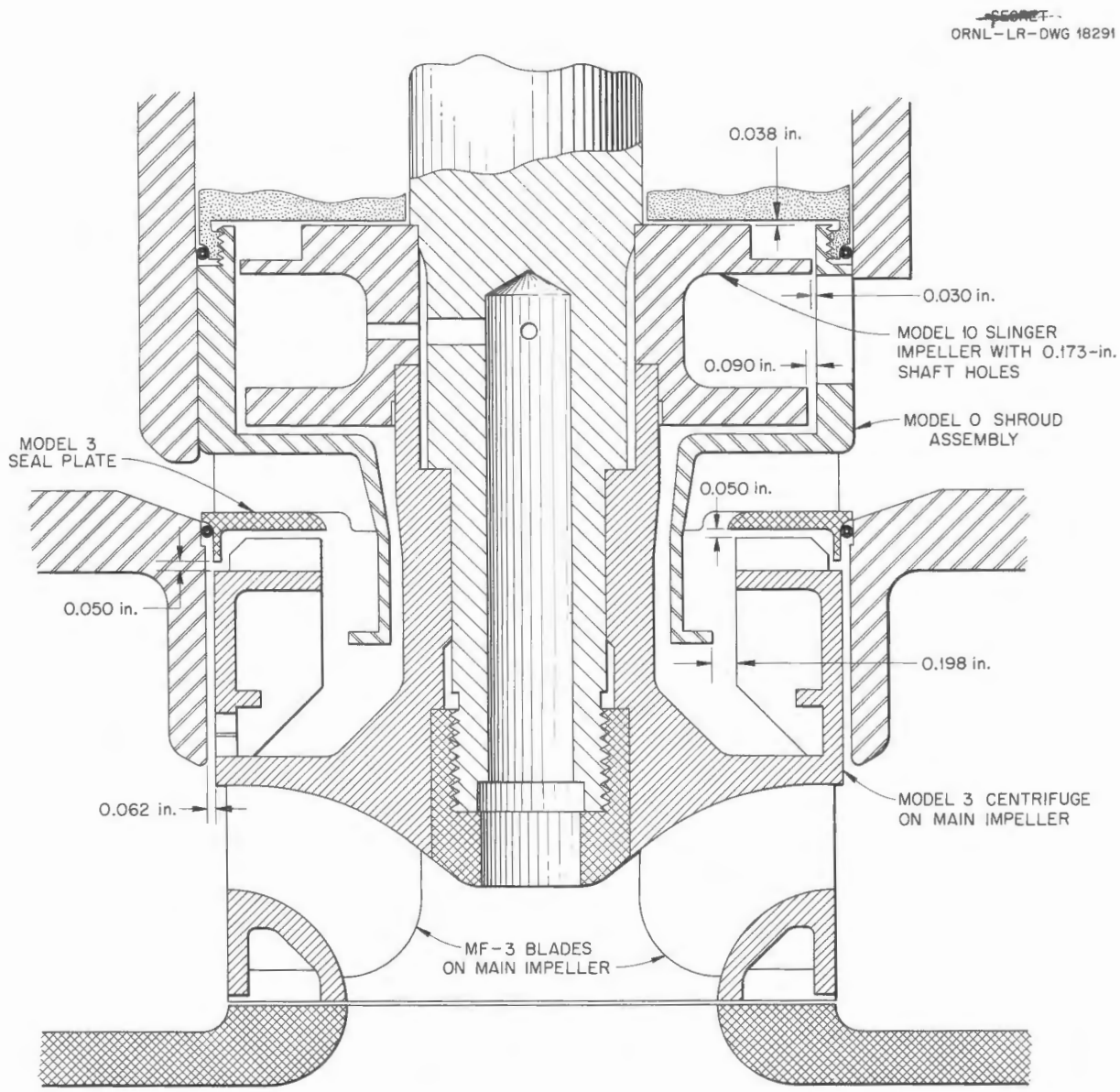

Fig. 1.4.5. ART Fuel Pump with Model 32 Impeller.

Model 32 impellers are being installed on fuel pumps for testing in the twin pumps of the aluminum north-head water test loop. The effects of one pump on the other at equal, as well as mismatched, operating speeds will be studied. Also a model 32 impeller fabricated of Inconel is to be used in high-temperature tests of the pump with the fuel mixture (No. 30) $NaF\text{-}ZrF_4\text{-}UF_4$ (50-46-4 mole %) as the circulated fluid.

Fuel Pump High-Temperature Performance Tests

H. C. Young[1] P. G. Smith

A test loop has been prepared for high-temperature operation of an ART fuel pump with a model 32 impeller and the fuel mixture (No. 30) $NaF\text{-}ZrF_4\text{-}UF_4$ (50-46-4 mole %) as the circulated fluid. The assembled loop has been cleaned by circulating a

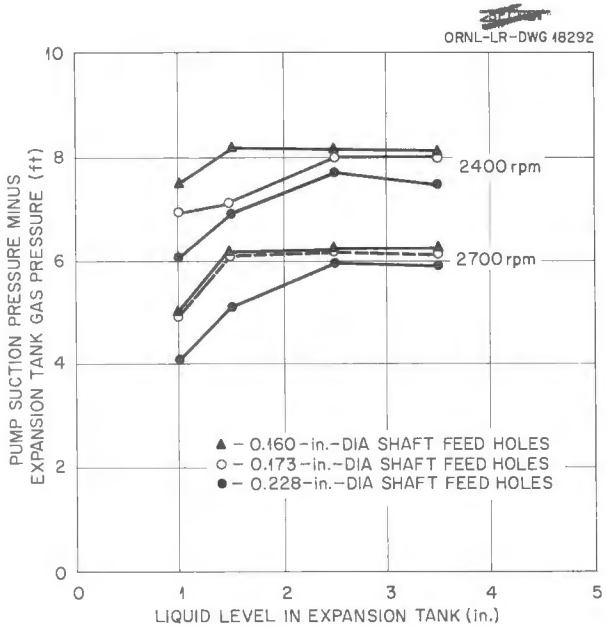

Fig. 1.4.6. Pressure Differential at a Flow Rate of 645 gpm in ART Fuel Pump with Model 32 Impeller (Development Test Data).

cleansing fuel mixture, and it has been filled with the test fluid. Performance data will be obtained during the next quarter.

Fuel Pump Endurance Tests

P. G. Smith

The ART fuel pump (model MF) being tested for endurance has continued to operate satisfactorily at high temperatures with the fuel mixture (No. 30) $NaF\text{-}ZrF_4\text{-}UF_4$ (50-46-4 mole %) as the circulated fluid. The test has been interrupted three times as a result of hydraulic drive failures. However, 1896 hr of trouble-free operation of the pump at temperatures from 1100 to 1400°F has been accumulated. During the last 932 hr of this test, the pump has been thermally cycled 41 times over the temperature range of 1100 to 1400°F. These relatively slow thermal cycles required about 5-hr intervals.

Sodium Pump Tests with Water

P. G. Smith R. Curry[1]
J. J. W. Simon

The sodium pump tests with water as the circulated fluid were continued.[6] During the quarter,

[6]S. M. DeCamp, Jr., *ANP Quar. Prog. Rep. Sept. 10, 1956*, ORNL-2157, p 43.

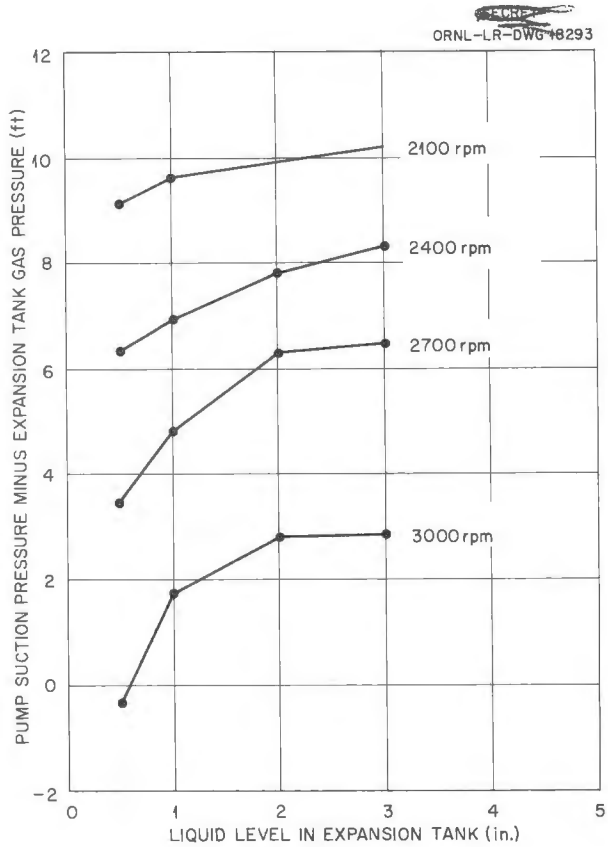

Fig. 1.4.7. Pressure Differential at a Flow Rate of 645 gpm in ART Fuel Pump with Model 32 Impeller and 0.173-in.-dia Shaft Feed Holes (Evaluation Data).

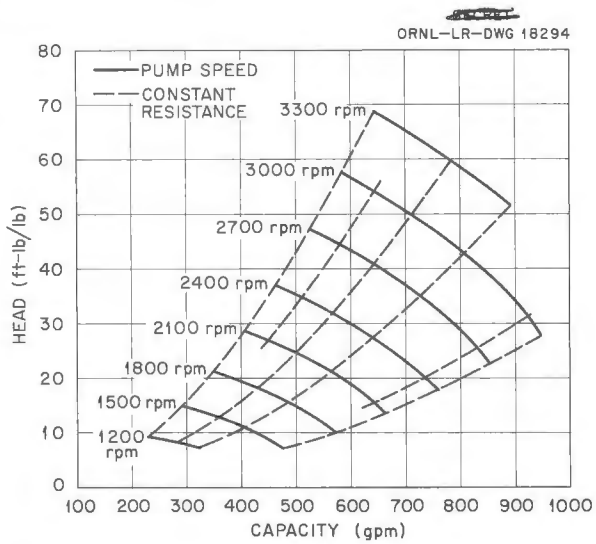

Fig. 1.4.8. Performance Curves for ART Fuel Pump with Model 32 Impeller and a 3-in. Depth of Liquid in the Expansion Tank.

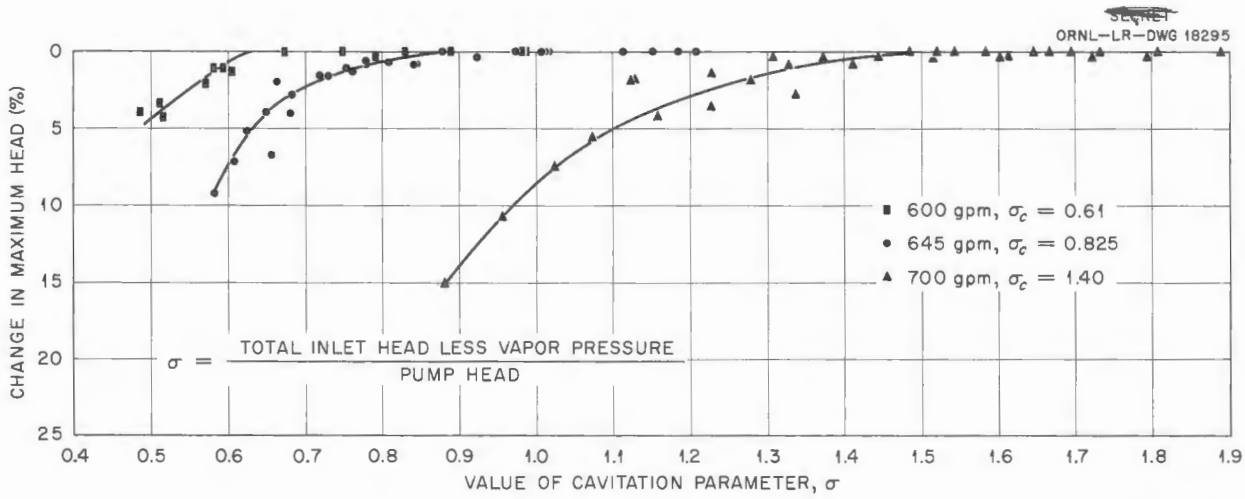

Fig. 1.4.9. Cavitation Characteristics of ART Fuel Pump with Model 32 Impeller at a Pump Speed of 2400 rpm and a 3-in. Depth of Liquid (Water) in the Expansion Tank.

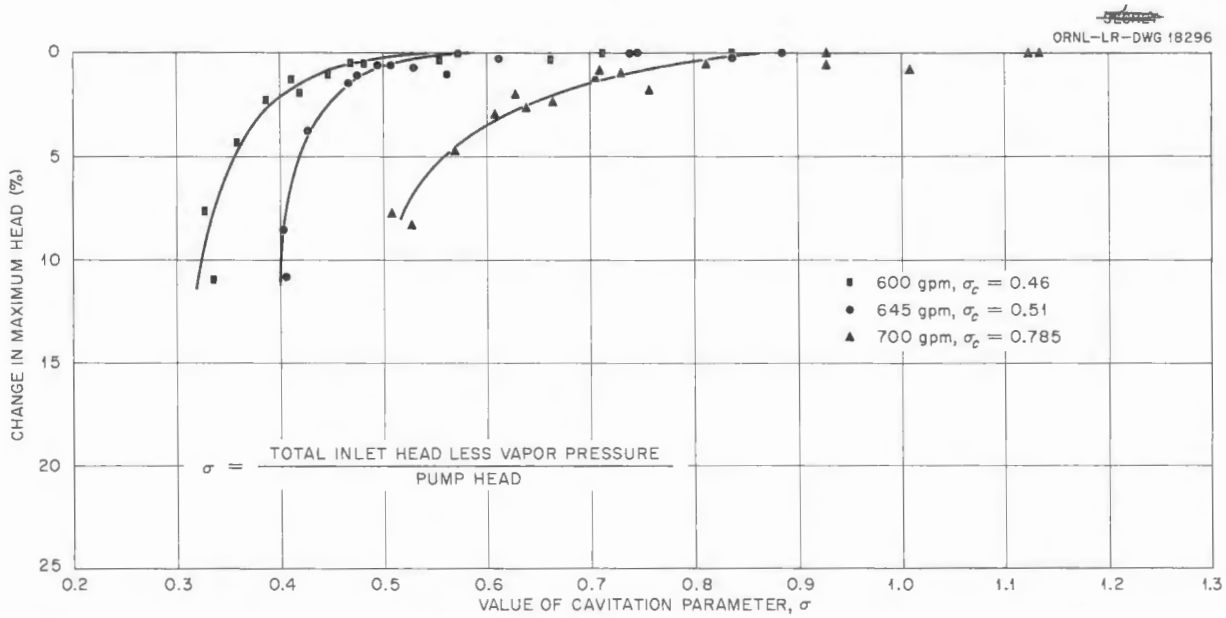

Fig. 1.4.10. Cavitation Characteristics of ART Fuel Pump with Model 32 Impeller at a Pump Speed of 2700 rpm and a 3-in. Depth of Liquid (Water) in the Expansion Tank.

the maximum head required for the ART sodium pumps was increased to approximately 165 ft at 440 gpm, and water tests at these operating conditions revealed ingassing. Tests have therefore been programed to evaluate the impeller-volute configuration under the new operating conditions with respect to the radial unbalance force and deflection and the centrifuge performance and to determine the pump head and flow characteristics.

Sodium Pump Tests with Sodium

P. G. Smith

An ART sodium pump was placed in a high-temperature test rig for testing with sodium at

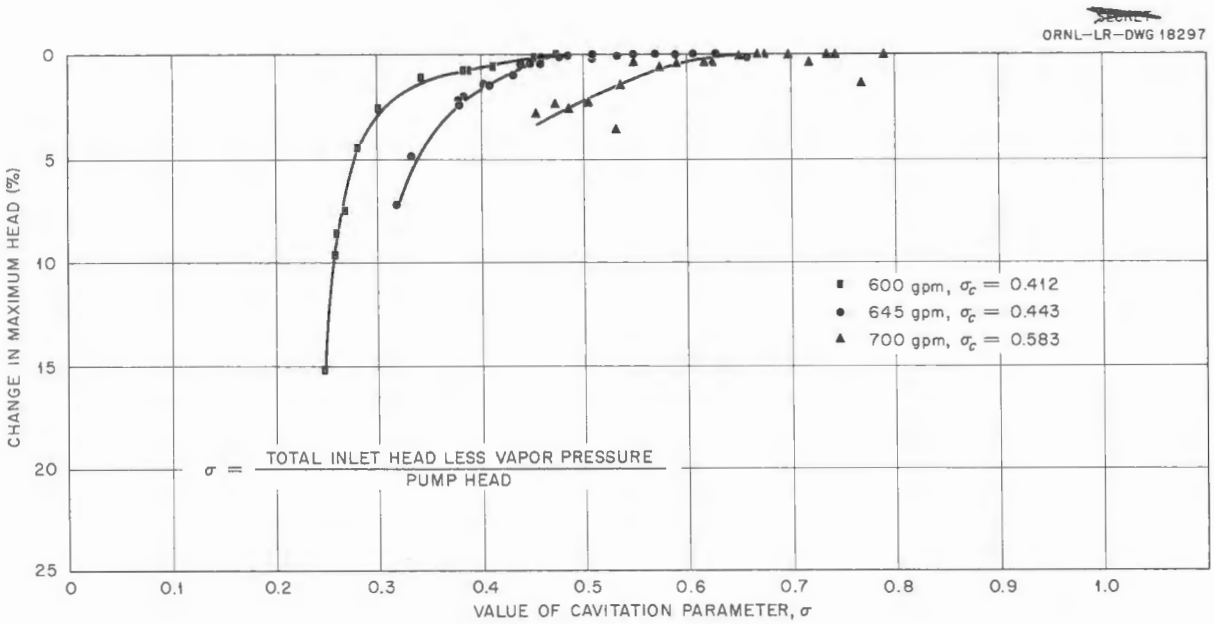

Fig. 1.4.11. Cavitation Characteristics of ART Fuel Pump with Model 32 Impeller at a Pump Speed of 3000 rpm and a 3-in. Depth of Liquid (Water) in the Expansion Tank.

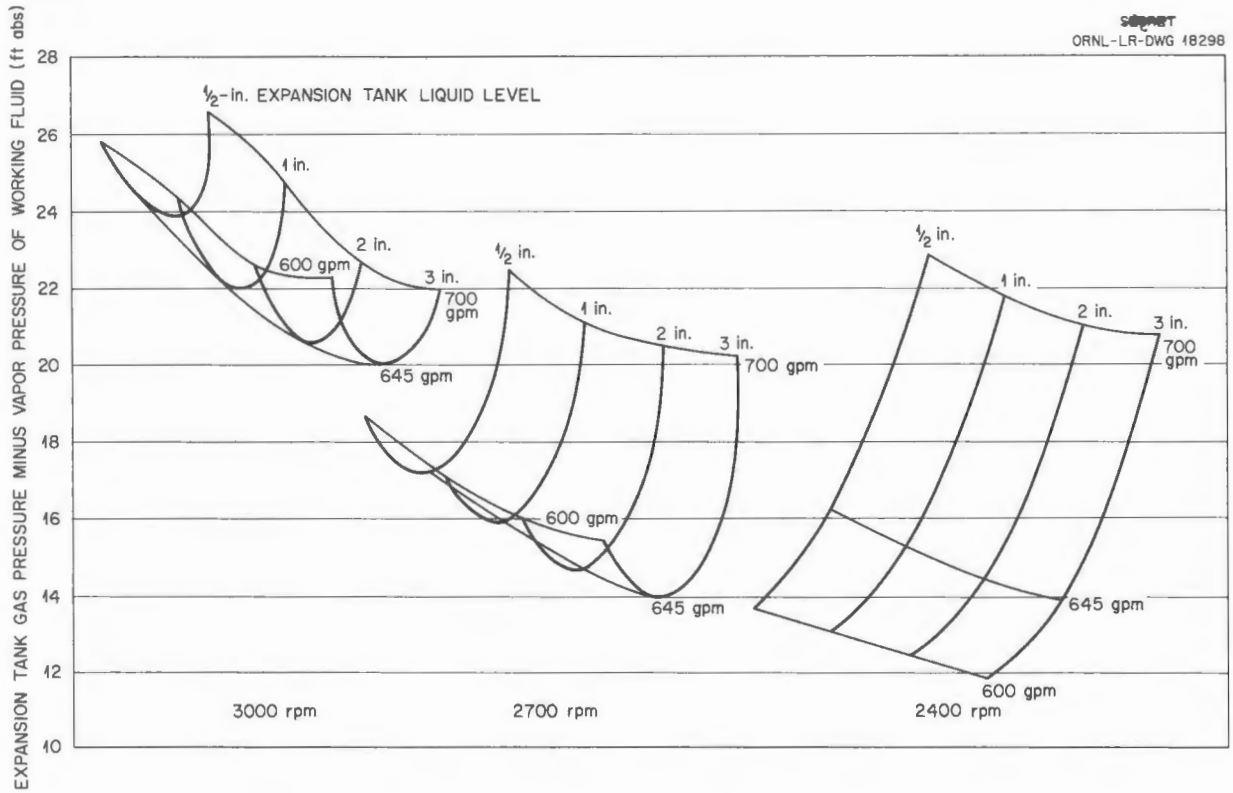

Fig. 1.4.12. Water Performance Characteristics of ART Fuel Pump with Model 32 Impeller.

temperatures of 1200 to 1350°F, and it has been operated for three short periods (total of 200 hr). These tests revealed several problems that were not evident in water tests, but which were brought out by the high temperature and the use of sodium. A bearing seizure occurred, and it was found to be necessary to increase the bearing clearance and to decrease the cold shrinkage tolerance. During one run sodium leaked past the O-ring seals and into the catch basin. Investigations revealed that the O-rings supplied by the manufacturer did not meet the tolerance specifications, and this problem is being studied further. Priming difficulties were encountered that may have resulted from gross ingassing on startup, and this problem will be investigated at the startup of the next test. Also the next test will be run with a lower sodium level in the pump pot in an attempt to prevent plugging of the off-gas lines with sodium. When these difficulties have been overcome the pump will be endurance tested.

Primary NaK Pump Development Tests

H. C. Young J. N. Simpson[1]

Water tests of the first primary NaK pumps fabricated from Inconel were completed. Heaters, insulation, and other equipment required for high-temperature testing with NaK were then added, and the high-temperature tests were started in late September. Performance curves obtained at a NaK temperature of 1200°F are presented in Fig. 1.4.13 and compared with the water test data for the same Inconel impeller and volute. The head was 2 to 3% higher for the test with NaK. Approximately 2% of the increase in the head can be attributed to an increase in the diameter of the impeller as a result of thermal expansion, and some of the increase, possibly 1%, may be attributed to errors in the calibration of the pressure-measuring instruments.

Cavitation data were obtained at the design flow rate for several different heads and at flow rates above and below the design rate. The data indicate that the cavitation parameters determined by the water tests are reasonably accurate for predicting the cavitation with NaK, if the difference between the vapor pressures of the fluids is considered. Two typical cavitation curves obtained with NaK at 1200°F are shown in Fig. 1.4.14. The critical cavitation values, σ_c, for NaK and for water at the

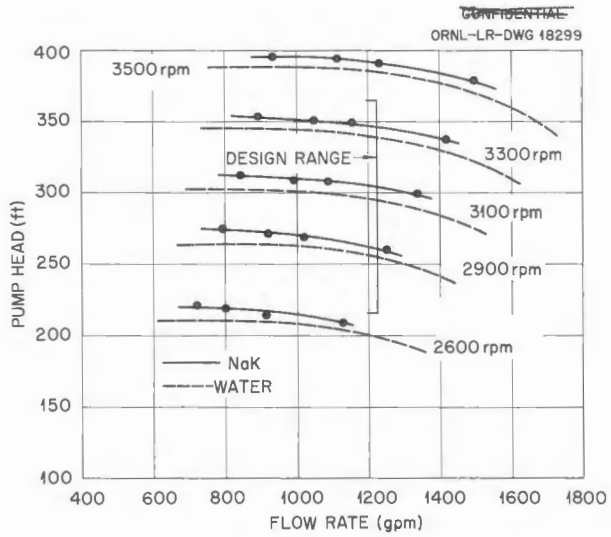

Fig. 1.4.13. Comparison of Performance Curves Obtained for the ART Primary NaK Pump Fabricated of Inconel When Tested with Water and with NaK at 1200°F.

similar heads and pump speeds for the same flow rate are also shown for comparison. As may be seen, both the performance and the cavitation data for operation with NaK correlate well with the water test data, and it was also found that the pump efficiency over the design range was 73 to 75% both for water and for NaK.

This first Inconel pump has operated at temperatures from 1000 to 1400°F for approximately 1000 hr. The oil seal leakage rates have remained within acceptable limits. Gas which was trapped in the pump discharge pipe during filling vented through the vent hole to the pump tank, and the pump primed satisfactorily on startup. The major operational problems encountered were plugging of off-gas lines with NaK vapor and ingassing during the cavitation tests. A condenser made of a 2-in. stainless steel pipe, 24 in. long, filled with Demister wool was connected to the off-gas lines, but some NaK vapor passed through this condenser and caused malfunctioning of helium pressure regulators. An auxiliary vapor separator, 3 in. in diameter and 8 in. long, has been installed in the off-gas line after the condenser, in an attempt to solve this problem, but more operational time will be required to evaluate the effectiveness of this separator.

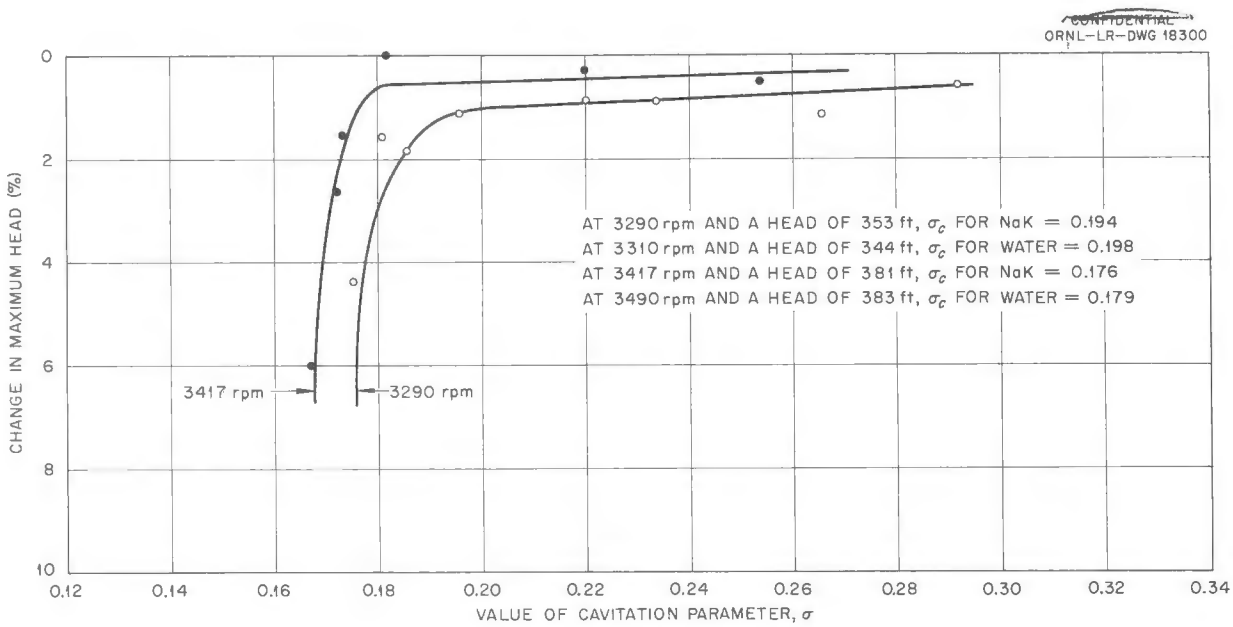

Fig. 1.4.14. Cavitation Characteristics of ART Primary NaK Pump Operated with NaK at 1200°F and a Flow Rate of 1220 gpm.

It was found that when the pump tank gas pressure was lowered to slightly below the pressure at which cavitation occurred, the pump ingassed, as evidenced by a rapid rise in the liquid level in the pump tank and a sudden drop in the head and the flow rate. This situation can, of course, be avoided by assuring adequate gas pressure in the pump tank. It is planned to continue operation of this pump to determine its long-time reliability. Tests are to be conducted to determine the heat removal by lubricating-cooling oil and the temperature gradient in the neck of the pump tank for various liquid levels and operating conditions.

WATER FLOW TESTS OF ALUMINUM NORTH-HEAD MOCKUP

E. R. Dytko
R. E. MacPherson
D. R. Ward
R. Curry
J. W. Cooke[1]

Tests of the ART twin fuel pump system have been run as part of the water flow tests of the aluminum north-head mockup in order to investigate (1) fluctuations of flow rate and pump suction pressure in the main circuit, (2) flow characteristics in the xenon-removal expansion tank, (3) ingassing of the main circuit when it is being filled with the pumps rotating or when one pump is being slowed or stopped while the other is still running, and (4) flow characteristics with one pump stopped and the other running. In particular, it was desired to ascertain whether liquid would rise up the annulus between the pump shaft and the radiation barrier when one pump was stopped with the other still running.

Tests with the original xenon-removal system have been completed, and the results of the investigation of items 1 and 3 were reported previously.[7] The system was found to be unsatisfactory with respect to items 2 and 4 and has therefore been modified. An improved xenon-removal system was developed and incorporated in the model 32 impeller, which, as described above, has been evaluated with water in a single-pump loop. Model 32 impellers have been installed in the twin-pump assembly and preliminary results indicate that fluid can be kept from rising up the shaft of the stopped pump or the running pump if helium flow is maintained in both pumps. The initial tests have also indicated that substantial improvement of the

[7] E. R. Dytko *et al.*, *ANP Quar. Prog. Rep. Sept. 10, 1956*, ORNL-2157, p 52.

flow characteristics in the xenon-removal expansion tank has been achieved.

Design work was completed on two new external circuit configurations that are to be tested in the aluminum north-head mockup. One of the configurations mocks up the reactor pump inlet region, including the tops of the intermediate heat exchanger tube bundles. A straight annular downcomer will be used for the pump discharge region. For the second configuration the straight downcomer will be replaced with a full-scale aluminum mockup of the reactor core. These configurations will be tested to determine flow patterns in the pump inlet and outlet regions.

REACTOR COMPONENT DEVELOPMENT TESTS

E. R. Dytko R. E. MacPherson

Heat Exchanger and Radiator Tests

J. C. Amos J. G. Turner
L. H. Devlin D. R. Ward

A summary of heat exchanger and radiator test operations during the quarter is presented in Table 1.4.2. The test of Process Engineering Corp. heat exchanger No. 1, type SHE-2 (ref 8), in conjunction with York Corp. radiator No. 7 (ref 9) in SHE test stand B was terminated on schedule after more than 2500 hr of operation. These units were replaced by Process Engineering Corp. heat exchanger No. 2, type SHE-7 (ref 10), and Black, Sivalls & Bryson radiator No. 1, which is of the same design as that used for York Corp. radiator No. 7. The effects of temperature, temperature gradient, and time on mass transfer in the NaK system are being investigated in the tests of these units. The temperature conditions being used for this study are given in Table 1.4.3. The relationship of radiator pressure drop to NaK Reynolds number is determined before, at the middle, and at the end of each run. Four runs have been completed, and the program will be continued during the next quarter.

After the failure of York Corp. radiator No. 5 in test stand C (previously reported[11]), tests of Process Engineering Corp. heat exchanger No. 1, type SHE-7, at ART operating conditions were

[8] The design of heat exchanger type SHE-2 is illustrated in Fig. 2.22, p 52, of *ANP Quar. Prog. Rep. Dec. 10, 1955*, ORNL-2012.

[9] Radiator No. 7 is shown in Fig. 1.4.8, p 60, of *ANP Quar. Prog. Rep. June 10, 1956*, ORNL-2106.

[10] The design of heat exchanger type SHE-7 is illustrated in Fig. 1.4.5, p 50, of *ANP Quar. Prog. Rep. Sept. 10, 1956*, ORNL-2157.

[11] L. H. Devlin and J. G. Turner, *ANP Quar. Prog. Rep. Sept. 10, 1956*, ORNL-2157, p 47.

TABLE 1.4.2. SUMMARY OF HEAT EXCHANGER AND RADIATOR TEST OPERATIONS

Test Unit	Hours of Nonisothermal Operation	Total Hours of Operation	Number of Thermal Cycles	Status of Test
Process Engineering Corp. heat exchanger No. 1 (type SHE-2)	1520	2574	15	Test completed
Process Engineering Corp. heat exchanger No. 1 (type SHE-7)	761	1217	36	Test completed
Process Engineering Corp. heat exchanger No. 2 (type SHE-7)	537	694	12	Test continuing
York Corp. radiator No. 7	1520	2574	15	Test completed
York Corp. radiator No. 8	434	629	26 ½	Terminated by radiator failure
Black, Sivalls & Bryson radiator No. 1	537	694	12	Test continuing
Black, Sivalls & Bryson radiator No. 2	211	293	3	Terminated by radiator failure

TABLE 1.4.3. RADIATOR TEMPERATURE CONDITIONS FOR INVESTIGATION OF MASS TRANSFER IN THE NaK SYSTEM OF A HEAT EXCHANGER–RADIATOR TEST LOOP

Run	Radiator Inlet Temperature (°F)	Radiator Outlet Temperature (°F)	Temperature Gradient (°F)
1	1375	1100	275
2	1546	1317	229
3	1421	1317	104
4	1447	1244	203
5	1546	1317	229
6	1550	1491	59
7	1447	1244	203
8	1500	1100	400
9	1250	1100	150
10	1500	1100	400
11	1447	1244	203
12	1349	1172	117
13	1474	1172	302
14	1519	1389	130
15	1350	1350	Isothermal

resumed; York Corp. radiator No. 8, which is identical to radiator No. 7, was used as a heat sink. As indicated in Table 1.4.2 this radiator failed after 629 hr of operation because of a leak in a radiator tube between the hot-NaK inlet header and the tube-fin matrix. A photograph of the failure area, taken after the unit had been cleaned, is shown in Fig. 1.4.15.

York Corp. radiator No. 8 was replaced by Black, Sivalls & Bryson radiator No. 2, and, again, the heat exchanger endurance test was resumed at ART operating conditions. Failure of this radiator occurred after 293 hr of operation as a result of cold-trap malfunction. Loss of cooling water caused the cold trap to heat to approximately 1000°F and to introduce large quantities of oxides into the system. The oxides apparently caused nearly complete plugging of one or more of the radiator tubes. Failure occurred approximately 2 hr after loss of the cold-trap cooling water. The differential thermal expansion between the tubes carrying NaK and the plugged tube, or tubes, was possibly one of the factors that contributed to the failure. A photograph of the failure area on the hot-air outlet face of the radiator is shown in Fig. 1.4.16. An attempt was made to determine the extent of tube plugging in the radiator, and the results are presented in Fig. 1.4.17. It is quite possible that the extensive plugging shown is not representative of the condition of the radiator at the time of failure. Although reasonable precautions were taken, air could have entered the radiator during removal and inspection operations and reacted with residual NaK to form additional oxide not present at the time of failure.

Since the test heat exchanger had operated 1217 hr, 761 of which was at ART full-power operating conditions, it was removed along with the radiator for metallurgical examination. Process Engineering Corp. heat exchanger No. 3, type SHE-7, is currently installed in test stand C, and testing of this unit will begin when a radiator is available.

Black, Sivalls & Bryson heat exchangers Nos. 1, 2, and 3, type IHE-8 (ref 12), were received during the quarter. Units 1 and 2 are currently installed in the IHE test stand B in conjunction with York Corp. radiators Nos. 11 and 12, and testing will begin early next quarter. Current programing calls for running the exchanger in which heat is transferred from fuel to NaK at a fuel inlet temperature of 1600°F to simulate ART design temperature conditions. This will require operating the companion NaK-to-fuel heat exchanger at a NaK inlet temperature of 1700°F. In view of the extreme corcorrosion found in previous units operated at a NaK inlet temperature of 1600°F, it is planned to replace the NaK-to-fuel unit after 500 hr of operation at these extreme conditions. A summary of the pertinent heat exchanger corrosion data is presented in Table 1.4.4.

Fig. 1.4.15. York Corp. Radiator No. 8 Which Failed After 629 hr of Service in Small Heat Exchanger Test Stand C.

The IHE test stand C has been modified for performance and reliability testing of a prototype ART radiator. The unit is being fabricated by York Corp. and is shown in Fig. 1.4.18 during assembly.

Valve Development Tests

L. P. Carpenter I. T. Dudley
M. H. Cooper[1]

Prototype ART Dump Valves. – No new valves were received from the vendor during the quarter, but several valves were tested that were rebuilt with components previously tested. Valve 5A, which was assembled by combining a cylindrical copper seat and a swiveled conical poppet made of molybdenum, leaked after being cycled, that is,

[12]The design of heat exchanger type IHE-8 is illustrated in Fig. 2.13, p 42, of *ANP Quar. Prog. Rep. Dec. 10, 1955*, ORNL-2012.

TABLE 1.4.4. SUMMARY OF CORROSION OF FUEL-TO-NaK HEAT EXCHANGERS OPERATED IN TEST STANDS

Heat Exchanger Designation	Total Operating Time (hr)	Nonisothermal Operating Time (hr)	Maximum Fuel-Wall Interface Temperature (°F)		Maximum Depth of Attack in Heat Exchanger (mils)	Reason for Termination of Test
			In Heat Exchanger	In System		
ORNL-1, 2; type IHE-3	1809*	993	1550	1550	25	NaK-to-fuel leak
Black, Sivalls & Bryson 1 and 2; type IHE-3	1398	1008	1550	1550	25	Scheduled
ORNL-1; type SHE-1	1557	1540	1460	1650**	7	Scheduled
ORNL-1; type SHE-2	2071	1041	1535	1700**	6	Scheduled
Process Engineering 1; type SHE-2	2574	1520	1535	1700**	8	Scheduled

*Previously reported incorrectly as 1129 hr. The 1129-hr value was actually the total time with fuel in the system.
**In resistance heater.

Fig. 1.4.16. Failure Area of Black, Sivalls & Bryson Radiator No. 2 Which Operated for 293 hr in Small Heat Exchanger Test Stand C.

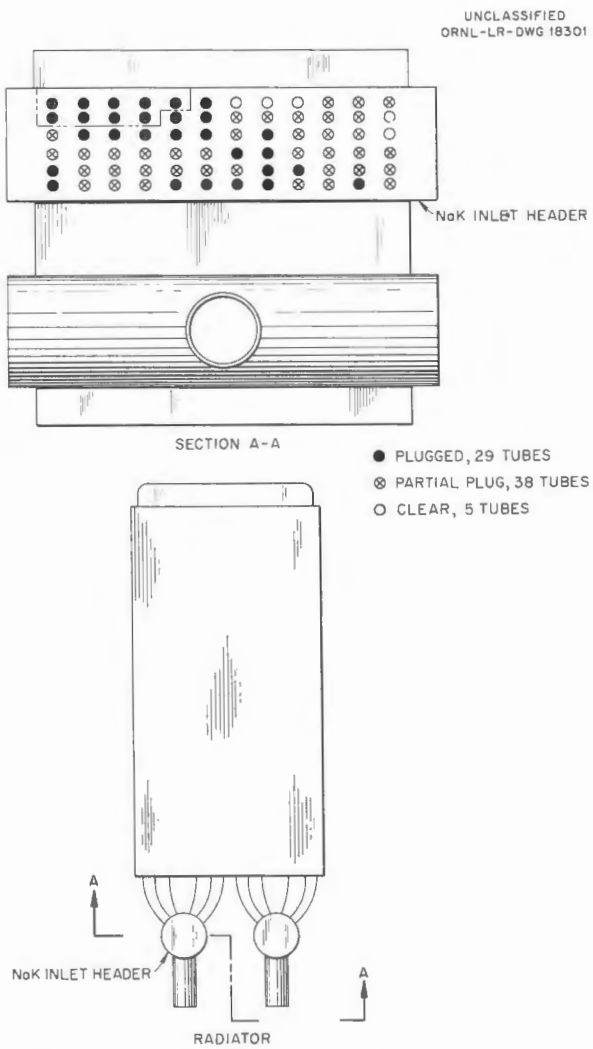

Fig. 1.4.17. Extent of Oxide Plugging of Tubes of Black, Sivalls & Bryson Radiator No. 2.

closed-opened-closed. Valve 5B, which was rebuilt with a fixed spherical molybdenum poppet and a conical copper seat, is presently being tested. Valve 4B, which was rebuilt after previous tests,[13] leaked severely when retested. The fuel mixture (No. 30) $NaF-ZrF_4-UF_4$ (50-46-4 mole %) at temperatures in the range of 1200 to 1350°F was used for these tests. The operating conditions and results are summarized in Table 1.4.5, and valve 4B is shown in Fig. 1.4.19 before assembly.

[13]E. R. Dytko *et al.*, *ANP Quar. Prog. Rep. Sept. 10, 1956*, ORNL-2157, p 53.

Valve 5A, which had a copper seat and a swiveled molybdenum poppet, initially had a low leakage rate but the leakage increased with the valve operating cycles. Increasing the seating force reduced the leakage, but cycling again caused unacceptable leak rates. Examination of the valve after termination of the test showed that the copper seat had been deformed elliptically. The deformation was apparently caused by the swiveled poppet, which did not seat in the same position after each cycle.

Valve 5B, in which the spherical molybdenum poppet is fixed rigidly to the stem and the copper seating ring is conical, is still being tested and has operated satisfactorily for 200 hr through 14 operating cycles. The fixed spherical plug and the conical ring mate in the same position each time the valve is closed, and hence the nonuniform deformation encountered with swiveled plugs is not produced.

Valve 4B, which has a swiveled Kentanium 151A plug and a Kentanium 152B seat, leaked excessively, and testing was terminated after 120 hr. Deep grooves on one side of the poppet indicated misalignment of the plug and seat. The valve will be rebuilt with a fixed plug and retested. It is hoped that further improvement of the seat and poppet alignment can be obtained by mounting the plug guide close to the seat ring. This should overcome any misalignment of poppet and seat which might occur when the end connection carrying the seat is welded to the valve body.

Seat and Plug Materials. – Twelve seat and poppet materials combinations have been tested to date in the fuel mixture (No. 30) $NaF-ZrF_4-UF_4$ (50-46-4 mole %). The Kentanium cermets[14] appear to be adequate valve materials; the copper-molybdenum combination shows promise of positive leakage control and tolerable self-welding characteristics. Valves of the refractory metals, tungsten and molybdenum, exhibit low opening forces, but they leaked badly for several days after being cycled.

The results of the seat materials tests are presented in Table 1.4.6. Three Kentanium combinations (tests 1, 2, and 4) have met ART performance specifications. One Kentanium combination (test 3) failed because of misalignment

[14]For the compositions of these cermets see Table 3.4.8, p 198, *ANP Quar. Prog. Rep. Sept. 10, 1956*, ORNL-2157.

Fig. 1.4.18. Prototype ART Radiator Being Assembled at York Corp.

UNCLASSIFIED
PHOTO 27399

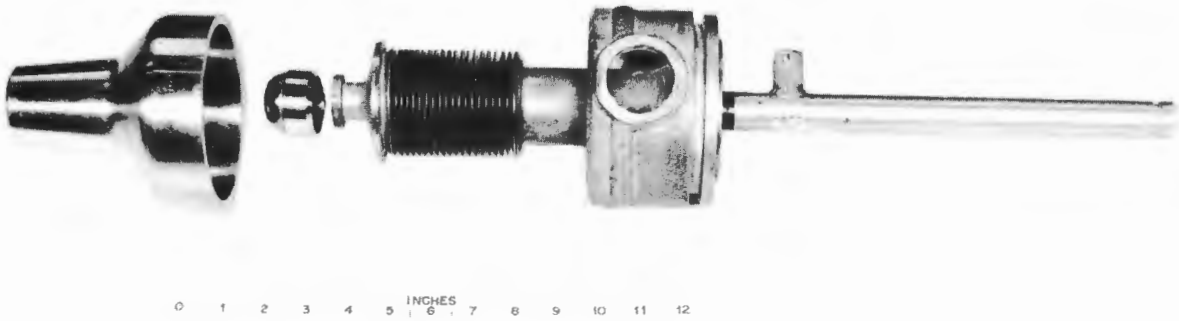

Fig. 1.4.19. Prototype ART Dump Valve with a Kentanium 152B Seat and a Kentanium 152A Plug Before Assembly. (Confidential with caption)

TABLE 1.4.5. OPERATING CONDITIONS AND RESULTS OF PROTOTYPE ART DUMP VALVE TESTS WITH FUEL MIXTURE (No. 30) $NaF\text{-}ZrF_4\text{-}UF_4$ (50-46-4 MOLE %)

Pressure differential across seat: 50 psi

	Valve 4B	Valve 5A	Valve 5B
Seat material	K152B	Copper	Copper
Plug material	K151A	Molybdenum	Molybdenum
Operating time, hr	120	312	In test
Valve temperature, °F	1200 1240	 1300	 1350
Stem thrust, lb	750 1200	750 1000	750
Opening force, lb	500 800	700 2000	500
Leakage, cm^3/hr			
Minimum	6.4	0	0
Maximum	46.2	19.5	0.6
No. of cycles	5	20	14

TABLE 1.4.6. CONDITIONS AND RESULTS OF TESTS OF VALVE SEAT AND PLUG MATERIAL

Pressure differential across seat: 50 psi

Test	Seat Material	Plug Material	Operating Time (hr)	Valve Temperature (°F)	No. of Cycles	Leak Rate (cm^3/hr)	Stem Thurst (lb)	Opening Force (lb)	Comments
1	K162B	K152B	2285	1225–1240	32	0–3.9	1000–750	500–1500	Test terminated for examination of materials
2	K152B	K162B	1683	1225–1325, 1500	48	0–7.1	750	170–2240	Initial high leakage decreased; operating force after 500-hr closure at 1500°F was 2340 lb
3	K162B	K151A	24	1210–1220	1	100	750		Seat and plug misaligned; plug cracked
4	K152B	K151A	1213	1310–1325	43	0–5.0	750	140–1400	Still operoting on a 500-hr closure period with no leakage
5	Cu	Mo	501	1250	7	0–37	750	250–1040	Leakage caused by crack in copper plug; test terminated
6	Cu	Mo	1452	1310–1325	44	0–12	750	252–1960	Initial low leakage increased; opening force after 500-hr closure was 1960 lb
7	Stellite		1160	1200–1350	18	9.4–52	750–1960	112–2000	Opening force at 1200°F low; higher at increased temperature
8	K162B	Cu	143	1320–1330	15	0–112	750	840–1760	Test terminated because of excessive leakage; grooves formed in plug
9	Cu	Mo	3185	1500	17	0–2.6	750	590–1680	Test terminated because plug welded to nickel base of seat
10	Mo	W	498	1300–1320	9	0–368	750–2140	140–840	High leakage after cycling decreased during closure period
11	Mo	Mo	405	1300–1310	6	2.0–22	750–2140	130–840	High leakage after cycling decreased during closure period
12	K162	Cu	357	1300–1310	2	1.5–20	750–1728	150–340	Leakage decreased with increased stem force
13	Mo	W							Installation completed
14	K94	K94							Being fabricated

and cracking of the plug. A photograph of the valve tested in test 1, which operated for 2285 hr in the fuel mixture (No. 30) $NaF-ZrF_4-UF_4$ (50-46-4 mole %) at 1240°F, is shown in Fig. 1.4.20.

Two copper-molybdenum combinations (tests 5 and 9) failed, and the leakage rate of a third copper-molybdenum combination (test 6) increased sharply from nearly zero to 12 cm^3/hr. The leakage increase in test 5 was caused by the cracking of the copper seat ring, which, along with the molybdenum plug, is shown in Fig. 1.4.21. The copper seat material is not expected to crack during ART operation, however, because the copper seat ring will be restrained from radial deformation by the Inconel walls of the valve end connection. Further, the molybdenum plug has been made spherical and the seat ring conical to minimize the deformation of the copper.

Fig. 1.4.20. Valve Seat Materials Test No. 1 Components After 2285 hr in the Fuel Mixture (No. 30) $NaF-ZrF_4-UF_4$ (50-46-4 mole %) at 1240°F. (Secret with caption)

The refractory-metal combinations, tungsten vs molybdenum and molybdenum vs molybdenum, exhibit low opening forces and low leakage rates after several days closure. However, high leakage rates are observed after completion of an operating cycle. Investigation of the effect of increased stem thrust on the leakage rates after cycling are in progress.

Zirconium Fluoride Vapor Traps

M. H. Cooper F. A. Anderson[15]

Several types of condensation traps for removing zirconium fluoride vapor from the reactor off-gas have been designed and tested. The zirconium fluoride condensation trap presently being considered for use in the ART is shown in Fig. 1.4.22. The trap, 9 in. in inside diameter and 25 in. long, consists of an inlet section with a central water-cooled coil and a water-cooled shell. The outlet section is a 12-in.-long shell-and-tube, gas-to-water heat exchanger. The inlet section is expected to condense the zirconium fluoride vapor in the off-gas during low power operation; at high power, the radiation heating in the inlet section is expected to cause most of the zirconium fluoride vapor to move into the shell-and-tube section, where the zirconium fluoride vapor should recondense. At high power, the radiation heating should prevent the formation of zirconium fluoride plugs, and it is expected that an equilibrium will be established when the temperature of the radiation heated surface of the zirconium fluoride layer equals the condensation temperature of the vapor in the off-gas. The calculated equilibrium zirconium fluoride layer thickness for this trap is 0.075 in. at full reactor power.

Two other condensation traps, shown in Figs. 1.4.23 and 1.4.24, were designed to prevent plugging of off-gas lines with condensed zirconium fluoride by providing surfaces with temperatures above the condensation temperature of the zirconium fluoride. The results of tests of these traps are summarized in Table 1.4.7. Neither of these traps can be used in the ART in its simple form because of the excessive length required to contain the evolved zirconium fluoride in a 0.075-in.-thick equilibrium layer during full-power operation.

[15]Consultant from the University of Mississippi.

Fig. 1.4.21. Copper Seat and Molybdenum Plug (Test 5) After 501 hr at 1250°F in Fuel Mixture (No. 30) NaF-ZrF_4-UF_4 (50-46-4 mole %). Note cracks in copper seat ring. (Secret with caption)

TABLE 1.4.7. SUMMARY OF RESULTS OF TESTS OF ZIRCONIUM FLUORIDE VAPOR TRAPS

Trap	Operating Time (hr)	Helium Flow Rate (liters/min)	Sump Temperature (°F)	Hot-Wall Temperature (°F)	Comments
Icicle	132	2	1350	1270–1300	No plugging in these tests; small quantities of ZrF_4 carried through trap at higher helium flow rate
	28	2.5	1450	1450–1500	
	54	3	1425	1400–1425	
	28	3	1425	1400–1480	
	190	3.5	1425	1400–1480	Plugged
	285	3.5	1400	1250–1270	Plugged
Hot Finger	300	3.5	1400	1250–1500	Plugged

Chemical reaction traps packed with aluminum oxide were tested at several gas velocities to provide design data for the traps to be used in the Pratt & Whitney Aircraft high-temperature critical experiment. This type of trap was also operated at 1700°F to simulate predicted axial temperatures of ART traps when the reactor is operating at full power. The results of these tests are presented in Table 1.4.8. The aluminum oxide used in tests of trap No. 1 may not have been thoroughly dried prior to use, and heating of this material may have resulted in some particle disintegration and entrainment, with subsequent plugging of the trap outlet line. The traps for the high-temperature critical experiment were designed for a superficial gas velocity of 0.8 fps through alumina packing at 1300°F.

Alumina was tested in a similar apparatus at 1700°F. This is the estimated central temperature of the alumina packing at reactor full-power operation for the particular trap design being considered. The trop operated for 90 hr before the test section became plugged. Examination of the test section indicated that the reaction products

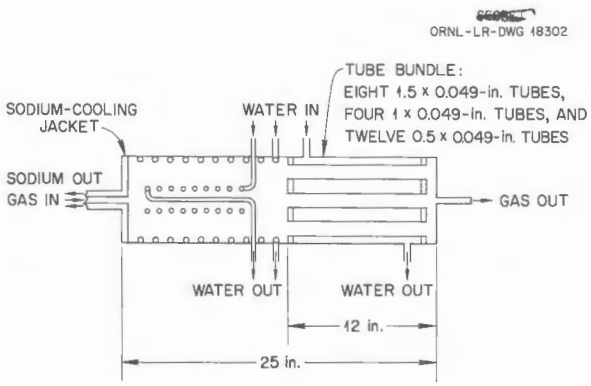

Fig. 1.4.22. Diagram of Zirconium Fluoride Vapor Condensation Trap Presently Being Considered for Use in the ART.

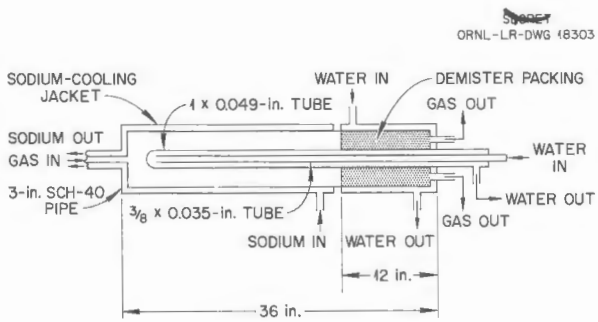

Fig. 1.4.23. Diagram of Icicle Trap for Zirconium Fluoride Vapor.

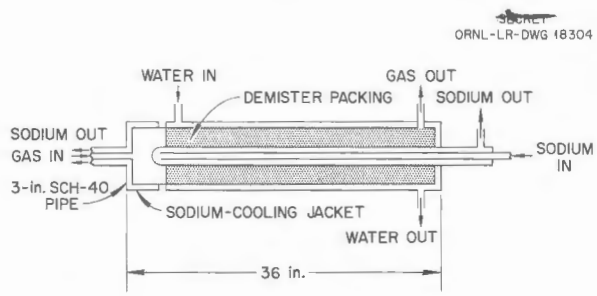

Fig. 1.4.24. Diagram of Hot-Finger Trap for Zirconium Fluoride Vapor.

TABLE 1.4.8. RESULTS OF TESTS OF ALUMINA REACTION TRAPS FOR ZIRCONIUM FLUORIDE VAPOR

Trap No.	Sump Temperature (°F)	Trap Temperature (°F)	Operating Time (hr)	Gas Flow Rate (liters/min)	Gas Velocity (ft/sec)	Comments
1	1300	1350	69	4	0.39	No plugging; Al_2O_3 found in exit line
	1300	1350	72	2	0.19	Al_2O_3 found in exit line
	1300	1350	34	6	0.58	Exit line plugged with Al_2O_3
2	1310	1350	90	8	0.79	Exit line clean
3	1500	1700	90	1	0.10	Test section plugged with reaction products

formed the plug, but further tests will be carried out to confirm the cause of plugging.

Liquid-Metal-Vapor Condensers

M. H. Cooper

Work continued on the development of condensers for removing liquid metal vapor from the purge gases bled from the ART sodium and NaK pumps. The condensers tested this quarter consisted of 24-in. sections of 2-in. sched-40 Inconel pipe filled with Inconel Demister packing. In a test of this condenser with sodium vapor in helium flowing at a rate of 500 liters/day and with a condenser inlet temperature of 1200°F and an outlet temperature of 70°F, the outlet line plugged after 500 hr. In a test made under the same conditions with NaK vapor, the condenser did not plug. However, when this condenser was tested at gas velocities approaching those expected during NaK dumping operations (~1.7 ft^3/min), the unit was unsatisfactory in that entrained NaK was observed in the outlet lines. The test setups illustrated previously were used for these experiments.[16]

The plug in the outlet of the condenser in sodium service was caused by the condensation of sodium as a result of vapor channeling through the center of the trap. Although the trap wall temperatures near the outlet approached room temperature, the temperature of the gas in the center of the trap was probably much higher because of channeling at the low gas flow. The sodium-vapor condenser has been redesigned, as shown in Fig. 1.4.25, to include baffles to prevent channeling of the gas.

The condenser for use during NaK dumping operations has also been modified, as shown in Fig. 1.4.26, to provide a 24-in. section of 4-in. pipe at the condenser outlet that functions as an entrainment separator. It is expected that NaK removed from the gas stream during the dumping operation will drain out of the trap during intervening periods of low gas flow.

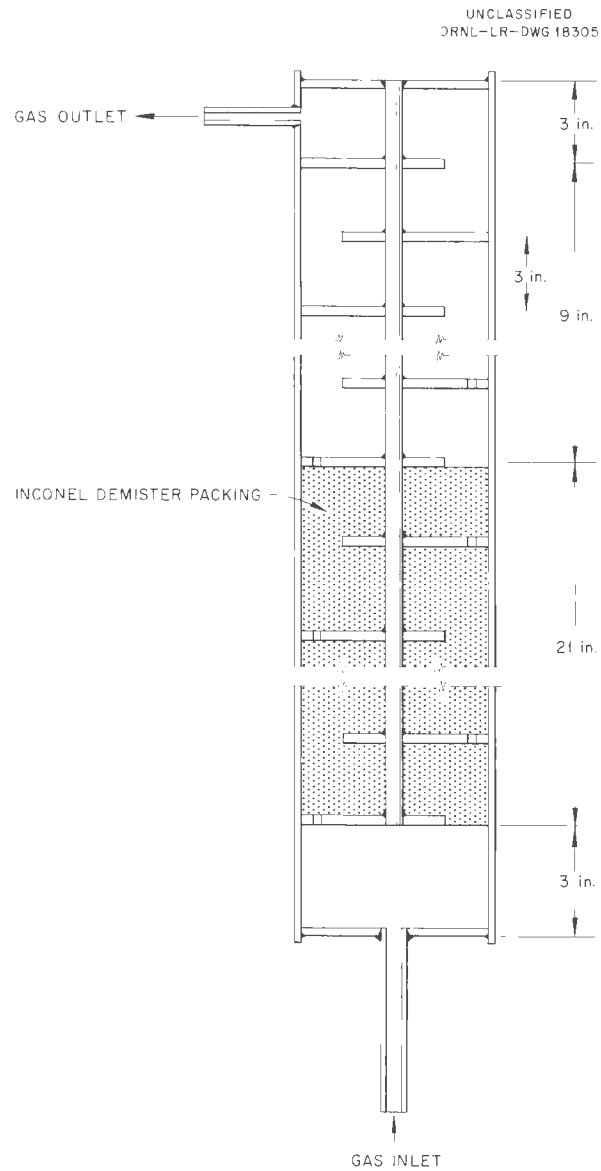

Fig. 1.4.25. Modified Sodium-Vapor Condenser.

AUXILIARY COMPONENT DEVELOPMENT TESTS

J. J. Keyes

High-Frequency Thermal-Cycling Test

J. E. Mott[1] A. G. Smith, Jr.[1]

Development of a pulse generator for producing temperature oscillations in a fused-salt stream of 150 to 200°F at a frequency of up to 10 cps has been completed, and the generator has been built but, as yet, not tested. The design of the unit is shown in Fig. 1.4.27. The loop in which the generator will operate has been designed as shown in Fig. 1.4.28, and it is being fabricated.

[16] M. H. Cooper, *ANP Quar. Prog. Rep. Sept. 10, 1956*, ORNL-2157, p 60.

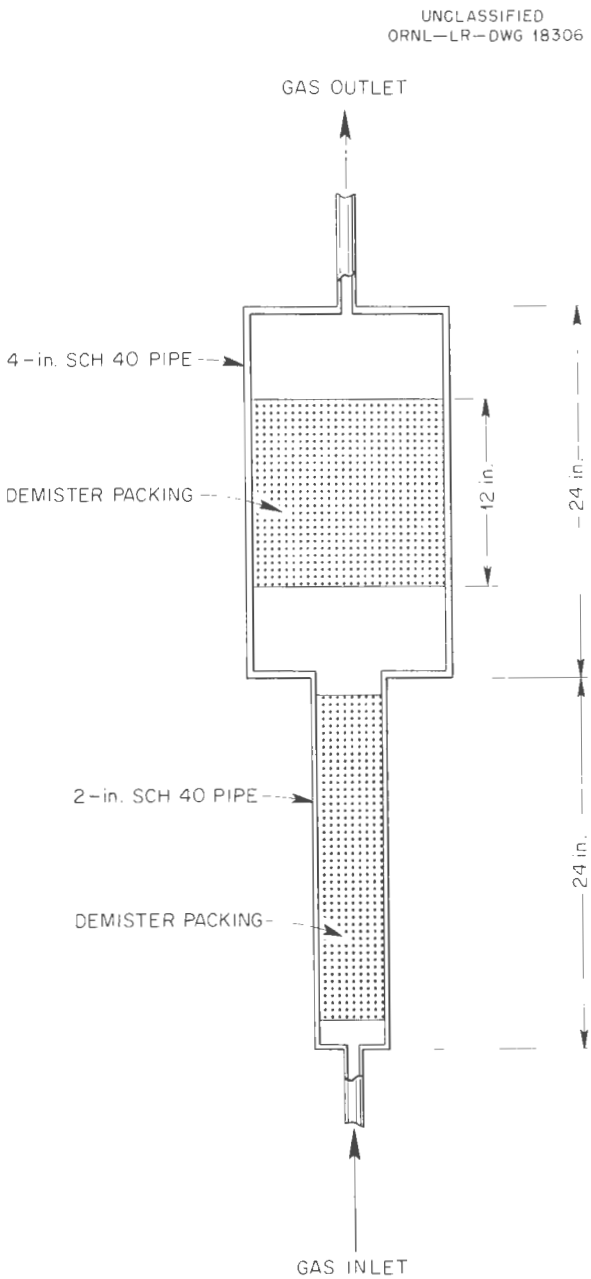

Fig. 1.4.26. Modified NaK-Vapor Condenser for Use During NaK Dumping Operations.

An investigation of techniques for measuring rapid temperature oscillations in the liquid streams and at the tube walls is under way, for which a mockup of the pulse generator, previously described,[17] is being used to generate thermal oscillations in water. Data have been obtained with which to evaluate thermocouples and recording equipment. The investigations of several types of thermocouples for temperature measurements of metal surfaces in contact with water have led to the adoption of the so-called "gun barrel" probe manufactured by the Midwest Research Institute. This probe consists of a thick-walled steel tube (0.09 in. OD) plated at one end with a 1-μ layer of nickel. The interface between the nickel and the end of the steel tube form the plane of emf generation, as shown in Fig. 1.4.29. The nickel lead wire to the plated end is nickel oxide coated for electrical insulation from the steel tube. The time constant of this thermocouple is reported to be about 0.25 μsec. Stream measurements were made with a two-wire, 5-mil, Chromel-Alumel immersed junction, the response of which has been calculated to be adequate (that is, well below 0.1 sec).

The mockup of the generator has been used for water tests of two tubular test sections consisting of a 0.460-in.-ID, 0.250-in.-wall Inconel tube insulated on its outer surface and a 0.460-in.-ID, 0.250-in.-wall Lucite tube. The data for the Inconel tube, tested with an inner surface film coefficient of 3100 Btu/hr·ft^2·°F, are plotted in Fig. 1.4.29. The theoretical curves presented for Inconel and steel are based on derivations of Jakob[18] for the case of a flat plate of infinite thickness. Because of the small surface penetration at high frequency, this case is believed to hold approximately for thick-walled tubes. The positions of the data points with respect to the theoretical curves illustrate the influence of the steel thermocouple wall on the measured oscillations. Inconel-nickel thermocouples of the same design should eliminate this difficulty, and they have been ordered. Data have been obtained with other film heat transfer coefficients, and they show similar relationships to the theoretical curves.

Wall temperature measurements were made for the Lucite tube with a conventional two-wire thermocouple junction that was embedded in the Lucite and ground flush. For this application, 5-mil Chromel-Alumel wires were used. The data and calculations are in reasonable agreement, as

[17] W. J. Stelzman and J. M. Trummel, *ANP Quar. Prog. Rep. Sept. 10, 1956*, ORNL-2157, p 56.

[18] M. Jakob, *Heat Transfer*, vol 1, p 297, Wiley, New York (1949).

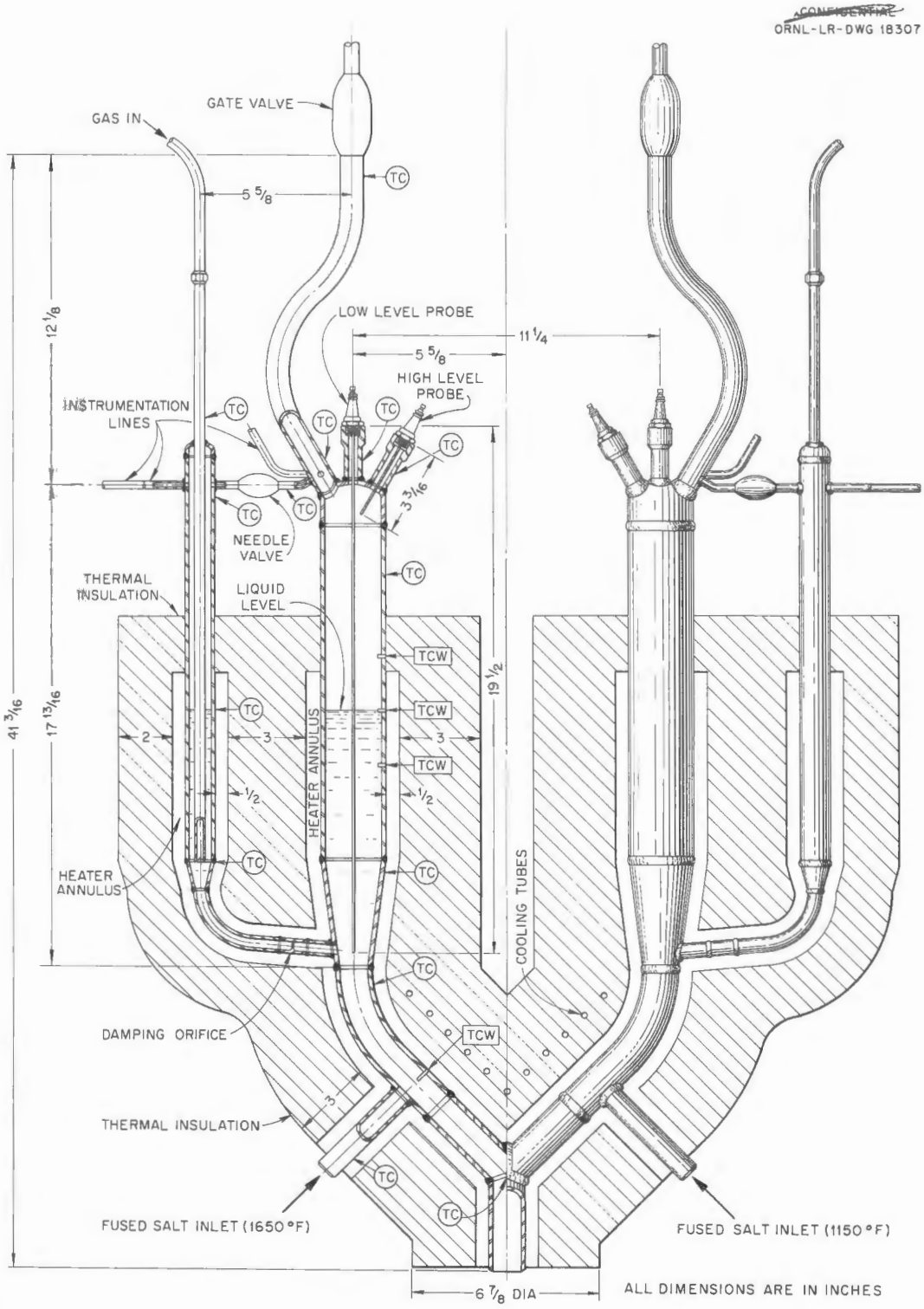

Fig. 1.4.27. High-Frequency Pulse Generator for Producing Temperature Oscillations in a High-Temperature Fused-Salt Stream.

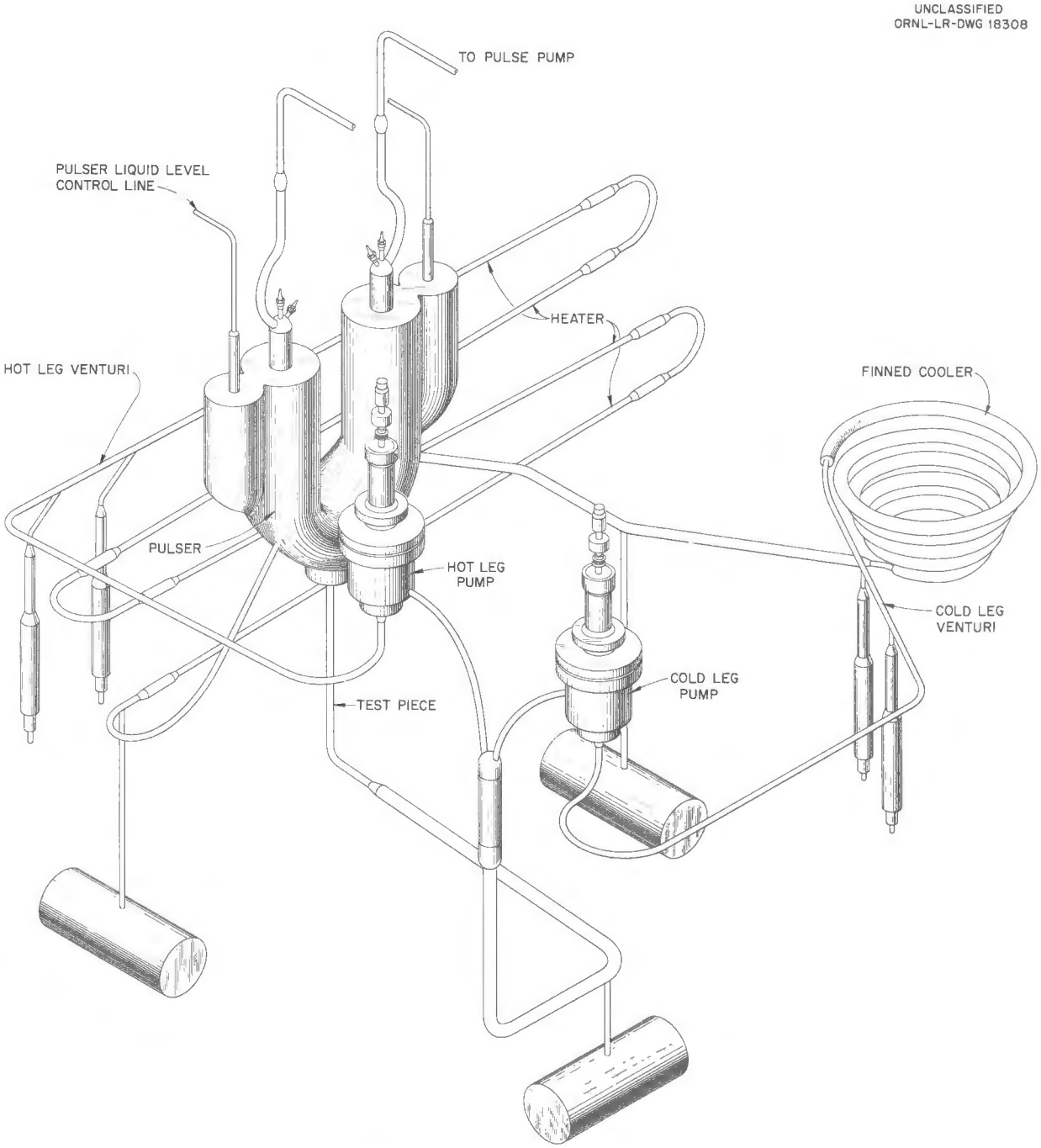

Fig. 1.4.28. High-Frequency Thermal-Cycling Loop.

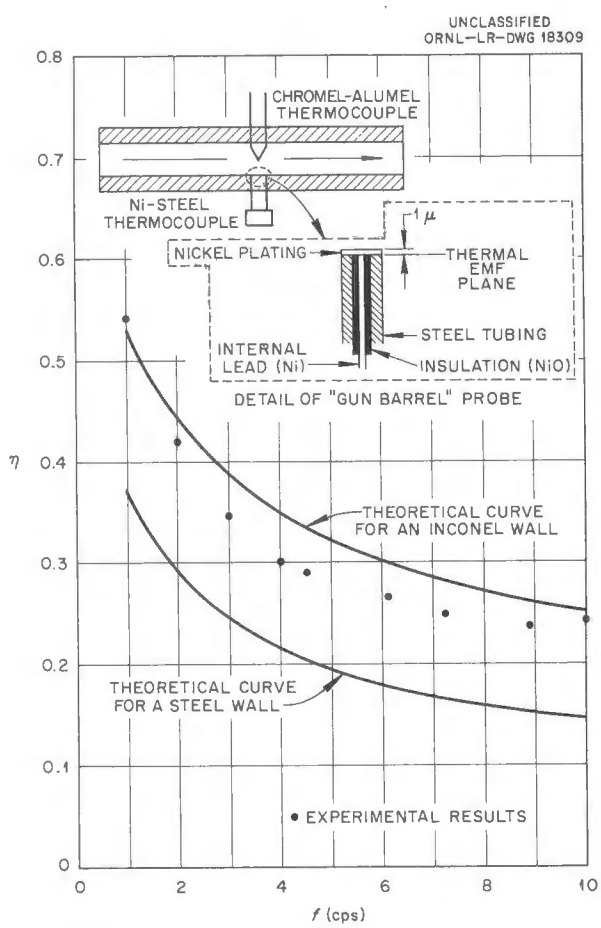

Fig. 1.4.29. Ratio of Thermal Amplitude of the Inner Surface of a Tube to the Thermal Amplitude of the Stream Flowing Through the Tube, η, as a Function of the Frequency, f, of the Thermal Cycle Imposed on the Stream for a Thick-Walled Tube with a Film Heat Transfer Coefficient of 3100 Btu/hr·ft^2·°F.

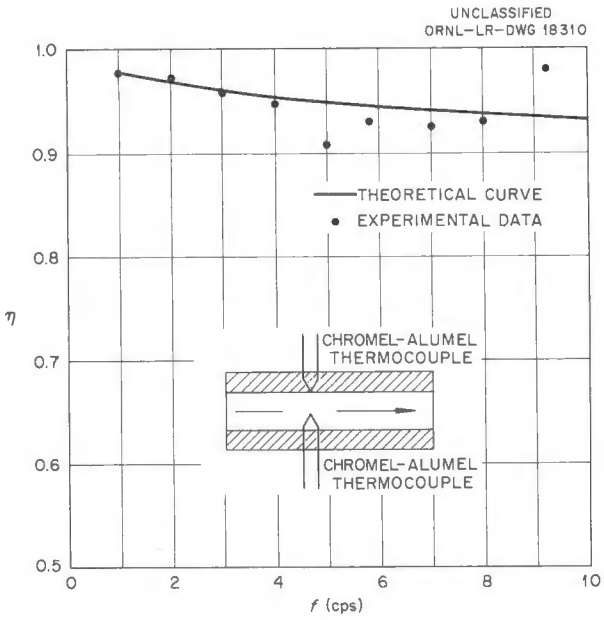

Fig. 1.4.30. Ratio of Thermal Amplitude of the Inner Surface of a Tube to the Thermal Amplitude of the Stream Flowing Through the Tube, η, as a Function of the Frequency, f, of the Thermal Cycle Imposed on the Stream for a Thick-Walled Lucite Tube with a Film Heat Transfer Coefficient of 3100 Btu/hr·ft^2·°F.

illustrated in Fig. 1.4.30. The good thermal insulating properties of the Lucite may be seen to have had an effect on the relationship of the experimental data to the theoretical curve.

A thin-walled (20-mil) test section has been fabricated that has provisions for water cooling of the outer surface. It is planned to investigate the influence of finite wall thickness and outer surface cooling on the ratio of the thermal amplitude of the inner surface to the thermal amplitude of the stream.[19]

ART Sodium Circuit Water Flow Tests

S. Kress[1] R. D. Peak[1]

The total pressure loss in the ART sodium circuit is being determined by calculations and by measuring the loss across mockups of those regions of the circuit which are difficult to analyze and to calculate. One region that had to be mocked up, called the island entrance region, occurs at the point where the island cooling sodium stream from one sodium pump meets the corresponding stream from the other pump and turns down into the annulus around the control rod thimble on its way to the island. This region is illustrated in Fig. 1.4.31, in a 100-deg section view, which shows only one of the two inlet pipes. The mockup of this sodium flow passage was made of steel, and it was tested with water. The measured pressure loss for this

[19] D. H. Platus and R. V. Meghreblian, *Conduction of Heat in a Finite Plate in Contact with an Environment in Which the Temperature Varies as a Prescribed Function of Time*, ORNL CF-56-9-60 (Sept. 12, 1956).

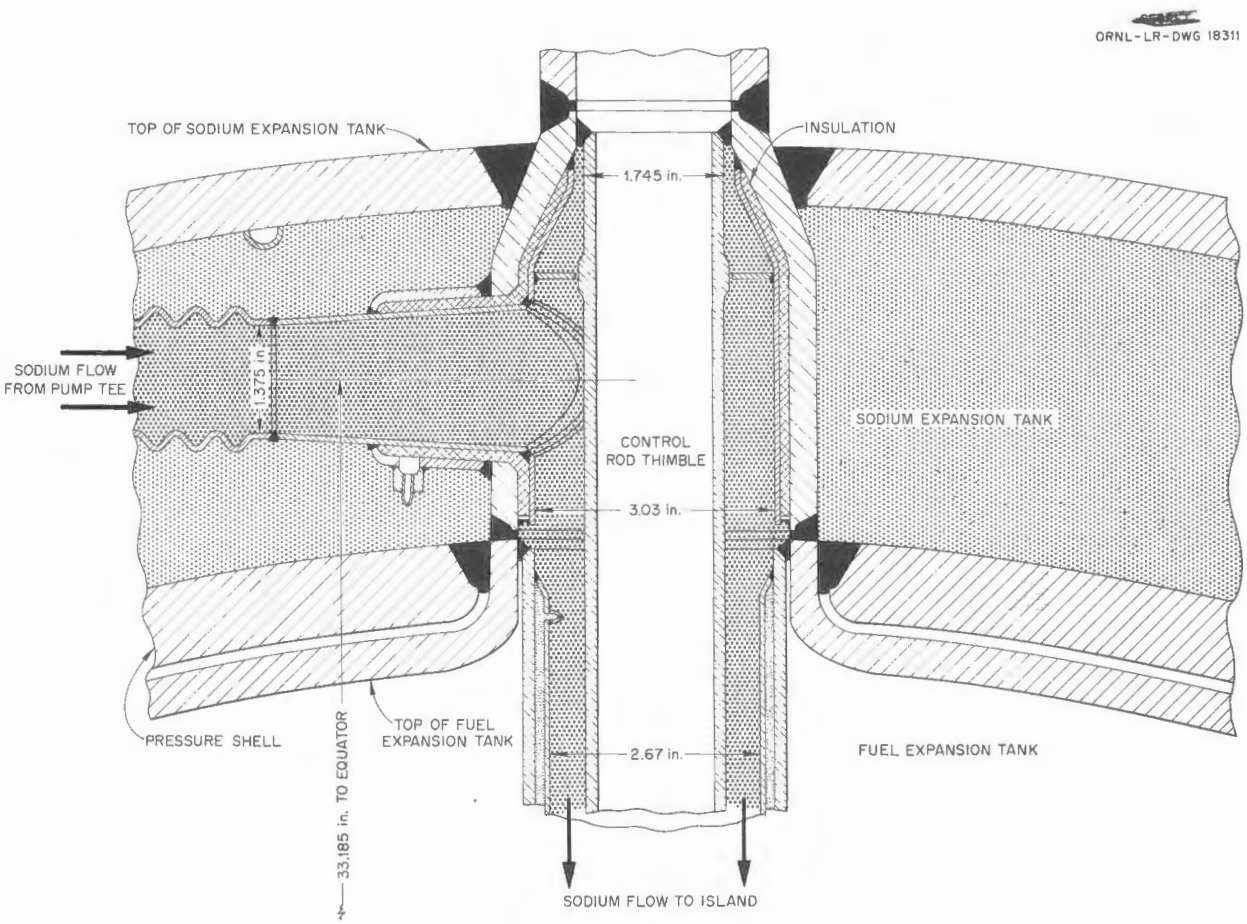

Fig. 1.4.31. ART Island Cooling System Entrance Region Showing Sodium Flow Channels in a 100-deg Section View.

region at the design flow rate to the island of 0.68 ft^3/sec was 13.8 ft of head.

A pressure loss measurement was made for spacers of the type which will be used to position the island and reflector beryllium with respect to the Inconel core shells. The test piece, shown in Fig. 1.4.32, had eight full-size spacers in each row around the aluminum bullet. The bullet was mounted in a 4-in., sched-40 pipe equipped with suitable pressure taps for measurements of the pressure drop across several rows of spacers. The test was run both with and without the spacers mounted on the bullet so that the pressure loss as a result of the spacers could be determined directly. The spacer pressure loss, expressed as a loss coefficient, $\Delta H/(V^2/2g)$, was only 0.0805, which was considerably lower than the loss coefficient of 0.15 measured by Copenhaver and Lynch[20] on a $^5/_{22}$-scale model of the annulus region.

Since the heat loads in the island vary with position and lengths of the four rows of cooling holes through the beryllium are different, the sodium flow through these cooling holes must be controlled in some manner in order to obtain uniform temperatures throughout the beryllium. A convenient way to control the sodium flow in the individual holes will be to vary the orifice size of the nominally $^3/_{16}$-in. holes at the equator joint of the island beryllium by inserting $^1/_4$-in.-thick orifice disks. The results of tests with various orifice sizes are shown in Fig. 1.4.33 as pressure loss coefficients

[20]C. M. Copenhaver and F. E. Lynch, *ART Reflector Sodium Annulus Study*, ORNL CF-56-7-155 (July 31, 1956).

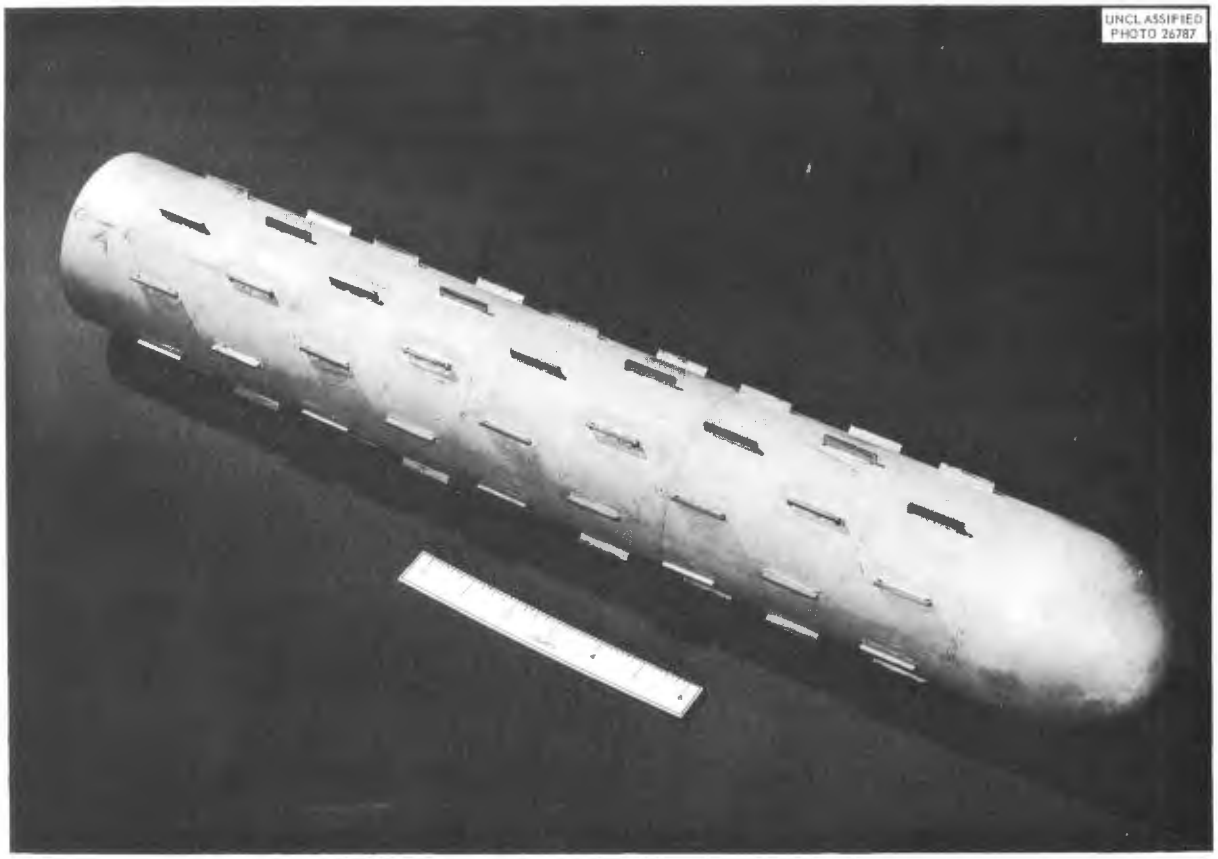

Fig. 1.4.32. Test Piece for Experimental Measurement of Pressure Loss in the Annulus Region Between the ART Beryllium Reflector or the Island and the Inconel Core Shells as a Result of the Spacers. (Secret with caption)

vs orifice diameter. In the investigation, measurements were made for orifice diameters of $^3/_{16}$ in. (no orifice disk) to 0.104 in. The smallest orifice in the longest island cooling hole was found to limit the flow to about 64% of the flow without the orifice disk. Also, this same orifice (0.104 in. in diameter) in the shortest island cooling hole limited the flow to about 74% of the flow through the longest hole without an orifice disk.

The other regions of the sodium circuit which will be tested include the orifices at the equator joint of the reflector beryllium, the various entrances to the cooling holes through the beryllium reflector and island, the top of the reflector, the pump tees, and certain slot passages in the north head.

ETU Component Water Flow Tests

W. J. Stelzman

Four water flow tests of ETU components are planned in order to determine the flow distribution in the sodium circuits through, and around, the reflector-moderator and island regions and the pressure losses in these circuits. Design work was completed and fabrication was begun on the facility for test No. 1, which is designed for studying flow in the sodium cooling circuits through and around the reflector-moderator region. Where possible, the actual ETU components will be used. It is anticipated, however, that the facility for test No. 1 will be completed in advance of ETU component assembly. The flow diagram for test No. 1 is shown in Fig. 1.4.34.

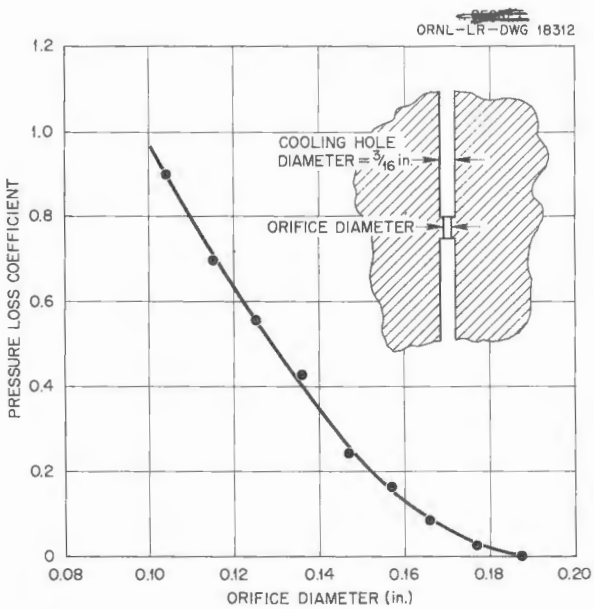

Fig. 1.4.33. Pressure Loss Coefficients for Sodium Cooling Holes with Various Sizes of Orifice Disks Placed at the Island Equator Joint.

Cold-Trap Evaluation Tests

R. D. Peak

Cooling tests were run on several cold traps installed on two test stands, small heat exchanger stand C (SHE-C) and cold-trap stand 1 (CTS-1). The cold traps tested on stand SHE-C were a standard 4-in.-dia cold trap, 60 in. long, wound with ½-in.-dia copper-tubing cooling coil, which was described previously,[21] and a very similar 4-in.-dia cold trap wound with a ⅝-in.-dia stainless-steel-tubing cooling coil. The cold trap tested on CTS-1 was similar to the standard 4-in. trap, but it was 8 in. in diameter, 60 in. long, and wound with a ⅝-in. stainless-steel-tubing cooling coil.[22] Also tested on each stand were 40-in.-long NaK-to-NaK economizers made of ⅜-in., sched-40 pipe inside a 1-in., sched-40 pipe. All the test data were correlated so that the operation of the ART cold-trap systems could be predicted.

With air cooling in the coils of the cold traps, a substantial amount, ranging from 10 to 55%, of the total heat lost by the NaK was lost by natural convection and radiation from the uninsulated cooling coil and thus was not picked up by the cooling air. This heat loss by natural convection and radiation was measured for the 8-in. cold trap, and it was found to correlate with the measured coil surface temperatures, which, in turn, were found to correlate with the average cooling-air temperatures. Over-all heat transfer coefficients for the traps were based on the inside areas of the traps covered by the cooling coils. These inside areas were 3.87 ft^2 for the 4-in. traps and 7.35 ft^2 for the 8-in. trap.

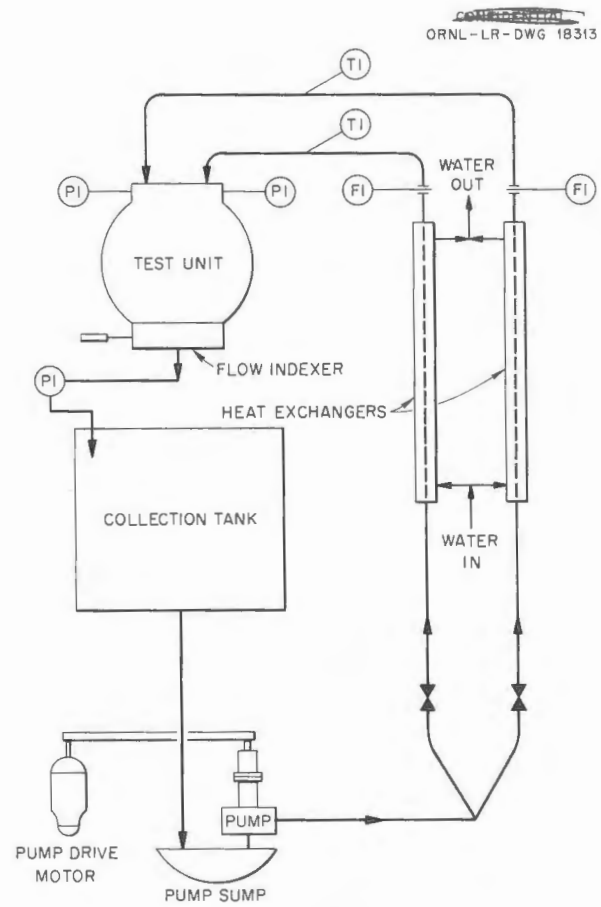

Fig. 1.4.34. Flow Diagram for ETU Component Water Flow Test No. 1.

The over-all heat transfer coefficients for air cooling, based on the heat picked up by the air, were correlated with the air flow rates and are shown in Fig. 1.4.35. Since no correction was

[21] F. A. Anderson and J. J. Milich, *ANP Quar. Prog. Rep. Sept. 10, 1955*, ORNL-1947, p 54.

[22] R. D. Peak, *ANP Quar. Prog. Rep. Sept. 10, 1956*, ORNL-2157, p 60.

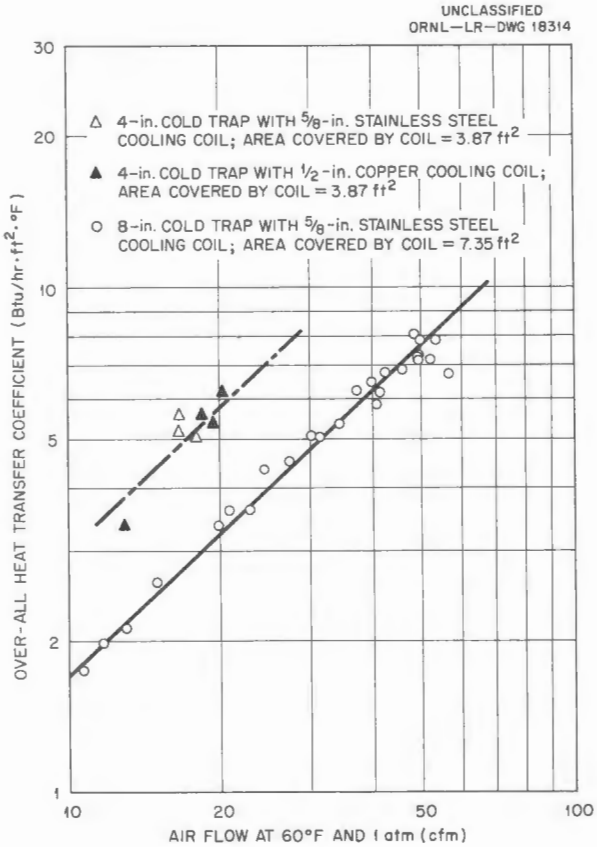

Fig. 1.4.35. Air Heat Transfer Coefficients in Cooling Coils of Cold Traps Based on Area of Cold Trap Covered by the Cooling Coil.

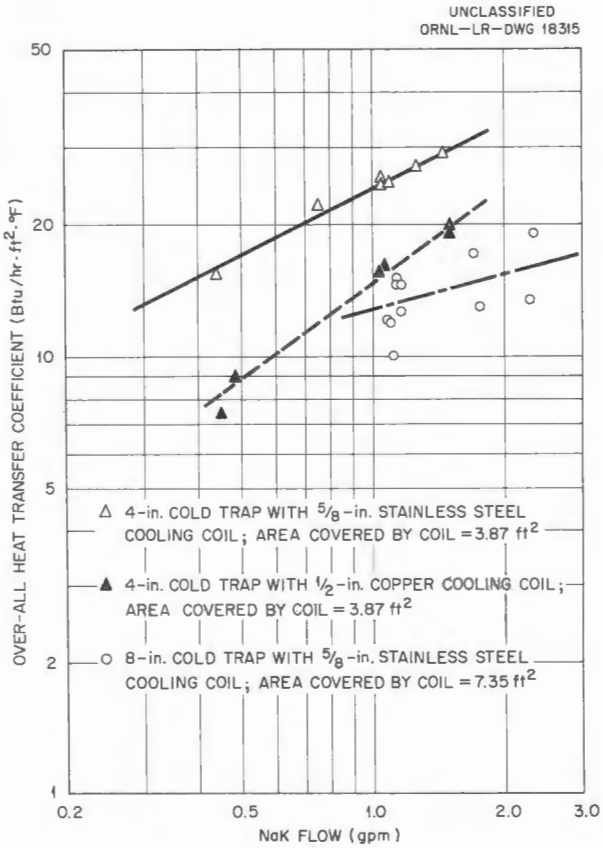

Fig. 1.4.36. Water Heat Transfer Coefficients in Cooling Coils of Cold Traps Based on Area of Cold Trap Covered by the Cooling Coil.

applied for the heat lost by radiation and convection from the external coil, these values should only be applied to cold traps of similar design. The coefficients for the 4-in. trap were similar for either the copper or the stainless steel coil and were higher than those for the 8-in. trap with its stainless steel coil. The test NaK flow range was from 0.29 to 2.88 gpm.

With water cooling in the coil of the cold traps, essentially no heat was lost by natural convection or radiation. The over-all heat transfer coefficients calculated for water cooling correlated best with NaK flow rates through the cold trap, as shown in Fig. 1.4.36. The coefficients for the 4-in. trap with the stainless steel coil were higher than the coefficients for either of the two other traps. The water flow range was from 0.25 to 6.0 gpm.

The test data on the 40-in. NaK-to-NaK economizers were correlated on the basis of over-all heat transfer coefficients based on a mean heat transfer area of 0.51 ft^2. Twenty-five of the 27 test points fell between the over-all coefficient line predicted by using the Martinelli and Lyon equation[23] and the line predicted by using the Lubarsky and Kaufmann equation[24] as shown in Fig. 1.4.37.

Temperature patterns were measured in both the 4- and 8-in. cold traps at three cross sections: (1) just entering the packed area, (2) halfway through the packed area, and (3) just leaving the packed area. The temperatures were measured ½ in. in from the top and bottom of the trap, at the center, and halfway into the center from the side. The patterns for the 4-in. trap are shown in Fig. 1.4.38,

[23] In W. H. McAdams, *Heat Transmission*, 3d ed., p 213, McGraw-Hill, New York, 1954.

[24] B. Lubarsky and S. J. Kaufmann, *Review of Experimental Investigations of Liquid-Metal Heat Transfer*, NACA TN 3336 (March 1955).

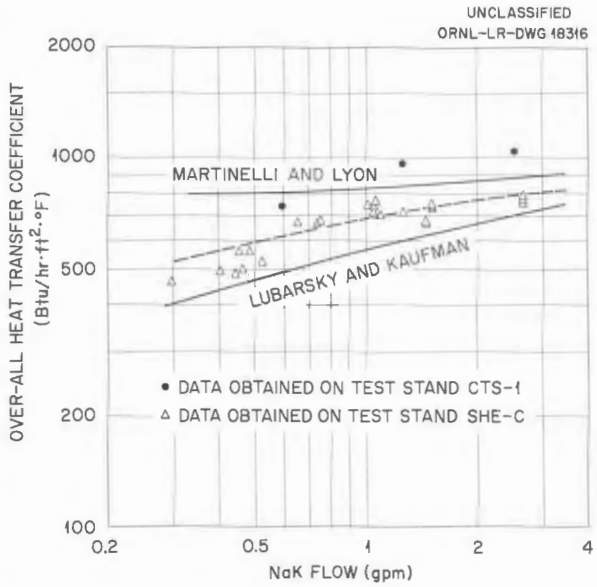

Fig. 1.4.37. Over-All Heat Transfer Coefficient of NaK-to-NaK Economizer, 40-in. Long, Made of a $\frac{3}{8}$-in. Pipe Inside a 1-in. Pipe.

and the patterns for the 8-in. trap are shown in Fig. 1.4.39. The patterns for the 4-in. trap show more extreme temperature differences than those for the 8-in. trap for some unknown reason. These patterns demonstrate the fallacy of attempting to correlate plug-indicator break temperatures with cold-trap exit or center temperatures when substantially lower temperatures exist near the walls in the trap.

Water Flow Studies of NaK Systems for Cooling Fuel Fill-and-Drain Tank

W. J. Stelzman

The ART fuel fill-and-drain tank is to be cooled by two separate NaK systems which will serve separate sets of U-tubes that will permeate the fuel volume from opposite ends of the tank. One of these two systems will also feed NaK through an annular jacket around the tank to provide wall cooling. Tests are being conducted on mockups of part of the annular jacket and part of the U-tube cooling system.

The first mockup tested represented one-half the annular jacket. Observation of the flow pattern indicated some regions of relative stagnation which may be eliminated by inserting baffles in the flow channel.

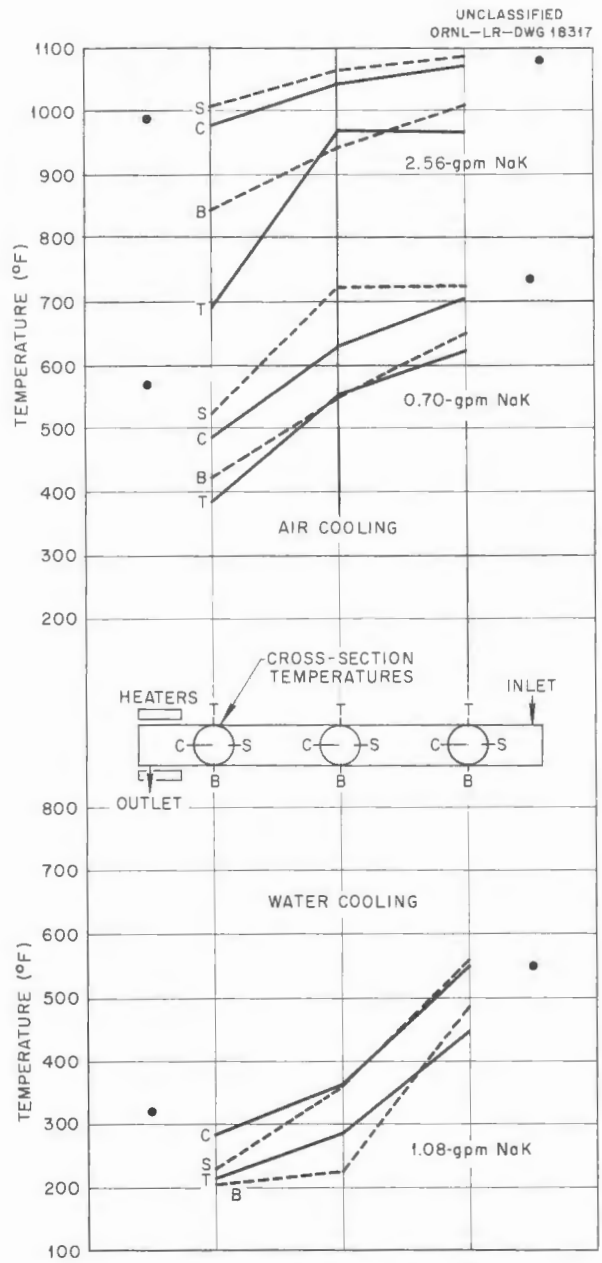

Fig. 1.4.38. Temperature Patterns in 4-in. Cold Trap.

The second mockup, which is being tested, represents one-half the bank of U-tubes that carry the NaK and are not associated with the annular jacket. This test will indicate the flow distribution across the tube sheet for the proposed drain-tank entrance and exit configurations.

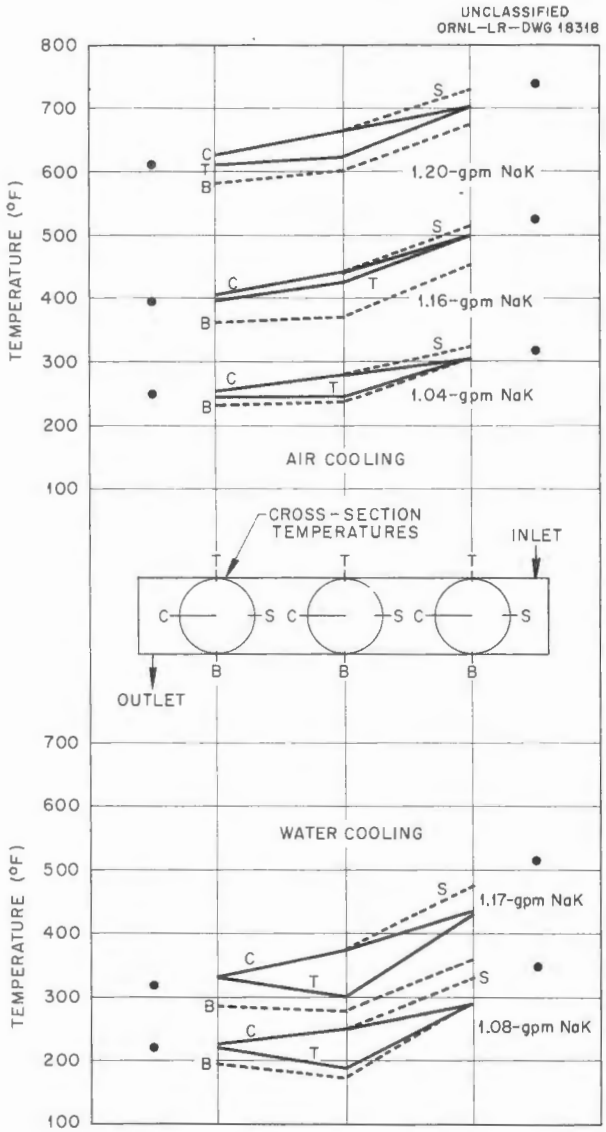

Fig. 1.4.39. Temperature Patterns in 8-in. Cold Trap.

1.5. PROCUREMENT AND CONSTRUCTION

W. F. Boudreau

ART FACILITY

F. R. McQuilkin

Contract work on the Aircraft Reactor Test (ART) facility is being done in four stages, package 1, package A, package 2, and package 3A, as determined by the design program. Package 1 work, which included the building alterations, the building addition, and the cell installation, and package A work on the installation of auxiliary services piping have been completed. A summary of the costs incurred during work on packages 1 and A is presented in Table 1.5.1. Package 2 work on the installation of the diesel generators and facility, electrical control centers, and spectrometer-room electrical and air-conditioning equipment has been completed, with the exception of the installation of three diesel control panels, performance testing of diesel-generator sets, and installation of penthouse anchor bolts. Design work on the process piping and process equipment (package 3) is continuing.

A portion of the work, termed package 3A, was recently prepared for lump-sum prime contracting by negotiation with the two contractors, V. L. Nicholson Company and Rentenbach Engineering Company, who were awarded the package 1 and 2 contracts. A supplemental agreement has been issued authorizing the Rentenbach Engineering

TABLE 1.5.1. COST OF PACKAGE 1 AND PACKAGE A CONSTRUCTION AT ART FACILITY

Package 1		
Initial total contract price		$765,835.00
Construction of addition to Building 7503	$501,462.00	
Construction of 7503 cell	$264,373.00	
Final total contract price*		$881,852.25
Construction of addition to Building 7503	$607,526.68	
Construction of 7503 cell	$274,325.57	
Total number of contract deviations	45	
Official starting date	August 23, 1955	
Official scheduled completion date	June 1, 1956	
Actual completion date	October 9, 1956	
Contract liquidated damage rate		
Phase I	$100 per day	
Phase II	$300 per day	
Liquidated damages charged for delay	None	
Reason damage charges not invoked	Contract deviations plus equipment delivery delays resulting from Westinghouse strike	
Package A		
Initial total contract price		$50,351.62
Final total contract price		$50,351.62
Official starting date	April 10, 1956	
Official scheduled completion date	June 29, 1956	
Actual completion date	September 26, 1956	

*This includes the $50,351.62 contract price for Package A.

Company to perform the package 3A work, which will include provision of a distribution system for supplying electrical power to the pipe and equipment heaters, a dry-air plant, and a building to house the air plant and wound-rotor-motor controllers. The electrical distribution system will include distribution centers, conduit, cable, cable trays, Powerstats, and induction regulators. The building will be a prefabricated type located west of the blower house and will be provided with the required auxiliary services. The dry-air plant will consist of two compressors, a dryer unit, and the necessary auxiliaries and piping. Package 3A provides for installation of the government-furnished wound-rotor-motor controllers and induction regulators; all other equipment is to be furnished, installed, and tested.

Work performed during the quarter included installation and testing of four 480-v circuit breakers, installation of a repaired radiator for diesel unit No. 4, mechanical testing to ascertain damage of diesel-generator units Nos. 3 and 4, drilling of holes for penthouse anchor bolts, installation of flashing around diesel-generator radiators, installation of two main blowers, completion of cell floor structure, demolition of the crane-bay parapet walls, completion of the high-pressure nitrogen manifolds, and removal of blocks which formed a 5-ft shield wall for the ARE reactor pits.

Some of the construction work may be seen in Figs. 1.5.1 through 1.5.5. A view of the cell floor structure immediately prior to installation within the cell is shown in Fig. 1.5.1. The fill-and-drain tank support pad and the support pads for the sampling tanks may be seen in Figs. 1.5.1 and 1.5.2, which show the cell floor structure after installation within the cell. The fill-and-drain tank support shaft will pass through the rectangular hole ($\sim 3 \times 6$ in.), which may be seen in the support pad as installed in the cell (Fig. 1.5.2). A photograph of the crane bay, Fig. 1.5.3, which was taken looking south toward the cell and the penthouse, illustrates the increased floor area made available by removal of the parapet walls on the ARE pits. One of the two main blowers that is now installed and is in operating condition may be seen in Fig. 1.5.4.

The startup of one of the Buda diesel-generator sets for mechanical testing is shown in Fig. 1.5.5. Two of the diesel-generator sets broke loose from their supports during shipment and were therefore checked for mechanical damage by this test.

Preliminary planning work continued on the program of reactor disassembly and examination. As outlined previously,[1] this activity is being developed in two basic parts, the first being that of removal of the reactor from the cell and the second that of transportation to, and hot disassembly in, a new large hot-cell facility. Tentatively, the new facility is being called the Central High-Level Laboratory.

The problems associated with removal of radioactive equipment and the reactor from the cell have been the subject of intensive study in order to determine whether such considerations would require design changes in the reactor, the cell equipment, or the cell. (For details of this study see Chap. 1.6, "ART, ETU, and In-Pile Operations.")

Thirteen possible building sites for the disassembly facility were investigated. Of these, three appeared to be sufficiently desirable to merit favorable recommendation. They are all located on Central Avenue of the Oak Ridge National Laboratory area near important associated facilities, such as the permanent reactor buildings, existing hot cells, and the contaminated waste and recovery facilities. A final choice for the site is expected to be made during the next quarter.

Present planning for the engineering work required includes the employment of an architect-engineer for the structure, building services, and large hot cell of the disassembly facility and employment of design jobbers to prepare detail drawings and specifications for the tools, fixtures, gages, and measuring devices required for hot disassembly work. Design criteria for the facility and design concept sketches for tools and gages are being prepared by ORNL personnel.

A mockup of the large hot-cell facility is proposed to provide a facility for disassembly tool shakedown, disassembly procedures shakedown, and personnel training. Because the time of need for such a setup is expected to conflict with the large-cell construction schedule, a separate location for the mockup is being considered.

[1] F. R. McQuilkin, *ANP Quar. Prog. Rep. Sept. 10, 1956*, ORNL-2157, p 64.

Fig. 1.5.1. Floor Structure Ready for Installation in Cell.

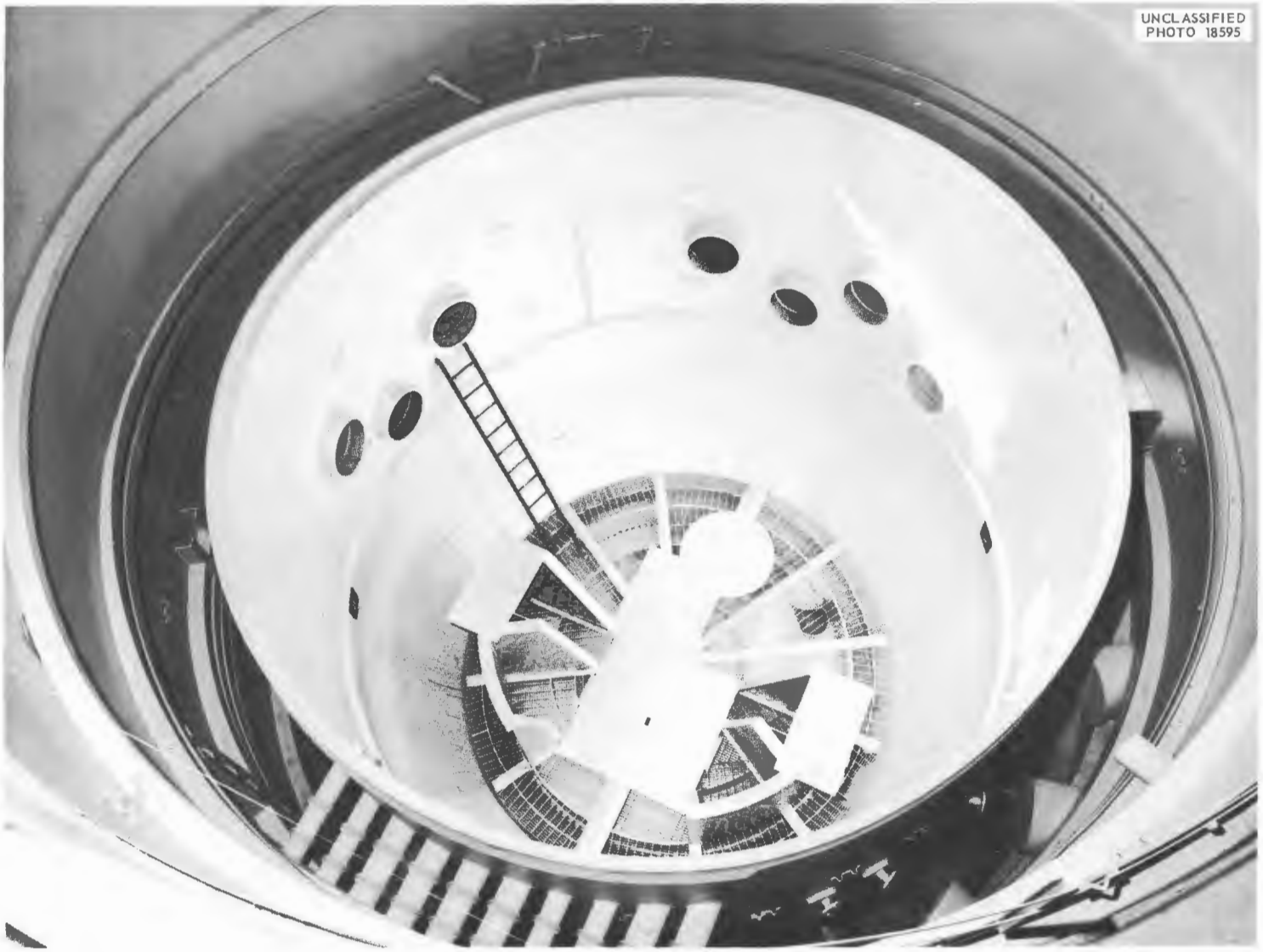

Fig. 1.5.2. Floor Structure Installed in Reactor Cell Showing Support Pads for Fuel Fill-and-Drain Tank and Sampling Tanks. ~~(Secret with caption)~~

Fig. 1.5.3. ART Facility Crane Bay After Removal of Parapet Walls on ARE Pits.

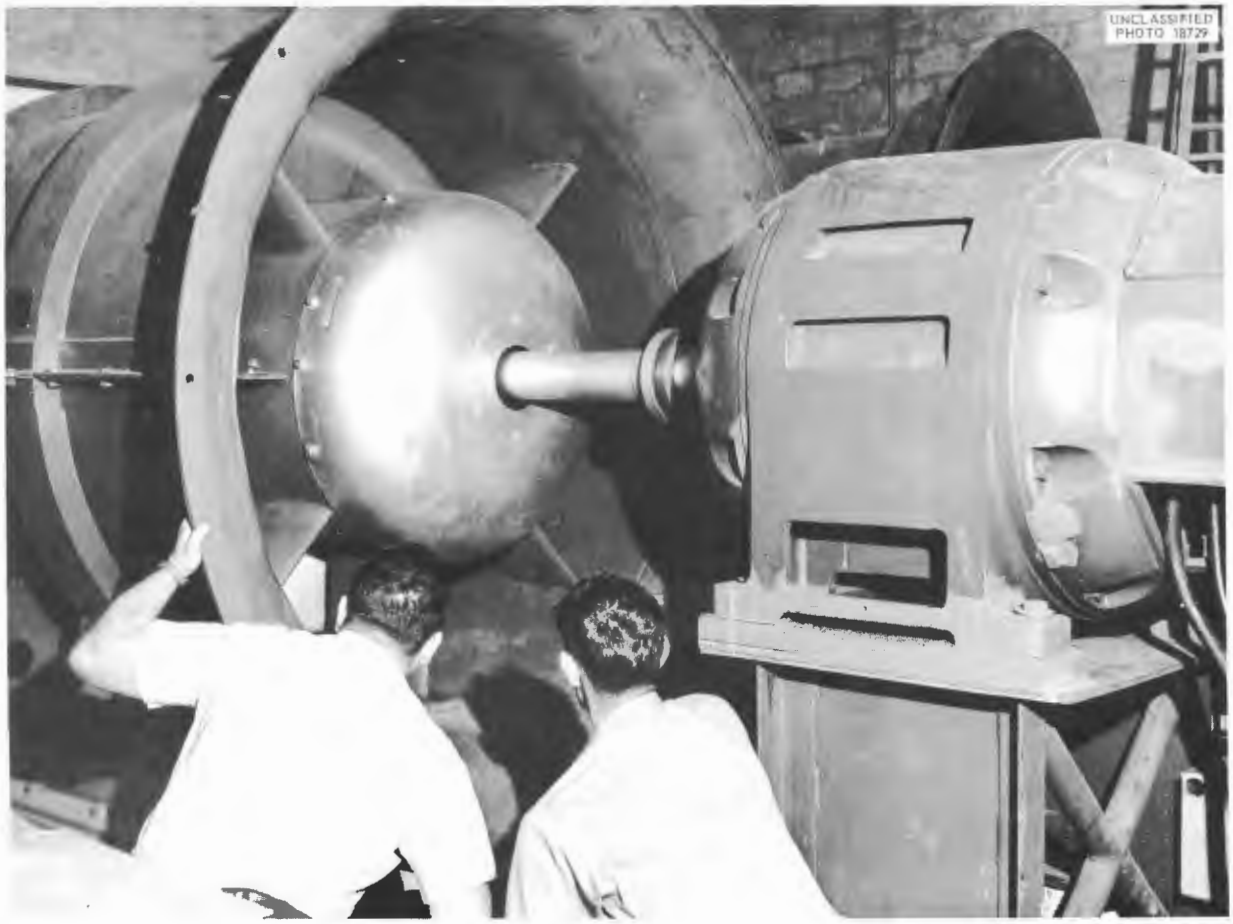

Fig. 1.5.4. One of Two Main Blowers, As Installed and in Operating Condition.

ART-ETU REACTOR CONSTRUCTION

M. Bender G. D. Whitman

Reactor Assembly

H. M. Abele C. K. McGlothlan
G. W. Peach

The preparation of reactor-assembly and inspection procedures was continued. Component procurement is under way, and weld-shrinkage tests are being made. Inspection procedures and data sheets have been completed for the reactor shells and beryllium parts, and general descriptions of the inspection methods for other components have been prepared.

One set of contoured beryllium parts for the ETU reactor has been received. These components are being processed through the local shops for hole drilling and inspection operations. The lower half of the hemispherical reflector-moderator has been completed and is ready for assembly in the first water flow test. This lower beryllium hemisphere is shown in Figs. 1.5.6 and 1.5.7 in the horizontal boring mill used to drill the holes that provide the passages for the sodium coolant.

The thin Inconel core shells that form the fuel annulus continue to be a difficult fabrication problem. Several shells have been received from the vendor for metallurgical examination and for use as weld test specimens, but none of these components has yet been within the established design tolerance. These shells are being fabricated by a shear forming process that is known commercially as "Hydrospinning." The progress to date indicates that the technique will ultimately produce acceptable inner and outer core shells, but problems still remain on raw material finish

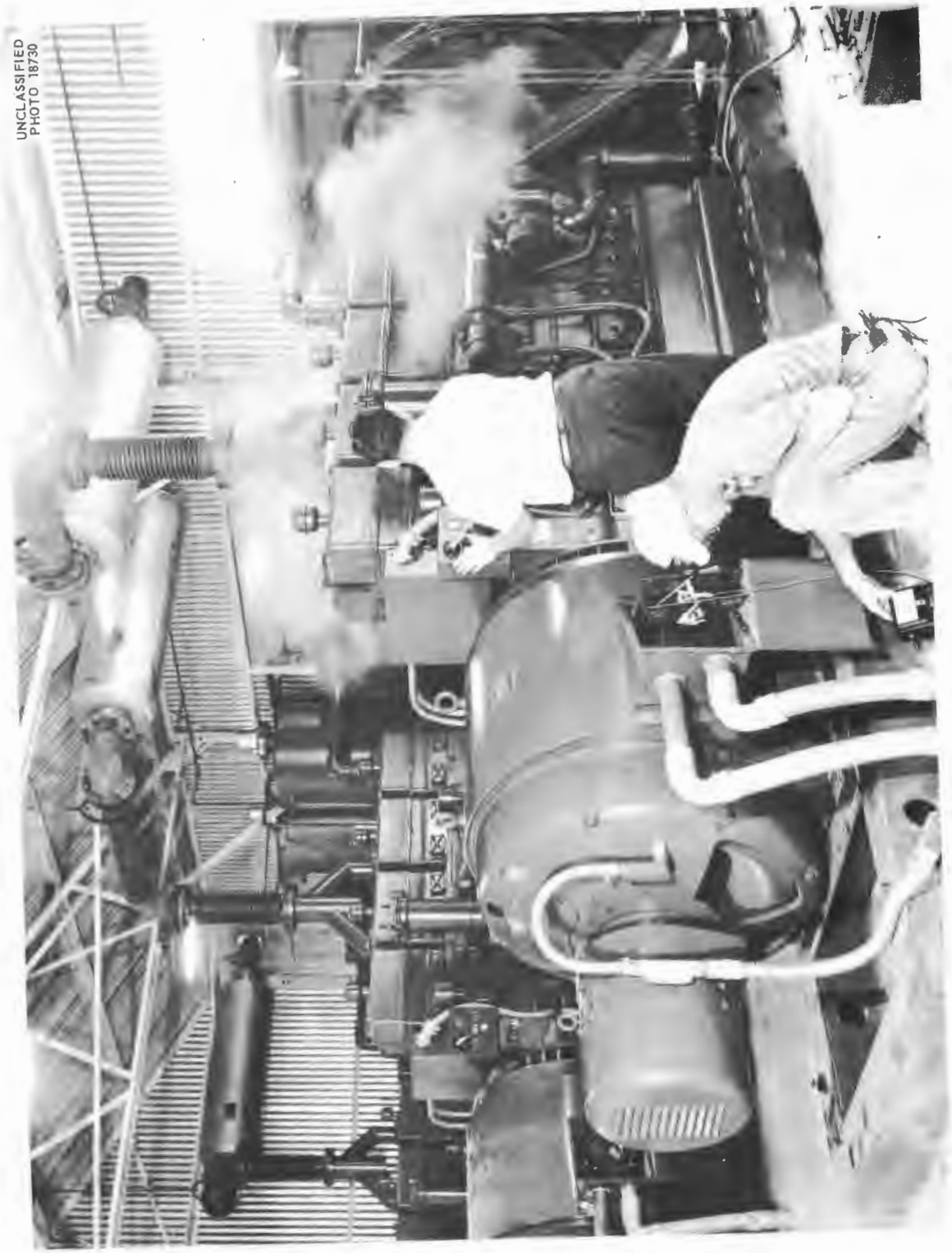

Fig. 1.5.5. One of the Diesel Generators Undergoing Mechanical Testing.

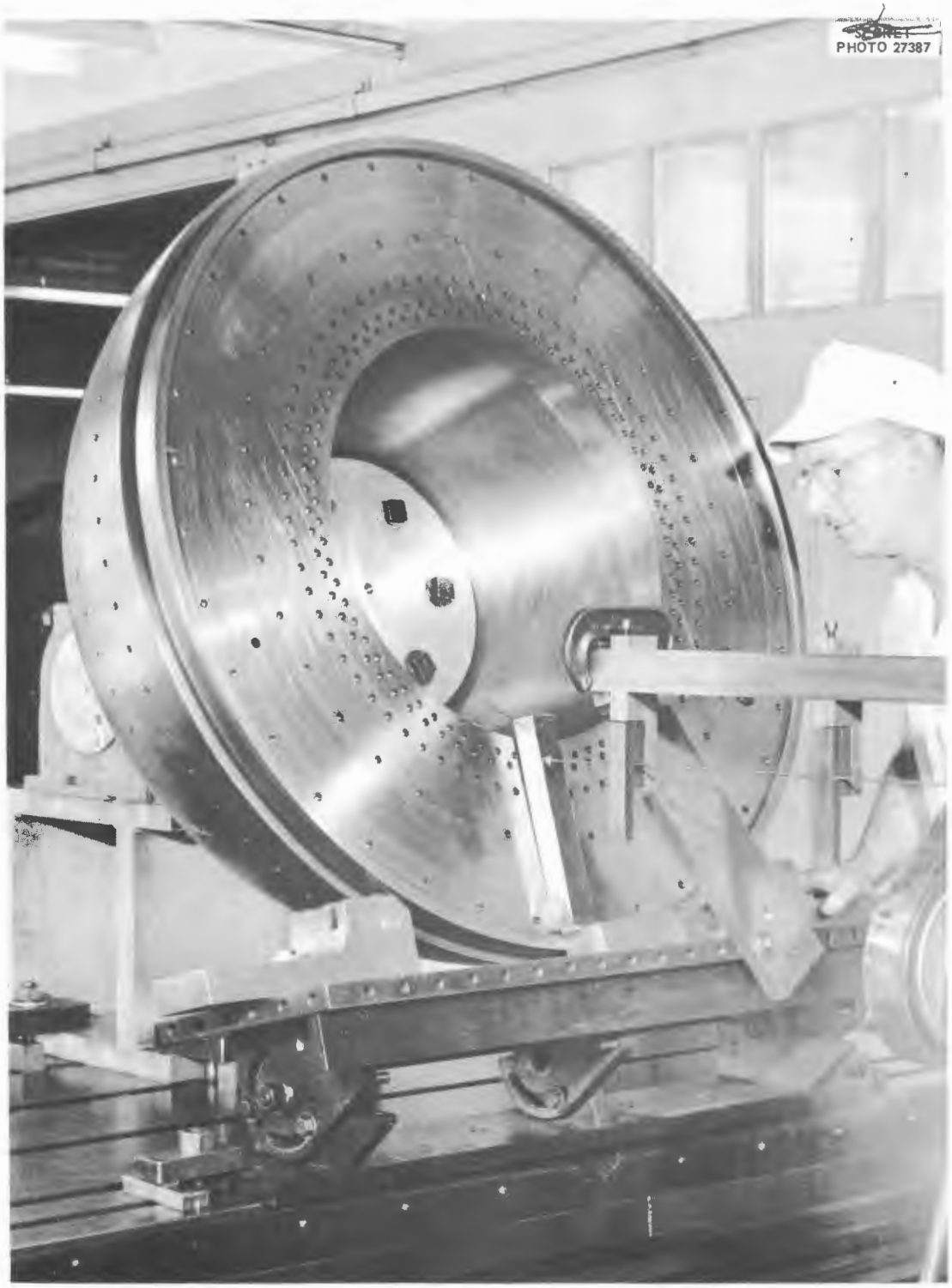

Fig. 1.5.6. Reflector-Moderator Southern Hemisphere Viewed from Equator.

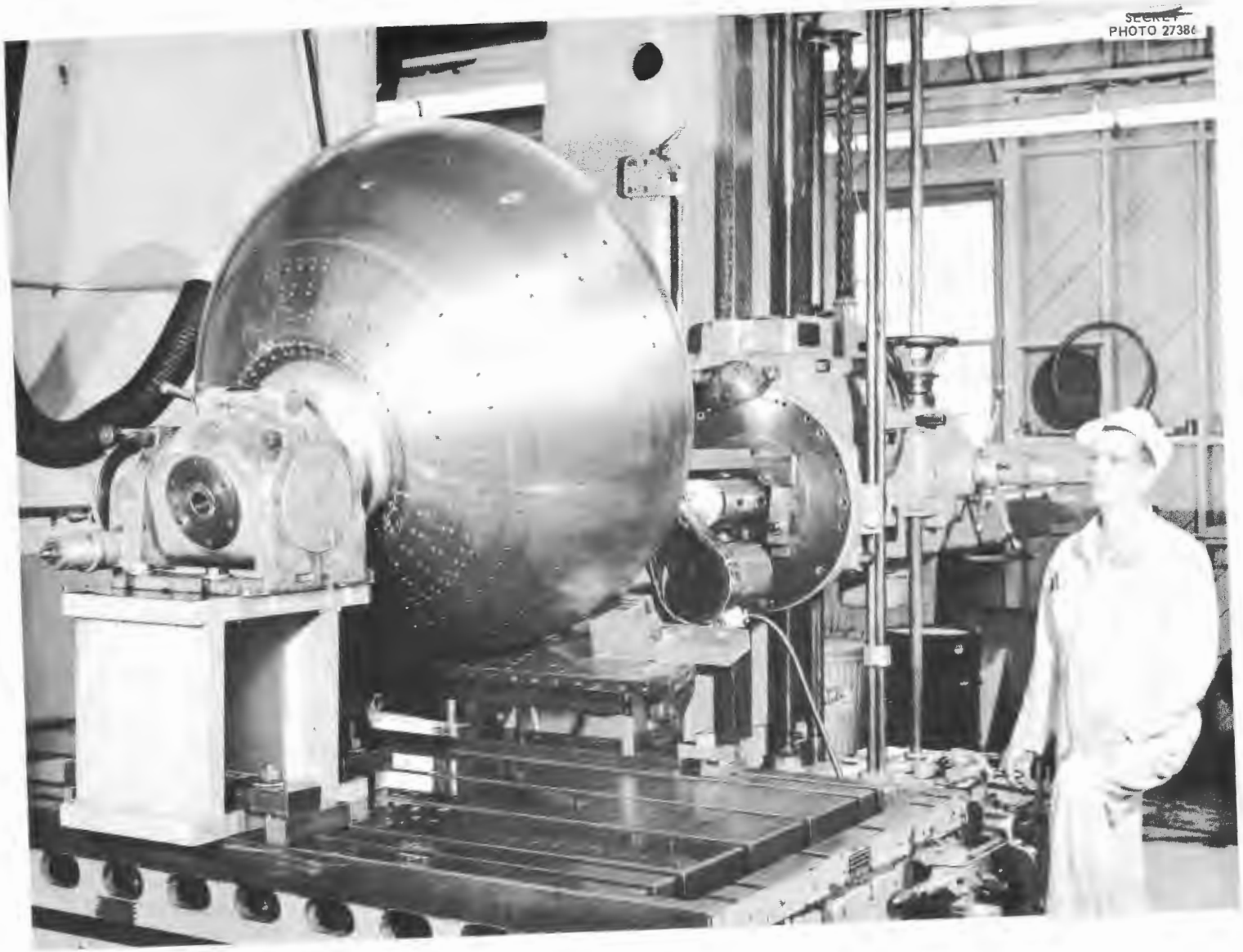

Fig. 1.5.7. Reflector-Moderator Southern Hemisphere Viewed from Bottom.

requirements, final mandrel sizing, and inspection techniques.

Samples of fabricated stainless-steel-clad boron-copper cermet parts have been received and are being given metallurgical and dimensional checks. These items appear to be acceptable. The surface finish is good. Some difficulty has been experienced in holding the raw stock to the thickness tolerance and in obtaining the proper thickness ratio between the stainless steel cladding and the cermet.

Considerable effort has been put forth on weld tests which not only give data on weld shrinkage of particular reactor geometries but will also serve to train the craftsmen on setup and welding techniques that will be required on the actual reactor parts. In addition to shrinkage information, data is taken on welding current, rod consumed, welding time, and gas flow rates. To date, the reproducibility of the shrinkage data on similar geometries has not been good enough to hold the spacing allowance between many of the parts in the reactor.

Tests have been performed on flat plates to determine the effect of joint preparation on weld quality and to determine the effect of gap and parent stock thickness on transverse shrinkage. Hoops of diameters and thicknesses that simulate those of the reactor shells are being welded to obtain information on transverse and diametral shrinkage, and rejected shells are being welded whenever they are available and suitable for weld tests. The setup used in making the equatorial weld of an inner core shell is shown in Fig. 1.5.8.

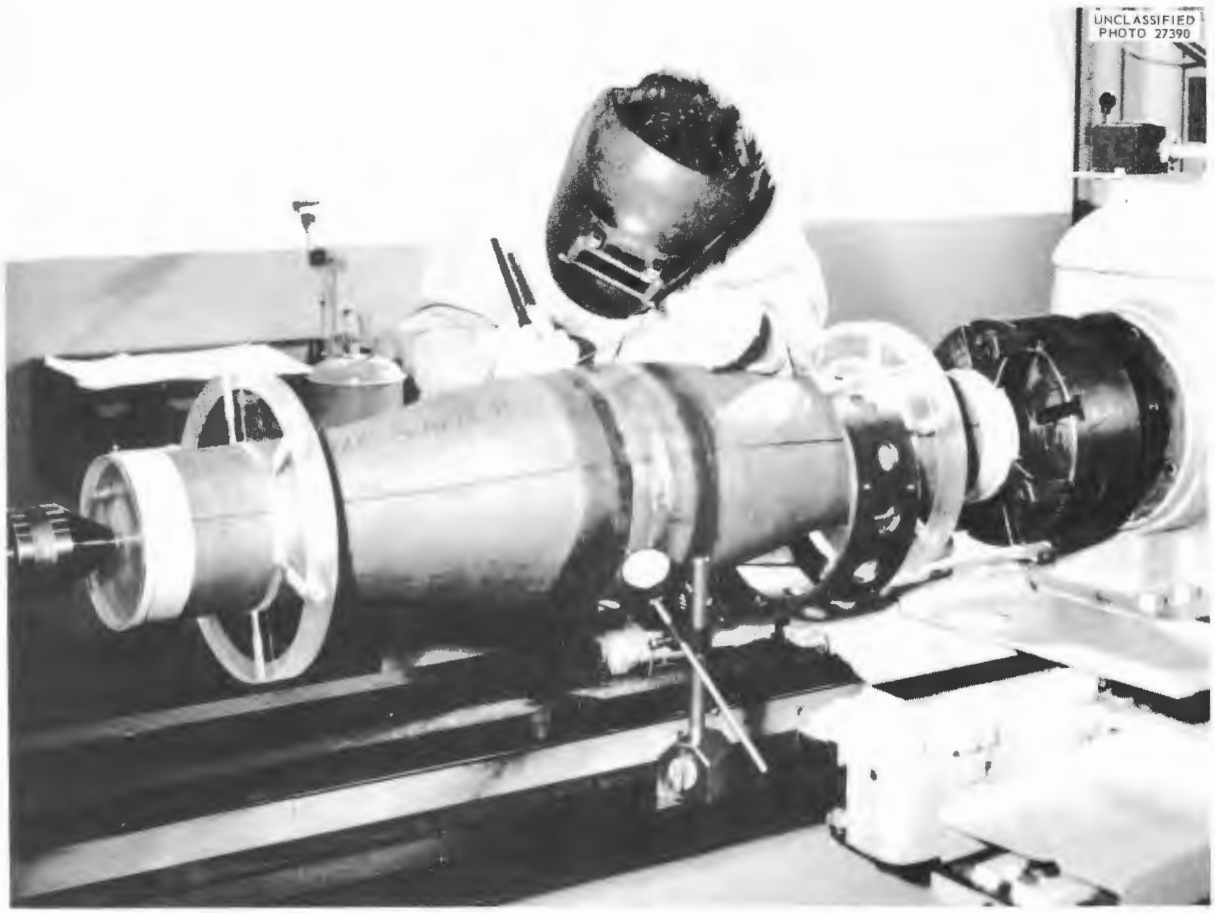

Fig. 1.5.8. Practice Welding of Inconel Inner Core Shell. ~~(Secret with caption)~~

ETU Facility

P. A. Gnadt A. M. Smith

The ETU facility is now being constructed. All the main NaK piping supports have been installed, as shown in Fig. 1.5.9, as well as most of the additional floor supports required. Many of the main NaK piping runs, such as those shown in Fig. 1.5.10, have been bench assembled and are ready for installation into the piping support frame. Design of the individual pipe hangers is 90% complete, and material procurement has been initiated. Cold-trap and plug-indicator piping circuits are being bench fabricated. Long delivery times for some components will delay the completion date of the NaK piping installation until approximately June 1, 1957.

The materials for the control-room enclosure have been ordered, and the scheduled completion date is February 1, 1957. The design of the enclosure is complete, except for the air-conditioning system and its associated auxiliary equipment. The main air duct is now being fabricated. The delivery date of the NaK-to-air radiators will delay the installation of this component until the summer of 1957. Detailed design of the electrical system is approximately 40% complete. The designs of motor control centers, heater distribution cabinets, cable trays, and voltage-adjusting devices have been completed, and most of the equipment is now on hand. Advanced orders for tubular and ceramic clamshell heaters have been filled. Design work on the installation of individual heaters and their associated thermocouples is approximately 30% complete.

Changes in flow sheets have delayed the design and construction of the controls system and the control panels. Firm flow sheet information is expected to be available by January 1957. Some instruments and other controls components have been ordered. Design and construction of the control panels and control circuits is expected to take approximately ten months after approval of the instrument flow sheets.

The designs of the basement auxiliary service piping, lube oil, hydraulic oil, helium, and water systems have been completed, and approximately 15% of this equipment has been installed. Major portions of the piping to the individual lube oil and hydraulic drive units will be completed when the equipment is delivered early in 1957. The plant air header for the facility will be installed by ORNL forces during the period required to clear the basement area of the existing air compressor and other equipment. The design layout of the auxiliary service piping in the reactor area has been started.

Cell Components

A. M. Smith

Present planning for use of the ART cell drawings where possible in the fabrication of the ETU makes the over-all design of both the ETU and ART cell components approximately 20% complete. Mockups of the ART components not required for the ETU are to be made for the ETU assembly in order to determine assembly procedures and techniques for the ART.

Layout drawings have been prepared for 12 of these items, including the main and auxiliary NaK manifolds, the reactor lead shield, the dual cooling system for the fuel fill-and-drain tank, the fill-and-drain tank shielding, the fuel dump valves and actuators, the junction-panel expansion joints, and the reactor support platform. Design details for these are to be provided by outside vendors. Details of the designs for the enricher, the enricher line assembly, and two auxiliary-piping junction panels have been completed, and these items are presently being fabricated.

The vendor selected for fabrication of the lead shield has proposed a chimney type of shield to replace the segment shield designed for the northhead region of the reactor. Sketches are to be prepared and presented for approval. Detail drawings for the remainder of the shield are presently being reviewed.

Planning for disassembly of the ART has brought out problems which involve several of the items already designed. These include the reactor support platform and support columns, the NaK manifolds, the fuel fill-and-drain tank and its shielding, and some piping layouts. The reactor-support-platform design is presently being revised, and other design conflicts are being studied.

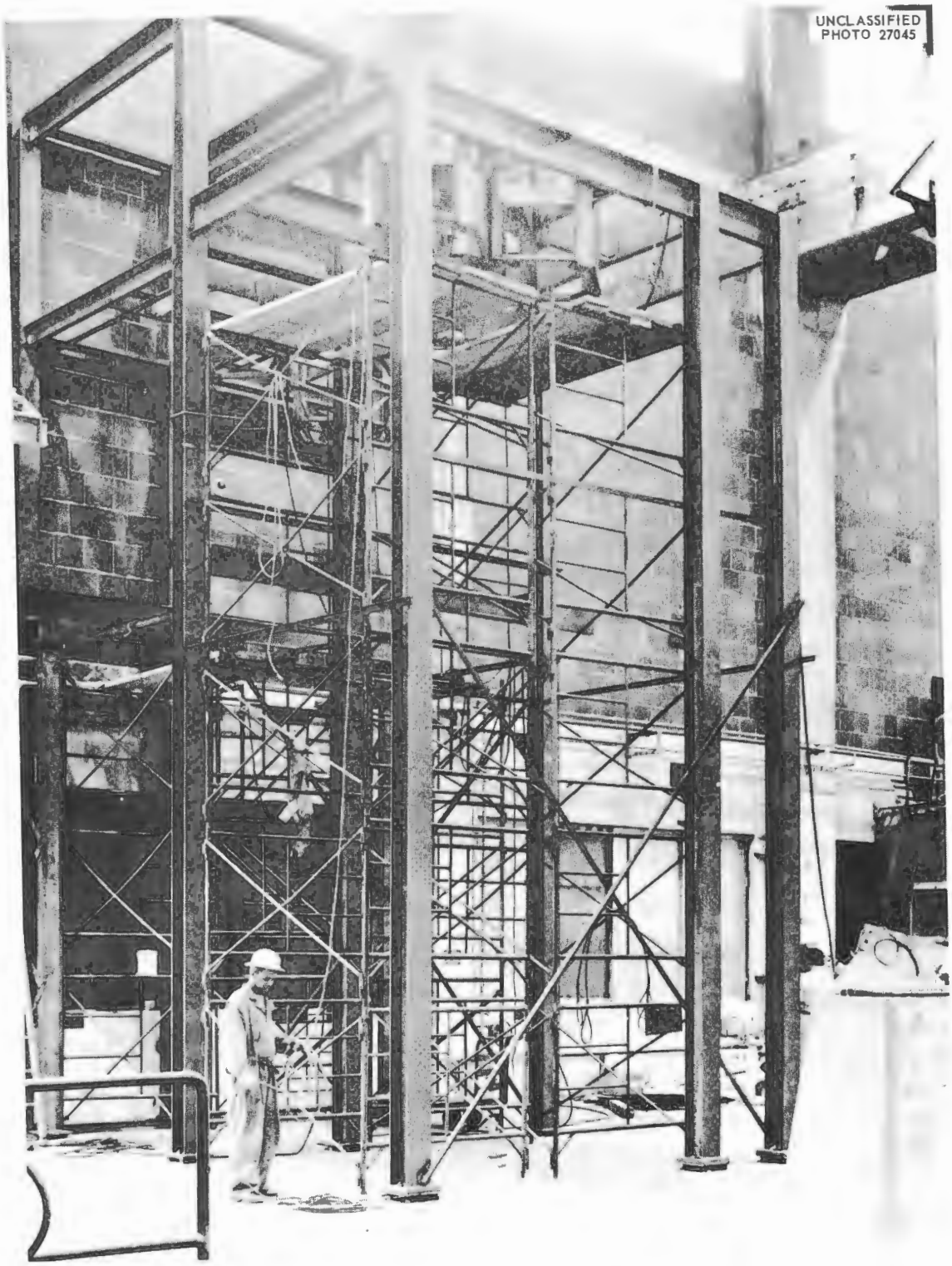

Fig. 1.5.9. ETU NaK Piping Support Structure.

Fig. 1.5.10. ETU NaK Piping.

ART-ETU REACTOR COMPONENT PROCUREMENT

M. Bender J. Zasler

Fuel-to-NaK Heat Exchangers

The York Corp. has fabricated a steel mockup of the channel and header assembly for the fuel-to-NaK heat exchanger in order to obtain additional information on the nature of the problems which might be encountered with the York method of fabrication. The Black, Sivalls & Bryson Company has completed the extensive modification of a large vertical boring mill required for machining the heat exchanger channels to final dimensions, and the first test channel is now being machined. Both companies have done considerable work on the problems of tube forming, welding, and machining, and both are developing suitable assembly and brazing fixtures.

Sodium-to-NaK Heat Exchangers

The Griscom-Russell Co. has been actively working on the more than thirty individual fixtures required to bend the tubes for the sodium-to-NaK heat exchangers. It has been found more difficult than anticipated to solve the springback problem, and much of the last quarter was devoted to making up the first four fixtures. Fixture production is now starting to move much more rapidly, however, since a great deal of knowledge has been gained from the work that has been accomplished to date.

Brazing Problems

Recent experimental and metallurgical work has indicated that the high-temperature brazing operation used for radiators, for all heat exchangers, and for the dump tanks must be subject to extremely close control, if excessive grain growth is

to be avoided in the tubing walls. The lower the brazing temperature, the less the chance for excessive grain growth. Successful brazing at the lowest possible temperature involves very careful control of furnace conditions (uniformity and close control of temperature and careful attention to drying and to distribution of the hydrogen), cleanliness of the work before brazing, adequate fitup of the parts to be brazed, and careful control and application of the brazing alloy. A great deal of work is being carried out with the vendors to ensure close control of all these variables.

Inconel Stock

The problem of obtaining adequate quantities of acceptable CX-900 tubing continues and is being discussed at frequent intervals with the Superior Tube Co. Obtaining plates or sheets having an adequate surface finish for the thin shells is a second currently urgent problem. Discussions have been held with representatives of the International Nickel Company concerning raw material production problems and inspection techniques for special forms of Inconel required for heat exchanger, radiator, and other parts.

1.6. ART, ETU, AND IN-PILE OPERATIONS

W. F. Boudreau H. W. Savage
D. B. Trauger

ART AND ETU OPERATION

D. B. Trauger W. B. Cottrell

A critical study of ART and ETU operational problems was initiated several months ago. This review has as an ultimate objective the formulation of operation procedures and operator training manuals, but it has also been conducted as an analysis of the reactor design. The real test of the design of a complex installation such as the ART is, of course, the operation of the complete unit, but the preparation of operating procedures can serve to reveal certain design deficiencies at an early stage when changes can be effected without undue delay and cost. This has been a major objective during the development of the operation procedures. The review has been extended to include analysis and revision of process flow sheets and control circuitry. It also is serving to familiarize a core of operating personnel with reactor and installation details.

Operating Procedures

ART. – Operating procedures are being formalized for the entire ART test program. This effort has been accompanied by the maintenance of up-to-date flow sheets of the various systems involved. There are 15 flow sheets which include all the components, valves, lines, instrumentation, and design operating values for the experiment. These flow sheets were first issued in November 1955, were revised during June and July of 1956, and a third revision is now nearly completed.

The operating procedures for the ART are based on the experimental objectives of the program, the physical requirements and limitations of the system and its components, the controls and instrumentation available, and the layout of the test facility. The fact that it was not deemed advisable to have all the controls centered in a single control room requires not only good coordination between the two major control centers but an elaborate system of permissives, interlocks, and annunciators to react in various situations.

In addition to the two major control centers the ART will have an electrical center, information centers, and miscellaneous operating stations. The two major control centers will be comprised of the main control room from which the fuel, sodium, and heat dump systems will be controlled and the nuclear operations will be performed and of the auxiliary control room from which the NaK, hydraulic, and lubrication systems will be operated. This arrangement, which will minimize the number of routine process operations controlled from the main control room, will leave the nuclear operators free to concentrate on the nuclear aspects of the test program. The auxiliary control room, on the other hand, will be the center for all process information and control not required in the main control room.

An outline of the ART operating procedures has been prepared, and the first draft is about 50% complete. The procedures will include details of operation for the following phases of the program:

1. acceptance tests,
2. cleaning of the systems,
3. charging of the NaK systems,
4. system heating,
5. charging of the sodium and fuel systems,
6. fluid shakedown tests,
7. enriching the fuel mixture,
8. low-power operation,
9. high-power operation, and
10. shutdown.

To date, procedures have been prepared for phases 2, 6, 7, and 8, and the procedural sequences involved in phases 3, 4, and 5 have been analyzed.

In order to minimize cleaning problems when the various systems have been assembled, precautions are to be taken during assembly to assure extreme cleanliness. Nevertheless, it is anticipated that acetone rinses of the fuel, sodium, and NaK systems will be desirable as a final cleanup and also as a preliminary check on the operability of the various systems and their associated instrumentation.

After the cleaning has been completed and the acetone removed, the NaK system can be filled with NaK. The heat generated by the pumps and by the piping heaters will combine to bring the reactor up to the desired temperature. When the reactor temperature is about 300°F, the sodium systems will be filled (the control-rod sodium system is

independent of the reflector-moderator sodium system) and the reactor will be heated to 1200°F, the design isothermal temperature for the system. The fuel carrier will then be charged to the fuel fill-and-drain tank, the NaK cold traps will be placed in operation, and the reactor will be ready for the fluid shakedown tests.

In the fluid shakedown tests, a check will be made of the operation of all the system components and of all operating procedures that will be required when criticality is achieved. Thus this phase of the test will assure the indoctrination of the operating crews, as well as determine the system characteristics and the applicability of the operating procedures.

The enriching operation will consist in discrete quantities of a fluoride mixture that is rich in U^{235} being added to the fuel carrier in the fill-and-drain tank. After each such addition, the fuel will be pressurized into the reactor, with the control rod inserted, and counts will be taken as the rod is withdrawn. The amount of uranium added will be small compared with the rod poisoning, and therefore criticality may be safely attained.

The low-power-operation phase will involve principally the calibration of the control rod and the determination of the nuclear characteristics of the reactor, including the reactor temperature coefficients, the effect of delayed neutrons, etc. Upon completion of these tests the reactor will be brought to power in a number of steps and operated at 60 Mw. During operation at design power a number of experiments pertaining to the nuclear characteristics of the reactor and to tests simulating an aircraft power plant will be performed. Following the completion of these tests, the experiment will be terminated and the reactor will be prepared for disassembly.

ETU. – The principal objective of the ETU is the construction and operation of the reactor assembly under simulated reactor conditions of pressure, temperature, and flow with natural uranium in the fuel mixture so that the assembly will not be critical. This test should provide information on the adequacy of the reactor fabrication and assembly techniques in advance of ART operation. While it will be possible to duplicate ART flow and pressure conditions, it has proved impractical to attempt to obtain the large ART temperature differences in the absence of the 60-Mw nuclear heat source.

In order to derive the greatest value from operation of the ETU, the system has been kept as similar to the ART as possible, consistent, of course, with the limited objectives of the ETU program. The ETU flow sheets and operating procedures parallel those of the ART, and the ETU will serve as a training facility for ART operating personnel, as well as a proving ground for the reactor.

The ETU system differs from that of the ART, however, in many respects. It does not include the special NaK systems for cooling the fill-and-drain tank. Two of the four main NaK systems will have no radiators, and the other two will include gas furnaces in place of the radiators. The two gas furnaces will provide the bulk of the heat (total ~3 Mw) which will be used in the ETU to simulate reactor system temperatures. The ETU fuel will contain natural uranium. The ETU control system and instrumentation will not have the numerous controls and interlocks that will be associated with the ART heat-dump system or the ART nuclear instrumentation. The ETU will have no disaster containment system.

Despite these differences the ETU will be similar to the ART in many important respects, the most important being the reactor and the equipment within the cell area. Except for the differences noted above, the NaK systems will be similar to those of the ART, and the hydraulic drive and lubrication systems will be practically identical to those of the ART.

The revisions currently being made to ETU flow sheets are a counterpart of the revisions being made in ART flow sheets. However, it is essential that the ETU flow sheets be "frozen" earlier than the ART flow sheets, since the ETU will operate first. Similarly, the ETU operating procedures will have to be available in final form first, although the ETU procedures will be patterned after those of the ART, with modifications as required. However, since the ETU operational requirements have not been completely specified, no effort has yet been made to compile the ETU procedures.

The ETU facility will have only one principal control center, whereas the ART will have two. Although this is made possible by the omission of nuclear controls, the ETU control center will be so crowded that it will be necessary to operate remotely all heater controls and to make use of

multiple switching arrangements for both heater and thermocouple circuits. The centralized control center will permit good coordination of all phases of the operation, but the ETU will also require some operating functions at other locations.

Process Flow Diagrams

C. W. Cunningham R. A. Dreisbach[1]

ART. – The ART process flow diagrams are listed in Table 1.6.1 with the latest revision number and the date of issuance for the latest revision. Drawings which are either being revised or which are due to be revised are so indicated. For the convenience of the ART operators, the fuel fill-and-drain, enriching, sampling, and recovery systems diagrams were consolidated on one flow diagram. The main, auxiliary, and special NaK systems flow diagrams, likewise, were combined on one flow diagram.

The most significant recent changes which have been or are being incorporated in the ART process flow diagrams[2] are described below.

1. Jackets have been added to the off-gas line, the inlet end of the reactor vapor trap, the overflow line, the branched fill-and-drain line, and the dump valves, and provisions have been made for circulating sodium coolant in the annuli thus created.
2. Provisions have been made for measuring fuel pressure at the south head instead of at the fuel pump suction and discharge. The fuel pump suction and discharge pressures will be obtained on the ETU but not on the ART.
3. Helium bypass lines have been added for each fuel pump to permit a rapid fuel dump in the event of plugging of the reactor vapor trap.
4. A similar bypass line, including a frangible disk valve, has been added around the vapor trap on the fill-and-drain tank.
5. A helium-bubbler type of level indicator has been provided in the overflow line to follow the fuel level in the reactor during the filling and draining operations.
6. An auxiliary sodium expansion tank has been added in parallel with the reactor sodium expansion

[1]On assignment from Pratt & Whitney Aircraft.

[2]Flow diagrams that were up to date as of May 1956 are presented in Appendix A of ORNL-2095, *Design Report on the Aircraft Reactor Test* (Dec. 7, 1956).

TABLE 1.6.1. ART-PROCESS FLOW DIAGRAMS

System	Drawing Number	Last Revision Date	Being Revised	Revision Pending
Reactor Temperature Instrumentation	D-2-02-054-1451 Original	11-5-55 (issue date)	No	Yes
Fuel Fill-and-Drain, Enriching, Sampling, and Recovery Systems	D-2-02-054-1469 Rev A	11-29-56	Yes	
Sodium System	D-2-02-054-1453 Rev A	5-4-56	Yes	
Main, Auxiliary, and Special NaK Systems	D-2-02-054-1470 Rev A	7-18-56	Yes	
Cell Pumps Hydraulic-Drive Systems	E-2-02-054-1460 Rev B	10-9-56	No	Yes
Reactor Pumps Lube Oil System	E-2-02-054-1461 Rev B	9-24-56	No	No
NaK Pumps Lube Oil System	E-2-02-054-1462 Rev B	9-26-56	No	No
Helium System	E-2-02-054-1463 Rev A	4-26-56	Yes	
Off-Gas System	E-2-02-054-1464 Rev A	4-26-56	No	Yes
Nitrogen System	E-2-02-054-1465 Rev A	4-26-56	No	Yes
Process Water System	E-2-02-054-1466 Rev A	4-26-56	No	Yes
Process Air System	E-2-02-054-1467 Rev A	4-26-56	No	Yes
Compressed Air System	E-2-02-054-1468 Rev A	4-26-56	No	Yes

tank to assure that the sodium pumps will remain primed if the reactor temperature is reduced to below 1200°F.

7. Provisions have been made for manually adjusting the pressure differential across the bottom seals of the reactor pumps and the NaK pumps from the lube-oil-package control panels in order to eliminate more complex control equipment.

8. Thermocouples are being provided on the outlet of each of the 12 main fuel-to-NaK heat exchangers for the detection of a leak between fuel and NaK. A leak in either direction would cause a temperature perturbation.

ETU. – ETU process flow diagrams are listed in Table 1.6.2 with the latest revision number and date of issuance of the latest revision of each flow diagram. Diagrams which are either being revised or are due to be revised are so indicated. The most significant changes which have been made or are being made to the ETU flow diagrams are those described above for the ART diagrams, except that, in addition to provisions for the fuel pressure measurement at the south pole, provisions will also be made for measuring the fuel pump suction and discharge pressures.

Electrical Systems

S. M. DeCamp

ART. – Sufficient electrical drawings have been completed for analysis of the electrical systems from the operations standpoint. The system is divided into two sections – half of the main reactor loads are fed from purchased TVA power, and the other half are supplied by locally operated diesel-electric generating sets. This system was devised to ensure an orderly shutdown of the reactor following loss of one power system. Where necessary the loads will be automatically transferred from the failed system to the operating system, and where permissible the transfer of power will take place manually.

A load study has been made of the ART power system. Presently available data show that under normal operating conditions the 750-kva transformer will be loaded to 725 kva and that the 1500-kva transformer will operate at 1160 kva. Adequate transformer capacity is available to maintain 80% bus voltage while starting the large induction motors used to drive the main NaK pumps and the main radiator blowers.

The diesel system consists of five engines, each driving a separate generator. Each generator

TABLE 1.6.2. ETU-PROCESS FLOW DIAGRAMS

System	Drawing Number	Last Revision Date	Being Revised	Revision Pending
Reactor Temperature Instrumentation	D-2-02-054-1476 Original	2-17-56 (issue date)	No	Yes
Fuel Fill-and-Drain, Enriching, Sampling, and Recovery Systems	D-2-02-054-1477 Rev A	4-2-56	Yes	
Sodium System	D-2-02-054-1478 Rev A	4-2-56	Yes	
Main, Auxiliary, and Special NaK Systems	D-2-02-054-1485 Rev A	4-2-56	Yes	
Cell Pumps Hydraulic-Drive Systems	D-2-02-054-1481 Rev A	10-21-56	No	No
Reactor Pumps Lube Oil System	D-2-02-054-1482 Rev A	10-2-56	No	No
NaK Pumps Lube Oil System	D-2-02-054-1483 Rev A	10-3-56	No	No
Helium System	D-2-02-054-1484 Original	2-17-56 (issue date)	Yes	
Process Water System	D-2-02-054-1487 Rev A	4-2-56	Yes	
Process Air System	D-2-02-054-1488 Original	2-17-56 (issue date)	Yes	

is rated at 375 kva. One machine, larger than the other four, while rated at only 375 kva, will be capable of supplying some leading current to help correct the system power factor. The total load on the diesel system is expected to be 1545 kva. The system rating is 1875 kva with five generators running or 1500 kva with four machines running. In the event that only four machines are in operation, it may not be possible to start the last main blower.

Normal control power will be taken from both the TVA and diesel bus. Controls and instruments will be fed from the bus that feeds their associated equipment. A d-c–a-c motor-generator set with a battery floating on the bus will provide a third source of control power. In case of a power failure the battery will continue to run the d-c–a-c motor-generator set. This third source of power will be used to power vital reactor control equipment, such as the control-rod drive motors, critical relays, and control instruments.

ETU. – Drawings of the ETU electrical system have also been reviewed from the standpoint of operations. Originally the ETU design was to follow the design of the ART electrical systems as closely as possible. However, the fact that the ETU will not contain a critical assembly has made possible the elimination of many controls required for the ART, and the space limitations for the ETU have made such omissions essential. The provision of only one control room for the ETU also decreases the similarity between the two systems.

Control of all ETU reactor pumps will be from the control room, but the lube oil pumps and the hydraulic equipment will be locally controlled. The speeds of the hydraulic motors for driving the fuel and sodium pumps will be varied by remote means from the control room.

Since the ETU reactor will not be critical, a power outage will not be so dangerous as for the ART. However, certain key equipment must be kept in operation until power is restored. Therefore a 300-kw diesel-driven generator has been provided. In case of a power outage this unit will maintain lube oil circulation to the pumps, will supply control power, and will maintain heating on vital lines. At the present time the system is designed so that a voltage drop to 80% of rated voltage will cause the same action as a loss of power. Since loss of power will not cause a thermal shock to the system, this type of operation will be satisfactory.

Electrical heating for the ETU will be controlled by induction regulators and Powerstats, which will be remotely operated from the control room. A selector switch and push button will make possible the operation of several heaters with a minimum of control equipment and yet achieve the desired degree of control. All heater circuits are being wired to provide for the use of a clip-on ammeter to check heater loads.

Leak Testing of the ART

J. R. Sites

L. O. Gilpatrick C. F. Harrison

It will be desirable to have assurance that no material transfer path exists between the fuel system and the cooling systems of the ART before and during startup. A very sensitive technique for such a check is that of isotopic dilution as determined with a mass spectrometer. The testing can be done during one of several stages of startup. If the cooling systems are loaded with helium and the fuel system is loaded with a higher pressure of krypton, any buildup of part-per-million amounts of krypton in the helium, with time, can be detected and an estimate of the size of a single equivalent leak can be calculated. The position of the gases could also be reversed in the systems.

A subsequent check would be desirable when the sodium and the NaK had been loaded into their respective systems and there was helium in the fuel system. In this case, however, there does not seem to be any effective technique for using a mass spectrometer that is sensitive enough to detect very small leaks.

With the sodium and NaK in their systems and with fuel in the fuel system, an increase in the amount of potassium (from the NaK system) in the fuel can be detected, but there is no sensitive way to detect a leak from the sodium system into the fuel system. If the pressure differential were in the opposite direction, it would be possible to look for an increase in the zirconium content of the sodium or the NaK.

The methods used for detecting trace amounts of krypton in helium were developed and used on the ARE, with a sensitivity of about 1 ppm. For the check of the NaK content of the fuel, potassium-free chemical reagents must be used. Superdistilled water, NH_4Cl, NH_4OH, and HCl have been made with less than 10 ppm of potassium, but the HF required for the analysis is less pure.

Samples of the fuel carrier have been put through ion exchange columns to remove the zirconium and to separate the relatively large amount of sodium from the desired potassium. Some attempts have been made to determine the potassium content of the fuel carrier without removing the other constituents, but the results obtained thus far have not been entirely satisfactory.

ART DISASSEMBLY

W. B. Cottrell

W. E. Browning R. P. Shields
D. B. Trauger

An obvious corollary to the operation of the ART is the analysis of its performance. To a degree this can be obtained from a study of the instrument records, but a final analysis must depend on information which can be obtained only from the disassembly, examination, and destructive testing of the reactor parts. Accordingly, a disassembly facility has been proposed in which sectioning of the reactor and subsequent examination of the parts may be accomplished. Also, techniques and procedures are being devised for removing the reactor from the ART facility after the test has been completed and for transporting it to the disassembly facility.

The procedure for disassembly at the ART facility from the time that the reactor test is terminated until the last major radioactive component is removed from the cell has been prepared. The designs of the features which must be built into the system in order to effect this procedure in the desired manner were thus established, and the necessary changes were initiated in the reactor system and facility designs.

Inasmuch as the disassembly program involves the handling of not only radioactive components but also an entire system which at one time contained radioactive fluids, estimates were made of the after-shutdown doses from the reactor resulting from residual activity and the doses from the ART cell that would result if there were an off-gas system leak. While the dose from the residual activity would not be so great as to prevent personnel access to the shield surface, the dose from a presumed off-gas-system leak would restrict access to the cell, since daughter products of the gases could not be purged. Accordingly, the disassembly procedures have been based on the assumption that cell entry is not permissible.

Disassembly Procedures in ART Cell

W. B. Cottrell

The operating procedures covering the disassembly of the ART cell components provide for remote control of the fluid (fuel, sodium, and NaK) removal and flushing operations. All reactor fluids will be removed except the control-rod sodium, which will be allowed to freeze in the control-rod thimble. When these operations have been effected, the cell will be opened and the fuel recovery tank will be removed. The cell interior will then be decontaminated, if necessary, by a water rinse. The reactor and all components within the cell will then be cut loose by remotely operated guillotines and removed from the cell for transportation to the disassembly facility. The detailed techniques for effecting the removal of the reactor from the ART cell have not been resolved; that is, it has not been determined whether the top of the cell will be removed before or after the reactor is cut loose, whether these operations will be performed in a water or a controlled air environment, and what the means of support and control of the remotely operated tools will be.

The sequence of operations involved in removing the reactor is outlined below:

1. Transfer fuel to recovery tank.
2. Transfer fuel carrier to fuel fill-and-drain tank for flushing reactor.
3. Flush reactor and dump fuel carrier.
4. Cool system to about 300°F.
5. Drain sodium from reactor.
6. Cool system to about 100°F.
7. Drain NaK systems.
8. Flush sodium system with alcohol.
9. Flush NaK systems with kerosene and alcohol.
10. Open all manholes.
11. Remove recovery tank from cell.
12. Flush cell with water.
13. Flood cell with water.[3]
14. Cut off top of cell.[4]
15. Remove postpower fuel samples.
16. Prepare reactor for removal.
17. Remove reactor from cell.

[3] Flooding the cell with water is only one of the proposed techniques for effecting the subsequent operations.

[4] Depending on the disassembly technique ultimately adopted, the top of the cell may be opened at this time or after the reactor is ready for removal.

18. Remove fill-and-drain tank from cell.
19. Clean cell.

After-Shutdown Dose from the Reactor

K. W. Edwards T. J. Bales[5]

The after-shutdown dose from the reactor was calculated for the following reactor shield conditions: reactor shielded by the as-designed lead and water shield, reactor shielded only by the lead, and reactor unshielded. For each of these three conditions the dose level at the surface of the water shield at the equator was determined as a function of time after shutdown following operation at 60 Mw for 100 and for 1000 hr. In each of these calculations it was assumed that 2% of the fuel remained in the reactor, as well as all the sodium. It is currently believed that flushing the reactor with carrier will leave less than 0.04% of the fuel in the reactor and that all but trace amounts of sodium will be removed from the reflector-moderator cooling system. The dose data presented in Figs. 1.6.1 through 1.6.6 were based on activation studies made by Bertini.[6]

Contamination in ART Cell from Off-Gas Leak

D. E. Guss[7]

Calculations have been made for determining the contamination that could occur in the ART cell as a result of a leak in the fuel-pump expansion-chamber seal or in the fission-gas purge line. These calculations were based on an expansion chamber volume of 90 in.^{3}, an off-gas flow rate of 3000 liters/day, and a continuous 1% leak of purge gas into the reactor cell during 500 hr of operation at 60 Mw.

The beta activity data are presented in Fig. 1.6.7 as the total number of curies present in the reactor cell. The average energy of the beta rays present will be about 500 kev, and the maximum energy present will be 2.2 Mev.

The gamma-ray activity data are presented in Fig. 1.6.8 as the dose rate at a distance of 12 ft from a point source whose intensity is that of all

[5]On assignment from Pratt & Whitney Aircraft.

[6]H. Bertini, private communication to T. J. Balles.

[7]On assignment from U. S. Air Force.

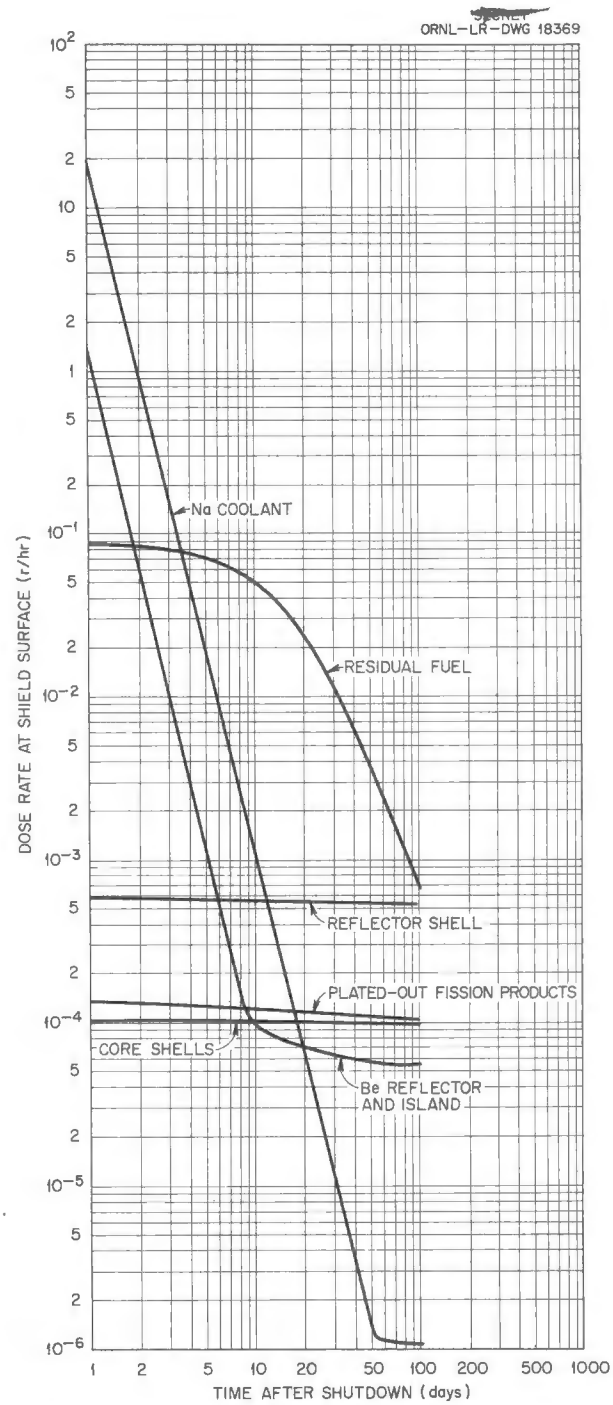

Fig. 1.6.1. Dose from Reactor with Lead and Water Shields After 100 hr of Operation at 60 Mw.

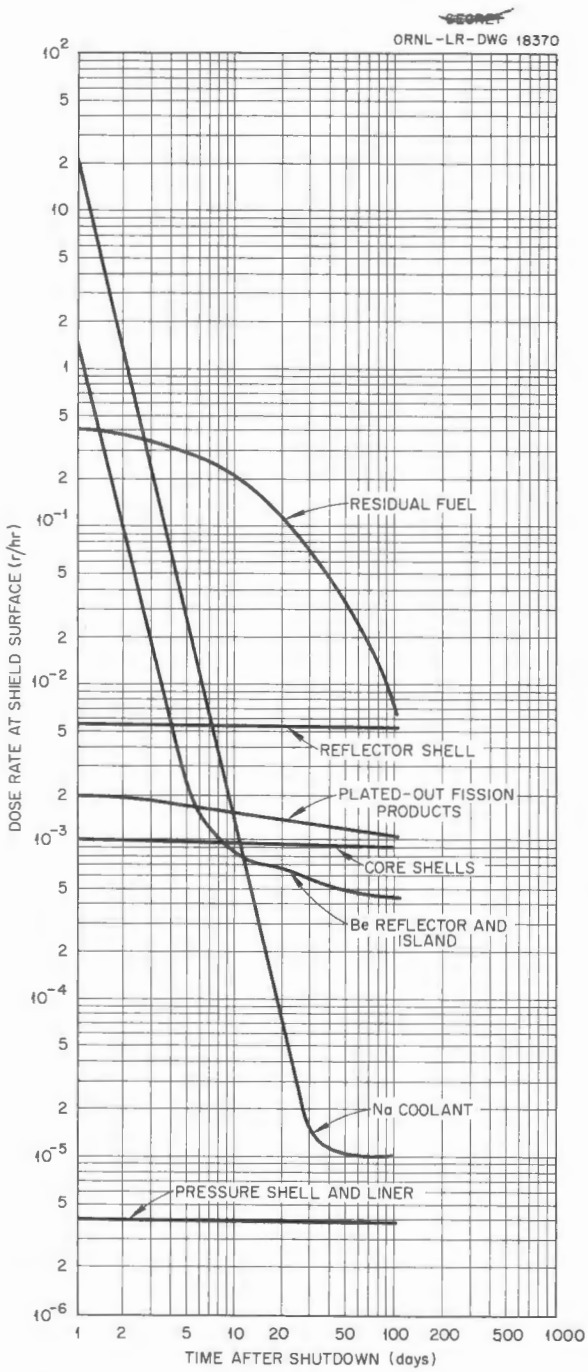

Fig. 1.6.2. Dose from Reactor with Lead and Water Shields After 1000 hr of Operation at 60 Mw.

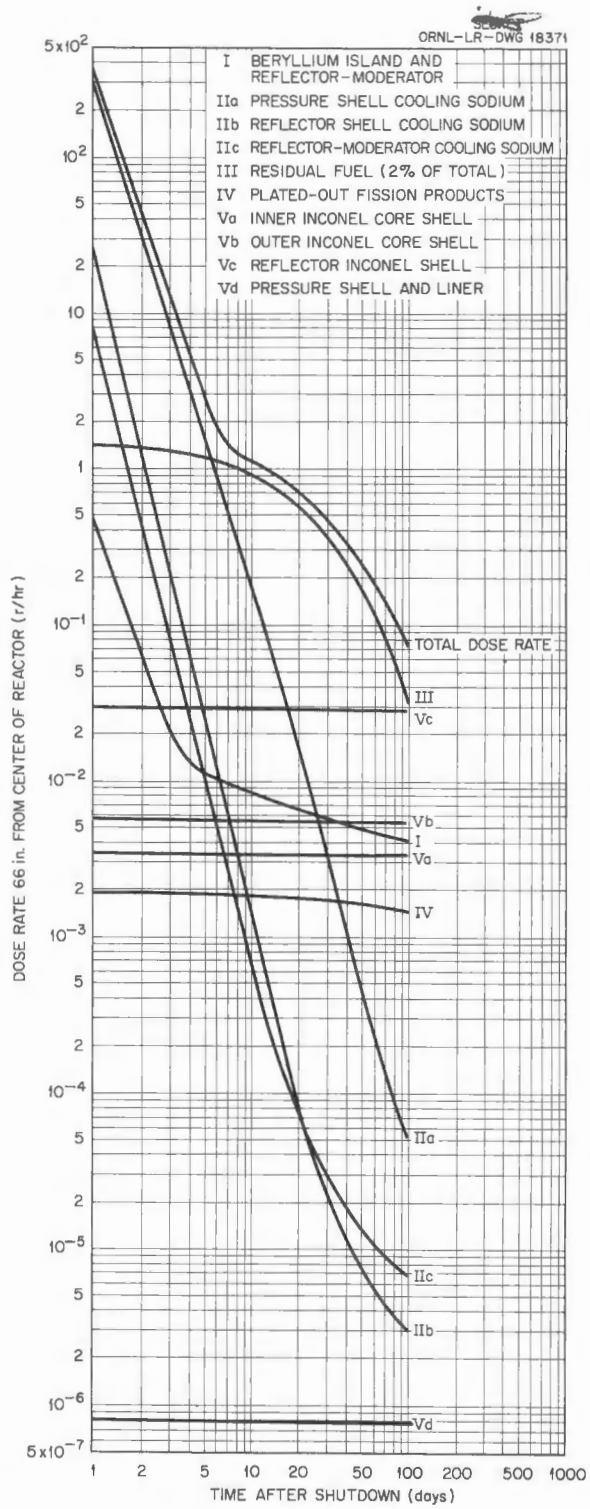

Fig. 1.6.3. Dose from Reactor with Lead Shield (No Water Shield) After 100 hr of Operation at 60 Mw.

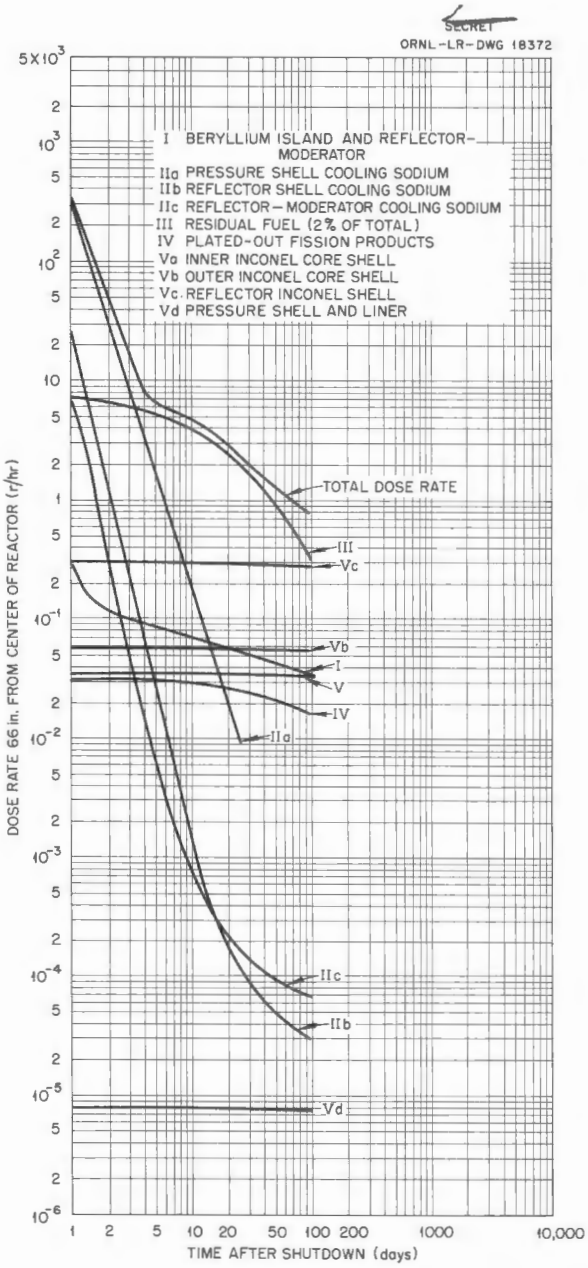

Fig. 1.6.4. Dose from Reactor with Lead Shield (No Water Shield) After 1000 hr of Operation at 60 Mw.

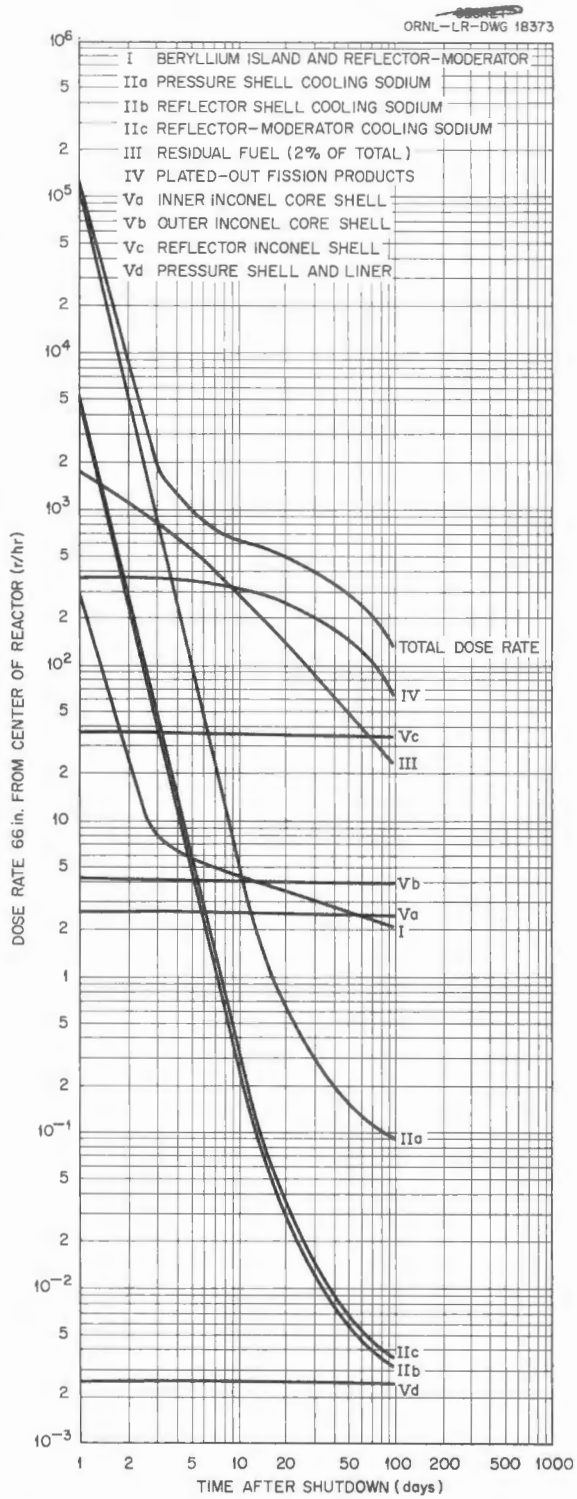

Fig. 1.6.5. Dose from Reactor Without Lead and Water Shields After 100 hr of Operation at 60 Mw.

the gamma-ray activity present in the cell. The result, if wall scattering is neglected, provides the total body dose a man would receive in the center of a 12-ft sphere if the gaseous fission-product daughters are assumed to be plated on the spherical surface. The bulk of the gamma-ray activity arises from Ba^{140} and La^{140}, and the residual activity for times after 140 days arises from Ba^{137} and follows the 33-year Cs^{137} half life.

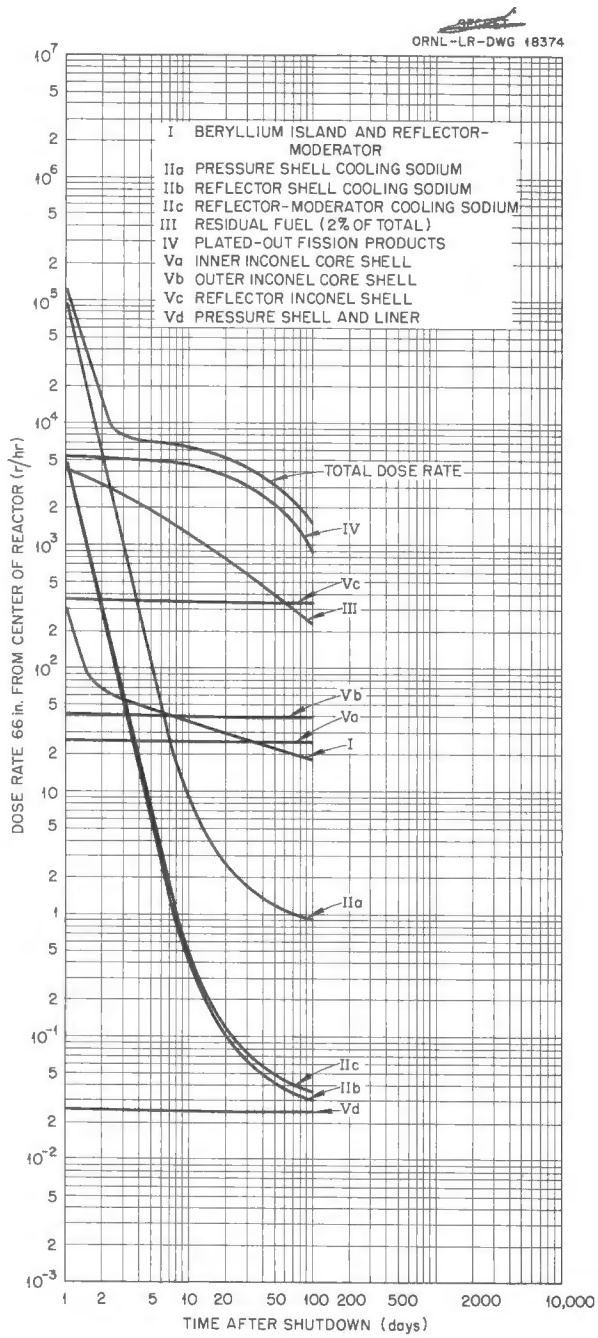

Fig. 1.6.6. Dose from Reactor Without Lead and Water Shields After 1000 hr of Operation at 60 Mw.

Particle-Size Distribution from Cutting Operations

J. C. Bolger[8] S. F. D'Urso[8]
M. H. Fontana[8]

A study was made of the air-borne-particle yields and size distribution that would result from each of four proposed disassembly methods. The methods are saw cutting, grinding, Heliarc-torch cutting, and shearing, and the materials studied were Inconel and 18-8 stainless steel. The range

[8]Massachusetts Institute of Technology Practice School students.

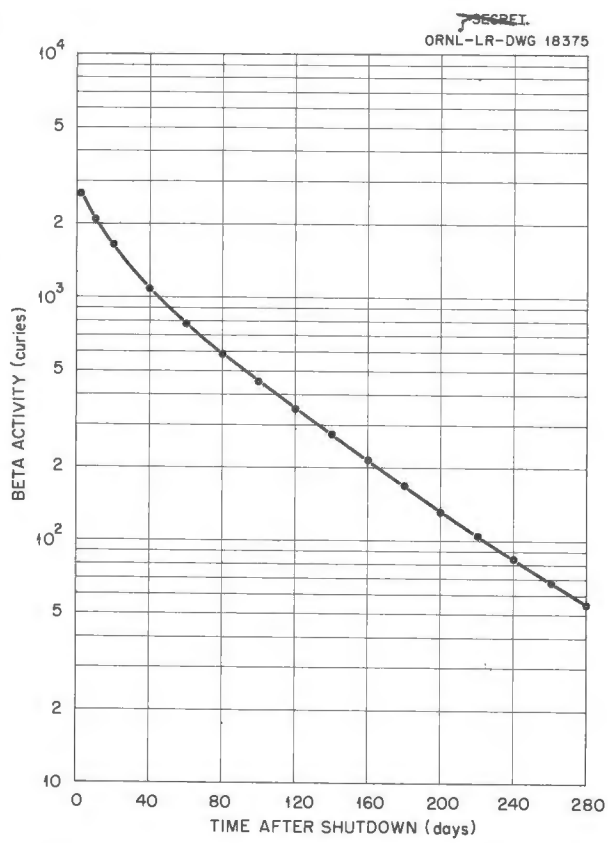

Fig. 1.6.7. Beta Activity in ART Cell as a Function of Time After Shutdown for a Continuous 1% Off-Gas Leak into the Cell During 500 hr of Operation at 60 Mw.

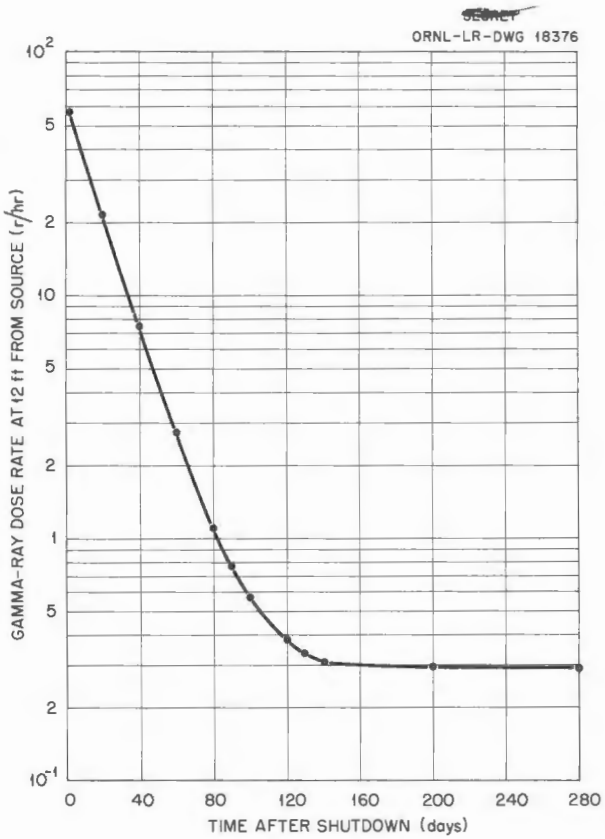

Fig. 1.6.8. Gamma-Ray Dose Rate as a Function of Time After Shutdown at 12 ft from Source for a Continuous 1% Off-Gas Leak During 500 hr of Operation at 60 Mw.

of this investigation extended from particles approximately 2 μ in diameter down to 0.0016 μ in diameter. Particles were detected and analyzed by use of a General Electric Company condensation nuclei meter and by electron-microscope photography.

Heliarc-torch cutting yielded the largest number of air-borne particles. Condensed vapors from both Heliarc-torch-cut Inconel and stainless steel specimens produced aerosols containing greater than 10^7 particles/cm^3. Few large particles were produced, that is, less than 0.1% were greater than 1 μ, and the average particle size was less than 0.01 μ.

Grinding with a diamond-wheel cutter, 8¾ in. in diameter at 2500 fpm rim speed, yielded both Inconel and stainless steel particles in quantities ranging from 5 to 8 $\times$ 10^6 particles/cm^3 that were 0.0016 μ or larger. The mean particle diameter was approximately 0.04 μ, and about 20% of the particles were greater than 1 μ in diameter. Inconel and stainless steel yield roughly the same number and size of particles. Whether the sample was ground wet or dry had no appreciable effect on particle yield. Dry grinding, however, caused severe overheating, especially with Inconel.

The band saw used in the saw cutting experiments was operated over a range of blade speeds from 44 to 2842 fpm and with blades having 10 and 14 teeth per inch. It was found that the number of air-borne particles per unit of material cut increased roughly in proportion to blade speed. The large-tooth blades produced less fines than did the small-tooth blades. When cut under the same conditions, Inconel yielded more and smaller fines than stainless steel yielded. With a saw speed of 114 fpm and a blade having 10 teeth per inch, the total particle yields were approximately 50,000 particles/cm^3 for stainless steel and 100,000 particles/cm^3 for Inconel. The average particles were large, 0.2 μ for stainless steel and 0.05 μ for Inconel.

A Manco guillotine was used to shear Inconel and stainless steel tubing ½ to ¾ in. in outside diameter. With the measuring techniques available no air-borne particles produced by this cutting process could be detected.

These results imply that disassembly of small piping and thin-walled sections should be carried out by shearing whenever possible. For cutting larger metal sections, sawing with the largest blades and the slowest cutting speeds will be satisfactory. Grinding produces from 10 to 100 times as many fines as saw cutting does at the same feed rates and is therefore a secondary method for cutting large sections. Grinding should be performed wet whenever possible, especially with Inconel, to avoid serious overheating. Heliarc-torch cutting yields the largest number of air-borne particles and would therefore require the most elaborate air-filtering equipment.

IN-PILE EXPERIMENTATION

D. B. Trauger

In-Pile Loop No. 6

J. A. Conlin
R. A. Dreisbach
C. C. Bolta[9]
D. M. Haines[9]

In-pile loop No. 6, described previously,[10] was inserted in the MTR on September 3, and was

[9]On assignment from Pratt & Whitney Aircraft.

[10]C. C. Bolta *et al.*, *ANP Quar. Prog. Rep. Sept. 10, 1956*, ORNL-2157, p 81.

removed on September 15 as a result of a long series of difficulties that culminated in pump malfunctioning and apparent breakage of the heat exchanger sniffer tube. Since this sniffer tube is part of a gas-monitoring system that would indicate impending failure of the heat exchanger tubes, its loss necessitated the shutdown. Both these troubles are thought to have been caused by the severe thermal cycling to which the loop was subjected as a result of numerous reactor scrams and malfunctioning of the temperature controller. The loop performance is summarized below:

Total operating time	224 hr
Operating time at some power	134 hr
Operating time at full power	70 hr
Loop high temperature	1600 to 1630°F
Average heat removal by air at full power	33.7 kw
Power density based on air heat removal at full power	0.866 kw/cm^3
Total heat removal	4167 kwhr

The loop is now at the MTR awaiting sectioning prior to shipment to ORNL for examination.

Higher power densities and higher maximum loop temperatures, of the order of 1600°F, are being considered in the planning of the future in-pile loop program. The higher power density may be obtained, in part, by fully inserting the loop into the reactor beam hole. Additional power may be obtained by increasing the uranium concentration of the fuel salt and, possibly, by having the MTR reactor loaded more heavily in the region of the HB-3 beam hole. To handle the increased power, a higher capacity heat exchanger must be developed, and to ensure satisfactory operation of the loop at the higher temperatures for more than one reactor cycle, an improved pump purge system must be developed. The required developmental work is under way, as described below. The next in-pile loop test is scheduled for June 1957.

In-Pile Loop Heat Exchanger

J. A. Conlin C. C. Bolta

As indicated above, future in-pile loops may be operated at higher power densities and will require larger capacity heat exchangers. The present unit is capable of removing a little over 30 kw of heat energy. Future loops having significantly higher specific power will require heat exchangers with capacities of 45 kw or more. A number of methods are available for increasing the heat exchanger capacity without gross redesign of the loop. The principal methods under consideration are: increasing the air-side heat transfer area by the use of fins, increasing the air pressure and flow, and injecting water into the air stream to increase the heat capacity. Increasing the air flow will require the use of a larger capacity, higher pressure air system. This can be obtained at the MTR from the GE-ANP installation by supplying the GE-ANP facility with low pressure air in return. It is expected that one, or a combination, of these approaches will provide the required increase in capacity. A heat exchanger test rig with more complete instrumentation than can be incorporated in-pile has been set up, and a heat exchanger of the original design is currently being tested to obtain the test data needed as a basis for evaluating proposed design changes.

Prototype In-Pile Loop Pump

J. A. Conlin D. M. Haines

The future in-pile loops require a pump capable of operating at higher temperatures for longer periods than in previous loops. To satisfy these requirements, developmental work is under way on a pump capable of operating at 1500°F and 4500 rpm for 2000 hr – that is, 100% more life and 50% greater speed than are required for proposed in-pile loops. The shaft of the first test pump seized after 1020 hr, and the shaft of the second pump, previously described,[11] seized after 986 hr. Both stoppages were due to zirconium fluoride buildup on the shaft. Seizure occurred in the slinger region of the shaft in both cases, even though the slinger clearance in the second pump was increased from 0.006 to 0.060 in. The rate of fluoride buildup was much greater with the larger clearance, possibly because of increased eddy currents, with the result that pump life was not improved. A third pump is being tested that has completed 750 hr of the 2000-hr test. This pump has clearances of about 0.030 in. around the pump slinger. In addition, a chemical vapor trap, which is packed with alumina, has been incorporated in the system. The pump purge flow is split so that one half follows the

[11] J. A. Conlin, D. M. Haines, and W. S. Karn, *ANP Quar. Prog. Rep. Sept. 10, 1956*, ORNL-2157, p 81.

original path to the bearing housing seal and out, and the other half flows across the slinger, over the pump sump, through the vapor trap, and out to a new off-gas line. It is hoped that this latter portion of the purge gas will sweep the zirconium fluoride vapor away from the slinger and into the vapor trap. Also, the fuel has been changed from the mixture $NaF-ZrF_4-UF_4$ (53.5-40-6.5 mole %, No. 44) to the mixture $NaF-ZrF_4-UF_4$ (56-39-5 mole %, No. 70), which has a lower zirconium fluoride vapor pressure

In-Pile Lubricant and Seal Test

J. A. Conlin D. M. Haines

Refined estimates of the ART fast-neutron fluxes and radiation-damage data from in-pile loops and other sources have indicated a need for irradiation testing of the reactor pump seal system. It is proposed to determine whether the present seal and cooling passage design is adequate for the high dose rate of 2.5×10^7 rep/hr (including prompt and delayed neutrons and gamma rays). The test will also serve to screen various lubricants for use in high-flux regions. The bulk of the lubricating oil may not suffer excessive damage because of the 150 to 1 dilution factor in this circulation system. However, provision has been made for changing the oil during ART operation.

The principal points of suspected trouble are the seal and the seal oil leakage removal system. In the first instance, the possibility exists that the oil on the seal itself may not be diluted with new oil with sufficient rapidity to prevent the accumulation of coke or resins that might cause increased leakage. The second possible trouble spot, the seal leakage removal system, consists of a 0.137-in.-ID tube that reaches to the bottom of an annulus into which the seal oil leakage drains. The seal oil leakage is blown from the annulus up the tube by a helium purge. There is the possibility that this oil removal system may become plugged by coked oil.

It is planned to use gamma radiation to test a full-scale pump bearing housing under simulated operating conditions. It appears that gamma radiation will be adequate for this test, since there is no appreciable difference between the effect of gamma and neutron radiation on hydrocarbons for equal energy absorption. A special gamma irradiation facility will be set up in the MTR canal that will consist of an 8-in.-dia pipe surrounded by an array of eight partly used reactor fuel elements, that is, elements which are normally set in racks for xenon decay. It is estimated that this installation will provide a 5×10^6 r/hr flux. A sealed pump bearing housing will be lowered to the region of maximum flux in the pipe, and the bearing will be operated until the desired exposure is obtained.

In-Pile Tests of Reactor Moderator Materials

J. A. Conlin D. M. Haines
C. C. Bolta

It has been proposed that moderator materials such as beryllium oxide, graphite, and certain metal hydrides be investigated for possible use in high-temperature, circulating-fuel reactors. The moderator material would be encased in a metallic sheath in the reactor. (For further information on the proposed reactor use, see Chap. 1.7, "Advanced Reactor Design," this report.)

A series of in-pile tests have been undertaken to check the mechanical stability of the moderator materials under simulated reactor operating conditions. In reactor use, the material will become an externally cooled volume heat source. This will cause thermal stresses which may cause spalling of the surface and possibly rupture of the metallic sheath.

For the first in-pile test, four beryllium oxide cermets, each 1 in. long and 1 in. in diameter, were inserted in a single close-fitting Inconel capsule with a 0.020-in.-thick wall. This capsule was installed horizontally on the axis of an in-pile plug in a forward position and was inserted in the HB-3 beam hole of the MTR on October 15, with removal scheduled for November 26. The capsule was surrounded by a helium atmosphere, and the maximum sheath temperature was 1495°F from gamma-ray heating.

1.7. ADVANCED REACTOR DESIGN

W. K. Ergen
A. P. Fraas
A. M. Perry
W. T. Furgerson

Preliminary design work has been done on advanced reactor concepts along the lines described previously,[1] with the objective of achieving an aircraft reactor system that is simpler than the ART system and which will operate at a higher temperature. Efforts toward simplification have been based upon the concept of a reactor in which the circulating fuel cools the moderator. As stated previously, if the fuel is to accept heat from the moderator, the moderator must be at a higher temperature than the fuel. Thus beryllium metal cannot be used as it is in the ART for the moderator because of problems of containing it and because of its poor mechanical properties at temperatures above the fuel temperature of interest, that is, 1750°F. Graphite, beryllium oxide, and the hydrides of zirconium and yttrium are being considered as possible moderators.

Elimination of the moderator cooling reactor would be a major simplification of a system such as the ART in that the system would not require the two sodium pumps, with their associated drive and purge systems, the two sodium-to-NaK heat exchangers, and the sodium expansion tank, along with the critical internal welds at points which separate the sodium and the fuel systems. A corollary of this simplification would be a simplification of fabrication and assembly problems.

The use of the fuel to remove heat from the moderator also presents the possibility of increasing the effective heat output of the reactor, since the heat would be added to that in the high-temperature fuel circuit rather than being disposed of through the sodium system. Many possible sources of trouble and some important hazards would also be eliminated if the separate moderator-cooling circuit were not required.

DESIGN CONSIDERATIONS

A circulating-fuel reactor in which the fuel cools a high temperature moderator is likely to be a core-moderated reactor because thermal stresses limit the thickness of moderating material that can be used. In general, the choice of materials and the optimum distribution of materials for a core-moderated, one-fluid reactor depends very much on heat deposition rates and thermal stresses in the core-moderator elements and in the reflector. Since the relative performance of various reflector materials, and, indirectly, of various core materials, depends in part on the amount of fuel that may be required to cool the reflector and in part on the possible poisoning required to suppress fissioning in the reflector, it was found to be essential to investigate rather carefully the heat deposition rates to be expected in various reflectors. A fixed-core geometry and a flat power distribution were assumed for this study, and some preliminary results are presented in Fig. 1.7.1. The heat-deposition rates established in this way may be used for determining the size and spacing of the fuel coolant passages required to meet thermal stress limitations. Cladding requirements and the attendant poisoning effects must also be taken into account, and the fissioning rate in the reflector must be determined for various combinations of core and reflector materials so that the need for poison to suppress fissioning can be evaluated.

The information obtained through the study of reflector problems must then be examined in combination with core considerations and evaluated with respect to the three principal figures of merit: fuel concentration, NaK activation in the heat exchanger, and shield weight. Moderator volume fractions in the range from 0.2 to 0.6 (average) are of interest, and nonuniform loadings should be considered. Adequate moderator cladding materials must be provided and the effect of moderator-rod size considered. Further, inelastic scattering in metals must be taken into consideration in calculations.

The reflector will actually serve a triple purpose. Besides the usual effect of reducing the core size and critical mass, it will serve both as a part of the shield and as a neutron barrier to reduce activation in the heat exchanger. Since repeated attempts to achieve minimum shield weight have invariably led to an annular type of heat exchanger (except for heavily divided shields), and since the gamma-ray shield weight of such configurations

[1] W. K. Ergen and A. M. Perry, *ANP Quar. Prog. Rep. Sept. 10, 1956*, ORNL-2157, p 83.

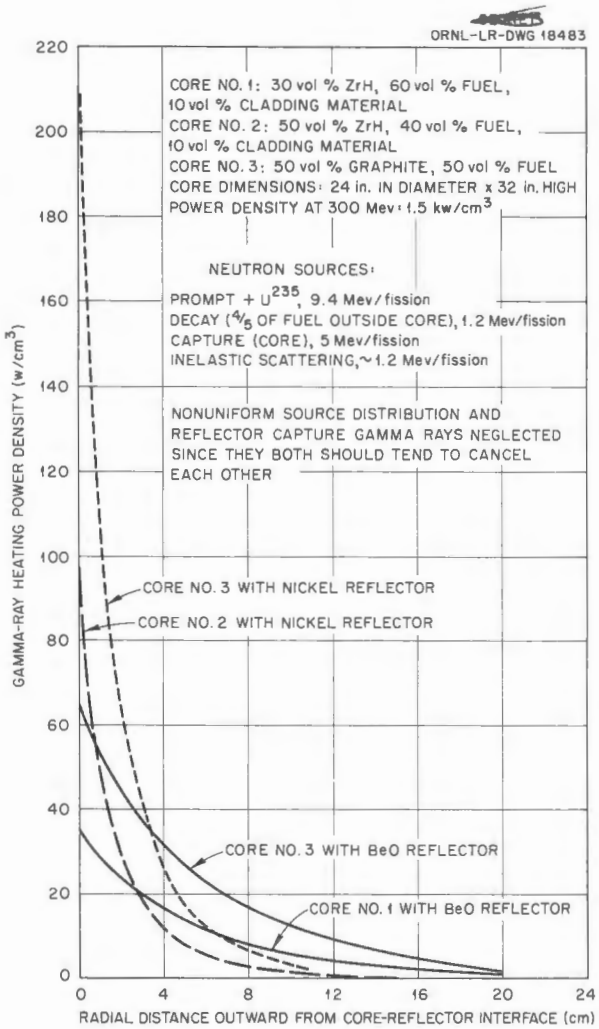

Fig. 1.7.1. Gamma-Ray Heating in Reflector of a Metal-Hydride-Moderated or Graphite-Moderated Circulating-Fuel Reactor.

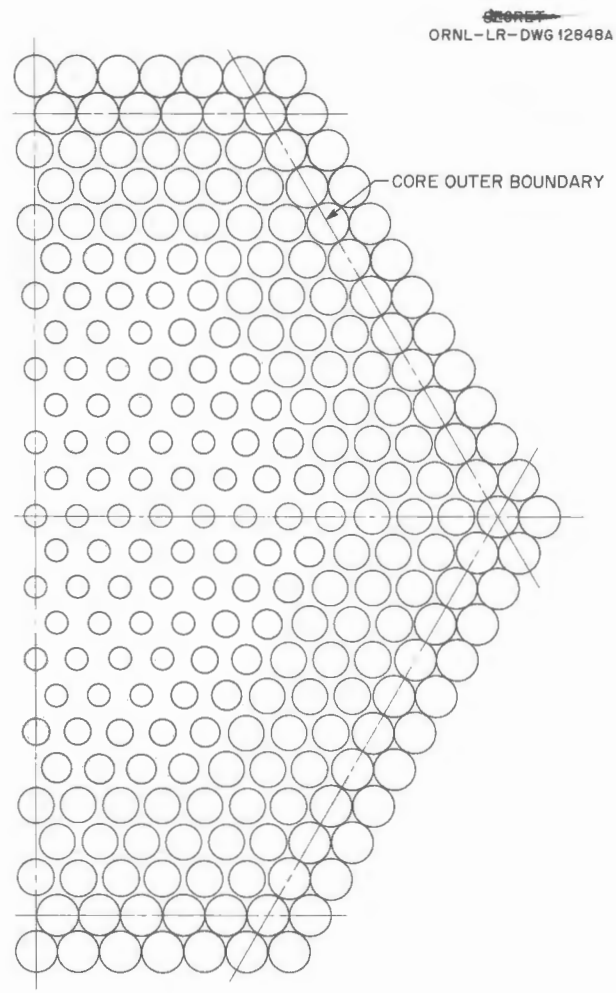

Fig. 1.7.2. Cross Section Through Core of Hydride-Moderated Circulating-Fuel Reactor.

grows rapidly with heat exchanger diameter, there is a strong incentive to minimize the reflector thickness. On the other hand, there is also a strong incentive to reduce neutron activation of the secondary fluid by increasing the reflector thickness. Careful evaluation of quite a variety of geometries and materials combinations will be required to establish the reflector design.

REACTOR CONFIGURATIONS

Two reactor configurations that are now being studied can be used to illustrate the problems. The design presented in Fig. 1.7.2 is comprised of rods of hydride placed in the core on uniform equilateral centers. The rod diameter is increased with radial distance from the center of the core in order to obtain a uniform power density in the fuel and to reduce the gamma-ray heating power density near the core boundary so that relatively large-diameter rods can be used in the reflector. The fuel volume at the outer periphery of such a core would be reduced to a minimum of 9 vol %, as is characteristic of close-packed cylindrical rods. The reflector would be poisoned in the region radially outward from where close packing began. The poisoning additions would be made so that fissioning would be suppressed to a level such that, at any given radius, the virgin neutrons

from the region would have little effect on the radiation escaping from the shield or on the activation of the secondary fluid in the heat exchanger. It is possible that the activation of NaK in the heat exchanger could be reduced to below the level expected in the ART because hydrogen moderation may be more effective than beryllium in isolating the heat exchanger from the core. Also, if zirconium hydride is used, the relatively good inelastic scattering cross section of the zirconium may help to increase the effectiveness of the isolation. The quantity of low neutron cross-section hydride required in the reactor would be small (of the order of 500 lb) because the bulk of the hydride in the reflector would be poisoned; consequently for the poisoned hydride the less expensive hafnium-containing zirconium or the rare-earth-containing yttrium could be used.

The second type of core being considered is shown in Fig. 1.7.3. It resembles the core shown in Fig. 1.7.2, except for the reflector, which would consist of a thick inner layer of copper surrounded by an outer layer of heavily poisoned hydride. Copper has such a high thermal conductivity that it can be used in a thick slab without serious thermal stresses. Further, it has the advantage that its high inelastic scattering cross section should make it both a good reflector and a good neutron shield. Since its density is fairly high it should also be very effective as a gamma-ray shield for the core. Thus it might make possible a significant saving in shield weight. Important questions which must be resolved for this type of reactor are the relative importance of decay gamma rays from the heat exchanger and secondary gamma rays from the shield. It is interesting to note that, in beryllium-moderated reactors proportioned as in the ART, the relatively low density beryllium appears to make the gamma-ray dose from the core roughly equal to that from the heat exchanger for shields designed to give 10 to 1000 r/hr at 50 ft. Much careful analytical work closely coupled with shielding experiments will be required to evaluate these problems.

Typical specifications for the design shown in Fig. 1.7.3 are given in Table 1.7.1, except that moderator-rod diameter and spacing have been reduced. A nickel-molybdenum alloy was presumed as the structural material and a lithium-base fluoride mixture as the fuel. While yttrium hydride would be the logical choice for the moderator, the absence of physical property data made it necessary to presume zirconium hydride, for which some data are available (see Table 1.7.2 in following section).

The three uniformly spaced fuel pumps that would discharge tangentially into a cylindrical plenum in essentially the same fashion as in the ART are not shown in Fig. 1.7.3. The fuel pump inlet and volute region would consist largely of solid copper or nickel to provide a good end reflector for the core and to minimize shield weight. The heat exchanger tube bundles would be in the form of helices in the cylindrical annulus indicated.

The grids for supporting and spacing the moderator rods are awkward, but no better arrangement has yet been devised. If it were practicable to build the moderator in the form of slabs, the drag loads could be carried by shear stresses into the reflector, and the fuel flow into and out of the core would be unobstructed. This would have the further advantage of giving a higher ratio of moderator to cladding volume for given allowable thermal stresses. On the other hand, such clad plates would probably be more difficult to fabricate, and perhaps a good bond between the cladding and the plate would not prove to be feasible metallurgically. Thermal stresses induced in the edges of the plates by changes in power level, fuel flow rates, or fuel temperature transients would be likely to be serious.

The choice of moderator-rod diameter and spacing depends in part on reactor physics requirements and in large measure on temperature limitations. Structural considerations make it desirable to make the rods 0.5 in. in diameter or larger. Similarly, for 0.010- to 0.020-in. thicknesses of molybdenum and Ni-Mo alloy cladding, the poisoning effect of the structure causes a marked increase in critical mass if the moderator-rod diameter is reduced to much below 0.5 in. Thus the effects of moderator-rod spacing for 0.5-in. rods are of interest. The effects of rod spacing on core volumes and fuel-passage hydraulic radius for a typical set of core porportions are shown in Fig. 1.7.4, and the effects of rod spacing on power density in the fuel moderator and on the temperature differences between the moderator and the fuel are shown in Figs. 1.7.5 and 1.7.6. The curves shown give the temperature difference induced by radiation heating between the center

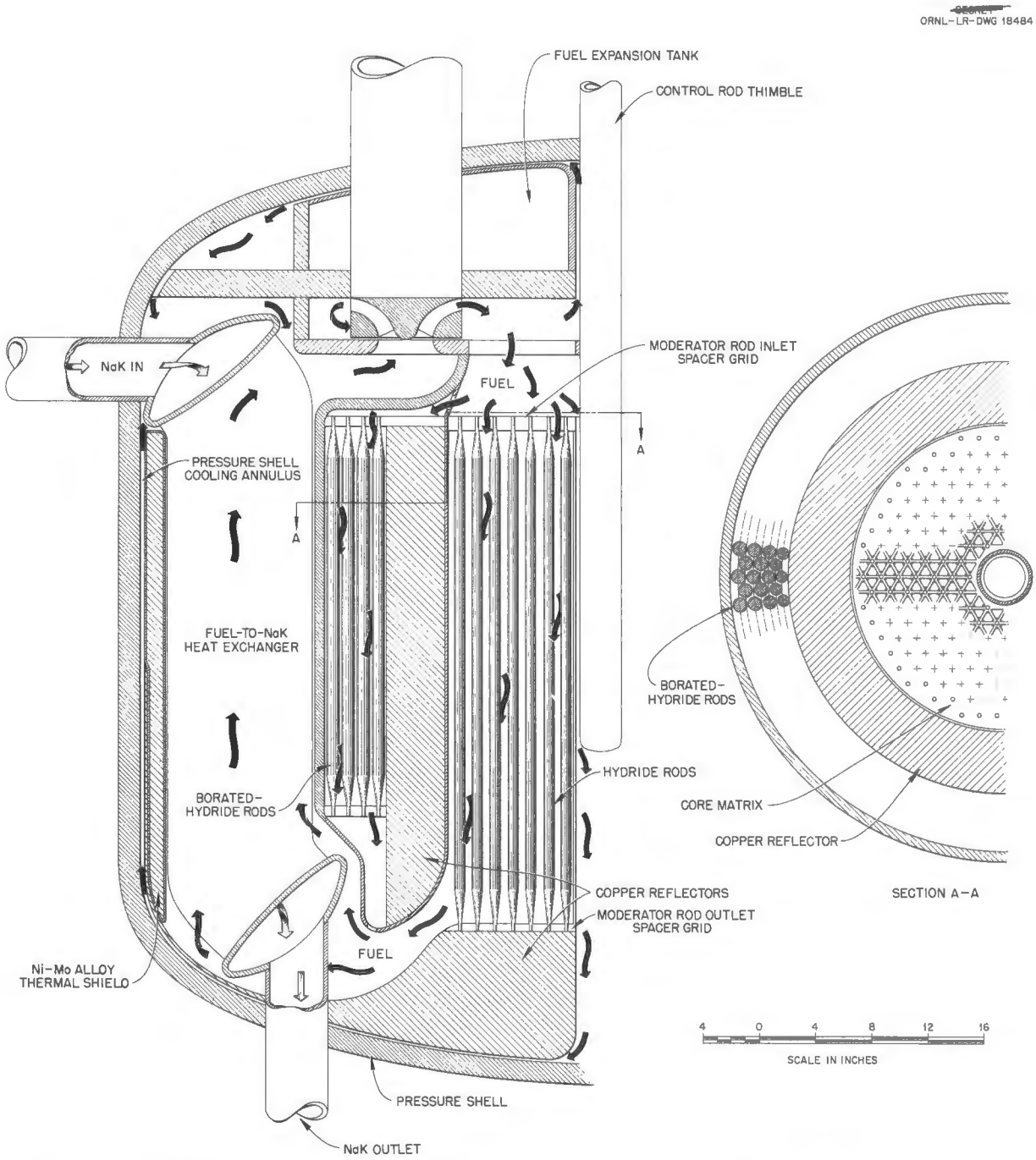

Fig. 1.7.3. Schematic Layout of a 180-Mw Hydride-Moderated Circulating-Fuel Reactor with a 21-in.-dia Core.

TABLE 1.7.1. PRELIMINARY DESIGN SPECIFICATIONS FOR A HYDRIDE-MODERATED CIRCULATING-FUEL REACTOR

Power	180 Mw
Fuel	$NaF-KF-LiF-UF_4$
Structure	Nickel-molybdenum alloy
Moderator	$ZrH(N_H = 3.5)$* or $YH(N_H = 4.5)$*
Moderator-rod outside diameter	0.5 in.
Rod cladding	0.015 in. of Mo + 0.015 in. of Ni-Mo alloy
Core diameter	21 in.
Core height	32 in.
Core volume	180,000 cm^3, 6.4 ft^3
Average core power density	1.0 kw/cm^3
Peak core power density	1.5 kw/cm^3
Core volume percentages	
Fuel	54
Moderator	36
Structure	10
Reflector	6 in. of copper
Axial reflector and header	8 in. of copper
North-head height from impeller inlet level	12 in.
Heat exchanger shield	6 in. of poisoned hydride
Heat exchanger	36 in. high × 10.5 in. thick, helical tube bundles
Pressure shell	$1\frac{1}{2}$ in. thick, 69 in. OD
Control rod	3 × 20 in. stroke (hollow rod filled with moderator)

*Number of hydrogen atoms per cubic centimeter multiplied by 10^{-22}.

and the surface of a rod, the temperature difference between the fuel-passage wall and the mixed mean fuel temperature induced by volume heat source effects, and the total difference in temperature between the moderator-rod surface and the mixed mean fuel temperature after allowance for the temperature drop required to transmit the heat generated in the rod by radiation to the fuel. The higher fuel flow rate in the 180-Mw reactor, as compared with that in the 60-Mw reactor, essentially compensates for the higher power density, so far as the difference between the moderator-rod surface and the mixed mean fuel temperatures is concerned. The internal temperature difference in the rod is, of course, directly proportional to power density. For a given fuel temperature rise through the core these curves indicate that fairly close spacing of the moderator rods gives the lowest values of temperature difference. The higher fuel velocities and smaller fuel-passage hydraulic radii reduce the boundary-layer heating effect (at the cost of greater pressure drops), while the larger moderator surface area reduces the temperature difference required to remove heat from the moderator rods.

It is evident that the hottest point in a ZrH- or YH-moderated reactor with 0.5-in.-dia moderator rods will be about 300°F above the mixed mean fuel temperature if there is a good thermal bond between the cladding and the hydride. If the bond is not good and is replaced by a hydrogen-filled gap, the temperature drop will be about 60°F per mil of gap. From Fig. 1.7.9 (see below) it appears that the gap thickness that might be induced by

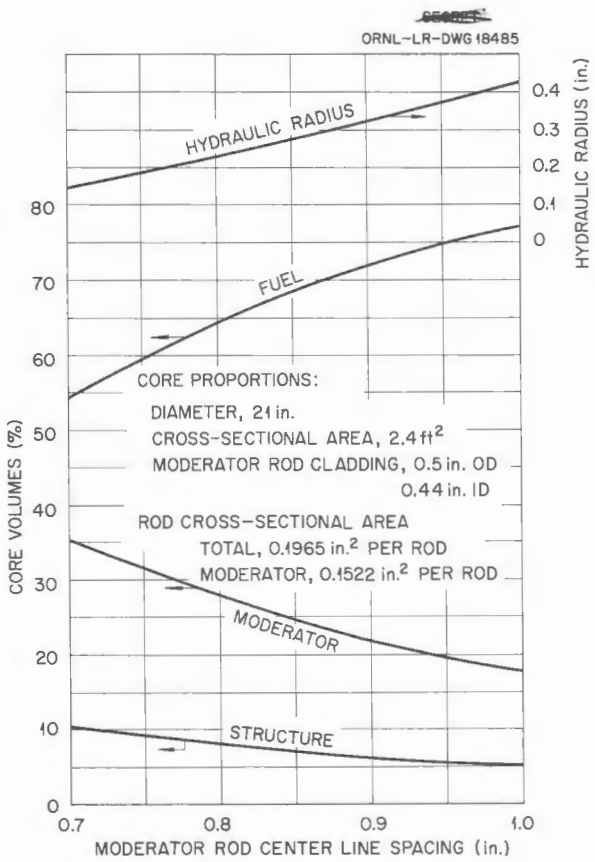

Fig. 1.7.4. Effects of Moderator Rod Spacing on Core Volumes and Fuel Passage Hydraulic Radius.

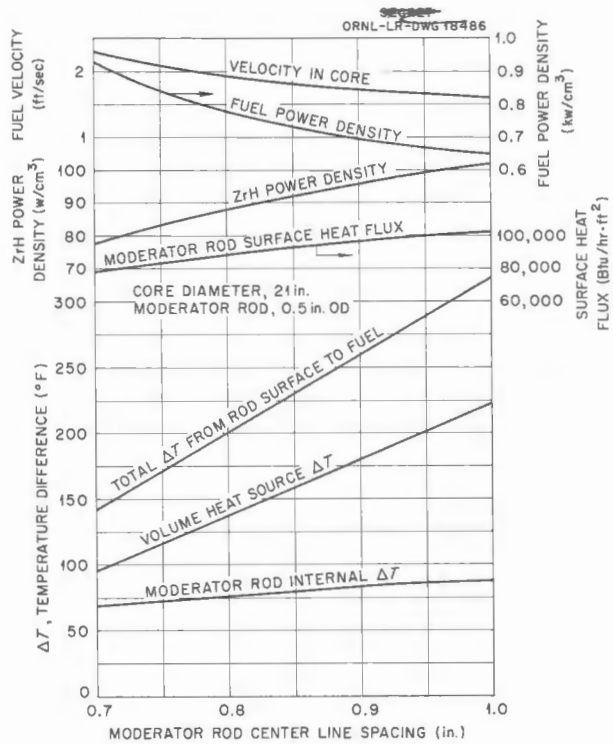

Fig. 1.7.5. Effects of Moderator Rod Spacing on Fuel Velocity, Power Density, Core Temperature Differences, and Moderator Rod Surface Heat Flux for a Fuel Flow Rate of 3 ft³/sec and a Power of 60 Mw.

differential thermal expansion would be less than 0.001 in. for 0.5-in.-dia clad rods.

MATERIALS PROBLEMS

The principal materials that must be tested and evaluated for use in advanced reactors are beryllium oxide, several forms of high-density graphite, zirconium hydride, and yttrium hydride. The key properties of these four materials, insofar as information is available, are indicated in Table 1.7.2. It may be seen that beryllium oxide would be likely to give trouble from thermal stress cracking and "ratcheting" if used in the configurations being considered. No material has been tested thus far to the point where it could be used with confidence. Additional data must be obtained before a significant advanced design can be worked out.

The problems associated with the use of moderating material at a high temperature vary somewhat with the particular material being considered, but, except perhaps for graphite, cladding will be required to isolate the moderator from the circulating fuel in order to minimize corrosion. The most convenient geometry for such a system will probably be one in which rods of moderator will be enclosed in long cans, roughly 0.5 in. to 2 in. in diameter with a can-wall thickness of from 0.010 to 0.040 in. This configuration seems much superior to the ARE type of core from the standpoints of differential thermal expansion and thermal stress because the rods can be individually supported with one end free to slide and thus accomodate relative movement between structural members. Either a good thermal bond between the can wall and the moderator or a close clearance, with helium or hydrogen filling the gap, must be provided. If the radial clearance between the can and the moderator can be kept to about 1 mil and the end clearances to a few mils, sodium could probably be

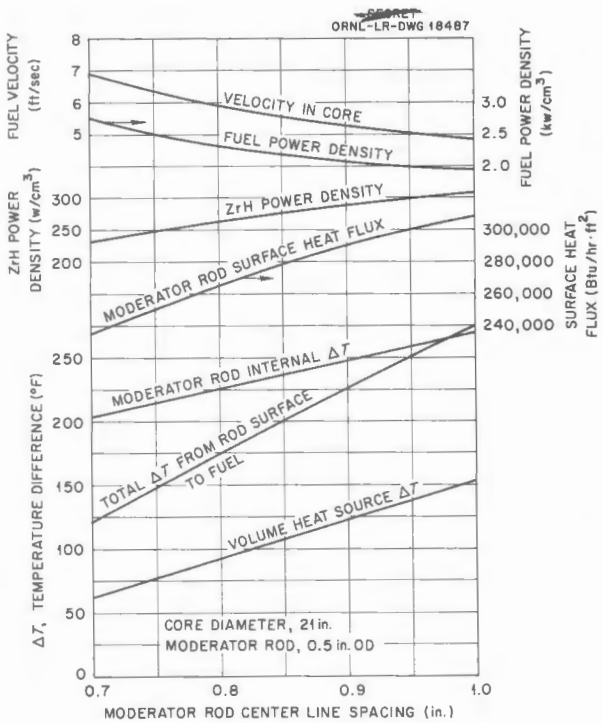

Fig. 1.7.6. Effects of Moderator Rod Spacing on Fuel Velocity, Power Density, Core Temperature Differences, and Moderator Rod Surface Heat Flux for a Fuel Flow Rate of 9 ft³/sec and a Power of 180 Mw.

used to provide a thermal bond, since the stresses in the cladding induced by the high coefficient of thermal expansion of the sodium probably could be kept to a tolerable level. However, the use of sodium would have the disadvantage that if a leak appeared in the can, a reaction between the sodium and the fuel would result, and some of the disadvantages of the ART sodium cooling system would reappear.

It appears that the principal strength requirement for the rods will be that they be strong enough to stay in place under moderate fluid dynamic forces. It seems likely that the can will supply an adequate amount of strength and that the only function of the moderator, from the stress-analysis standpoint, would be to prevent collapse of the can under external pressure during operating conditions in which the fuel pressure would be substantially in excess of the pressure in the interior of the can.

Apart from the possible hydrogen losses by the hydride, the damage or ill effects which would be expected to present problems in the use of any particular high-temperature moderating material will arise primarily from thermal effects, that is, differential expansion between the moderator and the can caused both by differences in coefficient of expansion and by differences in temperature, since the temperature of the moderator will be

TABLE 1.7.2. TYPICAL MATERIAL PROPERTIES THAT AFFECT ALLOWABLE THERMAL STRESSES AT ABOUT 1200°F

	Melting Point (°F)	Thermal Conductivity, k [Btu/hr·ft²(°F/ft)]	Modulus of Elasticity, E ($\times 10^{-6}$ psi)	Coefficient of Thermal Expansion ($\times 10^{-6}$ in./in.·°F)	Poisson's Ratio, ν	Estimated Allowable Thermal Stress (psi)
Be	2460	48.3	40	9	0.10	15,000
BeO	4660	14.5	10	5.5	0.23	4,000
Inconel	2600	15	21	9	0.29	60,000
Graphite		45	1	3	0.2	2,000
Stainless steel	2550	16	20	8	0.3	60,000
Mo	4760	60	42	4	0.3	30,000
Zr	3200	12	11	6	0.34	15,000
ZrH		12	13	6.5	0.34	15,000
Y	2710			7		

higher than that of the can. The stresses associated with the thermal gradient in the moderating material will tend to cause cracking in that material. If the cracking led to a substantial amount of fragmentation, it is felt that the fragments would tend to settle during successive heating and cooling cycles and to thus induce a phenomenon known as "ratcheting," which would cause distortion of the can in an irregular fashion. It is also possible that radiation damage by fast neutrons might aggravate the thermal stress conditions and cause a substantial degree of fragmentation that might not occur in out-of-pile tests designed to produce the same temperature distributions and thermal stresses.

In-Pile Tests of Moderator Materials

A volume heat source cannot be induced in beryllium oxide by electrical resistance heating, and since there is no other available means of simulating the temperature differential that would prevail in a reactor, at least in terms of the ratcheting phenomenon, actual in-pile tests are under way. Out-of-pile tests can be run on graphite and on hydride specimens by making use of an electrical-resistance type of volume heat source, and some favorable results have been obtained. However, in these materials, local electrical current concentrations associated with edge effects, variations in density, grain-boundary effects, etc. may produce peculiar results. Even more important, a high fast-neutron flux may substantially embrittle the material and reduce the thermal conductivity. Thus an out-of-pile test can give only an indication and not a conclusive picture of the reactor conditions. An in-pile test will be required for a determination of the dimensional stability of the graphite and hydride specimens. If the specimen is canned and the can does not grow or become distorted during the in-pile test, a similar rod would probably be satisfactory in a reactor even if the moderator material contained in the can showed a tendency to crack.

While the prime consideration in postirradiation examination of the specimens will be dimensional stability of the can, it will also be important to examine the moderating material visually to obtain a qualitative notion as to the character of the damage experienced. It may also prove desirable to make measurements of such characteristics as hardness and strength after irradiation. It will certainly be important to measure the hydrogen concentration of hydride specimens and possibly to measure some other physical properties, such as thermal conductivity, if observations made during or after the tests indicate the need for such data.

A series of simple experiments is being conducted in hole HB-3 of the MTR. The power density at the nose of the hole is of the same order as that to be expected about 2 in. outward from the surface of the core into the reflector. If specimens of the same size as the rods contemplated for use in a full-scale reactor are tested, the heat removal from the specimen can be accomplished by simple thermal radiation to the water-cooled wall of the thimble containing the specimens. Because of the fourth-power effect of temperature on radiation heat losses, it has been possible to design the test specimens so that the operating temperature will be between 1500 and 2000°F, even with allowances made for the many uncertainties associated with the tests. If specimens of different densities are used, the diameter of the specimen can be varied to yield essentially the desired temperature. This of course means that the operating temperature level cannot be established independently of the thermal stress level or the temperature difference existing within the specimen. However, for the materials under consideration (except for graphite) it seems that all these factors can be kept fairly close to the values to be expected in a full-scale reactor. Key values for representative specimens are given in Table 1.7.3.

The average temperature level required in a high-temperature moderator of a full-scale reactor will be about 100 to 200°F above the fuel temperature. This temperature difference is necessary to provide for the temperature drop through the boundary layer of the fuel stream which flows over the outside of the can and which is associated with removal of heat from the moderator. In addition, the volume-heat-source boundary-layer heating effect in the fuel will yield a temperature difference between the wall and the mean fluid temperature of the order of 50°F for the reactor proportions which currently seem to be interesting.

If the thimble is filled with helium so that the specimen is contained in a helium atmosphere, there will be no need to seal cans containing beryllium oxide or graphite specimens, and hence there will be no gas pressure differential across

TABLE 1.7.3. ESTIMATED OPERATING CONDITIONS FOR IN-PILE TESTS OF CANNED MODERATOR MATERIALS WITH AN 8-w/g VOLUME HEAT SOURCE

Specimen Properties and Test Operating Conditions	Test Materials			
	Be	BeO	Graphite	ZrH
Specimen diameter, in.	1.25	1.0	1.25	0.50
Estimated density, g/cm^3	1.8	3.0	1.9	5.5
Volume-heat-source power density, w/cm^3	14.4	24	15.2	44
Power developed per inch of length, w	270	280	282	142
Area for 1 in. length, ft^2	0.027	0.022	0.027	0.0109
Heat flux from surface, Btu/hr·ft^2	34,000	44,000	35,000	44,500
Temperature difference through helium film to can, °F	113	146	116	146
Temperature difference in specimen, °F	10	36	6.8	40
Thermal stress, psi	2600	3100	10	2500
Estimated equilibrium can surface temperature, °F (ϵ = 0.6)*	1400	1550	1410	1550

*Emissivity coefficient.

the can. This does not give an exact simulation of conditions to be expected in the reactor, but it is believed that the differences will not be important. The hydride specimens must of course be sealed to retain the hydrogen.

The first specimen tested was a beryllium oxide cylinder mounted with its axis horizontal and normal to the face of the reactor. This mounting gave a progressive reduction in power density (and hence in temperature along the length of the specimen) with distance away from the reactor face. Temperature data obtained from thermocouples installed along the length of the specimen are presented in Fig. 1.7.7. In later tests thermal radiation shields in the form of sheet metal baffles around the outboard portions of the specimens may be inserted to obtain higher temperatures. This first beryllium oxide specimen was irradiated for about 700 hr. It is expected that it will be examined in a hot cell in April 1957.

A second set of test specimens is being prepared that will include beryllium oxide, graphite, and zirconium hydride samples mounted vertically in the nose of the test pod. It is planned to thermally cycle these specimens approximately 100 times during irradiation. This will be done by alternately inserting and withdrawing the pod in order to vary the position of the specimens relative to the face

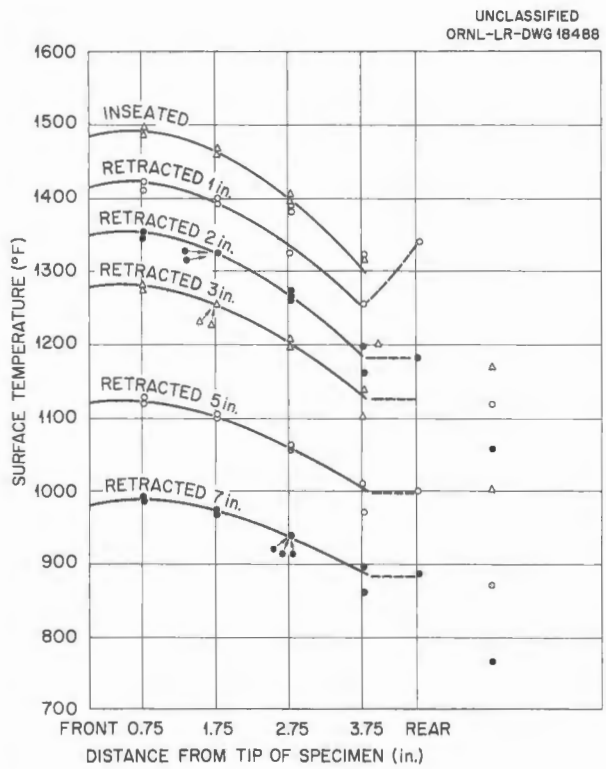

Fig. 1.7.7. Surface Temperature of BeO Specimen vs Distance from Core Face in MTR HB-3 Hole. Estimated power density, 24 w/cm^3.

of the reactor core and hence to vary the power density and temperature.

Thermal Stresses and Temperature Gradients in ZrH Cylinders

F. A. Field

The temperature difference between the center and the surface of a cylindrical rod of ZrH has been estimated and plotted in Fig. 1.7.8, for a constant radiation-heating power density of 100 w/cm^3, along with the estimated thermal stress. Both the temperature difference and the thermal stress are directly proportional to the power density, and hence values for any reactor design that employs round rods can be estimated quickly from this chart.

The total thermal expansion data for zirconium hydride and two possible cladding materials, Inconel and molybdenum, are shown in Fig. 1.7.9. As can be seen from these curves the total expansion of the hydride differs considerably from the expansion of both Inconel and molybdenum in the range from room temperature to 1500°F. These differences in expansion will make it quite difficult to maintain a solid bond between the hydride and its cladding under thermal cycling conditions; further, if there were a bond the differences in thermal expansion might cause buckling of the can.

The stresses in the bond and in the cladding can be calculated if certain simplifying assumptions are made. If the temperature difference between the hydride and the can is neglected, the difference between their total expansions up to any particular temperature is equal to the hoop strain in the can. For example, when an Inconel-clad element is heated from room temperature to an operating temperature of 1500°F a thermal hoop strain of 0.65% (an elastic stress, σ, of $0.0065 \times 15 \times 10^6 = 97{,}000$ psi) is induced in the Inconel can. The corresponding hydrostatic stress, p, in the bond can be found from the standard hoop stress-pressure

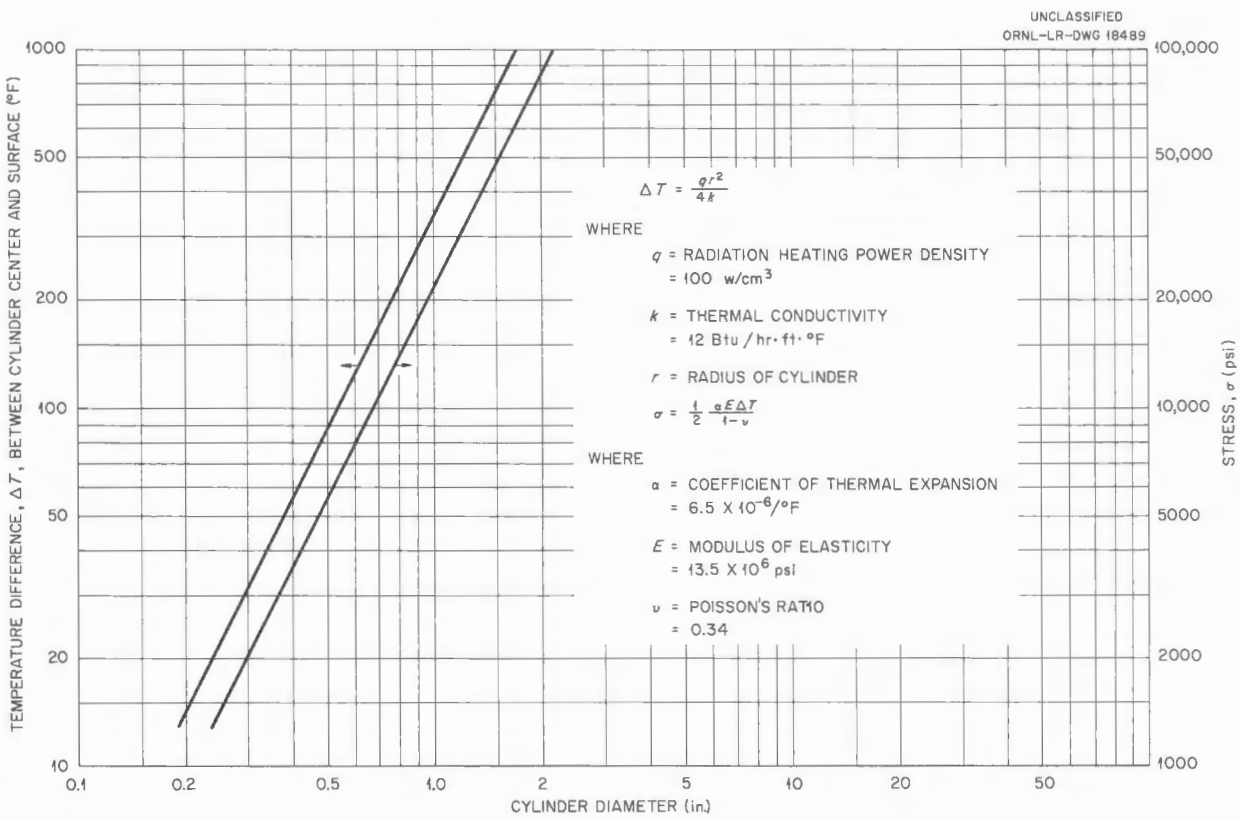

Fig. 1.7.8. Radial Temperature Difference and Thermal Stress in ZrH Cylinders with Uniform Internal Heat Generation.

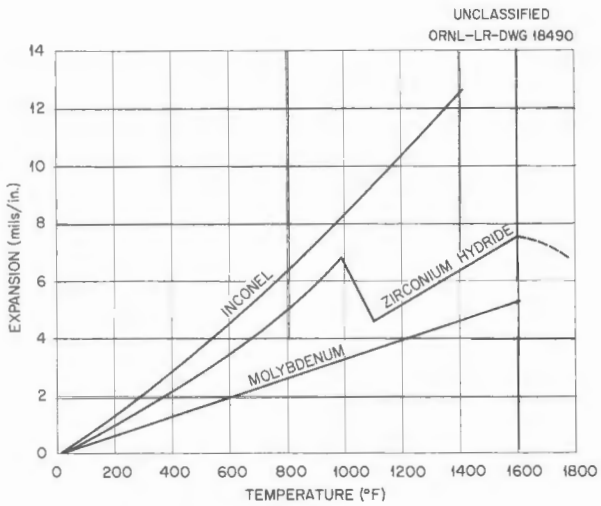

Fig. 1.7.9. Thermal Expansion of Inconel, Zirconium Hydride, and Molybdenum.

relation for cylindrical shells. If $\sigma = pd/2t$, then $p = 2\sigma t/d$. For example, where the can thickness, t, is 0.020 in., and the cylinder diameter, d, is 1 in., the stress on the bond is

$$p = \frac{2 \times 0.0065 \times 15 \times 10^6 \times 0.020}{1}$$

$$= 3900 \text{ psi} .$$

This represents quite severe cycling for both the can and the bond, which, of course, would be realized only during a large-scale thermal cycle from room temperature to operating temperature. A more frequent type of cycle from power to isothermal condition, that is, 1500 to 1100°F, would result in stresses that were about a factor of 3 lower. Both the can and bond stresses for equivalent temperatures would be about a factor of 3 lower for molybdenum cladding than for Inconel.

REACTOR CALCULATIONS

Curtiss-Wright Corporation

Two series of reactor calculations, in which 24-in.-dia reactor cores were assumed, were run on the computing facility at the Curtiss-Wright Corporation; the fuel was considered to be a mixture of $NaF \cdot ZrF_4$ and $2NaF \cdot UF_4$ that contained 4 mole % UF_4. For the first series of calculations, the reactor was considered to be made up of a 12-in.-thick BeO reflector, a core in which the volume percentage of fuel varies with radial position, moderator rods consisting of either graphite of density 1.8, or BeO, and cladding of various thicknesses of Inconel. Thermal stress considerations determined the size of the rods and, hence, the amount of Inconel required for a given thickness of rod cladding. In the case of graphite, the rods could be allowed to be large enough for each to occupy 10% of the reactor volume, but BeO rods could be only 0.26 in. in diameter.

The percentage of the core volume occupied by the fuel, the type of core moderator material assumed, and the thickness of the Inconel cladding required for each reactor calculated are given in Table 1.7.4, along with the resulting multiplication constants. All the reactors turned out to be considerably supercritical, but in a realistic reactor the fuel and cladding that would be required in the reflector would probably reduce the reactivity to below the values given in the table for the idealized reactors with solid BeO reflectors.

For graphite the cladding thickness has very little effect on the multiplication constant, since the large rod has a comparatively small surface, which requires a relatively small amount of cladding. For BeO, the cladding not only introduces substantial poisoning but also displaces BeO moderator. For graphite and for unclad BeO, it makes little difference whether the fuel occupies 80 or 60% of the core volume, but for clad BeO the poisoning of the rod cladding outweighs the reactivity increase of the additional moderator in a core with fuel occupying 60% of the volume. Unclad BeO would be better than unclad graphite, but for 20-mil cladding the advantage of BeO over graphite is only slight, and for 40-mil cladding the graphite is better than BeO.

In the second series of calculations, multiplication constants were determined for graphite-moderated cores with heavy-metal reflectors, such as Inconel and U^{238}. Heavy-metal reflectors would be advantageous in terms of heat removal and shielding. However, the reactors computed were far subcritical, and it appears that hydride moderators will be required for reactors with heavy-metal reflectors and with the core size and fuel concentration being considered.

The accuracy of the numerical values obtained in these calculations is in doubt, because the high-energy absorption cross sections used in the machine code were not correct but could not be changed. To illustrate this point Fig. 1.7.10 shows

TABLE 1.7.4. MULTIPLICATION CONSTANTS OF VARIOUS BeO-REFLECTED, CIRCULATING-FUEL REACTORS

Core Volume Occupied by Fuel (%)	Core Moderator Material	Thickness of Cladding (mils)	Multiplication Constant, k
80	Graphite	0	1.175
80	Graphite	20	1.175
80	Graphite	40	1.175
60	Graphite	0	1.16
60	Graphite	40	1.16
80	BeO	0	1.21
80	BeO	20	1.19
80	BeO	40	1.16
60	BeO	0	1.23
60	BeO	40	1.05

the zirconium absorption cross section values between 10^2 and 10^6 ev as used in the code[2] and as computed from data given by Greebler *et al.*,[3] along with an experimental value obtained by Diven and Terrell.[4] (Similar data for yttrium are given in Fig. 1.7.11.) Although the cross-section values of Greebler *et al.* are in doubt by a factor of 2 or 3, it is evident that the code used values that were far too low for the absorption cross section for zirconium at high neutron energies. The justification for using the code lies in the relatively small number of absorptions which occur at the high energies, and, for this reason, the general conclusions are believed to be valid. Efforts are being made to obtain better cross section data before further refinement of the calculations is undertaken.

[2]D. L. Kavanagh and C. B. Mills, *Neutron Cross Sections for Multigroup Reactor Calculations*, CWR-413 (Sept. 1, 1955).

[3]P. Greebler, H. Hurwitz, Jr., and M. L. Storm, *Statistical Evaluation of Fission-Product Absorption Cross Sections at Intermediate and High Energies*, Knolls Atomic Power Laboratory unclassified report (to be issued).

[4]*Progress Reports to the Nuclear Cross Sections Advisory Group for the Meeting at Argonne National Laboratory, Sept. 24–26, 1956*, see included "Report of Activities on Cross-Section Measurements from LASL Covering Period from 21 May 1956 to 20 August 1956."

Nuclear Development Corporation of America

As an initial study,[5] some spherical geometry multigroup calculations were run on the NDA Datatron in order to compare beryllium and iron reflectors for a reactor with the following specifications:

Core diameter	21 in.
Moderator material	ZrH (N_H = 3.5)
Moderator cladding	None
Fuel	$NaF \cdot UF_4$-$NaF \cdot ZrF_4$ (0.74 mole % UF_4)
Fuel volume fraction	0.5
Core fuel loading	2.04 kg of U^{235}
Reflector material	Be or Fe
Reflector thickness	6 in.
Reflector cooling provisions	None

This reactor was selected for the initial comparison since the results of a Wright Aeronautical Div. calculation for the case with the beryllium reflector were available. Iron was selected for the second case, rather than nickel, because inelastic scattering cross sections were available for iron but not

[5]Taken from a personal communication from D. M. Poole to W. K. Ergen, letter of December 13, 1956.

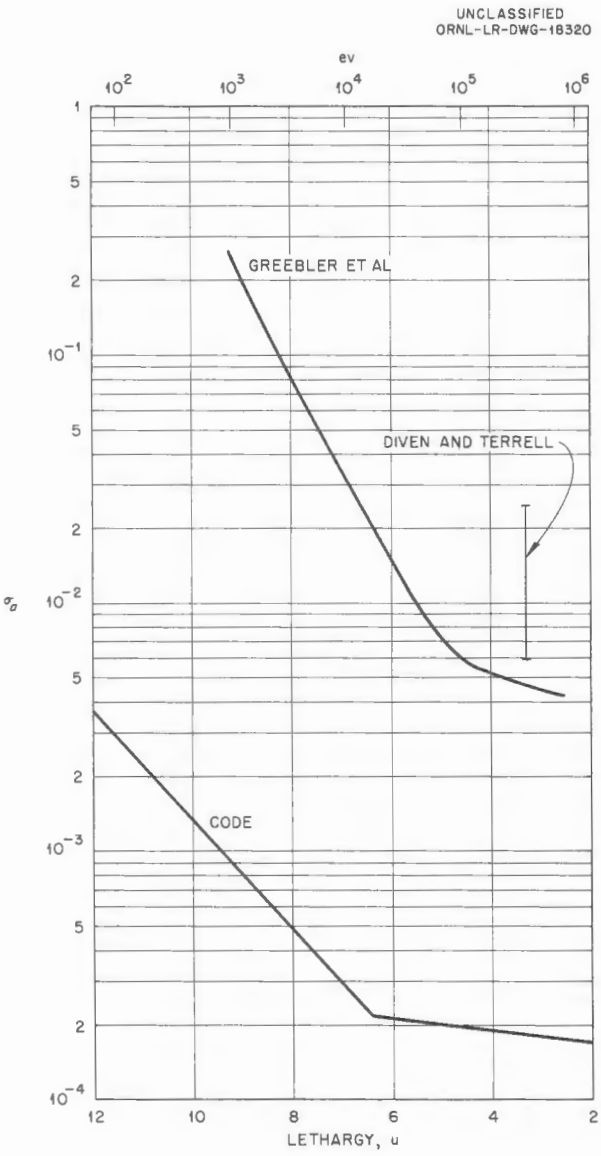

Fig. 1.7.10. Absorption Cross Section Values for Zirconium in the Neutron Energy Range from 10^2 to 10^6 ev.

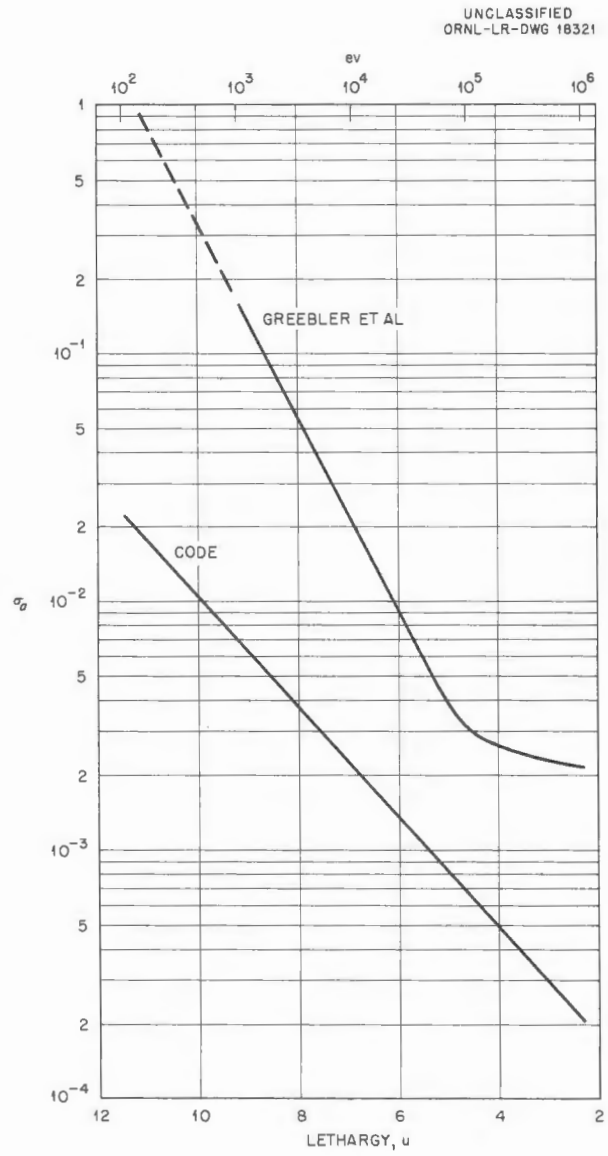

Fig. 1.7.11. Absorption Cross Section Values for Yttrium in the Neutron Energy Range from 10^2 to 10^6 ev.

for nickel. The core was assumed to be homogeneous.

The case with the beryllium reflector gave a multiplication constant of $k = 1.027$, which is in fairly good agreement with the Wright Aeronautical value of 1.00. The iron reflector gave a 20% reduction in k. A beryllium reflector is probably not practical for a single-fluid circulating-fuel reactor, but the comparison in reflector effectiveness provides some useful orientation.

A comparison of abbreviated neutron balances for the calculations, as given in Table 1.7.5, shows that the reduced reactivity of the iron-reflected reactor is largely caused by increased fast leakage and increased fast reflector absorption, as compared with the reactor with a beryllium reflector. The high rate of thermal absorptions in the iron reflector is partly counterbalanced by the higher thermal leakage from the beryllium reflector.

TABLE 1.7.5. COMPARISON OF NEUTRON ABSORPTION AND LEAKAGE IN BERYLLIUM AND IRON REFLECTORS

	Neutron Balance (%)	
	Beryllium Reflector	Iron Reflector
Fast leakage (all energies above thermal)	12.6	22.8
Thermal leakage	19.1	0.45
Fast absorptions in reflector	2.9	7.8
Thermal absorptions in reflector	1.7	18.2
Fast absorptions in core (including fissions)	10.4	11.0
Thermal absorptions in core (including fissions)	53.3	40.2

Approximately 90% of the thermal neutrons which are absorbed in the iron reflector originate in the core. Since almost all the core thermal neutrons can be expected to be born in the hydride, a two-region core consisting of a central region containing moderator and fuel and an annular region containing fuel only should reduce the thermal leakage into the reflector and thereby improve reactivity.

The effectiveness of this core arrangement was studied in three cylindrical multigroup calculations with the use of the same average core composition (atomic concentrations) as that used in the spherical calculations. The moderator rods were moved progressively closer to the center to give fuel annulus thicknesses of 0, 1, and 2 in. The results indicated that, while the thermal absorption in the reflector decreased as the fuel annulus thickness increased, for the rather dilute fuel concentration used the decrease in reflector absorption was more than offset by the increase in fast leakage caused by the shifting of fuel toward the core surface. The arrangement may prove more advantageous for higher fuel concentration.

Part 2

CHEMISTRY

W. R. Grimes

2.1. PHASE EQUILIBRIUM STUDIES[1]

C. J. Barton R. E. Moore R. E. Thoma
H. Insley, Consultant

THE SYSTEM $NaF-RbF-UF_4$

H. A. Friedman B. S. Landau

A phase equilibrium study of the system $NaF-RbF-UF_4$ has been completed, and the information presented here corrects that presented previously.[2] Equilibrium data were derived from petrographic and x-ray diffraction examination of quenched and slowly cooled melts. The boundary curves, compatibility triangles, and isotherms characteristic of the system are illustrated in Fig. 2.1.1. The eutectic and peritectic compositions and their temperatures are listed in Table 2.1.1. The phase relations of the compound $NaF \cdot RbF \cdot UF_4$ along the three joins on which it becomes the apex of a compatibility triangle are shown in Figs. 2.1.2, 2.1.3, and 2.1.4.

[1]The petrographic examinations reported here were performed by G. D. White, Metallurgy Division, and T. N. McVay and H. Insley, Consultants. The x-ray examinations were performed by R. E. Thoma and B. S. Landau, Chemistry Division.

[2]H. A. Friedman *et al.*, *ANP Quar. Prog. Rep. Sept. 10, 1956*, ORNL-2157, p 90.

TABLE 2.1.1. EUTECTIC AND PERITECTIC COMPOSITIONS IN THE SYSTEM $NaF-RbF-UF_4$

	Composition (mole %)			Temperature (°C)
	NaF	RbF	UF_4	
Eutectics	25	25	50	630
	26	27	47	620
	33	30	37	535
	46	32.5	21.5	470
	18	73	9	670
Peritectics	42	2.5	55.5	678
	32.5	14.5	53	655
	27	22	51	633
	32	29	39	540
	57	8	35	630
	41	26.5	32.5	550
	52	23	25	495
	45.5	29.5	25	485
	44	33	23	500
Eutectics on binary sections	25.5	26.5	48	635
	26.5	27	46.5	630
	40.35	26.35	33.3	555
	41	44	15	750

THE SYSTEM $RbF-CaF_2$

L. M. Bratcher R. J. Sheil

A new furnace was constructed that permits visual observation of small quantities of fused salts in an inert atmosphere at higher temperatures than those previously attainable in the visual-observation apparatus (about 850°C). The new furnace consisted of concentric Alundum tubes with platinum–10% rhodium wire wound on the inner tube. This assembly was fitted into the 2-in. stainless steel pipe on the bottom of a Lucite inert-atmosphere box similar to that previously described.[3] It was found that a temperature of 1200°C could be attained in the center of the inside furnace space in about 90 min by operating both the inside and the outside heaters at 75% of line voltage.

The new furnace arrangement was used to observe small portions of $RbF-CaF_2$ mixtures contained in 20-ml platinum crucibles. Temperatures were determined with a platinum–platinum-rhodium thermocouple junction that was dipped into the melt. The data obtained by using this apparatus are plotted as solid circles in Fig. 2.1.5. Thermal analysis data obtained previously with stirred melts are indicated in the diagram as open circles. The compositions given are values calculated from the weighed amounts of starting materials and may be slightly in error as a result of volatilization of the RbF component of the mixture. As shown by the diagram, $RbCaF_3$ melts congruently at 1110 ± 10°C and the eutectic between $RbCaF_3$ and CaF_2 melts at about 1090°C.

[3]M. S. Grim, *ANP Quar. Prog. Rep. Sept. 10, 1954*, ORNL-1771, p 56.

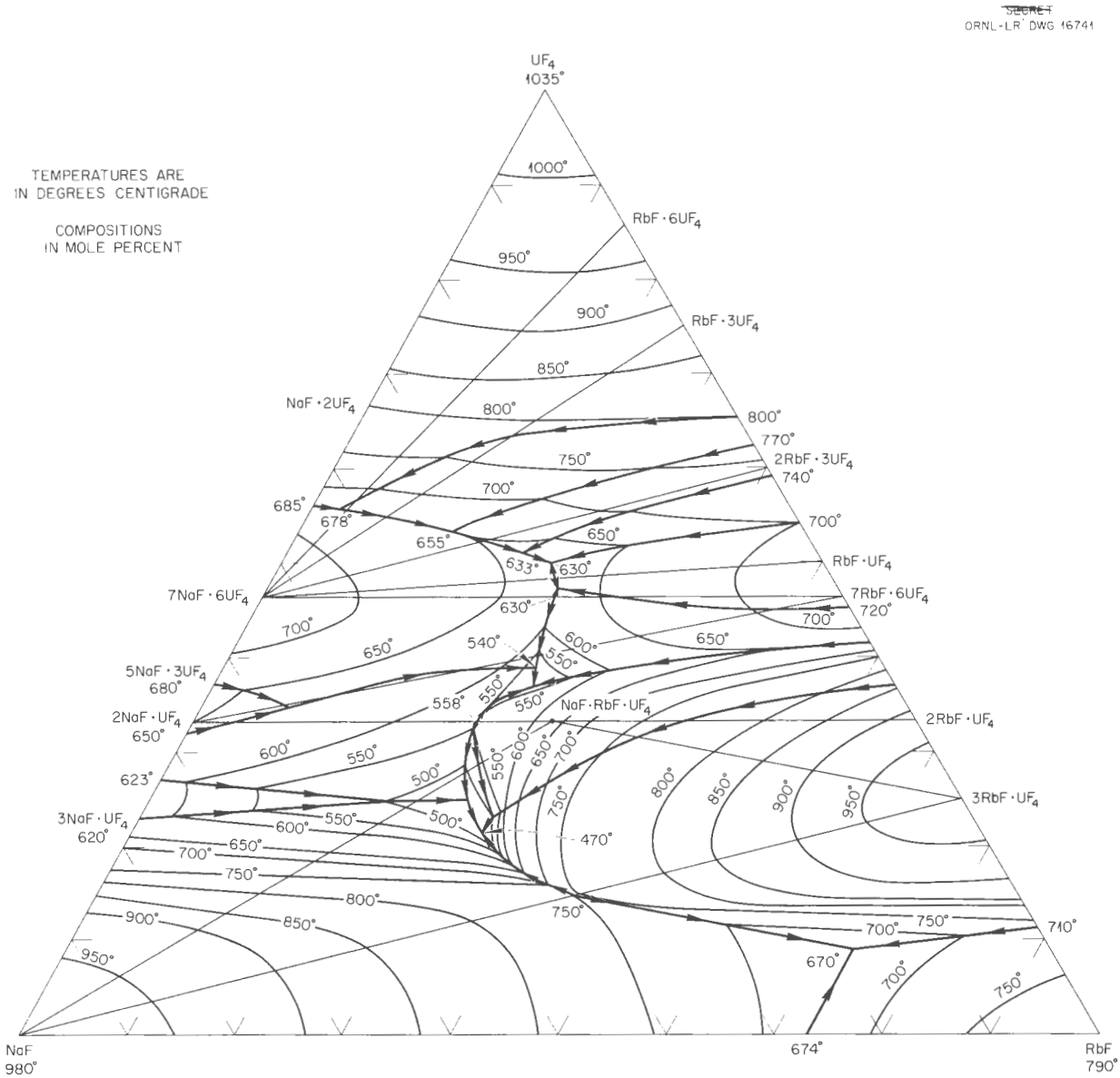

Fig. 2.1.1. The System NaF-RbF-UF_4.

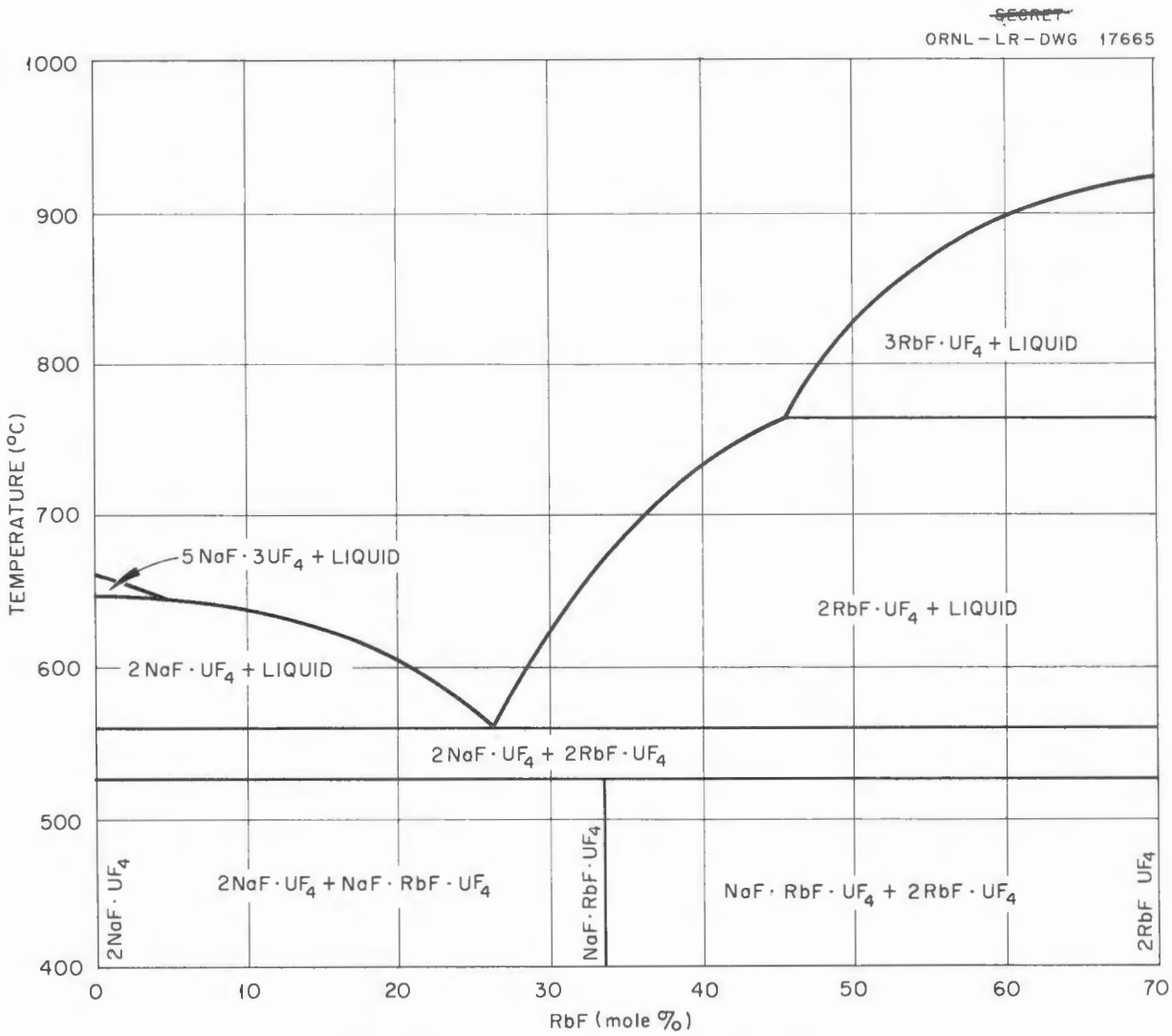

Fig. 2.1.2. The Join $2NaF \cdot UF_4$-$2RbF \cdot UF_4$.

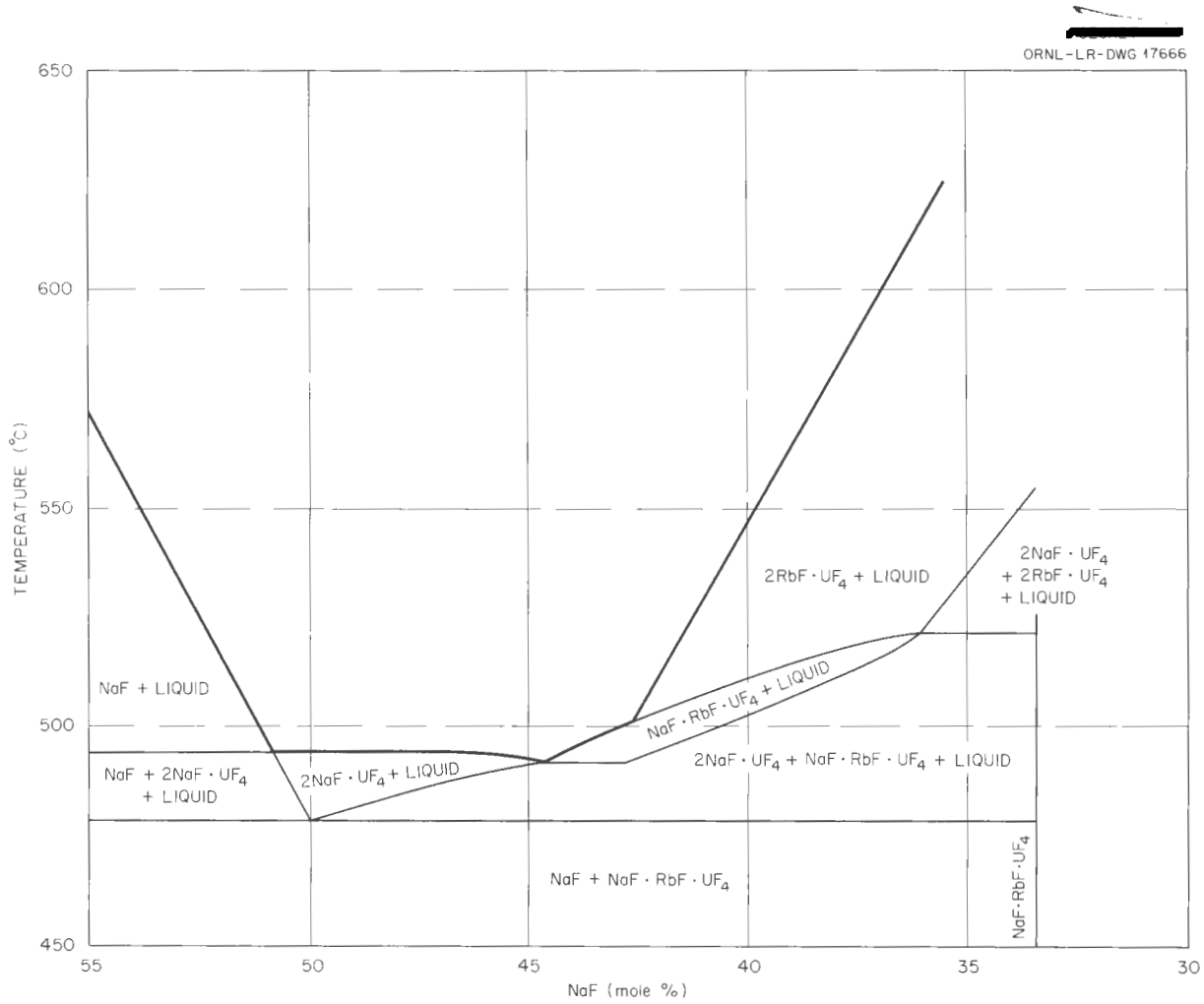

Fig. 2.1.3. The Join NaF-NaF·RbF·UF$_4$.

THE SYSTEM 7NaF·6ZrF$_4$-7NaF·6UF$_4$

H. A. Friedman H. Insley

The equilibrium relations in the solid solution 7NaF·6ZrF$_4$-7NaF·6UF$_4$ were established[4] following quenching studies of twelve compositions in this system. The solid solution displays neither a region of immiscibility nor a minimum liquidus or solidus temperature. A phase diagram of the system 7NaF·6ZrF$_4$-7NaF·6UF$_4$ is presented in Fig. 2.1.6.

[4]This solid solution, formerly thought to be NaF·ZrF$_4$-NaF·UF$_4$, was described previously by C. J. Barton *et al.* in *ANP Quar. Prog. Rep. Dec. 10, 1953*, ORNL-1649, p 54, and in *ANP Quar. Prog. Rep. Sept. 10, 1954*, ORNL-1771, p 54. The data previously obtained did not permit an accurate description of the liquidus-solidus relationships along this join or a determination of whether there is a miscibility gap or a minimum in the solid solution.

THE SYSTEM RbF-BeF$_2$

L. M. Bratcher R. E. Meadows

Quenching studies of the system RbF-BeF$_2$ were completed. The phase diagram presented in Fig. 2.1.7 is based on thermal analysis data obtained previously[5] and on x-ray diffraction examinations of quenched samples. Data from the experiments are given in Table 2.1.2.

[5]L. M. Bratcher, R. E. Meadows, and R. J. Sheil, *ANP Quar. Prog. Rep. March 10, 1956*, ORNL-2061, p 74.

TABLE 2.1.2. RESULTS OF QUENCHING STUDIES OF $RbF\cdot BeF_2$ MIXTURES

BeF_2 Content (mole %)	Quenching Temperature Range (°C)	Liquidus Temperature (°C)	Primary Phase	Solidus Temperature (°C)	Phases below Solidus	Remarks
20					$3RbF\cdot BeF_2$ (O), RbF (O)	
25	770–605	>710	$3RbF\cdot BeF_2$ (O)*	>710	$3RbF\cdot BeF_2$ (O)	
33.3	504–362					All samples contained pure $2RbF\cdot BeF_2$ (O)
40	504–368	>504	$2RbF\cdot BeF_2$ (O)	442	$2RbF\cdot BeF_2$ (O), $RbF\cdot BeF_2$ (O)	
48	498–462	>498	$2RbF\cdot BeF_2$ (O)	450	$2RbF\cdot BeF_2$ (O), $RbF\cdot BeF_2$ (O)	
50	563–396	475	$2RbF\cdot BeF_2$ (O)	434	$RbF\cdot BeF_2$ (O)	A small amount of another phase was also observed below the solidus
55	472–344	444	$RbF\cdot BeF_2$ (O)	374	$RbF\cdot BeF_2$ (O), $RbF\cdot 2BeF_2$ (O)	
60	488–354	393	$RbF\cdot BeF_2$ (O)	383	$RbF\cdot 2BeF_2$ (O, X),* $RbF\cdot BeF_2$ (O, X)	
63	471–344	450	$RbF\cdot 2BeF_2$ (O)	372	$RbF\cdot BeF_2$ (O), $RbF\cdot 2BeF_2$ (O)	
66.7	488–356	464	$RbF\cdot 2BeF_2$ (O)	464	$RbF\cdot 2BeF_2$ (O, X)	
73	486–345	450	$RbF\cdot 2BeF_2$ (O)			Crystalline BeF_2 used in the preparation of this composition
	486–354	448	$RbF\cdot 2BeF_2$ (O)			
80	414–296	409	$RbF\cdot 2BeF_2$ (O)	407	$RbF\cdot 2BeF_2$ (O, X), BeF_2 (X)	Crystalline BeF_2 used in the preparation of this composition
	440–315	413	$RbF\cdot 2BeF_2$ (O)	401	$RbF\cdot 2BeF_2$ (O), BeF_2 (O)	Crystalline BeF_2 used in the preparation of this composition
85	530–380	486	BeF_2 (O)	392		Crystalline BeF_2 used in the preparation of this composition

*The symbol (O) means that the phase was identified by petrographic examination. Formulas of phases identified by x-ray diffraction examination are followed by the symbol (X).

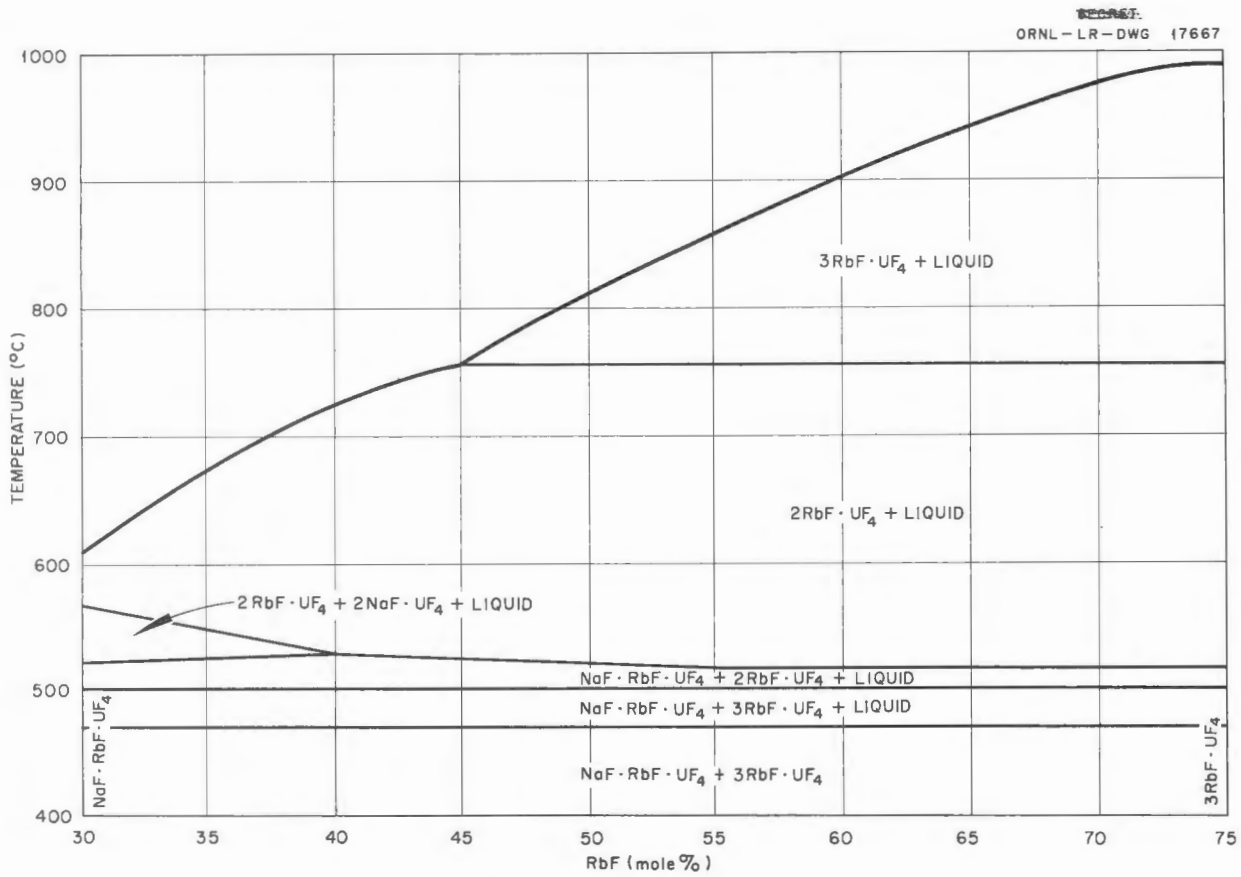

Fig. 2.1.4. The Join $NaF \cdot RbF \cdot UF_4$-$3RbF \cdot UF_4$.

The liquidus temperatures in the low BeF_2 part of the diagram, that is, below 50 mole % BeF_2, were obtained entirely by thermal analysis. Thermal analysis data were not so definitive above 50 mole % BeF_2, and in this region quenching methods were profitably employed. Most of the compositions used for quenching experiments in the highly viscous region between the compound $RbF \cdot 2BeF_2$ and BeF_2 were prepared by mixing $RbF \cdot 2BeF_2$ with crystalline BeF_2 obtained from Mound Laboratory.

If slowly cooled unpurified preparations made from glassy BeF_2 are used, the BeF_2 remains as glass during the heat treatment. This may indicate that a small amount of oxygen dissolved in the BeF_2 prevents its crystallization and that oxygen is more soluble in BeF_2 than in $RbF \cdot 2BeF_2$. It has been observed at Mound Laboratory that commercial, glassy BeF_2 can be converted to crystalline BeF_2 by treating the liquid BeF_2 with HF and H_2 gases to remove oxygen and then cooling the melt slowly. Even when crystalline material was used, however, the BeF_2 was not readily identifiable petrographically because of the small size of the crystals resulting from quenching, but the x-ray diffraction results were definitive. The very rapid inversion of BeF_2 from the high quartz temperature to the low quartz temperature is probably responsible for the petrographic difficulties.

THE SYSTEM NaF-RbF-BeF_2-UF_4

L. M. Bratcher

Liquidus temperatures were determined from cooling curves obtained for mixtures prepared by adding various amounts of UF_4 to two different solvent compositions in the NaF-RbF-BeF_2 ternary system, both solvents being on the $2NaF \cdot BeF_2$-$2RbF \cdot BeF_2$ join. The thermal data, as given in Table 2.1.3, show that liquidus temperatures in

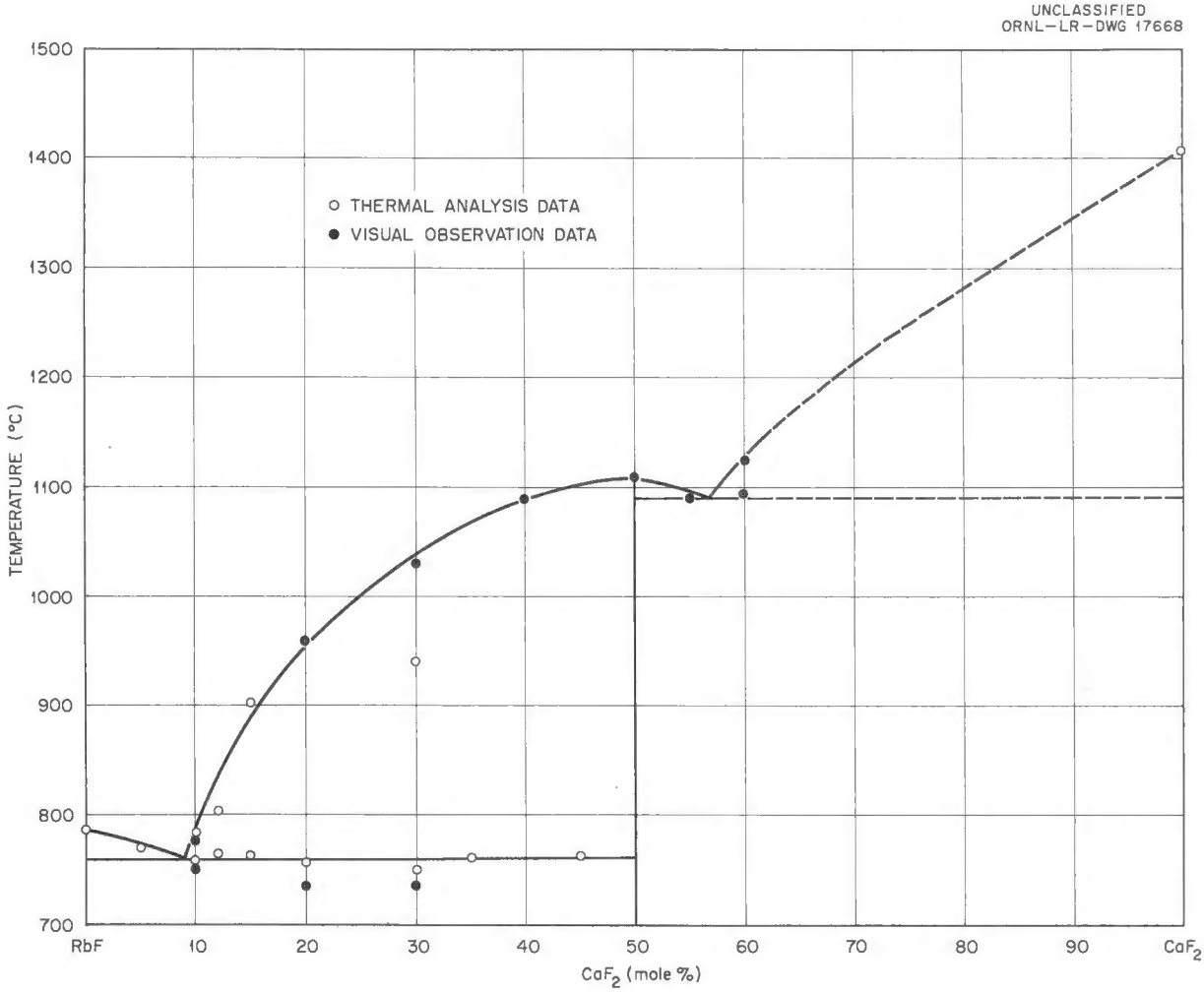

Fig. 2.1.5. The System RbF-CaF_2.

this system at UF_4 concentrations equivalent to those currently considered to be useful for aircraft-reactor fuel compare favorably with those obtained in the system NaF-ZrF_4-UF_4. Vapor pressure data are not available for mixtures in this system, but the vapor pressures are expected to be much lower than those of the ZrF_4-base fuel systems. Viscosity data likewise are not available for such mixtures but will be obtained in the near future. If the kinematic viscosity proves to be sufficiently low, mixtures in the NaF-RbF-BeF_2-UF_4 system will deserve serious consideration for use in future circulating-fuel reactors.

THE SYSTEM KF-BeF_2

L. M. Bratcher R. E. Meadows

Studies of the system KF-BeF_2 have been based entirely on thermal analysis data for mixtures containing up to 33 mole % BeF_2. It appears from the thermal data that KF-BeF_2 melts incongruently, but recent quenching experiments have cast some doubt upon this indication. The compound crystallizes too readily for a determination of its melting point to be made by quenching methods, and it has thus far not been possible to ascertain whether $2KF \cdot BeF_2$ is the primary phase at 50 mole %

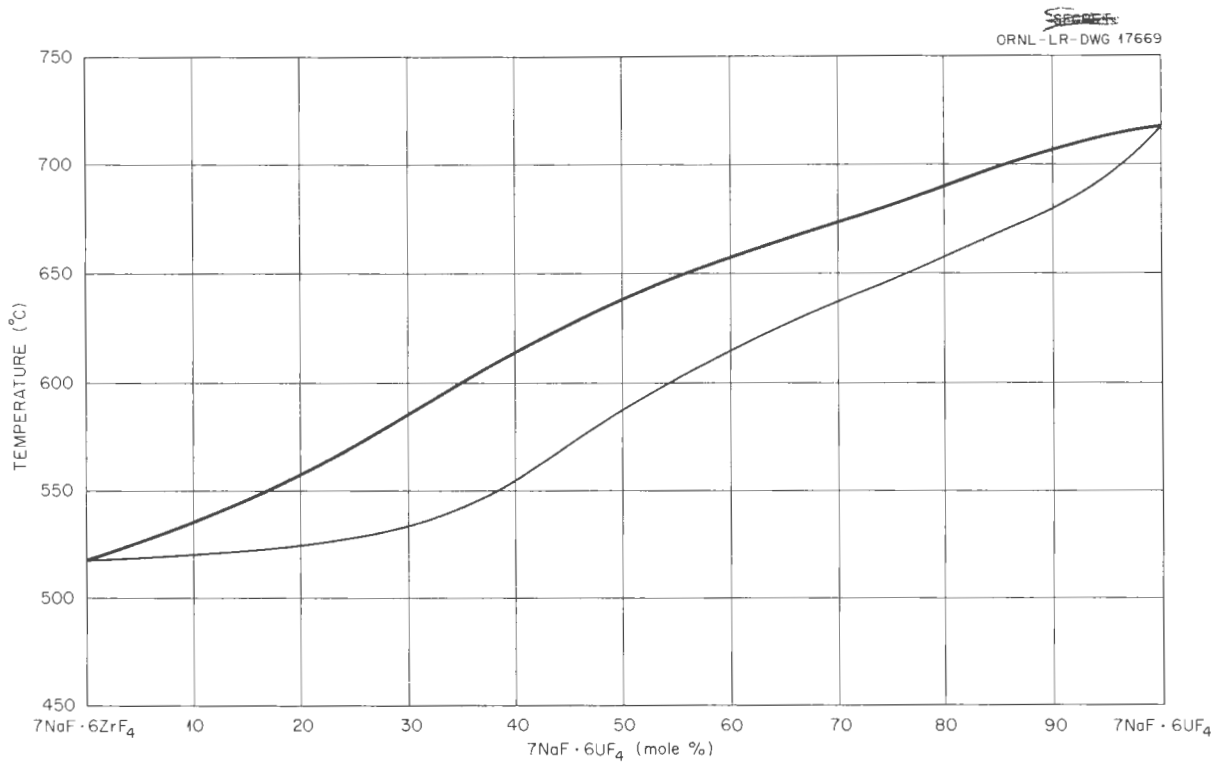

Fig. 2.1.6. The System $7NaF \cdot 6ZrF_4$-$7NaF \cdot 6UF_4$.

TABLE 2.1.3. LIQUIDUS TEMPERATURES OF NaF-RbF-BeF_2-UF_4 MIXTURES

Solvent Compositions (mole %)			UF_4 Concentration (mole %)	Liquidus Temperature (°C)	Temperatures of Other Thermal Effects (°C)
NaF	RbF	BeF_2			
$33\frac{1}{3}$	$33\frac{1}{3}$	$33\frac{1}{3}$	0	580	480
			2	560	430
			4	530	375
			6*	505	445, 390, 245
			8	460	370
			10	515	415
50	16.7	33.3	0	485	
			2	476	
			4	453	438, 429
			6	453	438, 420
			8	475	398, 280
			10	483	335, 280

*This was a purified mixture having slightly different concentrations of the solvent components. The unpurified mixture containing 6 mole % UF_4 gave variable thermal effects.

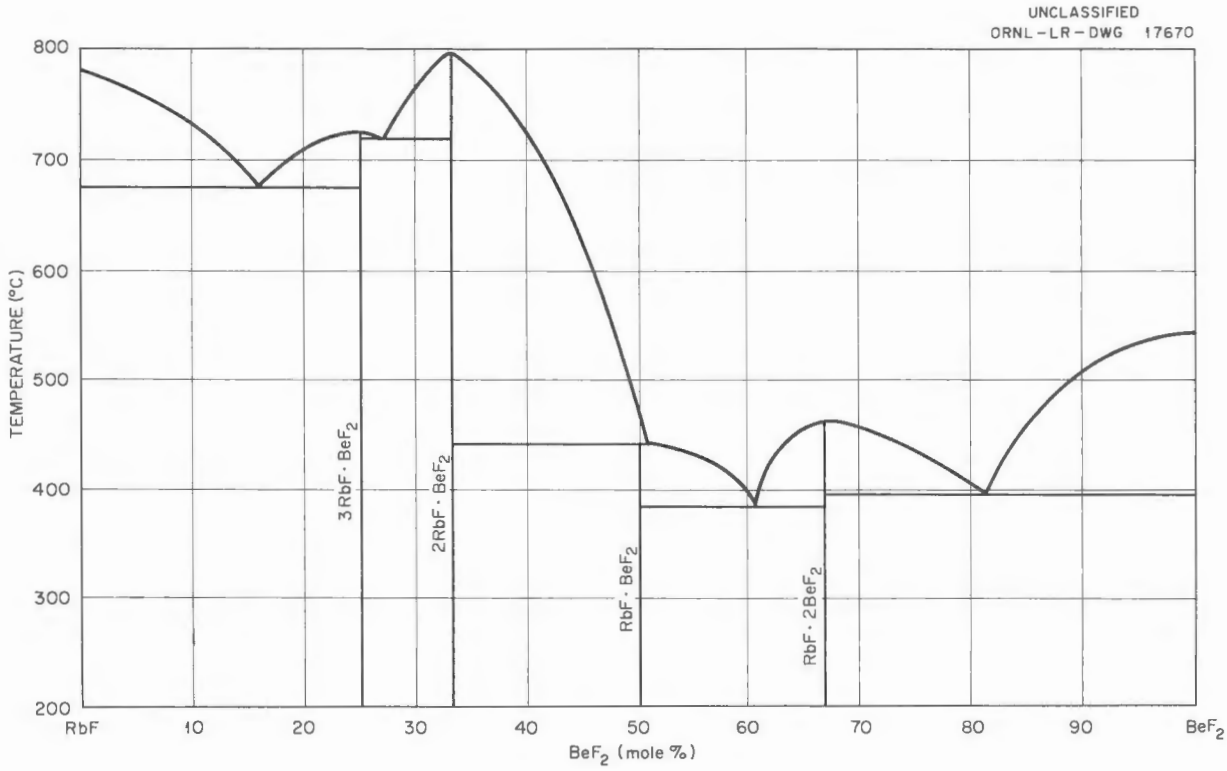

Fig. 2.1.7. The System RbF-BeF_2.

BeF_2. Quenched mixtures containing 37 and 40 mole % BeF_2 indicate a solidus temperature of about 375°C, which is considerably lower than the peritectic temperature, while petrographic examination of a series of quenched mixtures containing 55 mole % BeF_2 places the liquidus for that composition at 400°C. These data seem to show that KF·BeF_2 melts congruently, but this work is being pursued further since the quenching data cannot be reconciled with available thermal data.

The compound KF·2BeF_2 melts congruently at 358°C. Two modifications with very similar x-ray diffraction patterns have been found. The one found in slowly cooled preparations is uniaxial, while the one encountered in quenched samples is biaxial. Further quenching data are needed to determine the inversion temperature. Data obtained for quenched mixtures containing 55 and 60 mole % BeF_2 indicate that the eutectic between KF·BeF_2 and KF·2BeF_2 contains 59 mole % BeF_2 and melts at 338°C. Petrographic examination of quenched samples containing 71 and 75 mole % BeF_2 gave liquidus values of 352 and 397°C, respectively, with KF·2BeF_2 and BeF_2 as the primary phases. The solidus temperature was about 323°C in both cases. According to x-ray diffraction examination the material below the solidus consisted of KF·2BeF_2, KF·BeF_2, and BeF_2. Possibly there is slow decomposition of KF·2BeF_2 into KF·BeF_2 and BeF_2 just below the solidus. As was the case in the work on the RbF-BeF_2 system the samples used for quenching studies in the region between the compound KF·2BeF_2 and BeF_2 were prepared from crystalline BeF_2 obtained from Mound Laboratory.

THE SYSTEM CsF-BeF_2

L. M. Bratcher H. A. Friedman

A thermal analysis investigation of the CsF-BeF_2 system with mixtures containing 5 to 85 mole % BeF_2 was completed. Preliminary data were reported previously.[6] The effects observed

[6] L. M. Bratcher, *ANP Quar. Prog. Rep. Sept. 10, 1956*, ORNL-2157, p 92.

on cooling curves suggest the existence of incongruently melting compounds containing 25 and 50 mole % BeF_2 and a congruently melting compound containing 33⅓ mole % BeF_2. Examination of the slowly cooled melts by petrographic and x-ray diffraction techniques verified the existence of $2CsF{\cdot}BeF_2$ (mp, 755 ± 5°C) and $CsF{\cdot}BeF_2$ (incongruent mp, 455°C), but the existence of $3CsF{\cdot}BeF_2$ has not been verified. Since both components of this system are extremely hygroscopic, $NH_4F{\cdot}HF$ was added to each mixture to eliminate oxygen from the system. There is probably another compound having the composition $CsF{\cdot}2BeF_2$, since essentially single-phase material was found in the mixture containing 65 mole % BeF_2. There is a eutectic containing approximately 57.5 mole % BeF_2 between $CsF{\cdot}BeF_2$ and $CsF{\cdot}2BeF_2$, which melts at 365 ± 5°C, in addition to the previously reported[6] eutectic containing 14 mole % BeF_2, which melts at 605 ± 5°C. A new phase, apparently not BeF_2, appeared in mixtures containing 70 mole % BeF_2 or more. It was the predominant phase in the 75 mole % BeF_2 mixture. The slowly cooled mixture with 85 mole % BeF_2 contained only glass. Quenching data will be required to give a clear picture of phase relationships in this part of the system.

THE SYSTEM $NaCl{-}ZrCl_4$

R. J. Sheil

Thermal analysis data and petrographic examination of fused mixtures were the basis for the $NaCl{-}ZrCl_4$ phase diagram presented in Fig. 2.1.8. Published data for this system obtained by workers at Columbia University[7] are fragmentary, and the

[7] H. H. Kellogg, L. J. Howell, and R. C. Sommer, *Physical Chemical Properties of the Systems NaCl-ZrCl$_4$, KCl-ZrCl and NaCl-KCl-ZrCl$_4$. Summary Report*, NYO-3108, April 7, 1955.

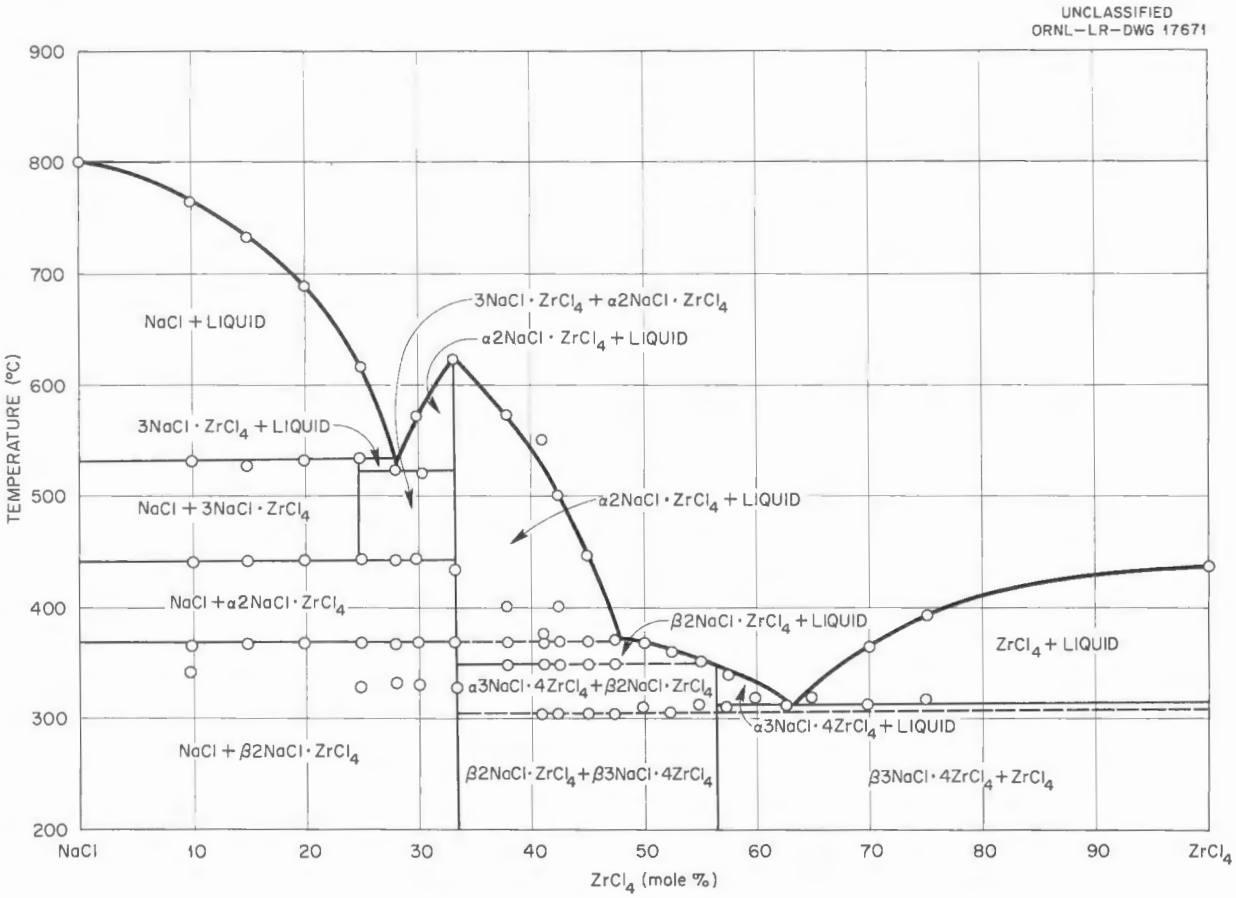

Fig. 2.1.8. Tentative Equilibrium Diagram of the System $NaCl{-}ZrCl_4$.

earlier Russian data[8] are obviously erroneous. A more recent Russian investigation[9] gave thermal data that agreed more closely with those shown in Fig. 2.1.8, but only one compound, $2NaCl \cdot ZrCl_4$, is reported in the Russian paper.

Since $2NaCl \cdot ZrCl_4$ and NaCl were the only phases identified in samples containing less than 33.3 mole % $ZrCl_4$, it is assumed that $3NaCl \cdot ZrCl_4$, which melts to NaCl and liquid at 535 ± 5°C, decomposes to $\alpha 2NaCl \cdot ZrCl_4$ and NaCl at 445 ± 5°C. It is planned to obtain quenching data to check this assumption. The series of thermal effects at 370 ± 5°C that spans the diagram to about 50 mole % $ZrCl_4$ is believed to represent an inversion of the 2:1 compound that was observed petrographically in mixtures containing up to 57.5 mole % $ZrCl_4$. A eutectic between $3NaCl \cdot ZrCl_4$ and $\alpha 2NaCl \cdot ZrCl_4$, which melts at 525 ± 5°C, is located at 72 mole % NaCl–28 mole % $ZrCl_4$.

As the concentration of $ZrCl_4$ was increased to beyond 33.3 mole %, a second compound appeared in slowly cooled melts that eventually became the predominant phase in mixtures containing 55 to 60 mole % $ZrCl_4$. Although thermal halts were noted at around 312°C in mixtures containing from 38 to 75 mole % $ZrCl_4$, visual observations of mixtures containing 38, 41, and 45 mole % $ZrCl_4$ did not show liquid below 360°C. Therefore, it is believed that a compound, possibly $3NaCl \cdot 4ZrCl_4$, melts incongruently to $\beta 2NaCl \cdot ZrCl_4$ and liquid at 352°C and that it inverts to the low-temperature form at approximately 312°C, the melting point of the eutectic containing 63 mole % $ZrCl_4$. This assumption will also be checked by quenching experiments. The diagram presented in Fig. 2.1.8 should be regarded as tentative.

OXIDES AND OXYFLUORIDES IN MOLTEN SALTS

B. S. Landau

Chemical analyses for small amounts of combined oxygen in a fluoride mixture would be very difficult to make, if not impossible, and x-ray diffraction techniques are of no value for determining these oxides and oxyfluorides at low concentration levels. Examination with the petrographic microscope is the most sensitive of the available methods and is routinely used on all material prepared for use in loops, heat exchangers, and other experimental equipment.

The specification for fuel mixtures for engineering tests calls for the oxygen compounds to be undetectable by petrographic examination. No quantitative data exist, however, for establishing exact criteria for the quality of such oxide-free fuels, since no experiments to date have provided a calibrated set of materials of known oxygen content. In a recent experiment an attempt was made to concentrate the oxides from a low-oxide-content batch of material for examination. Batches (2 kg) of $NaF\text{-}ZrF_4\text{-}UF_4$ (50-46-4 mole %) which were shown by petrographic examination to be oxide-free were carefully transferred to hydrogen-fired nickel containers with sloping bottoms to which had been welded short lengths of ½-in. tubing to serve as collection chambers for segregated oxygen compounds. These batches were then heated to 800°C, held for 1 hr, and slowly cooled to well below the freezing point of the material. After ten such cycles the samples in the collection chambers were carefully examined.

These samples (about 30 g of material) were shown by petrographic examination to contain appreciable quantities of oxyfluorides. These compounds were not detectable by x-ray diffraction and, accordingly, probably comprised much less than 5% of the sample. It is, of course, difficult to estimate the efficiency of collection of the oxygenated material by this sampling technique. If the collection were nearly complete, the original batch of fuel mixture probably contained less than 0.1% oxyfluoride compounds.

This series of tests indicates clearly that batches of material designated oxide-free would not be expected under thermal-cycling conditions to precipitate oxide materials that would plug loops or other equipment. The conclusion seems clear that in cases where clean fuel was introduced and trouble developed because of oxide precipitation, the trouble was a consequence of improper cleaning of the loop, exposure to atmospheric contamination, or other mishandling of the system or the fuel after its original examination.

[8] N. A. Belozerskts and O. A. Kucherenko, *Zhur. Priklad. Khim.* 13, 1552 (1940).

[9] I. S. Morozov and B. G. Korshunov, *Zhur. Neorg. Khim.* 1, 145 (1956).

2.2. CHEMICAL REACTIONS IN MOLTEN SALTS

F. F. Blankenship
R. F. Newton
L. G. Overholser
G. M. Watson

EQUILIBRIUM REDUCTION OF NiF_2 BY H_2 IN $NaF\text{-}ZrF_4$

C. M. Blood
G. A. Palmer

Investigation of the equilibrium

$$NiF_2\,(d) + H_2\,(g) \rightleftharpoons Ni\,(s) + 2HF\,(g)$$

in the reaction medium $NaF\text{-}ZrF_4$ (53-47 mole %) was continued. The results obtained this quarter for K_x are, as shown in Table 2.2.1, lower by about 30% than the average of a group of results published previously.[1] The reasons for the difference appear to be refinements in the experimental technique. These refinements included improvement of the accuracy of the determination of the hydrogen concentration in the H_2-He mixtures used, precise determination of the hydrogen concentration in the incipient HF vapor and adjustment of the data when necessary, much smaller temperature gradients in the reactor, and improvement of the precision of the analytical determination of nickel. The data given in Table 2.2.1 correlate very satisfactorily with changes of temperature. Additional measurements will be made at other temperatures.

SOLUBILITY AND STABILITY OF STRUCTURAL METAL FLUORIDES IN VARIOUS FLUORIDE MIXTURES

J. D. Redman

The results of studies of the solubility and stability of CrF_2, FeF_2, and NiF_2 in $NaF\text{-}ZrF_4$ (53-47 mole %),[2] $NaF\text{-}ZrF_4$ (59-41 mole %),[3] $LiF\text{-}ZrF_4$ (52-48 mole %),[3] and $KF\text{-}ZrF_4$ (52-48 mole %)[3] at 600 and at 800°C were reported previously. It was demonstrated that the solubility of FeF_2 and CrF_2 in these solvents increased as the quantity of solute added was increased. It appears that the solid phase in equilibrium with these solutions is a complex compound of ZrF_4 with the structural metal fluoride, and therefore the solvent becomes progressively richer in alkali fluoride as the amount of added solute increases. A less pronounced effect on the solubility of NiF_2 at 600°C was noted in $LiF\text{-}ZrF_4$ (52-48 mole %) and in $NaF\text{-}ZrF_4$ (53-47 mole %), while the solubility was found to be essentially unaffected by the excess of NiF_2 present in $KF\text{-}ZrF_4$ (52-48 mole %) and in $NaF\text{-}ZrF_4$ (59-41 mole %). By use of the same techniques these studies have been extended to include the behavior of $RbF\text{-}ZrF_4$ (60-40 mole %) as the solvent for these compounds.

The values given in Table 2.2.2 show that the solubility of NiF_2 at either 600 or 800°C is independent of the excess of solute present over the range tested. The solubilities of NiF_2 found in the $RbF\text{-}ZrF_4$ mixture are markedly lower at both 600 and 800°C than are the solubilities reported for any of the other solvents studied. The value of 0.2 wt % Ni^{++} at 800°C given in Table 2.2.2 is to be compared with the value of 1.0 wt % Ni^{++} previously given for the solubility in the $KF\text{-}ZrF_4$ mixture.

The data presented in Table 2.2.3 indicate that the solubility of FeF_2 at 600°C is independent of the excess of FeF_2 present, and at 800°C the excess FeF_2 has very little, if any, effect. The solubility of FeF_2 at 600°C in the $RbF\text{-}ZrF_4$ mixture with 1.0 wt % of Fe^{++} added approximates that found in $KF\text{-}ZrF_4$ (52-48 mole %), but it is greater than the solubility in $LiF\text{-}ZrF_4$ (52-48 mole %) and in $NaF\text{-}ZrF_4$ (53-47 mole %). The solubility of FeF_2 in the $RbF\text{-}ZrF_4$ mixture at 800°C is much smaller than that found in all the other solvents studied.

The ratio of Fe^{++} to total iron for the runs in which FeF_2 was added to the $RbF\text{-}ZrF_4$ mixture is significantly less than that previously reported for the other solvents studied. This would seem to indicate that FeF_2 is not completely stable toward disproportionation and that Fe^{++} and Fe^{+++} coexist in the $RbF\text{-}ZrF_4$ solvent. Data for the runs involving the FeF_3 additions indicate that a partial reduction of Fe^{+++} to Fe^{++} by the nickel container occurs. It is not certain that equilibrium was attained in these runs, and more complete

[1] C. M. Blood, *ANP Quar. Prog. Rep. June 10, 1956*, ORNL-2106, p 100; *ANP Quar. Prog. Rep. Sept. 10, 1956*, ORNL-2157, p 96.

[2] J. D. Redman, *ANP Quar. Prog. Rep. Dec. 10, 1955*, ORNL-2012, p 88; *ANP Quar. Prog. Rep. June 10, 1956*, ORNL-2106, p 101.

[3] J. D. Redman, *ANP Quar. Prog. Rep. Sept. 10, 1956*, ORNL-2157, p 100.

TABLE 2.2.1. EQUILIBRIUM RATIOS FOR THE REACTION

$$NiF_2(d) + H_2(g) \rightleftharpoons Ni(s) + 2HF(g)$$

Ni in Melt (ppm)	Pressure of H_2 (atm)	Pressure of HF (atm)	$K_x \times 10^{-4}$*
	Measurements Made at 625°C		
290	0.0316	0.597	2.3
270	0.0313	0.601	2.5
305	0.0303	0.614	2.4
280	0.0414	0.586	2.2
275	0.0321	0.590	2.3
220	0.0394	0.552	2.1
220	0.0396	0.550	2.0
290	0.0363	0.586	1.9
235	0.0381	0.566	2.1
190	0.0392	0.554	2.4
190	0.0395	0.551	2.4
195	0.0407	0.537	2.1
170	0.0426	0.515	2.1
190	0.0418	0.525	2.0
158	0.0421	0.521	2.4
190	0.0425	0.516	1.9
185	0.0428	0.513	2.0
140	0.0433	0.507	2.5
175	0.0436	0.496	2.0
155	0.0447	0.491	2.0
160	0.0449	0.489	2.0
145	0.0460	0.477	2.0
145	0.0465	0.471	1.9
100	0.0492	0.440	2.3
			Av 2.2 ± 0.2
	Measurements Made at 575°C		
150	0.0531	0.396	1.2
150	0.0543	0.382	1.1
150	0.0534	0.393	1.1
			Av 1.1

TABLE 2.2.1 (continued)

Ni in Melt (ppm)	Pressure of H_2 (atm)	Pressure of HF (atm)	$K_x \times 10^{-4}$*
	Measurements Made at 550°C		
265	0.0426	0.388	0.78
260	0.0424	0.391	0.81
250	0.0427	0.386	0.82
250	0.0438	0.370	0.73
240	0.0450	0.354	0.68
150	0.0480	0.311	0.79
160	0.0479	0.312	0.75
169	0.0478	0.313	0.75
165	0.0481	0.309	0.71
120	0.0499	0.283	0.79
105	0.0512	0.265	0.77
110	0.0516	0.259	0.69
			Av 0.76 ± 0.04

*$K_x = P^2_{HF}/X_{NiF_2}P_{H_2}$, where X is mole fraction and P is pressure in atmospheres.

TABLE 2.2.2. SOLUBILITY OF NiF_2 IN MOLTEN $RbF\text{-}ZrF_4$ (60-40 MOLE %) AT 600 AND AT 800°C

Conditions of Equilibrium		Total Ni Found in Filtrate (wt %)
Temperature (°C)	Ni^{++} (wt %)	
600	1	0.047
	1	0.047
	5	0.049
	5	0.050
800	5	0.22
	5	0.19
	10	0.22
	10	0.16

reduction might occur if the mixtures were heated for longer than 5 hr. No balance between the amounts of Fe^{++} and Ni^{++} found in the filtrates was to be expected because of the limited solubility of NiF_2 in this system.

The data given in Table 2.2.4 for CrF_2 are not sufficiently complete to establish what effect the excess of CrF_2 present may have on the solubility at either 600 or 800°C. The solubility at 800°C, which is in excess of 10 wt % Cr^{++}, is in line with the solubilities previously measured for the $KF\text{-}ZrF_4$, $LiF\text{-}ZrF_4$, and $NaF\text{-}ZrF_4$ mixtures. At 600°C with 5 wt % Cr^{++} added the solubility in the $RbF\text{-}ZrF_4$ mixture approximates that found in $NaF\text{-}ZrF_4$ (53-47 mole %), but it is considerably less than that obtained in the $KF\text{-}ZrF_4$, $LiF\text{-}ZrF_4$, and $NaF\text{-}ZrF_4$ (59-41 mole %) mixtures.

The data suggest that CrF_2 is less stable toward disproportionation in the $RbF\text{-}ZrF_4$ system than in any of the other solvents studied. The runs in which CrF_3 was added indicate that reduction of Cr^{+++} to Cr^{++} by the nickel container occurs but is rather far from complete. The data may represent equilibrium concentrations between Cr^0, Cr^{++}, and Cr^{+++}, but it also is possible that the reduction is incomplete after 5 hr because of a slow reduction rate.

TABLE 2.2.3. SOLUBILITY AND STABILITY OF FeF_2 AND FeF_3 IN MOLTEN $RbF\text{-}ZrF_4$ (60-40 MOLE %) AT 600 AND AT 800°C

Conditions of Equilibration			Found in Filtrate		
Temperature (°C)	Fe^{++} (wt %)	Fe^{+++} (wt %)	Fe^{++} (wt %)	Total Fe (wt %)	Total Ni (ppm)
600	1		0.75	0.96	120
	1		0.56	0.75	100
	5		0.72	0.93	125
	5		0.65	0.88	100
800	5		3.9	4.8	
	5		3.7	4.4	
	10		4.9	5.6	
	10		4.4	5.3	
600		1	0.59	0.74	600
		1	0.52	0.70	430
		5	0.72	0.92	840
		5	0.70	0.80	920
800		5	2.8	4.0	1840
		10	2.1	3.0	1820

REDUCTION OF UF_4 BY STRUCTURAL METALS

J. D. Redman

Further studies of the reduction of UF_4 by Cr^0 have been carried out in various reaction media by using a filtration method. The results obtained from earlier studies of this reaction with $NaF\text{-}ZrF_4$ (50-50 mole %,[4] 53-47 mole %,[5] 59-41 mole %[6]), $LiF\text{-}ZrF_4$ (52-48 mole %),[7] $KF\text{-}ZrF_4$ (52-48 mole %),[7] $NaF\text{-}LiF\text{-}ZrF_4$ (22-55-23 mole %),[8] NaF-LiF-KF (11.5-46.5-42 mole %),[9] or $LiF\text{-}BeF_2$ (48-52 mole %)[10] as the reaction medium were presented previously. Preliminary results obtained with $RbF\text{-}ZrF_4$ as the reaction medium were also given previously,[10] but more reliable data for this system are given in Table 2.2.5. Data also are presented (Table 2.2.6) for the interaction of UF_4 and Cr^0 in $LiF\text{-}BeF_2$ (48-52 mole %) at a UF_4 concentration considerably lower than that used previously.[10]

Data for the reaction of UF_4 with Cr^0 at 600 and at 800°C obtained with $RbF\text{-}ZrF_4$ (60-40 mole %) as the reaction medium are given in Table 2.2.5. In these runs approximately 2 g of Cr^0 was reacted with UF_4 (9.2 wt %, 4.0 mole %) dissolved in approximately 40 g of $RbF\text{-}ZrF_4$ mixture contained in nickel.

The chromium values given in Table 2.2.5 fall in the same range as those given previously.[10] However, the new values are more precise, and they demonstrate that the $UF_4\text{-}Cr^0$ reaction has a very

[4] J. D. Redman and C. F. Weaver, *ANP Quar. Prog. Rep. June 10, 1954*, ORNL-1729, p 50; *ANP Quar. Prog. Rep. Sept. 10, 1954*, ORNL-1771, p 60.

[5] J. D. Redman and C. F. Weaver, *ANP Quar. Prog. Rep. June 10, 1955*, ORNL-1896, p 60.

[6] J. D. Redman, *ANP Quar. Prog. Rep. March 10, 1956*, ORNL-2061, p 93.

[7] J. D. Redman, *ANP Quar. Prog. Rep. June 10, 1956*, ORNL-2106, p 94.

[8] J. D. Redman and C. F. Weaver, *ANP Quar. Prog. Rep. Sept. 10, 1955*, ORNL-1947, p 74.

[9] J. D. Redman and C. F. Weaver, *ANP Quar. Prog. Rep. March 10, 1955*, ORNL-1864, p 56.

[10] J. D. Redman, *ANP Quar. Prog. Rep. Sept. 10, 1956*, ORNL-2157, p 103.

TABLE 2.2.4. SOLUBILITY AND STABILITY OF CrF_2 AND CrF_3 IN MOLTEN $RbF\text{-}ZrF_4$ (60-40 MOLE %) AT 600 AND AT 800°C

Conditions of Equilibration			Found in Filtrate		
Temperature (°C)	Cr^{++} (wt %)	Cr^{+++} (wt %)	Cr^{++} (wt %)	Total Cr (wt %)	Total Ni (ppm)
600	1		0.56	1.02	110
	1		0.73	0.98	85
	5		1.3	1.7	70
	5		1.4	1.8	80
800	5		4.0	5.0	65
	5		4.1	5.1	65
	10		8.6	9.3	
	10		8.9	9.4	
600		1	0.38	0.69	200
		1	0.42	0.65	100
		5	0.38	0.65	185
		5	0.34	0.59	160
800		5	0.64	3.1	640
		5	0.65	3.1	410
		10	0.83	2.0	1050
		10	0.70	2.0	950
		10	0.86	2.4	1380
		10	0.80	2.5	890

small temperature coefficient in the temperature range studied. The equilibrium chromium concentrations given for this $RbF\text{-}ZrF_4$ mixture are considerably lower than those found in any of the other binary alkali fluoride–ZrF_4 mixtures examined, and they suggest that the fluoride ion activity is sufficiently large to reduce the activity of UF_4 quite effectively. It was postulated previously that the fluoride ion activity in the alkali fluoride–ZrF_4 mixture decreases in the order Rb, K, Na, Li.

The results given previously[10] for the reaction of UF_4 with Cr^0 in $LiF\text{-}BeF_2$ (48-52 mole %) were obtained with 1.5 mole % (11.5 wt %) UF_4 present. Data are presented in Table 2.2.6 for this system with only 0.074 mole % (0.7 wt %) UF_4 present. The other conditions of this study were comparable to the conditions of the earlier studies.

The results reported in Table 2.2.6 show that low equilibrium chromium concentrations prevail in this system if the original UF_4 concentration is low. The earlier studies with 1.5 mole % UF_4 gave chromium values of 930, 1300, and 2000 ppm, respectively, at 550, 650, and 800°C. It may be noted that the chromium blank found for this solvent is large, and, indeed, it approximates the chromium values measured in the runs with a low concentration of UF_4 present. However, visual observation of the solidified filtrates revealed rather extensive reduction of the UF_4. The solids were tan in color and sufficiently intense to mask the green color of any UF_4 present.

TABLE 2.2.5. DATA FOR THE REACTION OF UF_4 WITH Cr^0 IN MOLTEN $RbF\text{-}ZrF_4$ (60-40 MOLE %) AT 600 AND AT 800°C

Conditions of Equilibration		Present in Filtrate		
Temperature (°C)	Time (hr)	Total U (wt %)	Total Cr* (ppm)	Total Ni (ppm)
600	3	7.2	550	70
	3	6.9	630	70
	5	7.2	650	50
	5	7.1	680	65
800	3	7.2	550	85
	3	7.3	480	65
	5	7.3	650	55
	5	7.3	530	80

*Blank of 100 ppm of Cr at 800°C.

TABLE 2.2.6. DATA FOR THE REACTION OF UF_4 WITH Cr^0 IN MOLTEN $LiF\text{-}BeF_2$ (48-52 MOLE %)

Temperature of Equilibration (°C)	Present in Filtrate		
	Total U (wt %)	Total Cr* (ppm)	Total Ni (ppm)
550	0.57	420	115
	0.57	500	240
650	0.41	400	175
	0.55	530	180
800	0.54	470	160
	0.57	500	115

*Blank of 450 ppm of Cr at 800°C.

SOLUBILITY OF BaF_2 IN $NaF\text{-}ZrF_4$

W. T. Ward

Attempts have been made to determine the solubility of BaF_2 in molten $NaF\text{-}ZrF_4$ (50-50 mole %) as a function of temperature, since barium is an important fission product and it forms a relatively high-melting-point fluoride compound. The solubility of BaF_2 (16 wt % Ba at 560°C) is so high that no data on temperature dependence of its solubility has yet been obtained. This solubility is, of course, sufficient to preclude trouble from the deposition of fission-product barium in any practical system. It is possible, however, that much less soluble complex compounds of BaF_2 with other fission-product fluorides may be discovered.

SOLUBILITY OF LaF_3 AND OF CeF_3 IN MOLTEN FLUORIDE MIXTURES

W. T. Ward

The systematic investigation of the solubilities of LaF_3 and CeF_3 in molten fluorides of interest for aircraft reactor fuel was continued. Radioactive cerium and lanthanum and other radioactive tracers are being used in this study.

Determinations of solubility by filtration and chemical analysis are performed by techniques previously described.[11] All radiochemical determinations were performed, in general, by the technique described below.

An aqueous hydrochloric acid solution containing the radioactive element as the trichloride (10 mc of Ce^{141} in one case and the La^{140} separated from 3 mc of $Ba^{140}\text{-}La^{140}$ solution[12] in the other) was mixed with a similar solution containing about 60 g of the appropriate inert element as the trichloride. The rare earth was precipitated as the trifluoride, and the precipitate was washed, centrifuged, and dried. These labeled precipitates formed the master batches from which all experiments were run. Calibration curves were prepared by counting samples made by mixing, in 10 × 75 mm test tubes, weighed amounts of the labeled rare earths with 1 g of finely powdered $NaF\text{-}ZrF_4\text{-}UF_4$ mixture. The deviation of individual samples from the standard plot of counting rate vs quantity of rare earth added was about 1%. The standards were retained and were recounted along with samples obtained from the solubility experiments.

CeF_3 in $NaF\text{-}ZrF_4\text{-}UF_4$

The use of inert CeF_3, along with chemical determination of the cerium content of the filtrate obtained, yielded the results shown in Table 2.2.7. In these experiments, the CeF_3 content of the filtrates was obtained by redox titration. The values obtained clearly indicate that the solubility of the CeF_3 is independent of the quantity added.

[11] W. T. Ward, *ANP Quar. Prog. Rep. Sept. 10, 1956*, ORNL-2157, p 110.

[12] R. E. Druschel, "Strontium Activity and/or Barium Activity in Aqueous or Organic Solutions," Methods Nos. 2 21082 and 2 21801 (March 3, 1954) in *ORNL Master Analytical Manual*.

TABLE 2.2.7. CHEMICAL DETERMINATION OF SOLUBILITY OF CeF_3 IN $NaF-ZrF_4-UF_4$ (50-46-4 MOLE %)

CeF_3 Added (wt % Ce)	Filtration Temperature (°C)	Ce Found in Filtrate (wt %)
5	798	4.6
	710	3.1
	612	2.2
	552	1.6
>10	810	4.2
	707	3.3
	615	2.0
	556	1.9
>20	808	4.2
	700	2.8
	605	1.9
	547	1.6

This observation, along with petrographic and x-ray examination of the residues and filtrates, shows conclusively that CeF_3 crystallizes from such melts as the simple fluoride.

Solubility values obtained by adding 55 g of labeled CeF_3 to 936 g of the $NaF-ZrF_4-UF_4$ mixture, equilibrating the mixture at the proper temperature, filtering, and counting samples of the filtrate are presented in Table 2.2.8 below. These radiochemical values are believed to be more accurate than the substantially lower values obtained by chemical analysis.

LaF_3 in $NaF-KF-LiF-UF_4$ and in $NaF-ZrF_4-UF_4$

The data obtained for the solubility of LaF_3 in $NaF-KF-LiF-UF_4$ (11.2-41-45.3-2.5 mole %) at temperatures in the interval 525 to 800°C are presented in Table 2.2.9. It is obvious that the solubility of LaF_3 (and presumably of all the rare-earth fluorides) is very high in this fluoride fuel mixture.

Data obtained for solubility of LaF_3 in $NaF-ZrF_4-UF_4$ (50-46-4 mole %) by chemical analysis of filtrates are presented in Table 2.2.10. In this case the analysis was performed by oxalate precipitation. Within the fair precision of the analysis it appears that the solubility of LaF_3 is independent of quantity added. As in the case of CeF_3 there is no doubt that the saturating phase is the simple trifluoride.

TABLE 2.2.8. RADIOCHEMICAL DETERMINATION OF SOLUBILITY OF CeF_3 IN $NaF-ZrF_4-UF_4$ (50-46-4 MOLE %)

Filtration Temperature (°C)	Ce Found in Filtrate (wt %)
700	3.60
600	2.80
550	2.47

TABLE 2.2.9. CHEMICAL DETERMINATION OF SOLUBILITY OF LaF_3 IN $NaF-KF-LiF-UF_4$ (11.2-41-45.3-2.5 MOLE %)

LaF_3 Added (wt % La)	Filtration Temperature (°C)	La Found in Filtrate (wt %)
10	803	10.5
	707	10.6
	603	10.3
	533	10.4
>20	813	20.9
	703	22.1
	608	21.4
	532	22.3
>30	808	33.5
	705	33.4
	606	31.4
	540	22.9

The use of 5.4 wt % labeled LaF_3, along with subsequent counting of the filtrates, yielded the data shown in Table 2.2.11. These values, which agree rather well with those determined chemically, are considered to be the most precise values available.

PARTITION OF CeF_3 BETWEEN $NaF-ZrF_4-UF_4$ AND $LaF_3(CeF_3)$ SOLID SOLUTION

W. T. Ward

As the preceding discussion has shown, both LaF_3 and CeF_3 are sparingly soluble in the $NaF-ZrF_4-UF_4$ (50-46-4 mole %) fuel mixture, and each crystallizes from the melt as the simple trifluoride. Moreover, the solubilities of the two compounds

TABLE 2.2.10. CHEMICAL DETERMINATION OF SOLUBILITY OF LaF_3 IN NaF-ZrF_4-UF_4 (50-46-4 MOLE %)

LaF_3 Added (wt % La)	Filtration Temperature (°C)	La Found in Filtrate (wt %)
5	802	5.0
	703	3.6
	606	2.6
	555	3.3
10	804	5.1
	708	3.5
	610	2.7
	560	2.6
15	810	5.4
	705	3.2
	608	2.5
	550	2.1

TABLE 2.2.11. RADIOCHEMICAL DETERMINATION OF SOLUBILITY OF LaF_3 IN NaF-ZrF_4-UF_4 (50-46-4 MOLE %)

Filtration Temperature (°C)	La Found in Filtrate (wt %)
808	4.67
718	3.23
613	2.40
553	2.16

are very similar. In addition, CeF_3 and LaF_3 apparently form a continuous series of solid solutions. It is anticipated that all rare-earth trifluorides and yttrium trifluoride will show these similarities in behavior.

It should be possible therefore to remove fission-product rare-earth fluorides from a contaminated NaF-ZrF_4-UF_4 mixture to any desired degree by repeated addition of CeF_3 (for example), heating to dissolve the added CeF_3, cooling to crystallize the resulting CeF_3-rich solid solution, and filtering to remove the liquid. The "purified" fuel would, of course, be saturated with CeF_3 (with traces of all other rare-earth fluorides) at the filtration temperature; however, since this temperature could be safely below the lowest temperature in the operating cycle and since cerium has a low cross section for thermal neutrons, such a method might be very promising.

Experiments have conclusively demonstrated that the concentration of labeled CeF_3 in NaF-ZrF_4-UF_4 solution can be effectively lowered by the addition of LaF_3. In these experiments labeled CeF_3 (3.9 wt % Ce) was added to a purified batch of NaF-ZrF_4-UF_4, and the solubility of CeF_3 was obtained at various temperatures (see preceding discussion). Then, 6 wt % inert LaF_3 was added to the system, and, after equilibration, filtrates were obtained at 800, 700, 600, and 550°C. The CeF_3 content of the filtrate was determined by counting the activity of samples from each filtrate. The process was subsequently repeated after the addition of LaF_3 to a total of 11 wt % La. The values obtained for the concentration of CeF_3 in the melt are shown in Fig. 2.2.1.

It may be observed that the addition of 6 wt % LaF_3 to the system decreased the cerium concentration in the solution at 550°C by a factor of about 3 from its saturation value. Removal of the liquid phase from this solid and repetition of the process would, presumably, effect repeated lowering of the CeF_3 concentration.

For the simple case of partition of a material such as CeF_3 between two immiscible phases the equilibrium could be expressed as

$$MF_3(d) \rightleftharpoons MF_3(ss)$$

where the notations (d) and (ss) refer to dissolved MF_3 and to MF_3 in solid solution, respectively. When equilibrium is reached for such a system,

$$a_{MF_3(d)} = a_{MF_3(ss)} = N_{MF_3(d)} \cdot \gamma_{MF_3(d)} = N_{MF_3(ss)} \cdot \gamma_{MF_3(ss)} ,$$

where a refers to activity, N to mole fraction, and γ to activity coefficient of the species in the phases designated. If it can be assumed that the activity coefficient for the material in a specified phase is independent of the concentration in that phase, then

$$\frac{N_{MF_3(d)}}{N_{MF_3(ss)}} = K_{MF_3} ,$$

where K is the solubility of pure MF_3 in the liquid

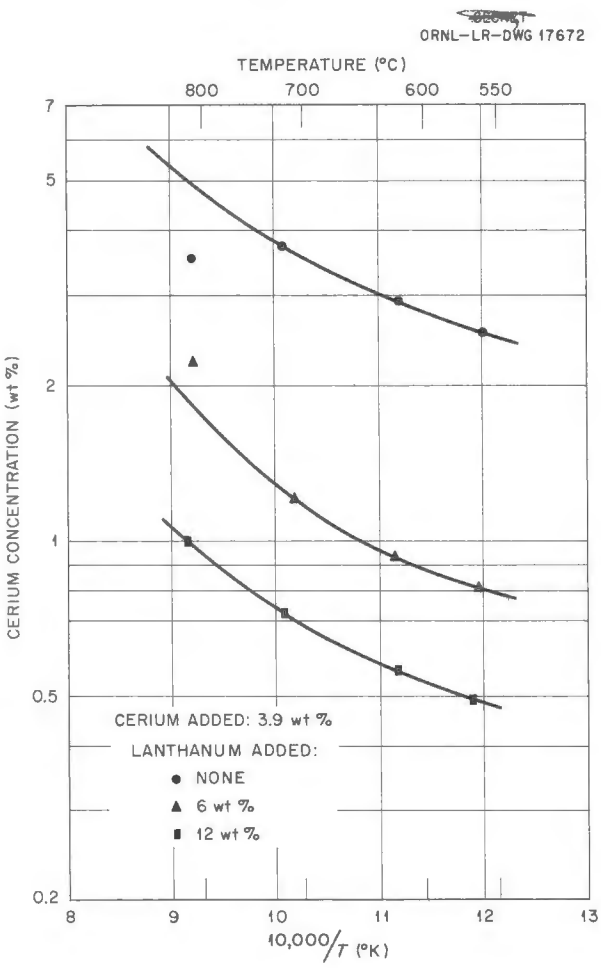

Fig. 2.2.1. Effect of Addition of LaF_3 on Concentration of CeF_3 in Solution in the Fuel Mixture $NaF\text{-}ZrF_4\text{-}UF_4$.

phase. For materials as similar as the fluorides of two consecutive rare earths this assumption seems not too unreasonable.

If the equilibrium between two rare-earth fluorides, CeF_3 and LaF_3, partitioned jointly between $NaF\text{-}ZrF_4\text{-}UF_4$ and their solid solution is considered, the reaction is

$$CeF_3(d) + LaF_3(ss) \rightleftharpoons LaF_3(d) + CeF_3(ss)$$

For this reaction at equilibrium

$$K_a = \frac{a_{CeF_3(ss)} \cdot a_{LaF_3(d)}}{a_{CeF_3(d)} \cdot a_{LaF_3(ss)}} = 1 .$$

If the same assumption as to constancy of γ with concentration is made, then

$$\frac{N_{CeF_3(ss)} \cdot N_{LaF_3(d)}}{N_{CeF_3(d)} \cdot N_{LaF_3(ss)}} = K_N = \frac{K_{LaF_3}}{K_{CeF_3}} .$$

The equilibrium constant for this reaction should, accordingly, be the ratio of the partition coefficients or the ratio of the solubilities of the pure rare earths. Since these solubilities are expected to be very similar, K_N should be nearly unity.

The partition coefficients and equilibrium constants calculated from the data plotted in Fig. 2.2.1 are given in Table 2.2.12. For purposes of this calculation it was assumed that the liquidus curve on the ternary phase diagram (LaF_3, CeF_3, $NaF\text{-}ZrF_4\text{-}UF_4$) was the straight line joining the solubilities of the pure rare-earth fluorides. From this assumption, along with the measured concentration of CeF_3 in the liquid and the known quantities of CeF_3 and LaF_3 in the system, the distribution of both trifluorides in both phases can be evaluated.

The data in Table 2.2.12 indicate that the distribution of CeF_3 and LaF_3 in systems containing both species follows, very well, the relationship

$$\frac{N_{MF_3(d)}}{N_{MF_3(ss)}} = K_{MF_3}$$

at each temperature studied. This finding and the constancy of K_N over the range studied strongly indicate that the system behaves predictably. Much additional work will be necessary to show that the technique is valuable for removing all rare earths, but the method seems to be very promising.

If such a partition of fission products is possible, it would be economical to accomplish the partition in a constant-temperature process, perhaps, by pouring the molten fluoride through a packed tower of the rare-earth fluoride at 550°C. To test whether such a scheme might be possible, a test was run to study the rate of exchange between labeled CeF_3 in $NaF\text{-}ZrF_4\text{-}UF_4$ solution and solid LaF_3. The data presented in Table 2.2.13 were obtained by adding 6 wt % LaF_3 to a solution containing 2.5 wt % cerium at 560°C, stirring the system by sparging with helium, and drawing samples through

TABLE 2.2.12. PHASE COMPOSITIONS AND EQUILIBRIUM CONSTANTS FOR PARTITION OF CeF_3 BETWEEN $NaF\text{-}ZrF_4\text{-}UF_4$ (50-46-4 MOLE %) SOLUTION AND LaF_3 SOLID SOLUTION

Total Composition (mole %)		Solid Phase Composition (mole %)		Temperature (°C)	Liquid Phase Composition (mole %)		Partition Coefficients		Equilibrium Quotients
CeF_3	LaF_3	CeF_3	LaF_3		CeF_3	LaF_3	$\left(\frac{N_{CeF_3(d)}}{N_{CeF_3(ss)}}\right)$	$\left(\frac{N_{LaF_3(d)}}{N_{LaF_3(ss)}}\right)$	$\left(\frac{N_{CeF_3(ss)}\,N_{LaF_3(d)}}{N_{CeF_3(d)}\,N_{LaF_3(ss)}}\right)$
3.3	0	100	0	700	2.9	0	0.029		
				600	2.2	0	0.022		
				550	1.9	0	0.019		
3.2	5.2	37.4	62.6	700	1.1	1.6	0.029	0.026	0.9
				600	0.8	1.2	0.021	0.019	0.9
				550	0.7	1.0	0.019	0.016	0.9
3.0	11.1	20.8	79.2	700	0.6	2.1	0.029	0.027	0.9
				600	0.45	1.55	0.022	0.020	0.9
				550	0.4	1.3	0.019	0.016	0.9
0	4	0	100	700	0	2.5		0.025	
				600	0	1.9		0.019	
				550	0	1.6		0.016	

TABLE 2.2.13. RATE OF EXCHANGE BETWEEN CeF_3 AND LaF_3 AT 560°C

Initial cerium concentration: 2.54 wt %

Time at Temperature (hr)	Cerium Found (wt %)
1.3	1.23
3.3	1.14
6.0	1.05
22.5	0.86
At equilibrium*	0.81

*Obtained by heating to a high temperature, cooling to 560°C, and filtering.

a filter at predetermined intervals. From the data it is apparent that the exchange rate is reasonably rapid even at 560°C and with relatively poor agitation. However, it is likely that diffusion in the solid solution is the slow step, and better contact would not greatly increase the rate. It still seems possible that the constant-temperature process may be successful. Additional studies of this system will be made as time permits.

SOLUBILITY OF HELIUM IN NaF-ZrF_4-UF_4

N. V. Smith

If xenon can be efficiently and continuously removed from the circulating-fuel system and kept at a few per cent of its equilibrium value (about 10^{-8} mole of xenon per cubic centimeter of fuel for the 60-Mw ART) important perturbations in reactivity can be avoided. If such efficient removal can be accomplished easily and with a minimum of equipment, important simplifications in the complex ART pump could perhaps be effected. One of the more important factors in the case of xenon removal is, of course, the absolute solubility of xenon in the molten fluoride system.

No information regarding solubility of gases in molten salts is available in the open literature. Preliminary values have been given[13] for the solubility of xenon in the KNO_3-$NaNO_3$ eutectic and in the NaF-KF-LiF eutectic. Xenon dissolves in the nitrate melt to the extent of 8.5×10^{-8} and 7×10^{-8} mole/cm^3 at 280 and 360°C, respectively. In the NaF-KF-LiF melt at 600°C a xenon solubility value of 10^{-7} mole/cm^3 was found. Subsequent experiments[14] indicated, however, that this figure was too high by perhaps as much as a factor of 10. The value suggested is of the order of 10^{-8} mole of xenon per cubic centimeter of melt, but there is considerable uncertainty in the determination.

Since the need for a more accurate value has become increasingly important, the present investigation was undertaken. The method being utilized for the determination involves saturating the melt with the desired gas in one section of the apparatus, transferring the melt by melting a frozen seal to another section of the equipment, stripping the dissolved gas by flushing with a known volume of a second gas in a closed system, and determining the relative concentrations of the two gases by using a mass spectrometer. Portions of the equipment are, in principle, similar to equipment employed in the previous study.[13] In order to test the equipment with a cheap and readily obtainable material that could be easily determined by analyses, the preliminary studies were made with helium as the saturating gas.

The experimental assembly is shown in Fig. 2.2.2, and a flowsheet of the system is shown in Fig. 2.2.3. The apparatus may be described in terms of several more or less independent units which serve different purposes during the operation. The units of the apparatus may be broadly described as the gas purification train, the solution-preparation assembly, the molten salt–gas saturator, and the molten-salt-stripping and gas-circulation assembly. Through a suitable system of valves any or all the units may be interconnected with one another or with a high-vacuum system.

The purpose of the gas purification train is to eliminate, by distillation, the helium impurities present in argon or in any other heavier noble gas used. Ideas for the construction of this unit were adapted from methods described elsewhere.[15–17] In the solution-preparation assembly, standard solutions of helium in argon are prepared in order to have a continuous check on the accuracy and precision of the analytical results.

[13] R. F. Newton and D. G. Hill, *ANP Quar. Prog. Rep. Sept. 10, 1954*, ORNL-1771, p 70.

[14] R. F. Newton, *ANP Quar. Prog. Rep. Sept. 10, 1955*, ORNL-1947, p 85.

[15] R. T. Sanderson, *Vacuum Manipulation of Volatile Compounds*, Wiley, New York, 1948.

[16] S. Dushman, *Scientific Foundations of Vacuum Technique*, Wiley, New York, 1949.

[17] R. B. Evans with G. M. Watson, *Compressibility Factors of Gaseous Nitrogen-n-Butane Mixtures*, Chemical and Engineering Data Series, Vol. I (in press).

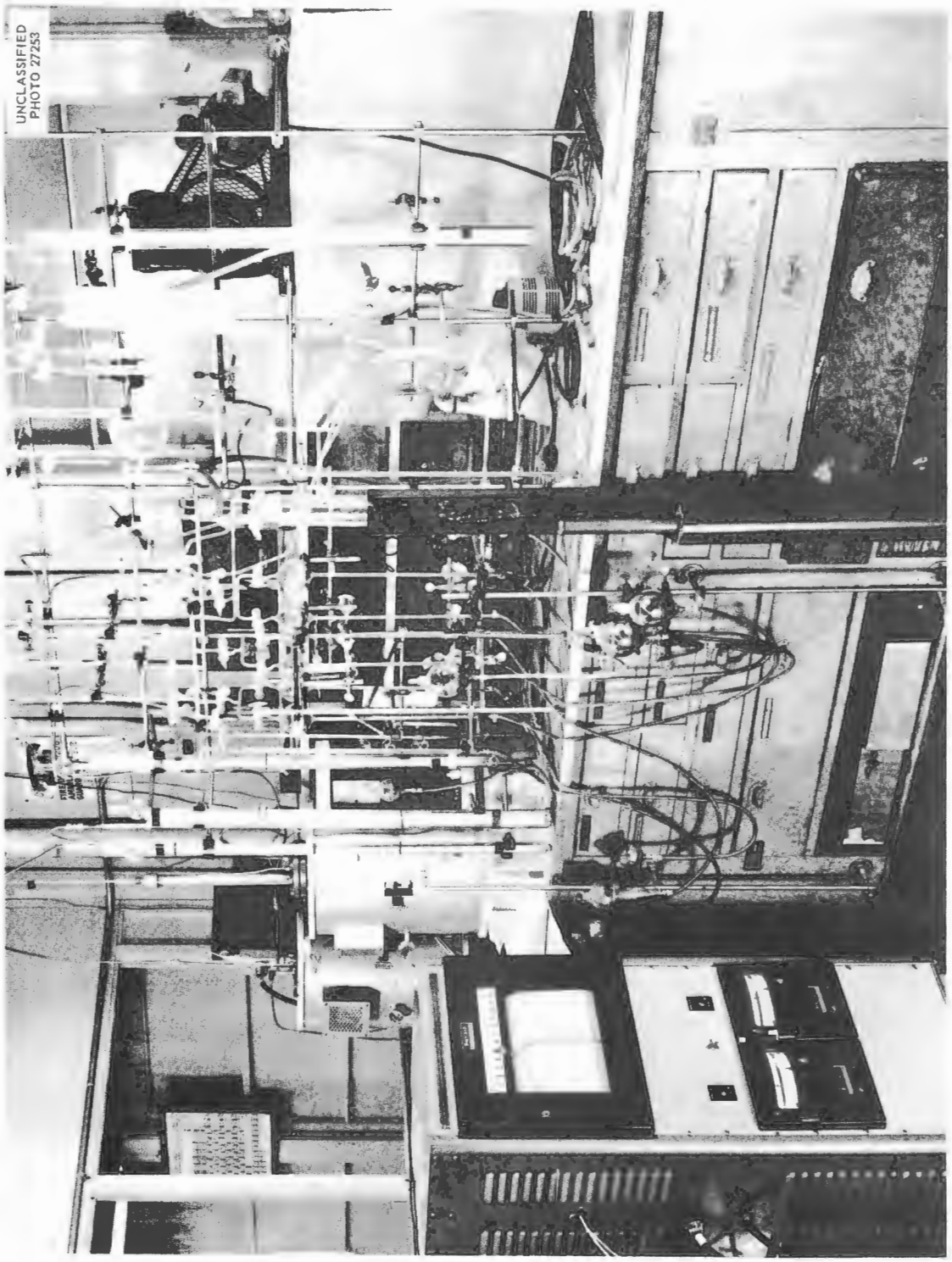

Fig. 2.2.2. Experimental Assembly for Determining the Solubility of Helium in Fused Salt Mixtures. (Confidential with caption)

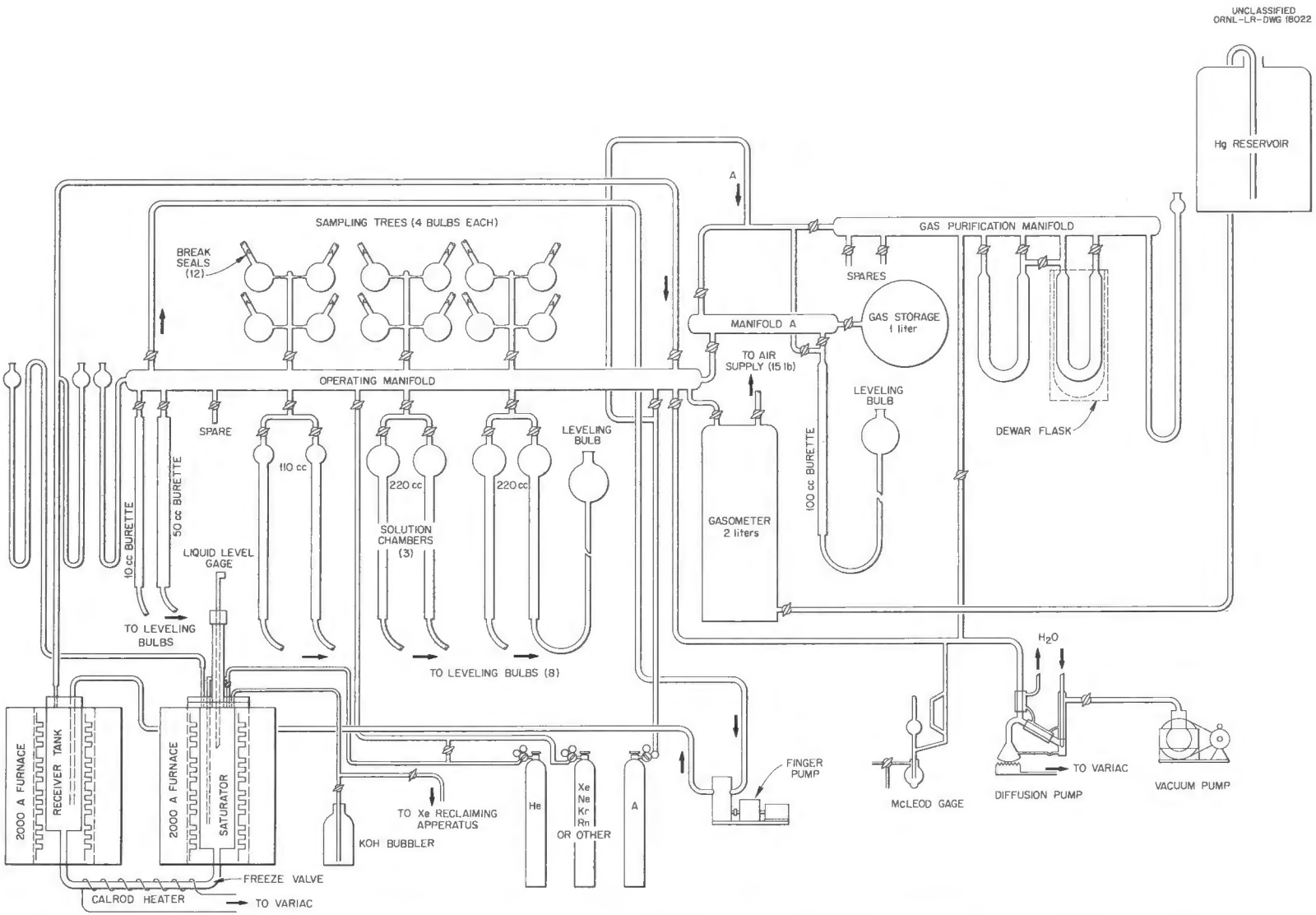

Fig. 2.2.3. Flowsheet for Apparatus for Determining the Solubility of Gases in Fused Salt Mixtures. ~~(Confidential with caption)~~

The molten salt–gas saturator system consists of a nickel container to hold the salt mixture and a freeze valve through the bottom of the container. The freeze valve, constructed of $\frac{3}{8}$-in.-wall nickel tubing, leads to a nickel receiver vessel which is part of the stripping assembly. Liquid-gas contact is attained by bubbling the gas through a dip leg. In order to prevent bubble entrainment, the dip leg delivers the gas 6 in. above the bottom of the container. The saturating pressure is regulated through inlet and outlet valves, and the pressure is measured directly by a mercury U-tube connected to the top of the saturator.

The molten-salt-stripping and gas-circulation unit consists of the nickel receiver, mentioned above, which is connected to the saturator through a freeze valve. In addition the receiver is fitted with a manometer, an outlet, and an inlet provided with a dip leg that extends to $\frac{1}{8}$ in. from the bottom. The inlet and outlet are part of a closed gas circuit, which includes a gas manifold and a finger pump. The gas manifold is made of glass tubing. Gas sampling bulbs are sealed to the manifold before each experiment. A gasometer, a gas burette, and a gas receiver may be tied into the manifold through the necessary valves. With this arrangement, it is possible to introduce accurately measured volumes of argon into the stripping section at any desired pressure.

For a typical solubility determination approximately 10 kg of salt mixture is placed in the saturating chamber, melted, and brought to temperature under continuous helium sparging. The saturating pressure can be adjusted from the start of the initial heating period. Sparging is continued for extended periods of time (about 20 hr) in an effort to saturate the liquid completely. Toward the end of the saturation period, the stripping section is evacuated, after the receiver has been brought to temperature. A carefully measured volume of argon is then introduced into the stripping section under a predetermined pressure. The value of the pressure used depends on the saturating pressure and is adjusted so that a volume displacement of about 1000 cm^3 causes the stripping section pressure to increase to the value of the saturating pressure. After the volume of argon has been measured, the gas-circulating pump is started, and the power is turned on through a Calrod heater in contact with the freeze valve. While the freeze valve is being melted, the gas sparging is discontinued so that the pressure can be kept constant by merely bypassing the dip leg. This procedure reduces the danger of bubble entrainment during transfer.

After the plug in the freeze valve has melted, the fused salt is transferred to the receiver by pressurizing the melt. The helium pressure on top of the melt is kept constant during transfer. As soon as the receiver pressure becomes essentially equal to the saturator pressure, the power is cut off from the transfer line, and the freeze plug is restored by cooling the valve with cold water. The melt in the receiver is stripped with argon, and the resulting helium-argon mixture is sampled at different times. The samples are analyzed by using a mass spectrometer. The volume of melt transferred is determined in three different ways – by weighing the receiver before and after the experiment, by measuring the melt level before and after transfer, and by weighing the salt recovered from the receiver. The results usually agree to within 50 cm^3. The sensitivity of the mass spectrometer is determined directly for each determination by analyzing standard solutions of the helium-argon mixture along with the unknowns. To avoid human bias, no information as to concentration of the standards or even as to which of a given set of samples are standards is given to the mass spectrometer operators. A summary of the experimental results obtained thus far is given in Table 2.2.14, and the results are plotted in Fig. 2.2.4.

The results given in Table 2.2.14 appear to correlate satisfactorily. Two of the values obtained at 700°C appear to be low relative to the other values. It is felt that the cause of the deviations may be either imperfect temperature control toward the end of these two experiments or analytical variations. Steps have been taken to increase the precision of the determinations.

It was somewhat surprising to observe that the solubility of helium increased with increasing temperature. This aspect of the investigation invites a correlation of melt composition, inert gas atom size, and postulated liquid structures; however, in the absence of a sizable body of experimental data, this discussion must be delayed. It has been observed that the solubility of helium in this solvent obeys Henry's law over the experimental range studied. The Henry's law constants obtained, in moles of helium per cubic centimeter of melt per atmosphere, were 3.9×10^{-7}, 2.7×10^{-7}, and 1.9×10^{-7} at 800, 700, and 600°C, respectively.

TABLE 2.2.14. SOLUBILITY OF HELIUM IN $NaF-ZrF_4-UF_4$ (50-46-4 MOLE %)

Temperature (°C)	Stripping Volume of Argon (cm^3 STP)	Stripping Gas Found (% He)	Helium Dissolved (mmoles)	Melt Transferred (g)	Melt Transferred (cm^3)	Helium Solubility (moles × 10^{-7} of He per cm^3 of melt)	Saturating Helium Pressure (atm)
600	785	0.95	0.34	4400	1300	2.6	1.42
	963	1.29	0.56	4900	1450	3.9	1.98
	555	0.80	0.20	3450	1024	2.0	1.01
	405	0.50	0.09	2900	861	1.0	0.45
	575	0.81	0.21	3786	1123	1.9	0.97
700	877	1.80	0.72	5040	1537	4.7	2.02
	510	1.11	0.25	3928	1198	2.1	0.97
	587	2.41	0.64	5294	1571	4.1	1.50
800	855	2.93	1.15	4850	1520	7.6	2.00
	565	1.99	0.51	3775	1183	4.3	0.99

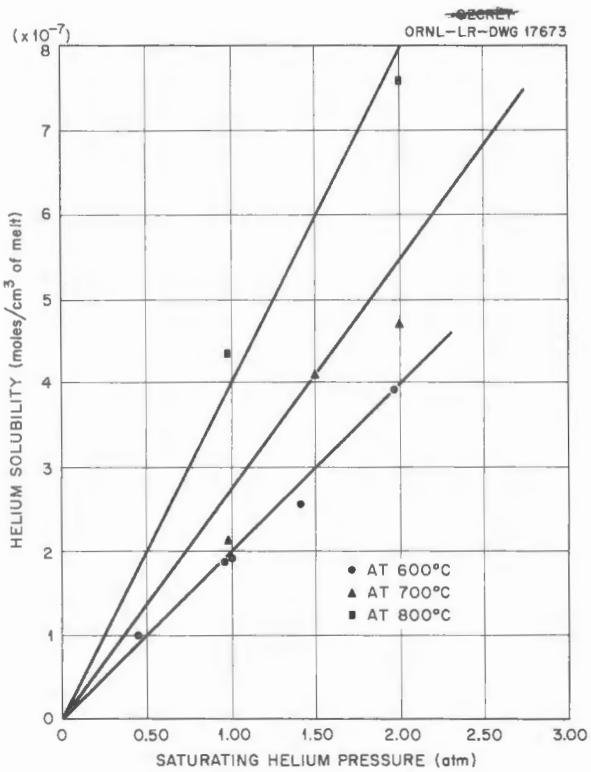

Fig. 2.2.4. Solubility of Helium in Molten $NaF-ZrF_4-UF_4$ (50-46-4 mole %) at Various Temperatures and Pressures.

NICKEL MASS TRANSFER IN $NaF-ZrF_4$

J. G. Eversole C. M. Blood

After the completion of several experiments designed to test the stability of NiF_2 in molten $NaF-ZrF_4$ (53-47 mole %), some large metallic nickel crystals were observed plated on the walls of the nickel containers, as shown in Fig. 2.2.5. During the course of the experiments, the salt mixtures which had been contaminated with approximately 3000 ppm of nickel as nickel fluoride were kept for several days at 800°C under continuous helium sparging. Examination of the nickel dip leg used during the sparging revealed that a considerable portion of the nickel metal had vanished from the tip. A new and a used dip leg are shown side by side in Fig. 2.2.6. The location of the dip-leg tip and the location of the nickel deposit indicate that nickel metal was transferred from a lower temperature region to a higher temperature region. In order to obtain some quantitative information regarding the temperature gradient with respect to nickel mass transfer in this system, the experiment was repeated.

In the second experiment an extra thermocouple well was welded to the nickel liner throughout the entire length of the container, and the usual thermocouple well was extended to the bottom of the liner without touching the walls. One kilogram

of $NaF\text{-}ZrF_4$ (53-47 mole %) contaminated with 2600 ppm of Ni as NiF_2 was then enclosed in the liner and was maintained at a temperature of 800°C for seven days under continuous helium sparging. Purified helium was used, and all the effluent gas was monitored for total liberation of HF from any impurities in the system. At intervals the temperature gradients along the wall and in the melt were determined. One filtrate sample of the melt was obtained at the beginning of the experiment, and two samples were obtained at the end. After one week the assembly was cooled, and the contents were examined. The usual amount of nickel mass transfer from the tip of the dip leg and from the center thermocouple well to the liner wall was found, as shown in Fig. 2.2.7. Some of the experimental data obtained are presented in Tables 2.2.15 and 2.2.16. The data indicate that nickel metal was transferred from the lower temperature regions of the assembly to the higher temperature regions.

Fig. 2.2.5. Nickel Crystals That Plated on the Walls of the Nickel Container During Experiments for Determining the Stability of NiF_2 in Molten $NaF\text{-}ZrF_4$. (Confidential with caption)

In an effort to determine whether NiF_2 is a necessary intermediate for nickel mass transfer in this system, the experiment was repeated with a solvent essentially free of NiF_2. The assembly and the melt were, in addition, purified *in situ* by hydrogen sparging prior to helium sparging. The system was then sparged with helium for seven days, and the temperature gradients observed were similar to those given in Table 2.2.16. At the conclusion of the experiment the melt was sampled and found to contain only 20 ppm nickel. Examination of the liner walls revealed no mass transfer, as shown in Fig. 2.2.8. On the basis of the results of this second experiment, it is concluded that NiF_2 is a necessary intermediate for nickel mass transfer.

The mass transfer mechanism may be explained by the postulation of a subfluoride which forms in the cooler regions and disproportionates in the

TABLE 2.2.15. MATERIAL BALANCE FOR NICKEL MASS TRANSFER EXPERIMENT

Initial charge: 1 kg $NaF\text{-}ZrF_4$ (53-47 mole %) with 2600 ppm Ni added as NiF_2

HF liberated: 13.5 meq in 689 liters of He

NiF_2 unaccounted for: 51.2 meq

Filtrate Sample Number	Time at Temperature (hr)	Found in Filtrate (ppm)		
		Ni	Fe	Cr
1	2	2485	220	25
2	168	900	255	25
3	169	905	210	25

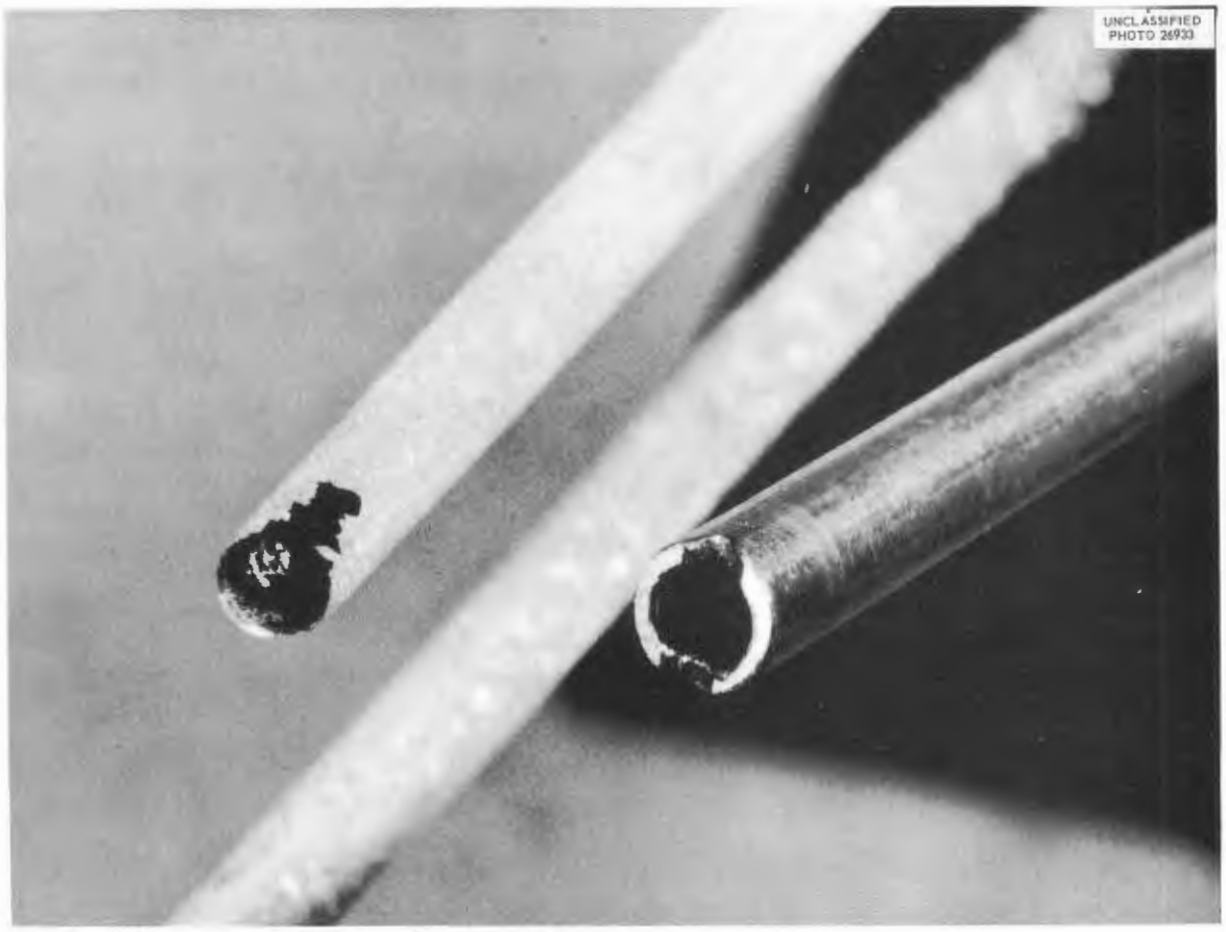

Fig. 2.2.6. An Unused Nickel Dip Leg and a Similar Dip Leg After Use in Experiments for Determining the Stability of NiF_2 in Molten $NaF\text{-}ZrF_4$. ~~(Confidential with caption)~~

hotter regions, as follows:

$$\text{Ni (wall)} + NiF_2 \underset{\text{Hotter}}{\overset{\text{Cooler}}{\rightleftharpoons}} 2\ NiF$$

There are a number of alternative explanations which may be just as plausible as the postulation of the unstable subhalide, and a very considerable amount of experimental work would be required to provide a basis for a reasonable choice among the postulated mechanisms. At present, however, no additional experiments are planned.

COLORS OF CORROSION PRODUCTS IN FUSED FLUORIDE SALTS

L. E. Topol

Most emf measurements of molten fluorides have been made by using a helium atmosphere furnace with a viewing port, and it was therefore relatively easy to make a survey of the colors displayed by various solutes in the half cells. The objective of the survey was to assess the prospects for a spectrophotometric study of the corrosion reaction participants. The results of the color survey appear in Table 2.2.17.

TABLE 2.2.16. TEMPERATURE GRADIENTS EXISTING DURING NICKEL MASS TRANSFER EXPERIMENT

Initial depth of melt: $7\frac{3}{4}$ in.

Final depth of melt after removal of three samples: $6\frac{1}{4}$ in.

Position of nickel crystals observed: $6\frac{1}{4}$ to $7\frac{3}{4}$ in. from bottom

Weight of nickel transferred: Approximately 8 g (4 g from lower end of dip leg and 4 g from thermocouple well)

Distance from Bottom of Nickel Liner (in.)	Wall Temperature (°C)	Melt Temperature (°C)
0	795	800
1	800	802
2	800	801
3	801	801
4	802	801
5	804	800
6	806	801
7	808	806
8	826	819

The equilibration interval varied with the solute, but it was usually 1 to 2 hr at 600°C. Trouble with scum formation was encountered, particularly with the $NaF\text{-}ZrF_4$ melts, but skimming usually permitted a good view of the melt color. Some of the earlier observations were made in ½-in. nickel crucibles of the type used for half cells, but better color distinctions were possible with dilute solution in the 30- to 50-ml crucibles which were usually used.

The color of a solute is attributed to the electronic configuration of the metal ion, and a change in color for the same valence state can be interpreted as a change in the complexing of the ion. The data of Table 2.2.17 show that NiF_2 is yellow in the alkali fluoride eutectic. This was not expected because FeF_2 and CrF_2 form a blue solution in this melt and, also, because both NiF_2 and $NiCl_2$ are blue in alkali chlorides. However, NiF_2 gives an orange solution in $NaNO_3$, which presumably represents an intermediate state between the yellow and red NiF_2 solutions reported in Table 2.2.17. Some attempts were made

Fig. 2.2.7. Nickel Mass-Transferred Crystals on Nickel Container That Was Exposed to $NaF\text{-}ZrF_4$ Containing Added NiF_2 for One Week at 800°C Under Continuous Helium Sparging. [redacted]

Fig. 2.2.8. Nickel Liner Exposed to NiF_2-Free $NaF\text{-}ZrF_4$ for One Week at 800°C Under Continuous Helium Sparging. Note absence of mass-transferred crystals. [redacted]

to change the color of the NiF_2 in the alkali fluoride eutectic from yellow to red by adding ZrF_4 and also to carry out the reverse color change by adding the eutectic, but the experimental conditions so restricted the amount of additive that no significant color changes were obtained.

It was interesting to note that the disproportionation of CrF_2 in the alkali fluoride eutectic could be followed visually by the blue to green color change indicated in the last entry of Table 2.2.17. No such behavior could be noted for FeF_2. The color changes confirm the conclusion reached

TABLE 2.2.17. COLORS OF CORROSION PRODUCTS IN FUSED FLUORIDE SALTS

Solvents: 1. $NaF-ZrF_4$ (53-47 mole %)
2. NaF-KF-LiF (11.5-42-46.5 mole %)

Corrosion Product Solute	Solvent	Crucible	Color
NiF_2	1	Nickel	Reddish or wine
	2	Nickel	Yellow
FeF_2	1	Nickel	Colorless
	2	Nickel	Blue
CrF_2	1	Nickel	Blue or blue-green
	2	Nickel	Blue
CuF_2	1	Nickel	Orange or copper colored (possibly result of reaction with Ni)
	1	Alumina	Blue-green (some dark material formed)
	2	Nickel	Muddy brown (result questionable)
	2	Alumina	Yellow-orange that turned to brown upon further addition of CuF_2
UF_4	1, 2	Nickel	Green
LaF_3	1, 2	Nickel	Colorless
FeF_3	1	Alumina	Yellow that turned to dark brown or black with further additions of FeF_3
	2	Nickel	Light green
	1	Nickel	Orange (possibly result of reaction with Ni)
CrF_3	1	Alumina	Brown
	2	Nickel	Green
$UF_4 + U^0$	1, 2	Nickel	Wine or red from UF_3
U^0	1, 2	Nickel	Wine or red from UF_3
CrF_2 (dilute)	2	Nickel	Blue that turned to green (CrF_3) upon standing overnight

earlier[18] that trivalent Fe and Cr are stable in the alkali fluoride eutectic but are reduced by Ni^0 in the $NaF\text{-}ZrF_4$ mixture. The trivalent salts were observed to be less soluble than the divalent salts in the $NaF\text{-}ZrF_4$ mixtures but to have appreciable solubility in the alkali fluoride eutectic. The CuF_2 solutions appeared to be reduced by Ni^0 in both solvents, and the solubility of CuF_2 seemed greater in the $NaF\text{-}ZrF_4$ melt than in the alkali fluoride eutectic.

The field for spectrophotometric studies of complexing and of the reaction mechanism is shown by this survey to be very promising.

SOLUBILITY DETERMINATIONS BY MEASUREMENT OF ELECTROMOTIVE FORCES OF CONCENTRATION CELLS

L. E. Topol

Work on the determination of the solubilities of metal fluorides in molten salts by measuring the emf's of appropriate cells was continued.[19] The method consists in measuring the potentials of concentration cells of the type

$$M|MF_2(c_1),\ NaF\text{-}ZrF_4\,||\,NaF\text{-}ZrF_4,\ MF_2(c_2)\,|M$$

where M is the metal, as a function of temperature. The solubility of the dissolved salt is determined by noting the point of discontinuity in a plot of voltage vs temperature. A helium atmosphere and a temperature range of 525 to 800°C were used for the experiments described here.

Cells with CuF_2 in $NaF\text{-}ZrF_4$ (53-47 mole %) contained in copper crucibles, which were previously treated with hydrogen, were investigated. Copper electrodes were used for these experiments. Preliminary measurements showed poor reproducibility,[19] and recent runs made with and without copper turnings added to the cells seem to verify the previous indications that a small amount of CuF, too little to measure, is formed in the melts. Because of this uncertainty in the melt composition, only tentative values for the solubility of CuF_2 are available. The data in Table 2.2.18 and Fig. 2.2.9 are probably too high, if they are in error, because the composition was determined from the amount of CuF_2 added, and

[18] J. D. Redman and C. F. Weaver, *ANP Quar. Prog. Rep. June 10, 1954*, ORNL-1729, p 50; *ANP Quar. Prog. Rep. Sept. 10, 1954*, ORNL-1771, p 63; *ANP Quar. Prog. Rep. Dec. 10, 1954*, ORNL-1816, p 63.

[19] L. E. Topol, *ANP Quar. Prog. Rep. Sept. 10, 1956*, ORNL-2157, p 106.

TABLE 2.2.18. TENTATIVE VALUES FOR THE SOLUBILITY OF CuF_2 IN $NaF\text{-}ZrF_4$ (53-47 MOLE %)

CuF_2 in Solution (mole % = wt %)	Temperature (°C)
0.135	560
0.143	550
0.152	540
0.156	565
0.213	610
0.225	610
0.230	605
0.273	620
0.301	620
0.314	650
0.359	650
0.362	660
0.434	690
0.439	685
0.573	715
0.797	785

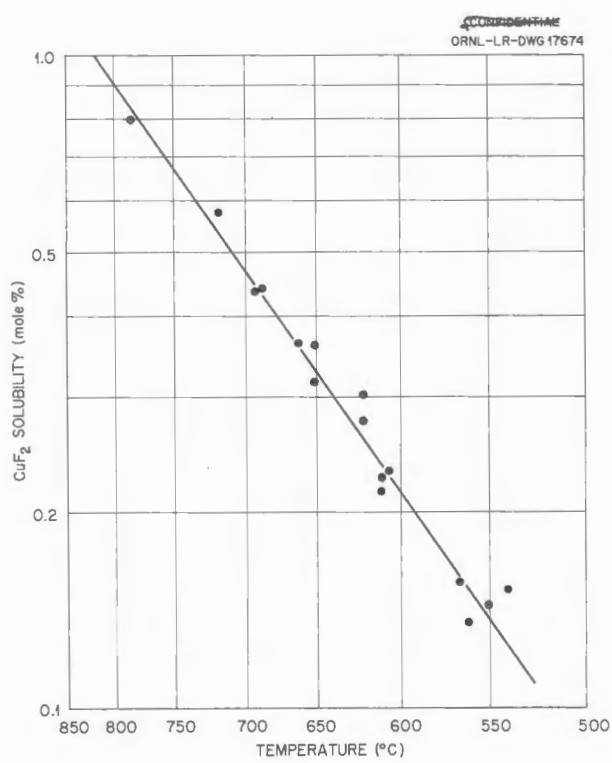

Fig. 2.2.9. Tentative Values for the Solubility of CuF_2 in $NaF\text{-}ZrF_4$ (53-47 mole %).

the CuF did not appear to be involved in the primary phase which precipitated.

The effect of temperature on the apparent solubility of CuF_2 in $NaF\text{-}ZrF_4$ (53-47 mole %) can be expressed by the relation

$$\log N = 0.68 - (13.3 \times 10^3/4.576T) ,$$

where N is the mole fraction of CuF_2 and T is the temperature in °K.

ACTIVITIES DETERMINED FROM FREEZING POINTS OF BINARY FLUORIDE MIXTURES

M. Blander

The choice of the best molten salt mixture for a practical application is essentially a matter of adjusting the composition to obtain an optimization of properties. For this reason it is of interest to analyze the effect of changes in composition on the properties in thermodynamic terms, to develop models and theories which account for the thermodynamic behavior, and to make correlations and predictions on the basis of these models and theories.

As an example, the effect of additions of one salt on the freezing point of another can be illustrated with the aid of data available for the constituents of fuel mixtures. For this purpose it is convenient to make use of the activity of a salt and the relation $a = \gamma N$, where a is the activity, γ is the activity coefficient, and N is the mole fraction of the salt. In an ideal salt melt, the activity coefficient will be unity,[20] and the activity will be the same as the mole fraction N; in other words, Raoult's law will be followed. In the case of fluorides, an ideal mixture has never been found; there is always a negative deviation from Raoult's law (activity coefficients less than unity) to a degree which depends chiefly on the difference in the value of Z/r (charge-to-radius ratio) for the cations involved.

The freezing point, the temperature below which a solid will precipitate, occurs when the activity of the salt as a solid is equal to its activity in solution. This leads to the following relation between the mole fraction, N, of the salt which is the precipitating phase and the freezing point, T (°K):

$$(1) \qquad \ln a = \ln \gamma + \ln N = \frac{-\Delta H_f}{R}\left(\frac{1}{T} - \frac{1}{T_0}\right) ,$$

where a, γ, and N refer to the salt in solution and ΔH_f and T_0 are the heat of fusion and melting point of the pure salt.[21] The chief difficulty in using Eq. 1 is the scarcity of reliable data on the heats of fusion of fluoride salts. Most of the heats of fusion in the literature were obtained from freezing-point curves, and the use of such values provides a comparison of one curve with another rather than the desired comparison with ideal behavior.

There are, however, calorimetrically determined heats of fusion for LiF (6467 cal/mole),[22] NaF (7780 cal/mole),[23] KF (6750 cal/mole),[23] and ZrF_4 (14,700 cal/mole).[24] By setting γ in Eq. 1 equal to unity, freezing points corresponding to ideal behavior were computed. The results are shown in Figs. 2.2.10 through 2.2.13 for mixtures that precipitate LiF, NaF, KF, and ZrF_4, respectively. Experimentally measured freezing points (or solubilities) are also plotted for comparison. The activity coefficient is equal to the ratio of the ideal solubility to the experimental solubility at any temperature ($\gamma = a/N = N_{ideal}/N$). Activity coefficients are tabulated in Tables 2.2.19 through 2.2.22; they are always less than unity, and thus they correspond to lower freezing points than those for ideal behavior. Described in terms of solubilities, the melts hold more salt without precipitation than if the solution were ideal because the activity of the salt is less than ideal. The extent of reduction of the activity, given by the activity coefficient, is more pronounced the larger the difference in the charge-to-radius ratios, Z/r, for the cations in the mixture. For example,

[20] This is equivalent to designating a pure liquid, supercooled, if necessary, as the standard state in the expression $\bar{F} - F^{\circ} = RT \ln a$, where $\bar{F}$ is the partial molal free energy in solution, F° is the free energy per mole in the standard state, R is the gas constant, and T is the temperature.

[21] Equation 1 is not valid if a solid solution precipitates. If a large temperature range is involved, the equation must be modified because of the change in ΔH_f with temperature. Useful comparisons can be made, however, at the extreme ends of the binary diagrams, where Eq. 1 is adequate, for combinations of fuel components.

[22] T. B. Douglas and J. L. Dever, WADC Technical Report No. 53-201, Part 1, National Bureau of Standards, October 1953.

[23] K. K. Kelley, *High-Temperature Heat-Content, Heat-Capacity, and Entropy Data for Inorganic Compounds*, U. S. Bur. Mines Bull. No. 476 (1949).

[24] W. D. Powers, this report, Chap. 4.1.

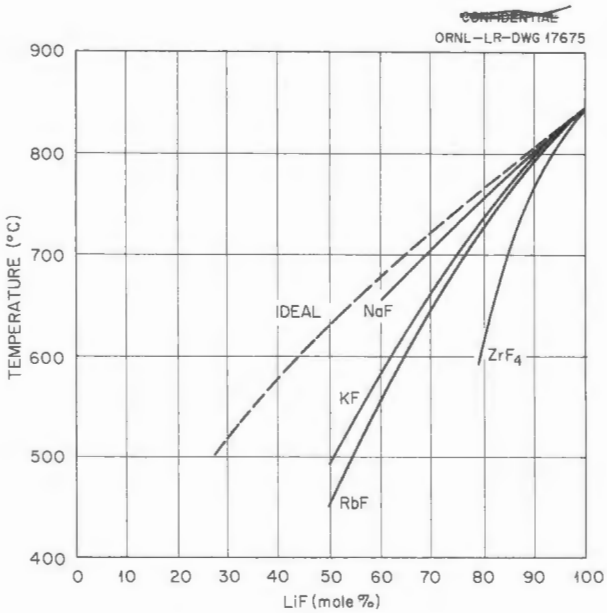

Fig. 2.2.10. Liquidus Temperatures of LiF in Binary Mixtures with NaF, KF, RbF, and ZrF_4.

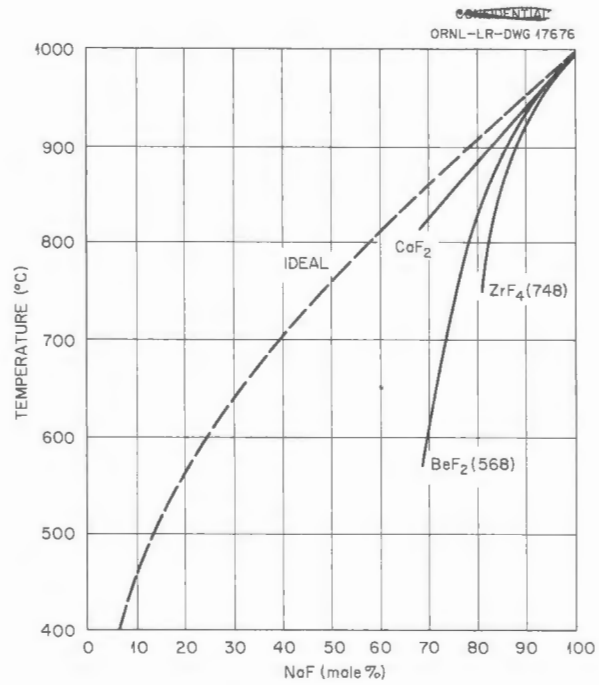

Fig. 2.2.11. Liquidus Temperatures of NaF in Binary Mixtures with CaF_2, BeF_2, and ZrF_4.

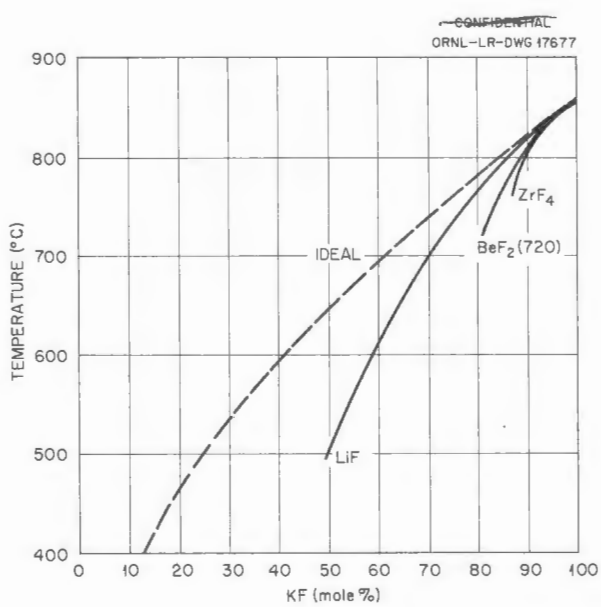

Fig. 2.2.12. Liquidus Temperatures of KF in Binary Mixtures with LiF, BeF_2, and ZrF_4.

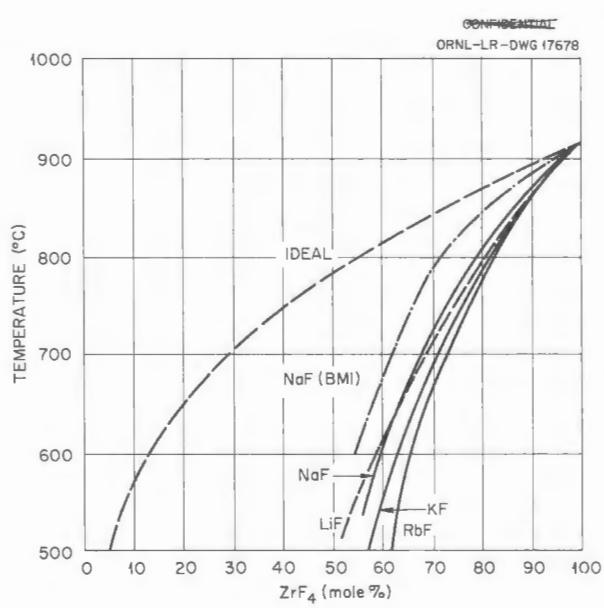

Fig. 2.2.13. Liquidus Temperatures of ZrF_4 in Binary Mixtures with LiF, NaF, KF, and RbF.

the addition of 40% of an alkali fluoride to ZrF_4 results in a freezing-point depression at least 200°C greater than the ideal depression.

The overlapping of the experimental curves for the effect of LiF and NaF on the freezing point of ZrF_4 is probably due to experimental error, since the activity of ZrF_4 with NaF should be less than that with LiF; vapor pressure measurements show that this is indeed the case.

A comparison of the freezing points obtained from thermal data with those obtained from vapor

TABLE 2.2.19. ACTIVITY COEFFICIENTS OF LiF IN SEVERAL BINARY FLUORIDES

Temperature (°C)	LiF-NaF		LiF-KF		LiF-RbF		LiF-ZrF_4	
	N*	γ*	N	γ	N	γ	N	γ
500			0.51	0.53	0.54	0.50		
600			0.61	0.72	0.64	0.69	0.79	0.56
700	0.68	0.94	0.74	0.87	0.76	0.85	0.85	0.76
800	0.90	0.97	0.91	0.96	0.91	0.96	0.94	0.94

*N is the mole fraction of LiF, and γ is the activity coefficient of LiF.

TABLE 2.2.20. ACTIVITY COEFFICIENTS OF NaF IN SEVERAL BINARY FLUORIDES

Temperature (°C)	NaF-CaF_2		NaF-BeF_2		NaF-ZrF_4	
	N*	γ*	N	γ	N	γ
600			0.70	0.38		
700			0.73	0.53		
800			0.78	0.73+	0.82	0.70
850	0.75	0.91	0.81	0.84	0.84	0.81
900	0.84	0.93	0.85	0.92	0.88	0.89
950	0.92	0.96	0.93	0.95	0.93	0.95

*N is the mole fraction of NaF, and γ is the activity coefficient of NaF.

TABLE 2.2.21. ACTIVITY COEFFICIENTS OF KF IN SEVERAL BINARY FLUORIDES

Temperature (°C)	KF-LiF		KF-BeF_2		KF-ZrF_4	
	N*	γ*	N	γ	N	γ
500	0.50	0.50				
600	0.59	0.70				
700	0.71	0.87				
750	0.78	0.94	0.83	0.87	0.87	0.86 (760°C)
800	0.87	0.98	0.89	0.95	0.89	0.95

*N is the mole fraction of KF, and γ is the activity coefficient of KF.

TABLE 2.2.22. ACTIVITY COEFFICIENTS OF ZrF_4 IN SEVERAL BINARY FLUORIDES

Temperature (°C)	ZrF_4-LiF		ZrF_4-NaF			ZrF_4-KF			ZrF_4-RbF		
	N*	γ*	N	γ	γ**	N	γ	γ**	N	γ	γ**
550	0.55	0.12	0.57	0.11	0.20	0.60	0.11	0.22	0.64	0.10	0.22
600	0.60	0.18	0.60	0.18	0.21	0.63	0.17	0.23	0.66	0.17	0.25
700	0.69	0.38	0.68	0.38	0.33	0.71	0.36		0.74	0.35	0.38
800	0.81	0.64	0.81	0.64		0.81	0.64		0.83	0.62	

*N is the mole fraction of ZrF_4, and γ is the activity coefficient of ZrF_4.

**Activity coefficient obtained from the vapor pressure; low-temperature values are inaccurate because of extrapolation uncertainties.

pressures[25] of a mixture of 30 to 40 mole % NaF in NaF-ZrF_4 reveals a discrepancy of 70 to 90°C in the freezing points. However, the difference in activity coefficients is only about 10%, and thus the discrepancy corresponds to a 10% error in the extrapolated vapor pressure. This could easily occur.

Little has been said regarding the central portion of the phase diagrams where the lowest melting mixtures usually occur. Here compound formation frequently complicates the picture, and the effect on freezing points must be discussed in terms of the relative stabilities of the solid lattice and "liquid lattice" at the same stoichiometry. Suffice it to say that the charge-to-radius ratios appear to be predominant factors, and that the same principles apply as in the precipitation of simple salts.

The cause for the deviations from ideality can be conveniently analyzed in the following manner. Since $\overline{F} - F^0 = RT \ln a$, where $\overline{F}$ is the partial molal free energy of the salt in solution, and F^0 is the free energy in the standard state (pure liquid, supercooled, if necessary),

$$\ln N + \ln \gamma = \frac{\overline{H} - H^0}{RT} - \frac{\overline{S} - S^0}{R}, \tag{2}$$

where the H's refer to heat contents and the S's to entropies of the same states as those for the F's. For random mixing such as that which occurs in an ideal solution, the partial molal entropy of mixing of a given component is $\overline{S}^i - S^0 = -R \ln N$, where $\overline{S}^i$ is the ideal partial molal entropy. If the difference $\overline{S} - S^i$ is designated as the partial excess molal entropy of mixing, S^E, then Eq. 2 may be rewritten as

$$\ln \gamma = \frac{\overline{H} - H^0}{RT} - \frac{S^E}{R}, \tag{3}$$

and thus the activity coefficient is resolved into an effect of the partial molal heat of solution $\overline{H} - H^0$ and an effect of deviations from the ideal entropy of mixing, S^E.

Activity coefficients less than unity can result from negative heats of solution or from positive excess entropies. In other words the ions in solution must have a lower heat content than they have when unmixed, and the mixing must result in a larger amount of "disordering"[26] than results from the formation of an ideal solution, $\overline{S}^i - S^0 = -R \ln N$.

This represents the limit of the application of thermodynamic theory to the subject. However, a number of models and theories have been proposed to account for the heats of solution and the entropies of mixing. The simplest models regard ionic melts as composed of charged balls. An important effect of the charge is that electrostatic forces require the cations to have anions for neighbors, and vice versa. In other words the ions are not mixed in a completely random fashion; the cations, for example, will distribute themselves so as to have anions between themselves and other cations. This results in a significant amount

[25] K. A. Sense, *et al.*, *Vapor Pressures of the Sodium Fluoride-Zirconium Fluoride System and Derived Information*, BMI-1064, Jan. 9, 1956.

[26] A larger number of configurations of equivalent energy than is the case with random mixing.

of ordering in comparison with the random mixing of black and white uncharged balls.

For a melt containing two alkali fluorides, such as NaF and KF, the effect of the ordering due to opposite charges can be incorporated in a model by considering a "liquid lattice" comprised of fluorides. Interpenetrating the fluoride lattice is a lattice of cation sites. Such a picture correctly describes the crystals of the pure solids. But the solids will not form a solution because the NaF and KF lattices are not the same size. An Na^+ ion is not "comfortable" in the KF lattice and a K^+ ion is not "comfortable" in the NaF lattice. The most "comfortable" of two alternate configurations is the one with the lowest energy, that is, the most stable. The liquid lattice resembles a solid lattice except for much greater flexibility and a lack of long-range order. Because of this flexibility, or lack of rigidity, the liquid lattices will mix to form a solution. The resulting mixed liquid lattice provides configurations of lower energy than the average energy of the unmixed lattices, and, also, the mixed lattice is distorted by local warping.

The lower energy configurations give rise to negative heats of solution. As an example of the factors contributing to this, it can be shown that the electrostatic repulsion between nearest cations is less when large and small cations alternate than the average of the repulsions between small cations and large cations among their own kind.[27] The difference is more pronounced the greater the difference in cation size, and similarly the negative heat of solution increases.

The warping of the fluoride lattice which permits the more stable configurations represents more disordering than would occur if the pure liquid lattices mixed without distortion. This gives rise to an increased entropy of mixing, above and beyond the value $\overline{S}^i - S^0 = -R \ln N$, which accounted only for the random distribution of cations among the cation sites. The resulting excess entropy of mixing will be greater for more pronounced warping, and the amount of warping increases with the difference in cation size. This explains the source of the positive excess entropies of mixing.

[27] This statement assumes that the distances between cations are proportional to the sum of the radii, and results from the fact that

$$\frac{e}{r_1 + r_2} + \frac{e}{r_2 + r_2} > \frac{e}{r_1 + r_2} .$$

The heat effect and the entropy effect go hand in hand, and with the model described here, it is impossible to have one without the other, although frequently one predominates. There is a prevalent practice of ascribing all negative deviations to complex formation. This places the emphasis on the entropy term and lattice distortions and causes the heat effect to be ignored, and, in the extreme view, it leads to the statement that NaF is complexed by KF because Na^+ ions have more attraction for the fluoride ion than do the K^+ ions. This statement is not wrong, but it implies a much less restricted definition of "complex" than is usually intended. For many solutions of salts of the same valence type, estimates of the expected heat of solution account for most of the deviation and leave very little to attribute to "complexing." Binary mixtures of alkali fluorides are examples. On the other hand a solution between salts of mixed valence types, such as $NaF\text{-}ZrF_4$, shows more deviation than can be accounted for by electrostatic forces and manifests large excess entropies of solution because of a definite preference by the fluoride ion for positions as Zr^{4+} neighbors. This is complexing in the sense that is usually intended, and it is more strongly influenced by charge than by size. For example, as shown in Table 2.2.23, the freezing point of NaF is depressed more by ZrF_4 than by BeF_2, although the Z/r ratio of Zr^{4+} ion differs from that of Na^+ ion less than that of Be^{++} ion.

TABLE 2.2.23. EFFECT OF CHARGE-TO-RADIUS RATIO (Z/r) ON THE FREEZING-POINT LOWERING OF LiF AND NaF BY 20 MOLE % QUANTITIES OF VARIOUS SOLUTES

Solute	Freezing Point	Z/r for Solute Cation
	Solvent: LiF (mp, 845°C)	
LiF		1.43
NaF	755	1.02
KF	740	0.75
RbF	730	0.67
ZrF_4	615	0.22
	Solvent: NaF (mp, 990°C)	
CaF_2	880	1.9
BeF_2	830	5.9
ZrF_4	750	4.6

2.3. PHYSICAL PROPERTIES OF MOLTEN MATERIALS

F. F. Blankenship

VAPOR PRESSURES AND ACTIVITIES IN THE $NaF-ZrF_4$ SYSTEM

S. Cantor

Measurements have been made of the vapor pressures of the $NaF-ZrF_4$ system by two groups of investigators who used two different methods. Sense and his co-workers[1] at Battelle Memorial Institute utilized the carrier-gas technique by which partial pressures could be obtained from the weights of condensates. Moore and his associates[2-4] at Oak Ridge National Laboratory used the Rodebush-Dixon[5] method in which total pressures were measured directly.

The two different methods gave data for total pressure which are in relatively good agreement. Sense found it necessary to postulate the existence of complex compounds in the vapor phase to account for concentrations of NaF in the condensate which would otherwise have required apparent activities higher than unity for NaF in some melts containing 35 mole % or more ZrF_4. Most of the compositions which Moore examined were so rich in ZrF_4 that virtually no NaF was expected in the condensates; moreover Moore was unable to detect the presence of NaF in sublimates from liquids containing as little as 43 mole % ZrF_4.

The studies reported here were made to check the data, by the Rodebush-Dixon method, for some of the compositions studied and to examine some compositions for which species other than ZrF_4 must be present in the vapor. The results obtained from the three compositions studied are given in Table 2.3.1. Analyses of the vapor sublimates show that there is a negligible difference between total pressures and vapor pressures of ZrF_4 for the compositions in Table 2.3.1 and the other compositions included in Table 2.3.2. The constants A and B are those expressed in the relation,

$$\log P \text{ (mm Hg)} = A - \frac{B}{T},$$

where T is in °K, and were obtained by treating the data by the method of least squares. On a plot of the data, the vapor pressures of the composition containing 66.4 mole % ZrF_4 fell approximately half way between the vapor pressures of compositions containing 57.8 and 75 mole % ZrF_4, as measured by Moore[2,3] and extrapolated to a liquidus temperature of 670°C, and thus the data agree exactly with accepted values obtained from phase studies. There is also relatively close agreement between the vapor pressures for the 38.7 mole % ZrF_4 mixture and those for a 38 mole % ZrF_4 mixture measured by the Battelle Memorial Institute.

TABLE 2.3.1. CONSTANTS FOR THE VAPOR PRESSURE EQUATION FOR THE $NaF-ZrF_4$ SYSTEM

Composition (mole % ZrF_4)	A	B
66.4	9.668 ± 0.040	8652 ± 43
38.7	7.567 ± 0.287	8268 ± 373
34.6	7.099 ± 0.122	8256 ± 158

One experiment was carried out to check the existence of an azeotrope at 75 mole % NaF–25 mole % ZrF_4, as reported by Sense.[1] A melt containing $NaF-ZrF_4$ (75-25 mole %) was held at 1200°C for 15 hr in an evacuated Rodebush-Dixon vapor-pressure cell. When the cooled cell was opened a small number of platelets were found to have condensed at the cold zone. Microscopic examination showed that the platelets were a single-phase material of the same index of refraction as $3NaF \cdot ZrF_4$ (although the crystals were biaxial instead of uniaxial as they usually are for $3NaF \cdot ZrF_4$). The fact that the sublimate was a single-phase material, coupled with the absence of other $NaF-ZrF_4$ components or complexes, confirms the azeotropic behavior of liquid $3NaF \cdot ZrF_4$. The similarity between the composition of the

[1] K. A. Sense *et al.*, *Vapor Pressures of the Sodium Fluoride–Zirconium Fluoride System and Derived Information*, BMI-1064 (Jan. 9, 1956).

[2] R. E. Moore, *ANP Quar. Prog. Rep. Sept. 10, 1954*, ORNL-1771, p 129.

[3] R. E. Moore and C. J. Barton, *ANP Quar. Prog. Rep. June 10, 1954*, ORNL-1729, p 101.

[4] R. E. Traber, Jr., R. E. Moore, and C. J. Barton, *ANP Quar. Prog. Rep. Dec. 10, 1953*, ORNL-1649, p 99.

[5] W. H. Rodebush and A. L. Dixon, *Phys. Rev.* 26, 851 (1925).

TABLE 2.3.2. APPROXIMATE ACTIVITIES OF ZrF_4 IN $NaF\text{-}ZrF_4$ SOLUTIONS AT SEVERAL TEMPERATURES

Composition (mole % ZrF_4)	Activity of ZrF_4			
	At 600°C	At 700°C	At 800°C	At 912°C
75	0.280	0.341	0.421	0.497
66.4	0.218	0.232	0.246	0.257
57.8	0.138	0.135	0.126	0.120
50	0.0871	0.0707	0.0601	0.0541
47	0.0580	0.0520	0.0417	0.0382
46.4	0.0538	0.0478	0.0379	0.0343
43	0.0350	0.0266	0.0210	0.0168
38.7	0.0138	0.00870	0.00620	0.00431
34.6	0.00167	0.00159	0.00159	0.00150

maximum-boiling-point azeotropic mixture and the composition of the stoichiometric mixture suggests that $3NaF\cdot ZrF_4$ may exist as a compound in the liquid and vapor. The existence of ZrF_7^{---} ions in the liquid is quite plausible, but confirmation of a complex molecule such as $3NaF\cdot ZrF_4$ in the vapor phase is lacking.

The activities of ZrF_4 in the $NaF\text{-}ZrF_4$ system, based on liquid standard states, can be obtained from the log P vs $1/T$ relation for a given composition by calculating the pressure at a given temperature and dividing by the pressure of pure liquid ZrF_4 at the same temperature. The vapor pressures given previously[6] for supercooled liquid ZrF_4 were used in combination with previously reported vapor pressures of solutions[2,3,4,6] for calculations of the activities of ZrF_4 in $NaF\text{-}ZrF_4$ solutions at 600, 700, 800, and 912°C. The assumption that ZrF_4 is the only volatile constituent and extrapolations, where necessary, gave rise to the approximate activities given in Table 2.3.2.

Empirically, the effect of composition on the activity of ZrF_4 at 912°C, as shown in Table 2.3.2, can be expressed as follows:

$$\frac{\log \gamma_{ZrF_4}}{X_{NaF}^2} = -6.49 + 4.93X_{ZrF_4} ,$$

where γ and X are the activity coefficient and mole fraction, respectively, of the compound designated by the subscript. If it is assumed that the empirical expression holds approximately for all composition ranges, the Gibbs-Duhem equation leads to the following expression for γ_{NaF}:

$$\frac{\log \gamma_{NaF}}{X_{ZrF_4}^2} = -8.96 + 4.93X_{ZrF_4} .$$

These two analytical equations for the activity coefficient as a function of composition lead to the activities of ZrF_4 and NaF plotted in Fig. 2.3.1. The activities calculated in this manner for NaF agree very well with those found experimentally at Battelle[1] for NaF at 1009°C in the range below 25 mole % ZrF_4. At higher ZrF_4 concentrations a comparison of the data is not valid because different assumptions were used in taking the complex formation into account. Activities were not obtained for NaF at lower temperatures because of the uncertainty in the necessary extrapolations.

EFFECT OF PARTIAL SUBSTITUTION OF UF_4 FOR ZrF_4 ON THE VAPOR PRESSURE OF ZrF_4 IN FUEL MIXTURES

S. D. Christian S. Cantor

Only surmises have been available regarding the effect of partial substitution of UF_4 for ZrF_4 on the vapor pressures of fuel mixtures. Most of the

[6] S. Cantor and S. D. Christian, *ANP Quar. Prog. Rep. Sept. 10, 1956*, ORNL-2157, p 108.

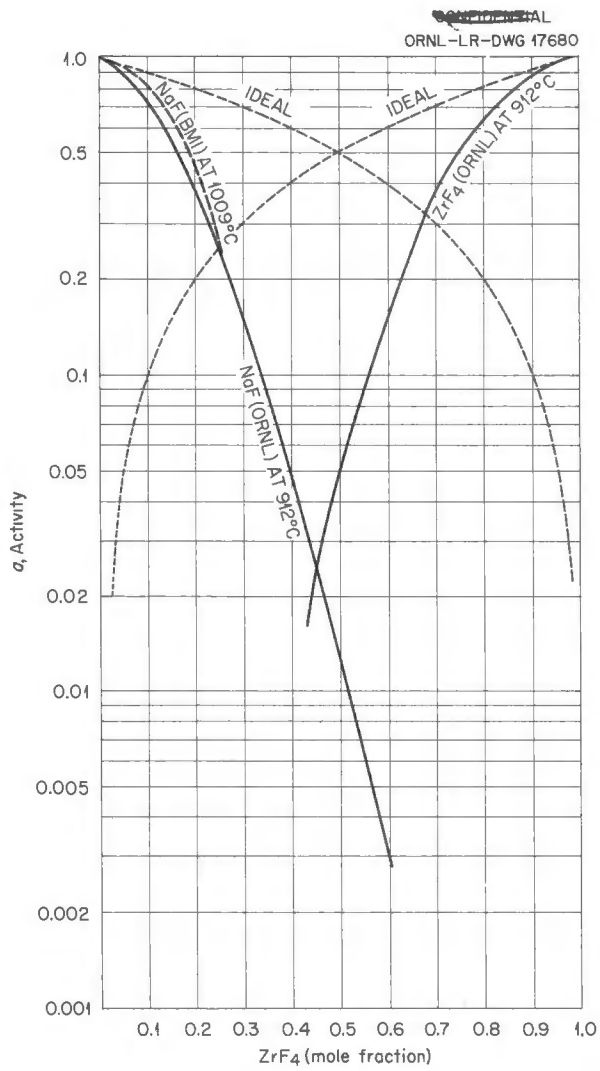

Fig. 2.3.1. Activities of NaF and ZrF_4 in the $NaF\cdot ZrF_4$ System.

vapor pressure measurements related to the volatility of ZrF_4 have dealt with the effect of altering the ZrF_4 concentration in binary mixtures with alkali fluorides. The effect of UF_4 has been studied by determining vapor pressures of compositions formed by varying the proportions of the compounds $7NaF\cdot 6ZrF_4$ and $7NaF\cdot 6UF_4$. In these mixtures the NaF content is constant, and UF_4 is substituted for ZrF_4 to give series of liquids which include regions of interest as fuels and which solidify to continuous series of solid solutions having the formula $7NaF\cdot 6(Zr,U)F_4$.

The Rodebush-Dixon apparatus in the form used for previous work in this laboratory was employed. Temperature ranges were chosen so that the vapor pressures were, in general, between 10 and 100 mm Hg. A least-squares straight-line representation of the data (Table 2.3.3) for each composition is shown in Fig. 2.3.2. Data on the apparent heat of vaporization, as found from the slope of the line and the vapor pressure equation, are also given in Table 2.3.3. When the data are interpreted in terms of the activity of ZrF_4 and when ZrF_4 is assumed to be the only volatile constituent, the results given in Table 2.3.4 are obtained. Also the Raoult's law activities, calculated on the basis of pressure as a linear function of composition (by assuming that $7NaF\cdot 6UF_4$ acts only as an inert diluent), are included in Table 2.3.4 for comparison.

The activities given in Table 2.3.4 and plotted in Fig. 2.3.3 are based on liquid $7NaF\cdot 6ZrF_4$ as the standard state, and if the slight differences in slopes at various compositions (Fig. 2.3.2) are neglected, there is no significant heat of mixing.

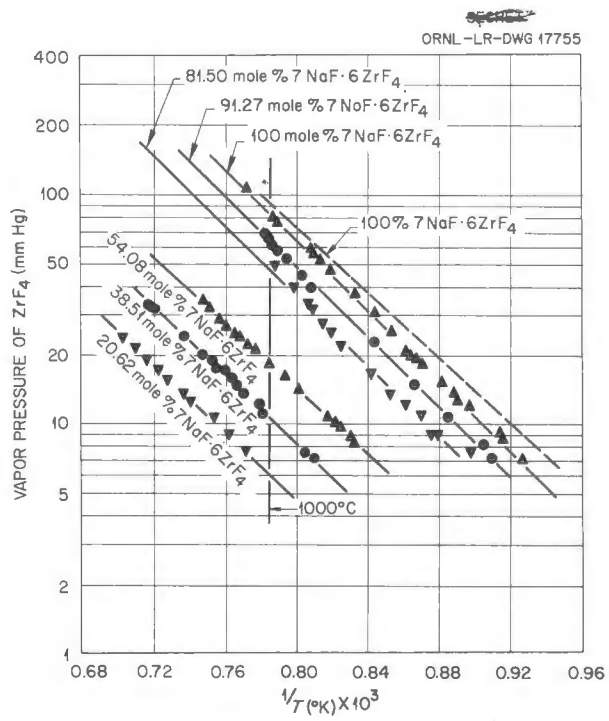

Fig. 2.3.2. Effect of Temperature on the Vapor Pressure of ZrF_4 from $7NaF\cdot 6UF_4$–$7NaF\cdot 6ZrF_4$ Mixtures.

TABLE 2.3.3. CONSTANTS FOR THE VAPOR PRESSURE EQUATION FOR $7NaF \cdot 6ZrF_4$–$7NaF \cdot 6UF_4$ MELTS

$$\text{Log } P \text{ (mm Hg)} = A - \frac{B}{T(^\circ K)}$$

Composition (mole % $7NaF \cdot 6ZrF_4$)	Temperature Range (°C)	A	B	ΔH_{vap} (kcal/mole)
100	800–1025	7.977 ± 0.068	7710 ± 80	35.3 ± 0.4
91.27	825–1025	7.747 ± 0.073	7588 ± 82	34.7 ± 0.4
81.50	825–975	7.691 ± 0.189	7662 ± 240	35.1 ± 1.1
54.08	925–1075	6.832 ± 0.057	7104 ± 72	32.5 ± 0.3
38.51	950–1125	6.834 ± 0.072	7400 ± 95	33.9 ± 0.4
20.62	1025–1150	6.343 ± 0.11	7072 ± 150	32.4 ± 0.7

TABLE 2.3.4. EFFECT OF UF_4 ON THE ACTIVITY OF ZrF_4 IN $7NaF \cdot 6(Zr,U)F_4$

Composition (mole % $7NaF \cdot 6ZrF_4$)	Activity of ZrF_4	Raoult's Law Activity of ZrF_4
100	1.00	1.00
90	0.74	0.90
80	0.54	0.80
70	0.40	0.70
60	0.28	0.60
50	0.20	0.50
40	0.13	0.40
30	0.08	0.30
20	0.04	0.20
10	0.02	0.10

This means that there is little change in activity with temperature and that the activities are approximately correct for lower temperatures, although they were compiled from 1000°C data. Empirical curve fitting showed that the experimental activities given in Table 2.3.4 are represented by the expression

$$a_{ZrF_4} = 0.15X\, e^{1.895X} ,$$

where X is the mole fraction of $7NaF \cdot 6ZrF_4$.

The effect of the UF_4 can be interpreted to be that of an additional supply of fluoride ions for the complexing of ZrF_4. The vapor pressure is accordingly reduced to a greater extent than would have been the case if UF_4 and ZrF_4 had equal attractions for fluoride ions. The vapor pressures obtained are experimental confirmation of the supposition that ZrF_4 is more strongly complexed in NaF mixtures than UF_4 because of the smaller size of the Zr^{4+} ion (0.80 Å) compared with the U^{4+} ion (0.97 Å), and they are compatible with previous data which indicated that UF_4 has lower activity coefficients in alkali fluoride mixtures which do not contain ZrF_4 than in mixtures which do contain ZrF_4. The substitution of UF_4 for ZrF_4 diminishes the vapor problem but is much less effective than increasing the amount of alkali fluoride.

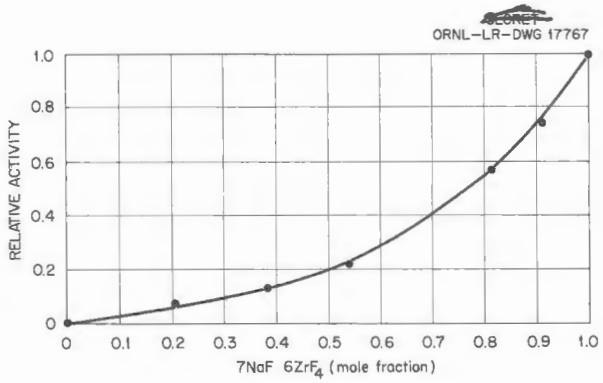

Fig. 2.3.3. Effect of Composition on the Activity of ZrF_4 in $7NaF \cdot 6UF_4$–$7NaF \cdot 6ZrF_4$ Mixtures.

VAPOR PRESSURES OF THE LiCl-$FeCl_2$ AND KCl-$FeCl_2$ SYSTEMS

C. C. Beusman

The determination of equilibrium constants for corrosion reactions that occur in fused salts on the basis of free-energy data requires that the activities of the corrosion-product salts be known accurately. Therefore measurements of the activities of structural metal halides, for example, $FeCl_2$, as a function of alkali cation size are being carried out as an aid in predicting the extent of corrosion reactions. Since $FeCl_2$ is a volatile salt, measurement of the vapor pressure as a function of composition yields information on the activity. The total vapor pressures in the $FeCl_2$-KCl and $FeCl_2$-LiCl systems have been measured over the entire range of composition by using the Rodebush-Dixon method. The data obtained for the various mixtures are shown graphically in Figs. 2.3.4 and 2.3.5. These data have been fitted by least-squares analysis to a linear relation of the type

$$\log P \text{ (mm Hg)} = B - \frac{A}{T(^\circ\text{K})} .$$

The constants obtained are given in Tables 2.3.5 and 2.3.6, along with the apparent heat of vaporization.

The $FeCl_2$ used in this work was prepared by drying $FeCl_2 \cdot 4H_2O$ under anhydrous HCl at 500°C for 4 hr. The LiCl used was similarly dried under anhydrous HCl, while the KCl was fused under dry helium. The salt mixtures were weighed and ground in a dry box and loaded into dry nickel vapor-pressure cells similar to the stainless steel cells used in fluoride salt experiments. During

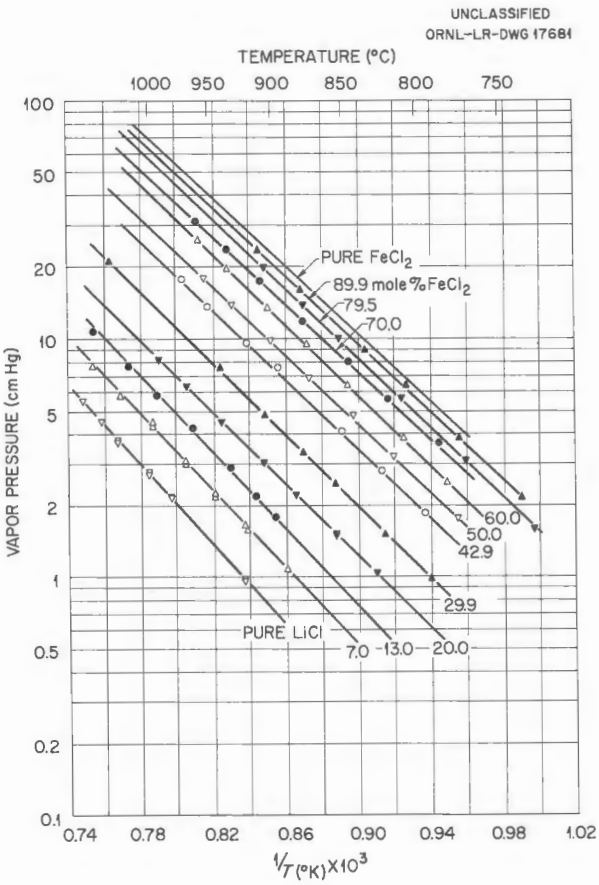

Fig. 2.3.4. Vapor Pressures vs Temperature for the $FeCl_2$-LiCl System.

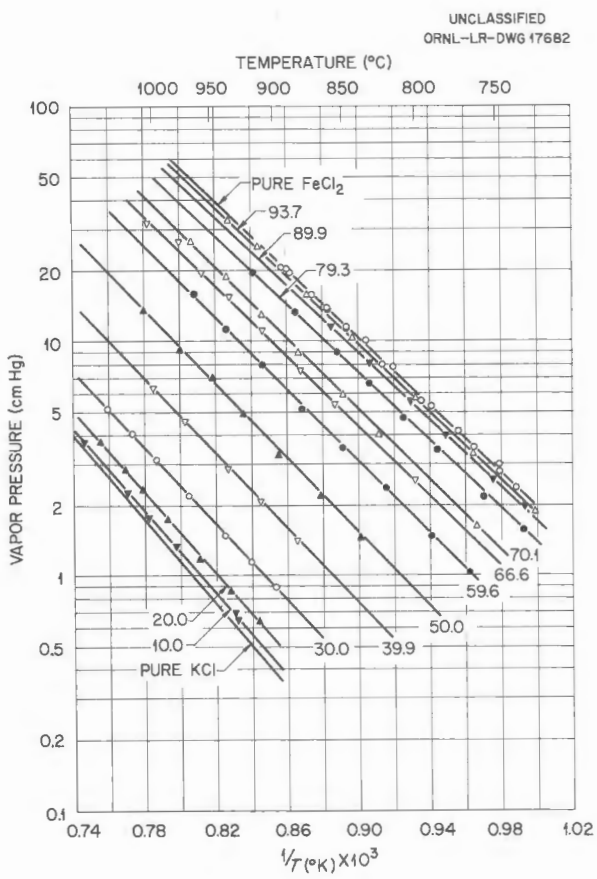

Fig. 2.3.5. Vapor Pressures vs Temperature for the $FeCl_2$-KCl System.

TABLE 2.3.5. VAPOR PRESSURE DATA FOR THE $LiCl\text{-}FeCl_2$ SYSTEM

$$\text{Log } P \text{ (mm Hg)} = B - \frac{A}{T(^\circ K)}$$

Composition (mole % $FeCl_2$)	Temperature Range (°C)	A	$-B$	ΔH_{vap} (kcal/mole)
100	750–890	8.5617	7274.5	33.29
89.9	740–910	8.5344	7288.9	33.35
79.5	730–905	8.3582	7275.9	33.31
70	790–960	8.3633	7228.3	33.08
60	780–960	8.4788	7472.0	34.19
50	775–950	8.2409	7335.9	33.57
42.9	795–975	8.1428	7345.7	33.61
29.9	790–1040	8.0480	7510.4	34.37
20	825–995	7.9114	7591.9	34.74
13	900–1055	7.9728	7876.0	36.04
7	865–1055	7.9594	8063.7	36.90
Pure LiCl	920–1105	8.01251	8388.1	38.38

TABLE 2.3.6. VAPOR PRESSURE DATA FOR THE $KCl\text{-}FeCl_2$ SYSTEM

$$\text{Log } P \text{ (mm Hg)} = B - \frac{A}{T(^\circ C)}$$

Composition (mole % $FeCl_2$)	Temperature Range (°C)	A	$-B$	ΔH_{vap} (kcal/mole)
100	750–890	8.5617	7274.5	33.29
93.7	730–935	8.6474	7397.4	33.85
89.9	735–860	8.3717	7144.2	32.69
85.1	730–910	8.5491	7373.5	33.74
79.3	735–915	8.5857	7476.3	34.21
70.1	765–970	8.6371	7709.1	35.28
66.6	855–1000	8.5385	7677.2	35.13
59.6	765–965	8.4542	7749.0	35.46
50	840–1010	8.3563	7976.1	36.50
39.9	885–1000	8.2117	8181.6	37.44
30	900–1045	8.0117	8297.5	37.97
20	915–1050	8.0996	8656.5	39.61
9.8	930–1065	8.0657	8719.6	39.90
Pure KCl	920–1150	8.3526	9115.0	41.71

the measurements small amounts of salt vapor volatilized and condensed in the cooler vertical gas lines. After each experimental point was obtained, the condensed material was returned to the body of the melt by heating the nickel tubes and allowing the salt to melt and run down. This procedure assures the restoration of the initial composition of the liquid.

The composition of the vapor was estimated from analyses of the condensates. When the pressure measurements on a composition were completed, the total inert gas pressure was reduced by pumping to a value lower than the equilibrium vapor pressure of the mixture. After refluxing for about 3 min and allowing vapor to condense on the cool upper section of the nickel tubes, the pressure was raised and the cell was cooled. The condensate was removed mechanically in a dry box from the inside of the tubes and analyzed chemically. Appreciable amounts of KCl were found in the vapor from mixtures of 40 mole % or less $FeCl_2$. Similarly, significant amounts of LiCl were present in the vapor from mixtures below 30 mole % $FeCl_2$. In order to clearly determine the vapor compositions and partial pressures in these ranges, transportation vapor-pressure determinations are currently being carried out.

The curves shown in Fig. 2.3.6 are of interest in the calculation of activities of $FeCl_2$ in these melts. These curves, which give the total vapor pressure at 900°C vs composition, were obtained by solution of the linear equations for the various mixtures studied. Strong depression of the vapor pressure of $FeCl_2$ is apparent in the KCl system. However, in the LiCl system, the $FeCl_2$ vapor pressure follows ideal behavior between 80 to 100 mole % $FeCl_2$ and shows a rather weak negative deviation from Raoult's law over the remaining composition range. The presence of KCl in the vapor precludes calculation of the $FeCl_2$ activity for the complete composition range from total vapor pressure data alone. It seems certain that either KCl or a KCl-$FeCl_2$ vapor complex contributes to the total vapor pressures of compositions below 40 mole % $FeCl_2$, as evidenced by condensate analyses. Thus complete calculations of the $FeCl_2$ and alkali chloride activities require the completion of the transportation vapor-pressure work.

The apparent heat of vaporization was calculated from the slope of the log P vs $1/T$ plots and is given as a function of composition for the two systems in Figs. 2.3.7 and 2.3.8. In the $FeCl_2$-LiCl system, essentially athermal mixing of LiCl in $FeCl_2$ occurs for compositions from 100 to 60 mole % $FeCl_2$, as was expected from the nearly ideal behavior of the total vapor pressure in this

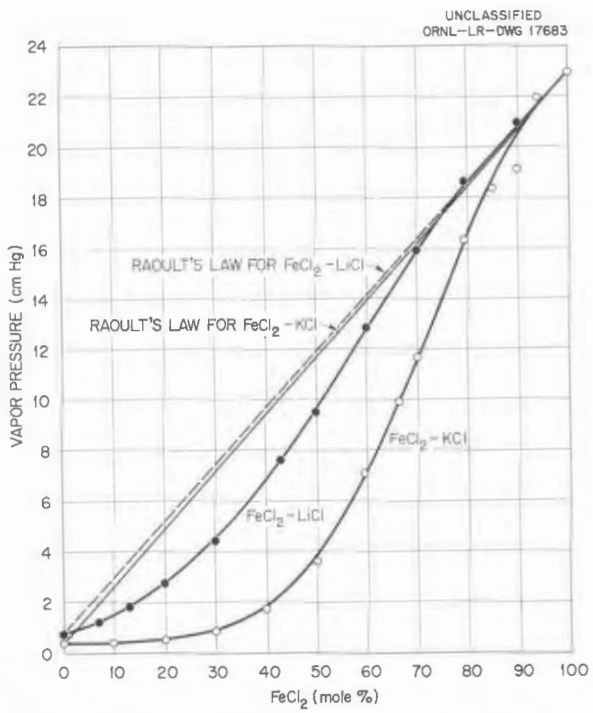

Fig. 2.3.6. Vapor Pressure at 900°C vs Composition in the $FeCl_2$-KCl and $FeCl_2$-LiCl Systems.

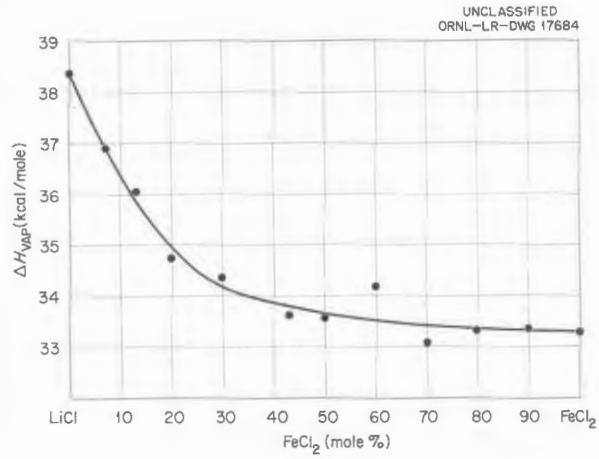

Fig. 2.3.7. Apparent Heat of Vaporization vs Composition in the $FeCl_2$-LiCl System.

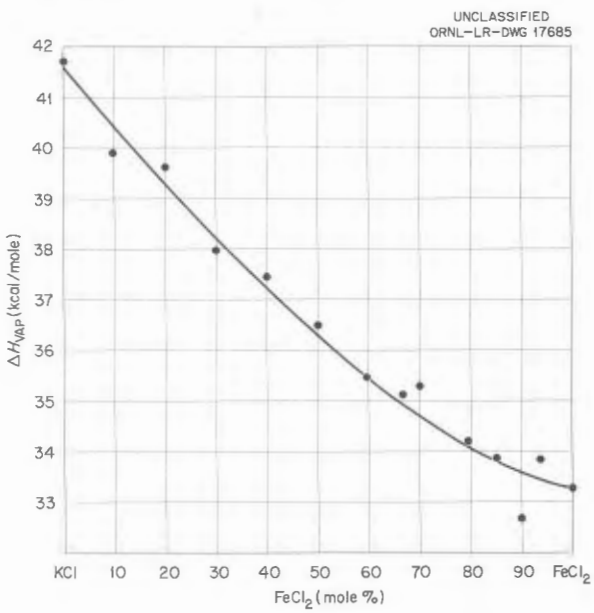

Fig. 2.3.8. Apparent Heat of Vaporization vs Composition in the $FeCl_2$-KCl System.

region. Such ideal behavior occurs only when solutions are formed athermally, and changes in the vapor pressure result from dilution effects. However, in the $FeCl_2$-KCl system, no athermal region exists, and thus it appears that neither the heat of solution nor the entropy of mixing is ideal.

SURFACE TENSIONS OF MOLTEN SALTS

S. Langer

Additional measurements of the surface tensions of NaF-ZrF_4 (53-47 mole %) were made by the sessile-drop method. The results obtained were in essential agreement with those previously reported. A study of the effect of time, temperature, and inert gas pressure on rate of change of composition of the drops is still incomplete.[7] Several attempts have been made to determine the surface tension of pure, liquid UF_4 by using plaques of graphite (both APC and C-18 grades) and boron nitride. While the products could not be identified, there was visible evidence of a reaction of the boron nitride with liquid UF_4. Values obtained with the graphite plaques for the ratio of surface tension to density are presented in Table 2.3.7. The density of liquid UF_4 has, apparently, not been measured. The approximate values given in the table were obtained by computing a density for liquid UF_4 from the published value for the room temperature solid by assuming negligible expansion of the solid on heating to 1036°C and a 25% expansion on melting.

TABLE 2.3.7. SURFACE TENSION OF URANIUM TETRAFLUORIDE

Calculated liquid density of UF_4: 5.30 g/cm^3

Temperature (°C)	Supporting Plaque	γ/d*	Approximate Surface Tension (dynes/cm)
1055	APC graphite	29.0713	154
1055	APC graphite	22.9945	122
1043	C-18 graphite	27.4712	146
1044	C-18 graphite	29.1405	154

*The γ/d is the surface-tension-to-density ratio in dynes·cm^2/g.

Photographs obtained in one attempt to make the measurement, data for which are not included in the table, showed many "whiskers" of solid UO_2 protruding from the surface of the drop. The approximate surface tensions calculated from these photographs ranged from 325 to 350 dynes/cm. It is apparent that small amounts of impurities may greatly affect the surface tension. An attempt will be made to use graphite pycnometers to measure the density of molten UF_4.

[7] S. Langer, *ANP Quar. Prog. Rep. March 10, 1956*, ORNL-2061, p 105; *ANP Quar. Prog. Rep. June 10, 1956*, ORNL-2106, p 118; *ANP Quar. Prog. Rep. Sept. 10, 1956*, ORNL-2157, p 118.

2.4 PRODUCTION OF PURIFIED FLUORIDE MIXTURES

G. J. Nessle

PREPARATION OF VARIOUS FLUORIDES

B. J. Sturm L. G. Overholser

Preparation of pure structural metal fluorides in small quantities for special studies was continued. In addition, quantities of rare-earth fluorides were prepared for use in fission-product removal studies.

Studies of the reduction of MoF_6 by FeF_2 were carried out in attempts to isolate molybdenum fluorides in which the valence state of the molydenum is less than six. Interaction of FeF_2 with MoF_6 at 300°C results in oxidation of the FeF_2 to FeF_3 and a reduction of the MoF_6 to a product which can be collected in a condenser maintained at 110°C. The reduction product was first observed to be yellow, but it was apparently very unstable with respect to traces of water, since it slowly turned to a brownish-blue color, even when exposed to the nearly inert atmosphere of a vacuum dry box. This material melts rather sharply at 60°C. Chemical analysis of the material yielded results corresponding to MoF_4; x-ray and petrographic examinations will be employed to positively identify it.

One batch of CrF_2 was prepared from anhydrous $CrCl_2$ by hydrofluorination at 500°C. Although a critical examination of the product has not been completed, it is believed that this material is purer than that previously obtained by the hydrogen reduction of CrF_3, since all batches prepared by this latter method were contaminated to some degree by metallic chromium. Additional FeF_2 for use in the reduction of MoF_6 was prepared by hydrofluorination of hydrated $FeCl_2$. Approximately 100 g of YF_3 was prepared by converting Y_2O_3 to YCl_3 through an aqueous HCl treatment, precipitating the fluoride by addition of aqueous HF, washing, and drying. A similar treatment was applied to Sm_2O_3 to produce about ½ lb of SmF_3. Some approximate values for the solubility of CeF_3 in various aqueous media were obtained by removing the solid phase from saturated solutions through filtering and centrifuging and then analyzing the liquid phase for cerium. Values found for the solubilities at 30°C, expressed in ppm of CeF_3, follow: distilled water, 50; 0.1 *M* HCl, 15; 0.1 *M* HF, 5. These values are to be considered as maximum values, since the removal of the solid phase may have been incomplete. Hydrofluorination of UF_4 and of an NaF-KF-ZrF_4 mixture for oxide removal was carried out.

PILOT-SCALE PURIFICATION OPERATIONS

C. R. Croft J. Truitt

During the past quarter the pilot scale (5, 10, 50 lb) fluoride preparation facilities processed 49 batches totaling approximately 1450 lb of various fluoride compositions to be used in small-scale corrosion testing, phase equilibrium studies, and physical property studies. Requests for the mixture NaF-KF-LiF-UF_4 (11.2-41-45.3-2.5 mole %) increased rather rapidly. Additional 50-lb storage containers for this material have been ordered, and two of the 50-lb units have been assigned to continuous production of this composition on an 8-hr-day basis. Production will average 600 lb or more per month under this arrangement, and presently known requirements can apparently be met. It has been found that many of the containers filled with this composition rupture when the material is remelted after freezing.

Metallographic examination of one container that failed revealed sulfur embrittlement; however, analysis of the fuel in that can and in six other cans gave sulfur contents of 6 ppm or less. It has been suggested that the nickel used in fabrication may be at fault, or improper degreasing of the cans may have allowed sulfur attack. However, these possibilities do not explain why the rapid incidence of failure is restricted to cans containing this composition. A possible explanation is that some sulfur embrittlement occurs on all nickel cans used and that the higher thermal-expansion coefficient of this particular material is sufficient to effect the observed damage.

PRODUCTION-SCALE OPERATIONS

J. E. Eorgan

During this quarter 25 batches totaling approximately 6150 lb of purified fluoride melts were processed in the 250-lb capacity facility. It was necessary to suspend operations for two weeks during the quarter because of the lack of storage containers. However, it is now believed that

sufficient containers will be available to allow continuous operation of the facility. An additional 40 containers were ordered; this order makes a total of 80 containers now being fabricated for Pratt & Whitney Aircraft.

Two copper-lined stainless steel reactor cans failed recently because of faulty temperature controllers. In each case the temperature reached or exceeded the melting point of the copper, and therefore the stainless steel shell was attacked by the molten fluorides. An alarm system has been installed to preclude this type of failure in the future. No copper-lined reactor can has yet failed as a consequence of standard operation of the equipment.

The preparation of $NaF\text{-}ZrF_4$ compositions is normally carried out by purifying hafnium-bearing Na_2ZrF_6 or $NaZrF_5$ plus small additions of NaF. However, the preparation of the material to be used as the fuel solvent for the Pratt & Whitney high-temperature critical experiment required the use of low-hafnium ZrF_4 and, consequently, a sizable quantity of NaF. The material was found, after processing, to contain excessive quantities of oxides. It was found later that the NaF which was presumed to have been purchased on specifications limiting the water content to 0.05% actually contained approximately 3.5% water. The fuel solvent for the Pratt & Whitney experiment is therefore being reprocessed to remove the oxides and oxyfluorides.

The first 4000 lb of $NaZrF_5$ ordered from a commercial vendor was received during the quarter. Analyses of this material showed it to be of very good quality. Establishment of a reliable commercial source of raw materials for this operation will be of great value in maintaining product quality.

The staff for operating the 250-lb production facility has been considerably increased, and, as of November 5, this facility was placed on 3-shift 7-day-week operation. This move became necessary when the projected requirements of Oak Ridge National Laboratory and of Pratt & Whitney Aircraft for calendar year 1957 were examined and when it was realized that the large Y-12 production facility could not be expected to be in operation much before January 1958. It now appears that 7-day operation of the present facility during fiscal year 1957 might result in somewhat more material than the Oak Ridge National Laboratory and Pratt & Whitney Aircraft will consume in that period; however, the surplus will almost certainly be needed to make up the deficit between production and requirements during the first half of fiscal year 1958.

BATCHING AND DISPENSING OPERATIONS

F. A. Doss D. C. Wood

During this quarter 139 batches totaling approximately 5450 lb of processed fluorides were dispensed in batch sizes ranging from 1 to 250 lb. Although the number of batches dispensed increased, the amount of salt handled decreased. Thus there was a sizable increase in the stock inventory. The amount dispensed decreased because no shipments were made to Pratt & Whitney Aircraft during the quarter; all Pratt & Whitney Aircraft shipments were postponed until November 19, 1956. A material balance for the quarter is given in Table 2.4.1.

TABLE 2.4.1. MATERIAL BALANCE FOR FLUORIDE MIXTURE PRODUCTION AND USE

	Material (lb)				Special Mixtures	Total
	Mixture No. 30, $NaF\text{-}ZrF_4\text{-}UF_4$ (50-46-4 mole %)	Mixture No. 31, $NaF\text{-}ZrF_4$ (50-50 mole %)	Mixture No. 108, $NaF\text{-}ZrF_4\text{-}UF_4$ (56-37.5-6.5 mole %)	Mixture No. 45, $NaF\text{-}ZrF_4$ (53-47 mole %)		
On hand at beginning of quarter	2444	1240	994	990	1027	6,695
Produced during quarter	1726	2671	990	747	1472	7,606
Total	4170	3911	1984	1737	2499	14,301
Dispensed during quarter	2469	1725			1279	5,473
On hand at end of quarter	1701	2186	1984	1737	1220	8,828

The main consumers of processed fluoride mixtures and their allotments during the quarter are given below:

	Amount (lb)
ORNL-ANP groups	
For chemical and physical property studies	757
For experimental engineering tests	3386
For metallurgical studies and fuel reprocessing development	540
Other contractors, including BMI, NRL, and WADC	150
Salvage and reprocessing	640
Total	5473

The increased production capacity increases the possibility that the storage-and-handling area will have to be enlarged. Recent examinations by the Health Physics Division have shown that this area presents some definite health hazards. Every effort is being made to follow the recommendations made by the Health Physics Division, since the congestion and activity in this area will increase considerably during the next few months. The most difficult problem at present is the installation of a "walk-in" type of hood for the maintenance and repair of storage cans and the handling of salvage material. The problems of space and proper location are being studied. It is hoped that installation of such a hood will be completed within the next two months.

PREPARATION OF ZrF_4 FROM $ZrCl_4$

J. E. Eorgan

The conversion of about 1850 lb of low-hafnium $ZrCl_4$ to ZrF_4 was completed during the quarter. Installation of a dust filter on the conversion unit decreased the dust loss from the 12% observed on early runs to about 3% in the later runs. The overall conversion showed a net yield of 93%. The quality of the ZrF_4 obtained is considered to be satisfactory, with the chloride content being 0.5% and the total structural metal (Fe, Cr, Ni) content ranging in various batches from 500 to 1000 ppm.

The best results were obtained from the dust filter by placing it on the loading section of the conversion chamber. The HF gas enters at each end of the chamber, passes through the powdered $ZrCl_4$ to the center section, and exits at the loading port through the dust filter. It was found that the filter rotors had to be run continuously to prevent plugging with dust to such an extent as to make restarting the rotors difficult.

SPECIAL SERVICES

F. A. Doss J. Truitt D. C. Wood

Filling, Draining, and Sampling Operations

Approximately 3400 lb of processed fluorides and 3000 lb of liquid metals were charged to engineering tests in charge sizes ranging from 1 to 500 lb in a total of 134 operations.

Shield Mockup Core Materials

Attempts to fill two "orange slices" which simulated heat exchanger sections of the Shield Mockup Core (SMC) were successful. The material used to simulate the fuel and the NaK coolant in the heat exchanger of the circulating-fuel reactor contained 61.7 mole % NaF, 16.4 mole % ZrF_4, 1.4 mole % UF_4, and 20.5 mole % KF; its melting point was close to 1300°F.

The first section was placed in a furnace and heated to 1500°F. It was provided with an overflow tank of sufficient size to allow for shrinkage of the melt in the section without void formation. The can containing the melt was then heated to 1650°F, and the melt was poured into the first section. The "orange slice" was allowed to cool slowly with the overflow tank maintained at 1500°F until the temperature of the section had fallen to well below the freezing point of the melt. When the section had cooled to room temperature the overflow tank was removed, and the section was cut open. The cast fluoride salt was very uniform in appearance, and no voids or cracks were found in the casting, aside from small gas bubbles. Some deformation of the critical dimensions of the "orange slice" had occurred but was considered to be tolerable. Analyses of the melt from top to bottom showed evidence of some uranium segregation toward the bottom.

The second "orange slice" was not heated for the casting operation. The overflow tank and connecting neck were maintained at 1500°F, and the 1650°F melt was poured into the cold section. Again the section was allowed to cool to well

below the freezing point of the melt with the overflow tank maintained at 1500°F. This section cooled to room temperature relatively rapidly as compared with the first section (about 6 hr as compared with 20 hr). Subsequent examination showed the cast fluoride salt to be uniform and dense, with no voids, and it was especially interesting that there were no gas bubbles entrained in the melt. Chemical analyses of the melt from top to bottom showed no evidence of uranium segregation.

As a result of these experiments, it appears that it will be possible to pour the melt into a cold half-shell that simulates the SMC with considerable chances of obtaining a good cast. One noticeable problem, however, is the shrinkage of the casting during cooling from the freezing point to room temperature. Sufficient shrinkage was noted to leave a space of as much as ½ in. on the long dimensions and ¼ in. on the short dimension of the heat exchanger section. Since the SMC is being redesigned no further work on this problem is planned.

Fuel Mixture for Pratt & Whitney Aircraft High-Temperature Critical Experiment

The processing of some 300 lb of $NaF\text{-}UF_4$ (66.6-33.4 mole %) with enriched uranium for the Pratt & Whitney Aircraft high-temperature critical experiment was completed. The production operation progressed smoothly with only one out of eleven batches having to be reprocessed because of oxide contamination. Preparation of the material was started on August 13, and the material was verified as acceptable on October 24. The analytical and accountability data relative to this material have been reported.[1] The material was loaded into the experimental fuel-enriching system on about November 20.

PREPARATION AND IDENTIFICATION OF THE OXIDES OF SODIUM AND POTASSIUM

E. E. Ketchen L. G. Overholser

The indices of refraction of sodium monoxide and potassium monoxide were determined because of interest in identifying the oxides of NaK collected in cold traps in circulating NaK systems. Sodium monoxide is commercially available, but potassium monoxide had to be prepared especially for this study. The indices of refraction, as determined by using the petrographic microscope, are, for sodium monoxide, 1.688, and, for potassium monoxide, 1.720.

A study related to the identification of the oxides taken from NaK systems was the determination of a method for removing all NaK from the alkali oxides. It was found that distillation in silver under vacuum gave a satisfactory separation. A recognized fault of this method is the possible change in the ratio of the two oxides during distillation so that the final oxide mixture may be different from that present prior to distillation. Other methods of separation studied were mechanical removal of NaK from the oxides and removal of NaK by amalgamation. With the first method it was not possible to remove all the NaK, and with the second method residual mercury interfered with the microscopic examination.

An attempted preparation of potassium monoxide by using a controlled reaction between potassium and oxygen yielded a mixture of potassium oxides. It was found in the literature[2] that sodium monoxide has been prepared by the reaction

$$5NaN_3 + NaNO_3 \longrightarrow 3Na_2O + 8N_2$$

and it seemed reasonable to expect the analogous reaction for potassium salts. Therefore potassium azide was precipitated from a dilute aqueous solution of hydrazoic acid by the addition of potassium hydroxide and alcohol. The potassium azide was filtered, air dried, mixed in a 4:1 weight ratio with potassium nitrate, and charged to a metal crucible enclosed in a heated quartz tube. The azide was decomposed slowly under vacuum by gentle heating to about 300°C. Reaction of the resulting potassium with the potassium nitrate took place at about 340°C, and any excess potassium was then distilled off by heating under vacuum to somewhat over 400°C. Three runs were carried out with approximately 5 g of charge material. The first two, made in nickel, were

[1] J. Truitt, *Analytical and Accountability Report on PWHCT Concentrate*, ORNL CF-56-10-107 (Oct. 25, 1956).

[2] E. Zintl and H. H. v. Baumbach, *Z. anorg. u. allgem. Chem.* 198, 88 (1931).

unsuccessful; the first yielded no product and the second gave a product badly contaminated with nickel oxide. The third run was made in silver and yielded somewhat less than 1 g of fairly pure potassium monoxide. A fourth run was attempted with about 40 g of charge material in a larger silver crucible. The run proceeded normally through decomposition of the azide and through the heating up to about 340°C, at which point a very violent explosion occurred, which was possibly caused by the reaction between the potassium metal and the potassium nitrate proceeding too rapidly and generating enough heat to explode the remaining potassium nitrate.

2.5. COMPATIBILITY OF MATERIALS AT HIGH TEMPERATURES

F. Kertesz

PENETRATION OF GRAPHITE BY MOLTEN FLUORIDES

H. J. Buttram

The study of the behavior of high-density graphite exposed to molten fluorides, reported previously,[1] was continued with graphite specimens which are not commercially available. These materials included a pitch-impregnated and fired sample obtained from the Graphite Specialties Corporation (density, 1.8 g/cm^3), an especially prepared experimental sample designated grade CN_F obtained from the Central Research Laboratory of the National Carbon Company (density, 1.92 g/cm^3), and a high-density sample obtained from the Degussa Company, Germany (density, 2.0 g/cm^3), which was probably prepared from purified natural graphite.

By determining the alpha counts inside and at the surface of specimens exposed to molten $NaF\text{-}ZrF_4\text{-}UF_4$ mixtures at 800°C for 24 hr, it was found that the Degussa graphite was not detectably penetrated by the melt and that the other two specimens were only slightly less resistant to penetration. All three materials had low ash content, as determined by igniting them at 650°C in oxygen. The sample prepared by the National Carbon Company had the lowest ash content (0.004%), and the others, including commercial APC graphite, ranged from 0.04 to 0.094% ash.

Attempts were made to pretreat APC graphite in such a manner as to reduce its penetrability. The three treatments tried included impregnation with $NaF\text{-}ZrF_4$ (53-47 mole %), impregnation with $NaF\text{-}ZrF_4$ (53-47 mole %) followed by heating in vacuum, and impregnation with $NaF\text{-}ZrF_4$ (53-47 mole %) followed by heating in a stream of wet helium. The heating of the impregnated graphite in vacuum resulted in the removal of ZrF_4 and yielded a higher melting $NaF\text{-}ZrF_4$ mixture that offered more resistance to diffusion of $NaF\text{-}ZrF_4\text{-}UF_4$. The heat treatment in wet helium resulted in the formation of ZrO_2 in the pores or, at least, on the surface of the graphite.

The specimens were impregnated with $NaF\text{-}ZrF_4$ (53-47 mole %) by heating them under vacuum for 2 hr and then immersing them in the $NaF\text{-}ZrF_4$.

The effectiveness of the pretreatment was determined by measuring the alpha count of the specimens after exposure to the $NaF\text{-}ZrF_4\text{-}UF_4$ (53.5-40-6.5 mole %) mixture. Measurements were made at the surface and at two depths, as shown in Table 2.5.1. The results indicate that impregnation alone reduces salt diffusion into the sample by a factor of 2 but does not prevent penetration. The pretreatment that consists of impregnating the material and then heating it in vacuum appears to be the most promising method

[1] H. J. Buttram and G. F. Schenck, *ANP Quar. Prog. Rep. Sept. 10, 1956*, ORNL-2157, p 123.

TABLE 2.5.1. ALPHA RADIATION IN PRETREATED APC GRAPHITE SAMPLES AFTER EXPOSURE TO $NaF\text{-}ZrF_4\text{-}UF_4$ (53.5-40-6.5 MOLE %)

Specimen Pretreatment	Radiation Penetration (counts/min)		
	At Surface	At 1/8-in. Depth	At 1/4-in. Depth
Impregnated with $NaF\text{-}ZrF_4$ (53-47 mole %)	14	12	12
Impregnated with $NaF\text{-}ZrF_4$ (53-47 mole %) and heated in vacuum	15	9	4
Impregnated with $NaF\text{-}ZrF_4$ (53-47 mole %) and heated in wet helium			
Sample A	49	23	19
Sample B	31	27	15

for reducing the penetration of APC graphite by UF_4-containing mixtures.

HYDROGEN PRESSURE OF THE NaOH-Ni REACTION

H. J. Buttram F. A. Knox

Previous investigations of the quantities of hydrogen evolved during the NaOH-Ni reaction revealed that after about 100 hr the hydrogen pressure within a quartz envelope containing a test capsule decreased.[2] It was postulated at that time that the rate of evolution of hydrogen from the system became slow after about 100 hr compared with the rate of loss by diffusion from the quartz envelope. Therefore, a series of tests was prepared to investigate the rate of diffusion through quartz at 800°C.

The experimental procedure used consisted of evacuating, flushing, and filling eight 1-in.-OD quartz tubes with hydrogen and sealing them at a measured pressure just below atmospheric pressure. Each tube was weighed and its volume was measured. After 27, 91, 191, 248, 331, and 380 hr of soaking at 800°C, one or two tubes were removed from the furnace, and their residual pressures were determined. The results of these tests are summarized in Table 2.5.2 and presented in Fig. 2.5.1.

The results indicate that under the conditions used (about 3 atm pressure at 800°C), hydrogen gas diffused quite readily through the 0.85-mm-thick silica wall; the calculated pressure after 380 hr at 800°C was down to 53 mm Hg.

The rate of diffusion was calculated, and the data are given in Table 2.5.3 and plotted in Fig. 2.5.2. For the shortest experimental period, an average value for hydrogen of 0.446 ml/hr·(dm^2/mm) was obtained. During this time the pressure inside the capsule went from about 3 to 2.3 atm. The corresponding value for hydrogen for the 380-hr diffusion experiment was 0.110 ml/hr·(dm^2/mm),

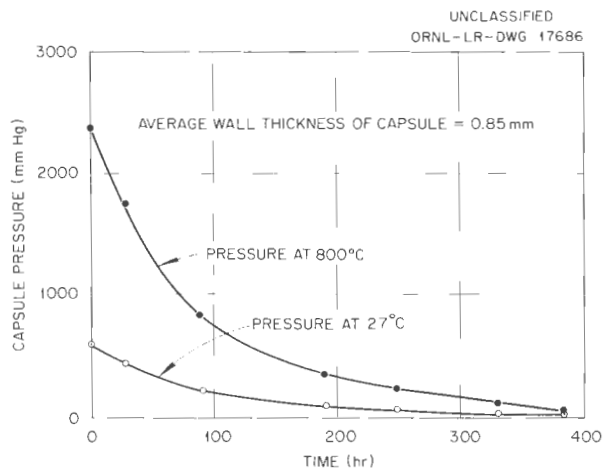

Fig. 2.5.1. Diffusion of Hydrogen Through Vitreous Silica at 800°C.

[2] H. J. Buttram and F. A. Knox, *ANP Quar. Prog. Rep. Sept. 10, 1956*, ORNL-2157, p 123.

TABLE 2.5.2. DIFFUSION OF HYDROGEN THROUGH VITREOUS SILICA CAPSULES AT 800°C

Average capsule wall thickness: 0.85 mm
Capsule volume: ~80 ml

Exposure Time (hr)	Original Pressure (mm Hg)		Pressure After Test (mm Hg)	
	At 27°C	At 800°C	At 27°C	At 800°C
27	662	2368	490	1752
	682	2440	483	1728
91	681	2436	247	884
	680	2431	225	805
191	678	2425	95	341
248	680	2431	72	258
331	677	2422	34	122
380	679	2429	15	53

TABLE 2.5.3. RATE OF DIFFUSION OF HYDROGEN THROUGH VITREOUS SILICA AT 800°C

Exposure Time (hr)	Pressure Loss at 0°C (mm Hg)	Volume (ml) of H_2 Corresponding to 1 mm Hg Pressure Drop at 0°C and 760 mm Hg	Volume (ml) of H_2 That Diffused Through Capsule Wall	Rate of Diffusion [ml/hr·(dm²/mm)]
27	156	0.133	20.7	0.412
	181	0.135	24.4	0.479
91	395	0.127	50.2	0.294
	413	0.118	48.7	0.280
191	530	0.126	66.8	0.185
248	552	0.130	71.8	0.154
331	585	0.130	76.1	0.122
380	604	0.130	78.5	0.110

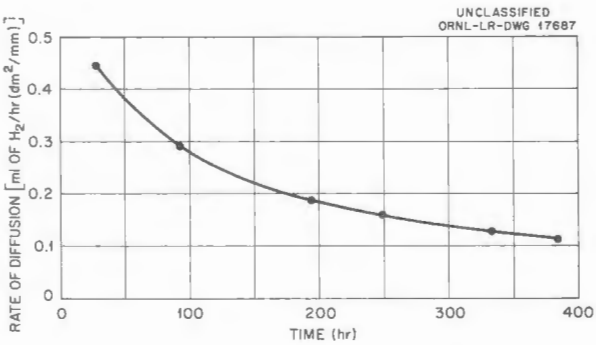

Fig. 2.5.2. Rate of Diffusion of Hydrogen Through Vitreous Silica at 800°C.

while the final pressure reached the low value of 53 mm Hg, as mentioned above.

ELECTROLYSIS OF THE NaOH-Ni SYSTEM

F. A. Knox

It was found in recent experiments that no detectable mass transfer occurred under isothermal conditions in an NaOH-Ni system with a current density of about 0.1 amp/cm² between nickel electrodes in an NaOH melt through which hydrogen was being bubbled at the electrodes. In these experiments the effects of both hydrogen and helium atmospheres were studied in NaOH-Ni systems with temperature gradients of 100 to 150°C. Either the nickel crucible or thermocouple well was used as the hot electrode and a ½-in. gas-cooled (hydrogen or helium) nickel tube served as the cold electrode. The hottest and coldest portions of the system were at temperatures of about 800 and 600°C, and the currents observed were in the order of 13 to 16 ma. When a helium atmosphere was employed, nickel deposits were found on the cold cathode, while no evidence of metal transfer was found with a hydrogen atmosphere. It was found, however, that with hydrogen, the direction of current flow was the reverse of that noted when helium was used; that is, the hot electrode became the cathode. In principle it could be possible to deposit nickel on the hot electrode, but this was not observed in this case.

In a hydrogen atmosphere a current density of about 3 amp/cm² was obtained by using an outside source and applying a 3.5-v potential, with the hot electrode negative. With a temperature gradient of nearly 200°C between electrodes, 60 mg of nickel was deposited on the hot electrode after 2 amp-hr had passed. At the same time about 1 mg was deposited on the cold electrode. Microscopic study of the cold electrode showed this deposit to be uneven.

Carbon monoxide was also used in the same manner as helium and hydrogen were used. Carbon was found to have deposited inside the crucible, and the NaOH melt contained Na_2CO_3. These results, of course, indicate that the CO disproportionated to yield C and CO_2.

PHYSICAL PROPERTIES OF ELASTOMERS EXPOSED TO ATTACK BY LIQUID METALS

D. Zucker

An apparatus for testing valve-seat materials under service conditions was built and placed in operation. This apparatus provides a facility for testing possible valve-seat materials in place in valves of the type scheduled for use in the ART NaK systems. In the apparatus the materials can be exposed to helium saturated with NaK vapor. The testing operation includes fairly rapid opening and closing of the valve containing the test seat under simulated ART operating conditions.

The materials described previously[3] were installed in valves and kept for about two weeks at a temperature of 180°C under helium before being tested at 50 psi with helium saturated with NaK vapor at 280°C. Some liquid NaK was also carried in the gas stream. As soon as the valves were exposed to NaK, they all began to leak. This effect occurred so fast, however, that it is not currently attributed to deterioration of the valve-seat material caused by the NaK but possibly to dirt in the test rig carried into the valve by the NaK (dislodged oxide, silver solder, flux, etc.). This supposition is borne out by the fact that subsequent measurement did not show noticeable changes in the leak rates in eleven days, in most cases. The leak rates of valves tested with DuPont silicone SR-5570 and General Electric silicone 81576 improved slightly during the tests. Currently G-E silicone 81576 shows the most promise, followed by G-E silicone SE-550 and Dow-Corning Silastic 80. Two other G-E samples, silicones 81578 and 81577, did not stand up well in contradiction of previous observations. The apparent improvements in the leak rates of several sample valves may have been caused by dislocation of dirt on the valve seat.

[3] D. Zucker, *ANP Quar. Prog. Rep. Sept. 10, 1956*, ORNL-2157, p 124.

2.6. ANALYTICAL CHEMISTRY

J. C. White J. R. Sites

DETERMINATION OF CARBON AND NITROGEN IN METALLIC LITHIUM

A. S. Meyer, Jr. T. W. Gilbert, Jr.

Carbon present in metallic lithium as lithium carbide is released as acetylene when the metal is dissolved in water. Hence, methods for the determination of carbon in metallic lithium ordinarily involve the determination of traces of acetylene in hydrogen. The acetylene is usually oxidized to carbon dioxide, which is subsequently determined gravimetrically. The sensitivity of this time-consuming method for the determination is extremely limited, however, and a method for the direct spectrophotometric determination of milligram and microgram quantities of acetylene was therefore developed. The spectrophotometric method may also be used for the determination of the lithium nitride in the same sample. The lithium nitride is released as ammonia along with the acetylene.

The spectrophotometric determination of the carbon is based on the measurement of the absorbance of the soluble complexes of silver carbide which are formed when acetylene is dissolved in concentrated solutions of silver salts. Silver perchlorate rather than silver nitrate was selected as the dissolvent for acetylene because of its low absorption of light in the ultraviolet spectrum. The absorption spectra of a solution of silver perchlorate and of solutions of acetylene in silver perchlorate at 30°C are shown in Fig. 2.6.1. Since the absorbance of the acetylene solution is to a great extent dependent on the wavelength used for the measurements, the sensitivity of the determination can be varied by the selection of the wavelength.

Wavelengths of 297 and 313 mμ were chosen for the determination of carbon in lithium. These wavelengths correspond to the emission lines of a mercury-vapor lamp, and therefore the reproducibility of the wavelengths used for the measurements can be checked. Calibration curves were established for the range of 5 to 120 μg per milliliter of acetylene at 297 mμ and from 30 to 600 μg/ml at 313 mμ. When a 2.5-g sample is taken and the acetylene is dissolved in 5 ml of a solution of silver perchlorate, the range of the determination is from 10 to 220 ppm of carbon at 297 mμ and from 50 to 1100 ppm at 313 mμ. The coefficient of variation of the method, as calculated from the results of the measurement of the absorption of known volumes of acetylene, is approximately 2%.

The absorbance of solutions of acetylene in silver perchlorate has an abnormally high temperature coefficient. Over the range of from 15 to 45°C the temperature coefficient of absorbance is −0.8%/°C. Control of the temperature of the solution to ±1°C is thus required during measurement of the absorbance. The solutions are stable at room temperature for a period of weeks.

In the proposed method the sample of metallic lithium is dissolved in water in a stainless steel bomb. The evolved gases, hydrogen, ammonia,

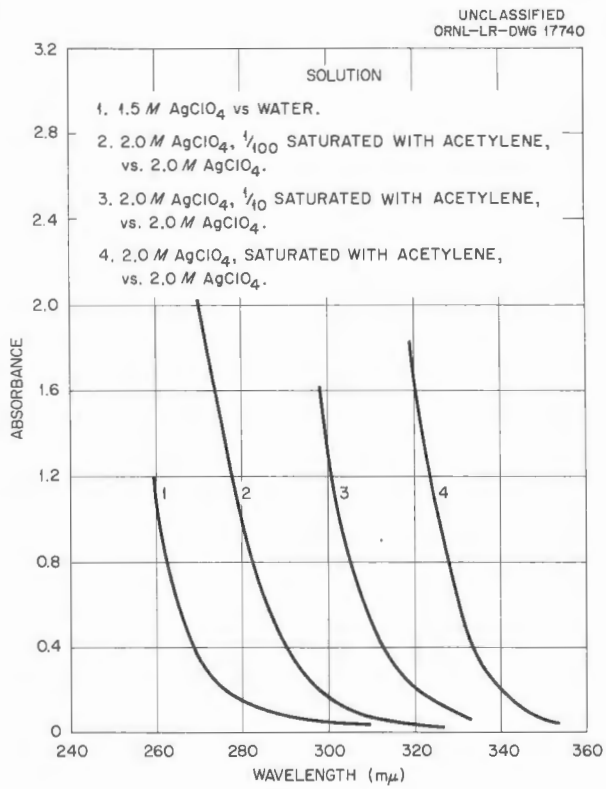

Fig. 2.6.1. Absorption Spectra of a Solution of $AgClO_4$ and of Solutions of Acetylene in $AgClO_4$ at 30°C.

and acetylene, are released from the bomb at a sufficiently low rate to permit absorption of the acetylene in a 5-ml volume of silver perchlorate solution. The gases are first passed through a 4% solution of boric acid to remove the ammonia, which is subsequently determined by the Nessler method,[1] and then through a series of tubes filled with silver perchlorate. More than 90% of the acetylene is absorbed in the first tube. Quantitative transfer of the gaseous products to the absorber train is completed by passing argon through the bomb while the solution containing the lithium sample is being boiled. Hydrogen interferes by causing the precipitation of finely divided metallic silver, which absorbs in the ultraviolet region. The extent of the precipitation can be minimized by maintaining the temperature of the silver perchlorate at 0°C. After the absorption of the acetylene is complete, the solutions are deaerated with argon and then heated on a steam bath to react with any remaining traces of hydrogen. The precipitated silver is removed by centrifuging the solutions before the absorbance measurements are made. The determination is carried out by using the apparatus shown in Fig. 2.6.2.

The method has been applied to samples of purified lithium and to samples of lithium which had been circulated in type 316 stainless steel thermal-convection loops at high temperatures (in the range 1400 to 1650°F, maximum) to study corrosion. Carbon in concentrations of from <10 ppm to 300 ppm was found in samples that contained up to 3% nitrogen, as determined by the Nessler method.[1]

[1] I. M. Kolthoff and E. B. Sandell, *Textbook of Quantitative Inorganic Analysis*, 3d ed., p 633, Macmillan, New York, 1952.

DETERMINATION OF OXYGEN IN METALLIC LITHIUM

A. S. Meyer, Jr. R. E. Feathers, Jr.

The amalgamation method for the determination of oxygen in metallic lithium, described previously,[2] was found to be impractical because of the

[2] A. S. Meyer, Jr., *et al.*, *ANP Quar. Prog. Rep. Sept. 10, 1956*, ORNL-2157, p 127.

UNCLASSIFIED
ORNL-LR-DWG 17741

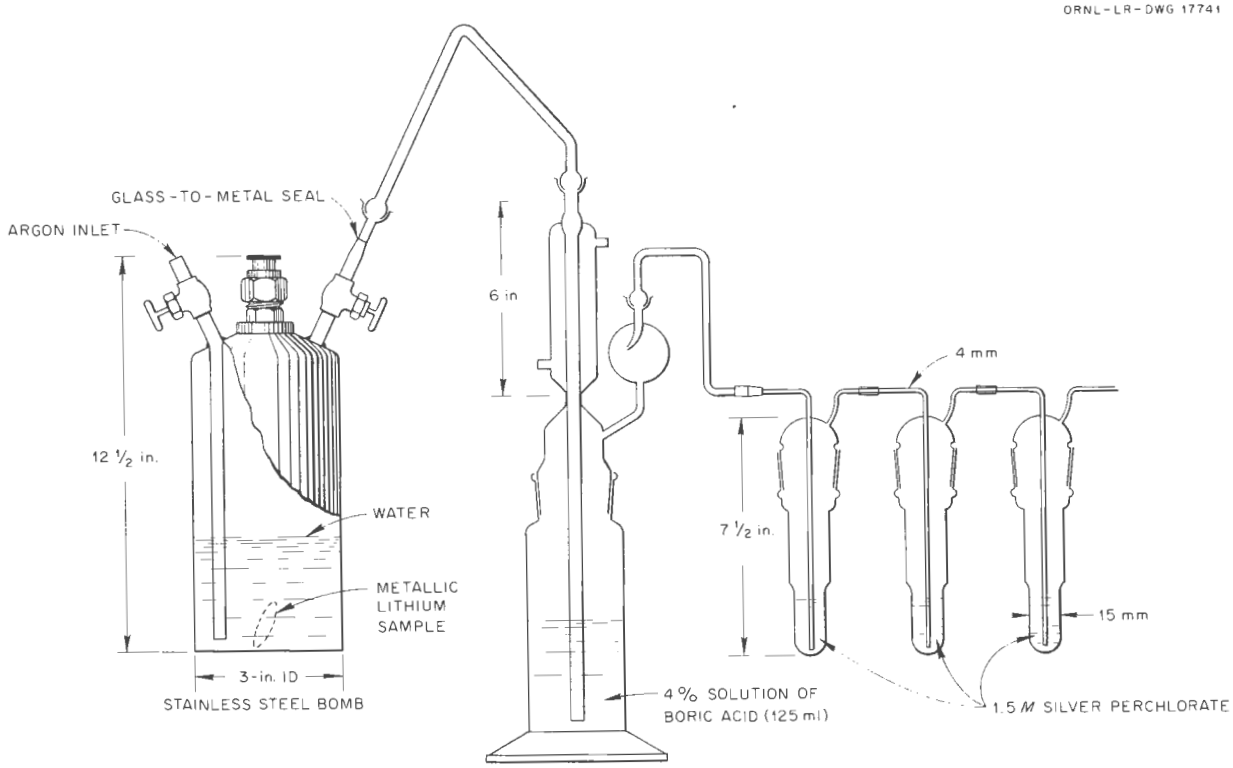

Fig. 2.6.2. Apparatus for the Determination of Carbon and Nitrogen in Metallic Lithium.

slow rate of filtration of the amalgam through the micrometallic filter which is used to separate Li_2O from the amalgam. Periods in excess of 8 hr were required to complete the filtration of the amalgam, which is produced from a 1-g sample, even when the amalgam was heated to a temperature of 250°C and a pressure differential of 50 psi was maintained across the filter.

The method for the determination of oxygen in lithium, which is based on the dissolution of the metal in an ethereal solution of *n*-butyl iodide and iodine, also described previously,[2] was studied further. The reaction

$$2Li_3N + 3I_2 \longrightarrow 6LiI + N_2$$

which was postulated to occur between lithium nitride and iodine during the dissolution of the samples was investigated by reacting pure Li_3N with the reagent solution. The reaction of the crystalline Li_3N was approximately 30% complete after 1-g samples of approximately 20-mesh particle size were refluxed with 300 ml of the reagent solution for periods of 8 to 12 hr. The extent of the reaction was determined by titrating the iodide which was formed during the reaction. Experiments are now being conducted in an effort to force the reaction to completion in a sealed vessel in which the yield of nitrogen can be measured.

Determinations of the concentration of oxygen in samples of purified lithium have yielded concentrations as low as 150 ppm. A comparison of the results obtained with various reagents indicates that traces of contaminants in the reagents contribute to the titration of oxygen. Analyses are being made for ascertaining the substances present in the reagents which could furnish active hydrogen, since water is carefully excluded from the reaction mixture.

An apparatus for the determination of traces of active hydrogen by a modification of the Zerewitinoff method[3] is now being assembled. In the proposed modification of this method the sample is treated with a solution of ethyl magnesium iodide in ether to liberate a volume of ethane equivalent to the active hydrogen in the sample according to the equation

$$ROH + C_2H_5{\cdot}MgI \longrightarrow ROMgI + C_2H_6$$

The ethane which is liberated in the reaction is transferred by means of a stream of helium to a trap that is cooled with liquid nitrogen. After the ethane has been collected, the trap is evacuated, and then the ethane is volatilized and measured under reduced pressure.

DETECTION OF TRACES OF NaK IN AIR

A. S. Meyer, Jr. J. P. Young

Investigations were continued on the development of a suitable instrument for the detection of leaks in NaK-to-air radiators and of methods for the introduction of reproducible quantities of NaK into air. The quantity of NaK in the air must be known in order to test the detection devices being considered.[4]

The detection devices are designed to analyze the ambient air in the radiator for traces of NaK. In order for the application of the devices to be successful, a major portion of the alkali-metal oxide present must be suspended in the air and must be detected rapidly. Experiments were therefore carried out to determine whether alkali-metal-oxide suspensions that are formed by the ignition of liquid NaK in air can be transferred to the detection elements of the proposed instruments.

A small test facility was fabricated in which the conditions of a radiator leak can be closely simulated. In this apparatus, NaK at temperatures up to 1200°F is injected, through a small orifice, into a stream of air which is drawn through a $\frac{3}{8}$-in. stainless steel tube at velocities up to 2400 lin ft/min. After the air traverses a distance of 4 ft from the point of injection, it is passed through a water-filled scrubbing system, which simulates the detection element.

In tests carried out in this apparatus, high-temperature NaK was injected under a pressure of 1000 psi into a room-temperature air stream which was moving at a velocity of 2400 lin ft/min. After approximately 2 ml of NaK had been injected, the apparatus was disassembled, and the concentration of alkali-metal oxides that had been deposited in various parts of the apparatus was determined by titration. It was found that more than 20% of the alkali-metal oxide had been collected in the scrubbers. The bulk of the oxide had deposited in the immediate vicinity of the point of injection,

[3] J. B. Niederl and V. Niederl, *Micromethods of Quantitative Organic Analysis*, 2d ed., p 263–272, Wiley, New York, 1942.

[4] A. S. Meyer, Jr., and J. P. Young, *ANP Quar. Prog. Rep. Sept. 10, 1956*, ORNL-2157, p 129.

while less than 5% was found in the 4-ft length of tubing. On the basis of the measured flow rates, the concentration of the alkali-metal oxides in the air delivered to the scrubbers was in excess of 2200 ppm, and less than 25% of the oxide formed was lost by deposition on the walls of the apparatus.

It is therefore apparent that the suspensions of alkali-metal oxide in air which are formed by the ignition of liquid NaK are more stable than those which are formed by the injection of helium saturated with alkali-metal vapor into air. It was demonstrated previously[4] that when helium saturated with sodium vapor is mixed with air a suspension is formed which rapidly deposits on the walls of the transfer line. The tests described above indicate that the suspensions formed by ignition in air are sufficiently stable for a leak in a NaK-to-air radiator to be detected by sampling the effluent air from the radiator duct.

Additional tests are in progress in which NaK at temperatures of 1200 to 1500°F is injected into air at pressures comparable to those to be used in the ART radiators. The construction of a larger test facility is planned in which the flow of air will be sufficient to permit the injection of NaK at a rate corresponding to 10 ppm of alkali metal in air.

The construction of the instrument for the detection of submicrogram quantities of NaK in air is essentially completed. This instrument is based on measurements of the absorbance of light of the frequency of the sodium doublet at 5890 Å. A functional description, together with the operational requirements of this instrument, was reported previously.[5]

SPECTROPHOTOMETRIC DETERMINATION OF NICKEL IN ALKALI METALS

A. S. Meyer, Jr. B. L. McDowell
R. E. Feathers, Jr.

The dioxime derivative 4-isopropyl-1,2-cyclohexanedionedioxime has been reported to be a sensitive, selective reagent for nickel.[6] This reagent is prepared by oxidizing 4-isopropylcyclohexanol to 4-isopropyl-1,2-cyclohexanedione and oximating the dione to 4-iospropyl-1,2-cyclohexanedionedioxime.

The chelate complex of nickel(II) with 4-isopropyl-1,2-cyclohexanedionedioxime, which is formed in a nearly neutral acetate buffer, extracts readily into chloroform. The partition coefficient for the complex in chloroform was found to be greater than 300. The chloroform solution of the chelate exhibited an absorption maximum at 383 mμ; the molar absorbance index for the complex is 4400. A plot of absorbance vs concentration of nickel was linear for concentrations of nickel from 1 to 15 μg/ml, with a coefficient of variation of 1%. Iron(II), iron(III), cobalt(III), and copper(I) are the only cations which are reported to cause serious interference in this method. Methods of masking these interferences are now being sought.

Since the distribution coefficient of the chelate complex is inordinately high, the extraction of this chelate with very small volumes of chloroform makes possible the utilization of a spectrophotometric method for the determination of traces of nickel in large volumes of aqueous solutions. Also, concentrations of nickel as low as 0.5 ppm can be determined in 5-g samples of alkali metals.

DETERMINATION OF TRACE AMOUNTS OF ZIRCONIUM WITH PYROCATECHOL VIOLET

J. P. Young J. R. French

The method for determining trace amounts of zirconium in sulfate solutions of fluoride salts with pyrocatechol violet is being studied. Pyrocatechol violet forms colored complexes with many cations. A procedure for the detection of zirconium,[7] based on the formation of the zirconium–pyrocatechol violet complex, served as a basis for this investigation. In a sulfate solution which has been buffered at a pH of 5 with sodium acetate, zirconium forms an intensely blue-colored complex.

The molar absorbancy index for the blue complex was determined as approximately 30,000 at a wavelength of 660 mμ, which indicates the ultimate sensitivity of this method. The zirconium–pyrocatechol violet complex flocculated after a short period of time, but precipitation was prevented by the addition of a small amount of gelatin. In the presence of gelatin, the absorbance of the complex conforms to Beer's law up to a concentration of

[5] A. S. Meyer, Jr., *et al.*, *ANP Quar. Prog. Rep. March 10, 1956*, ORNL-2061, p 207.

[6] D. T. Hooker and C. V. Banks, *Preparation, Properties, and Analytical Applications of Some Substituted Alicyclic* vic-*Dioximes*, ISC-597 (March 1955).

[7] H. Flaschka and F. Sodek, *Z. anal. Chem.* 150, 339 (1956).

2.5 μg of zirconium per milliliter of sulfate solution. The accuracy of the method is not affected by large concentrations of nickel or uranyl ions. Thorium causes slight interference; 4 μg of thorium per milliliter gives an error of 0.02 μg of zirconium per milliliter. Ferrous and ferric ions interfered seriously with the determination; however, in the presence of thioglycolic acid, an iron-to-zirconium ratio of 3:1 can be tolerated. The concentration of sulfate ion was found to have a slight effect on the sensitivity of the method. It has been reported that fluoride ion will bleach the color of the complex.[8] Further studies are planned to investigate the effect of other ions on this determination.

SPECTROPHOTOMETRIC DETERMINATION OF CERIUM IN MIXTURES OF FLUORIDE SALTS

A. S. Meyer, Jr. B. L. McDowell

Developmental work on the spectrophotometric determination of cerium with Tiron (disodium-1,2-dihydroxybenzene-3,5-disulfonate) in mixtures of fluoride salts was completed. Iron and uranium interfere by forming colored complexes with the reagent, and zirconium consumes the reagent to form a colorless complex. All these interfering materials were eliminated by extracting them into a solution of tri-*n*-octylphosphine oxide (TOPO) in cyclohexane.

Approximately 20 mg of zirconium or 25 mg of uranium can be extracted with 20 ml of a 0.1 *M* solution of TOPO in cyclohexane. Zirconium extracts readily from a sulfate solution, but chloride ions must be present for efficient extraction of uranium and iron. All the interfering cations in a 50-mg test portion of a sample of $NaF\text{-}ZrF_4\text{-}UF_4$ can be removed by the following procedure. A test portion of the sample in 10 ml of 0.5 *M* H_2SO_4 is extracted, during a 5-min period, with 20 ml of a 0.1 *M* solution of TOPO in cyclohexane. After separation of the phases, 5 ml of concentrated HCl is added to the aqueous phase. The resulting solution is extracted with another 20-ml portion of the TOPO solution. After the addition of 25 mg of Tiron, the color of the cerium-Tiron complex is developed in a test portion of the extracted solution, which contains 50 to 700 μg of cerium, by adjusting the solution to a pH greater than 8 with sodium hydroxide. In order to ensure more precise results, the ionic strength of the solution is adjusted by the addition of 1.25 g of Na_2SO_4 before dilution to a volume of 25 ml. After a period of 6 hr, the absorbance of the solution is measured at 500 mμ against a reference solution of the reagents. Concentrations of cerium as low as 0.1% in samples of $NaF\text{-}ZrF_4\text{-}UF_4$ can be determined in a sample of this size. A coefficient of variation of below 2% has been obtained for determinations of concentrations of cerium of from 3 to 12% in samples of $NaF\text{-}ZrF_4\text{-}UF_4$.

[8] L. Krahulec, *Ceskoslov. hyg., epidemiol., mikrobiol., imunol.* 4, 376 (1955).

PREPARATION OF RARE-EARTH FLUORIDE TRACERS

A. S. Meyer, Jr. G. Goldberg

Radioactive, tagged fluoride salts were prepared for use as tracers in studies of equilibria at high temperatures. The two tracer fluorides prepared were cerium fluoride tagged with Ce^{141} and lanthanum fluoride tagged with La^{140}. The cerium fluoride was precipitated by adding a solution of hydrogen fluoride to a solution of stable cerium chloride to which 10 mc of Ce^{140} had been added as the chloride. The resulting precipitate was centrifuged, and the supernatant liquid was discarded. The residue of cerium fluoride was transferred from the plastic centrifuge tube to an evaporating dish. The tagged fluoride salt was then dried in a vacuum-drying oven which was maintained at a temperature of 120°C.

The preparation of the tagged lanthanum fluoride included the separation of the La^{140} daughter from the isotopic Ba^{140} parent. This was accomplished by the addition of a large volume of fuming nitric acid to a small volume of solution which contained the barium and lanthanum isotopes and 20 mg of barium carrier. The reaction was carried out in a centrifuge tube which was cooled in an ice bath for 2 min after the addition of the nitric acid to the sample. The precipitate was then centrifuged to separate the insoluble barium nitrate from the soluble lanthanum nitrate. The supernatant liquid was then transferred to a second centrifuge tube.

The complete separation of the barium and the lanthanum was assured by the addition of barium carrier to the solution in the second centrifuge tube. The resulting precipitate was stirred and placed in an ice bath for 5 min. The precipitate was then centrifuged, and the supernatant liquid,

which contained approximately 3 mc of La^{140}, was added to a solution which contained 35 g of stable lanthanum as the nitrate. A solution of hydrogen fluoride was added to the solution of lanthanum nitrate. The resulting precipitate was centrifuged, and the supernate was discarded. The residue of lanthanum fluoride was transferred from the plastic centrifuge tube to an evaporating dish. The tagged fluoride salt was then dried in a vacuum-drying oven which was maintained at a temperature of 120° C.

DETERMINATION OF BORON IN GASES FROM THE REACTION OF BORON AND $NaF-ZrF_4-UF_4$

A. S. Meyer, Jr. G. Goldberg
W. J. Ross

In order to study the compatibility of elemental boron and $NaF-ZrF_4-UF_4$, the effluent gases from the reaction between these constituents were sampled to determine the concentration of boron as boron trifluoride in the gases. The boron was absorbed from the effluent gases by passing the gases through a scrubber which contained a 5% solution of sodium hydroxide. The scrubber consisted of a series of three 40-in. columns of $1\frac{1}{2}$-in. Tygon tubing which was supported in pyrex pipe. The absorber columns were packed with rings cut from $\frac{3}{8}$-in.-ID Tygon tubing. Boron was determined in the absorber solution by the carminic acid method. Approximately one-half the boron that had been added to the fluoride fuel as elemental boron was recovered from the absorber solution after a 3-hr period of sparging with helium. The details of this experiment have been reported.[9]

DETERMINATION OF METALLIC BORON IN MIXTURES OF FLUORIDE SALTS

A. S. Meyer, Jr. W. J. Ross

The method for the determination of boron[9] as the fluoride complex in mixtures of fluoride salts was modified to extend the application of the method to the determination of boron in fluoride salts in which the boron is present partially in the metallic state. Since elemental boron is not soluble in the solution of $AlCl_3$ and HCl which is used to dissolve the fluoride salts, it can be separated from the remainder of the sample solution by filtration. The boron in the filtrate is determined by the usual method.

The precipitate is treated with lime water to avoid loss of boron during the ignition of the filter paper. After the paper is ignited, the precipitate is fused with sodium carbonate, and then the melt is dissolved in hydrochloric acid. The boron in the resulting solution is determined directly by the carminic acid method.[9] The total boron is the sum of the boron found in the filtrate and that found in the residue.

COMPATIBILITY OF LUBRICANTS WITH MOLTEN ALKALI METALS AND FUSED FLUORIDE SALTS

A. S. Meyer, Jr. G. Goldberg

Tests were carried out to determine the compatibility of proposed lubricants for the ART pumps at 200° F with molten sodium and fused fluoride salts at 1100° F. The lubricants, Dowtherm-A, Cellulube, OS-45, Gulfspin-60, and Gulfcrest-34, were tested in an apparatus described previously,[10] in which small quantities of the high-temperature molten metal or salt are dropped into a reservoir of the lower temperature lubricant.

All the tests were carried out under an atmosphere of helium. With the exception of Cellulube, each of these lubricants was found to be inert both to sodium and to the fused fluorides salts. Cellulube (tricresyl phosphate) reacted vigorously with sodium with the evolution of a large volume of gas. A summary report of these experiments has been prepared.[11]

EXTRACTION OF ART FUEL COMPONENTS WITH ORGANO-PHOSPHORUS COMPOUNDS

W. J. Ross

Studies were continued of the analytical application of tri-*n*-octylphosphine oxide (TOPO) as a reagent for the concentration, separation, and determination of the components of ART fuels, corrosion products, and fission products. A study of the variables that influence the extraction of hexavalent chromium into solutions of TOPO in

[9] W. J. Ross, A. S. Meyer, Jr., and J. C. White, *Determination of Boron in Fluoride Salt*, ORNL-2135 (Aug. 7, 1956).

[10] A. S. Meyer, Jr., and G. Goldberg, *ANP Quar. Prog. Rep. Sept. 10, 1956*, ORNL-2157, p 129.

[11] G. Goldberg, A. S. Meyer, Jr., and J. C. White, *Compatibility of Pump Lubricants with Alkali Metals and Molten Fluoride Salts*, ORNL-2168 (Dec. 28, 1956).

organic solvents was completed. It was demonstrated that chromium can be concentrated one-hundredfold by a single extraction with 0.1 *M* TOPO in cyclohexane from solutions of HCl or H_2SO_4. Less efficient extractions can be carried out from solutions of HNO_3. The chromium is extracted as the complex $H_2Cr_2O_7 \cdot 2TOPO$.

The work of Blake *et al.*[12] has been extended by a systematic study of the variables that affect the extraction of UO_2^{++} into TOPO. These results have shown that 35 mg of UO_2^{++} can be extracted quantitatively in a single equilibration from 1 *M* HNO_3 into 0.5 mmole of TOPO in cyclohexane. Direct determination of UO_2^{++} in the organic phase can be carried out by measurement of the absorbance of the extract. Quantitative extraction of UO_2^{++} from solutions of sulfate, phosphate, and perchlorate can be achieved by making the aqueous solution 1 *M* with respect to HCl or HNO_3. The extraction is therefore a versatile method for the concentration of traces of UO_2^{++}.

A survey of the extractability of other ions which may be present as trace contaminants in ART fuels has been carried out to determine the selectivity of the reagent. Ions such as Ni^{++}, BO_2^-, Al^{+++}, the divalent alkaline-earth metals, and the trivalent rare-earth elements are not extracted by TOPO. No other elements were found to extract with partition coefficients comparable to those found for Cr^{6+}, Fe^{3+}, Zr^{4+}, and UO_2^{2+}. In an effort to find other selective extractants for application to the analysis of fused fluoride salt fuels, surveys of extractability with the other organophosphorus compounds are now being carried out.

The branched-chain phosphine oxide (*tris*-2-ethylhexylphosphine oxide) can be used to extract Fe^{+++} and UO_2^{++}, with partition coefficients comparable to those obtained with TOPO, but it is a less effective extractant for Cr^{6+} and Fe^{3+}. As was found with TOPO, ions such as Ni^{4+}, BO_2^-, Al^{3+}, the alkaline-earth metals, and the rare-earth elements are not extracted. Similar studies are now being carried out with trihexylphosphine oxide and di-2-ethylhexylphosphoric acid.

[12] C. A. Blake, K. B. Brown, and C. F. Coleman, *Solvent Extraction of Uranium (and Vanadium) from Acid Liquors with Trialkylphosphine Oxides*, ORNL-1964 (Nov. 4, 1955).

SERVICE LABORATORY

W. F. Vaughan

A total of 1358 samples was analyzed, which included 4601 determinations, for an average of 3.4 determinations per sample. A breakdown of the work is given below:

	Number of Samples	Number of Reported Results
Reactor Chemistry	693	2183
Experimental Engineering	502	2083
Metallurgy	17	23
Miscellaneous	146	312
Total	1358	4601

ANALYSES FOR CONTAMINANTS IN VERY PURE ARGON

J. R. Sites

C. E. Prather M. M. McMahan

Over 100 commercial cylinders of argon were sampled and checked on a mass spectrometer for contaminant gases in the parts-per-million range in an effort to find cylinders with less than 10 ppm of oxygen in the argon. In order to obtain reliable analyses for contaminants, all sampling must be done very carefully to prevent any addition of contaminant gases through in-leakage, especially of air. In the technique used, the cylinder to be tested is placed next to an auxiliary vacuum system and connected to it through a vacuum-tight pressure-reducing regulator and a double-ended gas-sample bulb. With the cylinder valve still closed, all the other valves, including the regulator valve, are opened, and the entire system is evacuated to at least 1×10^{-5} mm Hg. After this pressure is reached, the sample bulb is isolated from the vacuum system, and argon is carefully let into it and flushed through it to the atmosphere through a side stopcock. After 2 or 3 min of flushing, the two stopcocks on the sample bulb are closed. This sample of argon at atmospheric pressure is then put on the sample-inlet system of the gas mass spectrometer. After appropriate evacuation of the inlet system, the pressure in the expansion volume is increased until the A^{36} ion peak is nearly full scale on the "× 500" scale of the vibrating-reed electrometer. The VGIA ion gage rises from a base pressure of 4×10^{-8} mm

Hg to about 1.5×10^{-5} mm Hg. The scanning of the ion peaks is then accomplished in the normal way, including switching to the appropriate intensity ranges for each peak on the strip-chart recorder. The following ion peaks are scanned slowly: H_2 at mass 2, He at mass 4, CH_4 at mass 16, H_2O at mass 17 (doubly charged A^{36} precludes using mass 18 for H_2O), hydrocarbon at mass 27, N_2 at mass 28, O_2 at mass 32, argon at mass 36, and CO_2 at mass 44. Great care is taken not to let the enormous ion peaks of argon mass 40 and doubly charged A^{40} at mass 20 fall on the receiver slit, since their very large currents would cause unwanted effects in the 10^{10}-ohm electrometer-input resistor. The CO_2 peak is on the very large tail of the A^{40} peak.

The mass spectrometer must be clean so that it will have the minimum of residual background ion peaks, since their intensities must be subtracted from the mass spectrum obtained from the sample. The mass spectrometer has been calibrated for these contaminant gases, and the correction factors for their differences in ionization have been determined. An important feature of this method is that the relative abundance of the A^{36} isotope gives a "lever" of a factor of over 200 for total amount of argon.

A cylinder that has about 10 ppm of O_2 has been set aside as a control, and it is checked every few days in order to verify the delicate sampling technique and the day-to-day and week-to-week reproducibility of the mass spectrometer. The 95% confidence interval for 20 different loadings of this control is ±2 ppm out of 11 ppm. This interval even includes data taken when the mass spectrometer background was not so low as usual because of some "dirty" samples having been run. In the mass spectrometer used, it is impossible to separate N_2 and CO, which both have a mass of 28.

A few samples of helium were analyzed in the same manner, and the results are equally as good. In this case the electrometer-input resistor is switched to one, and there is 100 times less resistance for a "lever" on the very large helium peak at mass 4 than there is for A^{36}.

Part 3

METALLURGY

W. D. Manly

3.1. DYNAMIC CORROSION STUDIES

J. H. DeVan

FORCED-CIRCULATION LOOP TESTS

J. H. DeVan R. S. Crouse

Fuel Mixtures in Inconel

Effect of Flow Rate. – A comparison of corrosion results obtained from Inconel thermal-convection loops with those obtained from forced-circulation loops indicates that the flow rate has only a minor effect on the corrosion of Inconel by the fuel mixture (No. 30) $NaF-ZrF_4-UF_4$ (50-46-4 mole %). In order to further evaluate the effect of flow rate, three forced-circulation loops were operated under identical temperature conditions but with three different Reynolds numbers in the range 5,000 to 14,000. The conditions for these tests are given in Table 3.1.1. The operating period for each of the three loops was scheduled to be 1000 hr, but the initial loop with a high Reynolds number (loop 7425-19) operated for only 515 hr because of an instrument failure. A second loop (7425-24) was therefore operated with a high Reynolds number. Operation of this second loop was terminated by a pump failure, but 981 of the 1000 hr had been accumulated and it was therefore not considered necessary to make a third test.

The corrosion results presented in Table 3.1.1 show that the corrosion attack in the loop with the highest flow rate was slightly greater than the attack in the other loops. However, the table also shows that the attack in the loop operated at a Reynolds number of 5200 was worse than the attack in the loop operated at a Reynolds number of 9620. The small spread in the corrosion data and the lack of correlation between the flow rates and the depths of attack appear to confirm the previous observation that the effect of flow rate on corrosion is minor.

Effect of Temperature Drop. – Previous efforts to study the effect of temperature drop on attack in Inconel forced-circulation loops operated with the fuel mixture (No. 30) $NaF-ZrF_4-UF_4$ (50-46-4 mole %) gave rise to questionable results because of operational difficulties encountered in two of the tests involved.[1] The tests in question have been repeated with the operation of loops 7425-16 and 7425-10, and the operating conditions and corrosion results are presented in Table 3.1.2,

[1] J. H. DeVan, *ANP Quar. Prog. Rep. Dec. 10, 1955*, ORNL-2012, p 105.

TABLE 3.1.1. OPERATING CONDITIONS OF FORCED-CIRCULATION LOOP TESTS OF THE EFFECT OF FLOW RATE ON CORROSION OF INCONEL BY THE FUEL MIXTURE (NO. 30) $NaF-ZrF_4-UF_4$ (50-46-4 MOLE %)

Operating Conditions and Corrosion Results	Loop Number			
	7425-17	7425-18	7425-19	7425-24
Operating time, hr	1000	1000	515*	981**
Maximum fuel temperature, °F	1520	1510	1510	1515
Fuel temperature drop, °F	150	150	150	150
Maximum tube wall temperature, °F	1565	1565	1560	1570
Reynolds number of fuel	5200	9620	13,835	14,258
Fuel velocity, fps	3.49	6.49	9.32	9.61
Fuel flow rate, gpm	1.44	2.68	3.85	3.97
Maximum depth of attack, mils	4	3	3	6.5

*Terminated by instrument failure.

**Terminated by pump failure.

TABLE 3.1.2. OPERATING CONDITIONS AND RESULTS OF FORCED-CIRCULATION LOOP TESTS OF THE EFFECT OF TEMPERATURE DROP ON THE CORROSION OF INCONEL BY THE FUEL MIXTURE (NO. 30) $NaF-ZrF_4-UF_4$ (50-46-4 MOLE %)

Operating Conditions and Corrosion Results	Loop Number		
	7425-16	7425-10	4950-6
Operating time, hr	1040	1000	1000
Maximum fuel temperature, °F	1540	1500	1520
Maximum tube wall temperature, °F	1600	1580	1620
Temperature drop, °F	145	200	300
Reynolds number	10,000	10,000	8,000
Fuel velocity, fps	5.9	5.9	5.22
Maximum depth of attack, mils	4	4.5	8

along with similar data for loop 4950-6, which operated satisfactorily as part of the earlier series of tests. In the operation of these loops the maximum wall and fluid temperatures were maintained constant, insofar as possible, but different heat input and cooling rates were used to achieve the specified cold-zone temperatures and fluid temperature drops.

The temperature drops employed for this series of tests were 145, 200, and 300°F, and, as may be seen in Table 3.1.2, the depths of attack in the loops operated with the two lower temperature drops were quite similar and were significantly lower than the attack of the loop operated with a temperature drop of 300°F. This suggests that at the temperature levels employed temperature drops of above 200°F noticeably increase the attack and that temperature drops of below 200°F do not correspondingly reduce the attack. Such a conclusion supports a statement made previously[2] that the leaching of chromium from the hot leg is controlled by the rate of diffusion of chromium into the cold leg. In the loops with the higher cold-leg temperatures, which accompanied the smaller system temperature drops, the rate of diffusion of chromium into the cold leg was proportionately greater than in the loop with the lower cold-leg temperature. The increase in diffusion may have compensated for the loss in driving force toward mass transfer brought about by the lower temperature drop.

Effect of Operating Time. – A series of forced-circulation loops were recently operated under identical temperature conditions and for various periods of time in order to study the effect of time on the corrosion of Inconel by the fuel mixture (No. 30) $NaF-ZrF_4-UF_4$ (50-46-4 mole %). This series of tests supplemented an earlier series of tests operated for the same purpose but at a lower system temperature.[3] As may be seen in Table 3.1.3 in which the operating conditions and corrosion results of the latest series of tests are presented, the loops were operated with a maximum bulk fuel mixture temperature of 1600°F and a temperature drop of 300°F. Direct-resistance

[2] J. H. DeVan and R. S. Crouse, *ANP Quar. Prog. Rep. June 10, 1956*, ORNL-2106, p 134; W. R. Grimes, *ANP Quar. Prog. Rep. June 10, 1956*, ORNL-2106, p 96.

[3] G. M. Adamson and R. S. Crouse, *ANP Quar. Prog. Rep. Sept. 10, 1955*, ORNL-1947, p 95.

TABLE 3.1.3. OPERATING CONDITIONS AND RESULTS OF FORCED-CIRCULATION LOOP TESTS OF THE EFFECT OF TEST DURATION ON THE CORROSION OF INCONEL BY THE FUEL MIXTURE (NO. 30) $NaF-ZrF_4-UF_4$ (50-46-4 MOLE %)

Maximum fuel temperature: 1600°F
Maximum tube wall temperature: 1700°F
Fuel temperature drop: 300°F
Reynolds number: 6000
Ratio of hot-leg surface to total loop volume, $in.^2/in.^3$: 2.5

Loop No.	Operating Time (hr)	Maximum Attack (mils)
7425-23B	15	3
7425-23A	50	3
7425-23C	100	4
7425-21	304	4
7425-25	500	5
7425-22	1000	7
7425-9	3000	14

heating was used for all these tests, and the maximum wall temperatures, as measured on the external surface of the loop hot leg, were approximately 1700°F.

The test results are plotted in Fig. 3.1.1 as depth of attack vs operating time. The data indicate rapid attack during the first 15 hr and then a slower and relatively constant rate of attack thereafter. The slope of the straight line which approximates the curve of the data plotted in Fig. 3.1.1 indicates that the rate of attack after the first 15 hr is about 1 mil in 280 hr. Typical hot-leg sections of the loops are shown in Fig. 3.1.2. Chemical analyses of the fuel showed increases in chromium content during the first 50 hr of up to about 400 ppm, but subsequent analyses showed that the chromium content of the fuel mixture did not change appreciably with time of operation of the loop.

A comparison of these results with the results of the earlier tests in which a 1500°F maximum fluid temperature was used shows almost identical variations in attack with time. However, the loops tested previously had a smaller ratio of heated surface area to loop volume than that of the loops operated recently, and therefore a direct comparison of the results of the two series of tests on the basis of maximum depths of attack is not possible. If the difference in the ratio is considered, the series with the higher system temperature shows greater over-all removal of chromium from the hot leg, both during the first 15 hr of operation and subsequent periods.

Sodium in Various Structural Materials

Inconel. – Three Inconel forced-circulation loops were examined that had operated with sodium for 1000 hr at a hot-leg temperature of 1500°F. Cold-leg temperatures were used that produced temperature drops of 150, 300, and 400°F, respectively. The loops were of similar construction and each incorporated an oxide cold trap that was maintained at 300°F. The results of this series of tests are presented in Table 3.1.4. A definite increase in the amount of mass transfer with increased temperature drop is evident. The data, as plotted in Fig. 3.1.3, indicate an approximately linear relationship between temperature drop and

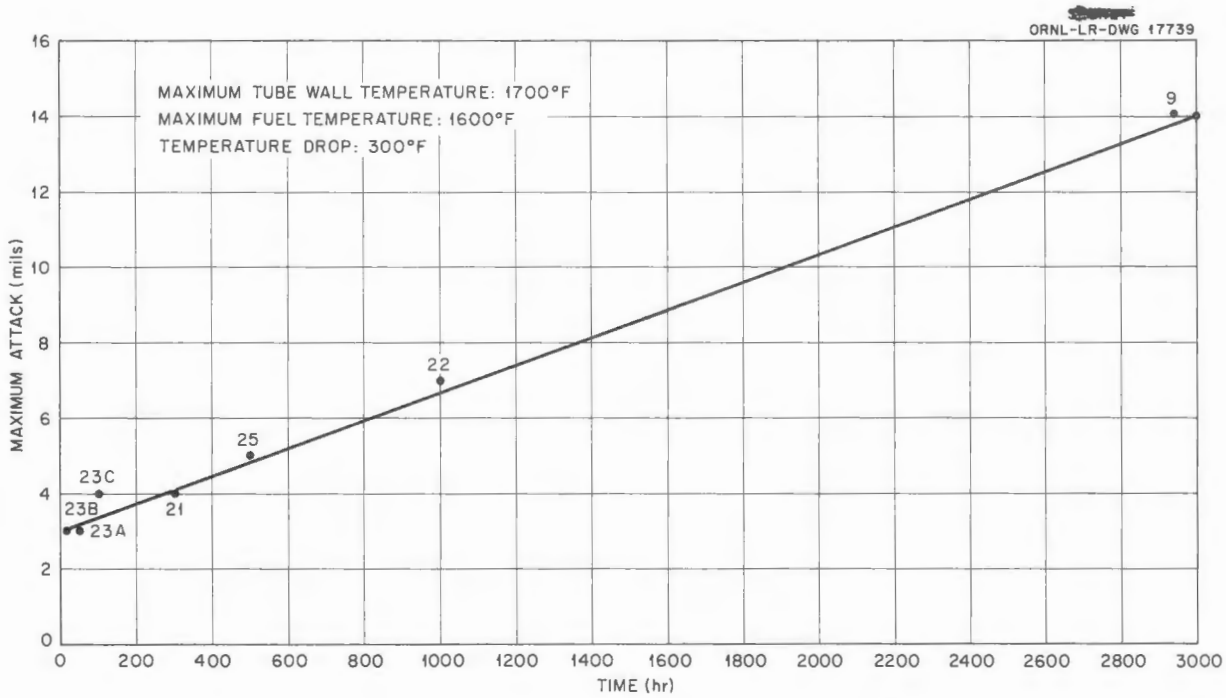

Fig. 3.1.1. Plot of Depth of Attack vs Operating Time for Inconel Forced-Circulation Loops Which Circulated the Fuel Mixture (No. 30) $NaF-ZrF_4-UF_4$ (50-46-4 mole %).

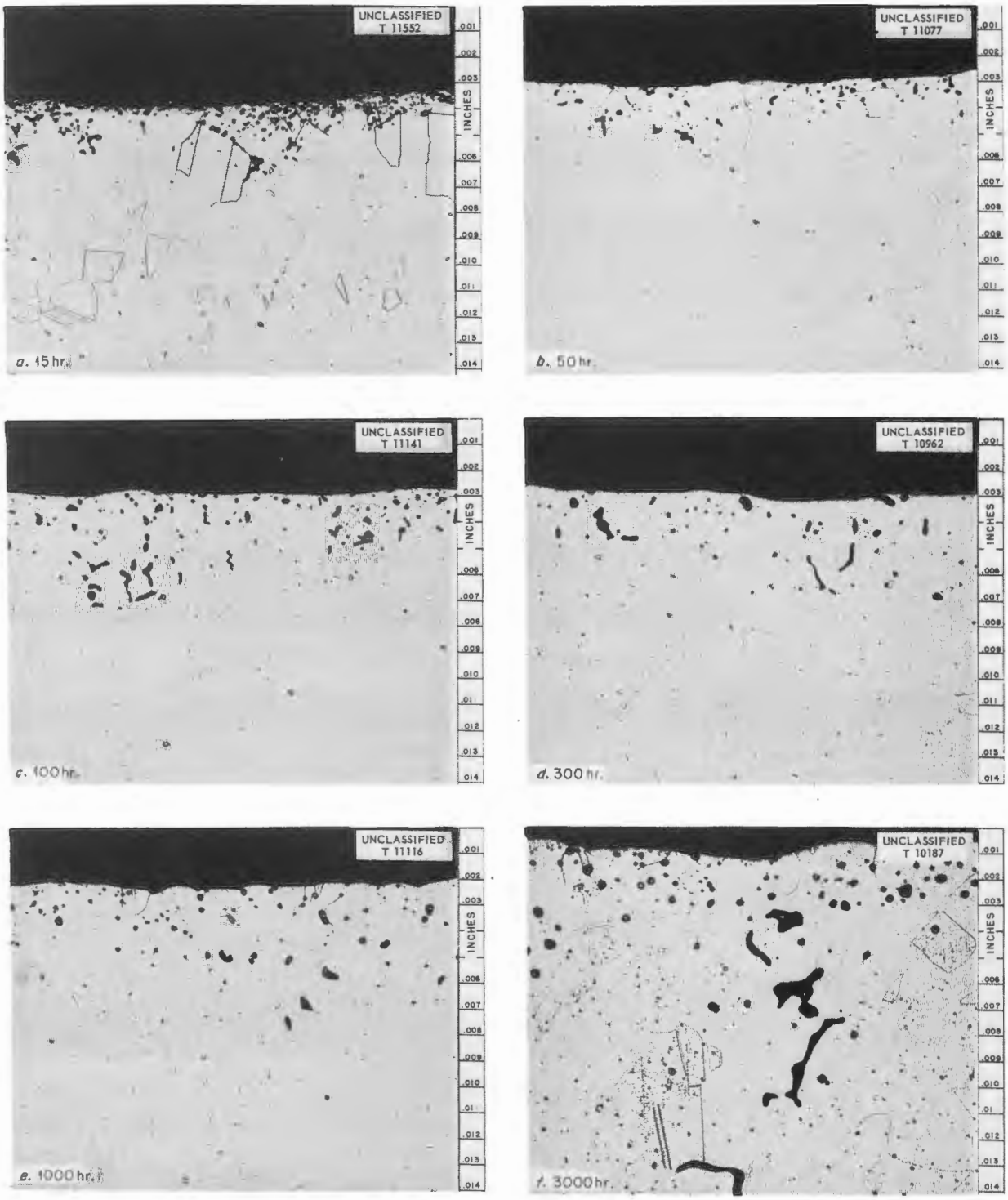

Fig. 3.1.2. Typical Hot-Leg Sections of Inconel Forced-Circulation Loops Operated with the Fuel Mixture (No. 30) $NaF-ZrF_4-UF_4$ (50-46-4 mole %) for Various Periods of Time. 250X. Reduced 31%. (Secret with caption)

TABLE 3.1.4. EFFECT OF TEMPERATURE DROP ON MASS TRANSFER IN INCONEL FORCED-CIRCULATION LOOPS OPERATED WITH SODIUM FOR 1000 hr

Loop No.	Temperature Drop (°F)	Maximum Thickness of Mass-Transferred Deposits (mils)	Total Weight* of Deposits (g)
7426-19	150	12	5.5
7426-6	300	18	15.0
7426-12	400	20	21.2

*Weight of material obtained by scraping deposits from loop walls.

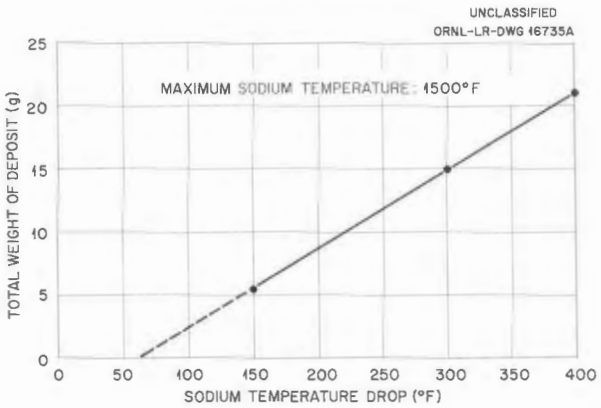

Fig. 3.1.3. Effect of Temperature Drop on Mass Transfer in Inconel Forced-Circulation Loops Operated with Sodium.

weight of mass-transferred deposit. All the deposits were found to be composed of approximately 90% nickel and 10% chromium.

A similar series of Inconel forced-circulation loops was operated to evaluate the effect on mass transfer of the addition of certain oxide formers to the sodium. The operating conditions for these loops and the test results are given in Table 3.1.5. The effect of adding magnesium was tested by exposing sodium to magnesium chips at a temperature of 800°F before introducing the sodium into the test loop. The sodium was kept at 800°F during the filling operation, and, if it is assumed that a saturated solution was attained, the magnesium concentration of the sodium was about 1%. Two analyses of the sodium which were made during filling indicated magnesium concentrations of 2.27 and 2.57 wt %, but these high values may possibly indicate that there was carry-over of the magnesium chips with the sodium. An oxide cold trap maintained at 300°F was used in the system, but it was valved off after the first 50 hr of operation. Flow through the cold trap had decreased during that period because of magnesium buildup at the entrance to the trap. After 1000 hr of operation at a hot-leg temperature of 1500°F and a temperature drop of 300°F, no difference could be seen in the amount of mass transfer in this loop as compared with that in a standard loop.

Inserts of titanium and zirconium were added to the hot legs of two other loops which were operated with sodium under similar temperature conditions. These loops too showed little difference in mass transfer as compared with a standard loop (see Table 3.1.5). The inserts, which were in the form of rods produced by the crystal-bar process, were composed of many incompletely joined crystals, and thus they provided relatively large surface areas. Intergranular hot-leg attack was found in these loops to a maximum depth of 1 mil.

Zirconium and titanium inserts were tested because of their oxide-gettering properties and because in certain other liquid metal systems they formed corrosion-resistant surface products on the loop walls. Metallographic examination of the loops failed, however, to show any surface layers which could be attributed to the presence of the inserts. In further experiments with these additions, finely divided powders are to be added directly to the liquid sodium.

Incoloy. – A forced-circulation loop constructed of Incoloy (34% Ni–20% Cr–bal Fe) tubing was operated with sodium for 1000 hr at a maximum sodium temperature of 1500°F. The temperature drop through the loop was 300°F, and the system included an oxide cold trap. Examination of the

TABLE 3.1.5. OPERATING CONDITIONS AND RESULTS OF FORCED-CIRCULATION LOOP TESTS OF THE EFFECTS ON MASS TRANSFER OF ADDING OXIDE FORMERS TO THE SODIUM CIRCULATED IN INCONEL

Maximum sodium temperature: 1500° F
Sodium temperature drop: 300° F

Loop No.	Type of Addition	Maximum Thickness of Mass-Transferred Deposits (mils)	Total Weight of Loop Deposit (g)
7426-16	Magnesium (1%) added directly to sodium	14	16
7426-20	Titanium insert added in loop hot leg	23	15
7426-21	Zirconium insert added in loop hot leg	13.5	13
7426-6	Standard loop with cold trap maintained at 300° F	11	15

loop revealed mass-transferred deposits in the colder portions of the loop that were similar to those found in Inconel loops. The deposits, however, in contrast to those in Inconel loops, did not adhere to the loop walls and they fell off when the loop was sectioned. Metallographic specimens did not therefore accurately reveal the extent of such deposits and thickness measurements could not be obtained. Chemical analyses of the deposits showed them to be predominantly nickel and chromium (in approximately equal amounts) with 1 to 4% iron. The hot-leg attack was similar to that found in Inconel loops, that is, intergranular attack to a depth of 2 mils.

Hastelloy B. – A Hastelloy B loop which operated 1000 hr with sodium was also examined. The loop (7642-51) had a gas-fired heat source and was operated with a maximum sodium temperature of 1500°F and a temperature drop of 300°F. Because of the limited amount of tubing available, it was not possible to adhere to the conventional loop design, and therefore the test results cannot be compared directly with those from standard Inconel loops. However, the nature and the extent of the mass-transferred deposits were, in general, similar to the nature and extent of the deposits found in standard Inconel loops, and therefore it appears that the sodium corrosion problem in Hastelloy B systems will be similar to the problem in Inconel systems.

The hot-leg attack appeared as uniform surface removal to a maximum depth of 1.5 mils, as shown in Fig. 3.1.4. Preferential attack along grain boundaries, which is characteristic of Inconel-sodium systems, was absent in this Hastelloy B–

Fig. 3.1.4. Hot-Leg Attack in Hastelloy B Forced-Circulation Loop Operated with Sodium for 1000 hr at 1500°F. 250X. Reduced 32%.

sodium system. In fact much of the second-phase material present in the grain boundaries and as precipitates throughout the metal was quite resistant to attack and remained unaltered in the corroded areas, even though the surrounding metal had been entirely removed. Metal deposits were present in the cold leg to a maximum thickness of 12 mils and were found by analyses to be 97.5% nickel, with traces of chromium, iron, manganese, and vanadium. Molybdenum was present in the deposits in the amount of only 0.06%.

HEAT EXCHANGER TEST EQUIPMENT

J. H. DeVan R. S. Crouse

Specimens from a gas-fired heater coil used in conjunction with intermediate heat exchanger test

stand A were examined to determine whether replacement of the coil would be required before the heater is operated as a heat source for the Engineering Test Unit. The heater is constructed of Inconel and has been operated with NaK for approximately 2700 hr. Fluid temperatures in the heater have varied from 1200 to 1600°F, with the majority of the operation having been in the range of 1400 to 1500°F. No surface changes other than removal of oxide films could be seen upon visual examination of the specimens. A specimen from the hottest point in the heater was found metallographically to be attacked intergranularly to a depth of 1.5 mils; however, no evidence of surface removal could be detected from wall-thickness measurements.

THERMAL-CONVECTION LOOP TESTS

E. A. Kovacevich D. A. Stoneburner

Special Nickel-Molybdenum Alloy Loops

A series of thermal-convection loops constructed from 0.5-in.-ID, 0.035-in.-wall tubing fabricated from several nickel-molybdenum base alloys were operated with the fuel mixture (No. 107) NaF-KF-LiF-UF_4 (11.2-41-45.3-2.5 mole %) and with sodium at 1500°F. The compositions of the alloys used are given in Table 3.1.6, and the operating conditions and results of the tests are given in Table 3.1.7.

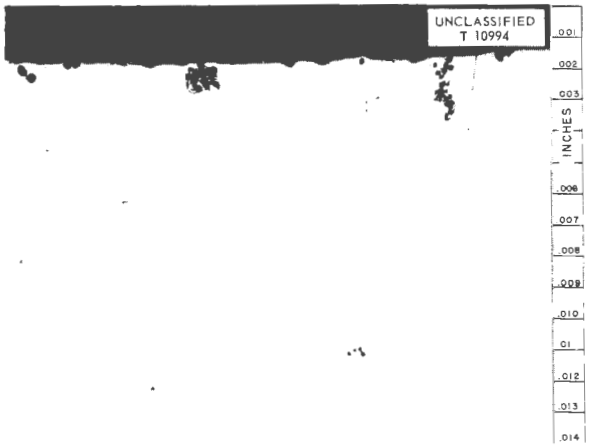

Fig. 3.1.5. Maximum Hot-Leg Attack in Loop (1025) Fabricated from a Nickel-Molybdenum Alloy (11% Mo–2% Al–bal Ni) and Operated with the Fuel Mixture (No. 107) NaF-KF-LiF-UF_4 (11.2-41-45.3-2.5 mole %) at 1500°F for 1000 hr. 250X. Reduced 32%. (Secret with caption)

TABLE 3.1.6. COMPOSITIONS OF NICKEL-MOLYBDENUM ALLOYS FROM WHICH THERMAL-CONVECTION LOOPS WERE FABRICATED

Loop No.	Heat No.	Composition (wt %)
1024 1025	1491	11.2 Mo–2.2 Al–0.1 Co–bal Ni
1066 1067	30-1	16.9 Mo–2.8 Cr–80.1 Ni
1068 1071 1075	30-2	16.7 Mo–4.6 Cr–77.6 Ni
1069	37A-1	20.4 Mo–2.6 Cr–bal Ni
1070	T-23012	17.4 Mo–0.17 Al–bal Ni
1076 1077	30-4	16.4 Mo–9.2 Cr–72.7 Ni
1078	B-2898	20.5 Mo–0.84 Mn–1.31 Nb–2.44 Ti–74.0 Ni
1079	43A-3	20.3 Mo–6.3 Cr–bal Ni
1080	T-23014	16.7 Mo–2.1 Ti–0.57 Al–bal Ni
1081	T-23011	15.1 Mo–3.8 Cr–2.7 Nb–3.2 W–0.13 Al–bal Ni
1082	T-23013	15.2 Mo–4.0 Nb–3.2 W–0.27 Al–bal Ni

The two loops (1024 and 1025) constructed from an alloy containing approximately 2% aluminum showed maximum hot-leg attack of 2 mils (Fig. 3.1.5) after 1000 hr of operation with fuel mixture No. 107 at 1500°F. The attack occurred as heavy surface pitting and shallow subsurface-void formation. The cold legs of both loops were found metallographically to have only light surface roughening, and no cold-leg deposits were visible in either loop.

Although the corrosion attack in these loops was relatively light, it should be noted (Table 3.1.8) that the chemical analyses of the fuel mixture indicate the aluminum pickup in the fuel to be high. This high concentration of aluminum is considered to be undesirable because of the ability of aluminum to reduce the UF_4 in the fuel to UF_3. Disproportionation of UF_3 could result in some diffusion of metallic uranium into the container walls.

Loops 1067, 1068, 1069, 1079, and 1076, which were constructed from alloys containing approximately 3, 5, 7, or 10 wt % chromium, were also evaluated after having circulated fuel No. 107. These tests were run to establish the amount of chromium which can be present in a nickel-molybdenum system without seriously detracting from the corrosion resistance of the alloy in the fuel mixture. Although the attack in each loop was 1 mil or less, the chromium pickup by the fuel, as shown in Fig. 3.1.6, increased noticeably as the chromium content of the alloy increased. The reason for the increased chromium content of the fuel can be seen by comparing Figs. 3.1.7 and 3.1.8, which show the maximum attack in the alloys containing approximately 5% and 10%

TABLE 3.1.7. RESULTS OF METALLOGRAPHIC EXAMINATIONS OF NICKEL-MOLYBDENUM THERMAL-CONVECTION LOOPS OPERATED WITH FUEL NO. 107 AND WITH SODIUM AT 1500°F

Loop No.	Heat No.*	Circulated Fluid	Operating Time (hr)	Metallographic Notes	
				Hot Leg	Cold Leg
1024	1491	Fuel No. 107	1000	Heavy surface pitting and voids to a depth of 2 mils	Light surface roughening
1025	1491	Fuel No. 107	1000	Heavy surface pitting and voids to a depth of 2 mils	Light surface roughening
1066	30-1	Sodium	290**	Intergranular voids to a depth of 4 mils	Light surface roughening
1067	30-1	Fuel No. 107	500	Few pits to a depth of 1 mil	No attack
1068	30-2	Fuel No. 107	500	Surface pitting to a depth of 1 mil	Few voids to a depth of 1 mil
1069	37A-1	Fuel No. 107	500	Few pits to a depth of 1 mil	Light surface roughening to a depth of 1 mil
1070	T-23012	Fuel No. 107	500	Few subsurface voids to a depth of less than 1 mil	No attack
1071	30-2	Sodium	1000	Heavy, shallow, surface roughening to a depth of less than 1 mil	Light surface roughening
1075	30-2	Fuel No. 107	1000	Heavy voids to a depth of 1 mil	Light surface roughening
1076	30-4	Fuel No. 107	500	Heavy subsurface voids to a depth of less than 1 mil	Light surface roughening
1077	30-4	Sodium	1000	Light surface roughening to a depth of 1 mil	Light surface roughening
1078	B-2898	Fuel No. 107	500	Few voids to a depth of 1 mil	No attack
1079	43A-3	Fuel No. 107	500	Few pits to a depth of 1 mil	No attack
1080	T-23014	Fuel No. 107	500	Few voids to a depth of 1 mil	Light surface roughening
1081	T-23011	Fuel No. 107	500	Heavy subsurface voids to depth of 2.5 mils	No attack
1082	T-23013	Fuel No. 107	500	Heavy surface roughening to a depth of less than 1 mil	No attack

*See Table 3.1.6 for compositions.

**Terminated because of a leak.

TABLE 3.1.8. CHEMICAL ANALYSES OF FUEL NO. 107 BEFORE AND AFTER CIRCULATION IN NICKEL-MOLYBDENUM THERMAL-CONVECTION LOOPS 1024 AND 1025 FOR 1000 hr AT 1500°F

Loop No.	Sample Taken	Uranium Content (wt %)	Impurity Analysis (ppm)				
			Mo	Al	Ni	Cr	Fe
1024	During Filling	12.4	6		150	40	140
	After operation*						
	Hot leg	11.4	100	2100	95	25	115
	Cold leg	11.0	55	2695	60	30	155
1025	During filling	12.7	2		240	80	170
	After operation*						
	Hot leg	12.1	60	1725	50	50	105
	Cold leg	12.3	25	2920	190	60	75

*No cobalt detected.

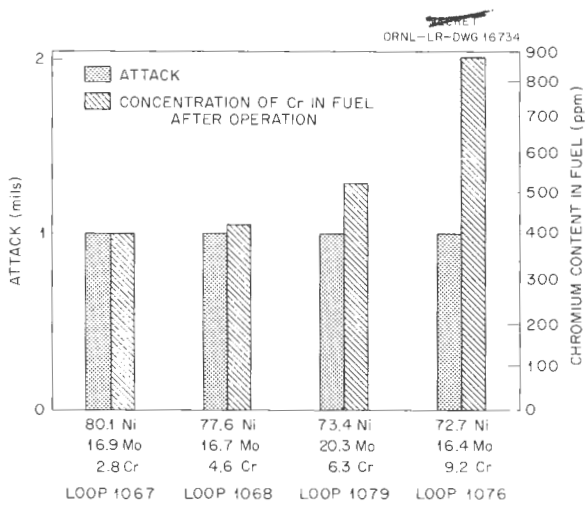

Fig. 3.1.6. Corrosion Results of Thermal-Convection Loop Tests of Special Nickel-Molybdenum Alloys Exposed to the Fuel Mixture (No. 107) NaF-KF-LiF-UF_4 (11.2-41-45.3-2.5 mole %) at 1500°F for 500 hr.

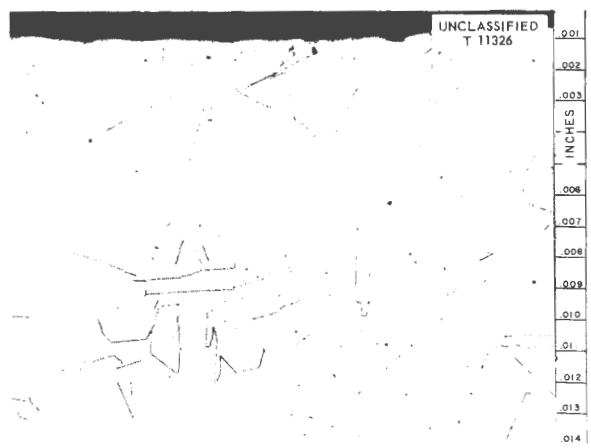

Fig. 3.1.7. Hot Leg of Loop (1068) Fabricated from a Nickel-Molybdenum Alloy Containing ~5% Chromium After Circulating Fuel No. 107 at 1500°F for 500 hr. 250X. Reduced 32%. (Secret with caption)

chromium. Although the depths of attack are similar, the concentration of the attack is higher in the alloy containing approximately 10% chromium.

An additional loop (1075) was constructed from the same material as that used for loop 1068 (nominal composition: 5% Cr–17% Mo–bal Ni), but it was operated an additional 500 hr with fuel No. 107. The longer operating period produced no increase in depth of attack, as compared with loop 1068, but, again, the concentration of the attack was increased, as shown in Fig. 3.1.9. Additional loops fabricated from alloys with various chromium concentrations are being operated for 1000 hr to substantiate this result. No cold-leg deposits were found in the loops.

Loop 1082, which was fabricated from a nickel-molybdenum alloy containing niobium, aluminum, and tungsten, and loop 1081, which was fabricated from an alloy containing similar additions plus

Fig. 3.1.8. Hot Leg of Loop (1076) Fabricated from a Nickel-Molybdenum Alloy Containing ~10% Chromium After Circulating Fuel No. 107 at 1500°F for 500 hr. 250X. Reduced 32%. (Secret with caption)

Fig. 3.1.9. Hot Leg of Loop (1075) Fabricated from a Nickel-Molybdenum Alloy Containing ~5% Chromium After Circulating Fuel No. 107 at 1500°F for 1000 hr. 250X. Reduced 32%. (Secret with caption)

3.8 wt % chromium, showed considerable differences in attack. A maximum attack of 2.5 mils was recorded for loop 1081, which contained the chromium addition, whereas the attack was to a depth of less than 1 mil in loop 1082. Further, loop 1082 showed somewhat more attack than loop 1068, which was fabricated from an alloy containing a similar chromium addition but not the other alloying elements. No cold-leg deposits were visible in either loop.

The other loops listed in Table 3.1.7 (1070, 1078, 1080), which were fabricated from alloys that contained various amounts of aluminum, niobium, or titanium, revealed negligible attack by fuel No. 107. In all the loops, the attack occurred predominantly as pitting, accompanied by a limited amount of subsurface-void formations.

Loops 1066, 1071, and 1077, which were fabricated from alloys that contained various chromium additions, were operated with sodium at 1500°F for 1000 hr. With the exception of loop 1066, which was terminated by a leak after 290 hr, all the loops operated the scheduled 1000-hr period. The attack in loop 1071 occurred as heavy surface roughening to a depth of less than 1 mil, as compared with light surface roughening to a depth of 1 mil in loop 1077. Macroexamination of these loops showed a small amount of mass transfer of as yet undetermined composition.

Special Fuel Mixtures in Inconel

Screening tests of special fluoride mixtures were completed for fuels Nos. 93, WR9, and WR12, whose compositions are given in Table 3.1.9. These tests were made with standard Inconel thermal-convection loops, and the mixtures were circulated at a maximum fluid temperature of 1500°F. Metallographic results of these tests are also presented in Table 3.1.9.

The results obtained for fuel No. 93 in loops 994 and 995 show less attack than that found previously[4] for this fuel under similar conditions. The attack remains, nevertheless, the highest found with the alkali-metal fluoride systems (Group 1), as was stated previously. Another loop (997), which operated with fuel WR9, was also a repeat test, and slightly more attack was found than was reported previously for this fuel under similar conditions. Segregation of fuel constituents was observed in all the tests of fuel WR9 and may account for the difference in test results.

Loops 946 and 947, which operated 500 hr with fuel WR12, showed essentially the same type and amount of attack as was found previously[4] in loops which operated with fuel WR7, $NaF-ZrF_4-UF_4$ (60-35-5 mole %). An increase of 5 mole % in the UF_4 content of the ZrF_4-base mixture apparently did not significantly increase the attack, although this result contradicts the known effects of UF_4 in such fuels. Cold-leg deposits were also observed in these loops.

[4]E. A. Kovacevich and J. H. DeVan, *ANP Quar. Prog. Rep. Sept. 10, 1956*, ORNL-2157, p 146.

TABLE 3.1.9. RESULTS OF METALLOGRAPHIC EXAMINATIONS OF STANDARD INCONEL THERMAL-CONVECTION LOOPS WHICH CIRCULATED SPECIAL FUEL MIXTURES AT 1500°F FOR 500 hr

Loop No.	Code Designation of Circulated Fluid	Composition of Circulated Fluid (mole %)	Metallographic Results	
			Hot-Leg Attack (mils)	Cold-Leg Appearance
994	93	50 LiF–46 ZrF_4–4 UF_4	13	Metallic crystals
995	93	50 LiF–46 ZrF_4–4 UF_4	13	Metallic crystals
997	WR9	60 NaF–14 ZrF_4–26 UF_4	14	No deposits
946	WR 12	58 NaF–32 ZrF_4–10 UF_4	10	Metallic layer
947	WR 12	58 NaF–32 ZrF_4–10 UF_4	11	Metallic layer

3.2. GENERAL CORROSION STUDIES

E. E. Hoffman

TESTS OF INCONEL TUBE-TO-HEADER JOINTS WITH RECRYSTALLIZED WELDS

D. H. Jansen

Additional Inconel tube-to-header joints with recrystallized welds were tested in NaK (56-44 wt %) and in the fuel mixture (No. 30) $NaF-ZrF_4-UF_4$ (50-46-4 mole %). The method used to fabricate these joints, which were supplied by the Glenn L. Martin Co., and the results of earlier tests were described previously.[1] The joints, as illustrated in Fig. 3.2.1, are of the "flange-during-welding" type, and they have, in addition, a fusion weld.

Corrosion tests of the specimens were conducted by exposing them to the test fluid in the tilting-furnace apparatus at a hot-zone temperature of 1500°F for 100 hr. No attack was observed on the weld metal or on the parent material of the specimen tested in NaK. A uniform attack to a depth of 2 mils was observed on the Inconel tube and the header of the specimen tested in the fuel mixture, but attack on the weld metal was nonuniform and spotty, and it was found to be about 1 mil in depth. Metallographic samples of the as-tested specimen are shown in Figs. 3.2.2 and 3.2.3.

[1] D. H. Jansen, *ANP Quar. Prog. Rep. Sept. 10, 1956*, ORNL-2157, p 149.

TESTS OF COAST METALS BRAZING ALLOYS

D. H. Jansen

Corrosion tests of Coast Metals brazing alloy No. 53 (81% Ni–8% Cr–4% Si–4% B–3% Fe) and Coast Metals brazing alloy No. 52 (89% Ni–5% Si–4% B–2% Fe) were continued in an effort to obtain

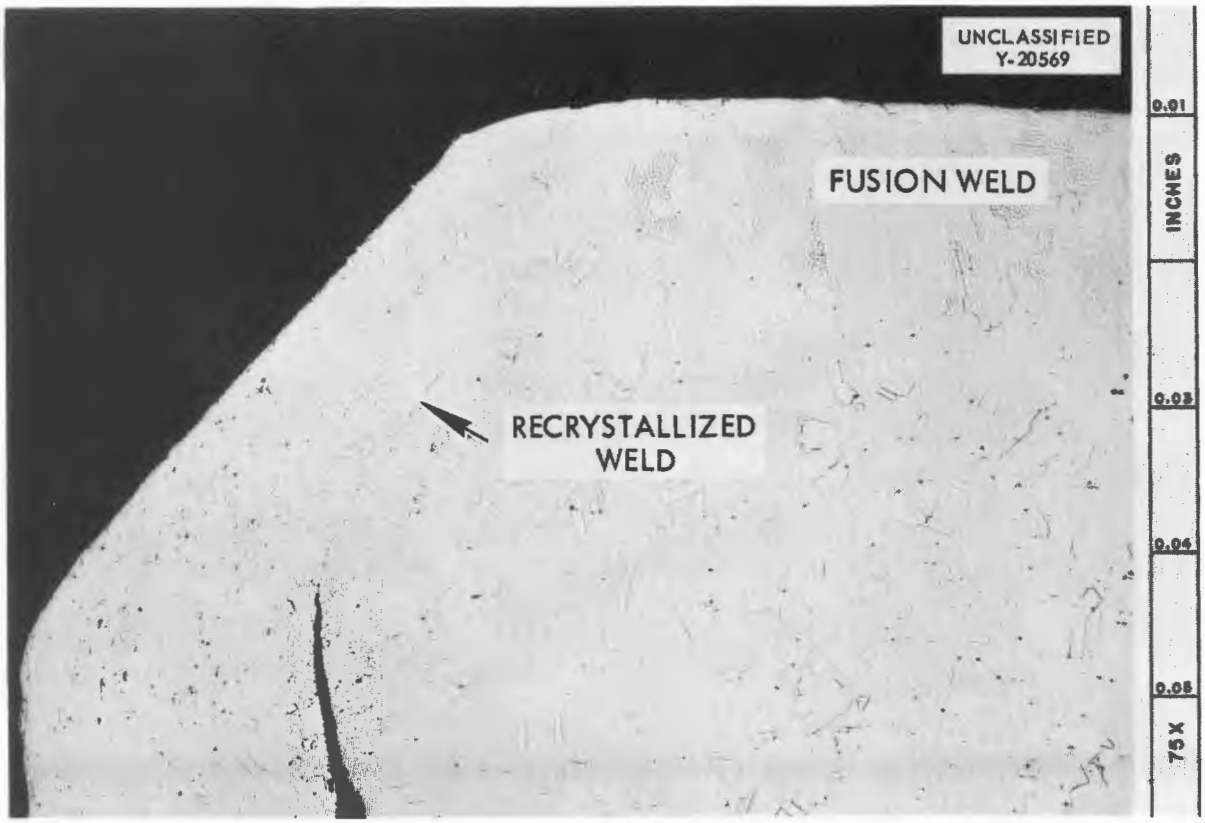

Fig. 3.2.1. As-Received Inconel Tube-to-Header Joint Fabricated by the Standard "Flange-During-Welding" Method and with an Additional Fusion Weld. Etchant: aqua regia. 75X.

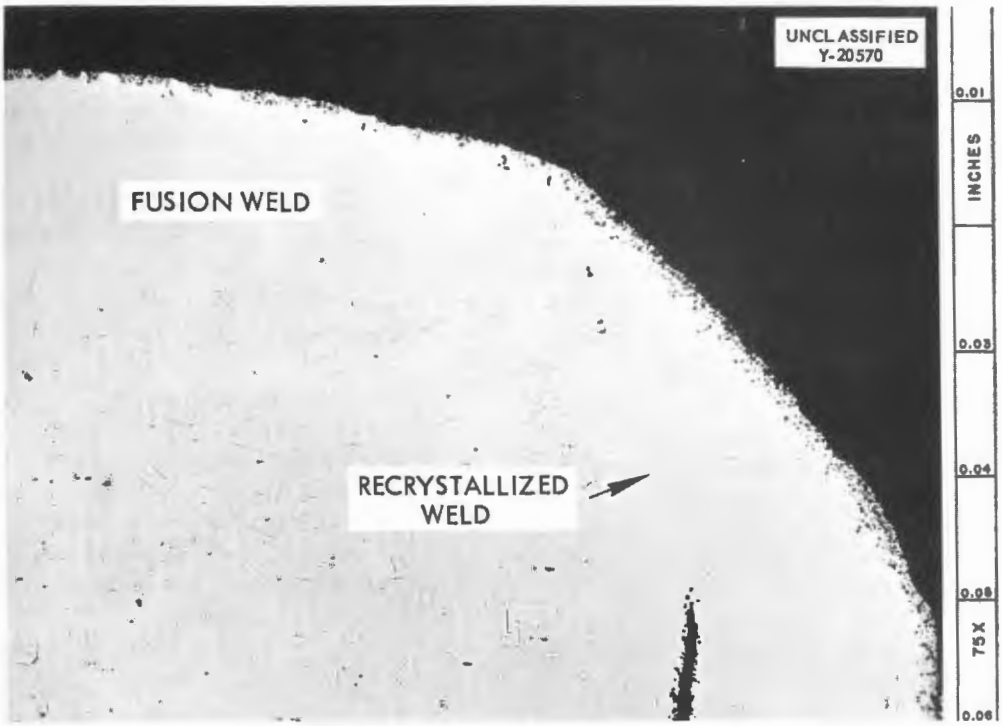

Fig. 3.2.2. Inconel Tube-to-Header Joint After Exposure to $NaF-ZrF_4-UF_4$ (50-46-4 mole %) at 1500°F for 100 hr. Etchant: aqua regia. 75X. Reduced 12%. (Secret with caption)

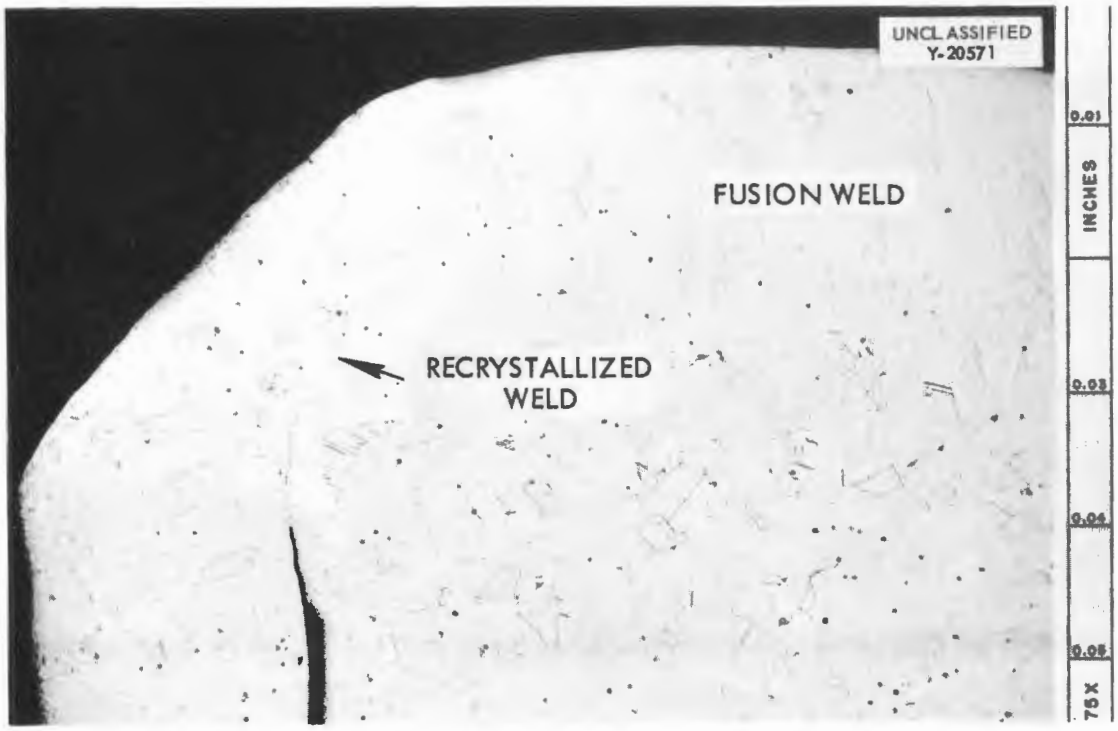

Fig. 3.2.3. Inconel Tube-to-Header Joint After Exposure to NaK (56-44 wt %) at 1500°F for 100 hr. Etchant: aqua regia. 75X. Reduced 6%.

further information on the rate at which boron is depleted from the surface of the brazing alloy when it is exposed to NaK or to a fused salt fuel mixture. The results of some preliminary corrosion tests of alloy No. 53 in NaK (56-44 wt %) and in $NaF-ZrF_4-UF_4$ (53.5-40-6.5 mole %) were reported previously.[2] In the recent tests both the alloys (Nos. 52 and 53) were exposed to both test mediums for 100 hr at 1400, 1500, and 1600°F and at 1500°F for 500 and 1000 hr. The specimens were examined metallographically, and microspark traverses were conducted on polished cross sections in order to detect variations in the boron compositions. In all the tests conducted to date, the depth of depletion of boron increased as the test temperature was increased and became more severe when the exposure time was increased from 100 to 500 hr, as shown in Fig. 3.2.4.

Metallographic results indicate that boron is leached from Coast Metals brazing alloy No. 52 (89% Ni–5% Si–4% B–2% Fe) to a depth of 4 mils in 1000 hr by $NaF-ZrF_4-UF_4$ (53.5-40-6.5 mole %) at 1500°F in seesaw apparatus. This depth of leaching was approximately the same as that found after a similar test of 500 hr.

For all the tests conducted to date, the ratio of the surface area of the specimen to the volume of the test fluid has been 0.83 in.^{2}/in.^{3}, in contrast to the 0.08-in.^{2}/in.^{3} value proposed for the ART. Therefore a special 500-hr test was conducted for which a 0.25-in. cube of the alloy was used and the volume of test fluid was adjusted to obtain a surface-area-to-volume ratio of 0.08 in.^{2}/in.^{3} in order to determine whether the depth of boron removal would be greater with a large volume of the test fluid present. Metallographic results show that the boron depletion extended to about the same depth as on the specimens tested with the higher surface-area-to-volume ratio. Microspark-traverse analyses of the test fluid and examinations of microdrillings from the edge of the alloy have not yet been completed.

[2]D. H. Jansen, *ANP Quar. Prog. Rep. Sept. 10, 1956*, ORNL-2157, p 152.

TESTS OF SPECIAL NICKEL-MOLYBDENUM ALLOYS

D. H. Jansen

A specimen of a special nickel-molybdenum alloy (17% Mo–3% Cr–0.075% C–bal Ni) was exposed to the fuel mixture (No. 107) $NaF-KF-LiF-UF_4$ (11.2-

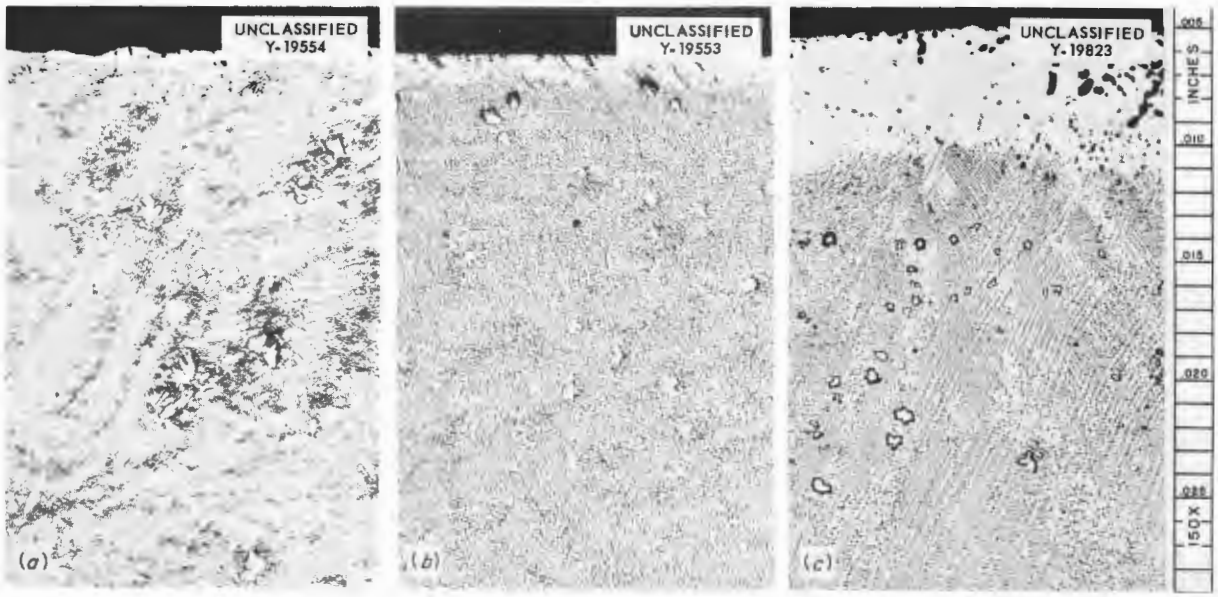

Fig. 3.2.4. Coast Metals Brazing Alloy No. 53 (81% Ni–8% Cr–4% Si–4% B–3% Fe) After Exposure in Seesaw Apparatus to $NaF-ZrF_4-UF_4$ (53.5-40-6.5 mole %) at (*a*) 1400°F for 100 hr, at (*b*) 1500°F for 100 hr, and at (*c*) 1500°F for 500 hr. Etchant: 10% oxalic acid. 150X. Reduced 17%. (Secret with caption)

41-45.3-2.5 mole %) for 1000 hr in seesaw apparatus with a hot-zone temperature of 1600°F and a cold-zone temperature of 1350°F. The container and the specimen were fabricated from the same alloy.

One purpose of this test was to determine the possibility of using the seesaw apparatus for screening tests of the nickel-molybdenum alloys in fuel No. 107. A thermal-convection loop made of the same material was attacked to a depth of 1 mil by this fuel mixture, whereas the specimen described above showed no attack after the seesaw test. Therefore, the seesaw test would not be a suitable screening test for nickel-molybdenum alloys in fuel No. 107.

A chemical analysis of the fuel mixture removed from the seesaw test capsule showed 0.089% Ni, 0.12% Cr, and 0.10% Mo. Since the specimen and test container were of the same material, the impurities in the fuel cannot be attributed to the specimen alone. The specimen, which was confined in the hot zone during the test, showed a weight loss of 0.13%. Metallographic examination of the specimen and of the capsule walls after the seesaw test showed no pits or irregularities on the surface, and therefore any removal of material from the surface was extremely uniform.

INCONEL–GRAPHITE–FUSED SALT SYSTEMS

W. H. Cook

An Inconel–graphite[3]–NaF-ZrF_4-UF_4 (50-46-4 mole %) system and an Inconel–NaF-ZrF_4-UF_4 (50-46-4 mole %) system were tested for 100 hr in seesaw apparatus with hot- and cold-zone temperatures of 1500 and 1250°F in order to determine whether the graphite would "tie up" the chromium in the Inconel as carbides and thus affect the depth of corrosion attack. The test results indicated that the presence of the graphite had no effect on the depth of corrosion of the Inconel. No attack of the graphite by the fused salt was detected. Essentially the same results were reported previously[4] for the compatibility of C-18 graphite and fluoride fuel mixtures at a lower temperature, 1112°F.

Two identical capsules made from 1-in. sched-40 Inconel pipe and loaded with equal quantities of the fused salt were used for the seesaw tests. One of the capsules was used as a control, and a ¼-in.-dia, 18-in.-long C-18 graphite rod was suspended in the other. Metallographic examinations of the two capsules showed typical fused salt attack to an average depth of 2 mils in the hot zones and no attack in the cold zones. This similarity in attack was substantiated by chemical analyses of the fused salts (Table 3.2.1).

Etchants and hardness tests revealed no detectable difference between the control and test capsules. There was a slight increase in hardness in both capsules as compared with the hardness of untested hydrogen-fired Inconel, but the etchants did not show signs of carburization. Examination of the C-18 graphite rod showed that it had sagged approximately ⅛ in. from its longitudinal center line; it had gained 1.28% in weight (presumably as the result of a thin fused-salt-vapor deposit); it had increased 0.06% in diameter (average of 16 values); there was no fused salt in the pores (based on metallographic examination); the structure had not been altered; and there were no signs of attack. A test of a similar Inconel–fused salt system with 0.25% of amorphous carbon added to the fused salt is planned.

[3] Commercial grade C-18.

[4] H. J. Buttram and G. F. Schenck, *ANP Quar. Prog. Rep. June 10, 1956*, p 125.

TABLE 3.2.1. CHEMICAL ANALYSES OF SAMPLES OF FUSED SALT FROM THE INCONEL–GRAPHITE–NaF-ZrF_4-UF_4 (50-46-4 MOLE %) SYSTEMS SEESAW TESTED FOR 100 hr AT A HOT-ZONE TEMPERATURE OF 1500°F

Source of Fused Salt Analyzed	Impurities Found (wt %)			
	Ni	Cr	Fe	C
As-received	0.002	<0.001	0.022	0.79
Control capsule without C-18 graphite rod	<0.001	0.008	0.008	0.63
Test capsule with C-18 graphite rod	<0.001	0.007	0.009	1.11

FUSED CHLORIDE CORROSION OF NICKEL AND INCONEL

D. H. Jansen

Screening tests of nickel and Inconel exposed to the fused chloride system $NaCl$-$MgCl_2$-UCl_3 (50-33.3-16.7 mole %) were performed. One set of Inconel and nickel capsules loaded with the chloride bath was tested in seesaw apparatus for 100 hr at a hot-zone temperature of 1800°F, and the second set of capsules was tested for 500 hr at a hot-zone temperature of 1350°F.

Both the Inconel and the nickel capsules tested at 1800°F showed evidence of mass-transferred crystals, the nickel capsules having the greater amount, as shown in Fig. 3.2.5. The hot zone of the inconel capsule showed a maximum attack of 2 mils in the form of subsurface voids, as shown in Fig. 3.2.6. The attack was thus similar to the attack of Inconel exposed to fused fluoride mixtures.

UNCLASSIFIED
Y-19663

UNCLASSIFIED
Y-19664

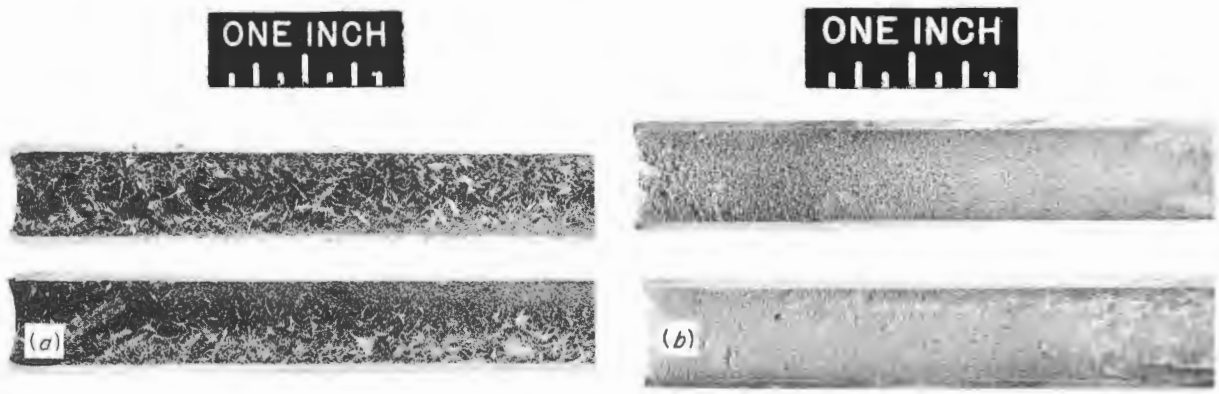

Fig. 3.2.5. Cold-Zone Portions of (*a*) Nickel and (*b*) Inconel Capsules Exposed to $NaCl$-$MgCl_2$-UCl_3 (50-33.3-16.7 mole %) in Seesaw Apparatus with a Hot-Zone Temperature of 1800°F for 100 hr. 1.2X. Reduced 9%. (Secret with caption)

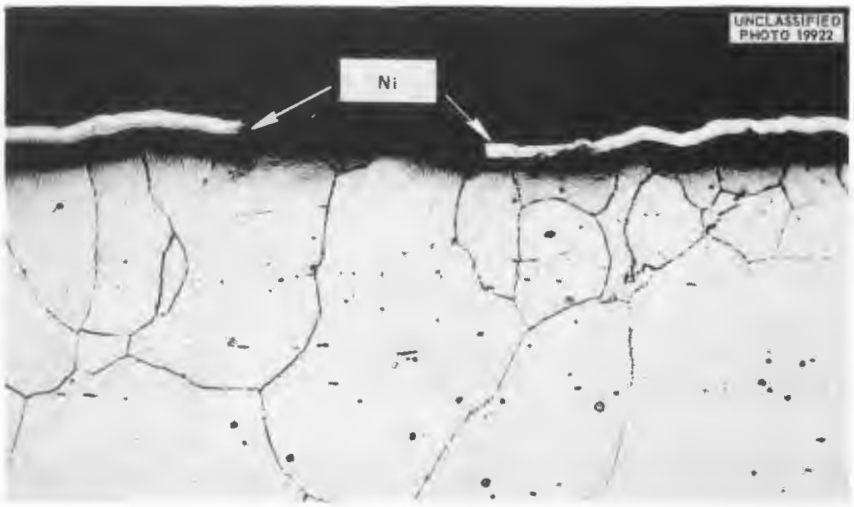

Fig. 3.2.6. Hot Zone from Inconel Capsule Exposed to $NaCl$-$MgCl_2$-UCl_3 (50-33.3-16.7 mole %) in Seesaw Apparatus for 500 hr at a Hot-Zone Temperature of 1350°F. Etchant: copper regia. 200X. ~~(Secret with caption)~~

The 500-hr tests with a hot-zone temperature of 1350°F showed no mass transfer in the nickel capsule, but a slight deposit of metallic crystals was observed in the cold zone of the Inconel capsule. Both the nickel capsule and the Inconel capsule were attacked to a depth of 0.5 mil.

POROUS RARE-EARTH OXIDES EXPOSED TO MOLTEN SODIUM IN INCONEL CAPSULES

W. H. Cook

The good corrosion resistance to sodium at 1300 and 1500°F of rare-earth oxide ceramics made from Lindsay Mix, with densities[5] of 3.53 and 6.58 g/cm^3, contributed to the proposal that the ART control rod be made from this commercial material. This material, which is obtained from the Lindsay Chemical Co. and is designated Code 920, has the following nominal composition: 45 to 49.5% Sm_2O_3, 22.5 to 27% Gd_2O_3, balance primarily other rare-earth oxides.[6] Since the corrosion resistance of ceramic materials is often dependent on how the materials are fabricated, it was decided that several of the shapes fabricated for the ART control rod should be tested in sodium under conditions as severe as or more severe than those anticipated in actual service. The purpose of the tests was to determine the distribution and quantities of corrosion products, if any. This information was needed for a determination of whether the corrosion products could seriously change the control-rod characteristics.

The ceramic sections for the ART control rod are, nominally, 1¼-in.-OD, ¾-in.-ID, 1-in.-long cylinders with average densities of 4.10 g/cm^3 and apparent porosities of 46.3%. Four such sections were tested in sodium which was thermally cycled in 3-hr periods between 1100 and 1350°F three times per day. The tests were continued for 500, 1000, 2000, and 3000 hr. The sodium used for each test has been examined, except that used for the 3000-hr test.

Three sodium samples (11 to 18 g, each) were taken from each test system for chemical analyses for rare earths. The test system used is shown in Fig. 3.2.7, and the locations from which the sodium samples were taken are indicated. In general, the

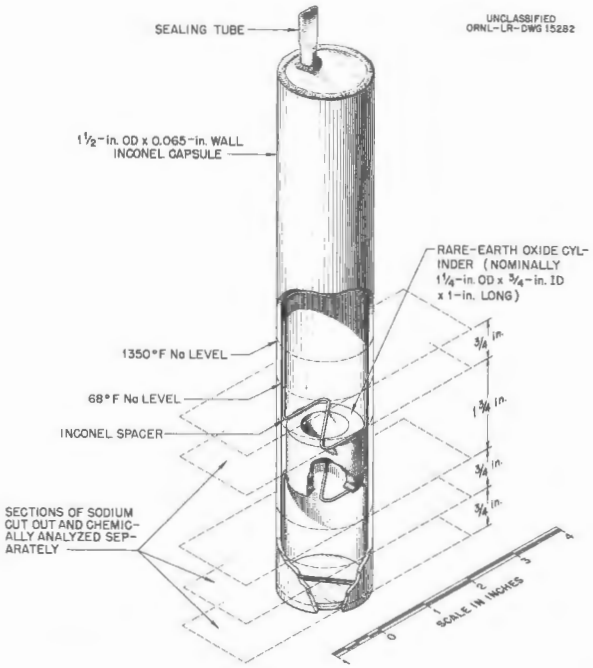

Fig. 3.2.7. Test System for Determining the Compatibility of Rare-Earth Oxides and Thermally Cycled Sodium in an Inconel Capsule.

chemical analyses of the sodium samples from the 500-, 1000-, and 2000-hr tests showed no rare earths, except in an alcohol-insoluble residue from the bottom sodium sample from the 2000-hr test. The detection limits for rare earths were 0.4 to 6.9 ppm, depending on the size of sample and the rare earth sought. The bottom sodium sample (17.48 g) from the 2000-hr test contained 73 ppm Sm, 40 ppm Gd, 7.3 ppm Eu, 7.3 ppm Dy, and 1.2 ppm Y in the alcohol-insoluble material. It is believed that all the rare-earth oxide specimens tested were attacked at approximately equal rates and that the quantities of rare earths found in the bottom sodium sample are in proportion to the respective quantities of rare-earth oxides in the original specimen. It is concluded therefore that these porous rare-earth oxides have good corrosion resistance to sodium under the test conditions outlined.

After the sodium was carefully vacuum distilled from the rare-earth oxide specimens, it was found that the specimen used for the 1000-hr test cracked and spalled to some extent, as shown in Fig. 3.2.8. The specimen from the 2000-hr test cracked into

[5] W. H. Cook, *ANP Quar. Prog. Rep. June 10, 1956*, ORNL-2106, p 155.

[6] Adapted from the Lindsay Chemical Co. analysis reported by J. A. Griffin and L. M. Doney, *ANP Quar. Prog. Rep. June 10, 1956*, ORNL-2106, p 213.

UNCLASSIFIED
Y-18867

UNCLASSIFIED
Y-19873

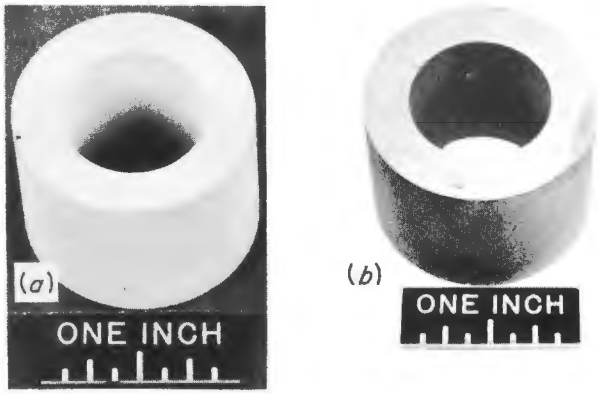

Fig. 3.2.8. A Rare-Earth Oxide Ceramic (*a*) Before and (*b*) After 1000 hr of Exposure to Sodium Thermally Cycled 66 Times Between 1100 and 1350°F. The cracking and spalling are considered to have occurred during removal of the sodium from the porous body by vacuum distillation after completion of the tests.

UNCLASSIFIED
Y-19944

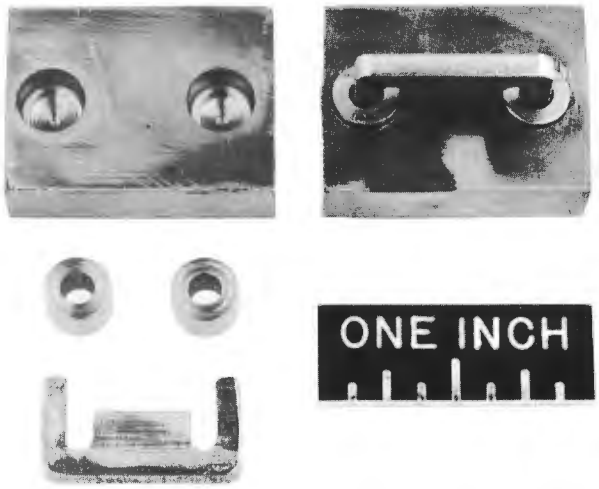

Fig. 3.2.9. Inconel Staples and Sleeves Before and After Insertion in a Beryllium Block. ~~(Secret with caption).~~

pieces. It was suspected that the vacuum distillation of the sodium might have caused the cracking and spalling. Radiographs of the 3000-hr test specimen before it was cut apart for examination support this theory; no cracks or faults were detected in the rare-earth oxide by this method.

This investigation will be concluded with the chemical analyses of the sodium samples from the 3000-hr test, metallographic examination of the test capsules and, if possible, the ceramic specimens, and the determination of the effects, if any, of the small quantities of corrosion products and their locations on the control-rod characteristics.

BERYLLIUM-INCONEL-SODIUM COMPATIBILITY

E. E. Hoffman

Inconel staples have been designed for insertion in Inconel sleeves in the beryllium reflector-moderator sections of the ART to prevent contact and subsequent alloying between the Inconel core shells and the beryllium. The Inconel staples will be driven into Inconel sleeves which will fit tightly into holes drilled in the beryllium, as shown in Fig. 3.2.9. Three such assemblies were tested in sodium for 1000 hr. During this period the test capsule was cycled from 1300 to 500 to 1300°F ten times. The temperature changes were at a rate of approximately 400°F/hr. One-half the total test time was at the lower temperature. An as-tested assembly is shown in Fig. 3.2.10.

The temperature cycling of the test assembly was carried out in order to determine to what extent the brittle nickel-beryllium intermetallic compound formed at the points of contact between the beryllium and the Inconel would spall. Some cracking of the beryllium specimens occurred when the Inconel sleeves were driven into the test blocks, but no additional cracking was detected following the tests. Examinations of six of the test assemblies revealed the formation of approximately 0.025 in. of $Be_{21}Ni_5$ compound between the Inconel sleeve and the beryllium, as shown in Figs. 3.2.11 and 3.2.12. The $Be_{21}Ni_5$ compound formed when flat beryllium and Inconel surfaces were held in contact (500-psi pressure) in sodium for 1000 hr at 1300°F was of the same thickness,[7] that is, 0.025 in. It may be noted in Fig. 3.2.11 that the greatest thickness of $Be_{21}Ni_5$ in the staple assembly occurred near the bottom of the Inconel sleeve, and thus the unalloyed Inconel near the surface will act as a barrier to prevent the brittle compound from spalling into the sodium stream.

[7] E. E. Hoffman and R. Carlander, *ANP Quar. Prog. Rep. Sept. 10, 1956*, ORNL-2157, p 160.

Fig. 3.2.10. Inconel Staple and Beryllium Block Assembly Following 1000 hr of Exposure to Sodium Thermally Cycled Between 500 and 1300°F Ten Times. [redacted]

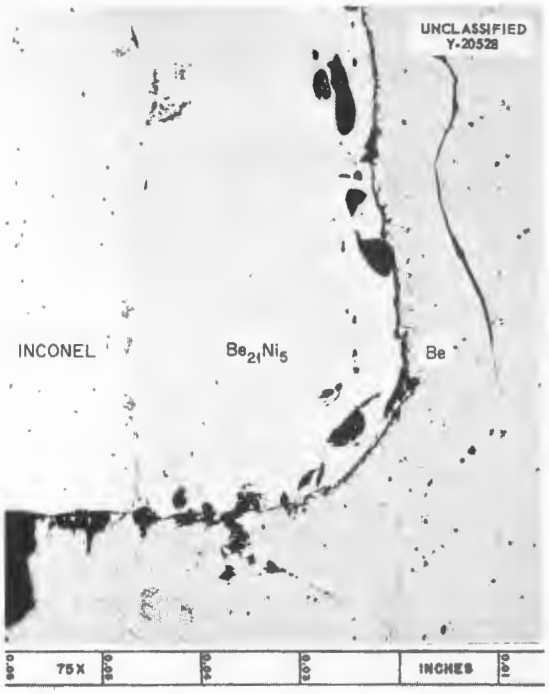

Fig. 3.2.12. Enlarged View of Area A of Fig. 3.2.11. Note alloying ($Be_{21}Ni_5$) between Inconel sleeve and beryllium wall. Unetched. 75X. Reduced 29%. [redacted]

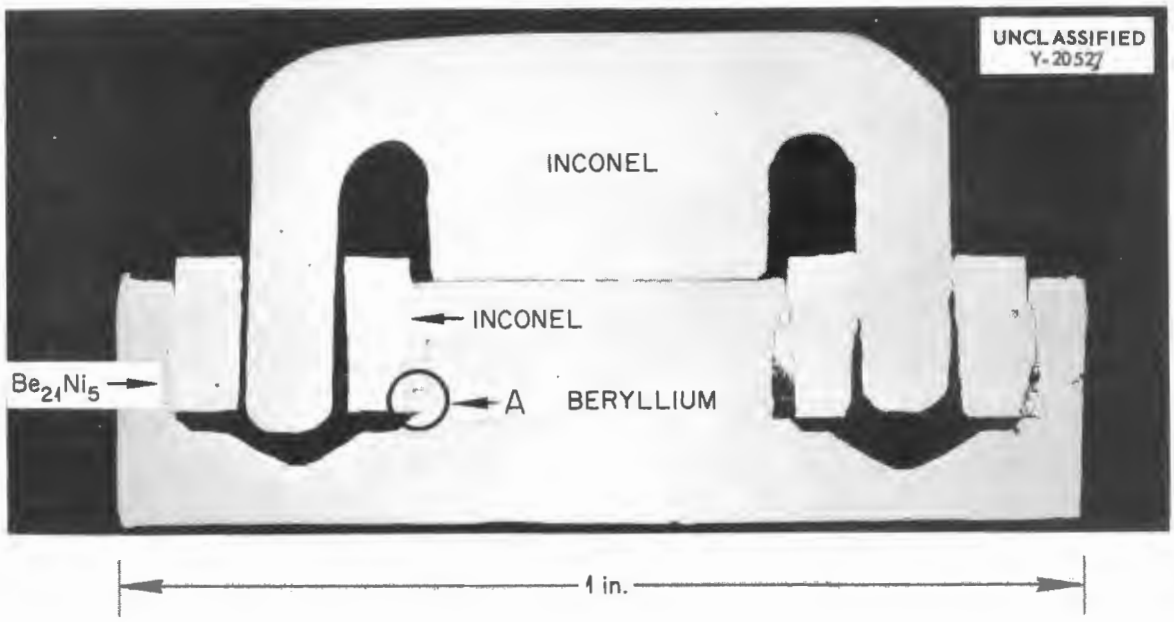

Fig. 3.2.11. Polished Cross Section of Inconel Staple, Inconel Sleeve, and Beryllium Block Following Exposure to Sodium for 1000 hr. Unetched. 5X.

INCONEL-SODIUM-ZIRCONIUM COMPATIBILITY

R. Carlander[8]

An Inconel thermal-convection loop, with a rectangular zirconium sleeve (1 × 1 × 5 in.) inserted in the hot leg, was filled with sodium and operated for 1000 hr with the hot leg at 1500°F and the cold leg at 1230°F. This test was run to determine the effect on the corrosion of the Inconel of the removal of oxygen from the sodium by the zirconium. No mass transfer and little attack (0.5 mil) of the Inconel occurred during the test. An adherent brownish-black film that resembled ZrO_2 was formed on the zirconium specimen, which indicated that it had picked up oxygen from the sodium, and the specimen increased 9.5×10^{-3} g/in.^{2} in weight. Metallographic examination of the specimen revealed a surface layer that was not present before the test, as shown in Fig. 3.2.13. This layer has not yet been identified, but, since traces of iron, nickel, and chromium were found on the surface of the zirconium, it is believed that the layer may be an intermetallic compound. The results of this test indicate that the presence of zirconium caused a decrease in the oxygen content of the sodium and a reduction in the extent of mass transfer by the sodium as compared with the mass transfer observed previously[9] in an Inconel-sodium thermal-convection loop operated under similar conditions. Standpipe tests are planned to confirm these results.

[8]On assignment from Pratt & Whitney Aircraft.

[9]E. E. Hoffman, W. H. Cook, and C. F. Leitten, Jr., *ANP Quar. Prog. Rep. June 10, 1955*, ORNL-1896, p 101.

Fig. 3.2.13. Zirconium Specimen from Hot Leg of Inconel Thermal-Convection Loop Which Circulated Sodium for 1000 hr at a Hot-Leg Temperature of 1500°F and a Cold-Leg Temperature of 1230°F. As-polished. 1000X. Reduced 44%. ~~(Secret with caption)~~

NaK-Li MIXTURES IN INCONEL

R. Carlander

A study of the lithium-sodium system[10] has revealed the existence of two melts, one lithium-rich and the other sodium-rich, in the temperature range of 340 to 825°F. Also, the lithium-rich mixture has been observed in the temperature range of 340 to 480°F during the preparation of the NaK-Li mixtures in an inert atmosphere chamber. Since nickel-base alloys exhibit poor corrosion resistance to molten lithium, the presence of a lithium-rich phase might alter their corrosion resistance to NaK-Li mixtures. Also, since this phase would be less dense than other phases existing in the system, it would tend to segregate in the upper portions of the bath and to cause severe corrosion in that area. Such segregation would occur only at low temperatures, since complete solution would exist at higher temperatures.

In order to test the corrosiveness of the NaK-Li system, an Inconel thermal-convection loop was filled with NaK (56-44 wt %) plus 5 wt % lithium and operated for 1000 hr with a hot-leg temperature of 1050°F and a cold-leg temperature of 740°F. No mass transfer or attack was found in any section of the Inconel loop. Therefore, the addition of up to 5 wt % lithium to NaK does not affect the low-temperature corrosion resistance of Inconel. Further tests will be performed to determine the effect of larger additions of lithium.

MOLYBDENUM AND ZIRCONIUM IN SODIUM AND IN LITHIUM

R. Carlander

Molybdenum and zirconium were exposed to sodium and to lithium for 100 hr in a tilting furnace (1 cpm) with the hot zone at a temperature of 1535°F and the cold zone at a temperature of 995°F in tests similar to those described previously[11] in which niobium was exposed to sodium and to lithium. A diagram of the test capsule is

[10]W. H. Howland *et al.*, paper presented at National ACS Meeting, Dallas, Texas, April 8–13, 1956.

[11]R. Carlander, *ANP Quar. Prog. Rep. Sept. 10, 1956*, ORNL-2157, p 154.

shown in Fig. 3.2.14, and no mass transfer or attack of the molybdenum or the zirconium occurred in any of the tests. A comparison of the test results with results of similar tests of niobium in sodium and in lithium[11] indicates that the corrosion resistance of all three materials to sodium is good. The best corrosion resistance to molten lithium (no attack) was exhibited by molybdenum, while the poorest corrosion resistance to molten lithium (2 mils of attack in hot zone) was exhibited by niobium.

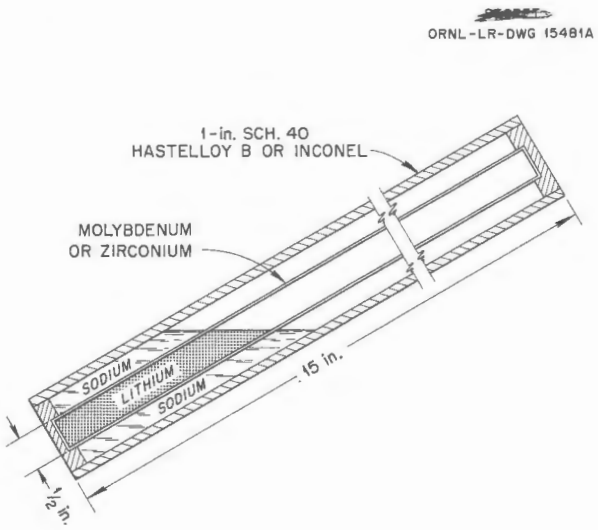

Fig. 3.2.14. Schematic Diagram of Capsule for Tilting Furnace Tests of Molybdenum and Zirconium in Sodium and in Lithium.

MOLYBDENUM AND HASTELLOY B IN RUBIDIUM

R. Carlander

Rubidium, because of its desirable properties, that is, low cross section (0.56 barn), low melting point (102°F), and high boiling point (1260°F), is being considered as a possible coolant for use in aircraft reactors. Therefore the search for structural materials with good corrosion resistance to rubidium and high strength at the elevated temperatures has been renewed. Preliminary corrosion studies of Inconel in static and in dynamic rubidium were reported previously.[12,13] Static tests of rubidium in Inconel at 1500 and 1650°F showed a maximum attack of 2 mils after 100 hr.[12] A boiling rubidium-Inconel thermal-convection loop operated at a hot-leg temperature of 1520°F showed no mass transfer and 1 mil of intergranular penetration in the hot leg after 312 hr.[13] In continuation of the search for a corrosion-resistant material with good high-temperature strength, molybdenum and Hastelloy B (a nickel-molybdenum alloy) have been tested as possible containers for rubidium. Two standpipe tests have been completed in which Hastelloy B was exposed to rubidium for 500 hr at bath-zone temperatures of 1400 and 1500°F and a cold-zone temperature of 1000°F. A diagram of the standpipe apparatus is shown in Fig. 3.2.15.

Tests of rubidium in Hastelloy B and in molybdenum were also performed in a tilting furnace at

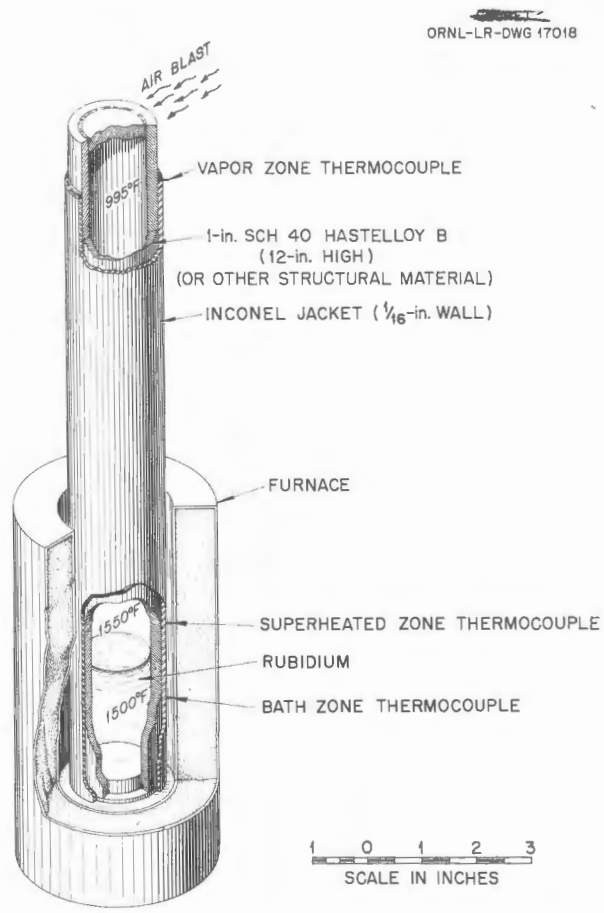

Fig. 3.2.15. Schematic Diagram of Standpipe Apparatus for Testing the Effect of Rubidium on Structural Materials.

[12] E. E. Hoffman *et al.*, *ANP Quar. Prog. Rep. Sept. 10, 1954*, ORNL-1771, p 86.

[13] E. E. Hoffman, W. H. Cook, and C. F. Leitten, *ANP Quar. Prog. Rep. Dec. 10, 1954*, ORNL-1816, p 87.

1 cpm for 500 hr. The hot zone of the Hastelloy B capsule was maintained at 1600°F (cold zone, 1000°F), and the hot zone of the molybdenum capsule was maintained at 1900°F (cold zone, 1350°F). The temperatures of the various portions of the test capsule and the results of metallographic examination are given in Table 3.2.2. No mass transfer occurred in any of the capsules. The maximum depth of attack of Hastelloy B in the standpipe tests, as shown in Fig. 3.2.16, was 2 mils. The maximum depth of attack of the Hastelloy B in the seesaw test, as shown in Fig. 3.2.17, was 1 mil. No attack occurred on the molybdenum in the seesaw test, as shown in Fig. 3.2.18. Results of these preliminary tests indicate that molybdenum and alloys of the nickel-molybdenum type would be suitable high-temperature containers for rubidium.

PROPERTIES OF LEAD-LITHIUM ALLOYS

D. H. Jansen E. E. Hoffman

An investigation has been initiated to determine the properties of a lead-lithium alloy (low lithium content) that is being considered for use as a combination neutron and gamma-ray shielding material. It has been specified that the alloy must be homogeneous.

A survey of the literature, including patents, did not reveal any references to the possibility of utilizing this type of an alloy as neutron and gamma-ray shielding material. The alloy is prepared by adding solid lithium to molten lead in an inert atmosphere chamber. Preliminary castings of lead containing 0.1 and 1.0% lithium have been made to determine the homogeneity of the cast alloy. Chemical analyses of various sections of these castings showed that segregation is not a problem when solidification occurs rapidly. Subsequent studies have been confined to the eutectic composition, which contains 0.69% Li, since segregation would be no problem with the eutectic regardless of cooling rate or size of casting. A phase diagram for the lead-lithium system in the low-lithium-content range, taken from the work of Hofmann,[14] is shown in Fig. 3.2.19.

The eutectic was cast as tensile bars for mechanical tests, and the results of the tests are given in Table 3.2.3. In addition, information concerning the amount of lithium lost in the alloying reaction was obtained during the casting operations. It was found that from 0.03 to 0.07% lithium is

[14] W. Hofmann, *Blei und bleilegierungen*, Edwards Brothers, Inc., Ann Arbor, 1944.

TABLE 3.2.2. SUMMARY OF THE TEST CONDITIONS AND METALLOGRAPHIC EXAMINATIONS OF HASTELLOY B AND MOLYBDENUM CORROSION TESTS IN RUBIDIUM

Test Designation	Structural Material Tested	Capsule Zone Sampled	Temperature of Sampled Zone During Test (°F)	Metallographic Notes
Standpipe No. 1	Hastelloy B	Bath zone	1400	1 mil of attack
		Superheated zone	1535	1.5 mils of attack
		Vapor zone	815	0.5 mil of attack
Standpipe No. 2	Hastelloy B	Bath zone	1500	2 mils of attack
		Superheated zone	1550	1.5 mils of attack
		Vapor zone	995	1 mil of attack
Seesaw test No. 1	Hastelloy B	Hot zone	1600	1 mil of voids
		Cold zone	1000	1 mil of voids
Seesaw test No. 2	Molybdenum	Hot zone	1900	No attack
		Cold zone	1350	No attack

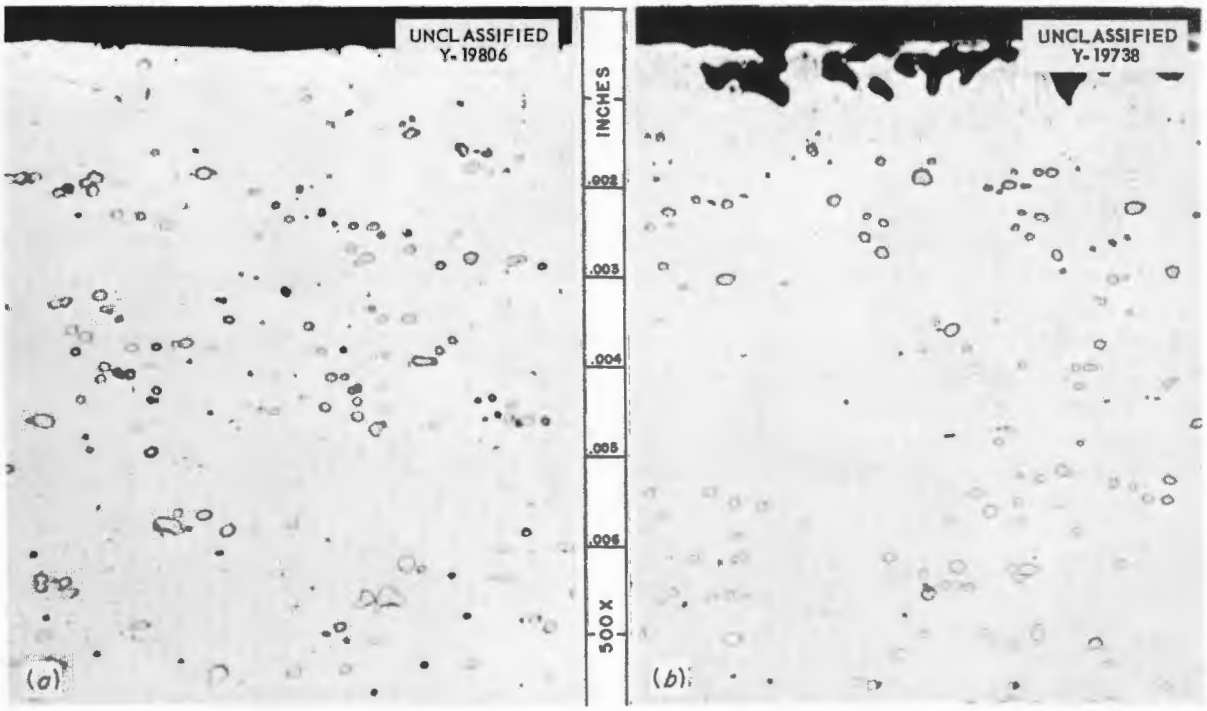

Fig. 3.2.16. (*a*) As-Received Hastelloy B and (*b*) Hastelloy B from Vapor Zone Standpipe Test No. 2 After Exposure to Rubidium Vapor for 500 hr at 1500°F. Attack of the bath zone was similar to that of the vapor zone. Etchant: 80% H_2O_2–20% H_3PO_4. 500X. Reduced 5%. [redacted]

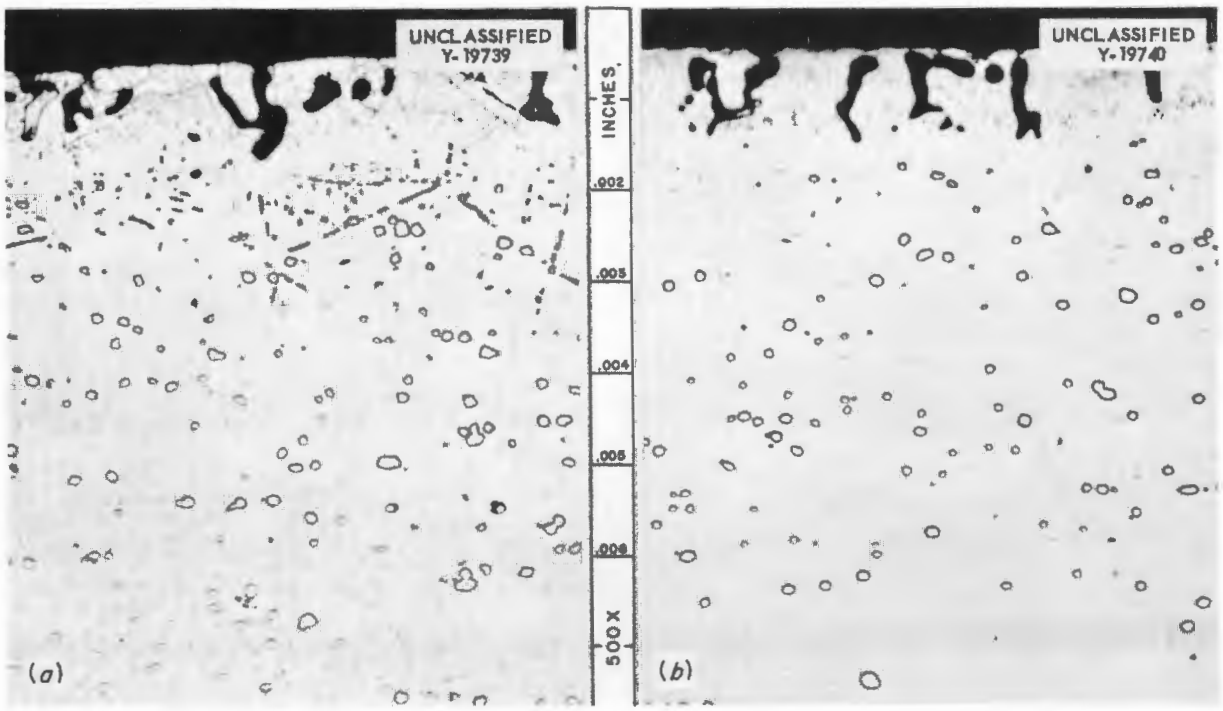

Fig. 3.2.17. (*a*) Hot Zone (1600°F) and (*b*) Cold Zone (1000°F) of Hastelloy B Seesaw Capsule After Exposure to Rubidium Vapor for 500 hr at 1600°F. Etchant: 80% H_2O_2–20% H_3PO_4. 500X. Reduced 4%. [redacted]

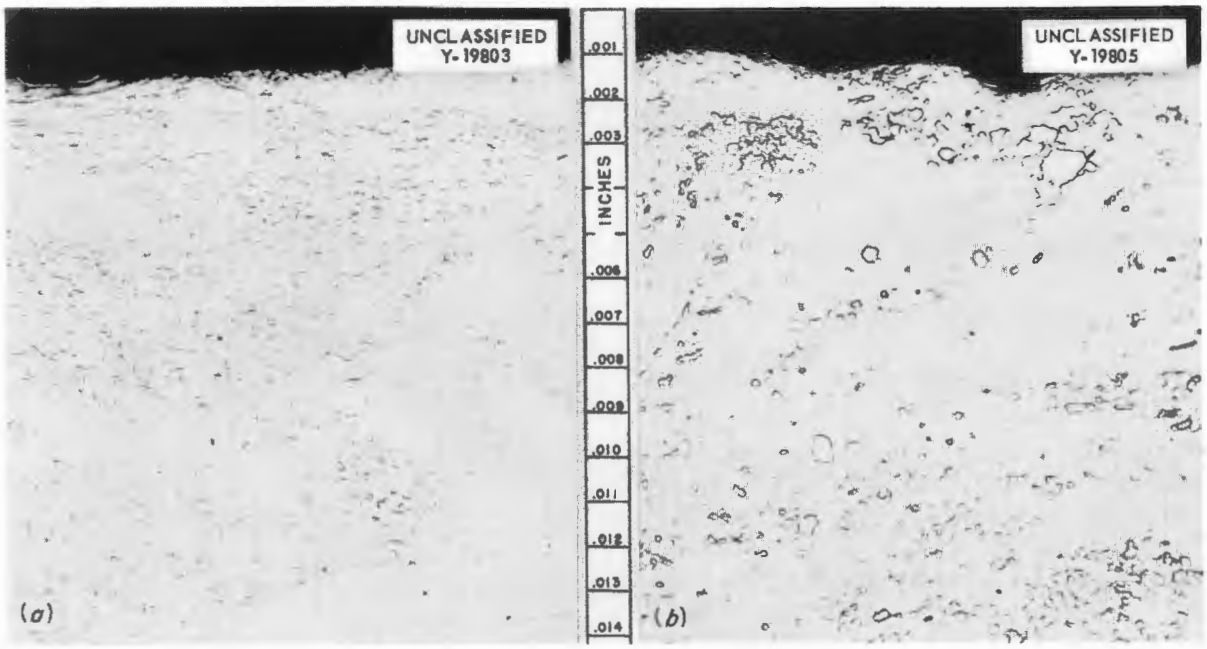

Fig. 3.2.18. (*a*) As-Received Molybdenum and (*b*) Hot Zone of a Molybdenum Seesaw Capsule After Exposure to Rubidium Vapor for 500 hr at 1900°F. Etchant: 50% H_2O_2–50% NH_4OH. 250X. Reduced 5%. [redacted]

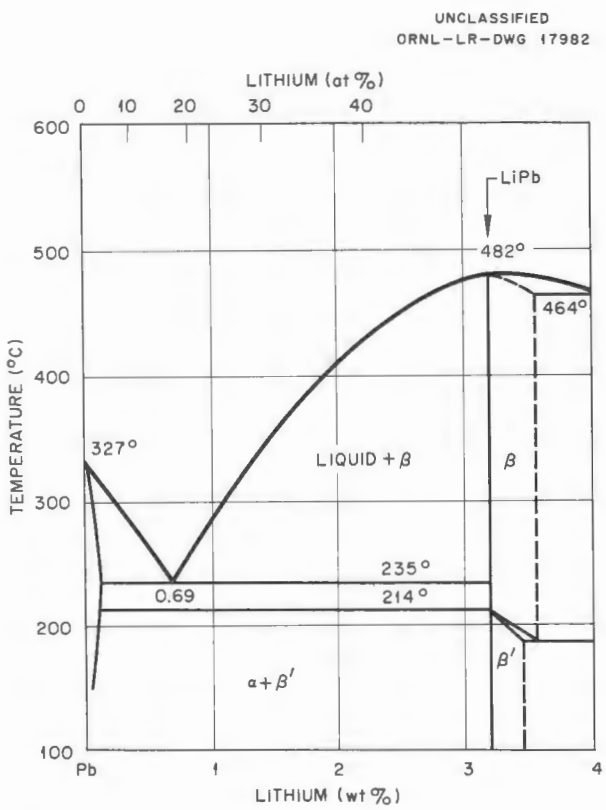

Fig. 3.2.19. Lead-Lithium Phase Diagram Showing the Low-Lithium Range.

lost when the lithium is added to the molten lead in an inert atmosphere. The loss of lithium is attributed to reduction of lead oxide by the lithium and reaction of lithium with small amounts of residual oxygen and nitrogen in the inert atmosphere during the exothermic reaction period.

It was found that about 0.02% Li is lost when the alloy is melted and cast in air. The lithium content of alloys 12 and 13 of Table 3.2.3 dropped from 0.75 to 0.70% Li upon remelting and casting in air. Alloys 15 and 16 dropped from 0.75% to 0.68% Li when remelted and recast in air twice. The structure of the eutectic alloy is shown in Fig. 3.2.20. The lithium content and mechanical properties of each casting that has been made are given in Table 3.2.3. An indication of the strength values obtained by these small lithium additions can be shown by comparing the results of a 1000-hr room-temperature stress-rupture test at 1000 psi on a Pb–0.67% Li casting with the results of a similar test of a Pb–0.06% Cu alloy which is being considered for ART shielding applications. The lead-lithium alloy showed 1.8% elongation after the 1000-hr test, whereas the lead-copper alloy failed in 130 hr under the same conditions. It was also found that the tensile strength of a lead-lithium alloy at 110°C was about twice that of a

TABLE 3.2.3. RESULTS OF MECHANICAL PROPERTY TESTS OF LEAD-LITHIUM ALLOYS

Alloy Designation	Li Added (wt %)	Li in Casting (wt %)	Diamond Pyramid Hardness, 1-kg Load	Stress Rupture Life at Room Temperature	Tensile Strength (psi) and Elongation (%) in 3-in. Gage at Room Temperature	Tensile Strength (psi) and Elongation (%) in 3-in. Gage at 110°C
Lead[a]	0.0	0.0	4.5	<5 hr at 1000 psi	1433; 33[b]	
Pb + 0.06% Cu	0.0	0.0	4.9	130 hr at 1000 psi	1746; 53[b]	
A	0.1		11.2			
B	1.0		17.0			
1	0.70	0.67	15.3	Test terminated after 1000 hr at 1000 psi; elongation, 1.8%		
2	0.70	0.65	15.1			3423; 11.6[b]
3	0.70	0.67	15.0			3553; 56[c]
4	0.70	0.66	14.9			In test
5	0.70	0.65	13.5		7654; 22[d]	
6	0.70	0.67	14.0		6308; 22[b]	
7	0.70	0.65	15.3		5485; 39[b]	
8	0.70	0.63	13.7			3502; 65[c]
9	0.70	0.66	16.1	41.8 hr at 3000 psi; elongation, 26.6%		
10	0.70	0.64	15.4			3019; 56[c]
11	0.75	0.72	14.4		7230; 23[d]	
12	0.75	0.70	14.6		7003[d]	
13	0.75	0.70	15.9		6860; 11[d]	
14	0.75	0.71	14.3		7892; 29[d]	
15	0.75	0.67	13.9		6490; 16[d]	
16	0.75	0.68	14.2		6879; 14[d]	

[a]Doe-run lead (99.9+ % Pb).
[b]Rate of test: 0.05 in./in./min.
[c]Rate of test: 0.17 in./in./min.
[d]Rate of test: 0.25 in./in./min.

lead-copper alloy tensile tested at room temperature.

Tests will be conducted in the future to determine possible methods of preparing and casting large amounts of the lead-lithium alloy under a protective atmosphere. Mechanical properties tests, including long-time creep experiments at 110°C in the stress range of 100 to 300 psi, are to be conducted. The corrosion resistance of the alloy in water under various conditions will be investigated. The possibilities of preparing large sheets (approximately 3 ft square) for nuclear tests in the Bulk Shielding Facility will be investigated.

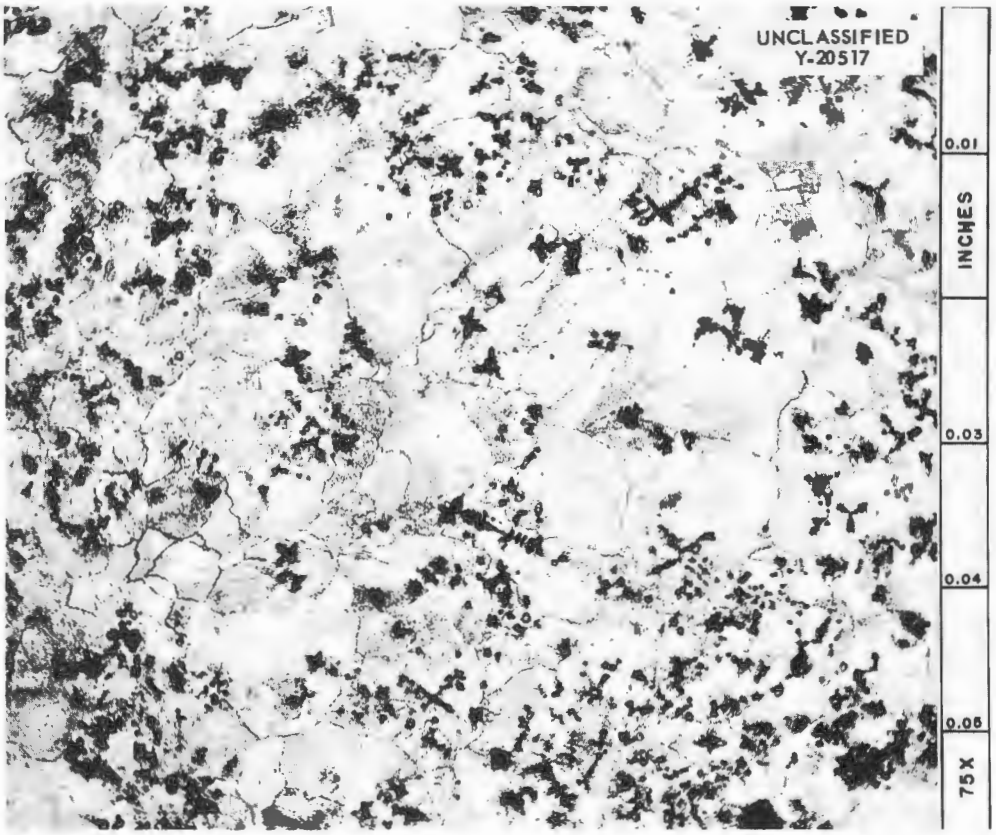

Fig. 3.2.20. As-Cast Lead-Lithium Alloy Containing 0.72% Li. Etchant: 16% acetic acid, 16% HNO_3, 68% glycerine. ~~(Confidential with caption)~~

3.3. FABRICATION RESEARCH

J. H. Coobs

NICKEL-MOLYBDENUM ALLOY DEVELOPMENT

H. Inouye T. K. Roche

Alloy Evaluation Norms

Based on experience with Hastelloys B and W, various binary nickel-molybdenum alloys, Inconel, and other nickel-base alloys, it has been concluded that if it were possible to develop an alloy having the best properties of Inconel and Hastelloy B, the container requirements for high-temperature fused-salt reactors would, in a large measure, be adequately solved. Because such an alloy is not available commercially, a coordinated effort is being made to develop it and to reduce its production to commercial practice.

The standards established for acceptability of the experimental alloys are listed below:

Fabricability. – The fabricability of the alloy must be equivalent to that of Inconel.

Oxidation Resistance. – The alloy must be oxidation resistant to air at 1500°F, and its oxide scale must not spall during thermal cycling. In the nickel-molybdenum system, the problem becomes one of suppressing the beta- to gamma-phase transformation of $NiMoO_4$ which occurs at about 600°F.

Stress-Rupture Properties. – In the environment of interest the alloy must have a minimum rupture life of 1000 hr at a temperature of 1500°F and a stress of 8000 psi.

Corrosion Resistance. – The alloy must have corrosion resistance equivalent to that of Hastelloy B.

Joining Characteristics. – The alloy must be satisfactorily weldable in sections varying from 0.020-in.-thick sheet to heavy plate. Furthermore it is desirable that the alloy be brazable by established procedures.

Aging Characteristics. – The alloy must not require an aging heat treatment to exhibit its best properties. A mild aging response is permissible if the alloy does not exhibit ductility of less than 10% in the aged condition.

Nuclear Properties. – Considerations of fuel inventory and shield weight indicate that the alloy should have a total neutron cross section near that of nickel and be free of elements which become strongly activated during irradiation.

These criteria coupled with thermodynamic and chemical considerations indicate the following maximum composition limits:

Element	Permissible Maximum Content (wt %)
Molybdenum	20
Chromium	5
Titanium plus aluminum	2.5
Tungsten	4
Iron	10
Niobium, vanadium, carbon	Limits to be determined by physical properties

Status of Development Program

A review of the data obtained during recent months has permitted some generalizations to be made regarding the properties of the experimental nickel-molybdenum alloys. The observations presented below indicate that satisfactory progress is being made toward the attainment of an alloy that meets the established requirements for acceptability:

Fabricability. – No difficulties have been experienced in fabricating the desired shapes from the majority of the compositions by conventional methods. For successful tube reducing and redrawing of seamless tubing, the titanium plus aluminum content of the alloy must be less than 4% (ref 1), and the carbon content must be less than 0.20%. Laboratory heats of an alloy with a titanium plus aluminum content of 3.5% were found to be forgeable, whereas a 4800-lb pilot-plant heat of the same composition cracked severely upon forging and became virtually scrap metal. The composition of this alloy was 16% Mo–1.5% Ti–2% Al–bal Ni.

Oxidation Resistance. – Numerous compositions have been found that can be classified as oxidation resistant. It has been established that their oxidation resistance depends almost entirely on the chromium content.

[1] This value of less than 4% was established on the basis of fabrication alone, and it is not in conflict with the over-all permissible maximum of 2.5% Ti plus Al.

Stress-Rupture Properties. – Most of the experimental compositions have stress-rupture strengths greater than that of Inconel, but they have less than the acceptable rupture strength (see standard above).

Corrosion Resistance. – The alloys have shown no appreciable corrosion after exposure to the fuel mixture (No. 107) NaF-KF-LiF-UF_4 (11.2-41-45.3-2.5 mole %) in 500-hr thermal-convection-loop tests. The depth of the corrosion found after most of the tests was about 1 mil.

Joining Characteristics. – No difficulties have been experienced in welding tubing of the various alloys into thermal-convection loops.

Aging Characteristics. – The experimental alloys have not exhibited aging embrittlement such as that found with the Hastelloys.

Much of the information collected thus far is of a preliminary nature, and in many cases the results of only a single test are available. Since many of the compositions can be considered as being of a certain class or similar with respect to the property being studied, a direct comparison of the properties of the numerous compositions has shown the effects of the carbon and chromium additions to the alloys. Based on the tube-reducing and redrawing properties of approximately 200 extruded tube blanks containing various amounts of carbon, it was concluded that carbon in excess of that necessary for deoxidation seriously reduces the cold fabricability of the alloy. Similarly the high-carbon-content alloys showed a greater tendency to edge-crack during hot rolling than the alloys with low carbon content.

The effect of carbon on the mechanical properties was most pronounced in the tensile tests of these alloys both at room temperature and at elevated temperatures. In Fig. 3.3.1 the tensile ductilities of various compositions[2] are listed in the order of

[2] The composition designations INOR-1 through INOR-8 refer to types of alloys rather than to specific compositions. The several different specific and nominal compositions given in this report for alloys of the INOR types are the compositions of the individual heats being discussed.

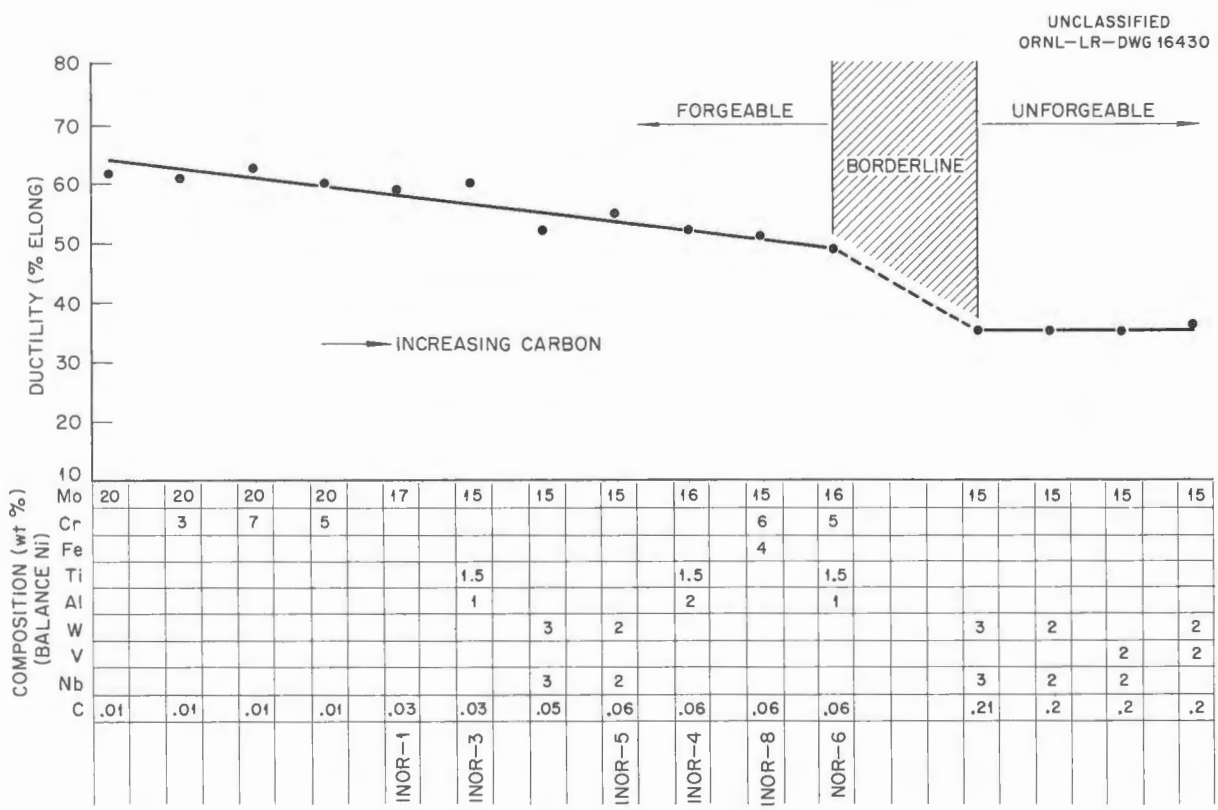

Fig. 3.3.1. Room-Temperature Tensile Ductility of Annealed Ni-Mo Alloys.

increasing carbon content. This graph clearly shows that the total elongation of the specimen decreases with the carbon content. As is usually the case, the yield point and the ultimate tensile strength increase as the ductility decreases. The alloys containing 0.06 to 0.20% carbon were borderline with respect to tube-reducing and redrawing properties.

Additions of chromium to the alloys have significant effects on the oxidation rate and the corrosion resistance. The data on the oxidation rates of numerous alloys tested in static air at 1500°F for 100 hr are summarized in Fig. 3.3.2. The dominant role of chromium in determining the oxidation rates of these alloys is quite evident. The other alloying elements appear to have only slight effects. All alloys listed as having a nonspalling oxide are considered to be heat resistant under the test conditions.

Preliminary thermal-convection loop tests in which the nickel-molybdenum alloys containing chromium were exposed to the fuel mixture (No. 107) $NaF-KF-LiF-UF_4$ (11.2-41-45.3-2.5 mole %) showed that the chromium content in the fused salt increases as the chromium content of the alloy increases. The details of these tests are reported in Chap. 3.1, "Dynamic Corrosion Studies."

The preliminary data obtained on the properties and the status of the development of several experimental alloys are listed in Table 3.3.1. The table is not a complete listing of the compositions

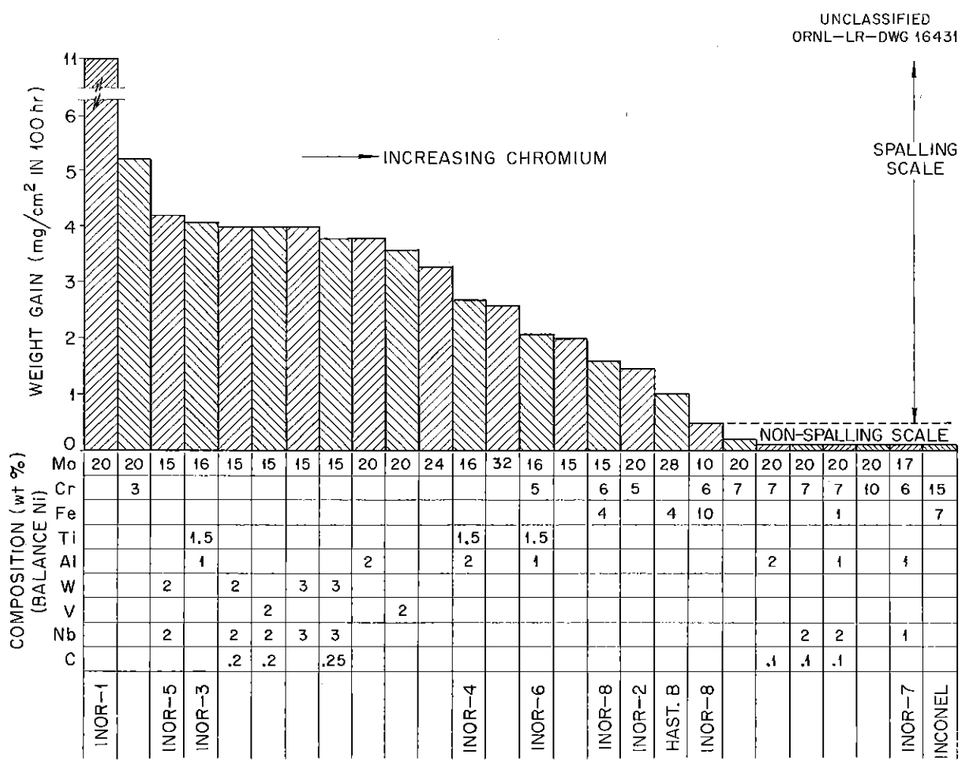

Fig. 3.3.2. Oxidation Rates of Ni-Mo Alloys at 1500°F in Air.

TABLE 3.3.1. PROPERTIES AND STATUS OF SELECTED NICKEL-MOLYBDENUM ALLOYS

	ORNL Alloys								Battelle Alloys			Special ORNL Alloy	Hastelloy B	Inconel
	INOR-1	INOR-2	INOR-3	INOR-4	INOR-5	INOR-6	INOR-7	INOR-8	B-3276	B-3278	B-3277			
Nominal Composition (wt %)	17 Mo–0.5 Al–bal Ni	20 Mo–5 Cr–bal Ni	16 Mo–1.5 Ti–1 Al–bal Ni	16 Mo–1.5 Ti–2 Al–bal Ni	15 Mo–2 Nb–2 W–bal Ni	16 Mo–5 Cr–1.5 Ti–1 Al–bal Ni	17 Mo–6 Cr–1 Nb–1 Al–bal Ni	10 Mo–6 Cr–10 Fe–bal Ni	20 Mo–7 Cr–2 Nb–1 Fe–0.12 C–bal Ni	20 Mo–7 Cr–2 Al–0.12 C–bal Ni	20 Mo–7 Cr–2 Nb–1 Al–0.12 C–bal Ni	20 Mo–2 Al–bal Ni	68 Ni–28 Mo–4 Fe	78 Ni–15 Cr–7 Fe
Fabricability														
Extrusion	Satisfactory	Satisfactory	Satisfactory	Satisfactory	Satisfactory	Satisfactory	Satisfactory	Satisfactory	Satisfactory	Satisfactory	Satisfactory	Satisfactory	Satisfactory	Satisfactory
Hot forging	Satisfactory	Satisfactory	Satisfactory	Satisfactory	Satisfactory	Satisfactory	Satisfactory	Satisfactory	No data	No data	Satisfactory	Satisfactory	Satisfactory	Satisfactory
Hot rolling	Satisfactory	Satisfactory	Satisfactory	Satisfactory	Satisfactory	Satisfactory	Satisfactory	Satisfactory	No data	No data	Satisfactory	Satisfactory	Satisfactory	Satisfactory
Cold rolling	Satisfactory	Satisfactory	Satisfactory	Satisfactory	Satisfactory	Satisfactory	Satisfactory	Satisfactory	No data	No data	Satisfactory	Satisfactory	Satisfactory	Satisfactory
Tube reducing	Satisfactory	Satisfactory	Satisfactory	Satisfactory	Satisfactory	Satisfactory	Satisfactory	Satisfactory	Satisfactory	Unsatisfactory	Satisfactory	Satisfactory	No data	Satisfactory
Redrawing	Satisfactory	Satisfactory	Satisfactory	Satisfactory	Satisfactory	Satisfactory	Satisfactory	Satisfactory	Satisfactory	Unsatisfactory	Satisfactory	Satisfactory	No data	Satisfactory
Oxidation in Air														
Rate (mg/cm^2 in 100 hr)	3.3	1.2	4	2.7	4.2	2.1	0.07	0.04	0.04	0.19	0.08	2.9	1.2	0.04
Spalling of oxide	Yes	Yes	Yes	Yes	Yes	Slight	No	No	No	No	No	Yes	Yes	No
Corrosion (mils) after 500 hr at 1500°F														
In fuel 107*	2	1.0	1.0	Tests in progress	0	Tests in progress	Tests in progress	No data	Tests in progress	No data	Tests in progress	2	2	11
In fuel 30*	1	0.5	No data	No data	No data	No data	No data	2	No data	No data	No data	No data	2	8
In sodium	No data	0	Tests in progress	Tests in progress	Tests in progress	Tests in progress	Tests in progress	No data	No data	No data	Tests in progress	Tests in progress	2	1
Joining														
Brazable in dry hydrogen	Yes	Yes	No	No	Yes	No	No data	Yes	Yes	No data	No data	No data	Yes	Yes
Weldability	Tests in progress	Tests in progress	Tests in progress	Tests in progress	Tests in progress	Tests in progress	Tests in progress	Tests in progress	Tests in progress	No data	No data	No data	No data	Satisfactory
Stress-Rupture at 8000 psi and 1500°F in Fuel 107*														
Time to 1% strain (hr)	No data	30	30	20	20	15	No data	No data	41	41	110	60	290	No data
Rupture life (hr)	40	444**	211	325	185	204	No data	242	442	679	Tests in progress	1374	>7000	80**
Rupture ductility (%)	50	28	63	73	58	69	No data	64	21	35	Tests in progress	28	10	50
Aging Characteristics	None	None	None	Yes	None	Yes	No data	No	No data	No data	No data	No data	Yes	None
Tensile Ductility (%)														
At room temperature, annealed	59	51	60	51	55	49	No data	51	40	34	No data	62	40	45
At room temperature, aged at 1300°F	56	52	55	36	50	42	No data	47	No data	No data	No data	32	0	No data
At 1300°F, annealed	37	8.5	30	No data	No data	No data	No data	14	No data	No data	No data	No data	13	No data
At 1300°F, aged	No data	16.5	41	2	11.0	No data	No data	21	No data	No data	No data	No data	2	No data
Single-Phased Alloy	Yes	Yes	No data	No data	No data	No data	No data	No data	No data	No data	No data	No data	No	Yes

*Fuel No. 107: $NaF-KF-LiF-UF_4$ (11.2-41-45.3-2.5 mole %).
Fuel No. 30: $NaF-ZrF_4-UF_4$ (50-46-4 mole %).

**In argon.

being studied. The results for the compositions listed as the INOR alloys are for the laboratory counterparts of the pilot-plant heats which are now being processed but have not been evaluated.

Examination of the table readily shows a deficiency in the data on welding and corrosion. The available data indicate that the corrosion rates and the creep strengths of the alloys are superior to those of Inconel. In contrast to the embrittlement which occurs in aged Hastelloy B, these alloys, in general, show no aging tendencies. An exception to this is the INOR-4 alloy, which exhibits low ductility at 1300°F after aging. The precipitation-hardening tendencies of alloys containing titanium and aluminum were determined by hardness tests, and the results are presented in Fig. 3.3.3. At a temperature of 1300°F the aging response is significant, while at 1500°F the alloys either overage in a short time or show no effect.

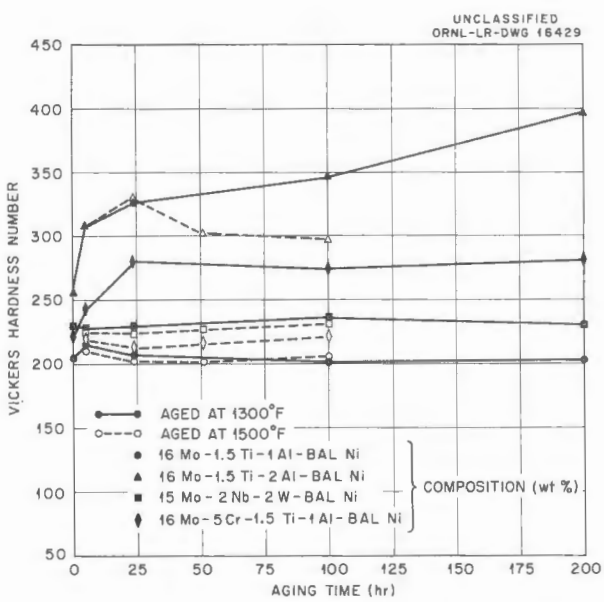

Fig. 3.3.3. Room-Temperature Hardness Data for Several Ni-Mo Alloys.

Fabrication of Battelle Alloys

Tubing processed from extrusions of Battelle Memorial Institute alloys designated B-3275, B-3276, B-3277, and B-3278, which were described previously,[3] was returned by the Superior Tube Co. The results obtained in the redrawing operation are summarized in Table 3.3.2. With the exception of alloys B-3276 and B-3278, the blanks were all converted to 0.500-in.-OD, 0.035-in.-wall tubing without difficulty. One of the two extrusions of alloy B-3276 and both extrusions of alloy B-3278 split during the tube-reducing operation and were scrapped. The relatively high carbon content of the Battelle alloys is believed to be responsible for the processing difficulties. Thermal-convection loops have been constructed from the tubing for testing with the fuel mixture (No. 107) NaF-KF-LiF-UF_4 (11.2-41-45.3-2.5 mole %).

Sixteen additional extrusion billets representing the four compositions listed below were received from Battelle and were successfully extruded at 2150°F at a ratio of 7:1:

Alloy No.	Nominal Composition (wt %)
B-3404	20 Mo–7 Cr–2 Al–0.8 Mn–0.12 C–bal Ni
B-3407	20 Mo–7 Cr–1 Al–2 Nb–1 Fe–0.8 Mn–0.12 C–bal Ni
B-3412	20 Mo–2 Al–1 Nb–0.5 Fe–0.8 Mn–0.12 C–bal Ni
B-3418	20 Mo–2 Nb–1 Fe–0.8 Mn–0.12 C–bal Ni

The tube blanks have been sent to Superior Tube Co. to be drawn to small-diameter tubing. These alloys were selected by Battelle for thermal-convection loop studies, as well as for tests to determine strength, ductility, and weldability, but it may be difficult to obtain the necessary tubing since these alloys contain 0.12% carbon and their tube-forming characteristics may therefore be marginal. The methods which are being considered for the tube fabrication are (1) extruding, tube reducing, and drawing to produce seamless tubing; (2) rolling to strip, forming, welding, and drawing to produce Weldrawn tubing; and (3) forging, machining, and drawing to produce seamless tubing. The last method is being considered as a means of bypassing the extrusion and tube-reducing steps. Battelle has indicated that the Superior Tube Co. is attempting to produce tubing of the alloys by the latter two methods. The tube-blank extrusions which were made successfully at ORNL are to be used for determining the feasibility of tubing fabrication by the first method. The results of these initial experiments will determine which method will be best suited for completing the fabrication

[3] H. Inouye and T. K. Roche, *ANP Quar. Prog. Rep. Sept. 10, 1956*, ORNL-2157, p 175.

TABLE 3.3.2. RESULTS OF REDRAWING BATTELLE MEMORIAL INSTITUTE AND ORNL ALLOYS TO 0.500-in.-OD, 0.035-in.-WALL TUBING AT THE SUPERIOR TUBE CO.

Alloy No.	Nominal Composition (wt %)	Number of Extruded Tube Blanks	Total Length of Tubing Received		Number of Loops Being Fabricated*	Remarks
			Feet	Inches		
	Battelle Memorial Institute Alloys					
B-3275	20 Mo–7 Cr–0.8 Mn–0.12 C–bal Ni	2	26	3	2	
B-3276	20 Mo–7 Cr–2 Nb–1 Fe–0.8 Mn–0.12 C–bal Ni	2	11	4	1	One tube blank split on tube reducer
B-3277	20 Mo–7 Cr–2 Nb–1 Fe–1 Al–0.8 Mn–0.12 C–bal Ni	2	27	6	2	
N-3278	20 Mo–7 Cr–2 Al–0.8 Mn–0.12 C–bal Ni	2	0	0	0	Both tube blanks split on tube reducer
	ORNL Alloys					
30-6	17 Mo–7 Cr–0.06 C–bal Ni	2	23	7	2	
30-7	17 Mo–2 Al–0.06 C–bal Ni	3	34	2	3	
30-17	17 Mo–4 Al–0.06 C–bal Ni	3	0	0	0	One tube blank defective; one split upon drawing; one split during final anneal
30-8	17 Mo–2 Ti–0.06 C–bal Ni	3	31	5	3	
30-18	17 Mo–4 Ti–0.06 C–bal Ni	3	28	2	0	Tubing cracked
30-9	17 Mo–2 W–0.06 C–bal Ni	3	31	7	3	
30-19	17 Mo–4 W–0.06 C–bal Ni	3	34	1	3	
30-10	17 Mo–2 V–0.06 C–bal Ni	3	33	4	3	
30-20	17 Mo–4 V–0.06 C–bal Ni	3	32	7	3	
30-11	17 Mo–4 Fe–0.06 C–bal Ni	3	29	9	3	
30-12	17 Mo–3 Nb–0.06 C–bal Ni	3	31	4	3	
30-21	17 Mo–5 Nb–0.06 C–bal Ni	3	34	11	3	
30-13	16 Mo–1 5 Ti–1 Al–0.06 C–bal Ni (INOR-3)	3	35	10	3	
30-14	16 Mo–1.5 Ti–2 Al–0.06 C–bal Ni (INOR-4)	3	33	10	3	
30-15	15 Mo–2 Nb–2 W–0.06 C–bal Ni (INOR-5)	2	21	0	2	
30-16	16 Mo–5 Cr–1.5 Ti–1 Al–0.06 C–bal Ni (INOR-6)	3	32	0	3	
30-22	16 Mo–6 Cr–1 Nb–1 Al–0.08 C–bal Ni (INOR-7)	3	32	0	3	
30-33	15 Mo–6 Cr–5 Fe–0.5 Al–0.5 Mn–0.06 C–bal Ni (INOR-8)	3				Processing incomplete
STC-5525**	17 Mo–4 Al–bal Ni	3				Processing incomplete
30-46	17 Mo–10 Cr–7 Fe–0.5 Al–0.5 Mn–0.06 C–bol Ni	3				Processing incomplete
30-47	17 Mo–10 Cr–7 Fe–0.5 Al–0.5 Mn–0.06 C–bal Ni	3				Processing incomplete

*Approximately 10 ft of tubing is required to fabricate a thermal-convection loop.

**Heat supplied by Superior Tube Co.

of the tubing needed for the loop tests to be made at Battelle.

Fabrication of ORNL Alloys

The initial effort at ORNL on the nickel-molybdenum alloy development program was largely concerned with supplying seamless tubing of various compositions for fused fluoride salt and sodium corrosion evaluation in thermal-convection-loop tests. Emphasis has been placed on ternary compositions in order to determine singly the effect of various alloy strengtheners on the corrosion resistance of the base composition, 17% Mo–bal Ni. The alloying elements being studied are Cr, Al, Ti, Nb, W, V, and Fe. In addition to the ternary-alloy studies an investigation is to be made of the corrosion resistance of the INOR compositions. Laboratory heats of the alloys have been prepared for conversion to seamless tubing.

The results of redrawing of the extruded tube blanks to 0.500-in.-OD, 0.035-in.-wall tubing at the Superior Tube Co. are summarized in Table 3.3.2. With the exception of alloys 30-17 (4% Al) and 30-18 (4% Ti), no difficulties were encountered in processing the extrusions. One of the three processed extrusions of alloy 30-17 was defective and could not be cleaned up by machining; it was returned as scrap. The two remaining extrusions

were consistently harder than those of other compositions; one split longitudinally at approximately 0.700-in.-OD, 0.040-in.-wall thickness, and the other developed cracks during the final anneal. Alloy 30-18 (4% Ti) was not excessively hard and appeared to be amenable to cold working, but the finished tubing contained numerous cracks.

Although it is readily apparent that composition 30-17 (17% Mo–4% Al–0.06% C–bal Ni) is of no value in the alloy development program other than for establishing the effect of a high aluminum content on the corrosion resistance of the base composition, three additional billets of this alloy, prepared from heat STC-5525 supplied by Superior Tube Co., were extruded with moderate success and returned for processing. These billets were extruded at 2300°F instead of 2200°F in the hope that the unit extrusion pressure would be lowered at the higher temperature. However, little, if any, difference from previous results was noted.

Tubing to be processed from alloys 30-46 and 30-47, also listed in Table 3.3.2, is to be fabricated into forced-circulation loops. Since chromium is required for oxidation resistance in nickel-molybdenum alloys and since chromium additions up to 10% result in only a limited amount of corrosion in thermal-convection-loop tests with the fuel mixture No. 107, the more severe forced-circulation-loop tests are in order. Such tests of alloys 30-46 and 30-47, which contain 10% Cr, should help to establish trends from a corrosion standpoint.

Since sufficient tubing of the ternary and INOR alloys has been made available for preliminary corrosion evaluation, attention has been directed toward the fabrication of weld wire and stress-rupture specimen blanks to fill material requirements for other phases of the alloy screening program. The procedure for preparing wire has been to extrude a solid billet to a $^7/_8$-in.-dia rod and cold-swage the rod to 0.125 in. in diameter, along with intermediate annealing treatments. The stress-rupture specimen blanks are prepared by extruding a 1.5-in.-dia rod, hot-rolling the rod to 0.300- to 0.250-in.-thick strip, and further reducing the strip to 0.065 in. in thickness by cold-rolling, along with intermediate anneals.

The status of the fabrication of wire and strip products is summarized in Table 3.3.3. The initial effort is being devoted to the fabrication of the INOR alloys to gain some knowledge of their properties prior to a more complete evaluation, which will be carried out on the products of the large air-melted heats being processed by the International Nickel Company.

A flow diagram that summarizes the procedure for fabricating experimental quantities of the various shapes required for alloy evaluation is presented in Fig. 3.3.4. Thus far no attempt has been made to produce 0.500-in.-thick plate for weldability studies, but a casting of the alloy INOR-8 has been prepared for this purpose. Two billets 5.5 in. long, 3 in. wide (maximum), and 1.875 in. thick will be machined from the casting, and each billet will be hot-rolled to a plate approximately 12 in. long, 5 in. wide, and 0.5 in. thick. No difficulties are expected, and it is anticipated that plate material of a variety of compositions can be supplied for welding studies.

Production of Commercial-Size Heats of Nickel-Molybdenum Alloys

In order to gain production experience with special nickel-molybdenum alloys, the International Nickel Company has prepared 4800-lb air-melted heats of six alloys which, according to their experience, should possess elevated temperature strengths superior to that of Inconel. The nominal compositions of these alloys, designated as INOR-1 through -6, are listed below:

	Composition (wt %)
INOR-1	20 Mo–bal Ni
INOR-2	16 Mo–5 Cr–bal Ni
INOR-3	16 Mo–1.5 Ti–1 Al–bal Ni
INOR-4	16 Mo–1.5 Ti–2 Al–bal Ni
INOR-5	15 Mo–2 Nb–2 W–0.10 C–bal Ni
INOR-6	16 Mo–5 Cr–1.5 Ti–1 Al–bal Ni

A materials inventory which was received from the International Nickel Company following breakdown of the ingots is presented in Table 3.3.4. It has been requested that the product of each composition remaining for processing be fabricated to seamless tubing, plate, sheet, wire, and rod for carrying out a complete evaluation program on each alloy. One composition, INOR-4, could not be forged very successfully, and only sufficient billet material remains for fabricating a small amount of plate and sheet product.

Hot-rolled rods prepared from usable billet stock of each alloy have already been submitted to the New England Materials Laboratory and to Rensselaer

TABLE 3.3.3. STATUS OF FABRICATION OF 0.125-in.-dia WELD WIRE AND 0.065-in.-THICK STRIP FROM ORNL ALLOYS

Alloy No.	Nominal Composition (wt %)	Diameter of Extruded Rod (in.)	Results
30-25 (INOR-2)	16 Mo–5 Cr–0.5 Al–0.5 Mn–0.06 C–bal Ni	0.875	Cold-swaged to 0.125-in.-dia weld wire; yield, $3\frac{3}{4}$ lb
		0.875	Cold-swaged to 0.125-in.-dia weld wire; yield, $3\frac{3}{4}$ lb
		1.5	Hot-rolled* to 0.250 in. in thickness; cold-rolled** to 0.065-in.-thick strip
30-26 (INOR-3)	16 Mo–1.5 Ti–1 Al–0.5 Mn–0.06 C–bal Ni	1.25	Cold-swaged to 0.125-in.-dia weld wire; yield, $4\frac{1}{4}$ lb
		0.875	Cold-swaged to 0.125-in.-dia weld wire; yield, $4\frac{1}{4}$ lb
		1.5	Slight edge cracking on hot rolling to 0.250 in. in thickness; cold-rolled to 0.065-in.-thick strip
30-27 (INOR-4)	16 Mo–1.5 Ti–2 Al–0.5 Mn–0.06 C–bal Ni	0.875	Cold-swaged to 0.125-in.-dia weld wire; yield, 4 lb
		0.875	Cold-swaged to 0.125-in.-dia weld wire; yield, 4 lb
		1.5	Slight edge cracking on hot rolling to 0.250 in. in thickness; cold-rolled to 0.065-in.-thick strip
30-28 (INOR-5)	16 Mo–2 Nb–2 W–0.5 Al–0.5 Mn–0.10 C–bal Ni	0.875	Processing incomplete
		1.5	Hot-rolled to 0.250 in. in thickness; cold-rolled to 0.065-in.-thick strip
30-29 (INOR-6)	16 Mo–5 Cr–1.5 Ti–1 Al–0.5 Mn–0.06 C–bal Ni	0.875	Processing incomplete
		1.25	Slight edge cracking on hot rolling to 0.250 in. in thickness; cold-rolled to 0.065-in.-thick strip
30-23 (INOR-7)	16 Mo–6 Cr–1 Al–1 Nb–0.5 Mn–0.08 C–bal Ni	0.875	Cold-swaged to 0.125-in.-dia weld wire; yield, $2\frac{3}{4}$ lb
		0.875	Cold-swaged to 0.125-in.-dia weld wire; yield, $2\frac{3}{4}$ lb
		1.5	Moderate edge cracking on hot rolling to 0.250 in. in thickness, cold-rolled to 0.065-in.-thick strip

*Hot rolling carried out at 2150°F at reductions of 3 to 10% per pass.

**Cold rolling carried out at approximately 2% per pass.

Polytechnic Institute for stress-rupture and weldability studies, respectively.

The Westinghouse Electric Corporation has submitted a contract proposal covering the melting, casting, and fabrication of large pilot heats of nickel-molybdenum alloys at their Blairsville, Pennsylvania, metals plant. In essence, the proposal calls for induction melting in air of 3000-lb heats of the two alloys listed below:

	Composition (wt %)
INOR-7	16 Mo–6 Cr–1 Nb–1 Al–bal Ni
INOR-8	15 Mo–6 Cr–5 Fe–bal Ni

Each heat is to be cast into two ingots of approximately 1150 lb each and three ingots of approximately 265 lb each. The small ingots will be used for pilot forging runs to determine the best forging techniques, including heating cycles, forging temperatures, reductions, etc.

After the most suitable forging practice for each alloy has been determined, one 1150-lb ingot will be forged to a suitable round for the preparation of $8\frac{3}{4}$-in.-dia extrusion billets to be subsequently extruded to tube blanks by the International Nickel Company. The second large ingot of each alloy will be forged by the best technique developed to

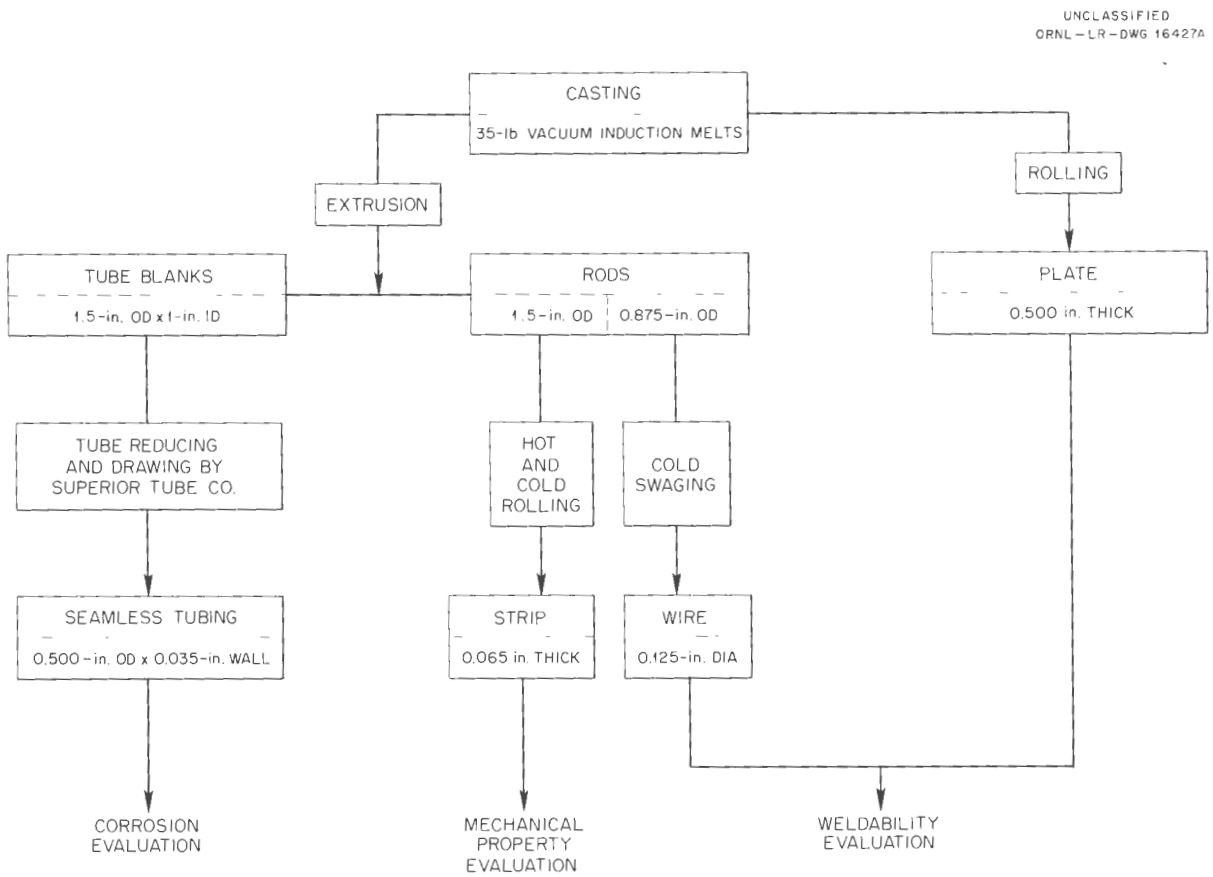

Fig. 3.3.4. Fabrication Procedure for Obtaining Material for Alloy Evaluation.

a billet suitable for the fabrication of plate, sheet, rod, and wire.

The second phase of the program will be an investigation and evaluation of fabricated products produced by induction-melting in vacuum and by arc-melting in vacuum. It is proposed that two ingots of approximately 1000 lb each of an alloy yet to be selected be produced by induction- and arc-melting in vacuum and fabricated into sheet and rod for evaluation to provide an indication of the effect of melting practice on mechanical properties of the alloy. For the third phase of the program it is proposed that five heats of 5000 lb each of a selected alloy be prepared by induction-melting in air and fabricated into typical shapes for a study of reproducibility of results and the reprocessing of developed scrap.

SHIELD PLUGS FOR ART PUMPS

J. P. Page

The shield plugs for the ART pumps are to consist of a layer of copper-B_4C neutron shielding, a layer of stabilized zirconia that will serve as a thermal shield, and a layer of a compact consisting of a mixture of tungsten carbide and Hastelloy C that will serve as a gamma-ray shield. Graphite dies for hot pressing the full-size gamma-ray shields were designed and obtained. A 42-lb batch of the shielding material, 75 wt % tungsten carbide and 25 wt % Hastelloy C, has been weighed, blended, and packed into one of the alumina-coated dies. A large, horizontal, hot-pressing unit is being readied for final fabrication of the shield material, which is to have a density greater than 12.0 g/cm^3, a thermal conductivity of less than

TABLE 3.3.4. INVENTORY OF MATERIAL FROM 4800-lb HEATS OF NICKEL-MOLYBDENUM ALLOYS PREPARED BY INTERNATIONAL NICKEL COMPANY

Alloy No.	Total Ingot Weight (lb)	Billet for Processing				Weight of Scrap (lb)	Rod Material Sent To					
							New England Materials Laboratory			Rensselaer Polytechnic Institute		
		Dimension	Length		Weight (lb)		Diameter (in.)	Length (ft)	Weight (lb)	Diameter (in.)	Length (ft)	Weight (lb)
			Feet	Inches								
INOR-1	4720	4 × 6 in.	15	2	1404	2495	½	26	21	½	13	10
		8¾ in. dia		20	390							
		8¾ in. dia		10	400[a]							
INOR-2	4614	3 × 3 in.	3		106	2585	½	44	36	7/16	20	12
		3 × 3 in.	28		890							
		8¾ in. dia		31	585[b]							
		8¾ in. dia		10	400[a]							
INOR-3	4621	4 × 5 in.	16		1152	3095	½	49	40	½	26	21
		3 × 3 in.	3		113							
		8¾ in. dia		10	200[c]							
INOR-4	4370	3 × 3 in.	3		113[b]	4195[d]	½	51½	41	½	26	20
INOR-5	4469	3 × 3 in.	3		102	2250	½	54½	41	7/16	26	16
		3 × 3 in.	36		1175							
		8¾ in. dia		25	485							
		8¾ in. dia		10	400[a]							
INOR-6	4557	3 × 3 in.	34		1095	2665	½	23½	18	½	11	9
		8¾ in. dia		30	570							
		8¾ in. dia		10	200							

[a] Two extrusion billets.
[b] Billet split on one end.
[c] One-piece extrusion billet.
[d] Ingot split on forge.

0.10 cal/cm·sec·°C, and must be brazable to Inconel.

Thermal shields of stabilized zirconia have been machined and are ready for insertion into the shield plug assemblies. The density of these pieces is approximately 3.25 g/cm^3, and the thermal conductivity at 600°C will be approximately 0.0016 cal/cm·sec·°C.

Stainless steel picture frames for the copper-B_4C for neutron shield portions of the shield plug assemblies have been designed and prepared. The composites will be assembled and rolled to 0.128 in. in thickness. The B^{10} content of the rolled composites will be somewhat greater than the 0.01 g/cm^2 minimum required.

NEUTRON SHIELD MATERIAL

M. R. D'Amore[4] J. H. Coobs

ART Neutron Shield Plates

Four batches of type 430 stainless-steel-clad copper-B_4C (20 vol %, 6.6 wt % B_4C) plates designed for use as neutron shielding in the ART and fabricated by the Allegheny Ludlum Steel Corp. were tested. The materials used for these evaluation tests were pieces that did not meet the material specifications because of minor flaws or insufficient size but were considered to be representative pieces of each batch. The Allegheny Ludlum batch numbers and the dimensions of the plates evaluated are listed below:

Batch No.	Size of Plate Evaluated (in.)
5503	$6\frac{3}{8} \times 8\frac{1}{2}$
5504	$3\frac{7}{8} \times 6\frac{7}{8}$
5505	$4\frac{7}{8} \times 7\frac{1}{2}$
5507	$7\frac{1}{2} \times 8\frac{1}{2}$

Another batch (No. 5506) of plates has been fabricated, but no pieces from this batch were evaluated because no scrap pieces are available. The evaluation tests included radiography, bend and tensile tests, thickness uniformity and core density measurements, microstructure analysis, and clad-to-core bonding examinations.

No segregation or cracking of the copper-B_4C cores was observed, and the claddings were well bonded to the cores on all the plates evaluated. The density of the cermet core of batch 5505 was 97.9% of theoretical. The densities of the cores of the plates from the remaining batches were not measured because the density of the core from batch 5505 was the same as the density of the first material produced by Allegheny Ludlum. Bend specimens $\frac{3}{8} \times 1\frac{1}{2}$ in. were sheared from each plate parallel and transverse to the rolling direction and annealed at 1750°F for 15 min. All the specimens were bent to less than a $\frac{3}{4}$-in. radius before cracking occurred in the copper-B_4C core. The thicknesses of the components of each composite plate were determined metallographically and are listed in Table 3.3.5. The minimum thickness of the copper barrier was thinner on all plates than the 0.001 to 0.002 in. specified. The plate from batch No. 5505 was within the specified over-all thickness tolerance of 0.100 ± 0.004 in. The remaining batches varied in over-all thickness to a maximum of 0.1065 in. The room-temperature tensile strengths of the plates, which indicate satisfactory ductility for subsequent forming operations, are given in Table 3.3.6. The room-temperature tensile strengths of the clad cermets were found to be comparable to the strength reported in the literature for pure copper, and the yield strengths are approximately double the value for pure copper.

Copper-B_4C Parts for Pratt & Whitney High-Temperature Critical Experiment

Fabrication was completed of a stainless-steel-clad copper-B_4C ring approximately 14 in. in diameter, 1.5 in. wide, and 0.4 in. thick for use as a neutron shield in the Pratt & Whitney Aircraft high-temperature critical experiment. The material for the ring was prepared by tamping a stainless steel tube with a powder mixture of 25 vol % B_4C–75 vol % Cu and then sealing and evacuating the tube. The tube was hot-rolled at 1750°F to consolidate the powders and to obtain the proper thickness. The density of the core material was approximately 95% of theoretical after the hot-rolling operation. The material was fabricated into a 14-in.-dia ring by cold forming and then machining to the required dimensions. Material for a larger ring approximately 19 in. in diameter, 3 in. wide, and 0.4 in. thick has been prepared by the same method, and the ring is currently being machined.

[4] On assignment from Pratt & Whitney Aircraft.

TABLE 3.3.5. COMPONENT THICKNESSES OF ALLEGHENY LUDLUM TYPE 430 STAINLESS-STEEL-CLAD COPPER-B_4C PLATE

Batch No.	Plate Component Thicknesses (in.)					
	Cladding		Copper Barrier		Copper Barrier and Core	
	Minimum	Maximum	Minimum	Maximum	Minimum	Maximum
5503	0.009	0.012	>0.00025	0.001	0.079	0.081
5504	0.010	0.014	>0.00025	0.001	0.078	0.078
5505	0.008	0.011	>0.00025	0.001	0.076	0.078
5507	0.010	0.011	>0.00025	0.001	0.080	0.081

TABLE 3.3.6. ROOM-TEMPERATURE TENSILE STRENGTH OF ALLEGHENY LUDLUM TYPE 430 STAINLESS-STEEL-CLAD COPPER-B_4C PLATES

All specimens annealed 15 min at 1750°F prior to test

Plate from Batch No.	Test Direction	Yield Strength (psi)	Ultimate Strength (psi)	Elongation (% in 2-in. gage)
5503	Transverse to rolling direction	17,770	31,700	8.0
5504	Transverse to rolling direction	19,470	33,000	7.5
5505	Transverse to rolling direction	18,020	32,000	8.8
5507	Transverse to rolling direction	19,115	30,200	4.0
5507	Parallel to rolling direction		33,900	7.5

TUBULAR CONTROL RODS

M. R. D'Amore

The feasibility study of extrusion of tubular control rods, described previously,[5] was continued. A series of tensile tests has been completed on 0.115-in.-thick specimens of the 30 wt % Lindsay oxide–70% nickel core material at 1500°F, and the data are presented in Table 3.3.7. The specimens were prepared as described previously[5] and were tested with and without 0.0065-in.-thick Inconel cladding. Three different particle-size fractions of Lindsay oxide were used: <200 μ, 52–200 μ, and the fine, as-received material, with a particle size of <3 μ.

The unclad material showed tensile strengths between 10,000 and 11,000 psi, and the strength of the clad specimens was about 10% greater. Both the strength and the modulus of elasticity increased slightly with increasing size of the Lindsay oxide particles. None of the specimens showed appreciable ductility, and fracturing occurred shortly after the yield point. The lack of ductility may be caused by the distribution of the oxide particles. Microstructures of the material revealed that the as-received Lindsay oxide (<3 μ) particles tended to agglomerate during fabrication, and they formed a nearly continuous phase throughout the

[5]M. R. D'Amore, *ANP Quar. Prog. Rep. Sept. 10, 1956*, ORNL-2157, p 181.

TABLE 3.3.7. TENSILE STRENGTH OF UNCLAD AND INCONEL-CLAD SPECIMENS OF 30 wt % LINDSAY OXIDE–70 wt % NICKEL CERMETS AT 1500°F

Specimen thickness: 0.115 in.
Cladding thickness: 0.0065 in.

Mesh Size of Lindsay Oxide	Specimen Condition	Yield Strength (psi)	Ultimate Strength (psi)	Modulus of Elasticity (psi × 10^6)	Elongation (% in 2-in. gage)
60 + 270 (52–200 μ)	Clad	10,642	12,210	12.5	0
	Clad	*	12,380	*	0
	Unclad	10,359	11,226	18.2	0
60 (<200 μ)	Clad	10,985	11,826	41.8	0
	Clad	10,690	12,310	7.76	0
	Unclad	10,128	10,300	7.7	0
As-received (<3 μ)	Clad	9,535	10,830	5.74	0
	Clad	8,227	9,732	8.2	1.8

*Specimen tested without extensometer.

nickel matrix, as shown in Fig. 3.3.5. The <200 and 52–200 μ Lindsay oxide particles were quite soft and porous, and they fractured during the hot-rolling operation. The fracturing resulted in severe stringering, as shown in Fig. 3.3.6. The larger particles were prepared by calcining compacts of the as-received Lindsay oxide at 1400°C and then grinding the material to the desired particle size. Higher firing temperatures will be used in future work to obtain higher density particles.

Two Hastelloy-X-clad Lindsay oxide–nickel billets were extruded during the quarter. The first billet was extruded at 2150°F at an extrusion ratio of 5:1, but the use of poor tools resulted in eccentricity and unsatisfactory surface quality in the extruded tube. The tube was cooled from a black heat after extrusion by quenching in water. Audible cracking of the cermet core occurred during the quenching treatment. The second Hastelloy-X-clad billet was extruded at 2200°F at a 7:1 ratio and was allowed to air cool. Examination revealed that the core layer of the air-cooled extruded tube had cracked under the less severe cooling conditions, and hot-short cracks were observed in the Hastelloy X cladding. A transverse section of the extruded tube is shown in Fig. 3.3.7, and the cracking which occurred in the core is shown in Fig. 3.3.8.

The linear thermal expansion of the 30 wt % Lindsay oxide–70 wt % nickel cermet was measured between room temperature and 900°C on specimens prepared by hot pressing and by hot swaging. The densities of the specimens, as measured by the water-displacement method, were 98.0 and 97.5% of theoretical, respectively. A slight difference noted in the thermal-expansion values for the two specimens was attributed to the difference in fabrication techniques. The mean coefficient of thermal expansion between 0 and 900°C for the hot-pressed specimen was 15.6×10^{-6} in./in.·°C.

NIOBIUM FABRICATION STUDIES

V. M. Kolba[6] J. P. Page

Evaluation of Arc-Melted Niobium

Three views of a macrosection of an as-received arc-melted niobium plate are presented in Fig. 3.3.9 which show the extremely large grain sizes usually present in arc-melted, cast, cold-worked ingots, as stated previously.[7] Evaluation of the physical properties of this material must be delayed until a fabrication schedule is developed which will yield a constant, reproducible grain size in

[6]On assignment from the Glenn L. Martin Company.

[7]H. Inouye, V. M. Kolba, and J. P. Page, *ANP Quar. Prog. Rep. Sept. 10, 1956*, ORNL-2157, p 183.

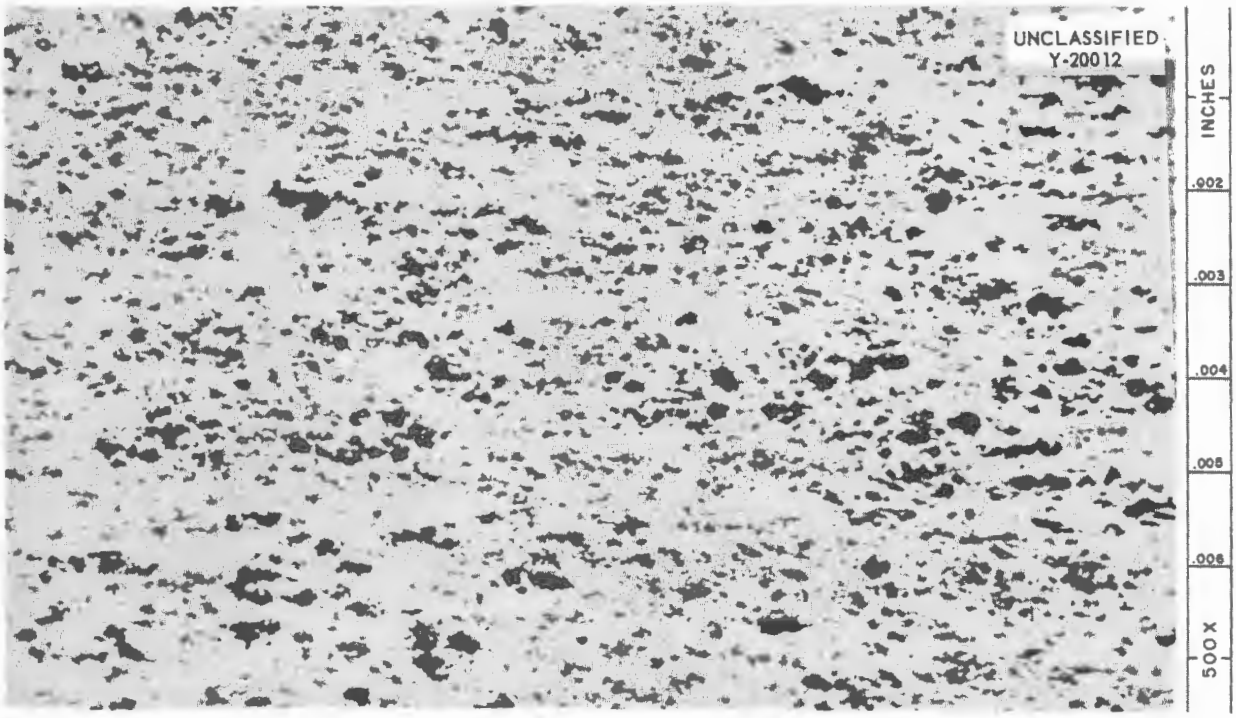

Fig. 3.3.5. Longitudinal Section of Core of Hot-Rolled Tensile Specimen of As-Received Lindsay Oxide (<3 μ) in a Nickel Matrix. 500X. Reduced 2%.

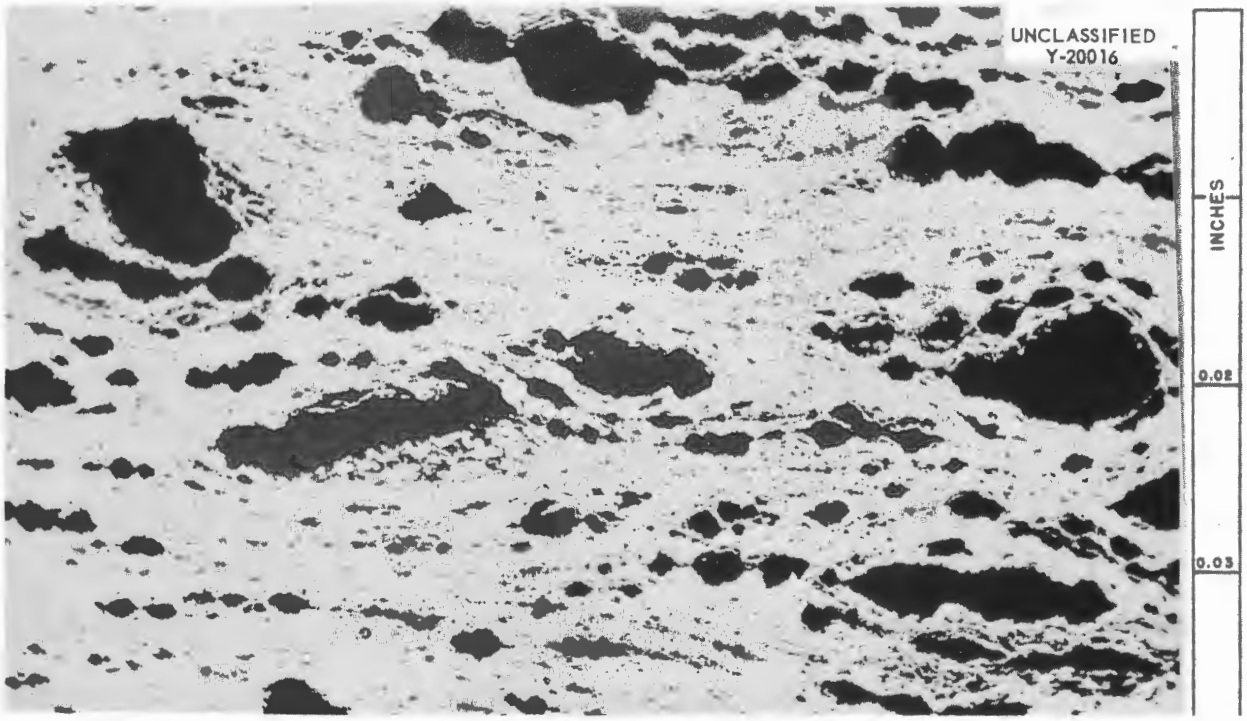

Fig. 3.3.6. Longitudinal Section of Core of Hot-Rolled Tensile Specimen of Lindsay Oxide (52–200 μ) in a Nickel Matrix. 100X. Reduced 2%.

Fig. 3.3.7. Traverse Section of Three-Ply Control Rod Extrusion. 2.5X. Reduced 25%.

the test specimens. A recrystallization study has been initiated that will involve an initial breakdown of the as-received structure and a determination of the recrystallization characteristics of the resultant fine-grained material. This study will require x-ray and metallographic examination of cold-worked niobium annealed for various times at several temperatures.

A Globar tube furnace is being adapted for inert-atmosphere annealing treatments. Preliminary data indicate that the very large-grained as-received and cold-worked material begins to recrystallize in less than ½ hr at temperatures of between 1100 and 1200°C. The time to the beginning of recrystallization depends on the amount of cold work. Recrystallization is not complete, however, in 4 hr at these temperatures. The arc-cast ingots have been analyzed for oxygen, nitrogen, hydrogen, and carbon, and the results of these analyses are given in Table 3.3.8.

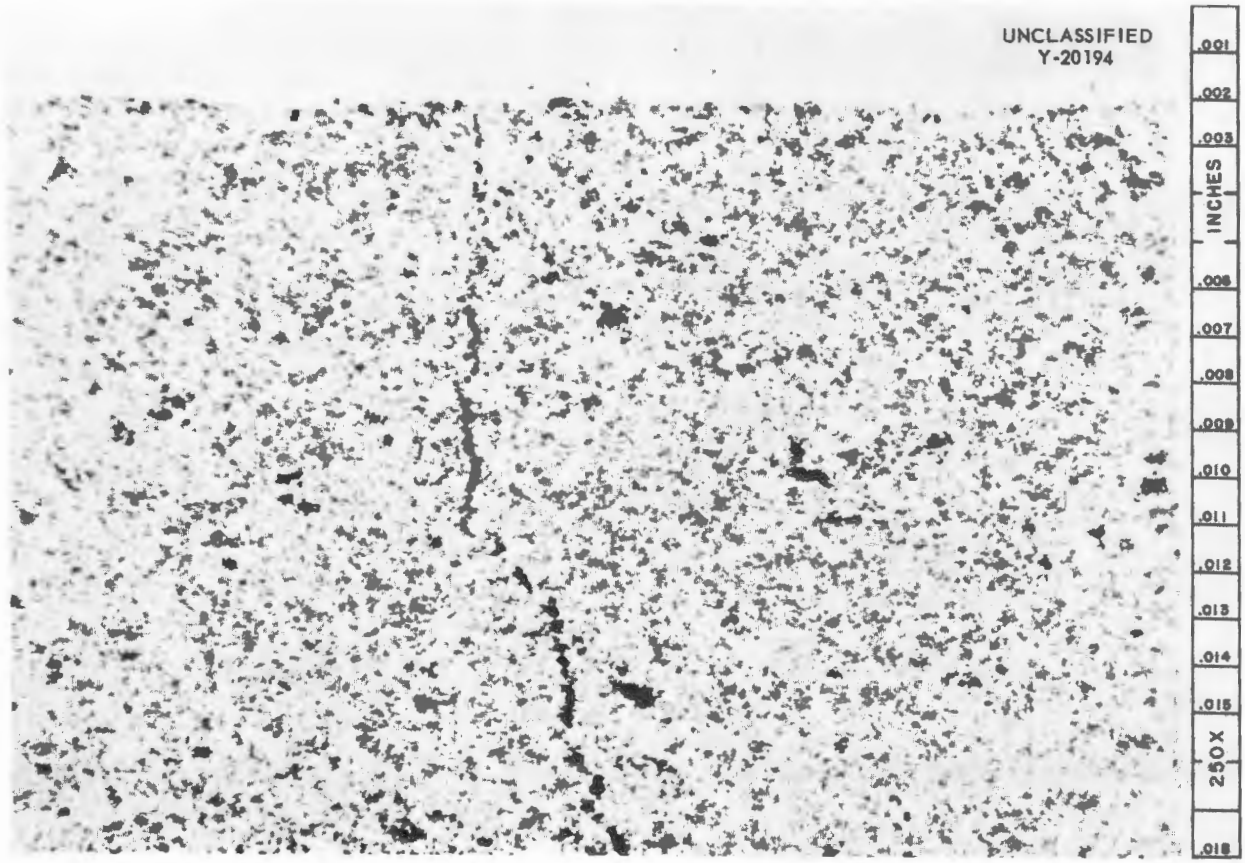

Fig. 3.3.8. Microstructure in Core of Extruded Three-Ply Control Rod Showing Cracking Which Occurred During Cooling. 250X.

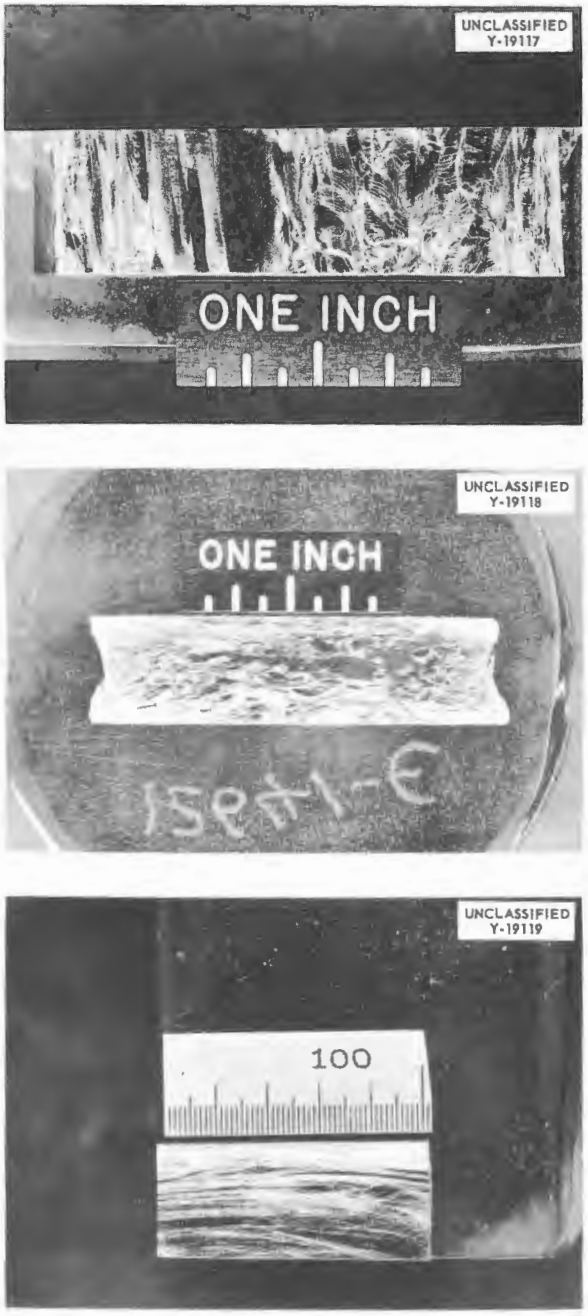

Fig. 3.3.9. Macrosections of As-Received Arc-Melted Niobium Plate.

Nb-UO_2 Compacts

The five Nb-UO_2 compacts, described previously,[7] which were vacuum-sintered for ½ hr at 2000°C showed slight weight losses – the maximum being 0.43%. The compacts were coined at 60 tsi to a density of 87.5% of theoretical. Cold rolling of one of the coined compacts was attempted, but severe cracking developed after 23% reduction. Two of the compacts were placed between wrought niobium sheets, encapsulated in stainless steel, and hot-rolled at 1100°C to a total reduction of 76% in thickness. The rolled plates showed no visible cracks, and radiographs showed good core integrity. However, metallographic examination revealed unsatisfactory bonding between the niobium cladding and the niobium in the core matrix.

Samples of the roll-clad plates were annealed, and the hardness data were obtained for comparison with the hardness data for starting materials. The results of the hardness determinations are shown in Table 3.3.9. Aging tests at 1000°C for 500 hr are in progress to check the stability of the compacts. Bend tests on samples of the as-rolled plate revealed that the core was brittle. The stainless steel capsules fractured after a 30-deg bend, and the niobium cladding and the Nb-UO_2 core cracked at a 70-deg bend angle.

An attempted extrusion at 1200°C of a 40 wt % UO_2–60 wt % Nb cold-pressed compact in a mild-steel can was unsuccessful. The compact was reduced only sufficiently to pass through the die opening, that is, from 1 in. in diameter to ~⅞ in. in diameter. A cold-pressed compact of Fansteel high-purity niobium powder in the same billet extruded unsatisfactorily. The density of the all-niobium extruded rod was 95% of theoretical. A second extrusion is planned in which the compact will be 30 wt % UO_2 in niobium with an addition of 8 wt % niobium–uranium alloy powder. A type 316 stainless steel container will be used. Powder for this compact has been made from wrought sheet material.

Niobium-Uranium Alloys

The fabrication of dispersion-type fuel elements presents several problems, the main ones being the attainment of homogeneity and the prevention of stringering of fuel particles. If a homogeneous uranium alloy were made in which UO_2 could be precipitated after final fabrication by a heat treatment, perhaps the stringering effect would be considerably reduced or even eliminated.

Preliminary calculations of the free-energy of formation of oxides have indicated that UO_2 would form in preference to Nb_2O_5 in niobium-

TABLE 3.3.8. IMPURITY ANALYSES OF ARC-CAST NIOBIUM INGOTS

Ingot No.	Location of Sample	Carbon (%)	Oxygen (ppm)	Nitrogen (ppm)	Hydrogen (ppm)
10	Top	0.04	900	360	13
		0.02	520	360	4
	Middle	0.01	640	350	5
	Bottom	0.06	500	360	11
13	Top	0.01	390	250	<1
	Middle	0.01	490	280	<1
		0.01	540	270	2
	Bottom	0.01	480	280	4
14	Top	0.01	470	260	4
	Middle	0.01	360	250	1
	Bottom	0.02	610	290	<1
		0.05	360	320	1
15	Top	0.03	520	250	6
	Middle	0.01	380	270	4
	Bottom	<0.01	520	270	14

TABLE 3.3.9. RESULTS OF HARDNESS DETERMINATIONS MADE DURING FABRICATION OF Nb-UO_2 PLATE CLAD WITH NIOBIUM

Fabrication Stage	Hardness (VHN)	
	Cladding	Core
Starting materials: sheet and powders	134	179–233
Sintered and coined		212
Hot-rolled	201	317
Vacuum-annealed 1 hr at 1150°C	177	188

uranium alloys. Additional verification of this was found in an article by McIntosh and Bagley[8] which states that "tests on Ta and Nb containing oxygen demonstrate that uranium, either solid or liquid, will remove oxygen from both these materials." The usefulness of this method of oxide precipitation *in situ* is dependent upon the reaction going in the correct direction to virtual completion and also upon the size of the particles produced. An independent study[9] of UO_2 particle size vs the radiation-damage affected area in a 30 vol % matrix showed that the minimum particle size which allows undamaged matrix material between particles is about 40 μ.

Attempts are under way presently to make a homogeneous niobium-uranium alloy which can be readily fabricated and which, by controlled oxidation and subsequent aging, will form discrete UO_2 particles. Efforts will be directed toward control of the size and distribution of the precipitated oxide particles. Such an alloy could also be added to Nb-UO_2 mixtures to remove the excess oxygen in the UO_2 system and thereby contribute to better ductility of the Nb-UO_2 compacts.

Annealing tests were conducted on a hot-rolled 80% Nb–20% U alloy which had been reduced 86.4% in thickness at 1050°C. The as-hot-rolled structure is shown in Fig. 3.3.10. Recrystallization

[8]A. B. McIntosh and K. Q. Bagley, *J. Inst. Metals* 84, 251 (1956).

[9]M. J. Feldman, *Radiation Effects in Solid Fuel Elements*, ORNL CF-55-1-18 (Feb. 2, 1955).

Fig. 3.3.10. An 80% Nb–20% U Alloy as Hot-Rolled at 1050°C. 500X. Reduced 2%. (Confidential with caption)

tests were conducted by vacuum annealing for 1 hr at 1100, 1200, and 1300°C. The recrystallized structure found after annealing for 1 hr at 1300°C is shown in Fig. 3.3.11. Additional annealing tests carried out at 1175 and 1250°C verified that the recrystallization temperature was near 1300°C. Hardness measurements on the vacuum-annealed samples revealed an increase in hardness as the temperature increased, as shown in Table 3.3.10. This was attributed to increasing contamination of the samples because of the poorer vacuum at the higher furnace operating temperatures. A sample which was annealed 1½ hr at 1100°C was successfully cold-rolled from 0.052 in. to 0.0065 in. in thickness at 0.002 in. per pass.

A second niobium-uranium alloy melt was encapsulated and hot-rolled at 1200°C. The hot-

TABLE 3.3.10. HARDNESS VALUES FOR AN 80% Nb–20% U ALLOY ANNEALED FOR 1 hr AT VARIOUS TEMPERATURES

Annealing Temperature (°C)	Annealing Vacuum (mm Hg)	Hardness (R_B)
As-hot-rolled at 1050°C		86
1100	10^{-5}	76.5
1175	10^{-5}	80.5
1200	10^{-5}	81.5
1250	10^{-4}	88.3
1300	$\sim 10^{-5}$	83.5

rolled alloy plate was then vacuum-annealed for 1½ hr at 1100°C and cold-rolled from 0.070 in. to 0.019 in. in thickness. Tensile specimens were prepared from this material, and tested in the as-cold-rolled condition and after an additional vacuum anneal at 1100°C. The test results are shown in Table 3.3.11.

Samples of the niobium-uranium alloy have been hydrided, crushed, and vacuum-annealed to make powders of the alloy which will be added to Nb-UO_2 compact cores.

Some attempts have been made to study the selective oxidation of uranium in the niobium-uranium alloy. The as-cast alloy was oxidized for 1½ hr at 600°C in air and aged in vacuum for 100 hr at 1200°C. During the 100-hr aging treatment the hardness of the oxidized edge decreased from 399 to 227 VHN, and the hardness of the core

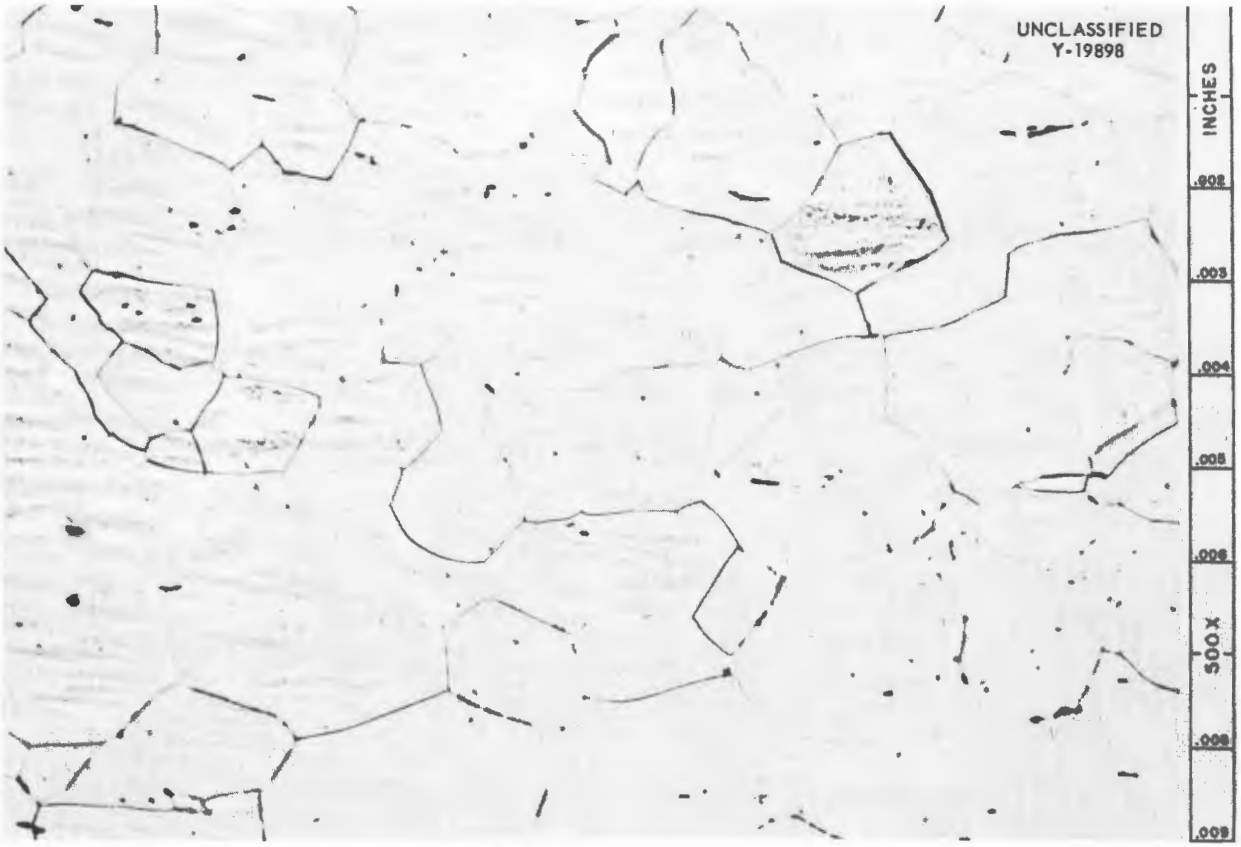

Fig. 3.3.11. An 80% Nb–20% U Alloy Hot-Rolled and Annealed 1 hr at 1300°F. 500X. Reduced 2%. ~~(Confidential with caption)~~

TABLE 3.3.11. RESULTS OF TENSILE STRENGTH TESTS OF A NIOBIUM-URANIUM ALLOY

Sample Condition	Ultimate Tensile Strength (psi)	Elongation (% in 2-in. gage)	Yield Strength 0.1% Offset (psi)	Hardness (VHN)
As-cold-rolled	104,300	1	93,000	285
Vacuum-annealed 1 hr at 1100°C	91,900	18	64,700	193

increased from 168 to 183 VHN. A section near the edge in which a precipitate can be seen clearly is shown in Fig. 3.3.12. X-ray diffraction studies revealed the following constituents and relative line intensity ratios: Nb, 84; U, 4; Nb_2O_5, 9; UO_2, 5.

Additional samples of the alloy have been oxidized in pure oxygen and attempts are being made to precipitate UO_2 from this alloy after it has been clad. A furnace is being constructed to study the precipitation in a partial pressure of oxygen at elevated temperatures and to determine the effect of interstitial compounds on the alloy.

FABRICATION OF HYDRIDES

R. E. McDonald[10]

A study of the fabrication of hydride moderating materials was initiated. The high-temperature controlled-atmosphere tensile rig has been redesigned for use with hydrides, and technology for the preparation of yttrium metal from its oxide is being acquired. The high-temperature controlled-atmosphere tensile rig, shown in Fig. 3.3.13, was originally used for the investigation of Ames thorium. It was designed to take a standard 0.505-in.-dia ASTM specimen. The extension of the specimen is measured by the movement of the pull rods which are mounted to blocks attached to the shoulders of the specimen. For the hydride moderator study a $^3/_{16}$-in.-dia ASTM specimen was chosen because of the scarcity and cost of the metal hydrides to be tested. It was necessary to modify the specimen holders and to make the specimens self-aligning. The complete rig is being checked

[10]On assignment from Pratt & Whitney Aircraft.

Fig. 3.3.12. Precipitate in Oxidized and Aged Niobium-Uranium Alloy. 500X. ~~(Confidential with caption)~~

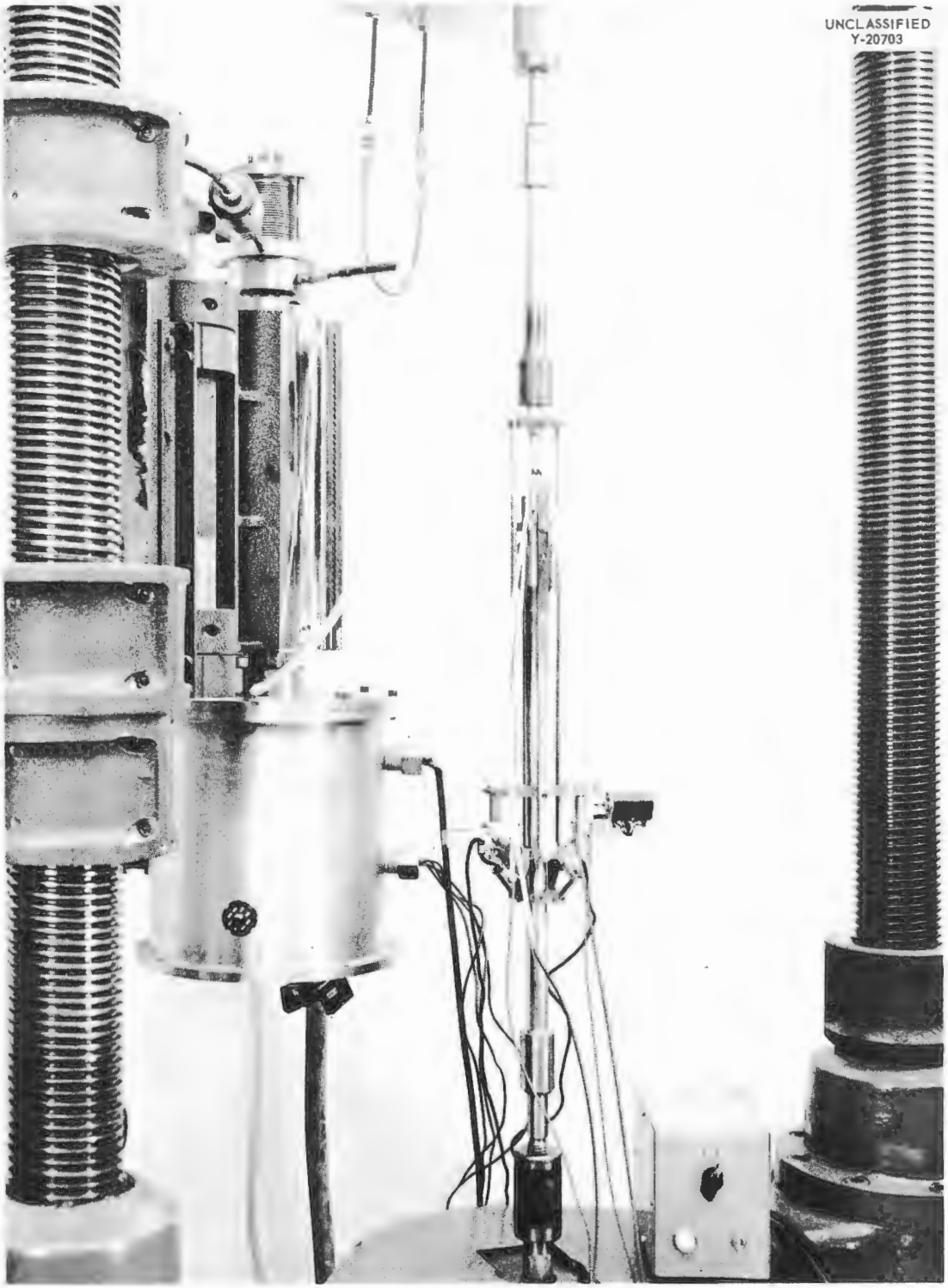

Fig. 3.3.13. Controlled-Atmosphere Tensile Test Rig Showing Extensometer and Control-Rod Setup.

by testing Inconel at various temperatures and comparing the resultant stress-strain curves with curves obtained by the standard method.

The fabrication of equipment necessary for the reduction of yttrium oxide to yttrium metal has begun. During the next quarter yttrium metal is to be produced by the Carlson process.[11] It is felt that this process is best suited to the available melting facilities.

[11] O. N. Carlson, F. A. Schmidt, and F. H. Spedding, *Preparation of Yttrium Metal by Reduction of Yttrium Trifluoride with Calcium*, ISC-744 (July 17, 1956).

3.4. WELDING AND BRAZING INVESTIGATIONS

P. Patriarca

WELDABILITY STUDIES OF NICKEL-MOLYBDENUM ALLOYS

P. Patriarca R. E. Clausing

A program has been initiated for a detailed investigation of the weldability of both commercial and experimental nickel-molybdenum alloys. The test specimens consist of a joint, $\frac{5}{8}$ in. wide, made between two $\frac{1}{2}$-in.-thick plates of the particular nickel-molybdenum alloy being studied. The filler metal is deposited by the inert-gas tungsten-arc process by qualified operators according to established procedures. The resulting joint is examined visually, with dye-penetrant, and radiographically and is then machined into all-weld-metal tensile, transverse-tensile, side bend, hardness, and metallographic specimens. The tensile and bend tests are conducted at room and elevated temperatures before and after aging.

Tensile Tests

The test plates described in Table 3.4.1 have been welded, and machining of 0.252-in.-dia reduced-section tensile specimens from the first few plates has been completed. A preliminary compilation of the as-welded data is presented in Table 3.4.2. All-weld-metal tensile and transverse-tensile data for Hastelloy B welds aged at 1300 and 1500°F for 200 hr are compiled in Tables 3.4.3 and 3.4.4. A summary of the all-weld-metal tensile data for Hastelloy W welds aged at 1300 and 1500°F for 200 hr is presented in Table 3.4.5.

An analysis of the data indicates that as-welded Hastelloy B joints failed in the weld metal, with good ductility, when tested at room temperature and failed in the base metal, with reduced ductility, when tested at 1500°F. Joints aged for 200 hr at 1300°F all failed with poor ductility; those tested at room temperature failed in the weld metal, while those tested at the aging temperature failed in the fusion line and heat-affected zone with lower ductility than that of all-weld-metal specimens tested under the same conditions. Hastelloy B welds aged for 200 hr at 1500°F showed a slight increase in strength and a slight decrease in ductility (compared with the as-welded ductility) when tested at room temperature, but no adverse effects were noted in tests at 1500°F.

Hastelloy W all-weld-metal specimens show strengths comparable to those of Hastelloy B and fair ductilities in all conditions tested. The Hastelloy W weld metal, however, apparently ages at 1300 and 1500°F, as evidenced by the decreased ductilities obtained upon holding for 200 hr at the aging temperature.

Hardness Tests

Small transverse-weld samples were machined from test plate No. 3 (Hastelloy B plate welded with Hastelloy B filler metal) and aged at 1100,

TABLE 3.4.1. NICKEL-MOLYBDENUM ALLOY WELDABILITY TEST PLATES

Plate No.	Plate	Filler Wire
1	Hastelloy B	85% Ni–15% Mo
2	Hastelloy B	Hastelloy B
3	Hastelloy B	Hastelloy B
4	Hastelloy B	Hastelloy B
5	Hastelloy W	Hastelloy W
6	Hastelloy W	Hastelloy W
7	Hastelloy W	Hastelloy W
8	Hastelloy B	Hastelloy B (vacuum melt)
9	Hastelloy B	Hastelloy W
10	Hastelloy W	85% Ni–15% Mo
11	Hastelloy W	INOR-2 (16% Mo–5% Cr–0.5% Al–0.5% Mn–0.06% C)
12	BMI-3405	BMI-3405 (20% Mo–7% Cr–2% Al–0.12% C)
13	BMI-3408	BMI-3408 (20% Mo–7% Cr–2% Nb–1% Al–0.12% C)
14	Hastelloy W	INOR-3 (16% Mo–1.5% Ti–1% Al–0.5% Mn–0.06% C)
15	BMI-3405	BMI-3405
16	BMI-3408	BMI-3408
17	Hastelloy W	INOR-7 (16% Mo–1% Al–1% Nb–0.5% Mn–3% Fe–0.08% C)
18	Hastelloy W	INOR-4 (16% Mo–1.5% Ti–2% Al–0.5% Mn–0.06% C)

1300, 1500, and 1650°F for 200 hr and at 1300°F for 24 and 500 hr. The results of hardness traverses made across the joints are plotted in Figs. 3.4.1 and 3.4.2. The variations in hardness between the base metal, heat-affected zone, and weld metal resulting from aging at the various temperatures are illustrated in Fig. 3.4.1. It may be seen that aging at 1300°F produced the highest hardness value, as measured with a Vickers diamond pyramid (10-kg load). The influence of aging time at 1300°F is shown in Fig. 3.4.2. Hardening is most pronounced along the weld metal–base metal interface and the heat-affected zone after aging at 1300°F.

TABLE 3.4.2. MECHANICAL PROPERTIES OF AS-WELDED NICKEL-MOLYBDENUM ALLOY

All-weld-metal tensile specimens

Type of Weld	Test Temperature (°F)	Tensile Strength (psi)	Yield Strength, 2% Offset (psi)	Elongation (% in 1-in. Gage)
Hastelloy B welded with 85% Ni–15% Mo* wire	Room	16,200	14,100	1
	Room	14,200	13,900	1
	1500	5,600		0
	1500	10,600	10,600	0
Hastelloy B welded with Hastelloy B	Room	118,300	84,200	25
	Room	124,000	80,400	22.5
	1500	66,700	52,600	9.5
	1500	62,300	55,600	12.5
Hastelloy W welded with Hastelloy W	Room	126,100	75,400	40
	Room	127,900	81,400	34.5
	1500	71,100	47,400	31
	1500	69,800	46,100	20

*All welds with the 85% Ni–15% Mo filler wire showed excessive porosity and weld cracking.

TABLE 3.4.3. MECHANICAL PROPERTIES OF HASTELLOY B WELDED WITH HASTELLOY B

All-weld-metal tensile specimens

Heat Treatment	Test Temperature (°F)	Tensile Strength (psi)	Elongation (% in 1-in. Gage)	Reduction in Area (%)
As welded	Room	118,300	25	20
	Room	124,000	22.5	23
Aged for 200 hr at 1500°F	Room	133,600	20	16
	Room	130,000	12	12
Aged for 200 hr at 1300°F	1300	114,300	8	5
	1300	116,200	6	3
Aged for 200 hr at 1500°F	1500	67,200	19.5	16
	1500	63,800	10	13
As welded	1500	66,700	9.5	9
	1500	62,300	12.5	13

Fabrication of Thermal-Convection Loops

Nickel-molybdenum alloy thermal-convection loops of various compositions are being fabricated for use in dynamic corrosion tests. A summary of the work performed this quarter is presented in Table 3.4.6.

BRAZING STUDIES OF NICKEL-MOLYBDENUM ALLOYS

G. M. Slaughter

The brazing characteristics of nickel-molybdenum alloys will largely determine whether these alloys can be used in heat exchanger and radiator appli-

TABLE 3.4.4. MECHANICAL PROPERTIES OF HASTELLOY B WELDED WITH HASTELLOY B

Transverse-weld tensile specimens

Heat Treatment	Test Temperature (°F)	Tensile Strength (psi)	Elongation (% in 1-in. Gage)	Reduction in Area (%)	Location of Fracture
As welded	Room	118,300	32.5	21	Weld
	Room	124,500	24.5	23	Weld
Aged for 200 hr at 1300°F	Room	146,100	2	5	Weld
	Room	140,500	5	2	Weld
Aged for 200 hr at 1300°F	1300	108,300	5	3	Fusion line
	1300	109,100	2	1	Base metal
Aged for 200 hr at 1500°F	1500	72,100	20	20	Weld
	1500	73,700	13.5	23	Base metal
As welded	1500	65,900	9.5	9	Base metal
	1500	68,000	9.5	9	Base metal

TABLE 3.4.5. MECHANICAL PROPERTIES OF HASTELLOY W WELDED WITH HASTELLOY W

All-weld-metal tensile specimens

Heat Treatment	Test Temperature (°F)	Tensile Strength (psi)	Elongation (% in 1-in. Gage)	Reduction in Area (%)
As welded	Room	126,100	40	30
	Room	127,900	36	27
Aged for 200 hr at 1500°F	Room	138,400	7.5	5
	Room	148,400	13	14
Aged for 200 hr at 1300°F	1300	105,300	15	14
	1300	117,600	13.5	15
Aged for 200 hr at 1500°F	1500	68,500	13.5	23
	1500	64,000	7.5	22
As welded	1500	71,100	31	16
	1500	69,800	20	18

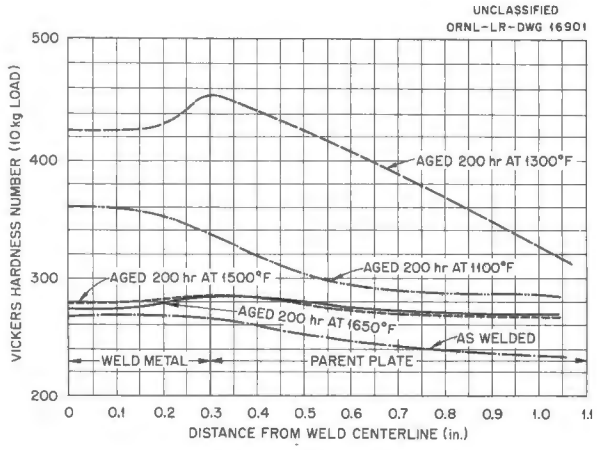

Fig. 3.4.1. Effect of Aging Temperature on Room-Temperature Hardness of Hastelloy B Welds.

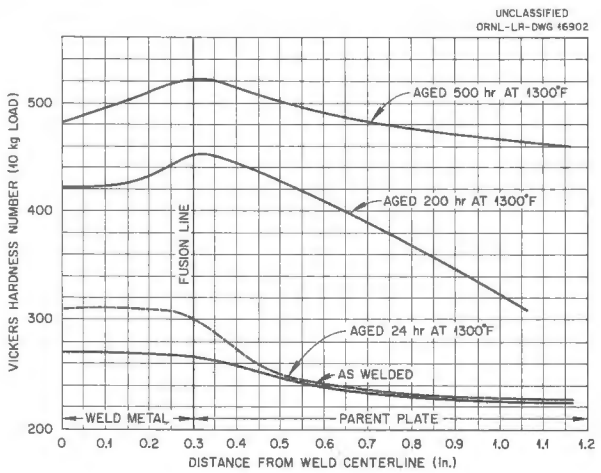

Fig. 3.4.2. Effect of Aging Time on Room-Temperature Hardness of Hastelloy B Welds After Aging at 1300°F.

cations. Since some of the common alloying elements (aluminum, titanium, and beryllium) form hard-to-wet oxide films on the alloy surface, dry-hydrogen brazing studies on the experimental alloys are being conducted. Flowability tests were conducted on several compositions with Coast Metals brazing alloy No. 52 and with an alloy containing 1% lithium for additional deoxidation and "gettering" of the atmosphere. No differences in the flowabilities of the two alloys were noted. A summary of the results is given in Table 3.4.7. Other techniques, such as flux brazing, are being investigated as possible means of joining these alloys.

TABLE 3.4.6. STATUS OF NICKEL-MOLYBDENUM ALLOY THERMAL-CONVECTION LOOP FABRICATION

Number of Loops	Alloy Composition (wt %)
	ORNL Alloys
1	20 Mo–3 Cr–bal Ni
2	17 Mo–3 Cr–bal Ni
3	17 Mo–5 Cr–bal Ni
3	17 Mo–2 Al–0.06 C–bal Ni
2	17 Mo–7 Cr–0.06 C–bal Ni
3	17 Mo–2 Ti–0.06 C–bal Ni
3	17 Mo–2 V–0.06 C–bal Ni
2	17 Mo–4 Fe–0.06 C–bal Ni
3	17 Mo–2 W–bal Ni
1	17 Mo–4 Fe–bal Ni
3	17 Mo–4 W–bal Ni
3	17 Mo–4 V–bal Ni
3	17 Mo–3 Nb–bal Ni
3	17 Mo–5 Nb–bal Ni
2	INOR-3, 16 Mo–1 Al–1.5 Ti–0.06 C–bal Ni
2	INOR-4, 16 Mo–2 Al–1.5 Ti–0.06 C–bal Ni
1	INOR-4, 16 Mo–2 Al–1.5 Ti–bal Ni
1	INOR-5, 15 Mo–2 Nb–2 W–bal Ni
2	INOR-6, 16 Mo–5 Cr–1.5 Ti–1 Al–0.06 C
3	INOR-7, 16 Mo–6 Cr–1 Nb–1 Al–bal Ni
	International Nickel Company Alloys
1	15 Mo–5 Cr–3 Nb–3 W–0.5 Al–bal Ni
1	17 Mo–0.5 Al–bal Ni
1	15 Mo–1.5 Ti–1 Al–bal Ni
1	15 Mo–3 Nb–3 W–0.5 Al–bal Ni
	Battelle Memorial Institute Alloys
1	20 Mo–2 Nb–7 Cr–1 Fe–bal Ni
1	20 Mo–1 Al–2 Nb–7 Cr–1 Fe–bal Ni
1	20 Mo–1 Al–2 Nb–7 Cr–bal Ni

NaK-TO-AIR RADIATOR FABRICATION

P. Patriarca G. M. Slaughter

Difficulties have been encountered at the York Corporation in attempts to braze high-conductivity-fin NaK-to-air radiators. The Coast Metals brazing alloy No. 52 rings have not melted adequately, and as a result the tube-to-fin joints have had poor adherence and poor fin-collar protection. Experiments were therefore conducted at ORNL to obtain

TABLE 3.4.7. RESULTS OF TESTS OF FLOWABILITY OF COAST METALS BRAZING ALLOY NO. 52 ON NICKEL-MOLYBDENUM ALLOYS

Alloy Composition (wt %)	Flowability
10 Mo–10 Fe–bal Ni	Good[a]
17 Mo–0.5 Al–bal Ni	Good
16 Mo–1 Al–1.5 Ti–bal Ni (INOR-3)	None[b]
16 Mo–2 Al–1.5 Ti–bal Ni (INOR-4)	None
18 Mo–0.5 Al–0.5 Be–bal Ni	None
18 Mo–0.5 Al–0.25 Be–2 Nb–0.5 Mn–bal Ni	None
15 Mo–0.5 Al–2 Nb–2 V–bal Ni	Good
15 Mo–0.5 Al–3 Nb–3 W–0.25 C–bal Ni	Fair[c]
15 Mo–0.5 Al–4 Fe–6 Cr–0.5 Mn–bal Ni (INOR-8)	Good
15 Mo–2 Nb–2 W–bal Ni (INOR-5)	Good

[a]Good; 3-in. of flow on a T-joint.
[b]None; no flow on a T-joint.
[c]Fair; 2-in. of flow on a T-joint.

a better understanding of the problem and to study possible means of overcoming it.

Effect of Temperature Rate-of-Rise on Brazing

Experiments by Coast Metals, Inc., indicated that the Coast Metals brazing alloy No. 52 rings melted and flowed satisfactorily when brought to the brazing temperature over a period of a few minutes. However, when brought to temperature in the York furnace (maximum rate of rise from room temperature approximately 100° F/hr), the brazing alloy ring still retained its original shape and, of course, did not provide a satisfactory tube-to-fin joint.

Experiments were therefore conducted to investigate the influence of various rates of temperature rise on the melting characteristics of the sintered rings of Coast Metals brazing alloy No. 52. Several thousand rings and several hundred high-conductivity fins were obtained from the York Corporation, and test samples similar to the sample shown in Fig. 3.4.3 were assembled and brazed with the tubes in the horizontal position. A thermocouple was welded to the specimen and was used for recording the thermal cycle.

UNCLASSIFIED
Y-18338

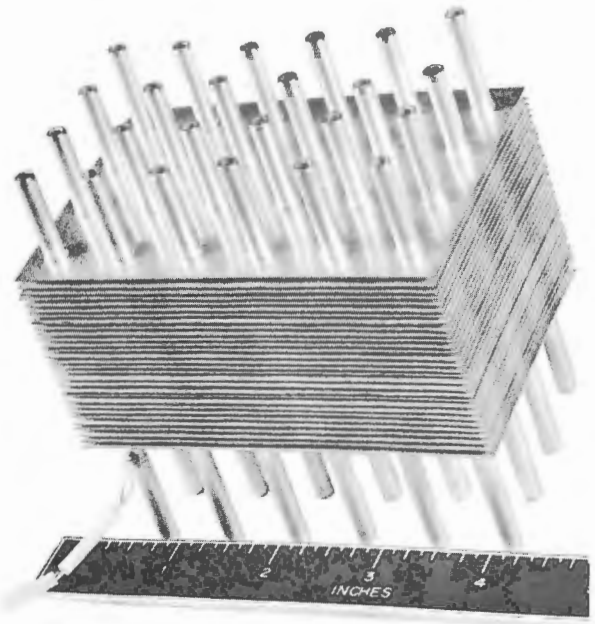

Fig. 3.4.3. Test Sample of Tube-to-Fin Joints for Use in Studying the Effect of the Rate of Temperature Rise on Brazing Characteristics.

The following rates of temperature rise through the temperature range 1700 to 1920° F were investigated: 100 (the York rate), 200, 300, and 550° F/hr. The degrees of melting obtained with these rates of temperature rise are illustrated in Figs. 3.4.4 through 3.4.7. Metallographic samples were taken from these specimens to determine the quality of braze obtained, and the results are presented below:

Rate of Temperature Rise (°F/hr)	Braze Quality
100	Poor adherence and poor fin-collar protection
200	Fair adherence and poor fin-collar protection
300	Good adherence and good fin-collar protection
550	Excellent adherence and excellent fin-collar protection

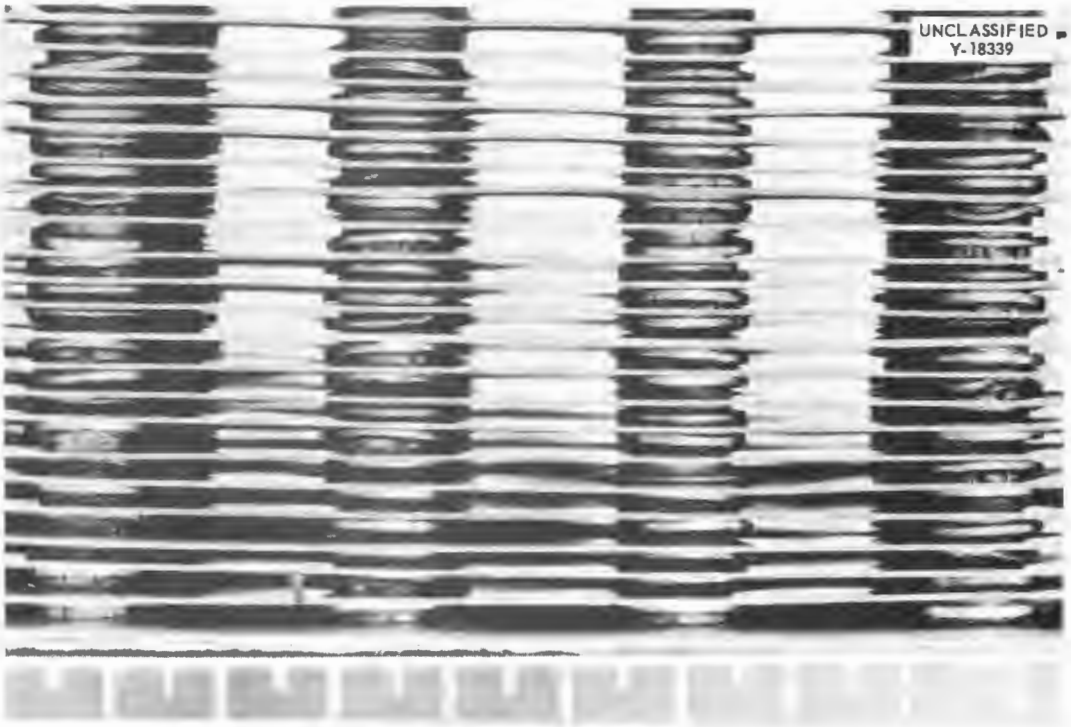

Fig. 3.4.4. Coast Metals Brazing Alloy No. 52 Rings on High-Conductivity-Fin Radiator Test Sample After Heating at a Rate of 100°F/hr. The alloy still appears as a ring.

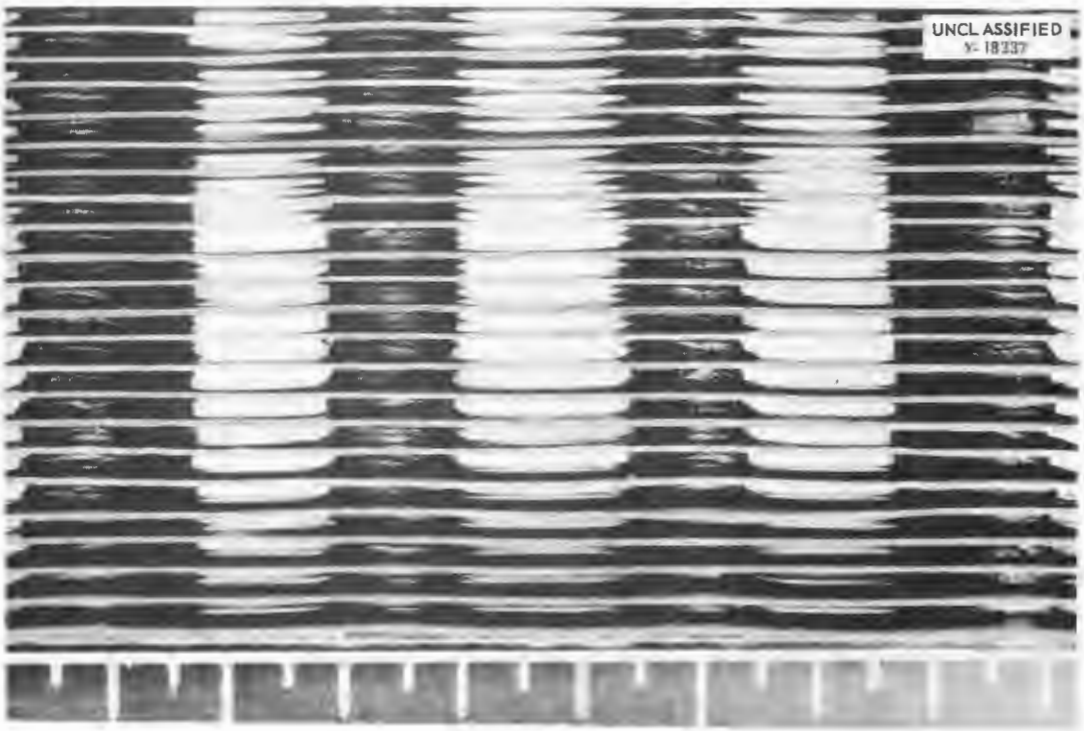

Fig. 3.4.5. Coast Metals Brazing Alloy No. 52 Rings on High-Conductivity-Fin Radiator Test Sample After Heating at a Rate of 200°F/hr. Incomplete melting of the ring is evident.

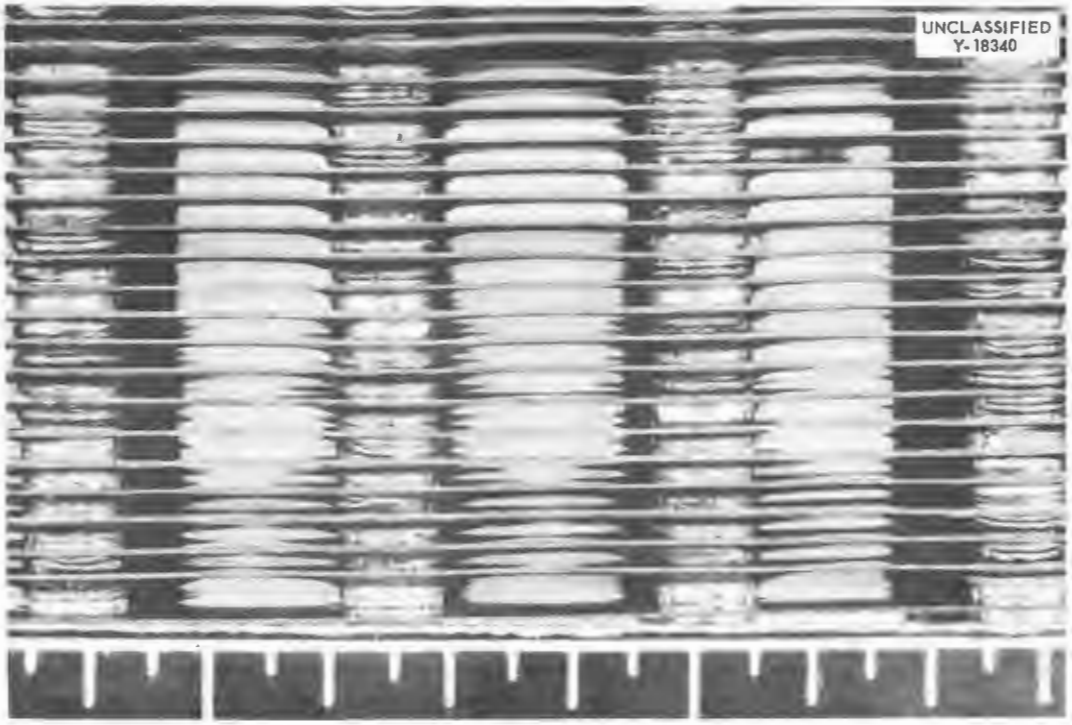

Fig. 3.4.6. Coast Metals Brazing Alloy No. 52 Rings on High-Conductivity-Fin Radiator Test Sample After Heating at a Rate of 300°F/hr. Generally satisfactory melting of the rings was obtained.

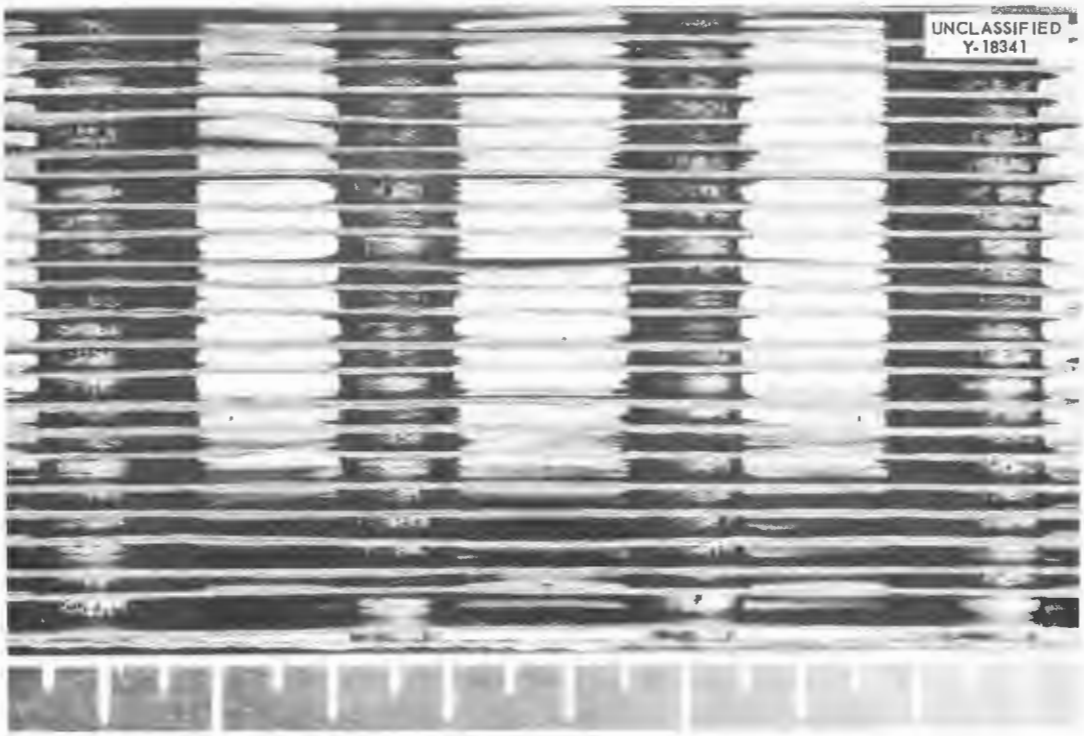

Fig. 3.4.7. Coast Metals Brazing Alloy No. 52 Rings on High-Conductivity-Fin Radiator Test Sample After Heating at a Rate of 550°F/hr. Complete melting of the ring is evident.

These experiments indicate that a minimum heating rate of 300° F/hr should be used in the brazing of the high-conductivity-fin radiators. However, since the experiments were conducted on small test samples under laboratory conditions, other experiments should be conducted by the vendor with the actual brazing equipment and test samples of mass comparable to that of the radiators.

Influence of Fin Materials on Brazing

Other experiments were conducted to study the effect of the fin material on the flow of the brazing alloy. High-conductivity-fin radiator test samples incorporating type 310 stainless-steel-clad copper fins revealed limited melting of the sintered brazing alloy rings at the 100° F/hr rate of temperature rise. The change in the brazing alloy that occurs upon liquation (removal of the lower melting constituents from the ring) is, however, shown in Fig. 3.4.8. As may be seen, the as-received brazing alloy rings fracture in a decidedly brittle manner, but a ring removed from a tube-to-fin joint brazed at a 100° F/hr rate of temperature rise could be manually deformed. Metallographic examination of the joints revealed no bonding in most instances and slight adherence in others. A high-magnification study of the joints indicated that the stainless steel cladding was readily wet by the brazing alloy to a distance surprisingly far from the initial position of the ring. The extent of boron diffusion into the stainless steel is shown in Fig. 3.4.9. A thin film of alloy apparently wet the surface during brazing, and the boron diffused rapidly into the cladding. In order to verify these observations, a sintered brazing alloy ring was placed on a sheet of type 310 stainless steel and subjected to an identical heating cycle. The sample was then carefully removed from the retort and coated with an electroplate of nickel to protect the surfaces during metallographic preparation. Examination at a magnification of 2000 revealed small particles of brazing alloy attached to the surface at a distance as far away as $\frac{1}{4}$ in. from the ring.

The liquation of the brazing alloy at a heating rate of 100° F/hr was found to be at a minimum when Inconel-clad copper high-conductivity fins were substituted for the stainless-steel-clad fins. The brazing alloy rings melted completely, as shown in Fig. 3.4.10, and adequate adherence and fin collar protection were achieved, as may be seen in Fig. 3.4.11. Only minor boron diffusion is evident in Fig. 3.4.12, which shows the joint at a higher magnification. The second phase visible in Fig. 3.4.12 resulted from the diffusion between the Inconel and copper, which is shown more clearly in Fig. 3.4.13. (Suitable barriers are available for minimizing diffusion between copper and Inconel.[1])

The results of these experiments indicate that the stainless steel cladding of the York fins, in contrast to Inconel-clad fins, is wet readily by the alloy and offers little resistance to spreading. A

[1] E. S. Bomar, J. H. Coobs, and H. Inouye, *ANP Quar. Prog. Rep. March 10, 1954*, ORNL-1692, p 91.

UNCLASSIFIED
PHOTO 18212

(*a*) (*b*) (*c*)

Fig. 3.4.8. Rings of Coast Metals Brazing Alloy No. 52 (*a*) As-Received, (*b*) As-Received and Fractured, and (*c*) Manually Deformed After Heating at a 100° F/hr Rate of Temperature Rise.

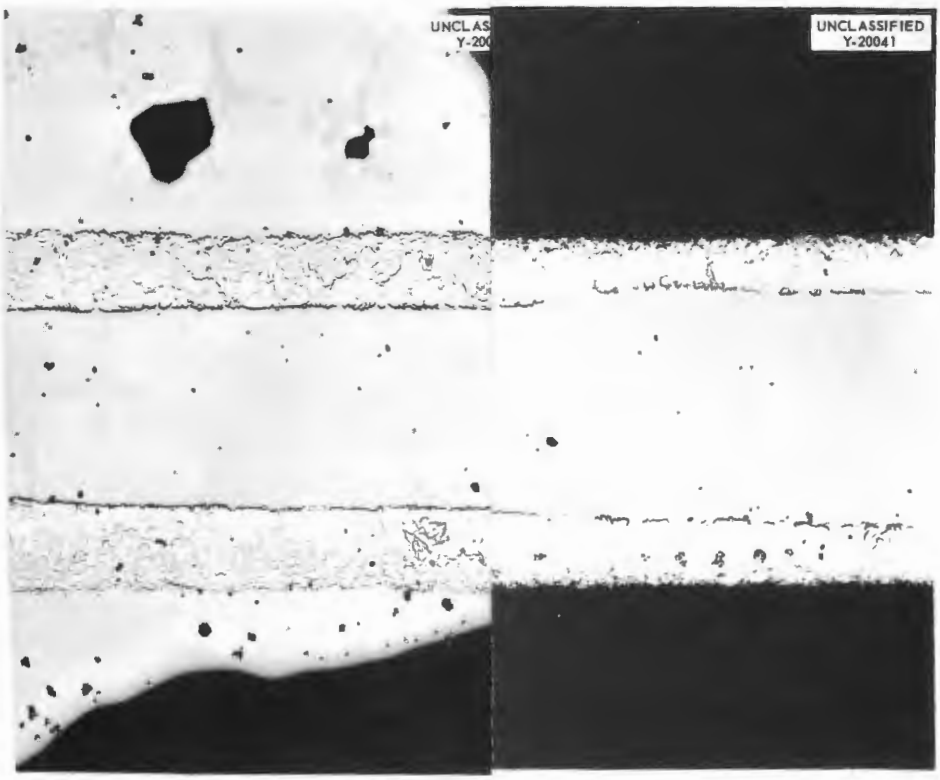

Fig. 3.4.9. Composite Photomicrogra Extensive Diffusion of boron into the cladding along the fin is evident. As-pol

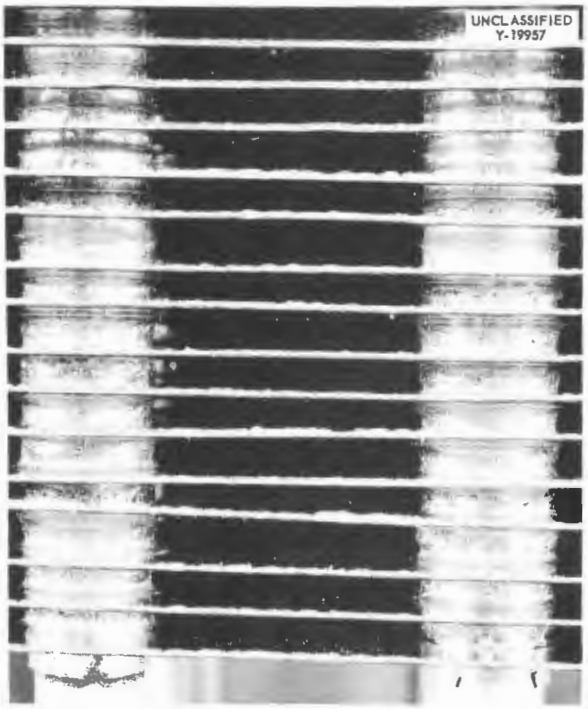

Fig. 3.4.10. Inconel-Clad Copper Fins and Coast Metals Brazing Alloy No. 52 Rings Heated at 100°F/hr. Note complete melting of brazing alloy rings.

more detailed study of these phenomena is to be made in an attempt to clarify the reported observations.

Influence of Atmosphere on Brazing

A metallographic study of hydrogen-brazed tube-to-fin joints indicated that the stainless steel cladding of the high-conductivity fins was readily wet by the brazing alloy and offered little resistance to spreading. A liquated film of alloy apparently wet the surface over a large area during brazing, and the boron diffused rapidly into the cladding.

Another stainless-steel-clad copper high-conductivity-fin radiator test sample obtained from York Corporation was assembled with Coast Metals brazing alloy rings and heated in dry helium (–70° F dew point) at a rate of 100° F/hr in order to compare the effects of a helium atmosphere with the effects described above that were obtained in a hydrogen atmosphere. The sample remained bright as it was removed from the retort, and complete melting of the rings was obtained, along with excellent braze adherence and fin-collar protection. The resultant high-quality braze is shown in Fig. 3.4.14. There was no evidence of

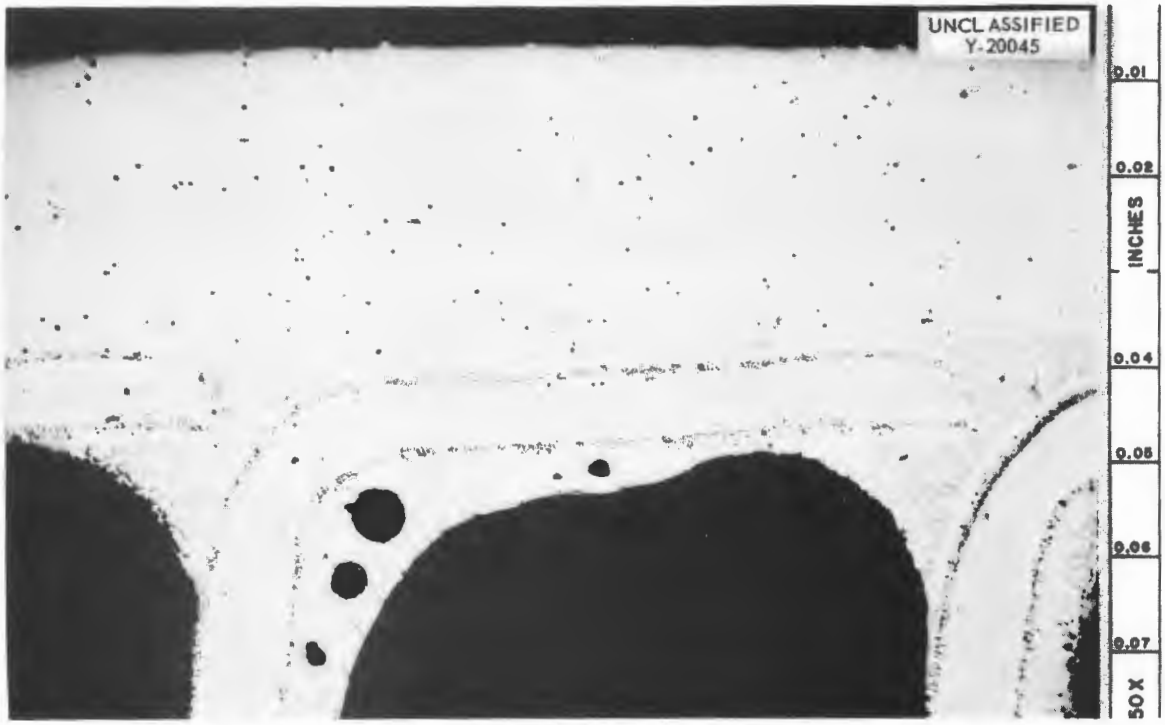

Fig. 3.4.11. Inconel-Clad Copper Fins Brazed to an Inconel Tube with Coast Metals Brazing Alloy No. 52 Sintered Rings. Note excellent melting. As-polished. 50X.

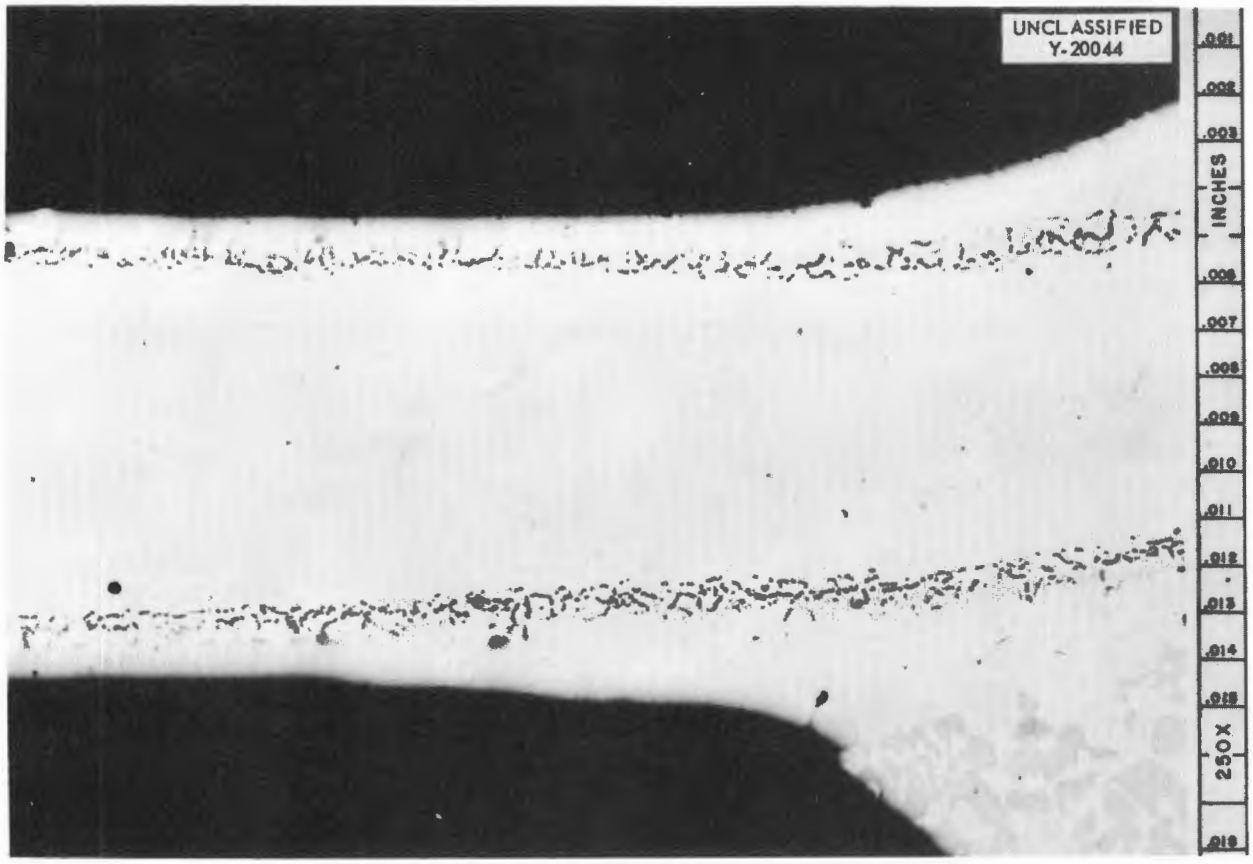

Fig. 3.4.12. Inconel-Clad Copper Fin Showing Limited Boron Diffusion. Some diffusion between copper and Inconel is evident. As-polished. 250X.

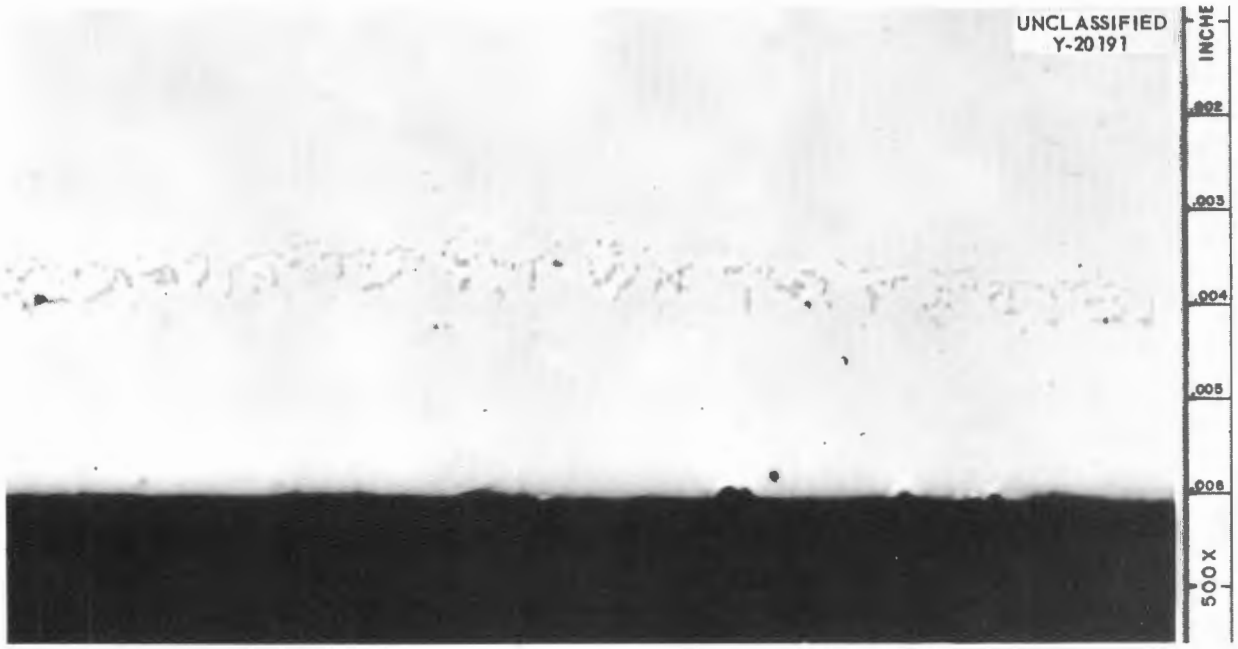

Fig. 3.4.13. Diffusion Layer Between Inconel Cladding and Copper Fin. As-polished. 500X.

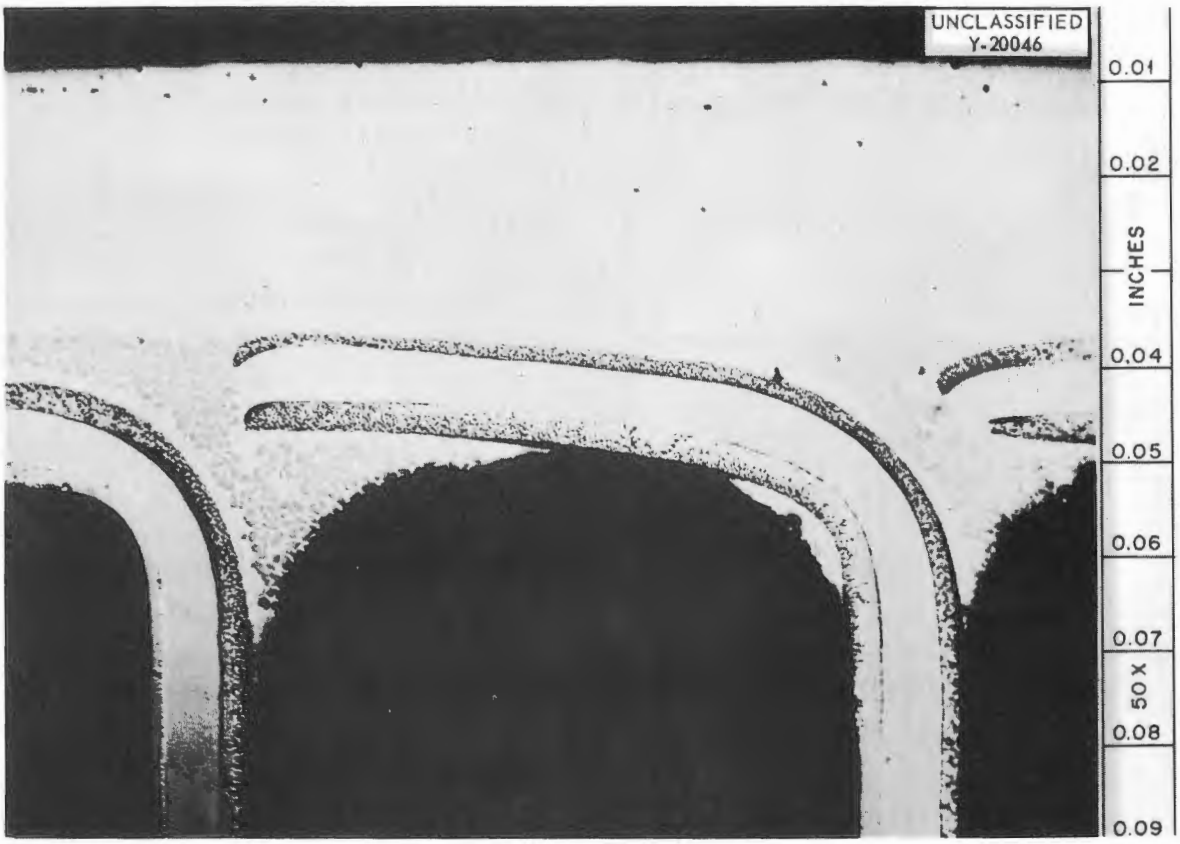

Fig. 3.4.14. Typical High-Quality Tube-to-Fin Joints Obtained by Brazing in Dry Helium at 100°F/hr. Unetched. 50X.

spreading of the alloy over the fin surface, as determined by the extent of boron diffusion into the cladding. In a high-magnification view (Fig. 3.4.15) of a fin area adjacent to a braze, it can be seen that the diffusion zone rapidly disappears with increasing distance from the brazing alloy. Possibly helium does not reduce pre-existing oxide films on the fins, which therefore impede spreading.

Dry-helium-atmosphere brazing thus appears to provide a possible alternate means of fabricating high-conductivity-fin radiators when exceptionally slow rates of rise to brazing temperature must be used. Before this method is adopted, extensive testing should be performed by a vendor to ensure duplication of the above results with the actual brazing equipment and procedures to be used.

BRAZING ALLOY DEVELOPMENT

R. E. Clausing

It would be desirable in most applications to use a brazing alloy with a coefficient of thermal expansion similar to that of the material to be brazed. Therefore the coefficients of thermal expansion of several conventional high-temperature brazing alloys were determined in the range from room temperature to 900°C. The data obtained do not take into consideration the base metal solution and brazing alloy dilution that occur during brazing, but they are useful in that they indicate the maximum deviation from the coefficient of thermal expansion of the base material.

Small ingots of the brazing alloys were cast in graphite molds and then centerless ground to

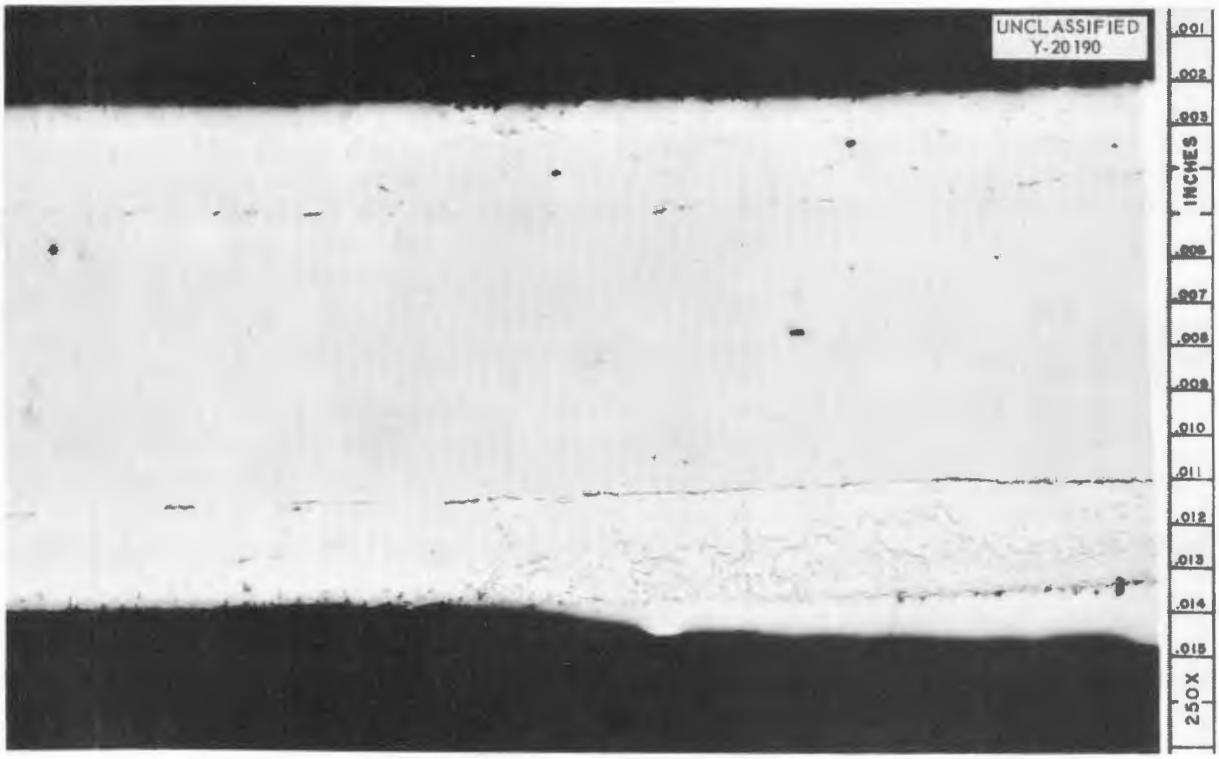

Fig. 3.4.15. Stainless-Steel-Clad Copper High-Conductivity-Fin Brazed in Dry Helium Showing Rapid Disappearance of Diffusion Zone with Increasing Distance from the Brazing Alloy. Unetched. 250X. Reduced 4%.

⅛-in.-dia, 1.0000-in.-long specimens for dilatometry studies. A convenient heating rate of 3°C/min was used for all the experiments. Plots of thermal expansion vs temperature for two of the brazing alloys studied are shown in Figs. 3.4.16 and 3.4.17. The thermal-expansion curve for Inconel is also plotted on each graph for comparison. It can be seen that the Coast Metals brazing alloy No. 52 possesses a nearly linear expansion characteristic over the temperature range investigated. The deviation from the linear relationship for the 82% Au–18% Ni alloy is associated with the formation of a second phase, as reported in the literature.[2] Comparison curves plotted from the data obtained for type 316 stainless steel, Inconel, and Hastelloy B are shown in Fig. 3.4.18. These curves are in good agreement with those available in the literature.

[2] *Metals Handbook*, p 1172, American Society for Metals, Cleveland, 1948.

The effect of subsequent heating and cooling on the thermal expansion and contraction characteristics of Coast Metals brazing alloy No. 52 was also studied, since this alloy is used extensively in the fabrication of heat exchanger components for high-temperature service. It may be noted in Fig. 3.4.19 that the expansion curve for the initial heating differs slightly from that for the second heating and cooling cycle. This variation probably results from the closer attainment of equilibrium conditions with each successive thermal cycle. A summary of the data obtained in this investigation is presented in Table 3.4.8.

STUDIES OF GRAIN GROWTH IN INCONEL TUBING

E. J. Wilson G. M. Slaughter

During assembly of the ART, several intermittent stress-relieving operations may be required to minimize the residual stresses in the system. Since visible surface films have been formed when

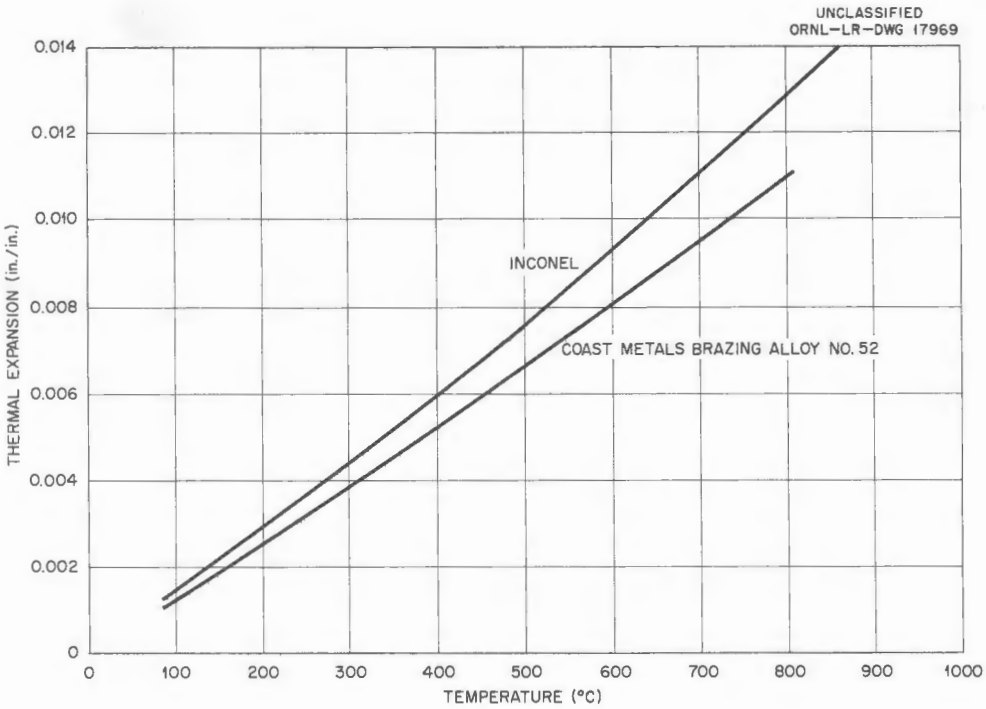

Fig. 3.4.16. Thermal Expansion of Coast Metals Brazing Alloy No. 52 as a Function of Temperature.

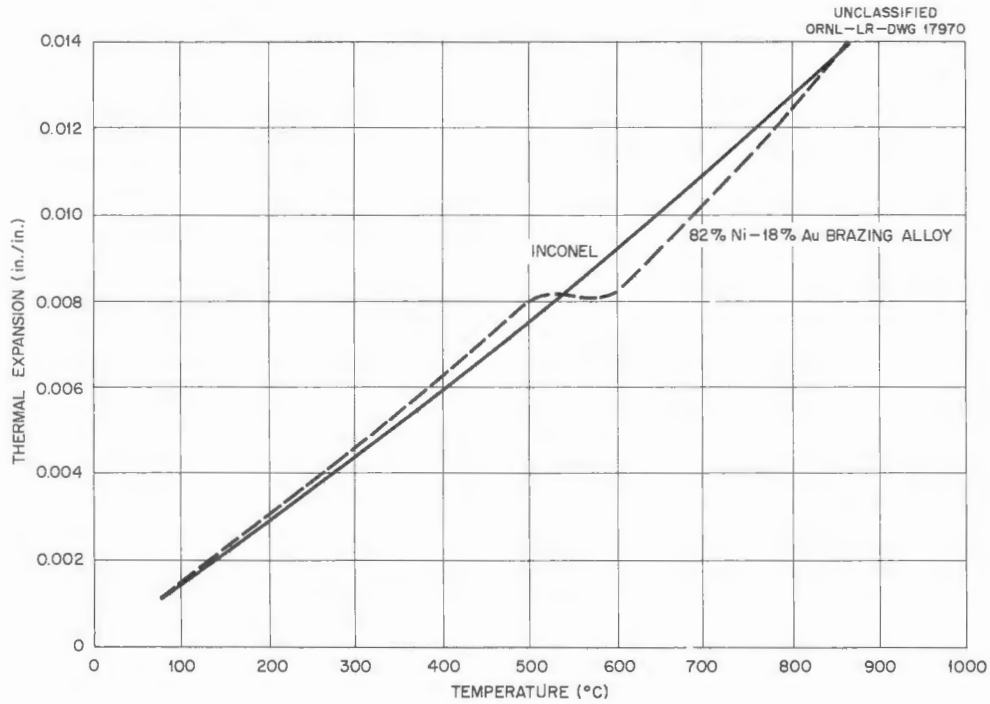

Fig. 3.4.17. Thermal Expansion of an 82% Au-18% Ni Brazing Alloy as a Function of Temperature.

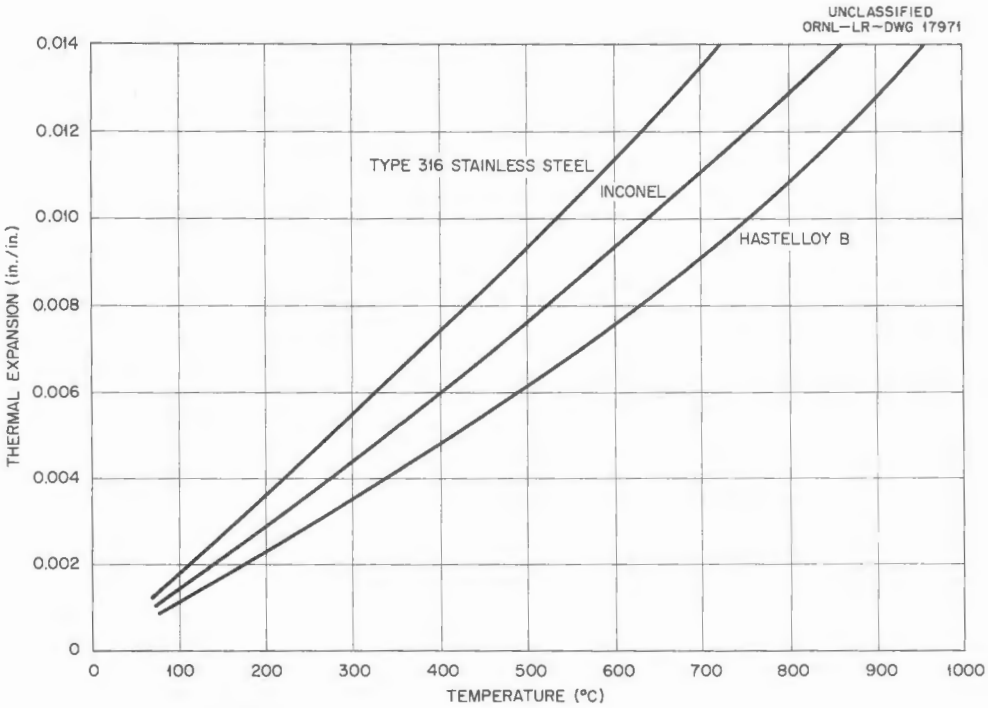

Fig. 3.4.18. Thermal Expansion of Inconel, Type 316 Stainless Steel, and Hastelloy-B as a Function of Temperature.

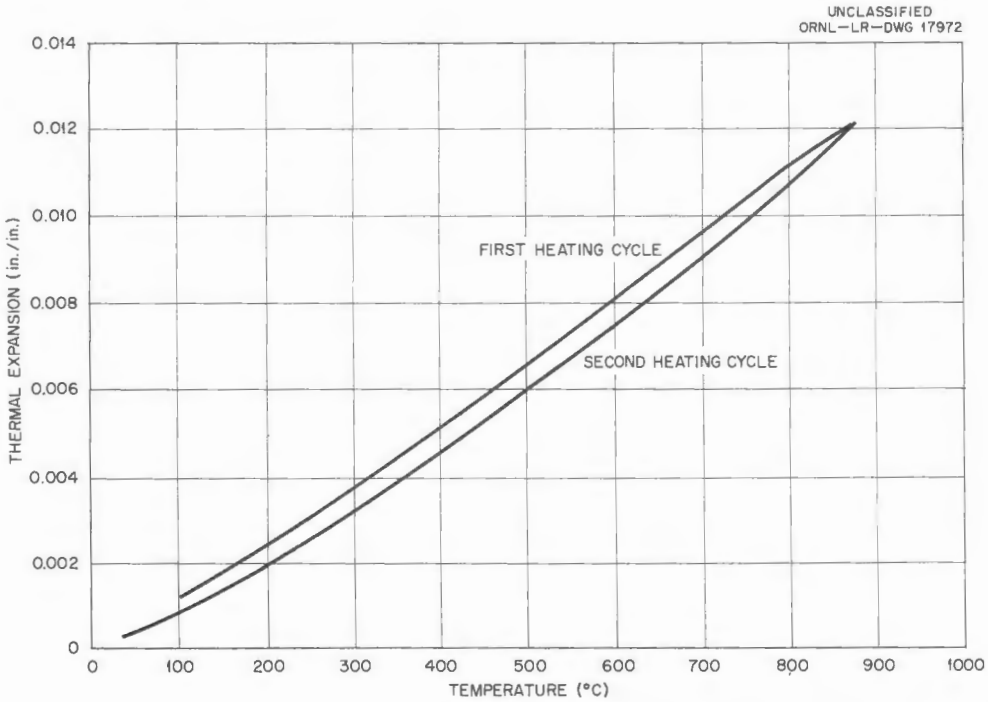

Fig. 3.4.19. Effect of Temperature Cycling on the Thermal Expansion of Coast Metals Brazing Alloy No. 52.

TABLE 3.4.8. MEAN COEFFICIENTS OF THERMAL EXPANSION FOR SEVERAL BRAZING ALLOYS AND STRUCTURAL MATERIALS IN VARIOUS TEMPERATURE RANGES

	Mean Coefficient of Thermal Expansion (in.·10^{-6}/in.·°C)			
	At 0–500°C	At 0–700°C	At 0–850°C	At 700–800°C
Coast Metals brazing alloy No. 52	13.24	13.79	13.76	13.4
Coast Metals brazing alloy No. 53	13.24	13.3	13.45	14.3
82% Au–18% Ni brazing alloy	15.90	14.71	15.89	21.5
90% Ni–10% P brazing alloy	13.80	14.17	14.37	14.5
Low-melting Nicrabraz	13.86	14.71	14.40	14.9
High-melting Nicrobraz	12.86	13.21	13.6	15.0
Inconel	15.14	15.81	16.03	17.1
Type 316 stainless steel	19.70	19.24	19.13	20.4
Hastelloy B	12.12	13.03	14.08	18.8

some heats of Inconel have been held for extended periods at or near 1500°F, even in a dry-hydrogen atmosphere, bright annealing of the components at a temperature of approximately 1830°F after the final stress-relief treatment may be required as a means of removing the film.

Recent metallographic examinations of components containing thin-walled tubes have indicated that the presence of large grains may be undesirable if the service conditions combine relatively high stresses and corrosion. Since grain growth is promoted by holding at elevated temperatures, a preliminary investigation was conducted to obtain information regarding the grain size to be expected in CX-900 tubing after each heat-treatment operation. The surfaces of the tubing were inspected for discoloration after each step.

For these initial experiments $\frac{3}{16}$-in.-OD, 0.025-in.-wall CX-900 tubing was used (heat No. 5759). Specimens were prepared by cutting fourteen 1-in. segments and cleaning them with acetone to remove dirt and grease. The samples were then subjected to the following heat-treating cycle:

1. Two samples from the as-received stock were identified and saved for comparison.
2. The remaining 12 specimens were heated in a furnace at 1922°F for $\frac{1}{2}$ hr and cooled. Two samples were removed.
3. The remaining 10 specimens were again heated in the furnace at 1500°F for 1 hr and cooled. Two samples were removed.
4. The remaining eight specimens were again heated in the furnace for 1 hr at 1500°F, as in step 3, and cooled. Two samples were removed.
5. The remaining six specimens were again heated at 1500°F for 1 hr, as in step 3. Two samples were removed.
6. The remaining four samples were again heated as in step 3 and cooled. Two samples were removed. These four samples had been at 1500°F for a total of 4 hr.
7. The remaining two samples were heated in the furnace at 1832°F for $\frac{1}{2}$ hr and cooled.

The temperature of 1922°F used in the second step is the brazing temperature. The stress-relieving temperature is 1500°F, and 1832°F is the bright-annealing temperature. All heat treatments were made in a dry-hydrogen atmosphere (dew point, ~–100°F). The tubes were examined for oxide films and sectioned for grain-size determination in the transverse position. The samples were examined metallographically, and photomicrographs of typical areas were made. No oxide films were noted after any of the stress-relief treatments. However, the data for the final bright-annealing treatment are important, since films may be formed on some of the complicated components during the actual fabrication. Measurements were also taken to determine the number of grains across the tube-wall thickness of 0.025 in. The results of these tests are correlated in Table 3.4.9.

TABLE 3.4.9. RESULTS OF GRAIN-SIZE MEASUREMENTS MADE ON CX-900 INCONEL TUBING AFTER VARIOUS HEAT TREATMENTS

Specimen No.	Heat Treatment	Number of Grains Across 0.025-in. Wall
1 and 2	As-received	20
3 and 4	Brazing temperature, 1922° F	10 to 12
5 and 6	First stress relief at 1500° F	10 to 12
7 and 8	Second stress relief at 1500° F	10 to 12
9 and 10	Third stress relief at 1500° F	10 to 12
11 and 12	Fourth stress relief at 1500° F	10 to 12
13 and 14	Bright anneal at 1832° F	9 to 10

Microscopic examination of the as-received samples revealed the fine-grained structure shown in Fig. 3.4.20. Upon heating at the brazing temperature of 1922° F, significant grain growth was evident on the exterior wall, while the interior wall of the tube still exhibited fine-grained structure, as shown in Fig. 3.4.21, which illustrates both typical and above-average (center of photograph) grain growth. Subsequent heat treatment at 1500° F, the stress-relief temperature, produced no noticeable increase in grain size. A structure typical of that found after the stress-relief treatment is shown in Fig. 3.4.22. A slight tendency for additional grain coarsening was noted during the final heat treatment at 1832° F.

Further experimentation is under way in this study of the effects of brazing temperature, time at temperature, and type of atmosphere on the grain-coarsening of Inconel tubes. The results of these studies will be reported as the data become available.

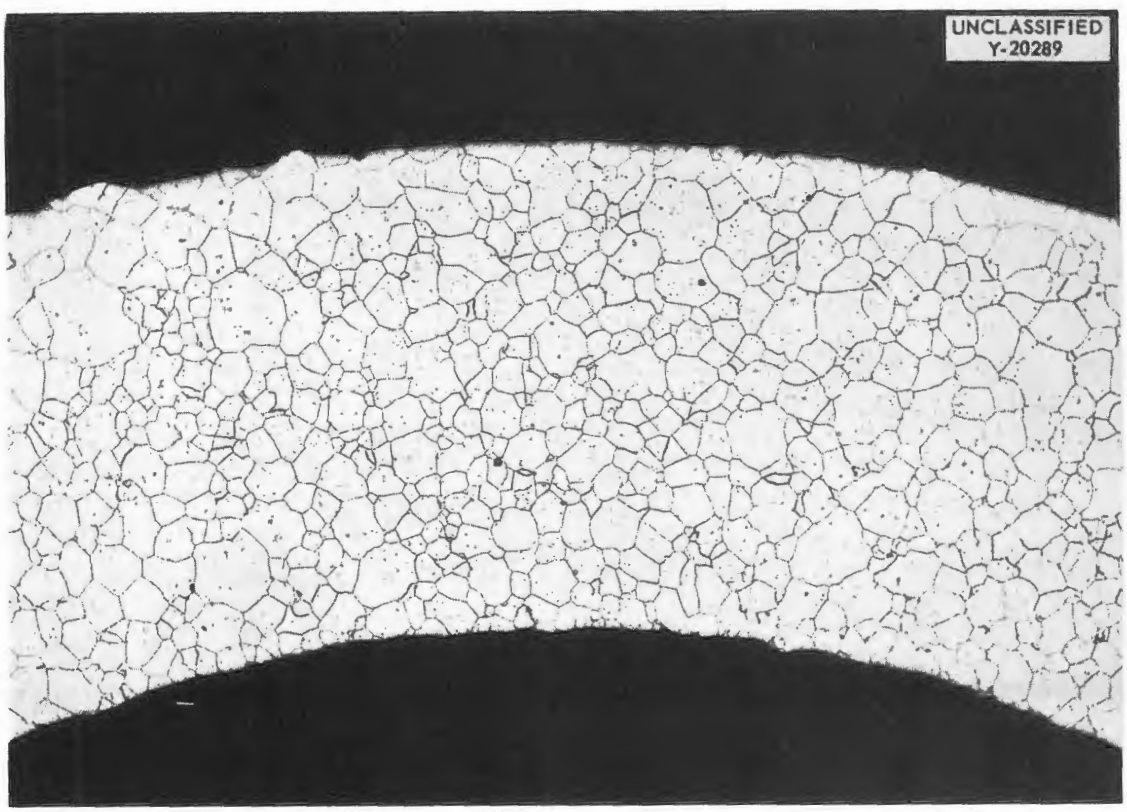

Fig. 3.4.20. Grain Structure of As-Received CX-900 Inconel Tubing. 100X.

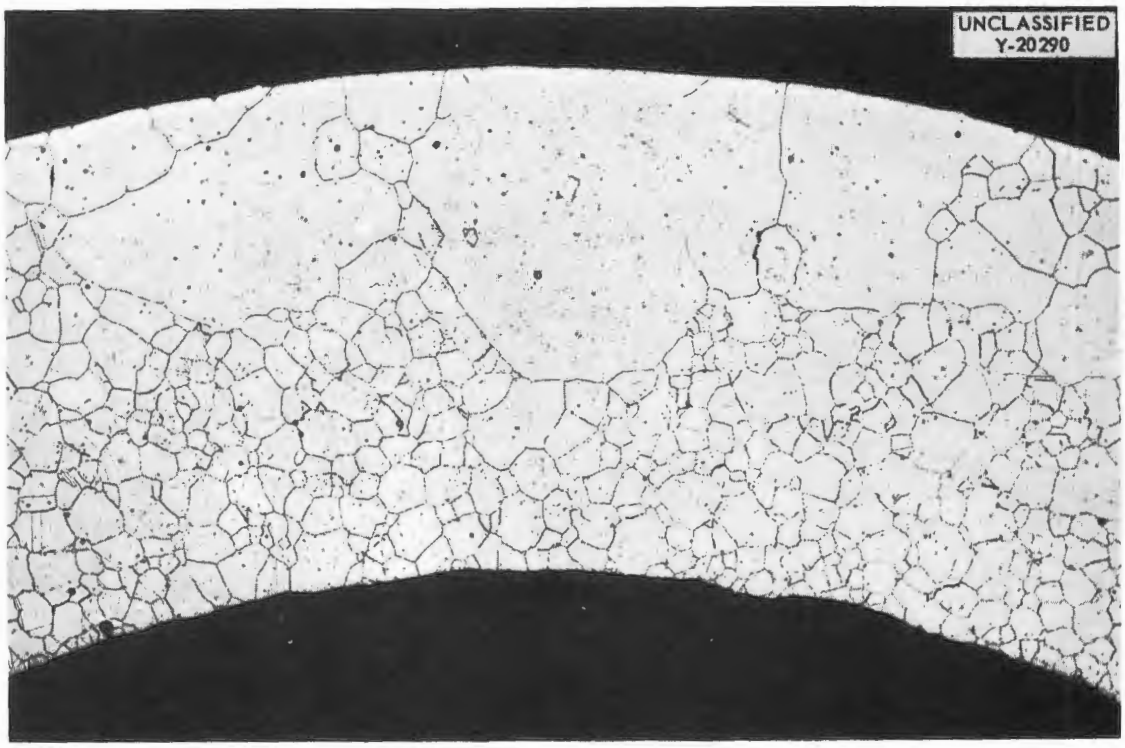

Fig. 3.4.21. Grain Structure of CX-900 Inconel Tubing After Heating at a Brazing Temperature of 1922°F for ½ hr. 100X.

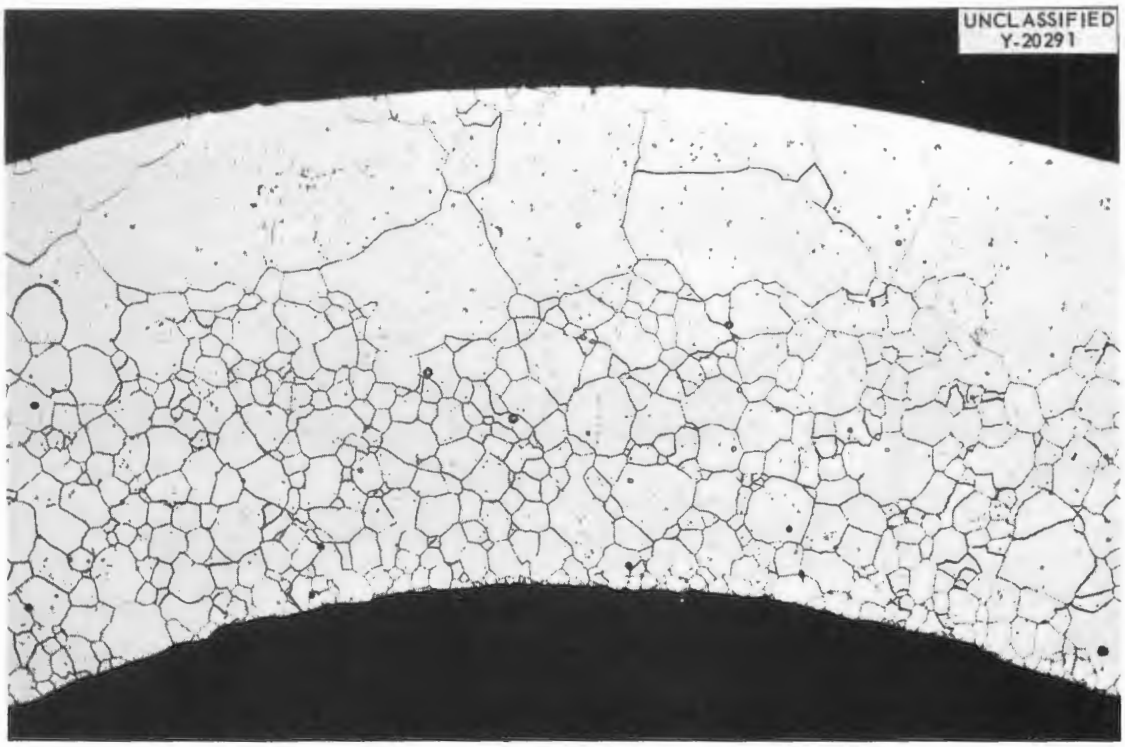

Fig. 3.4.22. Grain Structure of CX-900 Inconel Tubing After ½ hr at 1922°F and Four 1-hr Periods at the Stress-Relief Temperature of 1500°F. 100X.

WELDING OF BORON-CONTAINING STAINLESS STEEL

P. Patriarca

Stainless steels containing significant amounts of boron, for shielding purposes, were recently considered for use as load-carrying components that required welded construction. Therefore experiments were conducted in order to determine the properties of welded joints in a typical alloy. The preliminary results indicate that such materials should not be fabricated into load-carrying components.

A quantity of ⅛-in.-thick sheet with the following nominal composition was obtained: 18.03 wt % Cr, 11.4 wt % Ni, 0.09 wt % C, 1.07 wt % B, bal Fe. Two pieces ⅛ × 3 × 12 in. were butt welded by inert-arc welding procedures and with type 347 stainless steel filler wire. Several longitudinal and transverse bend specimens were then subjected to face and root bend tests, and the bend behavior was compared with that of the unwelded parent sheet. The lack of ductility exhibited by the weldments is shown in Fig. 3.4.23. The fracture was invariably initiated in the parent material at a relatively small bend angle, and it rapidly propagated through the weld metal. The partially fractured specimen in Fig. 3.4.23 illustrates a fracture in a partial state of propagation, the bending having been interrupted to preserve this condition. Transverse specimens also failed at comparable bend angles. The fractures had initiated in the fusion line and had propagated in an abrupt and brittle manner.

A typical microsection is shown in Fig. 3.4.24. As may be noted, the complex borides reacted with the matrix to form a eutectic at the fusion line. Such a reaction was to be expected, since both nickel and iron form relatively low-melting-point eutectics with their borides at 1140 and 1174°C, respectively.

Bend specimens of ⅛- and ¼-in.-thick parent material also exhibited low ductility and notch-sensitive behavior similar to that observed in welded specimens, as shown in Fig. 3.4.25, which illustrates the results of two such tests. The notch sensitivity of this material was further revealed by a bend test of a ¼-in. plate which had been intentionally scratched with a triangular file to a depth of approximately 0.020 in. The brittle behavior observed is illustrated in Fig. 3.4.26. These results clearly indicate that the use of a type 304 stainless steel containing 1% boron for load-carrying components is inadvisable.

UNCLASSIFIED
Y-19749

Fig. 3.4.23. Results of Guided-Bend Ductility Tests of Welded Type 304 Stainless Steel with 1% Boron Added. Weld metal, type 347 stainless steel. Bend radius, $2T$.

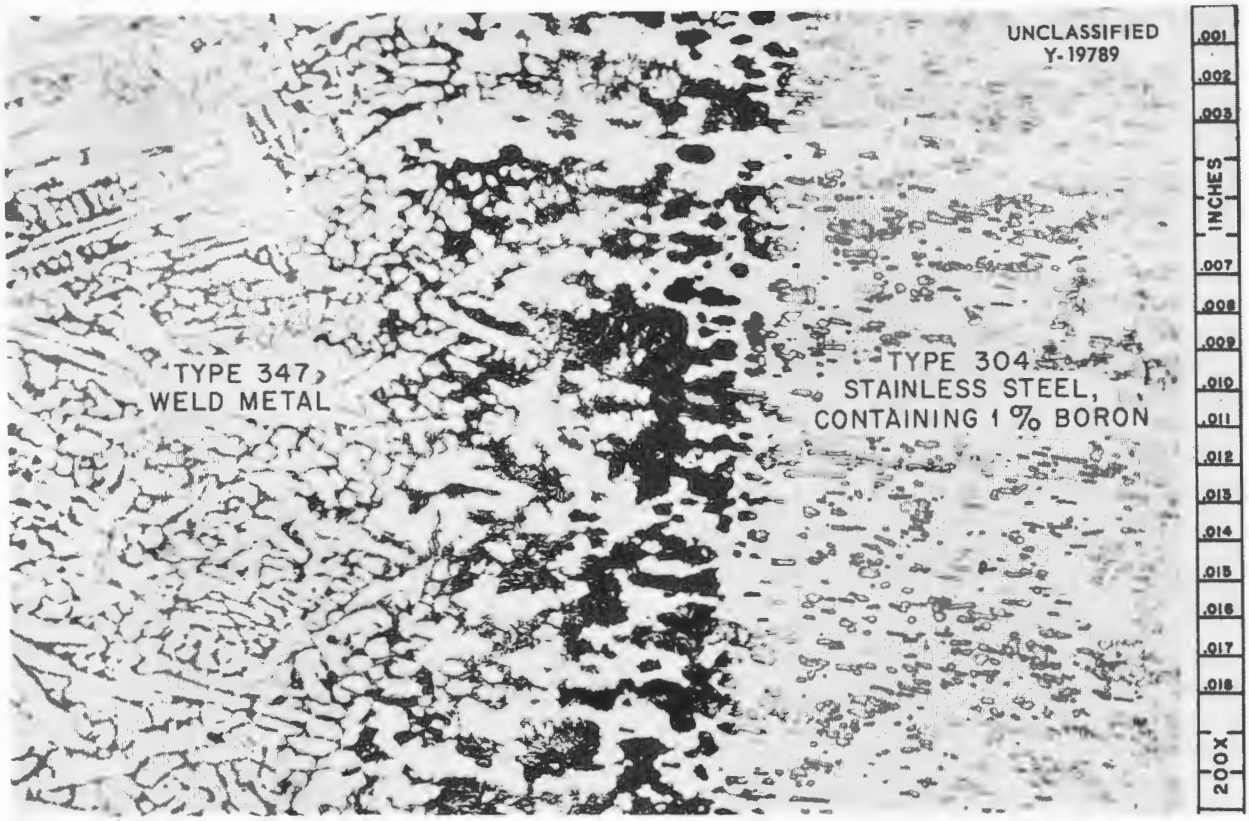

Fig. 3.4.24. Type 304 Stainless Steel Containing 1% Boron Inert-Arc Welded with Type 347 Stainless Steel Weld Metal. The complex borides visible as particles in the parent plate reacted with the type 304 stainless steel matrix and the weld metal to form a eutectic at the fusion line. 200X.

Fig. 3.4.25. Results of Guided-Bend Ductility Tests of Type 304 Stainless Steel Containing 1% Boron. Bend radius, $2T$.

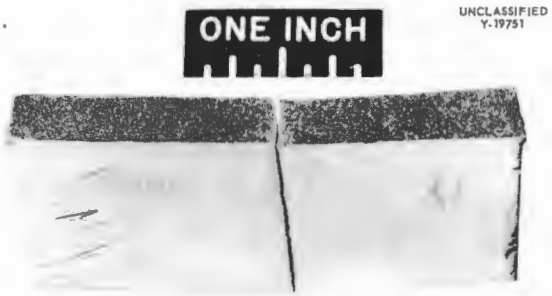

Fig. 3.4.26. Results of Guided-Bend Ductility Test of Type 304 Stainless Steel Containing 1% Boron. Specimen scratched to a depth of 0.020 in. before test.

EXAMINATION OF A NaK-TO-AIR RADIATOR

G. M. Slaughter A. E. Goldman

A 500-kw high-conductivity-fin NaK-to-air radiator, designated York HCF Radiator No. 9, was examined after test service for 1283 hr in the temperature range of 1000 to 1600°F, including 695 hr of service with a temperature drop across the system. This radiator was the first of the revised design to be tested. The revised design is different from the previous design in that the side plates are omitted; the rigid support plates, base plate, and top plate are omitted; the sump plates are fashioned from fin material; and the air shields on the top and bottom are made from 0.010-in. nickel sheet and are cut with over-size holes, as shown in Fig. 3.4.27. The radiator was brazed on its side with a slurry of Coast Metals brazing alloy No. 52.

UNCLASSIFIED
PHOTO 17881

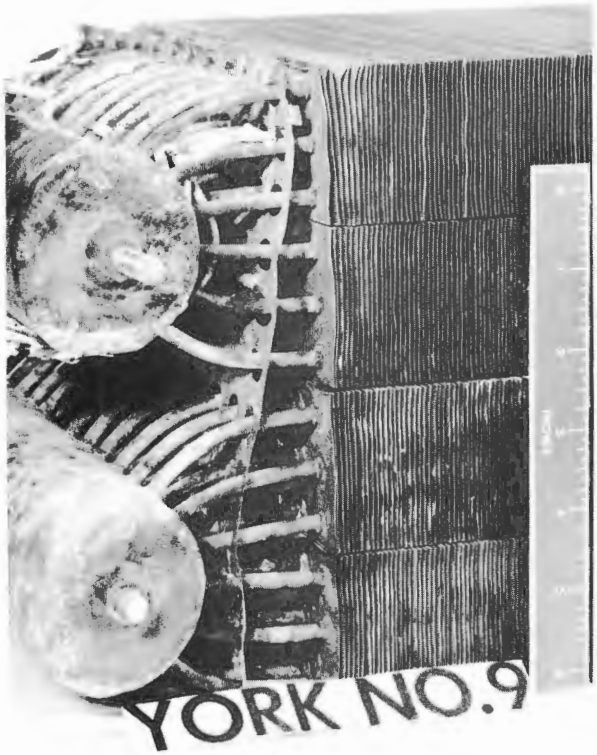

Fig. 3.4.27. York HCF Radiator No. 9 Showing the 0.010-in. Nickel-Sheet Air Shield Used in the Revised Design.

Twenty-four specimens were cut from the radiator, as shown in Fig. 3.4.28. Each specimen contained a portion of three tubes, with each tube joined to 19 or more fins. After the specimens were cross sectioned to reveal two opposed joint areas, they were mounted and then examined at 80X. A total of 2608 joint areas was examined. The percentages of fin-to-tube adherence and the degree of oxidation of the fin collars were noted and tabulated. The results of this examination are compared in Table 3.4.10 with the results of previous examinations of six other radiators. No cracks were found in tube-to-sump plate joint areas, and no evidence of incipient cracking was noted.

FABRICATION OF VALVE COMPONENTS

E. A. Franco-Ferreira G. M. Slaughter
E. J. Wilson

Attempts to attach cobalt-bonded cermets (K-M, K-138A) to Inconel by the high-temperature bonding technique described previously[3] have been unsuccessful. The wide difference in the thermal expansion coefficients of the cermet and nickel, coupled with insufficient toughness of the cobalt-bonded cermets of interest, resulted in prevalent shear-cracking.

The substitution of Mallory 1000 metal[4] (tungsten plus copper and nickel as binder materials) for nickel as a transition material has been studied, and preliminary tests are promising. The Mallory 1000 metal possesses a coefficient of thermal expansion which closely matches that of the cermet, and it is easily wet by conventional high-temperature brazing alloys. Test valve components have been successfully constructed by brazing the cobalt-bonded cermet to Mallory 1000 with the 60% Pd–40% Ni brazing alloy at 1270°C. The Mallory 1000 transition material was then copper-brazed to Inconel in a subsequent operation.

Tungsten carbide–nickel cermet valve components are also being studied. These components can be attached to a nickel-transition layer by copper-brazing. Other valve component materials

[3] P. Patriarca, A. E. Goldman, and G. M. Slaughter, *ANP Quar. Prog. Rep. March 10, 1956*, ORNL-2061, p 139, esp p 143.

[4] G. R. Van Houten, *Literature Survey – Bonding Cermets-to-Metals*, P. R. Mallory & Co., Inc., Chicago (to be published).

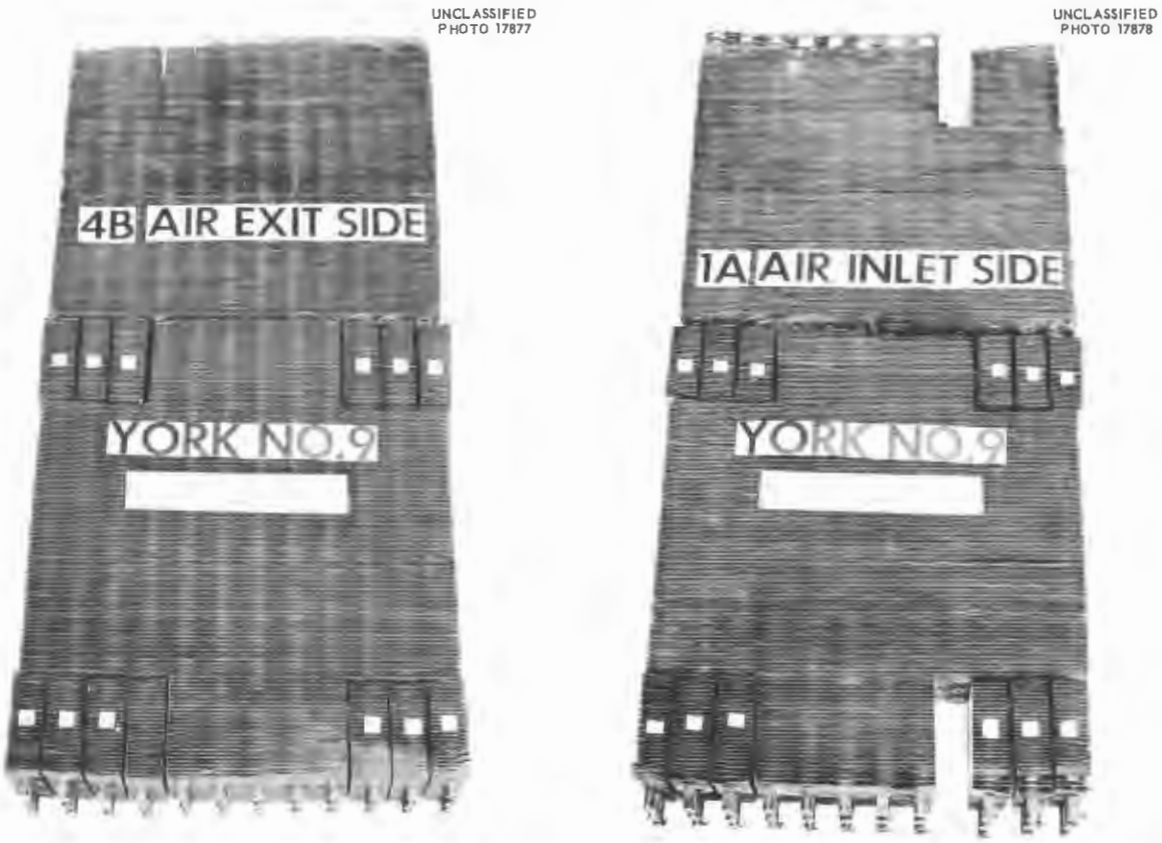

Fig. 3.4.28. Air Inlet and Exit Sides of York HCF Radiator No. 9 Showing Specimen Locations.

of interest include copper, tungsten, molybdenum, and Thermenol. A summary of the techniques utilized for attaching each of these materials is presented below.

Nickel-Bonded Cermets. – The cermet is bonded to nickel at a high temperature, with no filler-metal added. The nickel is brazed to Inconel in a subsequent operation.

Cobalt-Bonded Cermets. – Techniques are being developed. One method involves brazing the cermet to Mallory 1000 with the 60% Pd–40% Ni brazing alloy. The Mallory 1000 is brazed to Inconel in a subsequent operation.

Tungsten Carbide-Nickel Cermets. – The cermet is copper-brazed to a nickel-transition layer. The nickel is brazed to Inconel with Coast Metals brazing alloy No. 52 in a subsequent operation. (For sodium service, all brazing can be performed with Coast Metals brazing alloy No. 52.)

Copper. – A 0.005-in. electroplate of nickel is deposited on the faying surface of the copper valve material, which is then brazed to Inconel with Coast Metals brazing alloy No. 52 or the 82% Au–18% Ni alloy.

Molybdenum. – The molybdenum valve part is copper-brazed directly to Inconel.

Tungsten. – The tungsten valve part is copper-brazed to a nickel-transition layer which is brazed to Inconel with Coast Metals brazing alloy No. 52 in a subsequent operation.

Thermenol. – A 0.005-in. electroplate of nickel is deposited on the faying surface, which is then brazed with copper or Coast Metals brazing alloy No. 52 to Inconel.

TABLE 3.4.10. SUMMARY OF RESULTS OF EXAMINATIONS OF YORK HCF RADIATOR NO. 9 AND SIX PREVIOUSLY OPERATED RADIATORS

	Radiator Designation						
	York No. 9	York No. 4	York No. 3	York No. 1	PWA No. 2	ORNL No. 3	ORNL No. 1
Number of hours of service in the temperature range 1000 to 1600°F	1283	1356	361	152	1199	716	608
Number of joint areas examined	2608	2757	2684	3847	3210	2282	4150
Percentage of joint areas having 75 to 100% adherence	44.6	60.7	90.4	67.4	100	87.7	91.8
Percentage of joint areas having 50 to 74% adherence	21.2	18.8	5.9	13.0		3.5	4.2
Percentage of joint areas having 25 to 49% adherence	9.4	5.5	1.1	7.3		1.4	1.4
Percentage of joint areas having 0 to 24% adherence	24.8	15.0	2.6	12.3		7.4	2.6
Percentage of joint areas having nonoxidized copper fins	23.5	61.9	84.5	75.4	100	12.1	59.3
Per cent of joint areas having slightly oxidized copper fins	8.5	19.5	7.5	22.0		2.5	20.1
Per cent of joint areas having heavily oxidized copper fins	68.0	18.6	8.0	2.6		85.4	20.6

3.5. MECHANICAL PROPERTY STUDIES

D. A. Douglas

CREEP-RUPTURE PROPERTIES OF INCONEL

J. R. Weir, Jr.

Effect of Section Thickness

The applicability of creep-rupture design data for Inconel is limited in that the data are valid only when the alloy is subjected to operating conditions similar to those under which the material is tested. In a design where various shapes and thicknesses of material are employed in contact with corrosive media, the effect of section thickness becomes an important consideration in the use of the available data.

The effect of section thickness on the creep-rupture properties of fine-grained Inconel sheet completely immersed in the fuel mixture (No. 30) $NaF-ZrF_4-UF_4$ (50-46-4 mole %) is illustrated in Fig. 3.5.1, in which test time is plotted vs section thickness, with 2, 5, and 10% elongation, rupture, and elongation at rupture as parameters. The specimens were tested at 1500°F under a stress of 3500 psi. For sections less than 0.060 in. thick the strength and ductility are noticeably affected by the thickness of the section, being lower for the thinner sections, but for sections more than 0.060 in. thick the strength is not particularly sensitive to section thickness.

A more extensive comparison of the creep-rupture properties of 0.020- and 0.060-in.-thick fine-grained Inconel sheet tested in fuel mixture No. 30 at 1500°F is presented in Fig. 3.5.2. Although the data for the 0.060-in.-thick sheet are rather meager, some trends are established. The strength properties of the thinner sheet are somewhat less sensitive to stress and more sensitive to the time in the liquid than are the strength properties of the thicker sheet material. It is believed that for this fine-grained material a major portion of the strength decrement observed for the thinner sections may be attributed to the corrosive action of the fuel mixture.

Effect of Cold Work

The creep-rupture properties of an alloy depend to a great extent on the mechanical and thermal history of the alloy, and therefore an investigation was initiated to study the effect of cold work on the high-temperature strength and corrosion resistance of Inconel in fuel mixture No. 30. Cold-rolled (50% reduction in area) and as-recrystallized (annealed at 1650°F for 2 hr after cold rolling to 50% reduction in area) Inconel sheet specimens 0.060 in. thick were creep-rupture tested at 1500°F. A comparison of the stress-rupture properties of these specimens is shown in Fig. 3.5.3. The strength of the annealed specimen was found to be much higher than that of the cold-worked specimen.

Static corrosion tests were also made on Inconel specimens which had been previously cold worked in amounts varying from 0 to 25%. The cold work

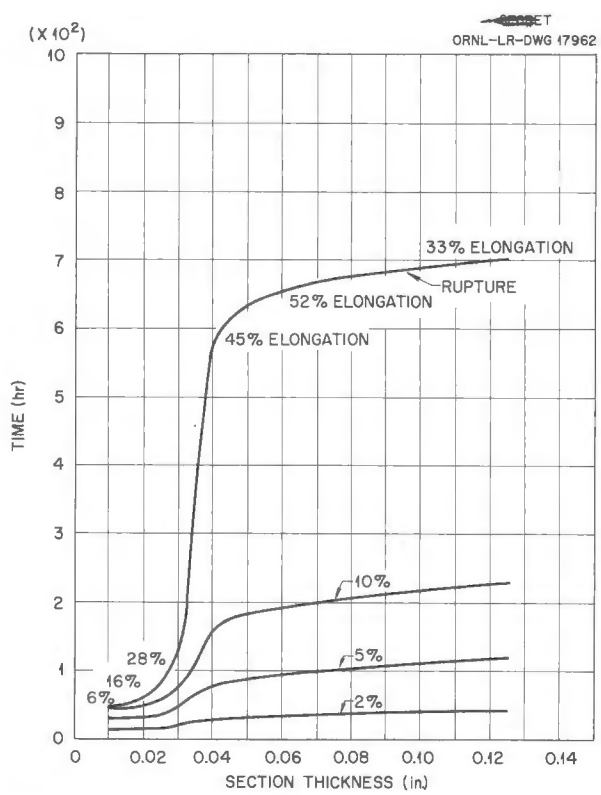

Fig. 3.5.1. Effect of Section Thickness on the Creep-Rupture Properties of Fine-Grained Inconel Sheet Tested at 1500°F and a Stress of 3500 psi in the Fuel Mixture (No. 30) $NaF-ZrF_4-UF_4$ (50-46-4 mole %).

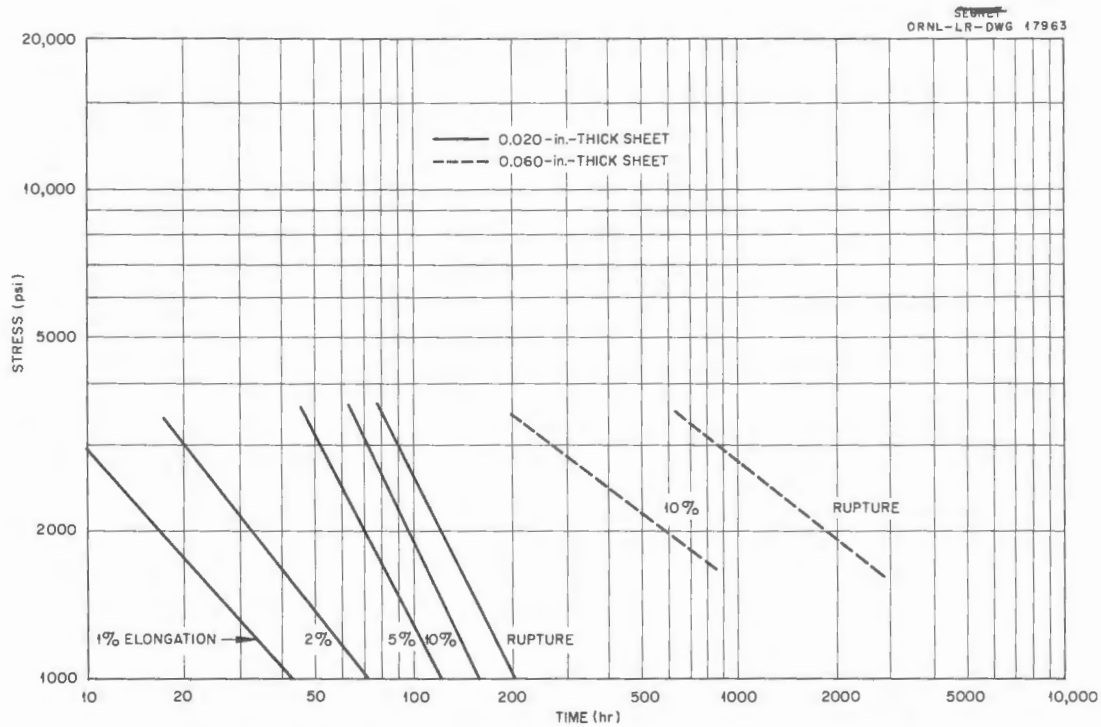

Fig. 3.5.2. Comparison of the Creep-Rupture Properties of 0.020- and 0.060-in.-Thick Fine-Grained Inconel Sheet Tested at 1500°F in the Fuel Mixture (No. 30) $NaF-ZrF_4-UF_4$ (50-46-4 mole %).

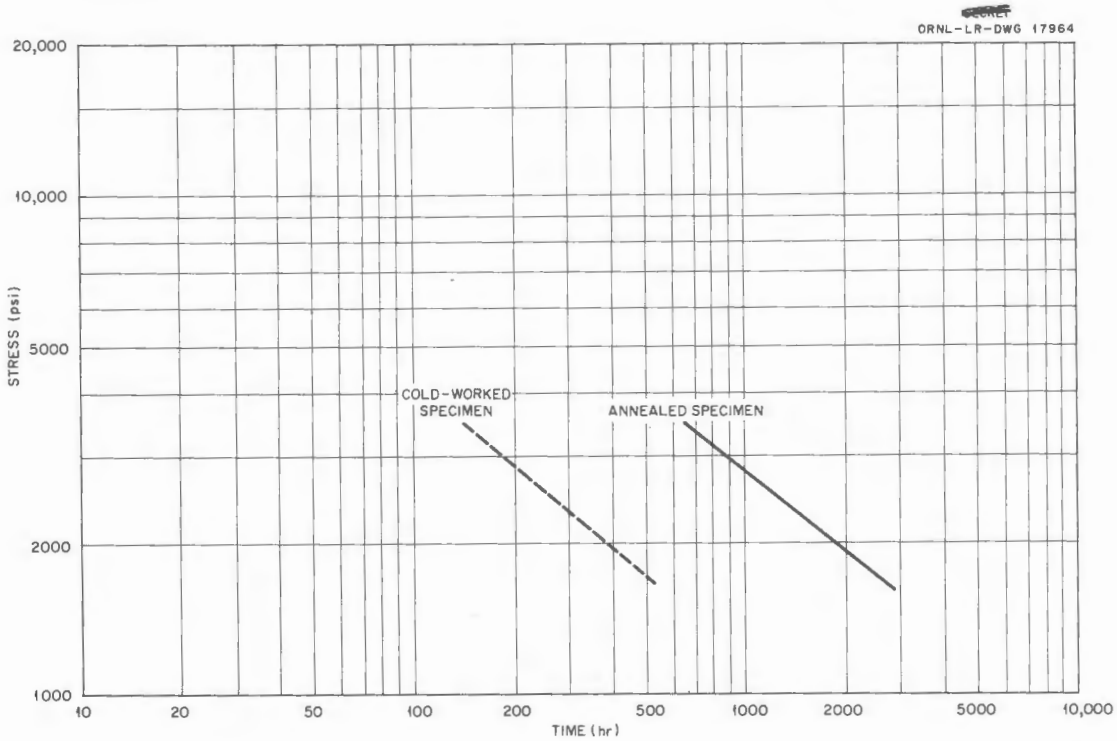

Fig. 3.5.3. Comparison of the Stress-Rupture Properties of Annealed and Cold-Worked 0.060-in.-Thick Inconel Sheet Specimens Tested at 1500°F in the Fuel Mixture (No. 30) $NaF-ZrF_4-UF_4$ (50-46-4 mole %).

was accomplished by bending, and the specimens were then immersed in the fuel mixture No. 30 for 140 hr at 1500°F. The sections shown in Figs. 3.5.4, 3.5.5, and 3.5.6 were taken from the surfaces of an as-received specimen, the tension side of a specimen cold worked 12%, and the tension side of a specimen cold worked 25%. The depth of attack on the compression side of the bends was observed to be of the same magnitude and appearance as that on the tension side, and therefore only the tension sides are shown. The results indicate that the depth of attack in static fuel mixture No. 30 is insensitive to the amount of cold work. Based on the observation that cold work has no effect on the depth of corrosive attack, the reduction in the strength of previously cold-worked Inconel at 1500°F is attributed to recrystallization during the test.

STRAIN CYCLING OF INCONEL

J. R. Weir, Jr.

Thermal fluctuations resulting from power changes or from flow characteristics in the bulk heated fluid in the ART will subject the structural material to strain cycles of varying frequency and magnitude, and therefore experimental investigations are being made in order to determine the effect of strain cycling on the properties of Inconel. The two experimental methods presently being used consist in stress relaxation testing[1] and mechanical strain cycle testing.

Development work was recently completed on equipment which may be used to strain cycle a

[1] C. R. Kennedy, *ANP Quar. Prog. Rep. Sept. 10, 1956*, ORNL-2157, p 205.

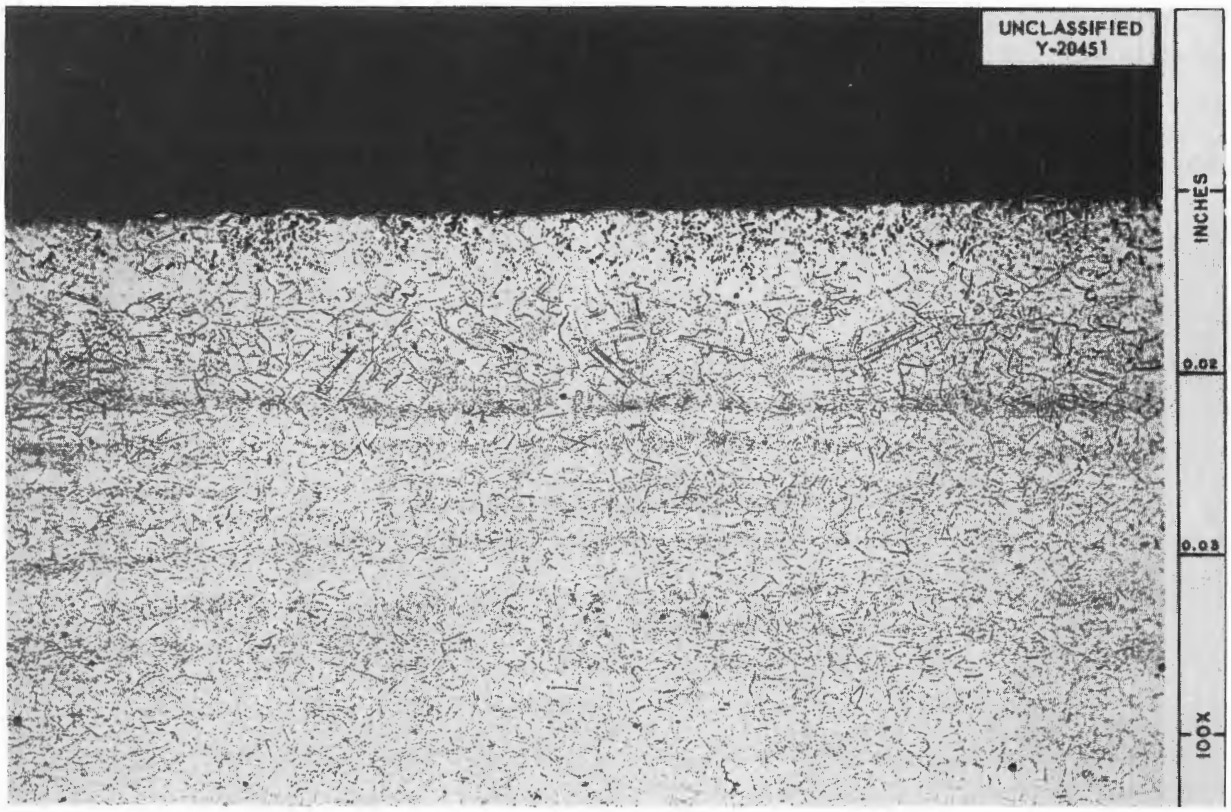

Fig. 3.5.4. As-Received Inconel Specimen After Exposure for 140 hr at 1500°F to the Fuel Mixture (No. 30) NaF-ZrF_4-UF_4 (50-46-4 mole %). 100X. Reduced 3%. ([redacted])

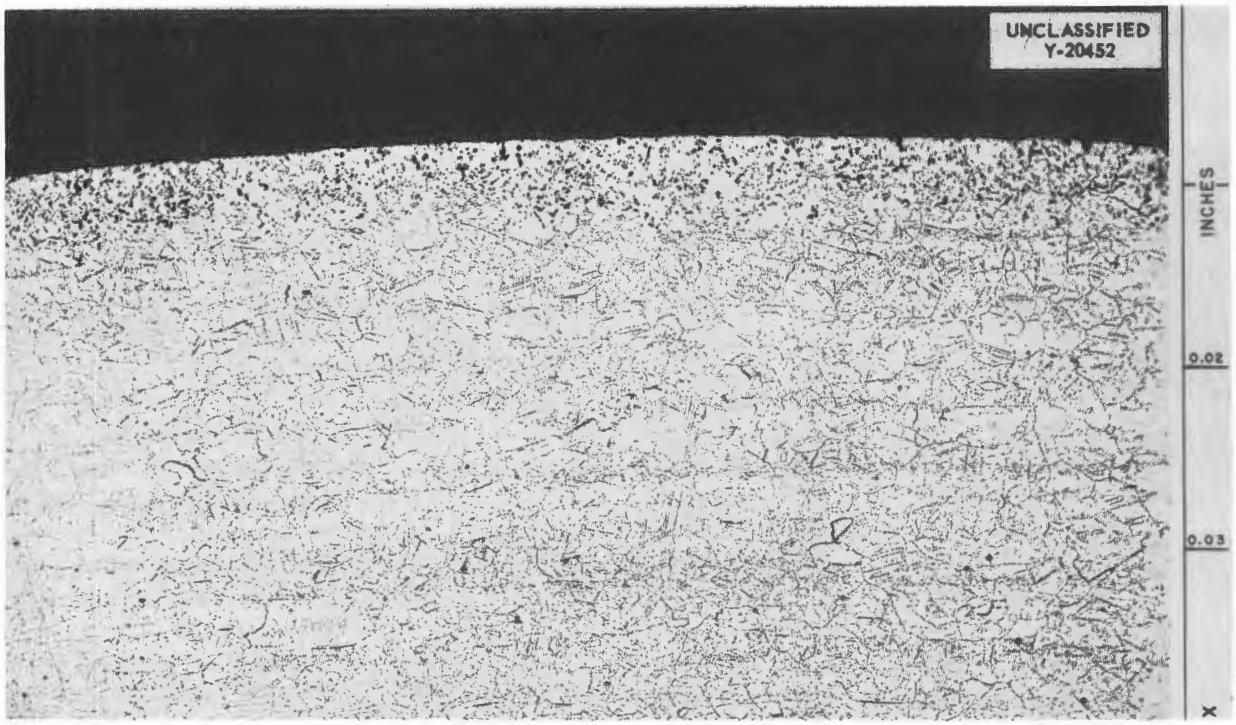

Fig. 3.5.5. Tension Side of Inconel Specimen Cold-Worked 12% and Exposed for 140 hr at 1500°F to the Fuel Mixture (No. 30) $NaF-ZrF_4-UF_4$ (50-46-4 mole %). 100X. Reduced 2%. [redacted]

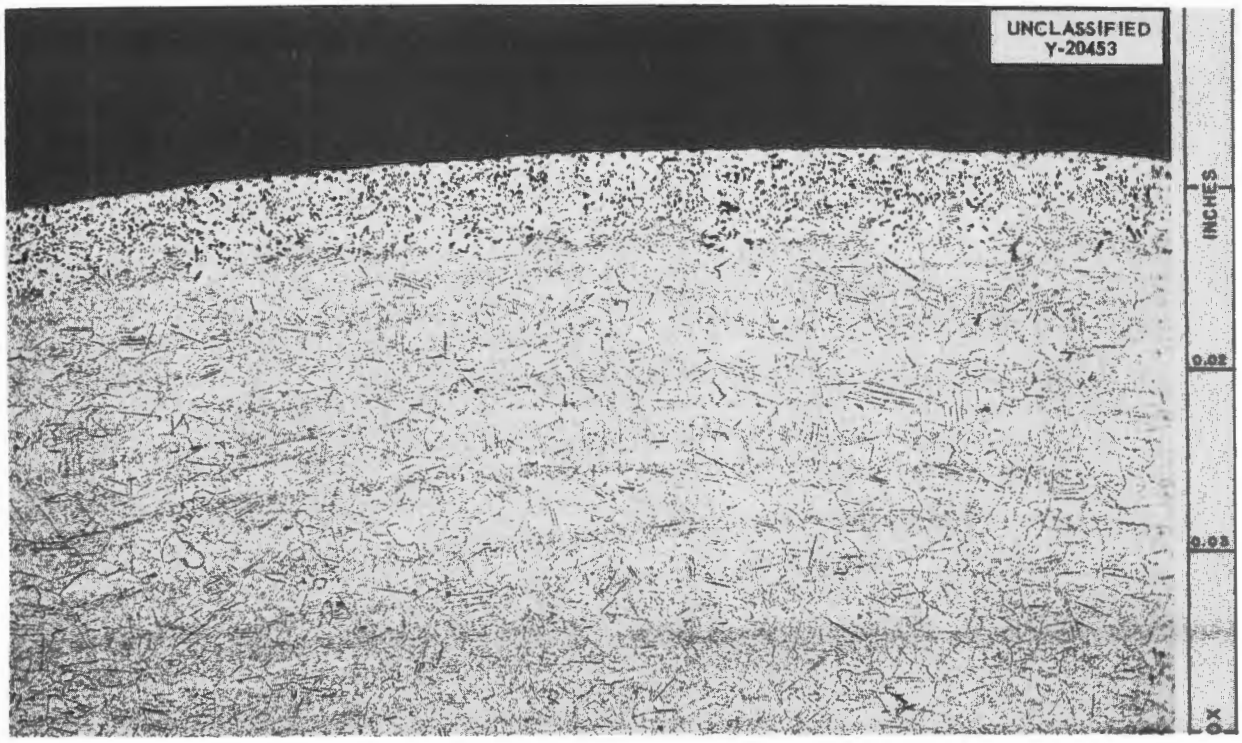

Fig. 3.5.6. Tension Side of Inconel Specimen Cold-Worked 25% and Exposed for 140 hr at 1500°F to the Fuel Mixture (No. 30) $NaF-ZrF_4-UF_4$ (50-46-4 mole %). 100X. Reduced 3%. [redacted]

specimen at elevated temperatures in controlled environments. A schematic diagram of the apparatus is shown in Fig. 3.5.7. The specimen is a $\frac{3}{4}$-in. tube with a 1-in.-long reduced section which serves as the test gage length. The top shoulder of the specimen is welded to the casement, and the piston rod is welded to the bottom shoulder of the specimen. The specimen is then loaded in tension or compression by means of controlled gas pressure on the top or bottom of the piston. The total strain is sensed through the small rod which is connected to the top of the large rod and extends through a pressure seal in the top of the pressure chamber. The total strain in each of the tension and compression cycles is monitored by means of a dial gage placed in contact with the top of the sensing rod. The total strain at which the stress in the specimen is to be reversed is controlled by a pneumatic device which changes small linear movements into pressure changes. These pressure changes are then sensed by pressure switches which actuate solenoid valves in the gas pressure lines leading to the top and bottom sides of the piston to change the axial direction of the stress in the specimen. The specimen is pressurized internally with gas at a very low pressure, and this internal pressure is monitored for failure of the specimen.

With this apparatus the total axial strain per cycle may be controlled to 0.5 to 25% per cycle with an accuracy of ±0.2% of the strain values. The plastic strain per cycle may be measured directly by removing the stress at the end of the

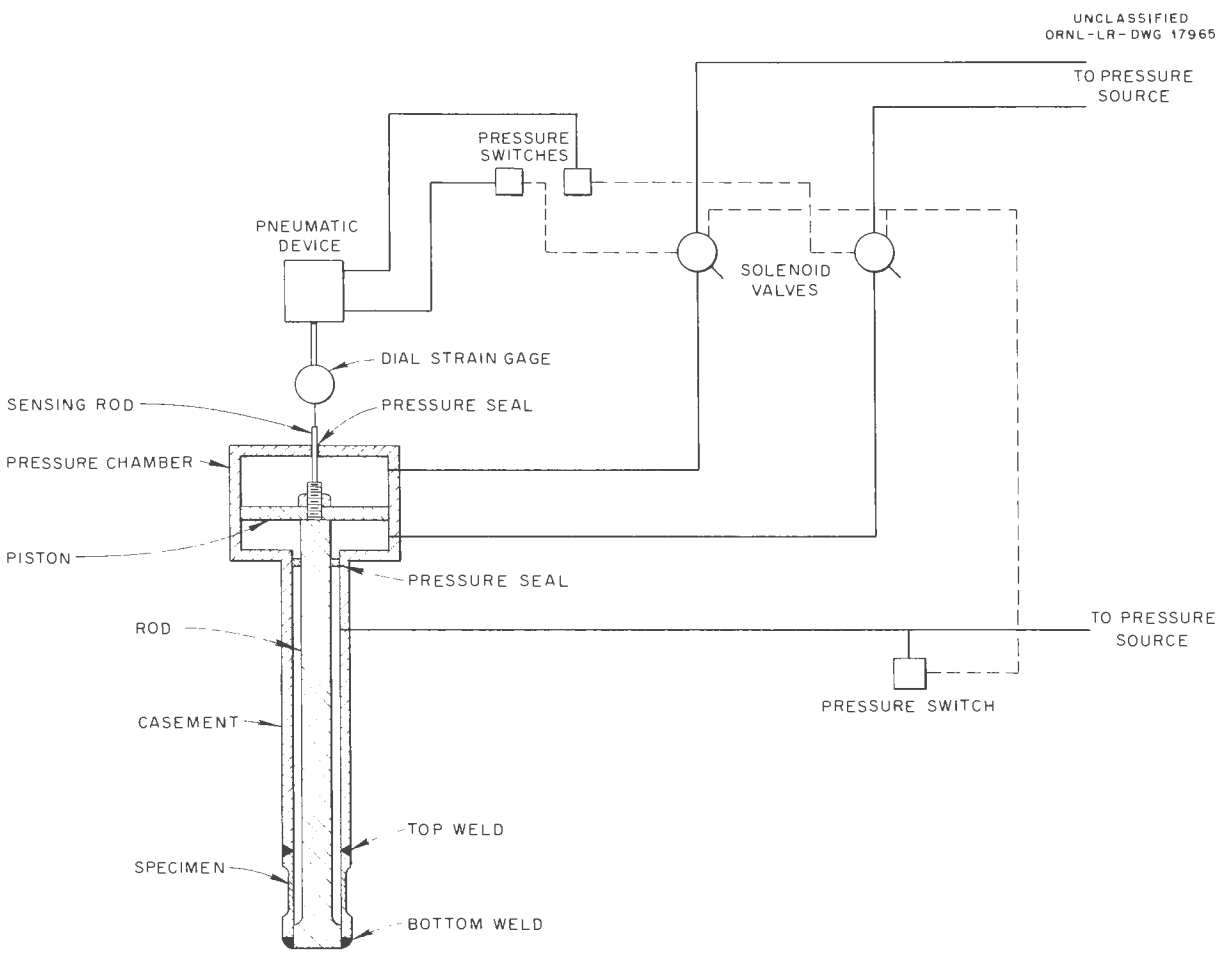

Fig. 3.5.7. Apparatus for Strain Cycling Inconel at High Temperatures.

tension and compression cycles and observing the dial gage readings. The highest cyclic frequency is roughly 1 cps. The lower frequencies may be varied at will. The highest stress value which may be produced in the specimen is roughly 30,000 psi, although it may be possible to increase this value somewhat. The maximum operating temperature is 1650°F. The environment to which the outside surface of the specimen may be exposed may be gaseous or liquid.

The operating conditions and results of the first test with this equipment are summarized below:

Temperature	1500°F
Total strain per full cycle	1%
Plastic strain per full cycle	0.12%
Cycle rate per full cycle	80 sec
Environment	Argon
Material	As-received fine-grained Inconel
Cycles to failure	3390
Time to failure	77 hr

The failure was intergranular, and metallographic examination disclosed no cracks in the gage length other than the single crack which propagated to failure. No grain growth or recrystallization appeared to have occurred during the test.

STRESS-RUPTURE PROPERTIES OF NICKEL-MOLYBDENUM ALLOYS

C. R. Kennedy[2]

Commercial nickel-molybdenum alloys, such as Hastelloys B and W, have always attracted much attention because of their excellent resistance to chemical corrosion and their relatively high strength at elevated temperatures. However, these alloys are not single phase, and their ductility is seriously reduced by precipitation of a brittle beta phase at ART design temperatures. Therefore special alloys designed to retain the inherent advantages of nickel-base molybdenum alloys and to eliminate their objectionable behavior are being studied. The effects of various amounts of molybdenum on the stress-rupture properties of nickel-molybdenum alloys are compared in Fig. 3.5.8. The plots were obtained from creep-rupture testing of solution-annealed specimens at 1500°F in argon. It is

[2]On assignment from Pratt & Whitney Aircraft.

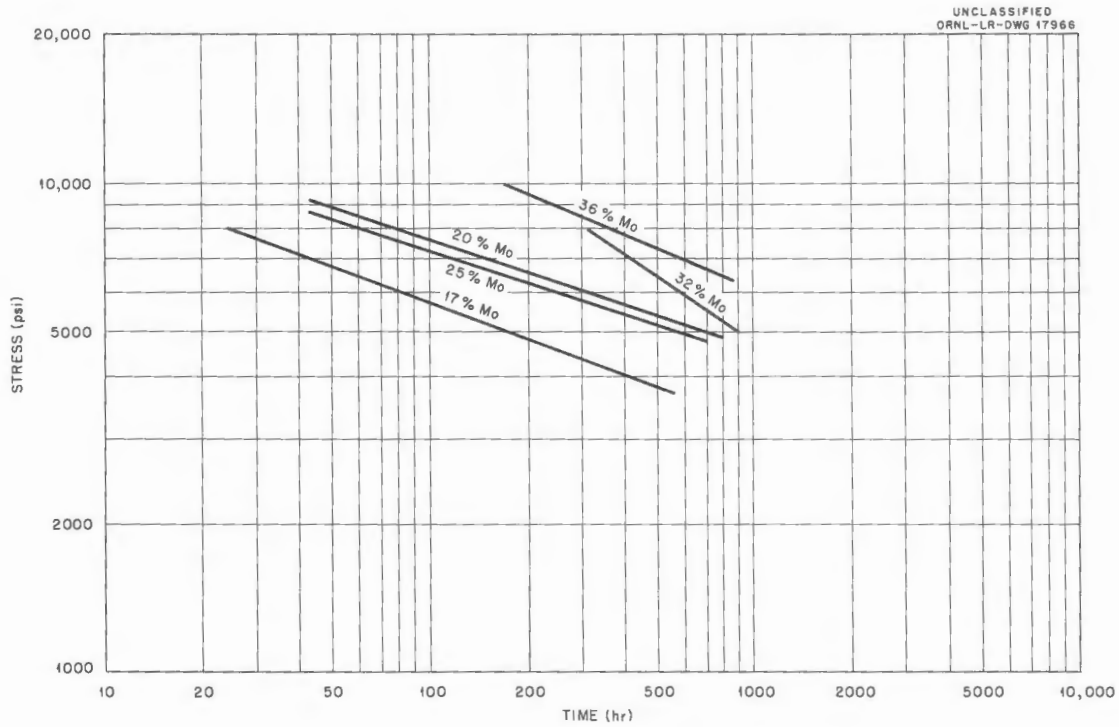

Fig. 3.5.8. Stress-Rupture Plots for Several Nickel-Molybdenum Binary Alloys Tested at 1500°F in Argon.

immediately evident that the strength of the alloy increases with increases in the molybdenum content. However, if the molybdenum content is greater than 20%, a two-phase alloy exists and the precipitation of the beta phase will cause a serious loss of ductility. Although the strength of the 80% Ni–20% Mo alloy is greater than that of Inconel, an even stronger material is desired for the future.

Chromium additions of up to 7% were made to the basic 80% Ni–20% Mo alloy for oxidation resistance, and then creep-rupture tests were made in argon at 1500°F to determine the effect of the chromium on the strength of the alloy. A comparison of the stress-rupture curves of the basic 80% Ni–20% Mo alloy with those for alloys with 3, 5, and 7% additions of chromium and corresponding reductions in the nickel content is presented in Fig. 3.5.9. All the alloys containing chromium were single phase, and no significant increase in strength was noted except for the alloy with 7% chromium. Similar alloys with niobium additions of 2 and 5% were also creep tested at 1500°F in argon. The comparison of the stress-rupture curves for these niobium-containing alloys with the curve for the basic alloy is presented in Fig. 3.5.10. Again there was an increase in strength with the addition of the third metal. However, the alloy with 5% niobium is two phase and therefore undesirable.

Screening tests are being made of the creep-rupture properties of the various experimental alloys exposed to the fuel mixture (No. 107) NaF-KF-LiF-UF_4 (11.2-41-45.3-2.5 mole %). For comparison, each alloy is being tested with a stress of 8000 psi at 1500°F in two conditions: annealed at 2000°F for 1 hr, and annealed at 2000°F for 1 hr and aged 50 hr at 1300°F. The alloy composition, source, type of melt, rupture life, and total strain are given in Table 3.5.1.

The low ductility of some of the first experimental alloys, reported previously,[3] appears to have been the result of the use of a melting technique that did not completely degas the material. It is shown in the table that all the alloys containing deoxidants, such as aluminum, are quite ductile. Metallographic examination of the tested specimens is incomplete; however, definite trends are indicated in Figs. 3.5.11 through 3.5.19. All the material tested contained less than 22% Mo, and therefore no beta phase is evident in any of the structures. Since most of the alloys were made in very small heats, segregation of carbides and complex compounds occurred. The segregation in turn resulted in grain growth in areas relatively free of precipitate, and the structures thus show mixed grain sizes. There was no corrosive attack evident on the alloys which contained no chromium. All specimens which contained chromium show intergranular corrosion of varying depths. The severity of attack was greater than was expected on the basis of the results obtained with thermal-convection loops. This may be explained by the fact that the creep-test chambers are made of Hastelloy B, which contains no chromium, and thus dissimilar metal transfer may have occurred.

---

[3]D. A. Douglas *et al.*, *ANP Quar. Prog. Rep. Dec. 10, 1955*, ORNL-2012, p 153.

TABLE 3.5.1. COMPOSITIONS OF ALLOYS CREEP TESTED AT 1500°F AND A STRESS OF 8000 psi EXPOSED TO THE FUEL MIXTURE (NO. 107) NaF-KF-LiF-UF_4 (11.2-41-45.3-2.5 MOLE %) AND TEST RESULTS

Alloy Composition (wt%)										Rupture Life (hr)	Elongation (%)	Treatment* of Specimen	Corrosion of Unstressed Specimen (in.)
Mo	Cr	Nb	W	Al	Ti	Mn	C	Fe	Ni				
ORNL Alloys, Vacuum Melted													
16				1	1.5	0.5	0.06		Bal	300	25	1	0
16				1	1.5	0.5	0.06		Bal	490	75	2	**
16				2	1.5	0.5	0.06		Bal	325	75	1	0
16				2	1.5	0.5	0.06		Bal	300	55	2	**
15		2	2						Bal	185	55	1	0
15		2	2						Bal	650	25	2	**
16	5			1	1.5				Bal	250	84	1	0.001
16	5			1	1.5				Bal	420	60	2	**
17	7			0.5			0.06		Bal	390	35	1	**
16	5	1		1		0.5	0.06		Bal	220	35	1	**
16	5			0.5		0.5	0.06		Bal	155	13	1	**
20				2					Bal	1373	25	1	0
International Nickel Company Alloys, Air Melted													
15	5	3	3						Bal	140	20	1	0.002
15	5	3	3						Bal	135	25	2	**
15		3	3						Bal	120	16	1	0
15		3	3						Bal	140	9	2	**
15				1	1.5				Bal	80	78	1	0
15				1	1.5				Bal	760	28	2	0
17				0.5					Bal	38	17	1	0
Battelle Memorial Institute Alloys, Air Melted													
20	7.4					0.8	0.14		Bal	280	20	1	0.004
20	7.4					0.8	0.14		Bal	280	25	2	**
21	7.58	2.16				0.8	0.15	1	Bal	450	21	1	0.006
21	7.58	2.16				0.8	0.15	1	Bal	460	21	2	**
21.6	7.82	2.32		1.31		0.8	0.15	1	Bal	911	14	1	0.005
21.6	7.82	2.32		1.31		0.8	0.15	1	Bal	1020	11	2	**
21	7.43			2.05		0.8	0.13		Bal	700	35	1	0.006
21	7.43			2.05		0.8	0.13		Bal	800	45	2	**

*Treatment 1: Annealed at 2000°F for 1 hr.

Treatment 2: Annealed at 2000°F for 1 hr and aged at 1300°F for 50 hr.

**Metallographic examination not completed.

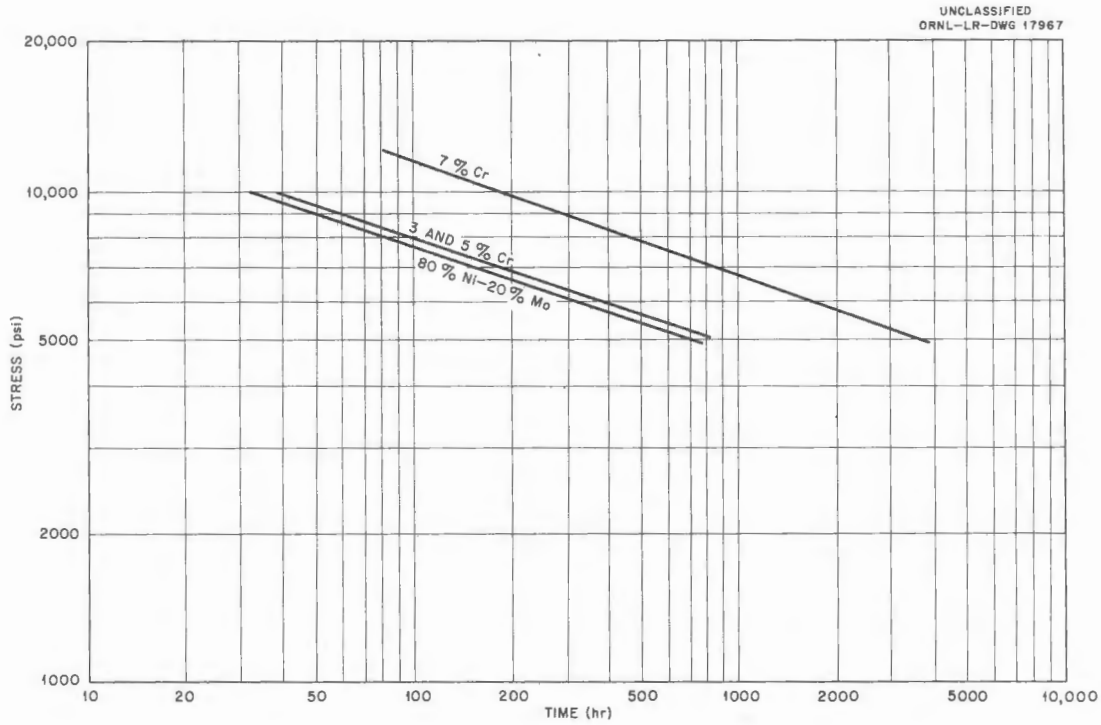

Fig. 3.5.9. Comparison of Stress-Rupture Properties at 1500°F in Argon of the Basic 80% Ni–20% Mo Alloy with Those of Alloys with 3, 5, and 7% Chromium Additions and Corresponding Nickel Reductions.

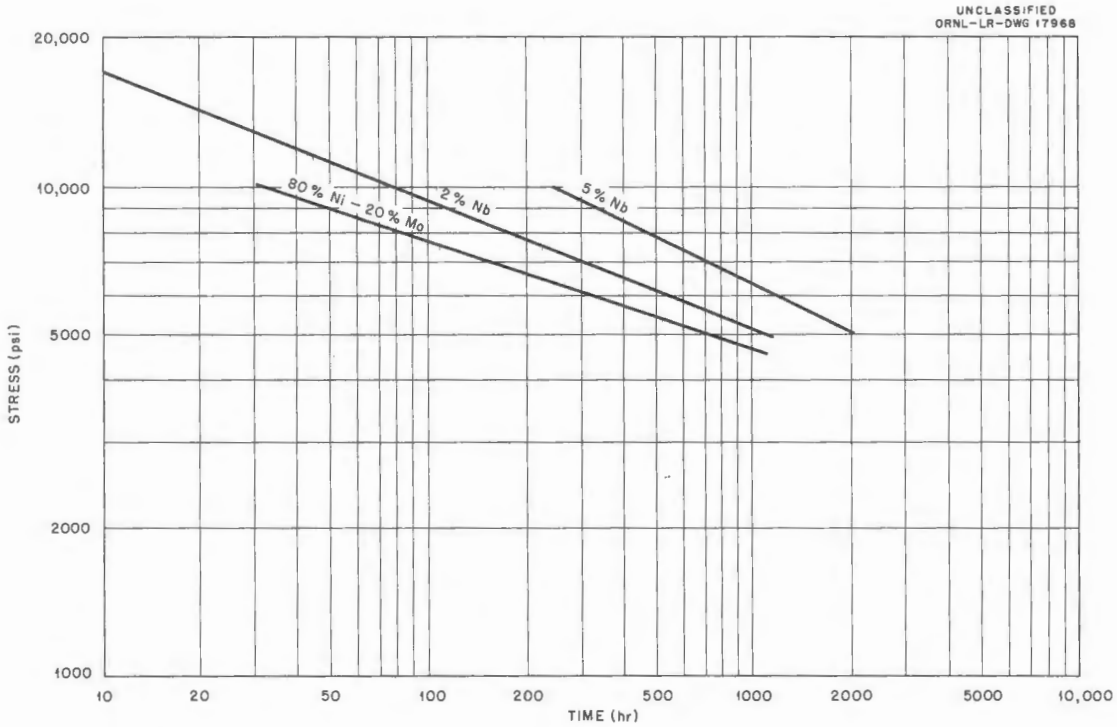

Fig. 3.5.10. Comparison of Stress-Rupture Properties at 1500°F in Argon of the Basic 80% Ni–20% Mo Alloy with Those of Alloys with 2 and 5% Niobium Additions and Corresponding Nickel Reductions.

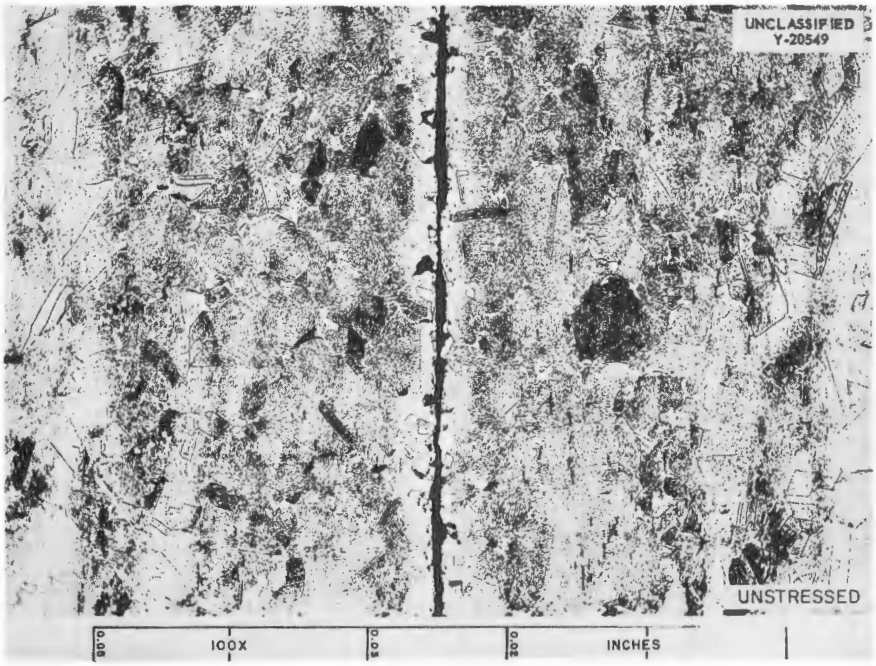

Fig. 3.5.11. Comparison of Stressed (8000 psi) and Unstressed Sections of a 20% Mo–2% Al–Bal Ni Alloy Creep Tested in the Fuel Mixture (No. 107) NaF-KF-LiF-UF_4 (11.2-41-45.3-2.5 mole %) at 1500°F in the Annealed Condition. Specimen ruptured in 1373 hr with 25% elongation. 100X. Reduced 26%. ~~(Secret with caption)~~

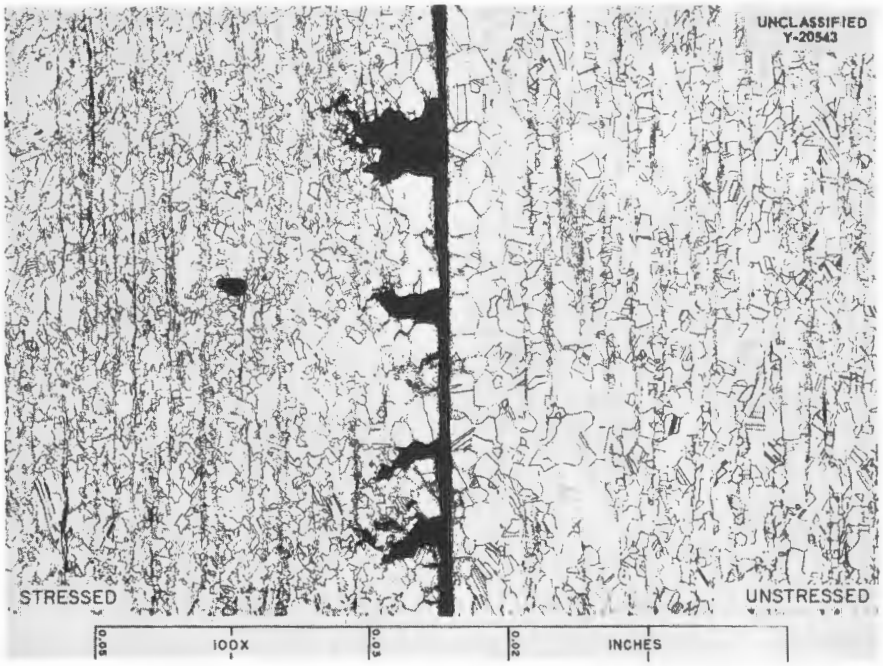

Fig. 3.5.12. Comparison of Stressed (8000 psi) and Unstressed Sections of a 16% Mo–1% Al–1.5% Ti–Bal Ni Alloy Creep Tested in the Fuel Mixture (No. 107) NaF-KF-LiF-UF_4 (11.2-41-45.3-2.5 mole %) at 1500°F in the Annealed Condition. Specimen ruptured in 211 hr with 55% elongation. 100X. Reduced 26%. ~~(Secret with caption)~~

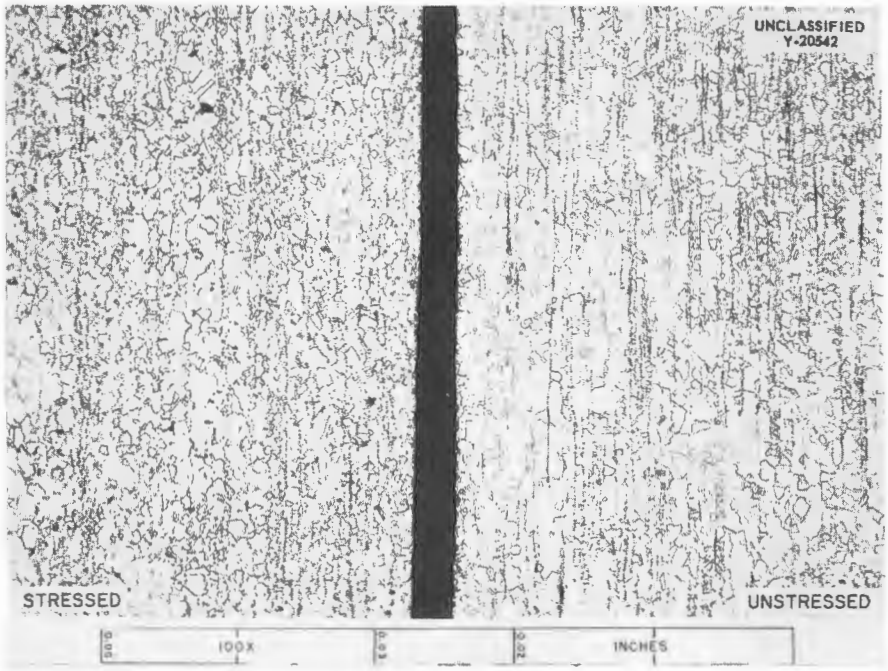

Fig. 3.5.13. Comparison of Stressed (8000 psi) and Unstressed Sections of a 16% Mo–2% Al–1.5% Ti–Bal Ni Alloy Creep Tested in the Fuel Mixture (No. 107) NaF-KF-LiF-UF_4 (11.2-41-45.3-2.5 mole %) at 1500°F in the Annealed Condition. Test discontinued in 325 hr with specimen elongation of 75%. 100X. Reduced 26%. ~~(Secret with caption)~~

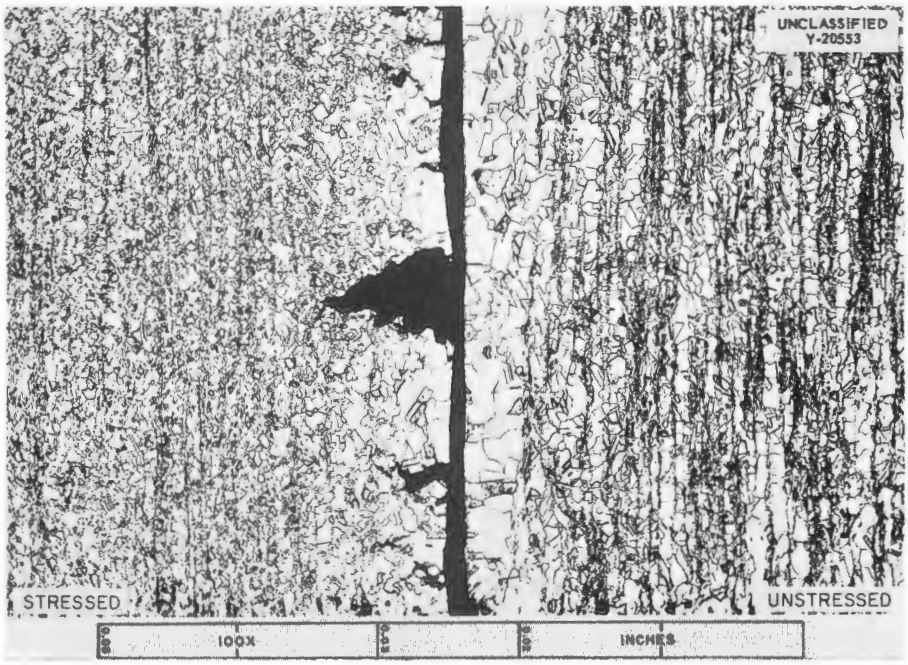

Fig. 3.5.14. Comparison of Stressed (8000 psi) and Unstressed Sections of a 15% Mo–2% Nb–2% W–Bal Ni Alloy Creep Tested in the Fuel Mixture (No. 107) NaF-KF-LiF-UF_4 (11.2-41-45.3-2.5 mole %) at 1500°F in the Annealed Condition. Specimen ruptured in 185 hr with 55% elongation. 100X. Reduced 25.5%. ~~(Secret with caption)~~

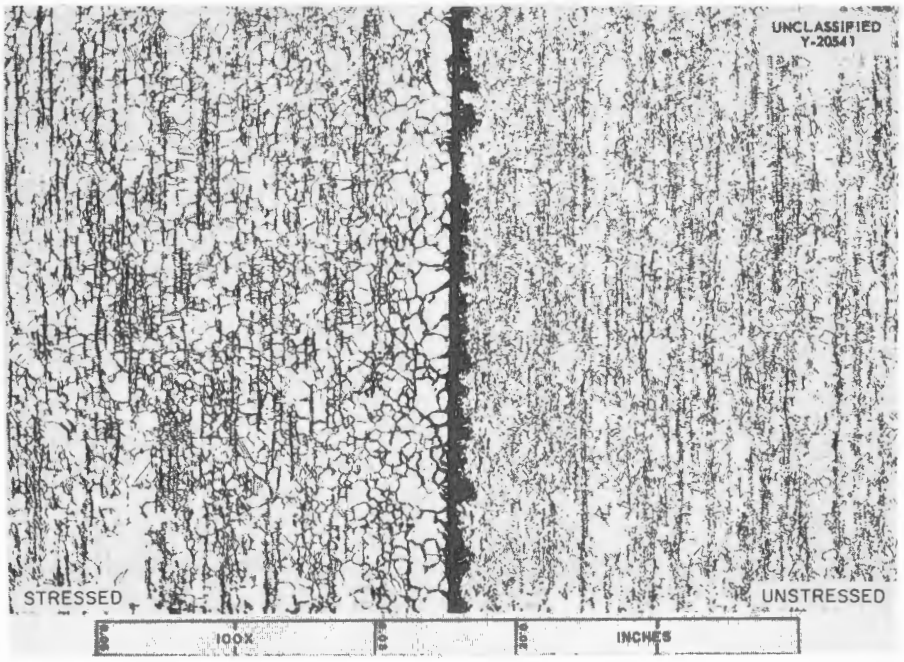

Fig. 3.5.15. Comparison of Stressed (8000 psi) and Unstressed Sections of a 16% Mo–5% Cr–1% Al–1.5% Ti–Bal Ni Alloy Creep Tested in the Fuel Mixture (No. 107) NaF-KF-LiF-UF_4 (11.2-41-45.3-2.5 mole %) at 1500°F in the Annealed Condition. Test discontinued in 230 hr with specimen elongation of 84%. 100X. Reduced 25.5%. [redacted]

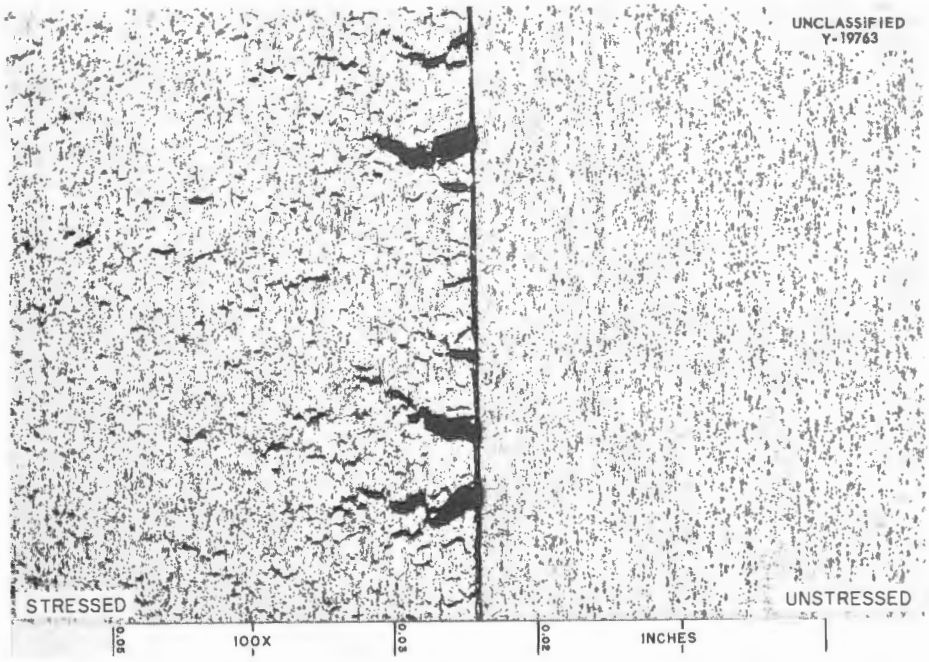

Fig. 3.5.16. Comparison of Stressed (8000 psi) and Unstressed Sections of a 15% Mo–5% Cr–3% Nb–3% W–Bal Ni Alloy Creep Tested in the Fuel Mixture (No. 107) NaF-KF-LiF-UF_4 (11.2-41-45.3-2.5 mole %) at 1500°F in the Annealed Condition. Specimen ruptured in 194 hr with 20% elongation. 100X. Reduced 24%. [redacted]

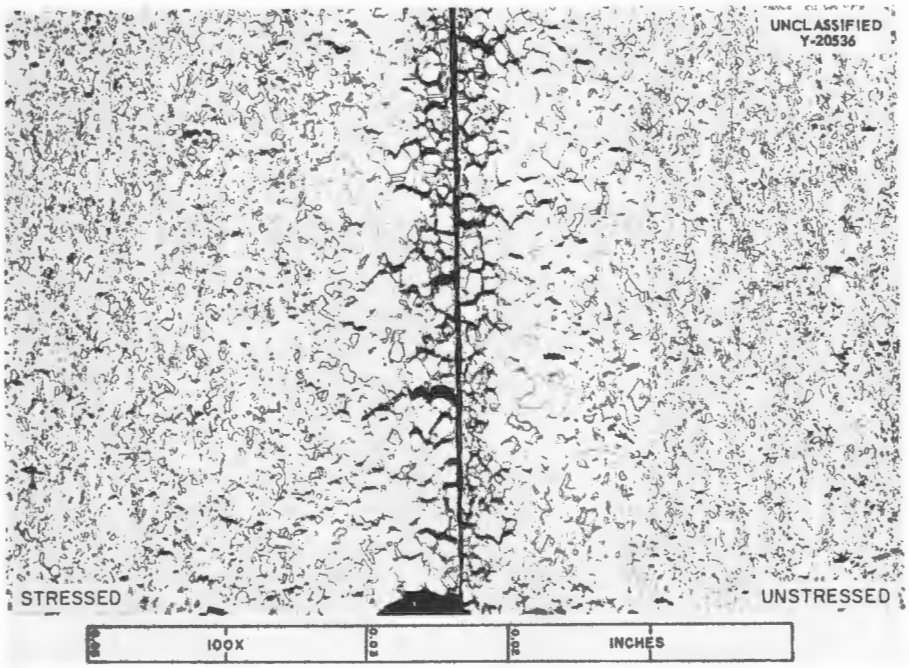

Fig. 3.5.17. Comparison of Stressed (8000 psi) and Unstressed Sections of a 15% Mo–1% Al–1.5% Ti–Bal Ni Alloy Creep Tested in the Fuel Mixture (No. 107) NaF-KF-LiF-UF_4 (11.2-41-45.3-2.5 mole %) at 1500°F in the Annealed Condition. Specimen ruptured in 911 hr with 14% elongation. 100X. Reduced 24.5%. ~~(Secret with caption)~~

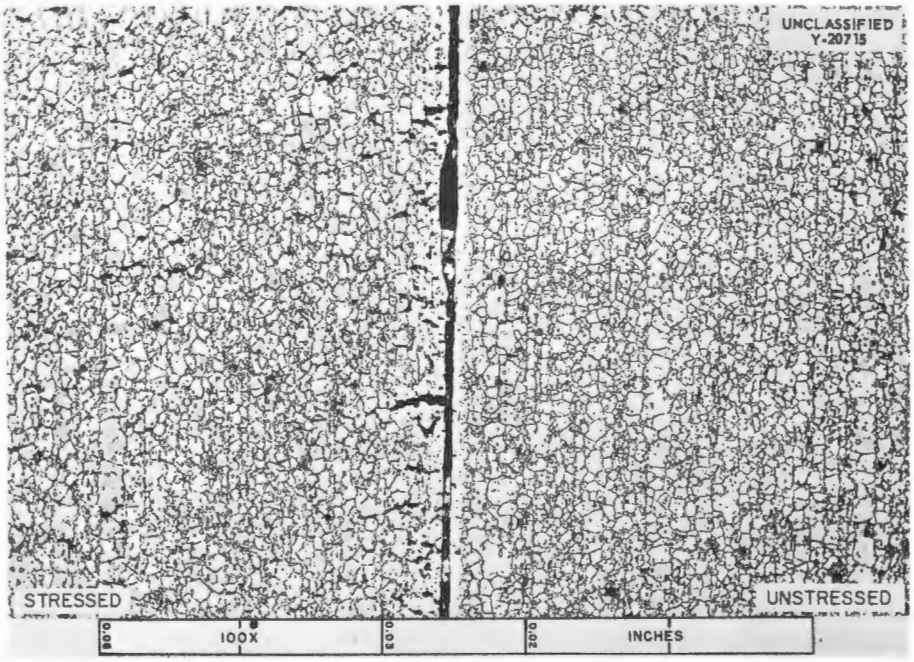

Fig. 3.5.18. Comparison of Stressed (8000 psi) and Unstressed Sections of a 20% Mo–7% Cr–2% Nb–1% Fe–0.8% Mn–0.12% C–Bal Ni Alloy Creep Tested in the Fuel Mixture (No. 107) NaF-KF-LiF-UF_4 (11.2-41-45.3-2.5 mole %) at 1500°F in the Annealed Condition. Specimen ruptured in 911 hr with 14% elongation. 100X. Reduced 24.5%. ~~(Secret with caption)~~

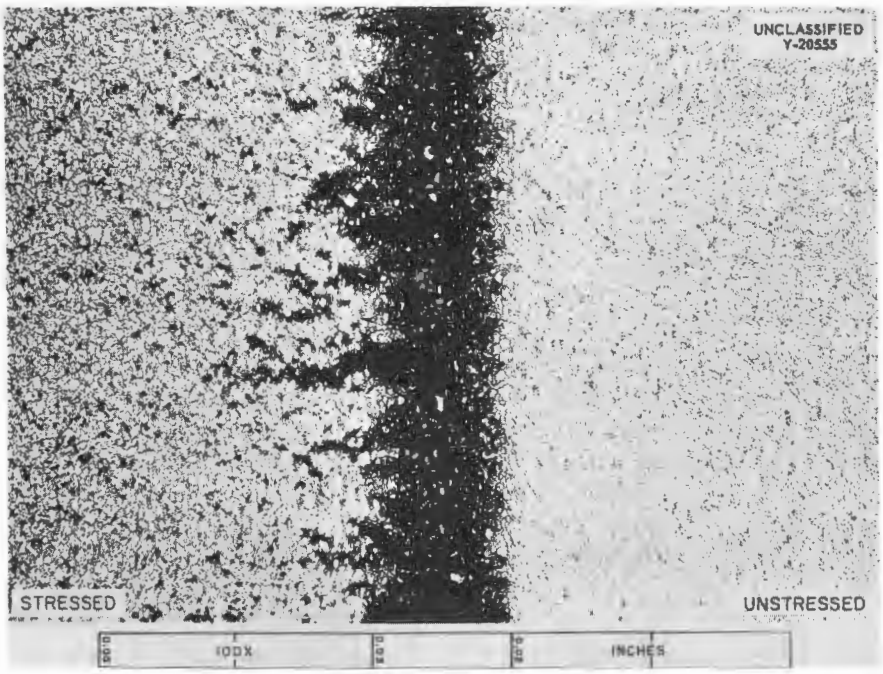

Fig. 3.5.19. Comparison of Stressed (8000 psi) and Unstressed Sections of a 20% Mo–7% Cr–2% Al–0.8% Mn–0.12% C–Bal Ni Alloy Creep Tested in the Fuel Mixture (No. 107) NaF-KF-LiF-UF_4 (11.2-41-45.3-2.5 mole %) at 1500°F in the Annealed Condition. Specimen ruptured in 697 hr with 35% elongation. 100X. Reduced 26%. [redacted]

3.6. CERAMICS RESEARCH

L. M. Doney

PRODUCTION OF METAL HYDRIDES

R. A. Potter

A system for the hydriding of yttrium and zirconium metals has been built and will be put into operation upon completion of the electrical installations now being made. Two hydriding furnaces and a gas purification train have been incorporated into the system to make possible the heating of 4 × 12 in. billets at temperatures of up to 2300°F in an atmosphere of purified hydrogen at constant pressures.

INVESTIGATIONS OF MODERATING MATERIALS

Beryllium Carbide

R. A. Potter A. J. Taylor

A small batch of Be_2C-SiC cermet was made for testing. There is a possibility that this material may be more oxidation resistant than Be_2C alone and may be more easily fabricated than either of the two carbides taken singly.

Beryllium Oxide

R. L. Hamner

A large hot-pressed block of BeO, 3.935 × 3.935 × 2.092 in., which was fabricated in Saclay, France, was received for sampling and testing. The block was found to have a bulk density of 98% of the theoretical density. Eight individual specimens selected throughout the block had densities ranging from 97.4 to 98.3% of theoretical. None of the specimens showed measurable porosity. The sonic modulus of elasticity for the material was found to be 52.073×10^6. The average modulus of rupture for specimens 0.116 × 0.501 × 2.00 in., tested with 1.5 in. between supports, was 42,527 psi. Values found for the coefficient of linear expansion at various temperatures are given below:

Temperature Range (°C)	Linear Expansion (in./in.·°C)
Perpendicular to Direction of Pressing	
100–400	0.77×10^{-5}
400–700	0.85×10^{-5}
700–1000	1.16×10^{-5}
1000–1200	1.21×10^{-5}
Parallel to Direction of Pressing	
100–400	0.78×10^{-5}
400–700	0.92×10^{-5}
700–1000	1.07×10^{-5}
1000–1200	1.21×10^{-5}

Four beryllium oxide specimens 1 in. in diameter and 1 in. in length and with a theoretical density of 95% were hot pressed for testing in the MTR. One additional specimen was fabricated for use as a control specimen.

PREPARATION OF RARE-EARTH-OXIDE CERMETS

C. E. Curtis L. M. Doney J. A. Griffin

Sufficient rings of 70% Ni–30% rare-earth oxide (Lindsay Code 921) were prepared for the Pratt & Whitney Aircraft high-temperature critical experiment. Research on the methods of compounding the nickel and rare-earth-oxide cermet has produced a means of achieving a high-density product.

Studies were initiated of methods for the fabrication of rare-earth-oxide hemispheres to be used for cross-section measurements.

PETROGRAPHIC AND X-RAY EXAMINATIONS

L. A. Harris T. N. McVay[1]
G. D. White

Fluoride Fuel Mixtures

Approximately 300 fluoride samples were examined, including samples from production batches, property measurement batches, and quenching studies. The bulk of the work was on quenched samples from the systems BeF_2-KF and BeF_2-RbF. These examinations were made in order to determine the composition and temperature ranges for the various phase regions of the system.

Optical Properties of Na_2O and K_2O

The refractive indices of K_2O and Na_2O were determined. Both these oxides are cubic and therefore isotropic, with $n = 1.688$ for Na_2O, and $n = 1.72$ for K_2O.

[1]Consultant.

3.7. NONDESTRUCTIVE TESTING AND INSPECTION OF MATERIALS AND COMPONENTS

R. B. Oliver A. Taboada

EDDY-CURRENT INSPECTION TECHNIQUES

J. W. Allen

It has been found that the encircling-coil eddy-current inspection equipment is of limited usefulness in the inspection of small-diameter tubing because the variations in the tubing influence the impedance of the testing coil. The only known method for separating the variations with reference to their nature and extent is that of employing an impedance-analysis[1] type of instrument which operates over a sufficient range of frequency to accommodate the required range of materials and sizes of tubing. Since the only available instruments of this type operate at fixed frequencies, a method is being developed to allow their operation over a wide range of frequencies. The obvious approach of "band-switching" and "ganging" variable components in the necessary large number of frequency- and phase-sensitive circuits has been rejected as being impractical.

An instrument has been conceived, however, and a developmental model has been built, which offers the advantages of both impedance analysis and variable frequency. This instrument consists basically of a cyclograph[2] type of circuit, which measures the a-c resistance of the testing coil, and a frequency discriminator, which measures the changes in the reactance of the testing coil as influenced by the tubing. The device exhibits the high sensitivity characteristic of the cyclograph, and it may be operated over a range of frequencies from about 15 to 600 kc/sec. Directly coupled signals are obtained from both the resistive and the reactive changes in the impedance of the coil, and thus the most difficult problem in obtaining a definitive eddy-current test for tubing is solved. The preliminary results obtained in test operation of the developmental model are very encouraging.

FLUORESCENT-PENETRANT INSPECTION TECHNIQUES

G. Tolson

An evaluation of the available penetrant inspection methods for the inspection of tubing has resulted in the replacement of dye-penetrant techniques with the postemulsification fluorescent-penetrant method known as Zyglo, which proved to be the most sensitive method tested for detecting small surface defects. Tests performed on defective tubes found during routine inspection indicated that this method had discovered all defects located by the dye-penetrant method and that it had located some flaws not found by using dye penetrant. An example of a defect and a small crack found by Zyglo inspection but not by any other method is shown in Fig. 3.7.1.

There are several additional advantages in the use of fluorescent-penetrant inspection. The method is less dependent on human variables, inherently more rapid, and more easily controllable than the dye-penetrant method, and the defects can be seen more easily because of the higher contrast. The disadvantages to this method are that it is difficult to differentiate actual defects from false indications and that it is possible to contaminate the material during the final stages of the test and thus introduce false indications. Shallow pit-type defects have not been found by this method. The equipment used in Zyglo inspection is shown in Figs. 3.7.2 and 3.7.3.

It is important in the use of this technique that the material be clean, that the time intervals for the various stages of operation be controlled, that

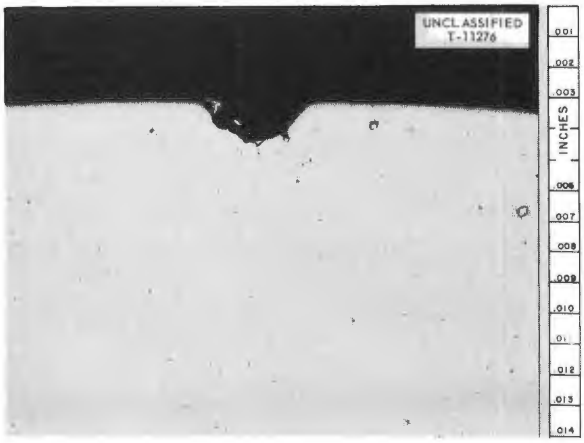

Fig. 3.7.1. Defect Detected by Fluorescent Penetrant but Not by Other Inspection Methods. 250X. Reduced 33%.

[1] R. B. Oliver *et al.*, *ANP Quar. Prog. Rep. Sept. 10, 1955*, ORNL-1947, p 136.

[2] J. W. Allen, *ANP Quar. Prog. Rep. June 10, 1956*, ORNL-2106, p 214.

Fig. 3.7.2. Equipment for Fluorescent-Penetrant Inspection of Tubing.

Fig. 3.7.3. Inspector Examining Tubing for Fluorescent-Penetrant Indications.

the intermediate washing operation be effective, and that the developer be kept free of contamination with fluorescent dye material. The time in the emulsifying bath appears to be the controlling factor in determining the sensitivity of the method. This time is held to a minimum of approximately 1 min. To minimize contamination, the powder developer is applied by enclosing the work in a chamber and blowing a cloud of powder about it. The technique for determining false indications involves inspecting the area under the indication, marking the area, and retesting the tube.

RADIOGRAPHIC TECHNIQUES FOR TUBING INSPECTION

A. Taboada G. Tolson

Radiographic techniques have been developed for the inspection of large quantities of tubing with a minimum of sacrifice in quality. Flaws of less than 2% of the wall thickness are located by these techniques. However, the ability to locate these defects is dependent on their general shape, orientation with respect to x-ray beam, and location in the tube. The latter two factors are minimized

by making three exposures of the same section of tubing, each exposure being 120 deg apart. This gives three views with different orientations at the same location on the tubes.

A group of tubes being prepared for radiographing is shown in Fig. 3.7.4. The conditions used for radiography are given below:

Tube voltage	120 kv
Tube current	6 ma
Tube-to-target distance	60 in.
Number of tubes per group	
For 0.187-in.-OD tubing	68
For 0.229-in.-OD tubing	54
Film density	2.6
Exposure time	2 min 15 sec
Filter at film	0.025 in. of Al
Intensifying screen	0.005 in. of lead
Backup screen	0.010 in. of lead
Machine	Norelco "150"
Film	Type M

Interpretation of the x-ray film and location of the defect are extremely tedious but very critical operations. To facilitate the interpretation and to eliminate errors, three views of each section of tubing are compared and the defects are matched. A typical flaw found by radiography is shown in Fig. 3.7.5.

Experimental work on the radiography of pipe weldments is being done in an attempt to minimize the number of exposures necessary for complete inspection and to improve the ability to locate defect positions. The weldments are being projected at an angle with the axis of the pipe. The optimum angle of projection, the number of exposures required, and the types of defects located are being investigated.

TUBING DEFECT ANALYSIS

G. Tolson

An attempt is being made to correlate the types of defects being found in tubing with the methods used to find them. Although the categories of defects listed below are not clear-cut or all-inclusive, most defects found to date may be included in them. Sizes of defects are still being investigated.

Cracks. – Cracks and scratches are usually detected by ultrasonic and eddy-current methods. When on the outer surface, they are most readily detected by penetrant inspection. This type of defect is not located by radiography if its orientation is wrong or if its width is small.

Pits. – Pits are usually detected by visual inspection. When accompanied by small cracks, the pits are found with penetrants (see Fig. 3.7.1). Ultrasonic and eddy-current inspections do not normally locate pits. Radiography will reveal the larger sized pits.

Gouges. – Wide, elongated defects with shallow, irregular bottoms, which are normally on the inside surface of a tube, as shown in Fig. 3.7.6, are usually found by radiography. Unless gouges have some sharp discontinuity, ultrasonic and eddy-current methods are not effective in their detection.

Handling Marks, Dents, and Laps. – These defects are most easily found by visual inspection or with penetrant, if any depth exists. Examples of these defects are shown in Fig. 3.7.7.

MATERIALS INSPECTION

Materials for ETU, ART, and test components are inspected for acceptability on the basis of their intended use. Efforts are made to repair and salvage defective material and to use rejected material for less critical application than originally intended. As reported above, developmental work has continued on penetrant and ultrasonic techniques in an effort to increase the reliability of inspection. Tubing and pipe inspection methods have been standardized, but developmental work on plate and sheet inspection methods has not yet been completed. Statistics on the inspection work accomplished during the quarter are presented in Table 3.7.1.

Tubing

J. W. Allen R. W. McClung
G. Tolson

The operations described in Table 3.7.2 are involved in the inspection of tubing for heat exchangers and radiators. Attempts are being made to improve automatic inspection methods in order to eliminate the less precise techniques, but at present all the methods listed must be used to ensure the necessary quality.

Inspection during the quarter of 5349 pieces of 0.187-in.-OD, 0.025-in.-wall, 42-in.-long CX-900

Fig. 3.7.4. Group of Tubes in Position for Radiography.

Fig. 3.7.5. Photomicrograph of Typical Tubing Flaw Detected by Radiography. 250X. Reduced 32%.

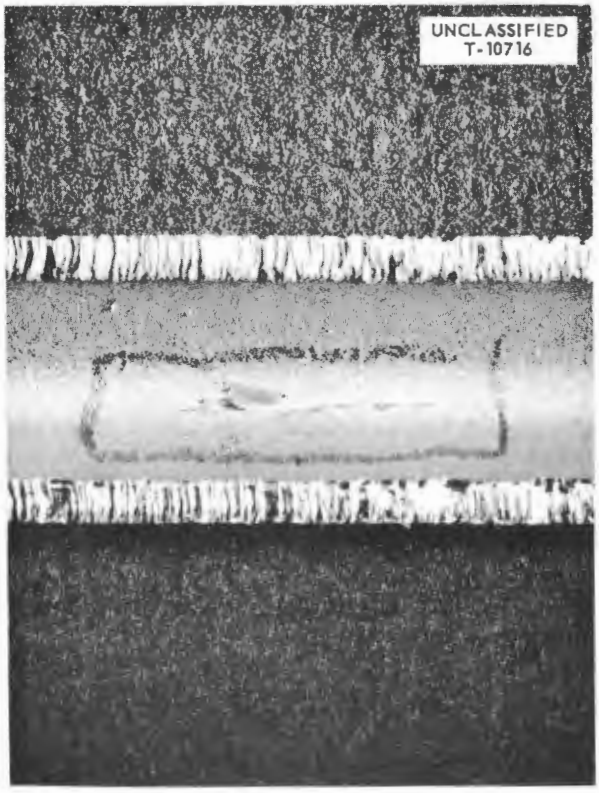

Fig. 3.7.6. Wide, Shallow, Gouge-Type Defect on Inner Surface of Tubing. This defect was detected by radiography. 8X. Reduced 7.5%.

Fig. 3.7.7. Handling Marks Detected by Visual Inspection. 6X. Reduced 32%.

Inconel tubing by the pulse-echo immersed-ultrasonic method resulted in the rejection of 119 lengths. Each of these pieces was rejected because of single, short defects. The encircling-coil, eddy-current inspection of 5574 pieces resulted in the rejection of 962 lengths, including 835 pieces rejected on the basis of slight dimensional variations. Of the remaining 127 pieces, 77 were rejected because of defect indications, 41 because of foreign metal pickup, and 9 because they were mashed or bent when received. By exercising a waiver of ±0.001 in. on the outside diameter tolerance, 781 of the rejected pieces will be acceptable. A crack approximately $\frac{1}{32}$ in. long and 0.015 in. deep that was detected in this lot of tubing by both ultrasound and eddy-current methods is shown in Fig. 3.7.8. A representative section of a smaller crack, about 0.006 in. in depth, is shown in Fig. 3.7.9, and Fig. 3.7.10 shows a scratch or gouge approximately 0.001 in. in depth that is typical of the defects found in many of the ultrasound rejects.

The immersed-ultrasonic method was also used for the inspection of 1559 pieces of 78-in.-long, 0.229-in.-OD, 0.025-in.-wall, CX-900 Inconel tubing. A length of tubing was considered rejectable if it contained a single detectable defect. A prevalent cause for rejection in this tubing seemed to be surface scratching, and repolishing of the outer surface resulted in salvaging about 70% of the ultrasound rejects. Subsequent eddy-current inspection of this tubing resulted in the

TABLE 3.7.1. MATERIALS INSPECTION SUMMARY

Item	Description	Quantity	Method of Inspection	Rejection Rate (%)	Remarks
Tubing	CX-900A Inconel; 0.187-in.-OD, 0.025-in.-wall thickness	13,194 ft	Visual, penetrant, radiographic, ultrasonic, and eddy current	16.5	2500 ft of this tubing, which was the initial order, was rejected because of improper processing and was downgraded for use in test radiators
	CX-900A Inconel; 0.229-in.-OD, 0.025-in.-wall thickness	9,847 ft	Visual, penetrant, radiographic, ultrasonic, and eddy current		Final visual inspection is not yet complete, but the onticipated rejection rate is approximately 15%
	Inconel; random sizes	653 ft	Visual penetrant, radiographic	50	220 ft of this tubing had no identification as to chemical or physical properties and was downgraded for noncritical use; the maximum allowable defect depth for this tubing was 5% of the wall thickness
Pipe	Inconel; random sizes	731 ft	Visual, penetrant, ultrasonic, and eddy current	33	175 ft of the rejected material was defective because of outside surface imperfections; the rejected material is being centerless ground to remove these defects and will be reinspected
	CX-900A Inconel; random sizes	686 ft	Visual, penetrant, ultrasonic, and eddy current	0	
	Hastelloy B; various sizes	1,620 ft	Visual, penetrant, ultrasonic, and eddy current	100	Both the seam welds and the parent material contained numerous flaws, but because of the scarcity of this material some of the least defective areas and some areas that could be repaired were used
Plate and sheet	Inconel; random thicknesses	1,713 ft^2	Visual, penetrant, ultrasonic, and eddy current	10	Defects were observed only in sections of plates; the defective areas were identified, but not removed, so that the fabricator could select areas around defects for use
	CX-900A Inconel; various thicknesses	325 ft^2	Visual, penetrant, ultrasonic, and eddy current	<1	
Rod and bar	Incanel; random sizes	473 ft	Visual, penetrant, ultrasonic, and eddy current	2	
	CX-900A Inconel; random sizes	27 ft	Visual, penetrant, ultrasonic, and eddy current	0	
Fittings	Inconel	104	Visual, penetrant	0	

TABLE 3.7.2. METHODS USED FOR INSPECTING TUBING FOR RADIATORS AND HEAT EXCHANGERS

Operation	Type and Amount	Purpose
Receiving inspection	Visual check of surfaces of all tubes; 5% of lot checked with the Boroscope	Check for outside surface flaws, oxidation, and miscellaneous defects
Metallographic examination	Metallographic samples taken of each lot	Check for grain size, inclusion, micro conditions, etc.
Chemical analysis	One sample taken of each heat	Verification of chemical compositions
Eddy-current test	100% inspection of each entire tube	Wall thickness test and gross flaw detection
Ultrasonic test	100% inspection of entire tube back and forth	Check for wall and inner surface flaws
Fluorescent-penetrant test	100% inspection of each tube	Detection of external surface imperfections and cracks
Radiography	100% inspection of three views (120 deg apart) of each tube	Detection of wall and inner surface flaws
Final visual inspection	100% visual check of each tube under bright light	Check for tubes damaged in handling during inspection

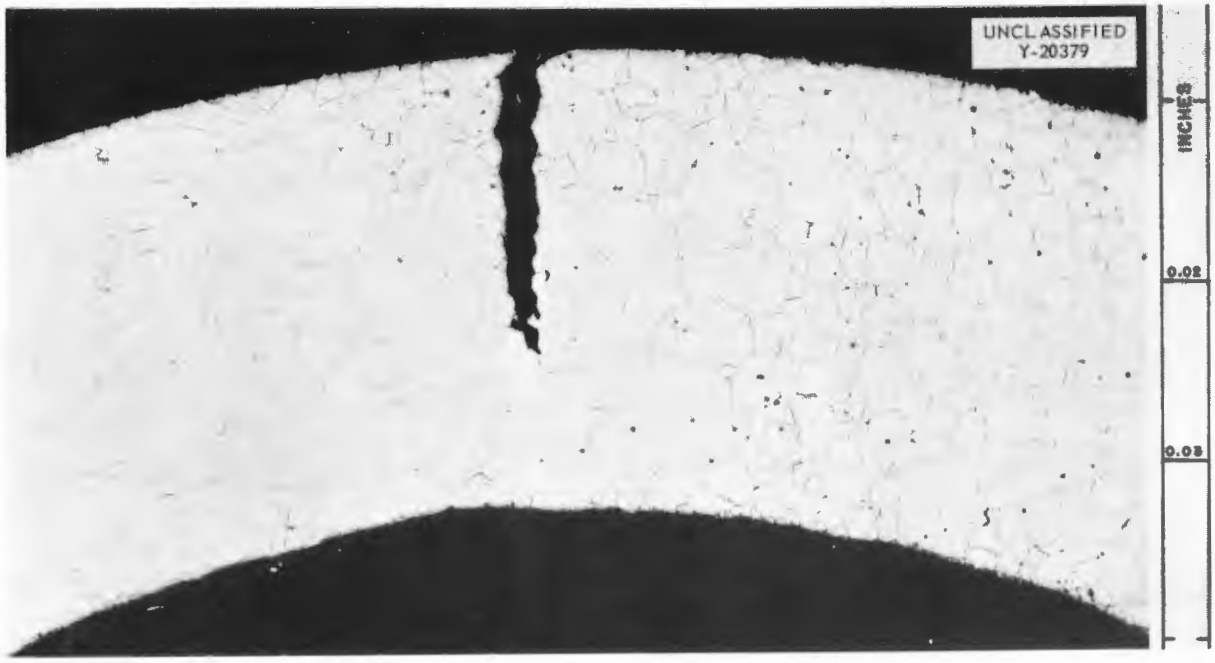

Fig. 3.7.8. A 0.187-in.-OD, 0.025-in.-Wall, CX-900 Inconel Tube Showing a $\frac{1}{32}$-in.-Long, 0.015-in.-Deep Crack Found by Ultrasound and Eddy-Current Inspection. 100X. Reduced 3.5%.

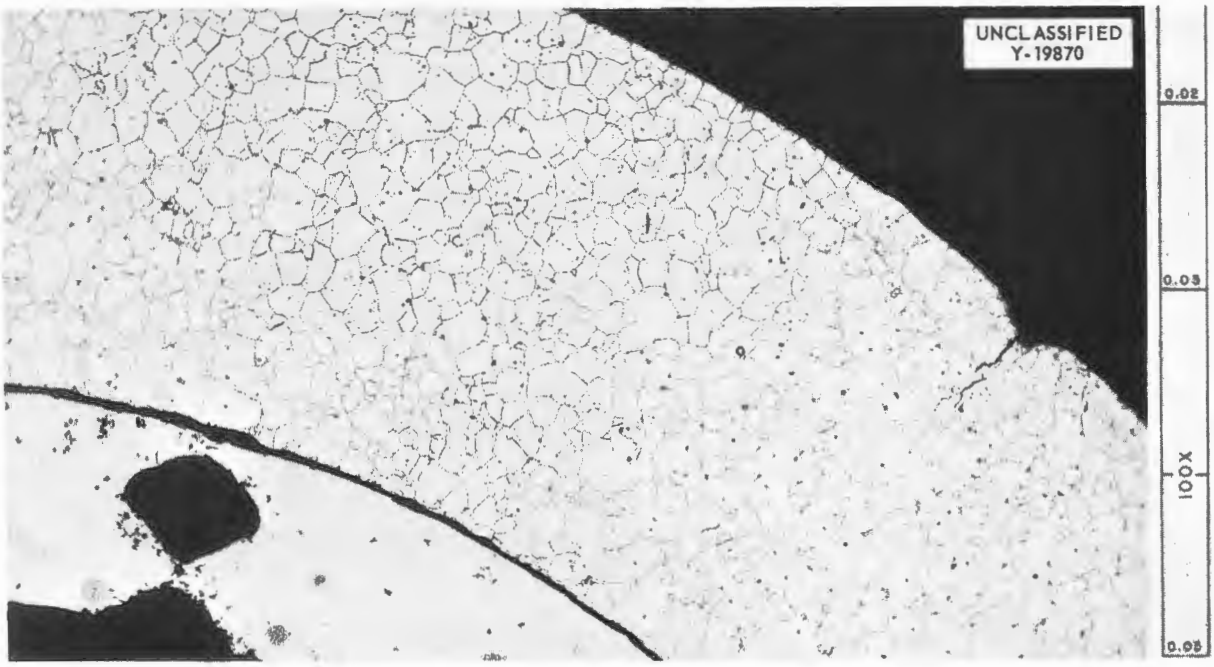

Fig. 3.7.9. A 0.187-in.-OD, 0.025-in.-Wall, CX-900 Inconel Tube Showing a Crack Approximately 0.006-in. Deep Found by Ultrasound and Eddy-Current Inspection. 100X. Reduced 1%.

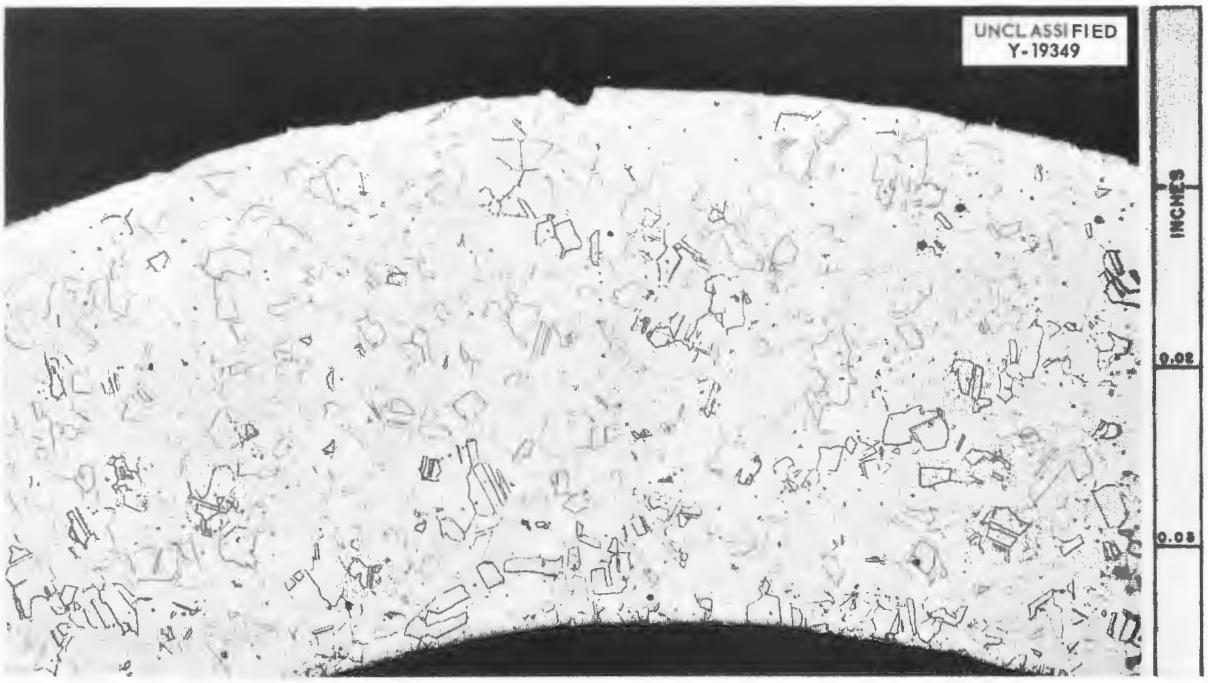

Fig. 3.7.10. Scratch Approximately 0.001 in. Deep Found by Ultrasound Inspection on Outer Surface of 0.187-in.-OD, 0.025-in.-Wall, CX-900 Inconel Tubing. 100X. Reduced 3%.

rejection of 201 lengths because of dimensional variations, but exercising the waiver of ±0.001 in. on the outside diameter tolerance again resulted in the salvaging of most of the pieces. Examples of the defects found in this tubing are shown in Figs. 3.7.11 and 3.7.12.

One lot of 1000 ft of $\frac{3}{8}$-in.-OD, 0.035-in. wall Hastelloy B tubing was completely rejected because of the presence of many cracks that were detected both by eddy-current and ultrasonic inspection. Typical clusters of small cracks that are 0.003 to 0.006 in. deep are shown in Fig. 3.7.13. One of several larger cracks that were found is shown in Fig. 3.7.14. Some of these large cracks were as much as 0.028 in. in depth; that is, they extended through 80% of the total wall thickness.

Some $\frac{1}{4}$-in.-OD, 0.035-in.-wall Hastelloy B tubing was also inspected, and typical defective areas located by ultrasound are shown in Figs. 3.7.15 and 3.7.16. The small cracks shown on the outer surface are 0.002 and 0.001 in. deep, respectively, and they are approximately $\frac{1}{4}$ in. in length.

Pipe

J. K. White

Examples of defects discovered by ultrasound inspection of Inconel pipe are shown in Figs. 3.7.17 and 3.7.18. As a result of the fabricating operations, most of the defects are longitudinal. Therefore the inspection technique that is most sensitive to longitudinal defects is being used along with a reference standard which simulates longitudinal defects.

Some progress has been made in machining reference standards. In the past it has been difficult to avoid whip in the shaping tool used to cut standard notches, particularly when cutting grooves on the inner surface of small-diameter pipe. For this reason the depth of inner surface notches has been uncertain in pipe of $\frac{3}{4}$-in. IPS or smaller. A new technique was devised which involves cutting circumferential rings at either end of the position chosen for the notch and to the same depth. The notch cutting operation can then proceed with relief of the tool at each end of the stroke.

A 1 × $\frac{1}{2}$ in. rectangular lithium sulfate transducer is now being used for pipe inspection. This larger transducer allows for a faster scanning operation than was possible with the $\frac{3}{4}$-in.-dia transducer.

Plate

R. W. McClung

Several lots of Inconel plate have been inspected by the pulse-echo immersed-ultrasonic method. Since laminar defects were expected, the reference standard used was a $\frac{1}{16}$-in.-dia, flat-bottom hole drilled in Inconel plate of the same thickness as the plate being inspected. Defect signals, if any, were then compared with the signal obtained from the flat bottom of the hole. In all the plate inspected to date no defect indications have been as large as those produced by the reference-standard hole.

Difficulties have been encountered in the inspection of thin plate because of excess surface roughness, warping, and twisting of the plates and because the opposite faces of the plates are not parallel. These factors all combine to scatter or refract the incident ultrasonic beam and thus reduce the sensitivity of such an inspection. The time required for continuous angular adjustment of the incident beam to maintain perpendicularity and thus offset the conditions described retarded the inspection rate considerably. Double inspection, once for each side, increased the confidence level of the inspection.

The plate was scanned at a linear rate of about 10 fpm, with successive scans being indexed $\frac{1}{8}$ in. from the previous scan. On plate $\frac{1}{2}$ in. thick and thinner, no alarm circuits could be used because of the excessive width of the existing electronic gates. However, on thicker plates, visual and audible alarm circuits were an aid to identification and interpretation of defect signals.

In all the plate inspected the only ultrasonic variation noted was an increase per unit thickness in ultrasonic attenuation, or sound loss, with increased plate thickness. Also there seemed to be changes in the attenuation characteristic along the length of many of the plates.

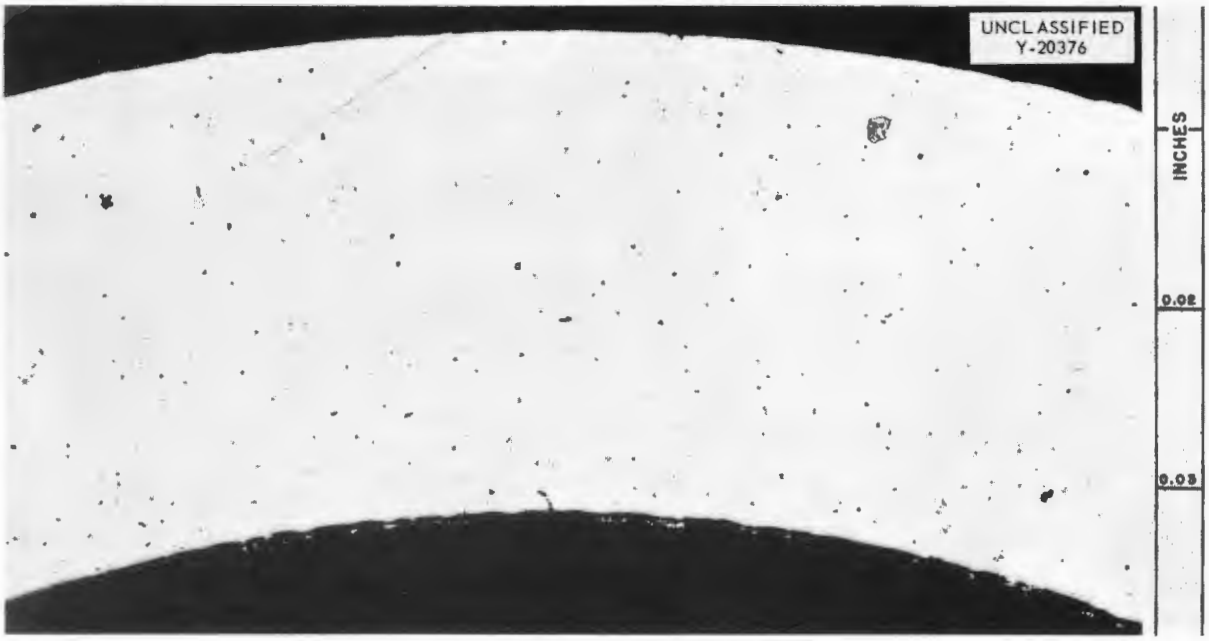

Fig. 3.7.11. A 0.229-in.-OD, 0.025-in.-Wall, CX-900 Inconel Tube Showing a Crack About 0.002 in. Deep on the Inner Surface That Was Found by Ultrasound Inspection. 100X. Reduced 4%.

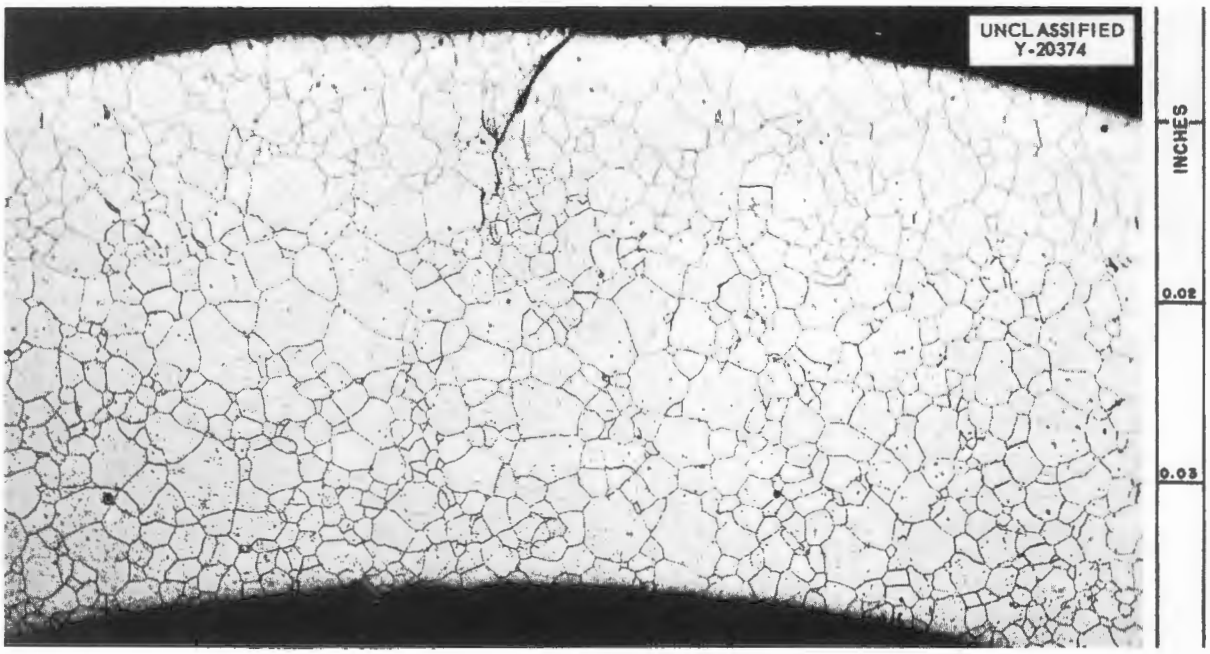

Fig. 3.7.12. A 0.229-in.-OD, 0.025-in.-Wall, CX-900 Inconel Tube Showing a Crack About 0.010 in. Deep on the Outer Surface That Was Found by Ultrasound Inspection. 100X. Reduced 3%.

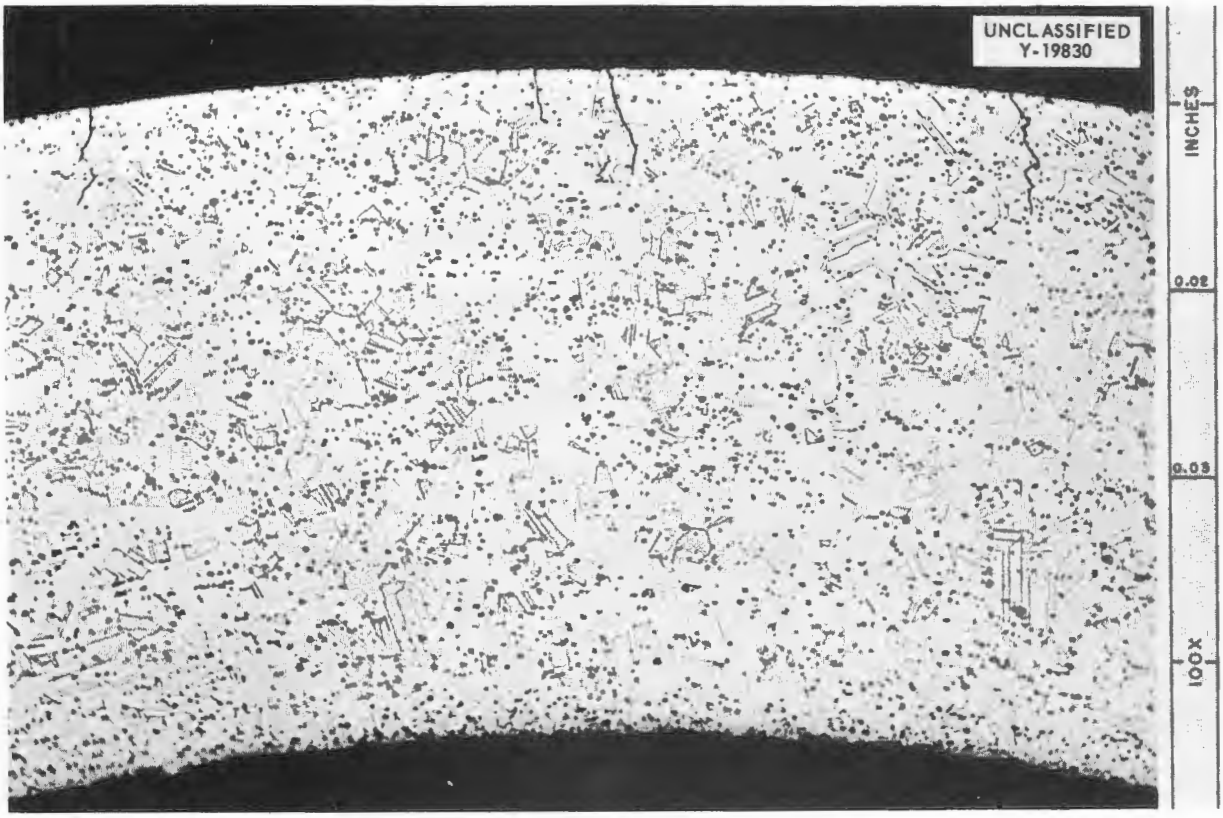

Fig. 3.7.13. A $^3/_8$-in.-OD, 0.035-in.-Wall, Hastelloy B Tube Showing Cracks from 0.003 to 0.006 in. Deep on the Outer Surface. 100X. Reduced 2%.

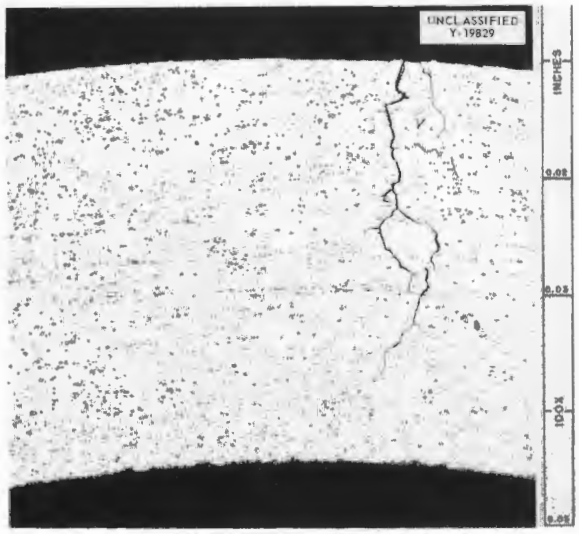

Fig. 3.7.14. A $^3/_8$-in.-OD, 0.035-in.-Wall, Hastelloy B Tube Showing a Crack About 0.027 in. Deep. 100X. Reduced 38%.

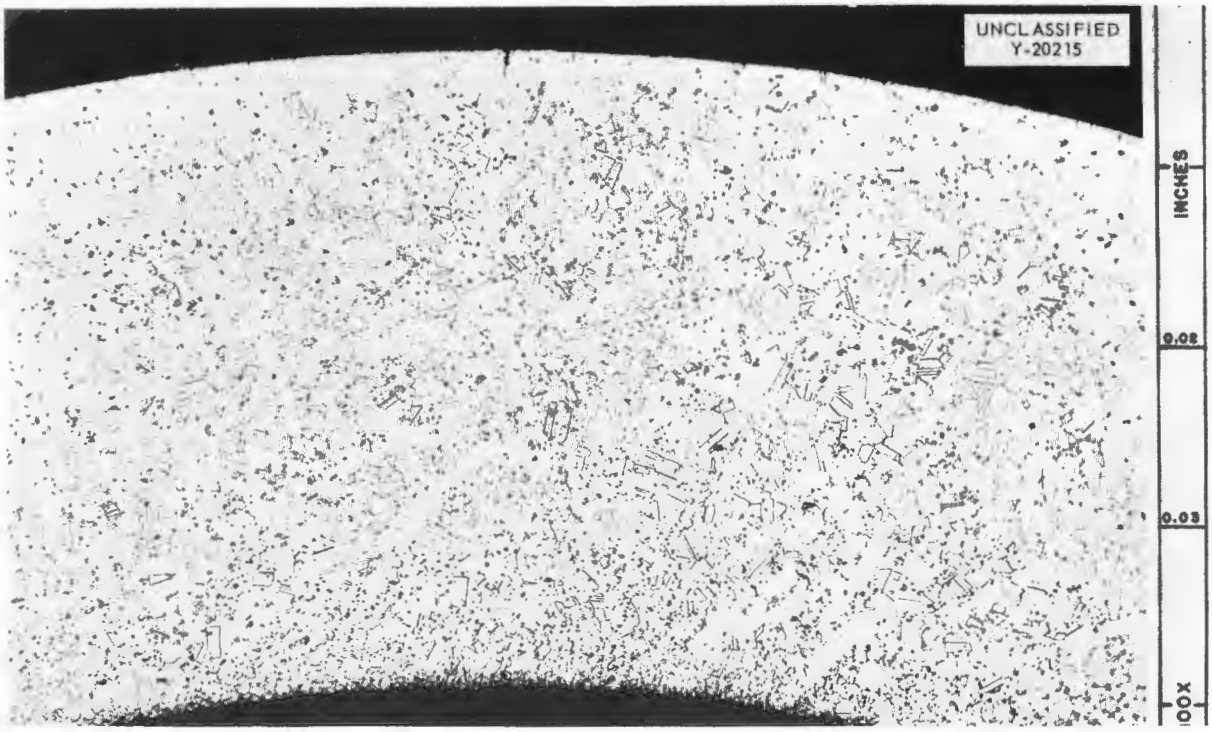

Fig. 3.7.15. A ¼-in.-OD, 0.035-in.-Wall, Hastelloy B Seamless Tube Showing a Crack About 0.002 in. Deep on the Outer Surface. 100X. Reduced 4%.

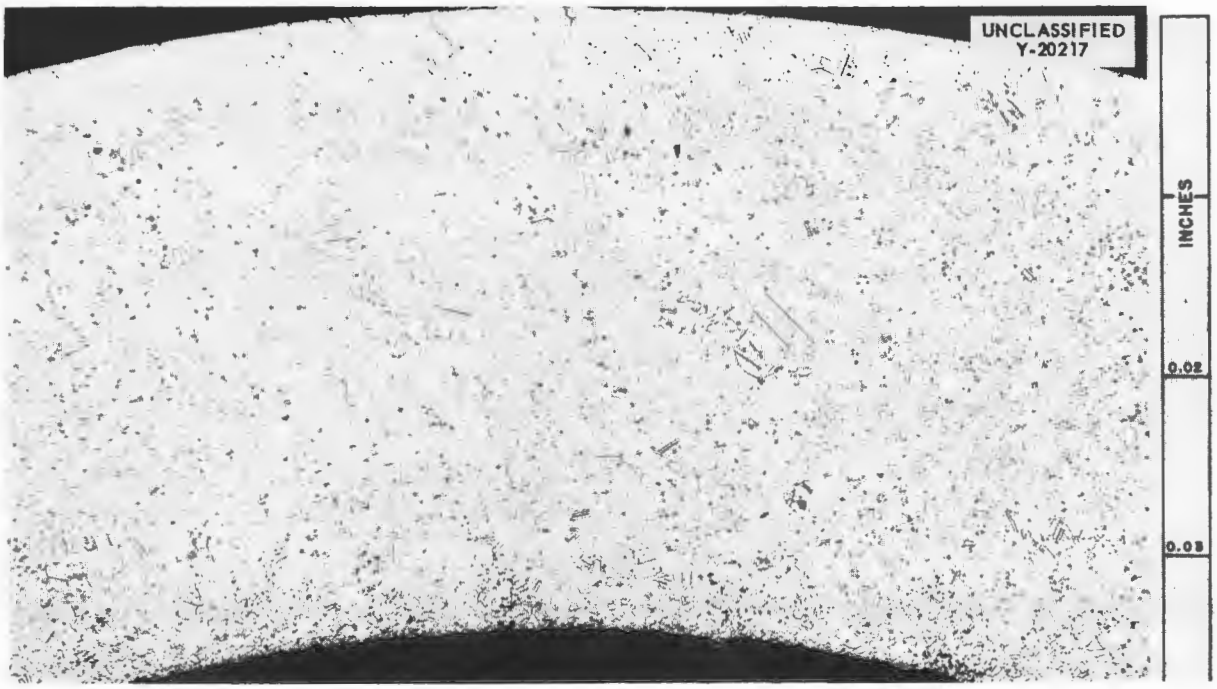

Fig. 3.7.16. A ¼-in.-OD, 0.035-in.-Wall, Hastelloy B Seamless Tube Showing a Crack About 0.001 in. Deep on the Outer Surface. 100X. Reduced 4%.

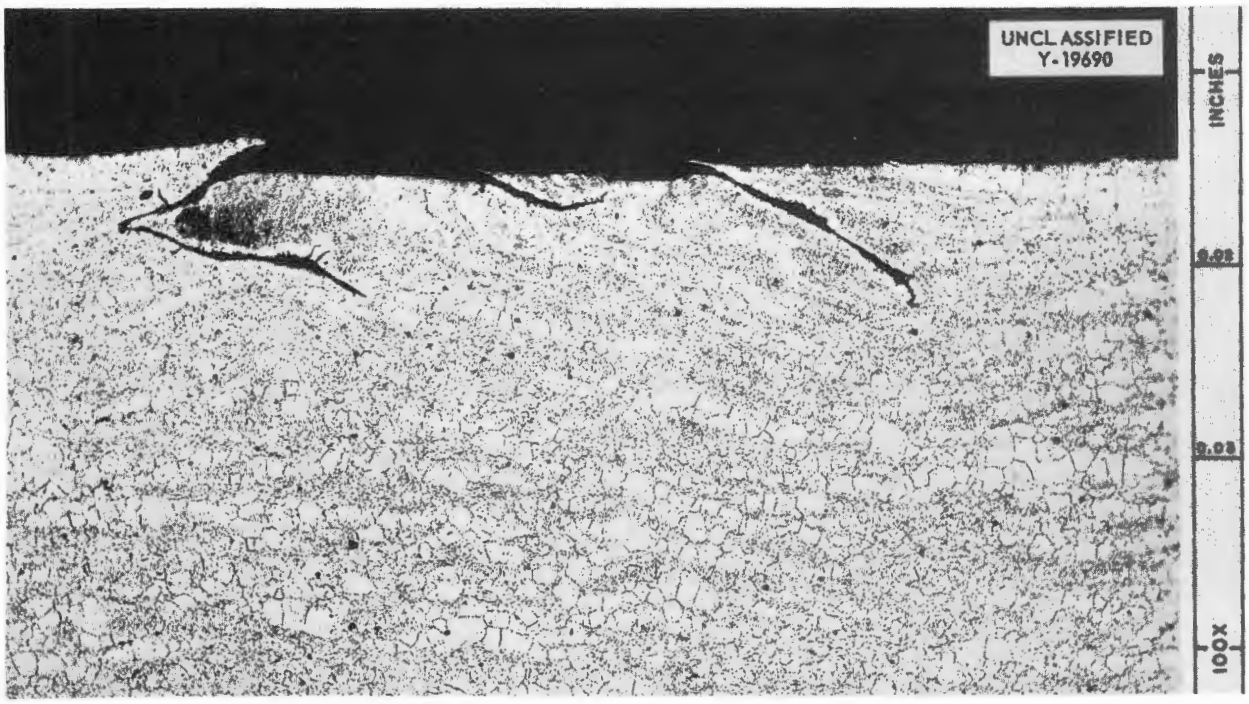

Fig. 3.7.17. Seamlike Fold Found by Immersed-Ultrasonic Inspection of $\frac{3}{4}$-in.-IPS Sched-40 CX-900 Inconel Pipe. 100X.

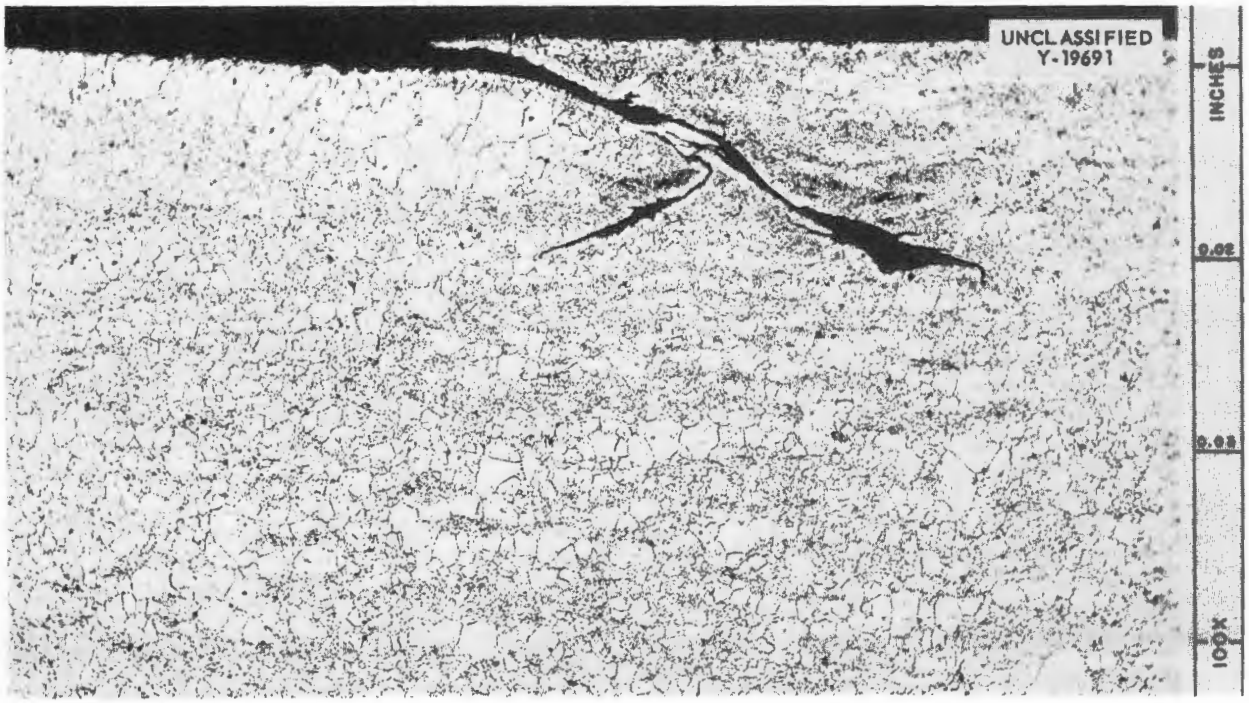

Fig. 3.7.18. Another Section of the Pipe Shown in Fig. 3.7.17. The defect extends through approximately 12% of the wall, approximately 20% of the circumference, and the entire 20-ft length. 100X.

Part 4

HEAT TRANSFER AND PHYSICAL PROPERTIES

H. F. Poppendiek

RADIATION DAMAGE

G. W. Keilholtz

FUEL RECOVERY AND REPROCESSING

R. B. Lindauer

4.1. HEAT TRANSFER AND PHYSICAL PROPERTIES

H. F. Poppendiek

ART FUEL-TO-NaK HEAT EXCHANGER

J. L. Wantland S. I. Cohen

The fluid friction characteristics on the fuel side of a full-scale mockup[1] simulating the present configuration of the 260-tube ART fuel-to-NaK heat exchanger were obtained between Reynolds numbers of 1000 and 8000. The data, shown in Fig. 4.1.1, were taken across a section having a length-to-hydraulic-diameter ratio of 586. The upstream pressure tap was 250 hydraulic diameters downstream of the entrance to the tube bundle. The friction characteristics determined fall 9% below those obtained from a 100-tube bundle with a similar spacing configuration.[2]

Experimental heat transfer and fluid friction characteristics were also obtained for a delta-array heat exchanger designed to have the same number of tubes, hydraulic diameter, and spacer density as the square-array heat exchanger studied previously.[3] The heat-transfer and fluid friction characteristics are given in Figs. 4.1.2 and 4.1.3, respectively, which also compare the data for the delta-array heat exchanger with those of the square-array heat exchanger. The over-all performance of the delta-array heat exchanger is superior to that of the square-array heat exchanger in the transition region. For example, at a Reynolds modulus of 4000, the fluid friction factor of the delta array is 16% lower than that of the square array, while the heat transfer parameter is 7% higher than that of the square array.

[1] S. I. Cohen and J. L. Wantland, *ANP Quar. Prog. Rep. June 10, 1956*, ORNL-2106, p 219.

[2] J. L. Wantland, *Transverse Pressure Difference Across Staggered and Inclined Spacers in the ART Fuel-to-NaK Heat Exchanger*, ORNL CF-56-6-143 (June 1956).

[3] J. L. Wantland, *Thermal Characteristics of the ART Fuel-to-NaK Heat Exchanger*, ORNL CF-55-12-120 (Dec. 22, 1955).

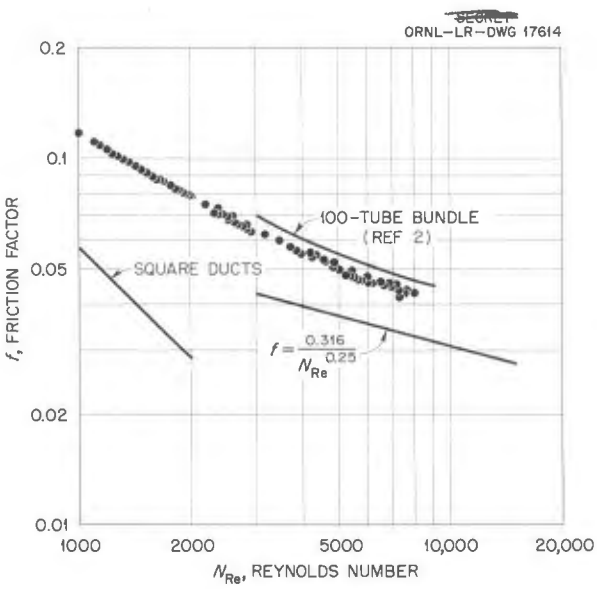

Fig. 4.1.1. Fluid Friction Characteristics on the Fuel Side of a 260-Tube Full-Scale Mockup of the ART Fuel-to-NaK Heat Exchanger.

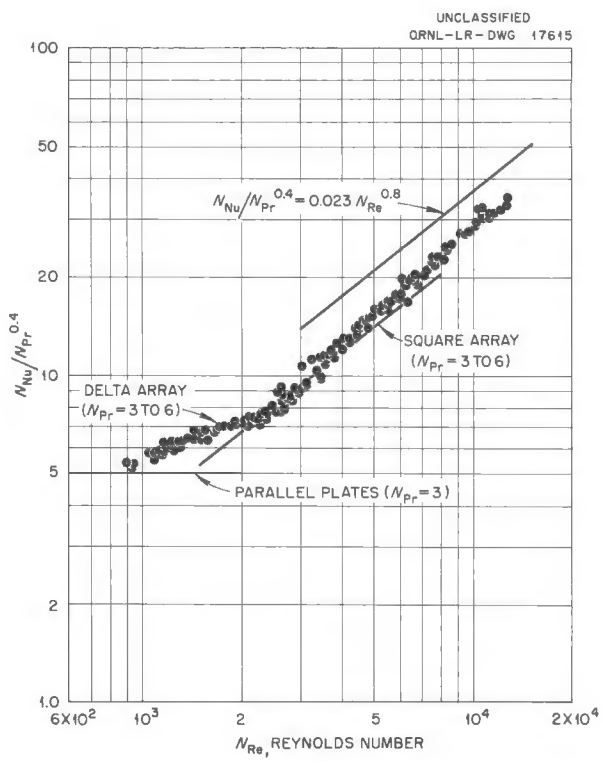

Fig. 4.1.2. Heat Transfer Characteristics of the Delta-Array Heat Exchanger.

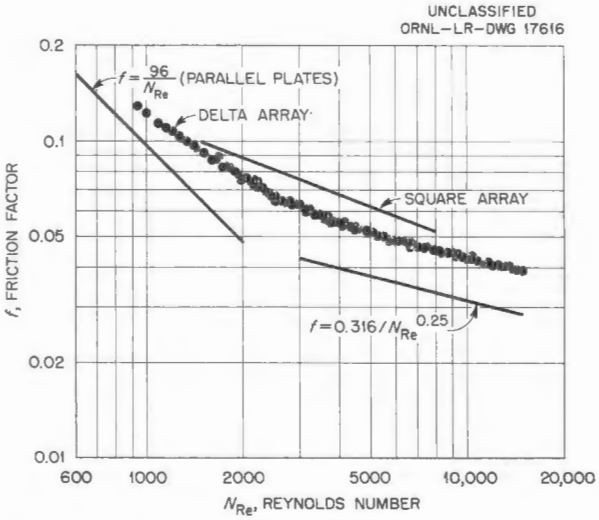

Fig. 4.1.3. Fluid Friction Characteristics of the Delta-Array Heat Exchanger.

ART HYDRODYNAMICS

L. D. Palmer F. E. Lynch
G. L. Muller[4]

Core Hydrodynamics

Additional research was conducted on fluid flow stabilization in fuel channels of circulating-fuel reactor cores through the use of screen packings. It was found that for a cylindrical annular core, such as that shown in Fig. 4.1.4, six 20 × 20 mesh, 0.0108-in.-wire-dia screens were needed in the divergent part of the channel to eliminate separation. However, separation occurred on the outer shell just before the sharp exit area contraction resulting from the sharp curvature of the flow channel. Removing the sharp curvature would probably eliminate the

[4]On assignment from Pratt & Whitney Aircraft.

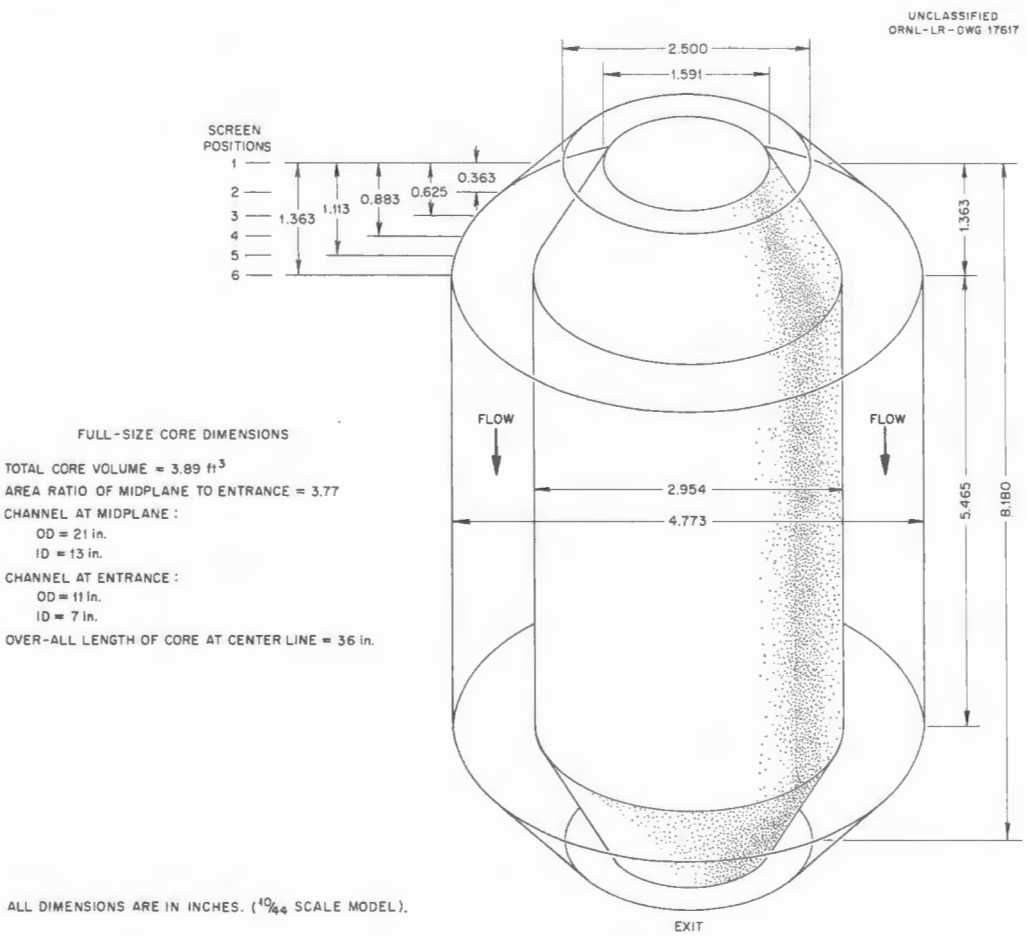

Fig. 4.1.4. Abrupt-Expansion, Straight, Annular Flow Channel of a 21-in.-dia Core.

separation. The qualitative velocity distributions in a cross section of the flow channel illustrated in Fig. 4.1.4, as determined by the phosphorescent-particle flow-visualization technique, are shown in Fig. 4.1.5. Also shown is the separation region, which was determined from observation of the motion of particles in the water flowing through the core under a strong light. The friction loss coefficient of this core was found to be about 57 at a mid-plane Reynolds number of 50,000.

Instantaneous Velocity-Profile Measurements

The phosphorescent-particle technique, which was used previously to observe instantaneous fluid flow phenomena in transparent ducts, has been converted to a quantitative method. The velocity profiles can now be recorded photographically. Optical distortion resulting from the transparent duct walls is accounted for by a photograph of a grid scale located within the duct being made prior to the velocity study and then being superimposed on the velocity photographs. An example of this technique is given in Fig. 4.1.6, which shows a velocity profile within a glass model of an in-pile loop helix (N_{Re} = 20,000). Another illustration is given in Fig. 4.1.7, in which the laminar-flow velocity

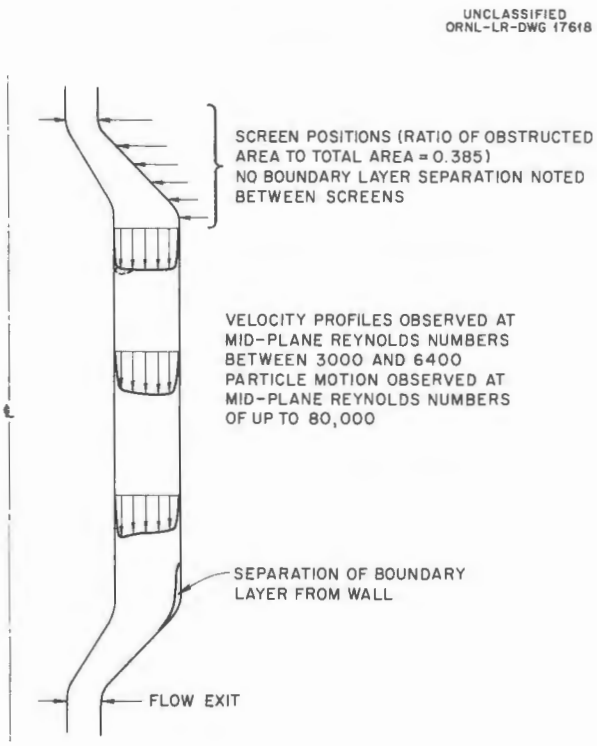

Fig. 4.1.5. Flow Features of Core Shown in Fig. 4.1.4.

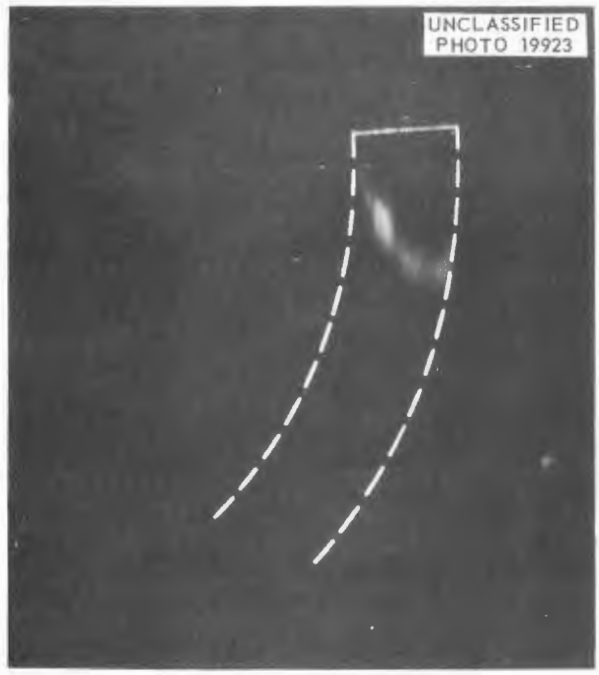

Fig. 4.1.6. Photograph of Instantaneous Velocity Profile Within a Glass Model of an In-Pile Loop Helix (N_{Re} = 20,000).

Fig. 4.1.7. Photograph of the Velocity Profile in a Circular Pipe Under Laminar-Flow Conditions.

profile in a circular pipe is shown. This new technique of determining quantitative, instantaneous velocity profiles should be very useful in characterizing both mean and transient flow phenomena in reactor fluid systems.

HEAT TRANSFER IN REFLECTOR-MODERATED REACTOR CORES

H. F. Poppendiek
N. D. Greene L. D. Palmer

ART Core

A mathematical analysis of the temperature structure within the fuel, Inconel core shells, and sodium coolant streams of an idealized ART core was carried out for the swirl entrance condition. A similar analysis was made previously for the straight-through flow case. A variable-gap channel representing the spiraling annular passage through which the fuel will flow in the actual ART was divided into a series of channels with parallel walls having different spacing. The heat transfer analyses of these individual channels were then performed as described previously.[5]

The analytical temperature increments between the uncooled-wall temperature and the mixed-mean fluid temperature, ΔT_{vhs}, were used in the study; these values fell between the corresponding experimental temperature increments for the inner and outer core walls. This simplification does not greatly influence the temperature structure because of compensating Nusselt number and ΔT_{vhs} relations. The latest volume-heat-source data for the core shells and the beryllium reflector were used in the study. It was presumed that the flow distributions in the sodium annuli were uniform; any nonuniform flow distribution in a cooling annulus would be directly reflected in the temperature structure in the form of hot and cold spots.

The calculated fuel, wall, and sodium temperature distributions within the ART core are plotted in Fig. 4.1.8. The sodium flow rates and cooling requirements used in the variable-gap-channel

[5]H. F. Poppendiek and L. D. Palmer, *Application of Temperature Solutions for Forced-Convection Systems with Volume Heat Sources to General Convection Problems*, ORNL-1933 (Sept. 29, 1955).

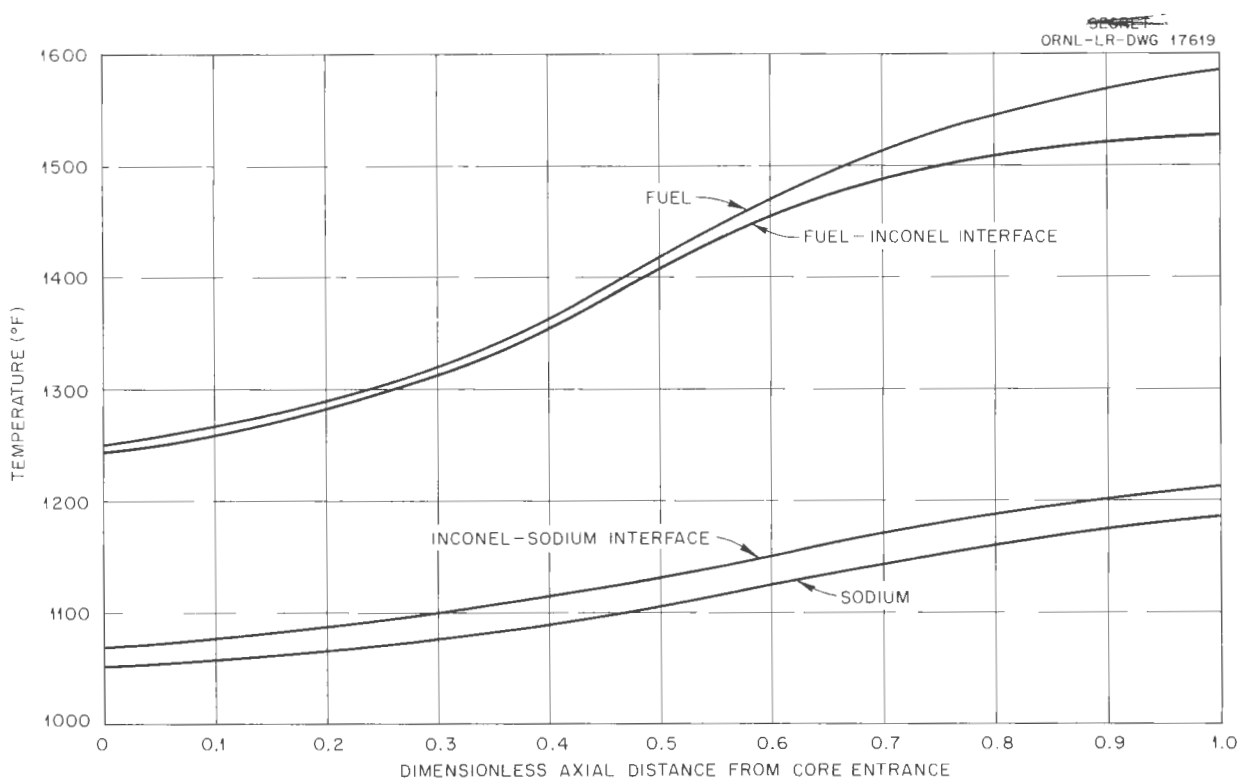

Fig. 4.1.8. Temperature Structure in Idealized ART Core with Swirl Entrance Conditions.

analysis pertained to a passage having identical wall areas from which heat was transferred to the coolant streams. Since in the actual ART annulus system the inner and outer wall areas will not be identical, the results of the variable-gap-channel analysis were apportioned to account for the ART outer wall area being somewhat larger than the inner wall area. The adjusted flow rates and cooling requirements were as follows:

Flow rate in inner sodium annulus	0.071×10^6 lb/hr
Flow rate in outer sodium annulus	0.133×10^6 lb/hr
Total cooling power required by sodium stream in inner annulus	0.89 Mw
Total cooling power required by sodium stream in outer annulus	1.65 Mw
Total cooling power required by both sodium streams	2.54 Mw

A New Reflector-Moderated Reactor Core

New reflector-moderated reactor core configurations have been studied in an effort to develop a core whose fuel temperature distribution is uniform with respect to radius. Under these circumstances the hot spot and thermal cycling problems would be mitigated, and a maximum thermodynamic efficiency based on some maximum metal interface temperature could be achieved. In the case of a simple reactor core with established flow and no wall heat transfer, a uniform radial temperature distribution can be obtained by generating an axial velocity profile having the same shape as the volume-heat-source profile. If the fuel were also cooling the surrounding moderator, the velocity distribution would have to be overcompensated somewhat to take care of the wall heat transfer. This elementary reasoning was used to design the vortex flow tube shown in Fig. 4.1.9. A unique vane system was developed which, when located at the entrance of a circular tube, generated a stable vortex throughout its whole length. The axial velocity distributions in the vortex flow tube are similar to the radial volume-heat-source distributions in cylindrical reflector-moderated reactor core systems; specifically, the axial fluid velocities near the pipe wall are higher than those near the pipe center.

The radial fuel temperature profiles of two simple cylindrical reactor cores are compared in

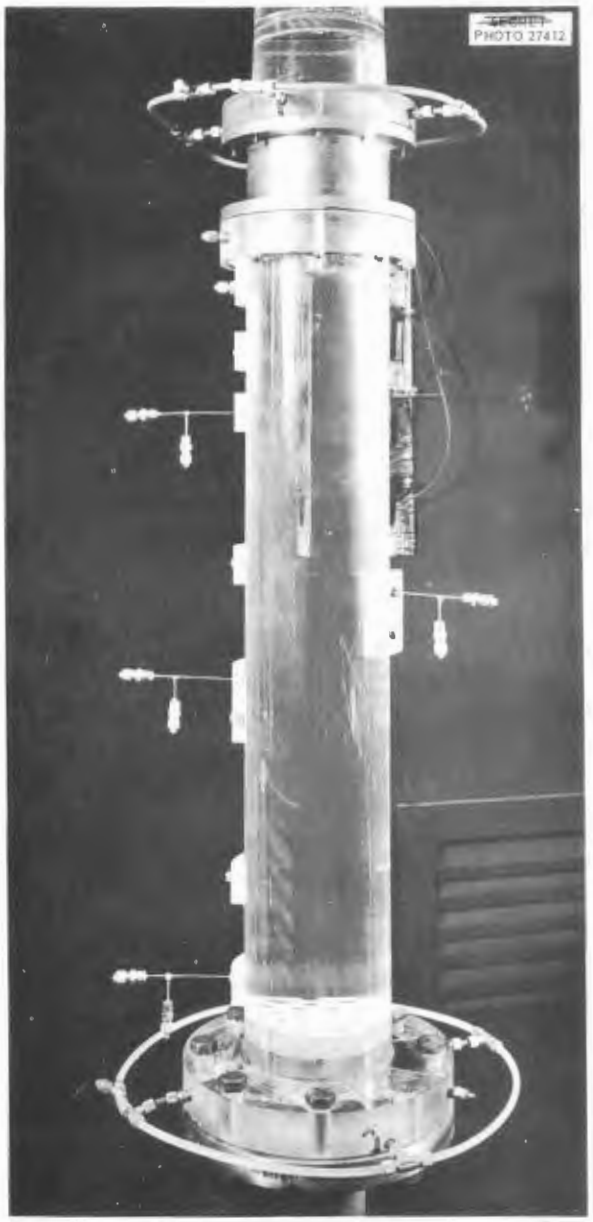

Fig. 4.1.9. Photograph of Vortex Flow Tube.

Fig. 4.1.10. Each core has Bessel-function radial volume-heat-source distributions and wall heat transfer to the fuel from the moderator which is being cooled. One core has ordinary straight-through flow and the other has the vortex flow described above. The mathematical radial fuel temperature distributions are plotted for each system. As may be seen, the maximum local

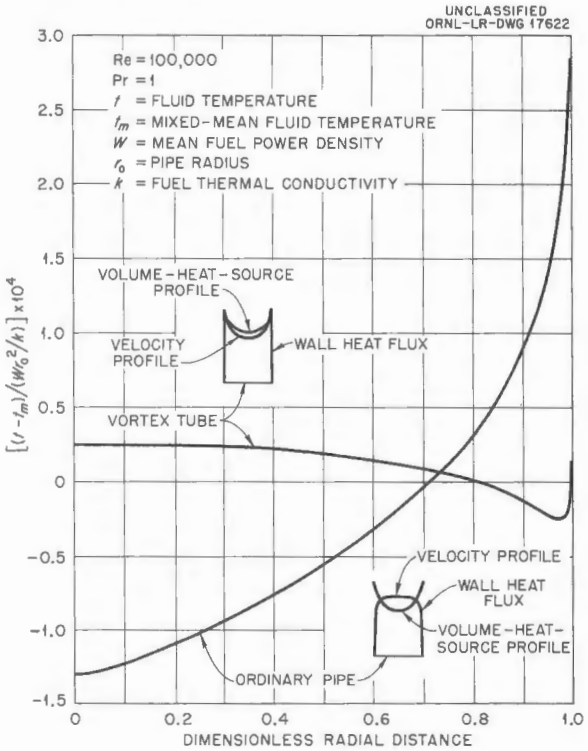

Fig. 4.1.10. Dimensionless Radial Temperature Distributions in Ordinary Pipe and Vortex Tube Fuel Elements with Wall Heat Transfer from Reflector-Moderator.

fuel temperature deviation from the mixed-mean temperature in the vortex tube was only one-eleventh of the corresponding value for the straight-through flow case.

It therefore appears that it will be possible to design a new reflector-moderated reactor core composed of a cluster of vortex flow tubes surrounded by a moderator. The advantages of such a reactor system would be the mitigation of hot-spot and thermal-cycling problems, the attainment of maximum thermodynamic efficiency, and the probable elimination of a separate cooling system for the moderator.

THERMAL-CYCLING EXPERIMENTS

H. W. Hoffman D. P. Gregory[4]

Studies of the effects of thermal cycling on Inconel exposed to flowing $NaF\text{-}ZrF_4\text{-}UF_4$ (50-46-4 mole %) were continued. No further modifications were made to the experimental system previously described.[6] The results obtained to date are summarized in Table 4.1.1. The penetrations observed in both the test section and the heater for runs ET-G to ET-K are illustrated in Figs. 4.1.11 through 4.1.15.

Run ET-F was performed under isothermal conditions to establish the effect of temperature level on metal attack in this specific system. The run was terminated after 5 hr of operation at an interface temperature of 1615°F for comparison with the preceding thermally cycled run, ET-E. The results of this comparison are inconclusive in that the relationship between the high heater temperature and the test section attack in run ET-E is not understood. For the runs following ET-F the maximum heater temperature was lowered to approximately 1900°F to reduce the stresses at the electrode-tube connection and thus to allow runs of longer duration.

In an attempt to answer the question raised by the comparison of runs ET-E and ET-F, run ET-J was made with the heater section maintained at the mean heater temperature of the high-frequency thermally cycled run ET-G. Hereafter, the experimental situation in which the heater is held at some steady-state temperature that is above the mixed-mean fluid temperature through the first half of the flow cycle and is held at the mixed-mean fluid temperature during the second half of the flow cycle will be referred to as low-frequency thermal cycling (~0.01 cps). The term "high-frequency thermal cycling" will then apply to the condition in which the heater temperature is periodically varied at a fixed frequency (in the range ¼ to 2 cps) through the first part of the cycle and is held at the fluid mixed-mean temperature during the return part of the fluid cycle. The comparison of runs ET-G and ET-J shows approximately the same depth of attack in the heater sections but somewhat less penetration in the test section for the low-frequency thermally cycled run, ET-J. The density of attack in the test section was lower in the low-frequency test (compare Figs. 4.1.11 and 4.1.14) than in the high-frequency test. The conclusions drawn must be tempered by two additional factors: the runs were of short duration, and fresh salt was used in run ET-G, while in run ET-J the salt

[6]H. W. Hoffman and D. P. Gregory, *ANP Quar. Prog. Rep. June 10, 1956*, ORNL-2106, p 227; H. W. Hoffman and D. P. Gregory, *ANP Quar. Prog. Rep. Sept. 10, 1956*, ORNL-2157, p 229.

TABLE 4.1.1. SUMMARY OF RESULTS OF THERMAL CYCLING EXPERIMENTS

Run	Duration (hr)	Heater Section				Test Section				Cause of Failure
		Interface Temperature (°F)		Depth (mils) and Type of Subsurface Voids		Interface Temperature (°F)		Depth (mils) and Type of Subsurface Voids		
		Average	Fluctuation	General	Intergranular	Average	Fluctuation	General	Intergranular	
ET-A	16	1455	±180	6; heavy	6; heavy	1273	± 8	None	1; heavy	Oxidized electrode
	14	1546	±225			1287	±12			
-B	240	1415	±170	9; heavy	None	1330	±17	1; heavy	None	Voluntary termination
-C	4	1755	±189	None	2.5; moderate to heavy	1613	±37	2; moderate to heavy	None	Melted electrode
-D	14	1845	±240	3; heavy	8; heavy	1590	±83	5; heavy	None	Tube break*
-E	5	1905	±235	None	8; localized, heavy	1635	±43	3; localized, heavy	None	Tube break*
-F	5	1615		No attack		1615		No attack		Voluntary termination
-G	23	1760	±190	None	3 to 6; localized, heavy	1583	±13	3.5; localized, heavy	None	Tube break*
-H	66	1730	±125	None	11; heavy	1600	±32	6; heavy	9; heavy	Tube break*
-I	106	1850	±125	None	11; heavy	1600	±22	6.5; moderate to heavy	None	Tube break*
-J	23	1800		5; localized, heavy	5; localized, heavy	1600		2; heavy	None	Mixing-pot leak
-K	100	1820		2; heavy	13; heavy	1620		2; localized, heavy	6; localized, heavy	Voluntary termination

*Break occurred at outlet end of heater immediately adjacent to electrode.

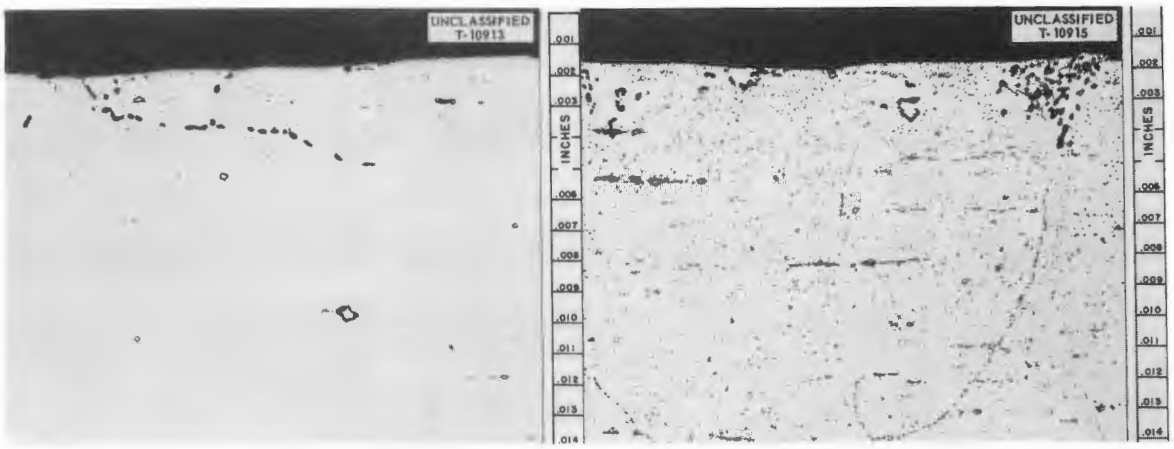

RUN: ET-G
DURATION OF RUN: 23 hr

SAMPLE POSITION: 2
AVERAGE INTERFACE TEMPERATURE: 1760°F
FLUCTUATION, ± 190°F

SAMPLE POSITION: 7
AVERAGE INTERFACE TEMPERATURE: 1583°F
FLUCTUATION, ± 13°F

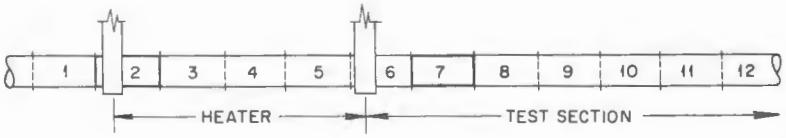

Fig. 4.1.11. Corrosion Results of Thermal-Cycling Test of Inconel Tubing Exposed to the Fuel Mixture (No. 30) NaF-ZrF_4-UF_4 (50-46-4 mole %). Run ET-G. 250X. Reduced 33.5%. ~~(Secret with caption)~~

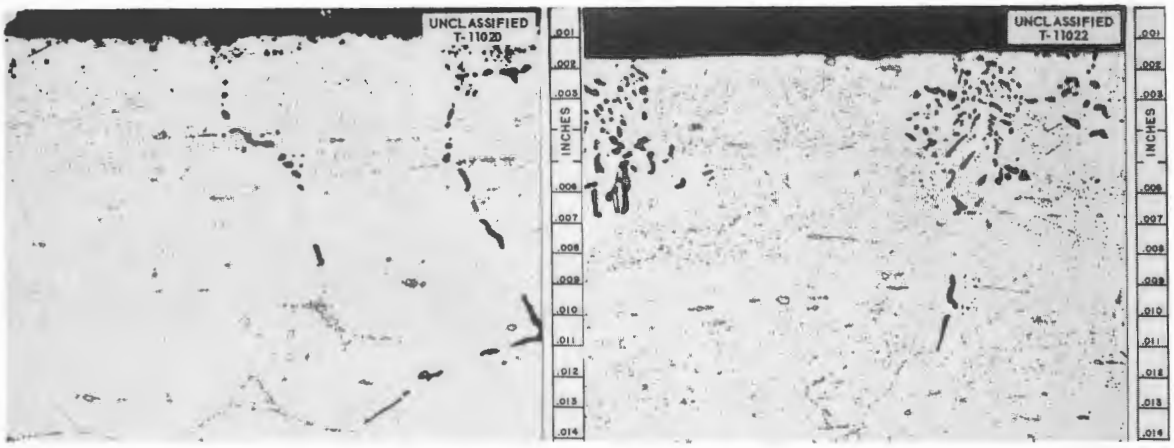

RUN: ET-H
DURATION OF RUN: 66 hr

SAMPLE POSITION: 2
AVERAGE INTERFACE TEMPERATURE: 1730°F
FLUCTUATION, ± 125°F

SAMPLE POSITION: 7
AVERAGE INTERFACE TEMPERATURE: 1600°F
FLUCTUATION, ± 32°F

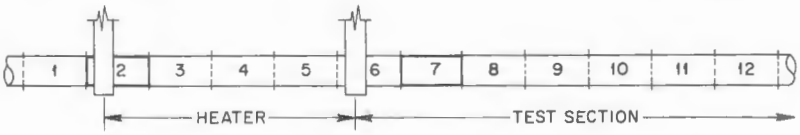

Fig. 4.1.12. Corrosion Results of Thermal-Cycling Test of Inconel Tubing Exposed to the Fuel Mixture (No. 30) NaF-ZrF_4-UF_4 (50-46-4 mole %). Run ET-H. 250X. Reduced 33.5%. ~~(Secret with caption)~~

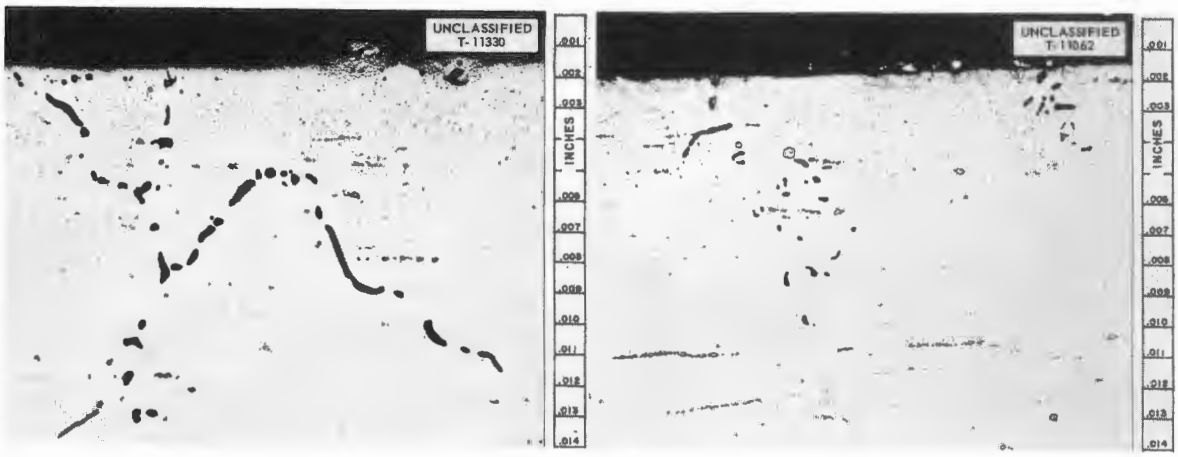

RUN: ET-I
DURATION OF RUN: 106 hr

SAMPLE POSITION: 5
AVERAGE INTERFACE TEMPERATURE: 1850°F
FLUCTUATIONS, ± 125°F

SAMPLE POSITION: 10
AVERAGE INTERFACE TEMPERATURE: 1600°F
FLUCTUATIONS, ± 22°F

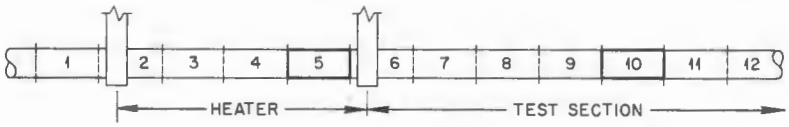

Fig. 4.1.13. Corrosion Results of Thermal-Cycling Test of Inconel Tubing Exposed to the Fuel Mixture (No. 30) NaF-ZrF$_4$-UF$_4$ (50-46-4 mole %). Run ET-I. 250X. Reduced 33.5% [redacted]

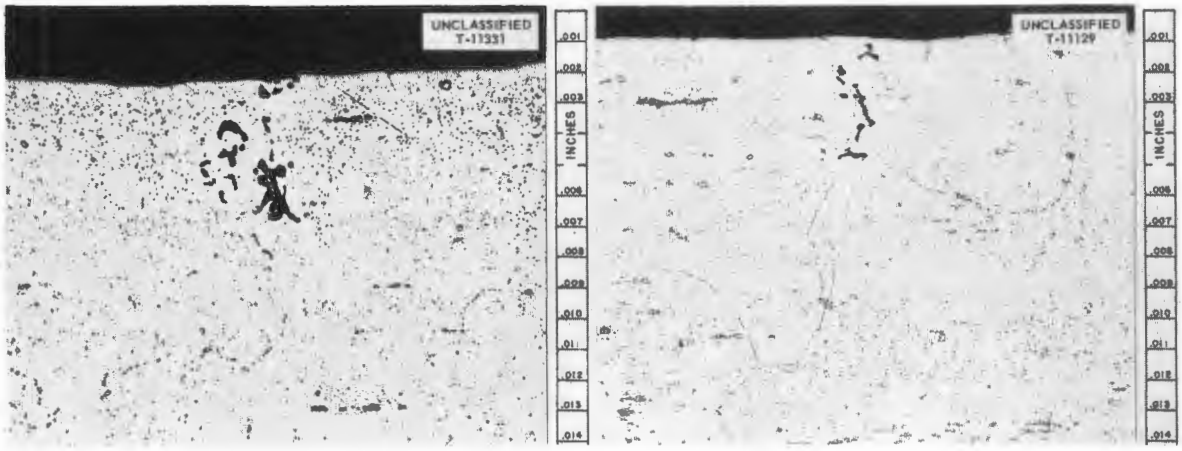

RUN: ET-J
DURATION OF RUN: 23 hr

SAMPLE POSITION: 2
INTERFACE TEMPERATURE: 1800°F

SAMPLE POSITION: 7
INTERFACE TEMPERATURE: 1600°F

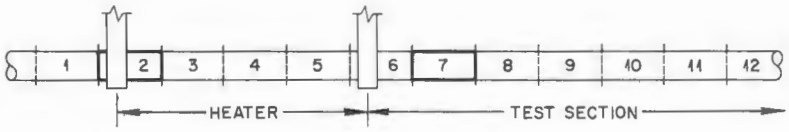

Fig. 4.1.14. Corrosion Results of Thermal-Cycling Test of Inconel Tubing Exposed to the Fuel Mixture (No. 30) NaF-ZrF$_4$-UF$_4$ (50-46-4 mole %). Run ET-J. 250X. Reduced 33.5%. ~~(Secret with caption)~~

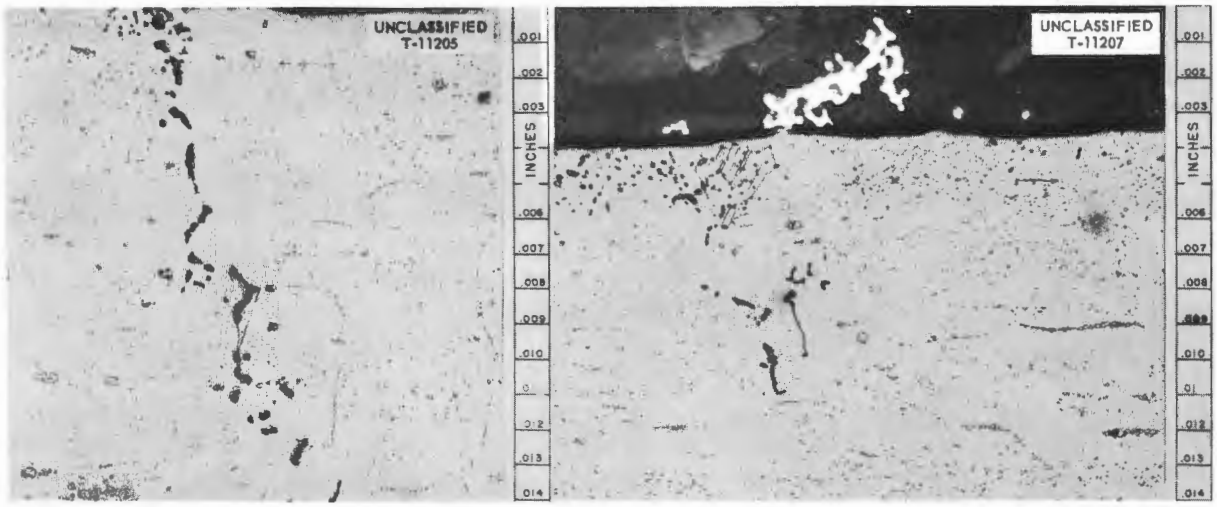

RUN: ET – K
DURATION OF RUN: 100 hr

SAMPLE POSITION: 4
INTERFACE TEMPERATURE: 1820°F

SAMPLE POSITION: 8
INTERFACE TEMPERATURE: 1620°F

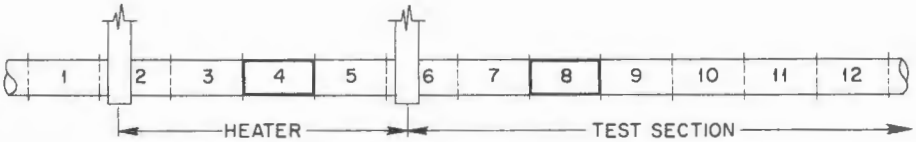

Fig. 4.1.15. Corrosion Results of Thermal-Cycling Test of Inconel Tubing Exposed to the Fuel Mixture (No. 30) $NaF-ZrF_4-UF_4$ (50-46-4 mole %). Run ET-K. 250X. Reduced 23.5%. [redacted]

previously exposed in runs ET-G and ET-I (~130 hr) was used. A comparison between runs ET-I (high-frequency test) and ET-K (low-frequency test) is complicated by a similar salt history.

A series of experiments will be conducted in which the effect of prior salt exposure will be reduced by equilibrating a large quantity of salt under isothermal conditions. Then this salt will be used in each test in a previously unexposed system. The series of tests will constitute a set of approximately 100-hr runs with test section temperatures in the vicinity of 1600°F and mean heater temperatures of 1800°F under high- and low-frequency thermal cycling, as well as isothermal, conditions.

Deeper subsurface void formation than was expected was observed in the test sections from both the high- and low-frequency thermal-cycling experiments run thus far. Whether this higher attack is to be ascribed in whole or in part to thermal cycling, to the temperature profile, or to the surface area-to-volume ratio of the system remains the pertinent question.

HEAT CAPACITY

W. D. Powers

The enthalpies and heat capacities of three salts were determined. The results are listed below.

ZrF_4

Solid (112 to 866°C)

$$H_T - H_{30°C} = -5.5 + 0.175T + (2.13 \times 10^{-5})T^2$$

$$c_p = 0.157 + (4.26 \times 10^{-5})T$$

Liquid (929 to 1075°C)

$$H_T - H_{30°C} = -201.5 + 0.659T - (18.74 \times 10^{-5})T^2$$

$$c_p = 0.659 - (37.47 \times 10^{-5})T$$

Heat of Fusion (912°C)

$$H_L - H_S = 88$$

In these and the following expressions
H = enthalpy in cal/g,
c_p = heat capacity in cal/g·°C),
T = temperature in °C.

$NaNO_2$-KNO_3-$NaNO_3$ (40-53-7 mole %)

Liquid (218 to 411°C)

$$H_T - H_{30°C} = 29.5 + 0.334T + (6.33 \times 10^{-5})T^2$$

$$c_p = 0.334 + (12.66 \times 10^{-5})T$$

This salt undergoes some decomposition when heated above 500°C during welding of the test capsule. The experimental enthalpy values plotted as a function of temperature show a minor discontinuity at 500°C. However, the slopes of the enthalpy curves remain constant.

NaCl-LiCl (28-72 mole %)

Solid (123 to 286°C)

$$H_T - H_{30°C} = -12.2 + 0.290T$$

$$c_p = 0.29$$

Solid (365 to 507°C)

$$H_T - H_{30°C} = -20.1 + 0.307T$$

$$c_p = 0.31$$

Liquid (589 to 940°C)

$$H_T - H_{30°C} = 20.2 + 0.415T - (4.58 \times 10^{-5})T^2$$

$$c_p = 0.415 - (9.16 \times 10^{-5})T$$

Heat of Fusion (552°C)

$$H_L - H_S = 86$$

In the solid state between 300 and 350°C there is an anomalous effect that causes an increase in the enthalpy of about 5 cal/g. For this reason the enthalpies and heat capacities were calculated for temperature intervals above and below this region. There is little, if any, heat of transition.

VISCOSITY

S. I. Cohen

A program for investigating the viscosities of some mixtures of fused chlorides is under way. Measurements have been made with two different viscometers on the KCl-LiCl (41.2-58.8 mole %) eutectic which melts at 352°C. Data were obtained in an Ostwald viscometer suspended in a molten salt bath and with the capillary "needle" viscometer previously described.[7] The two sets of measurements, which were in satisfactory agreement, are plotted in Fig. 4.1.16; average values ranged from 5.4 centipoises at 375°C to 1.8 centipoises at 600°C.

THERMAL CONDUCTIVITY

W. D. Powers W. R. Gambill

The thermal conductivity of molten $NaF-ZrF_4-UF_4$ (56-39-5 mole %) is being determined in a variable-gap apparatus. A preliminary value of about 1.5 Btu/hr·ft^2 (°F/ft) has been obtained. Some difficulties in obtaining unidirectional heat flow are being encountered, however.

[7] S. I. Cohen, *ANP Quar. Prog. Rep. June 10, 1956*, ORNL-2106, p 231.

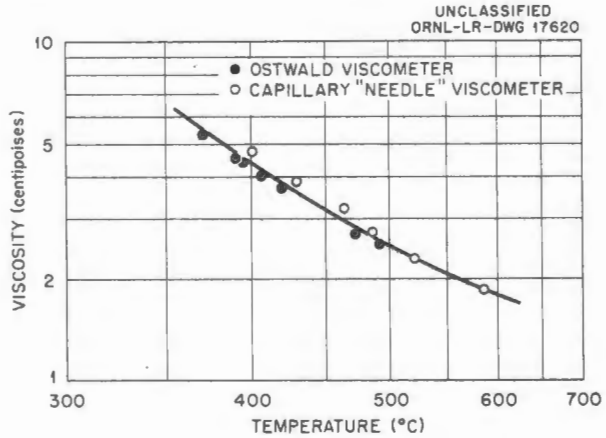

Fig. 4.1.16. Viscosity of KCl-LiCl (41.2-58.8 mole %).

The design of a new thermal-conductivity apparatus of the variable-gap type is presently being completed. Adequate means of guarding against heat losses are incorporated in the design so that unidirectional heat flow can be achieved.

A study is in progress on the effect of subsurface voids formed by corrosion on the over-all thermal conductivity of a metal wall. Metallurgical reports indicate that these porosities are true voids in that they are occupied by no matter. Their conductivity is therefore assumed to be zero in the following preliminary treatment. For the case in which Inconel is the metal ($k = 13$) and a homogeneous distribution of cavities exists in the corroded layer, the conductivity values shown in Fig. 4.1.17 were obtained. For example, if an

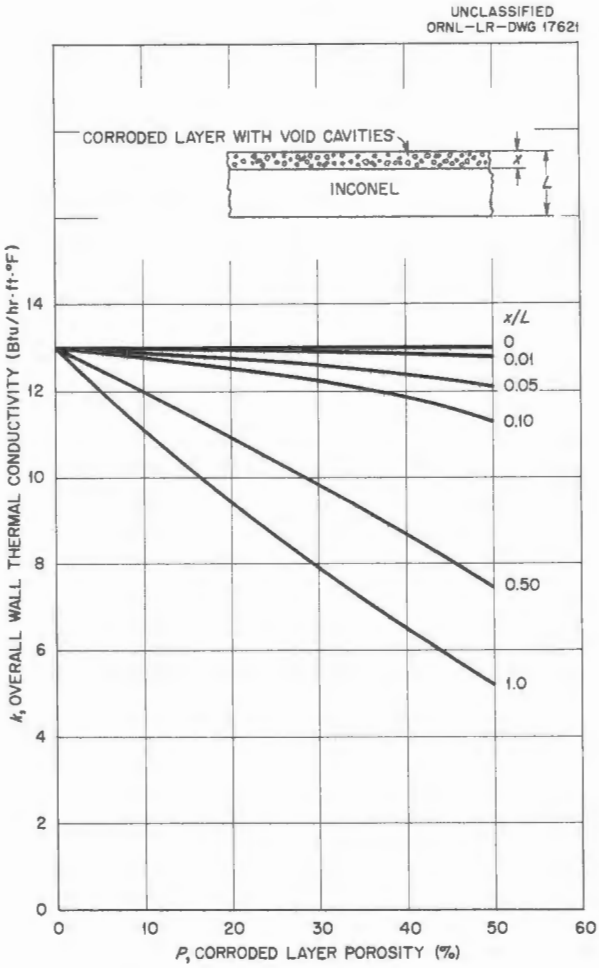

Fig. 4.1.17. Thermal Conductivity of an Inconel Wall with Empty Corrosion Cavities.

Inconel wall were corroded through one-half of its thickness with a void porosity of 30%, a 25% reduction in over-all wall thermal conductivity would result. The corroded layer porosity, P, is defined as the volume of corrosion voids divided by the total volume of the corroded layer. Further studies will involve determination of more accurate actual corrosion layer porosities and of the general validity of these results.

4.2. RADIATION DAMAGE

G. W. Keilholtz

EXAMINATION OF DISASSEMBLED MTR IN-PILE LOOPS

A. E. Richt E. J. Manthos
C. Ellis R. N. Ramsey
W. B. Parsley E. D. Sims
R. M. Wallace

Examination of MTR in-pile loop No. 3 was completed, and loop No. 4 was disassembled and partially examined. The operating conditions for these two loops, as described previously,[1] were similar. The maximum temperature in the fuel (No. 44), which was the mixture $NaF-ZrF_4-UF_4$ (53.5-40-6.5 mole %), was 1500°F and temperature differences of 155°F in loop No. 3 and 200°F in loop No. 4 were obtained. The total operating periods were similar, being 467 and 501 hr, as were the maximum fission power densities of about 800 w/cm^3 in both loops. During operation of these two loops, both the bearing housing and the pump-sump purge outlets plugged, and leaks in the pump bulkheads caused excessive activity in the cubicle and hampered removal of the loops from the MTR.

The only portion of loop No. 3 that remained to be examined during the quarter was a section of the pump impeller. As shown in Fig. 4.2.1, no evidence of attack was found on the impeller by metallographic examination. The results of ex-

[1] L. P. Carpenter *et al.*, *ANP Quar. Prog. Rep. Dec. 10, 1955*, ORNL-2012, p 27; C. C. Bolta *et al.*, *ANP Quar. Prog. Rep. June 10, 1956*, ORNL-2106, p 75.

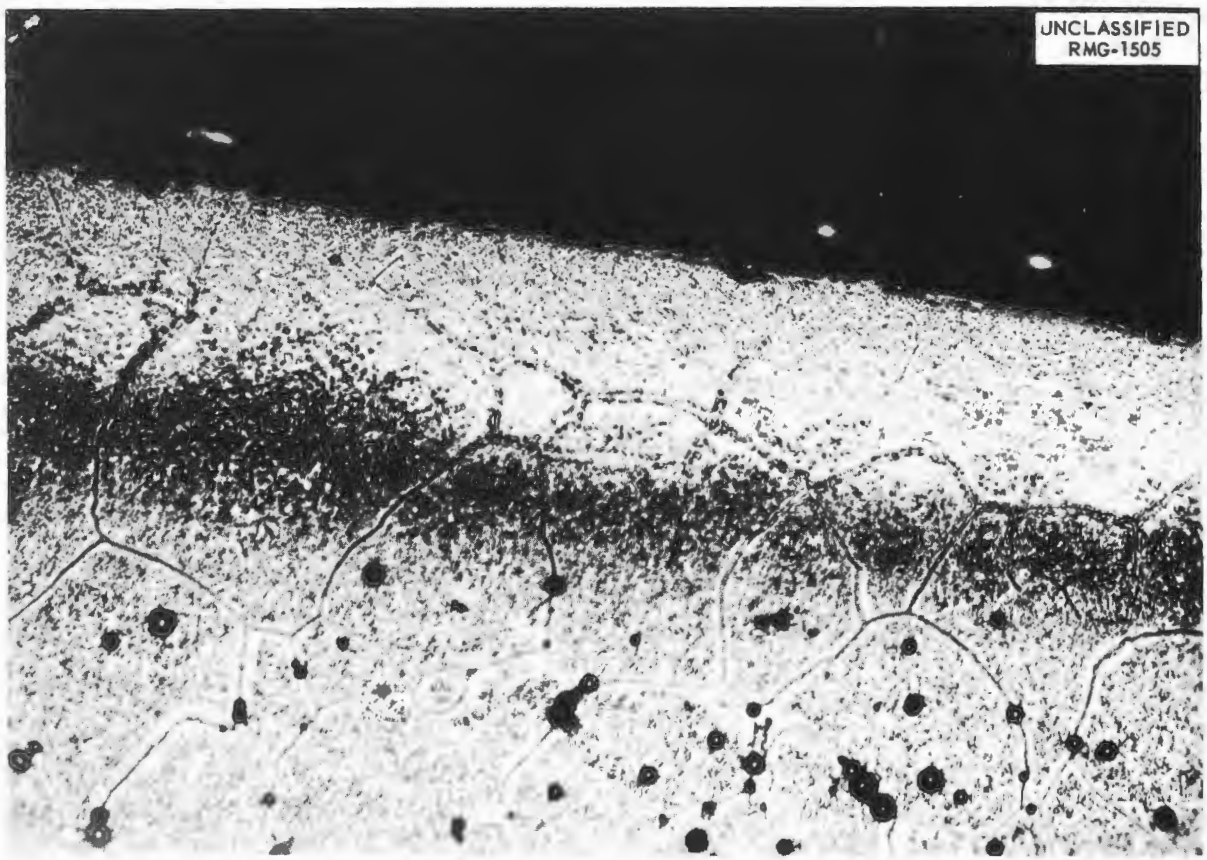

Fig. 4.2.1. Metallographic Specimen from Impeller of Fuel Pump Used in MTR In-Pile Loop No. 3. 250X. ~~(Secret with caption)~~

aminations of other portions of the loop were reported previously.[2]

The fuel-circulating pump from loop No. 4, which was similar to a pump illustrated previously,[3] was disassembled, except for the impeller housing, and was sectioned. Only a very small amount of fuel was found in the pump sump. A colored amorphous deposit similar to that found in the pump of loop No. 3 behind the slinger assembly and on the forward bellows was also present in the pump from loop No. 4. The forward bellows and the rotating copper block were found to be covered with a dark viscous oil. The oil finger, below the forward bellows, was filled with oil, while the oil overflow tank, behind the pump motor, was partially filled with oil. The oil finger and an oil sample from the tank for separating gas from the oil were saved for chemical analysis.

Ten samples were taken from the straight sections of fuel tubing[4] on both sides of the nose coil. Chemical analyses will be made of the fuel present in the tubing, and measurements will be made of the activation of the Inconel. Six samples of tubing from the nose coil and miscellaneous samples of various other portions of the loop will be examined similarly.

Only two of the six cobalt foils that were installed in loop No. 4 could be found after disassembly. However, sections of tubing have been cut at points where the foils were located, and the cobalt and/or chromium in the Inconel will be utilized as a flux monitor.

The nose-coil ends of the sniffer sleeves were removed and split. No obstructions or deposits were found in the spiral grooves of the sleeves, as shown in Figs. 4.2.2 and 4.2.3.

An attempt was made during disassembly of loop No. 4 not to disturb the thermocouple beads on the nose coil, and photographs were taken of the beads after the coil had been sectioned and the fuel had been melted out. The condition of thermocouple No. 2, where it was attached to the tube wall, is shown in Fig. 4.2.4. The same bead is shown in Fig. 4.2.5 after the tubing was cut and mounted for metallographic examination. The good adhesion between the bead and the tube wall may be seen.

[2] A. E. Richt *et al.*, *ANP Quar. Prog. Rep. Sept. 10, 1956*, ORNL-2157, p 236.

[3] J. A. Conlin, *ANP Quar. Prog. Rep. June 10, 1955*, ORNL-1896, p 27.

[4] For layout of loop see *ANP Quar. Prog. Rep. March 10, 1955*, ORNL-1864, Fig. 3.1, p 29.

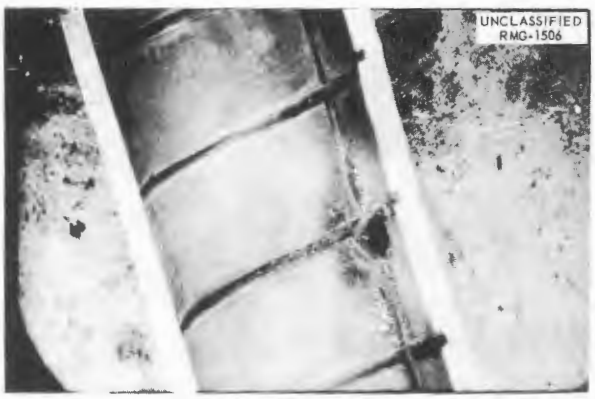

Fig. 4.2.2. Nose End of Split Sniffer Sleeve from Nose Inlet Side Showing Opening to Gas Exit Tube. 2X. Reduced 30.5%.

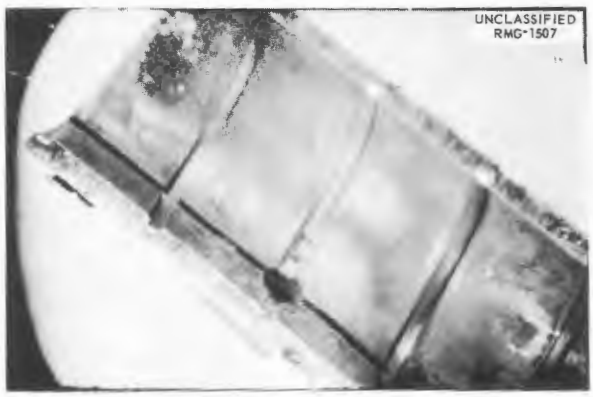

Fig. 4.2.3. Nose End of Split Sniffer Sleeve from Nose Outlet Side Showing Opening to Gas Exit Tube. 2X. Reduced 30.5%.

Fig. 4.2.4. Thermocouple No. 2 Attached to Fuel Line of MTR In-Pile Loop After Operation of Loop in MTR. 2X. Reduced 28.5%. (Secret with caption)

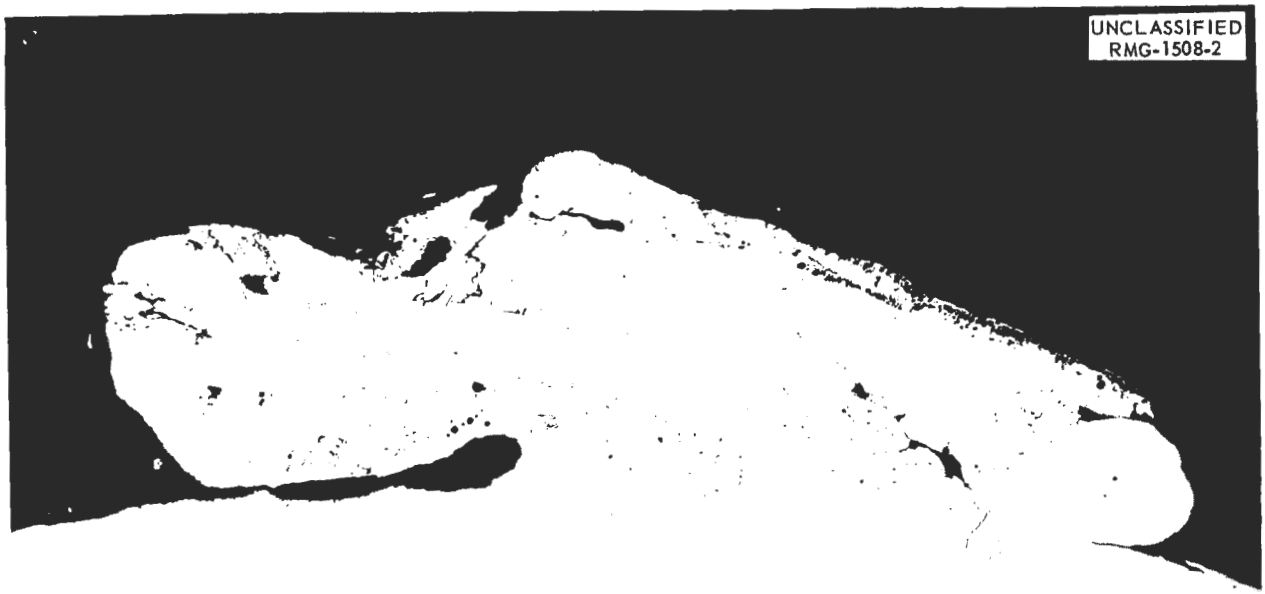

Fig. 4.2.5. Photomicrograph of Section Through Thermocouple Bead and Tube Shown in Fig. 4.2.4. As polished. 50X.

Sixteen of the 29 metallographic specimens taken from loop No. 4 have been mounted and examined. Nine of the 16 specimens were taken from the nose coil. Two more specimens from the nose coil remain to be cut and mounted. The fuel in the nose coil and in the fuel tubes was melted out in an inert atmosphere before the metallographic specimens were obtained. Samples from the nose coil that were adjacent to thermocouples were cut as close as possible to the thermocouple bead so that the exact temperature of the specimen would be known and so that a cross section of the thermocouple bead on the tube wall might possibly be obtained. An attempt was made to use an epoxy resin as a filler for the fuel tubes in the hope of preserving the inside edge of the specimens. However, the resin cracked badly under radiation and proved to be unsatisfactory.

Control specimens of tubing from loops Nos. 3 and 4 are shown in Fig. 4.2.6 for comparison with irradiated specimens. The control specimens also show that the tubing used in loop No. 4 was of smaller grain size than that used in loop No. 3. Metallographic specimens from loops Nos. 3 and 4 were etched with the same etchant as that indicated in Fig. 4.2.6. The inside edges of fuel-tube specimens obtained from loops Nos. 3 and 4 at the location of thermocouples 7 and 8 near the outlet of the nose coil are shown in Figs. 4.2.7 and 4.2.8. The as-polished specimens shown in Fig. 4.2.7 reveal that the depth of penetration was greater on the specimen from loop No. 3 than on the specimen from loop No. 4; however, the number of subsurface voids on the specimen from loop No. 4 seems to be slightly greater than the number on the specimen from loop No. 3. The etched structures in Fig. 4.2.8 show the voids enlarged, but the enlargement is due to the etching and is probably not a true picture of the attack. The depth of penetration of the specimen from loop No. 3 is approximately 3 mils, while the specimen from loop No. 4 shows penetration to a depth of 1.5 mils.

Specimens taken from loops Nos. 3 and 4 at the location of thermocouples 9, 10, and 22, which were 42½ in. from the pump on the nose outlet side, are shown in Figs. 4.2.9 and 4.2.10. Again the as-polished specimen from loop No. 3 shows the greater penetration, while the number of voids is greater on the specimen from loop No. 4. The depth of penetration on the specimen from loop No. 3 is 3 mils, while the specimen from loop

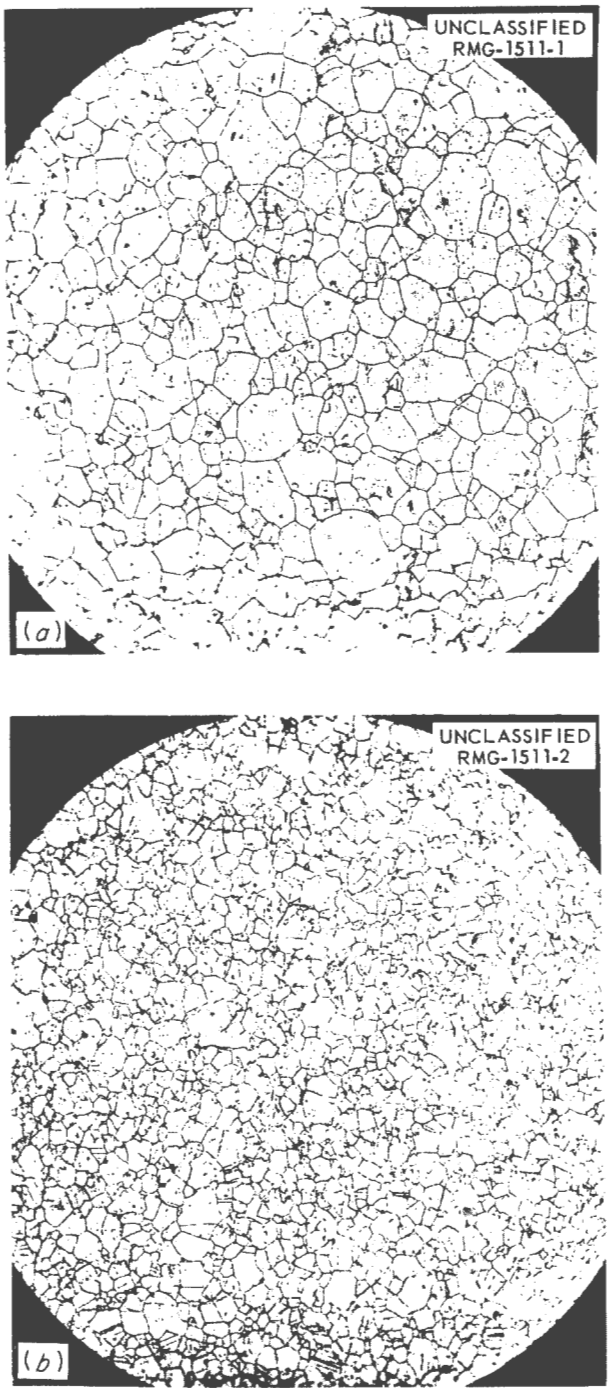

Fig. 4.2.6. Control Specimens of Inconel Tubing from (*a*) Loop No. 3 and (*b*) Loop No. 4. 100X.

No. 4 shows about 1.5 mils of penetration. No attack was apparent on specimens taken from loop No. 4 at points 25 and 30 in. from the pump on the nose inlet side, as shown in Fig. 4.2.11.

Loop No. 6 has been received for examination. Disassembly will begin as soon as the cells and the equipment have been decontaminated.

CHEMICAL PROBLEMS ENCOUNTERED IN ETCHING INCONEL

L. H. Jenkins R. M. Wallace

An investigation of the chemical processes involved in etching Inconel has been undertaken in an effort to determine the cause of the effects obtained by using various etchants. Since chromic, oxalic, and sulfuric acids are representative of the reagents used in etching processes, Inconel surfaces $\frac{1}{4} \times \frac{3}{4}$ in. were immersed in 25-ml portions of each of the acids in concentrations of 10, 10, and 5%, respectively. After four months at room temperature, the solutions were analyzed, and the results presented in Table 4.2.1 were obtained.

The data given in the table indicate that there was no selective etching of a major Inconel constituent. The Fe, Cr, and Ni concentrations in the etching solution correspond with those for Inconel. Hydrogen firing greatly decreased the attack on the rougher rolled surfaces. Surfaces which had been milled, however, were unaffected by hydrogen firing, except in the case of attack by H_2CrO_4. In all cases the attack on milled surfaces was less than the attack on the corresponding rolled surfaces.

Observation of the solutions and the Inconel specimens revealed that samples etched by H_2CrO_4 turned dark brown on the surface, with the exception of the milled, hydrogen-fired surfaces. The corresponding etching solutions were also darkened, with the exception of the chromic acid in which specimen No. 10 was exposed. Obviously, this represents a curious passivity in this sample. Inconel specimens 9 and 12 had light copper-colored coatings at the end of the test, and the corresponding solutions were a paler green than were the solutions in which specimens 3 and 6 were tested. This may indicate

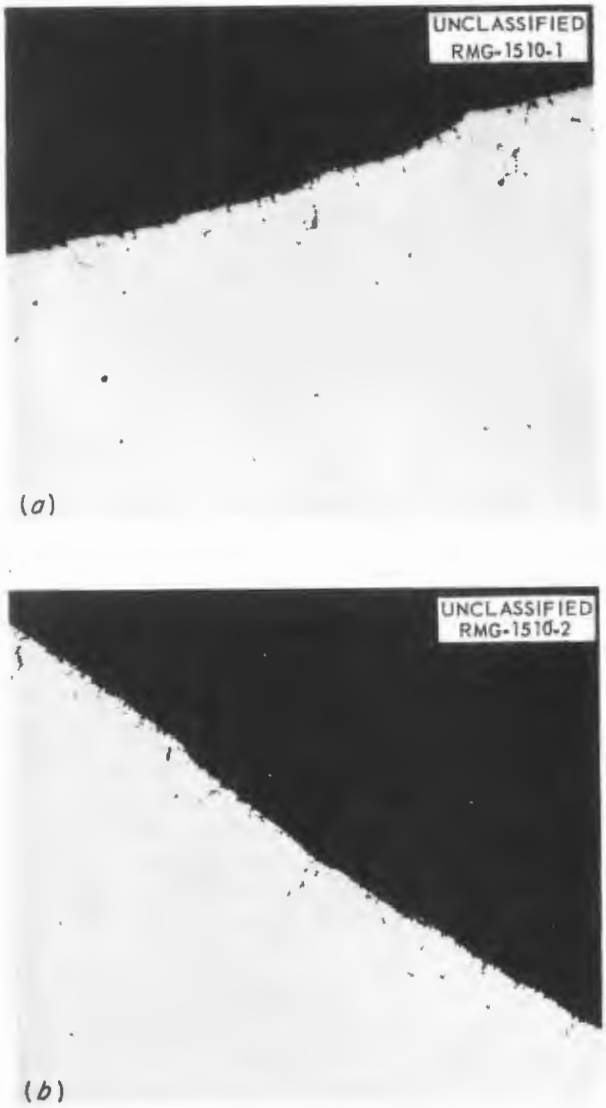

Fig. 4.2.7. Specimens of Inconel Tubing from Nose Coils of (*a*) Loop No. 3 and (*b*) Loop No. 4 Taken at the Location of Thermocouples 7 and 8 Near the Outlet of the Nose Coil. As polished. 250X.

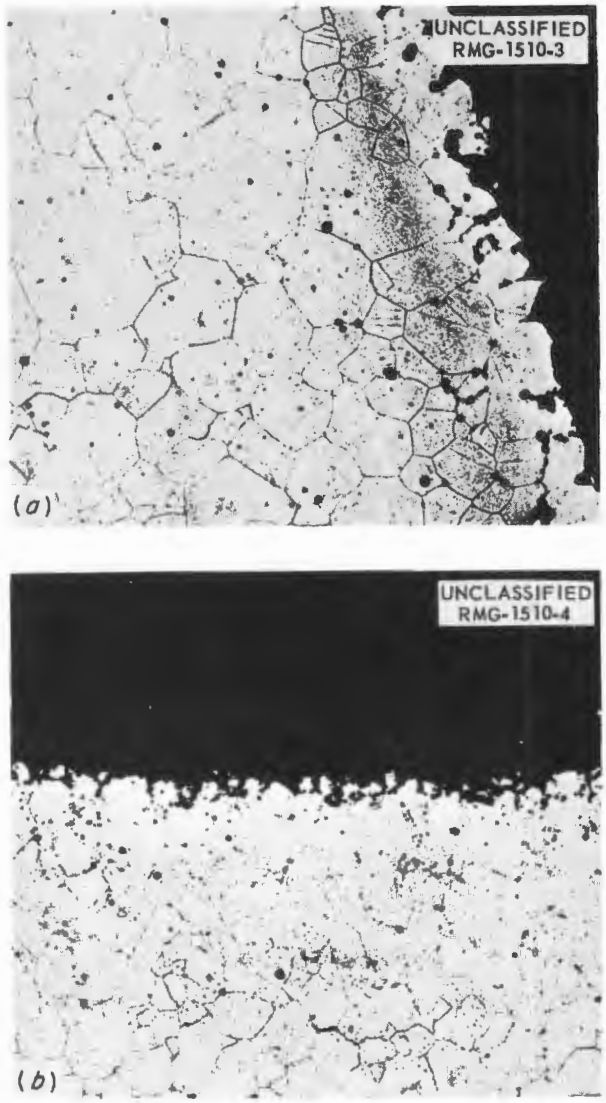

Fig. 4.2.8. Etched Structures of Specimens Shown in Fig. 4.2.7. (*a*) Specimen from loop No. 3. (*b*) Specimen from loop No. 4. 250X.

selective leaching of copper from Inconel exposed to sulfuric acid, since analyses indicated that the over-all attack of the Inconel was greatest for specimen 3, which was surface-rolled and exposed to 5% H_2SO_4.

Photomicrographs of the surfaces revealed no useful data regarding depth of etching. They did, however, demonstrate that a much clearer picture of the surface was obtained when the samples were electroplated with either copper or nickel or both, successively, before they were polished, since this prevented "rounding over" of the surface edges. Representative Inconel specimens are shown in Figs. 4.2.12 through 4.2.15, and it may be seen that the etching rate is not a function of grain size. This was found to be true in all cases. The large grains shown in Figs. 4.2.14 and 4.2.15 resulted from the hydrogen firing at 1750°F of the cold-worked specimens. The analytical results and evidences of grain growth

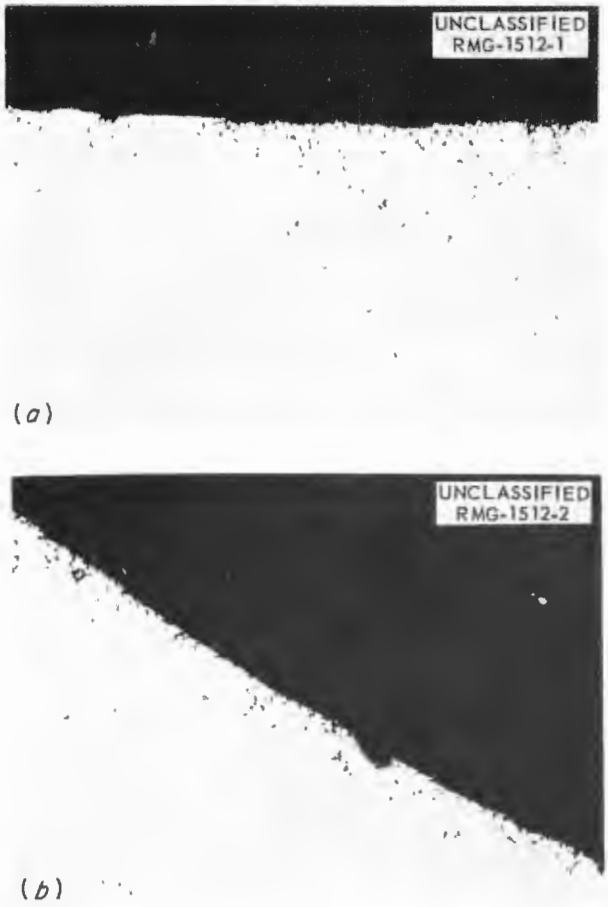

Fig. 4.2.9. Specimens of Inconel Tubing from (*a*) Loop No. 3 and (*b*) Loop No. 4 Taken at the Location of Thermocouples 9, 10, and 22, Which Were 42½ in. from the Pump on the Nose Outlet Side. As polished. 250X.

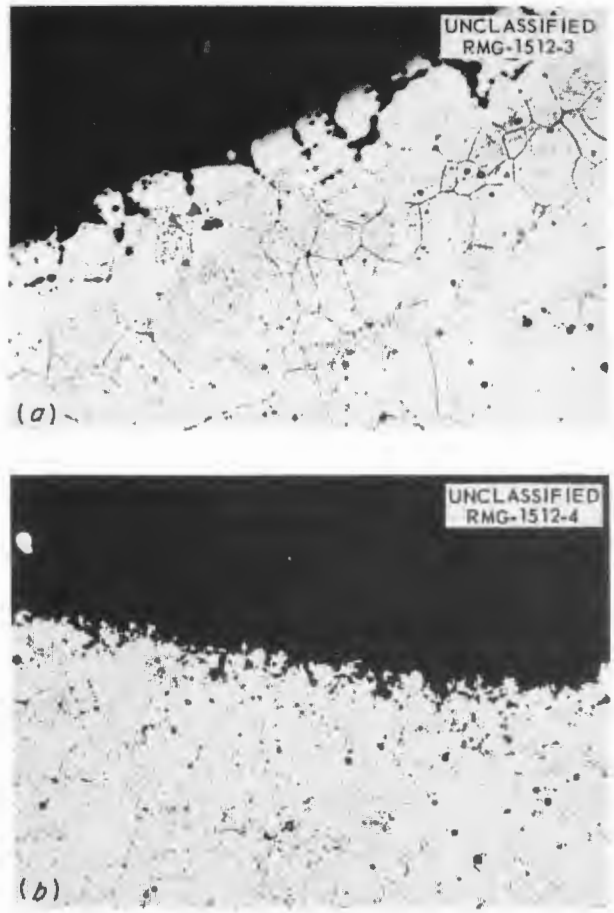

Fig. 4.2.10. Etched Structures of Specimens Shown in Fig. 4.2.9. (*a*) Specimen from loop No. 3. (*b*) Specimen from loop No. 4. 250X.

indicate a higher degree of cold work in the rolled surfaces than in milled surfaces.

These preliminary results emphasize the complexity of the subject and pose questions which apparently influence etching and which should be resolved. For example, it should be determined whether there is preferential attack along certain crystallographic axes which results either in superficial etching, such as was noted in one case in which chromic acid was used, or in selective leaching of trace constituents, such as copper, as was observed with sulfuric acid. The influence of the degree of cold work in the sample on the etching rate should be studied, and it should be determined whether surface conditions, other than cold work, influence the ease of etching. In an attempt to find answers to these and other questions concerning the chemistry of the etching process, additional Inconel surfaces are currently being tested.

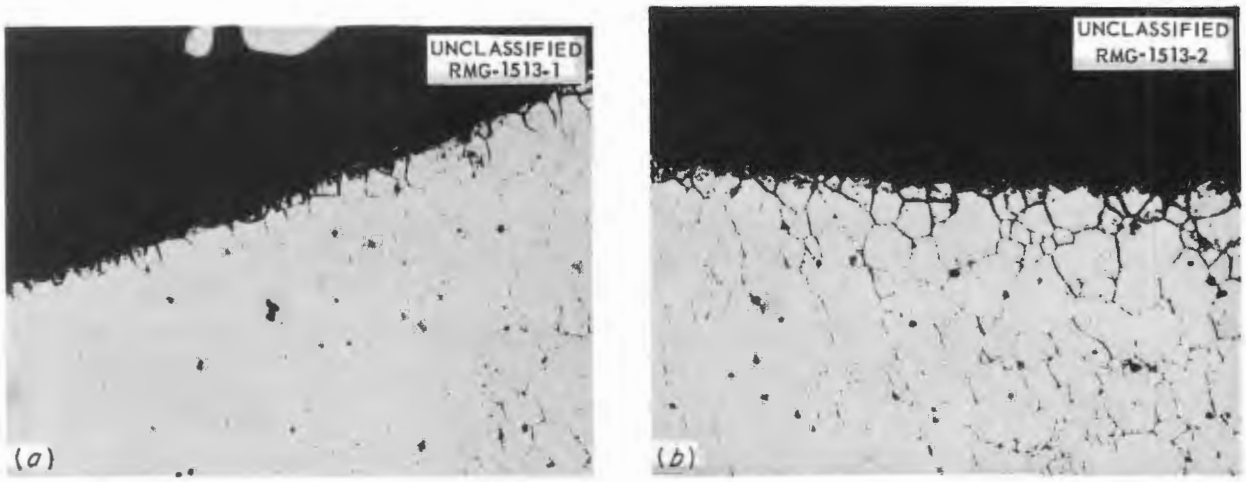

Fig. 4.2.11. Specimens of Inconel Tubing Taken (*a*) 25 and (*b*) 30 in. from the Pump on the Nose Inlet Side of Loop No. 4. 250X.

TABLE 4.2.1. RESULTS OF ANALYSES FOR THE PRINCIPAL CONSTITUENTS OF INCONEL IN ETCHING REAGENTS THAT WERE IN CONTACT WITH INCONEL FOR FOUR MONTHS AT ROOM TEMPERATURE

Inconel Specimen No.	Specimen Treatment	Etchant	Concentration of Inconel Constituents in Etchant (mg/ml)		
			Fe	Ni	Cr
1	Surface-rolled	10% H_2CrO_4	0.095	1.10	
2	Surface-rolled	10% $C_2H_2O_4$	0.07	0.58	0.348
3	Surface-rolled	5% H_2SO_4	0.224	3.07	0.566
4	Surface-milled	10% H_2CrO_4	0.08	0.98	
5	Surface-milled	10% $C_2H_2O_4$	0.06	0.44	0.210
6	Surface-milled	5% H_2SO_4	0.148	1.80	0.346
7	Surface-rolled and hydrogen-fired at 1750°F	10% H_2CrO_4	0.057	0.56	
8	Surface-rolled and hydrogen-fired at 1750°F	10% $C_2H_2O_4$	0.10	0.85	0.198
9	Surface-rolled and hydrogen-fired at 1750°F	5% H_2SO_4	0.204	2.77	0.493
10	Surface-milled and hydrogen-fired at 1750°F	10% H_2CrO_4	0.017	0.037	
11	Surface-milled and hydrogen-fired at 1750°F	10% $C_2H_2O_4$	0.07	0.57	0.190
12	Surface-milled and hydrogen-fired at 1750°F	5% H_2SO_4	0.146	1.87	0.362

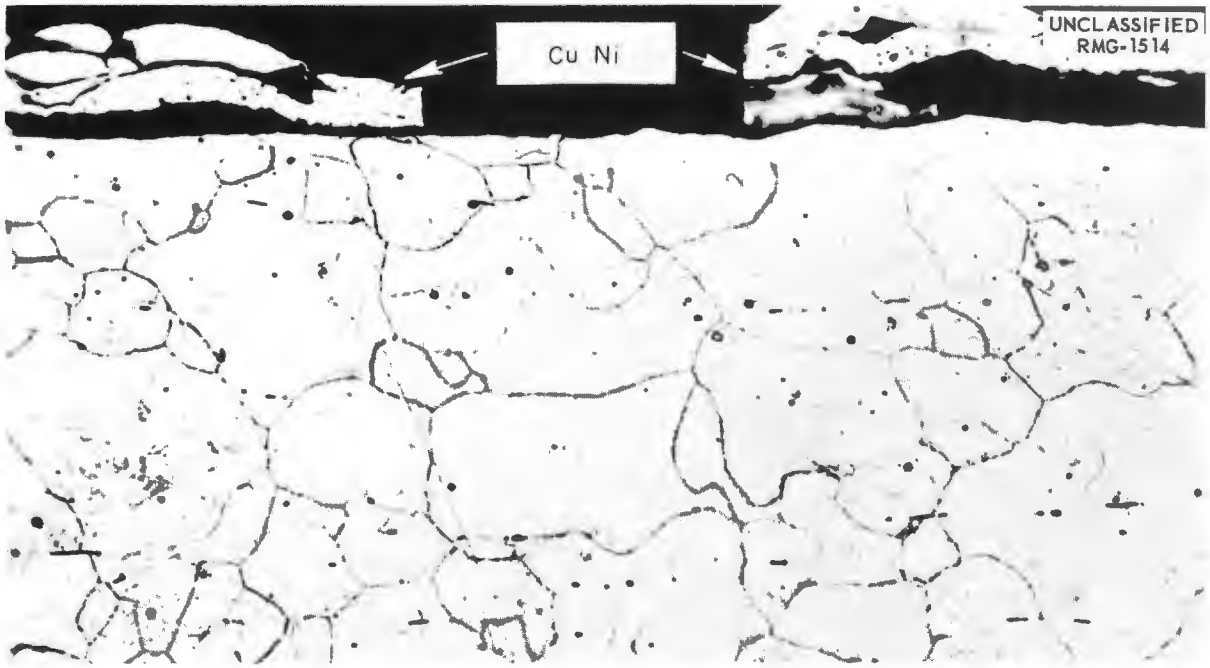

Fig. 4.2.12. Surface-Rolled Inconel Specimen After Exposure to 10% $C_2H_2O_4$ for Four Months at Room Temperature. Specimen surfaces copper plated and nickel plated, successively, before polishing and etching. Specimen No. 2. 250X.

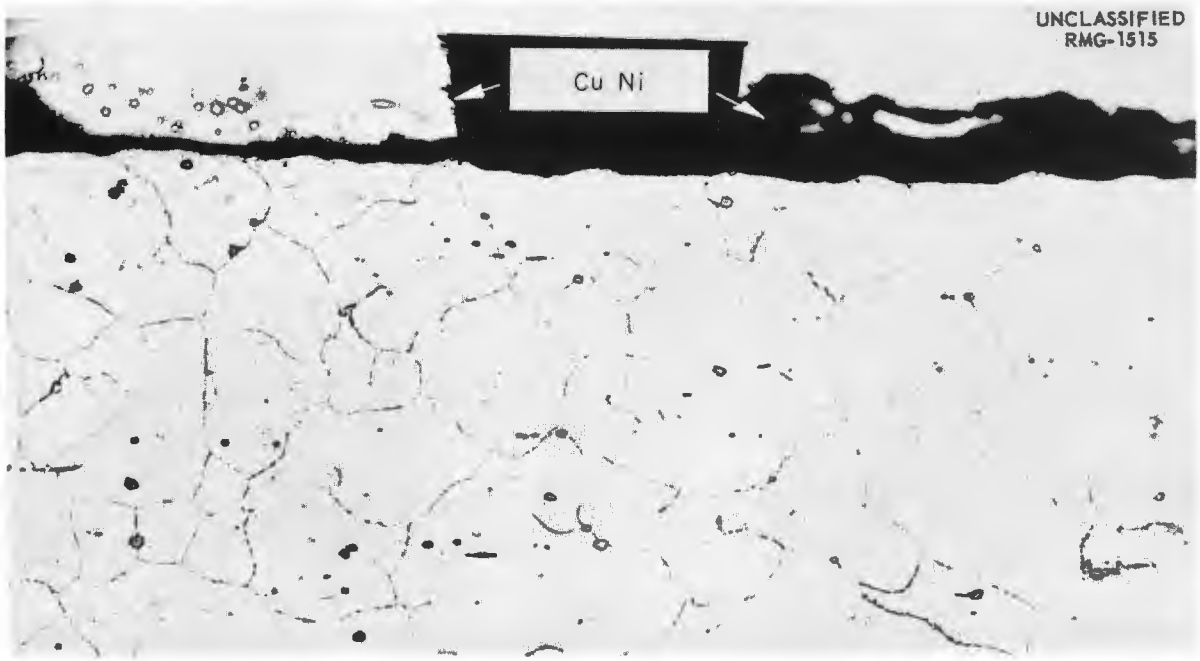

Fig. 4.2.13. Surface-Milled Inconel Specimen After Exposure to 10% $C_2H_2O_4$ for Four Months at Room Temperature. Specimen surfaces copper plated and nickel plated, successively, before polishing and etching. Specimen No. 5. 250X.

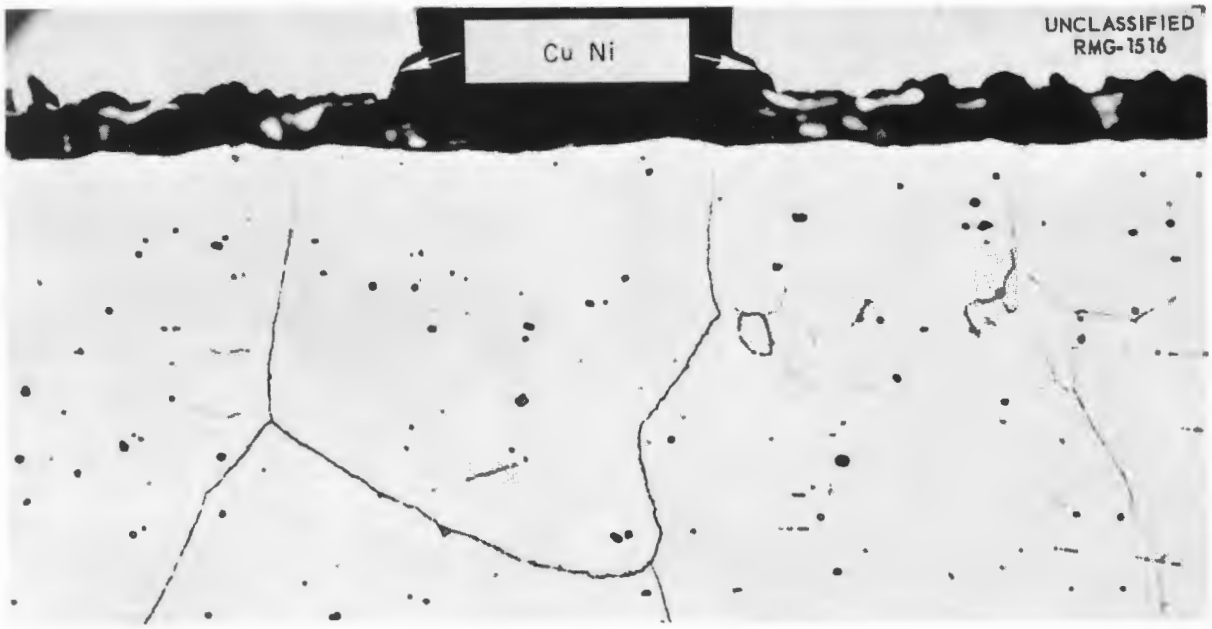

Fig. 4.2.14. Inconel Specimen Surface-Rolled and Hydrogen-Fired at 1750°F and Then Exposed to 10% $C_2H_2O_4$ for Four Months at Room Temperature. Specimen surfaces copper plated and nickel plated, successively, before polishing and etching. Specimen No. 8. 250X.

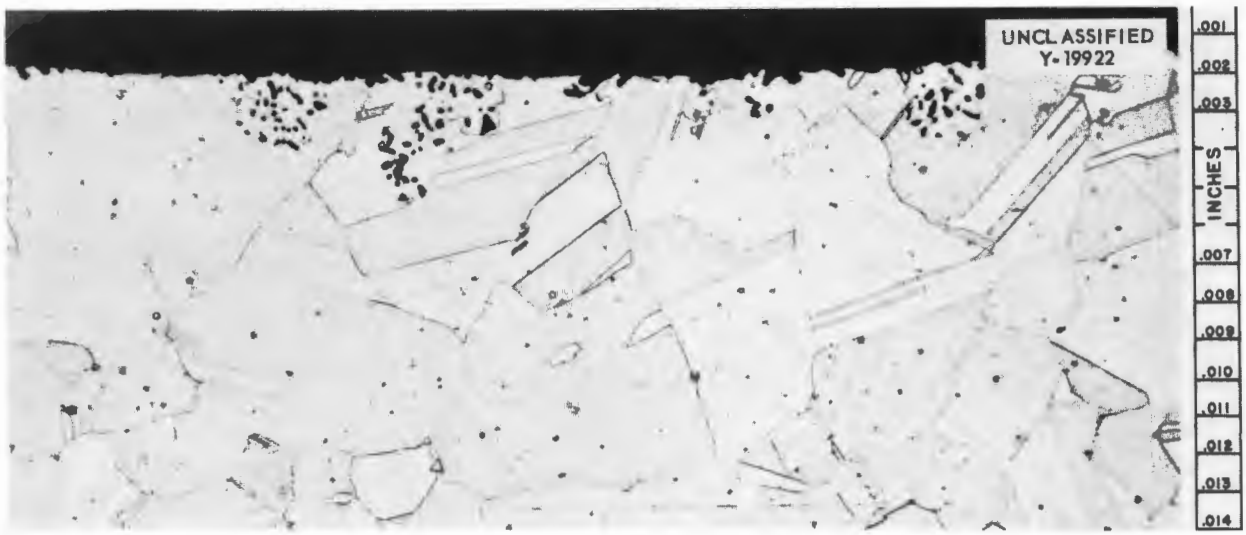

Fig. 4.2.15. Inconel Specimen Surface-Milled and Hydrogen-Fired at 1750°F and Then Exposed to 10% $C_2H_2O_4$ for Four Months at Room Temperature. Specimen surfaces nickel plated before polishing and etching. Specimen No. 11. 250X.

CREEP AND STRESS-CORROSION TESTS OF INCONEL

J. C. Wilson

C. D. Baumann
W. E. Brundage
W. W. Davis
N. E. Hinkle
T. C. Price[5]
J. C. Zukas

A series of experiments is under way in order to determine the effects of neutron irradiation on creep, stress-rupture life, and stress-corrosion of Inconel tubing in helium and in fused-salt fuel environments. One study is directed toward determining the effect of neutron bombardment on the stress-rupture life in helium of Inconel tubing of various wall thicknesses. Another study is directed toward determining the creep and stress-corrosion properties of Inconel tubing in helium and in fused-salt fuels under neutron bombardment.

The study of stress-rupture life is to be conducted in the MTR and is to consist of a series of tube burst tests in apparatus designed for operation in the HB-3 facility. The tube burst specimens will be fabricated from $\frac{3}{8}$-in., sched-40, Inconel pipe that has been carefully inspected by nondestructive testing. A helium atmosphere will be used, and the tubes will be at a temperature of 1500°F with stresses of 2000 and 4000 psi. Specimens with various wall thicknesses in the range 0.020 to 0.050 in. will be tested in order to determine the effect of wall thickness on stress-rupture life. Duplicate tests will be conducted without neutron bombardment for comparison.

Two specimen-holder and furnace assemblies are being tested for temperature uniformity and control, and the fabrication of equipment for the first MTR stress-rupture experiment is under way. The furnaces will accommodate 9 or 13 specimens.

Tensile-creep-test specimens of Inconel tubing irradiated previously[6] in the MTR in a helium atmosphere were found to have dark surface films throughout the high-temperature regions. The films, which were previously thought to have been the result of sulfur attack, have been identified as Cr_2O_3. Therefore equipment will be added to further purify the helium used for these tests and, in particular, to decrease the oxygen content.

Tube-burst experiments were continued in the LITR, and this study[7] of the stress-rupture life of Inconel tubing in a helium atmosphere is to be extended. The specimens now being tested were fabricated from ART radiator tubing that was inspected by nondestructive testing methods. Three of these specimens stressed at 2000 psi in a helium atmosphere have been in the LITR at a temperature of 1500°F for more than 1000 hr and have not yet ruptured. The reactor was operated at full power for approximately 800 hr during this period. This test indicates a stress-rupture life that is considerably in excess of the 260-hr arithmetic-mean rupture life reported previously[7] for substandard tubing tested under the same conditions.

Further heat-transfer studies of the apparatus designed for stress-rupture life tests in a fused-salt fuel environment in the HB-3 facility of the LITR have shown that operation at 1500°F is now feasible. Inconel tubing will be tested in this apparatus in contact with the fuel mixture (No. 46) $NaF\text{-}ZrF_4\text{-}UF_4$ (62.5-12.5-25 mole %).

The electrical resistivity of Inconel as a function of temperature was studied in order to obtain data needed in connection with the design and operation of electromagnetic flowmeters. Resistivity measurements were made on six heats of Inconel at temperatures from 80 to 1600°F. A resistivity maximum was observed at approximately 900°F. The resistivity values obtained at temperatures below 900°F were found to be dependent upon the length of time the specimen was held at temperatures between 600 and 900°F. Holding the specimen in this temperature range resulted in increases in resistivity, with the maximum increase in resistivity of about 2% being obtained by holding the specimen in this temperature range for 24 hr. Above 900°F, the resistivity was not dependent on time or on rates of heating or cooling. The curves presented in Fig. 4.2.16 are typical of the resistivity behavior observed during these tests.

LITR VERTICAL IN-PILE LOOP

W. E. Browning
M. F. Osborne
H. E. Robertson

The modified pump for circulating fused-salt fuel in the vertical in-pile loop was filled with the

[5] On assignment from Pratt & Whitney Aircraft.

[6] W. W. Davis, N. E. Hinkle, and J. C. Wilson, *ANP Quar. Prog. Rep. March 10, 1956*, ORNL-2061, p 190.

[7] J. C. Wilson *et al.*, *ANP Quar. Prog. Rep. Sept. 10, 1956*, ORNL-2157, p 240.

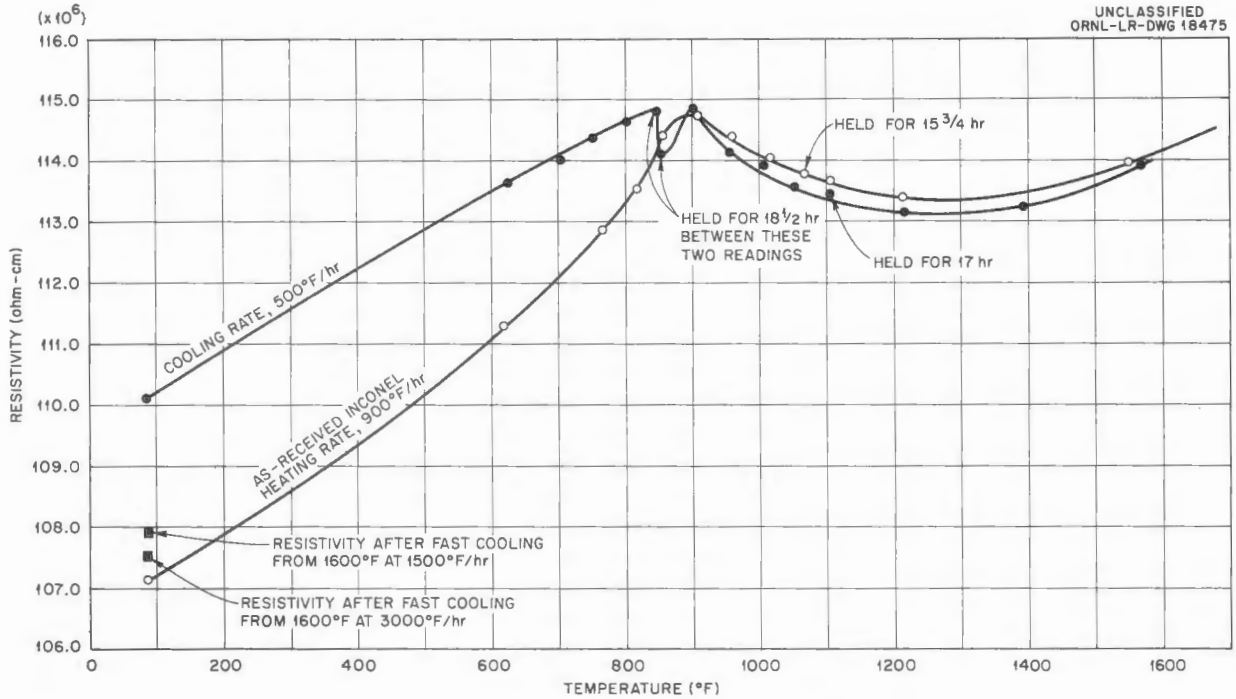

Fig. 4.2.16. Electrical Resistivity of Inconel as a Function of Temperature.

depleted fuel mixture (No. 30) $NaF-ZrF_4-UF_4$ (50-46-4 mole %) and was set up as a bench test in a loop mockup. This pump incorporates the modifications described previously,[8] and it has been operating quite satisfactorily for over 1700 hr. The loop in which this pump is operating is mechanically identical to the one being prepared for operation in the LITR, except that a somewhat shorter, but constricted, fuel circuit is used that provides the same resistance to flow. The pump has been running at a shaft speed of 2500 rpm and at a temperature of 1550 to 1580°F. There has been no perceptible change in its operation, except that the rotor turns somewhat more freely, as evidenced by a 10% increase in the length of time required to coast from 2500 to 500 rpm after the motor power is cut off. The successful operation of this pump indicates that there has been no significant condensation of ZrF_4 in critical areas, such as the region around the shaft at the Graphitar vapor baffle where the clearance is small. The high temperature in this region as a result of proximity to the fuel suppresses ZrF_4 condensation.

[8]W. E. Browning and D. E. Guss, *ANP Quar. Prog. Rep. Sept. 10, 1956*, ORNL-2157, p 245.

Loop No. 8 is now being assembled for operation in the LITR. The empty pump has been operated at room temperature, and the performance was found to be entirely normal. The fuel system has been welded and leak tested. Preparations are being made for filling the complete pump and loop assembly in a dry box. A system for individually controlling cooling air for the two legs of the loop has been adopted and tested. Essentially all the parts required for the assembly have been fabricated.

EFFECT OF RADIATION ON STATIC CORROSION OF STRUCTURAL MATERIALS BY FUSED SALTS

W. E. Browning
R. E. Adams H. L. Hemphill

Inconel Capsules Containing $NaF-ZrF_4-UF_4$

Irradiations of Inconel capsules filled with the fuel mixture (No. 44) $NaF-ZrF_4-UF_4$ (53.5-40-6.5 mole %) have been continued. Two capsules were irradiated for nine weeks at a power density of 6 kw/cm^3. Difficulties with the irradiation facility necessitated early withdrawal of two other capsules that had been irradiated for approximately

six weeks at 6 kw/cm^3. These capsules have not yet been examined.

Several leaks have occurred recently in the capsule irradiation facility in the MTR which resulted in water getting into the capsule cooling air. The leaks were caused by movement of the capsule-containing tubes in the reactor cooling water stream. Evolutionary changes in reactor operating conditions have increased this problem, and facility design modifications are therefore being prepared.

Three irradiated and four control capsules were opened and analyzed chemically and metallographically.[9] All these Inconel capsules had normal test histories and exhibited 1 mil or less corrosion, except irradiated capsules Nos. 2 and 3. The operating conditions and results of these tests are given in Table 4.2.2. Metallographic sections of these capsules are shown in Figs. 4.2.17 through 4.2.23.

Capsule No. 2 had one temperature excursion to 1600°F that lasted for 5 min, and it was cooled to below the freezing point of the fuel five times. Compared with histories of other capsules, the high-temperature excursion was somewhat unusual, but the number of low-temperature excursions was below average. All other phases of the operating history of this capsule were normal. Corrosion of this capsule was, however, slightly above normal.

Capsule No. 3 was subjected to a number of unusual conditions. Reactor operation was normal and the capsule was returned to ORNL in good condition, but, during preparation of the capsule for analysis, it was bent. The bend was concentrated near the midpoint of the test specimen. The capsule was straightened and specimen preparation was continued, but some distortion probably remained, which resulted in scoring of the wall of the capsule during drilling and, consequently, in high chromium, iron, and nickel contents of the fuel sample. The apparent depth of penetration may also be the result of the flexing of the capsule. Subsurface voids of submicroscopic dimensions may have been opened up and made visible as a result of the stresses created by the flexing. These observations are presumptive, and evaluation and interpretation studies of the data are to be continued.

[9] A. E. Richt and R. M. Wallace, *Metallographic Examination of Static Corrosion Capsules*, ORNL CF-56-10-96 (Oct. 23, 1956).

TABLE 4.2.2. OPERATING CONDITIONS AND RESULTS OF IN-PILE AND CONTROL STATIC-CORROSION TESTS OF INCONEL CAPSULES CONTAINING NaF-ZrF$_4$-UF$_4$

Capsule No.	Uranium Content of Fuel	Irradiation Time at 1500°F (hr)	Power Density* (w/cm^3)	Number of Excursions Below Melting Point of Fuel	Excursions Above 1500°F	Metallographic Results: Depth of Attack (mils)	Metallographic Results: Distribution of Attack	Impurities in Fuel After Test (ppm): Cr	Ni	Fe
				Irradiated Capsules						
1	2 mole % UF$_4$	918	1400	28	None	1	Uniform	175	3692	873
2	4 mole % UF$_4$	378	3600	5	5 min at 1600°F	4	Uniform	121	2909	491
3	4 mole % UF$_4$	623	3600	10	None	8	Heavy at highest temperature region of capsule	**	**	**
				Heat-Treated Unirradiated Control Capsule						
4	4 mole % UF$_4$	776		9	None	1	Uniform			
5	2 mole % UF$_4$	290		4	1 min at 1670°F 30 sec at 1612°F	1	Uniform	75	593	223
6	2 mole % UF$_3$	239		3	30 sec at 1650°F 30 sec at 1577°F 3 sec at 1550°F	1	Uniform			
7	2 mole % UF$_4$	295			1 min at 1543°F 1 min at 1522°F 1 min at 1512°F	1	Uniform			

*For reactor operation at 40 Mw.

**Analytical sample contaminated by Inconel during fuel removal.

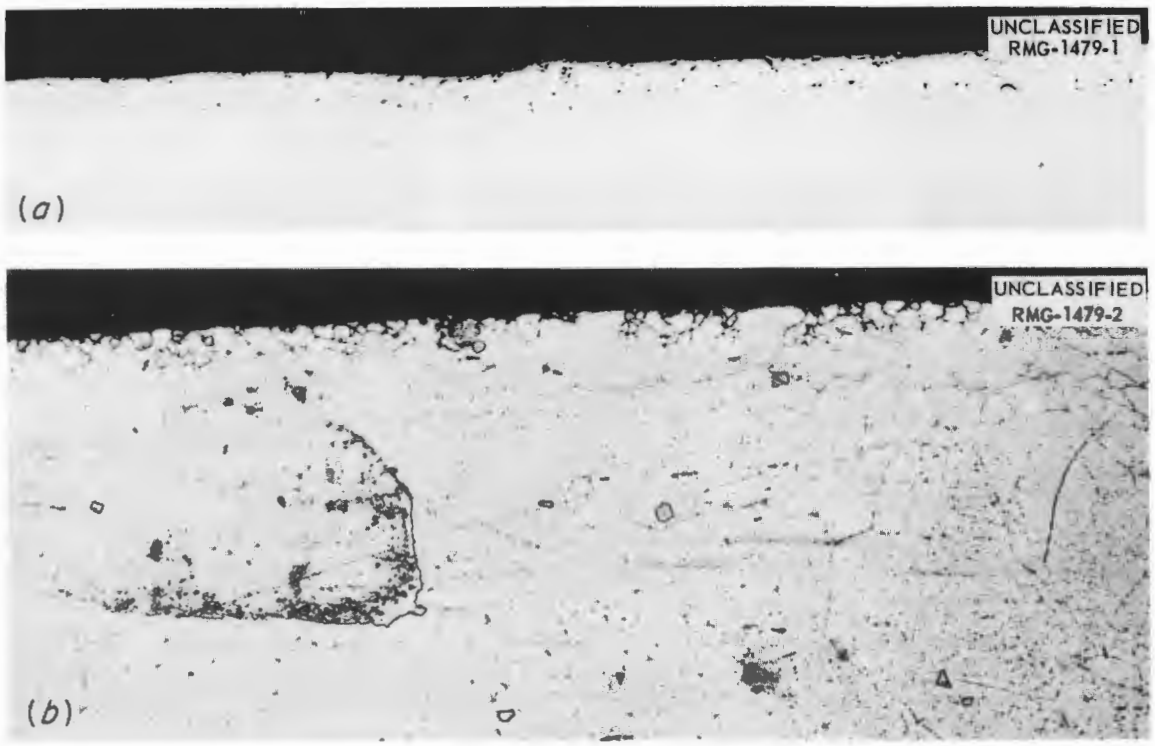

Fig. 4.2.17. Metallographic Sections of Irradiated Inconel Capsule No. 1. (*a*) Unetched. (*b*) Etched. 250X.

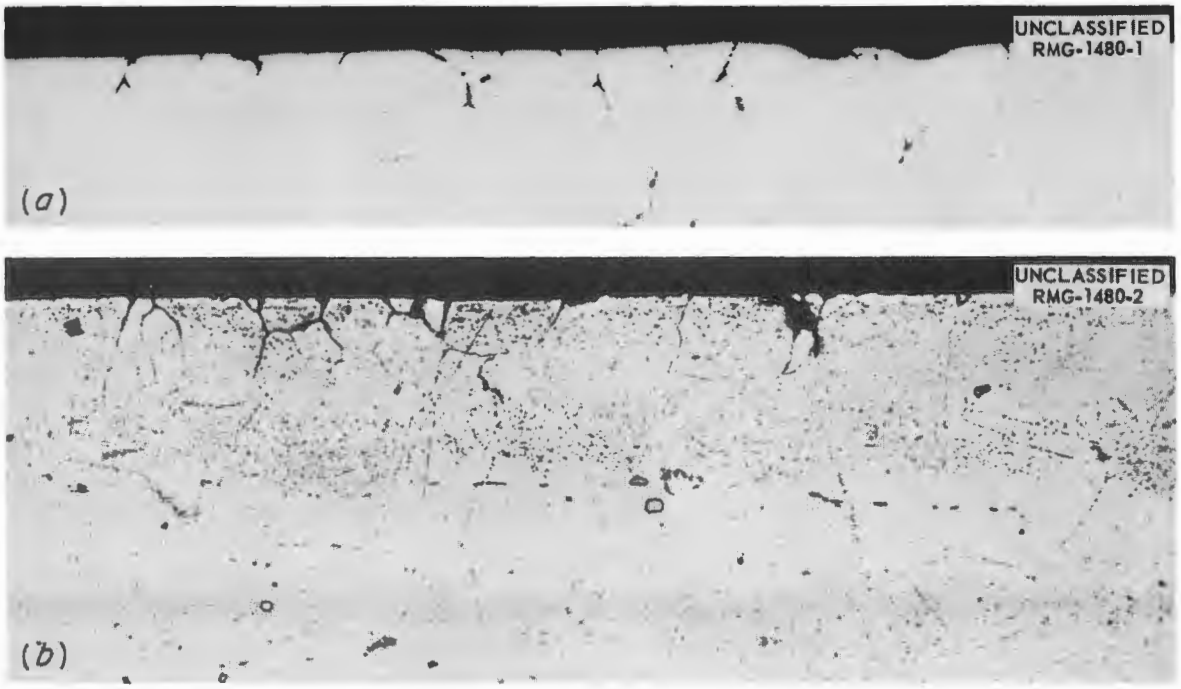

Fig. 4.2.18. Metallographic Sections of Irradiated Inconel Capsule No. 2. (*a*) Unetched. (*b*) Etched. 250X.

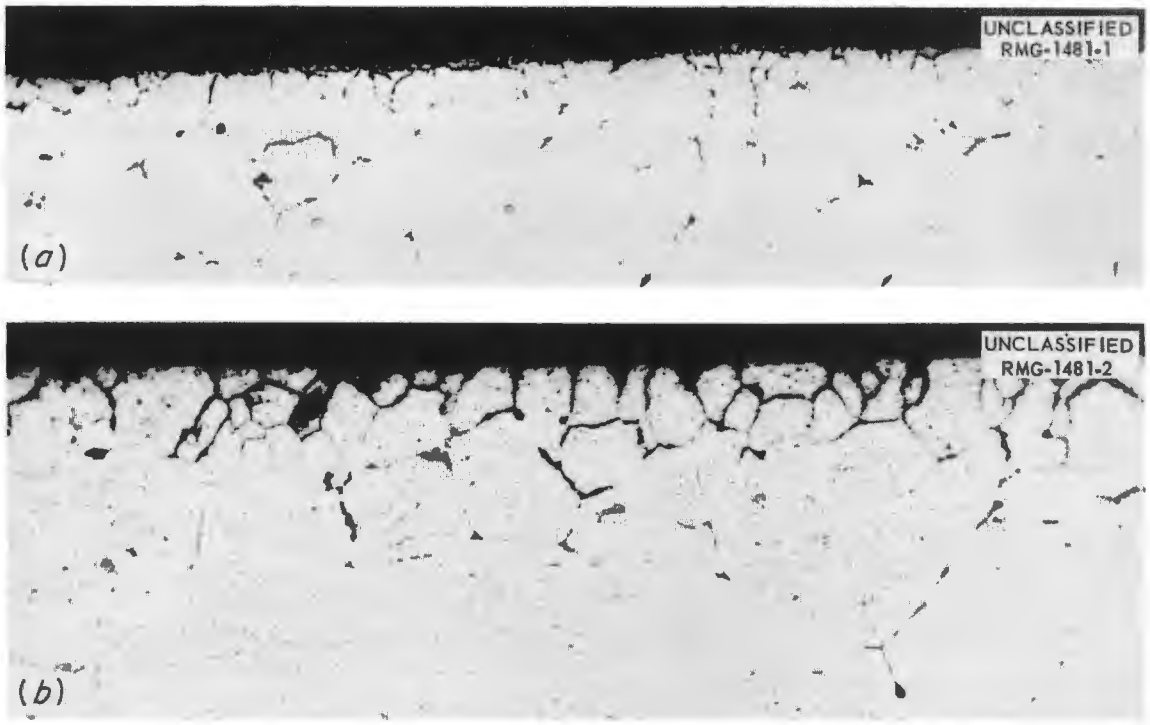

Fig. 4.2.19. Metallographic Sections of Irradiated Inconel Capsule No. 3. (*a*) Unetched. (*b*) Etched. 250X.

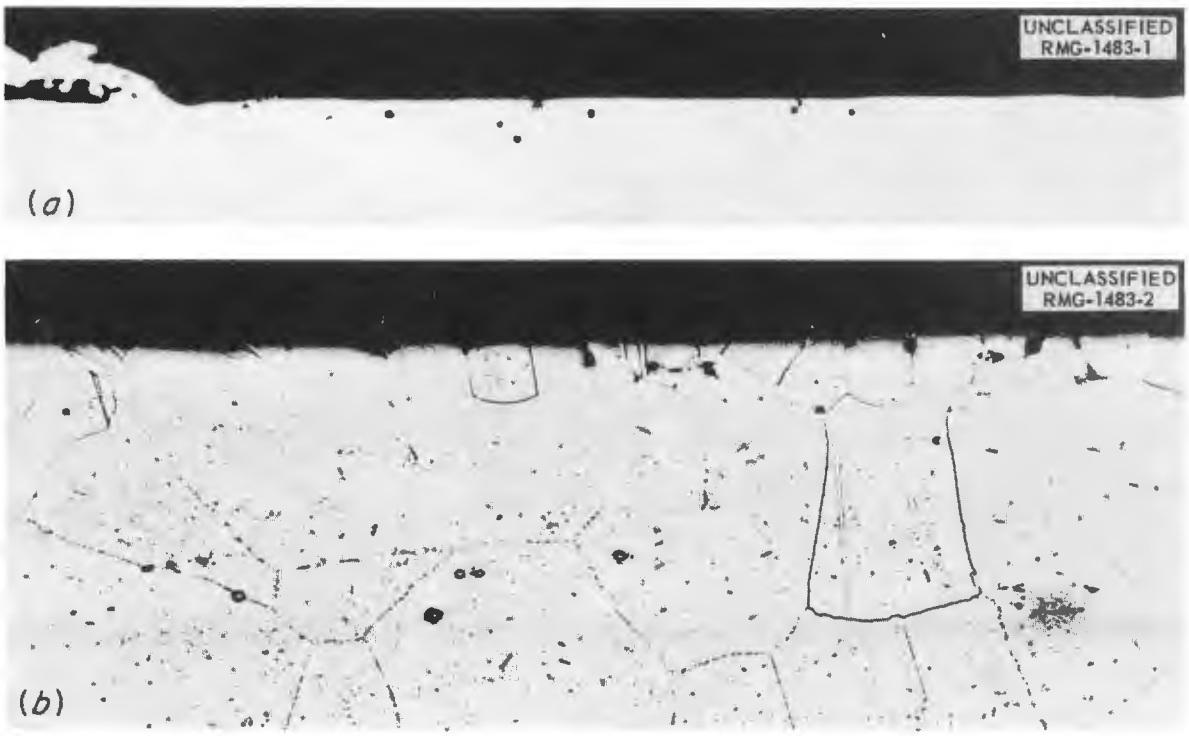

Fig. 4.2.20. Metallographic Sections of Unirradiated Inconel Capsule No. 4. (*a*) Unetched. (*b*) Etched. 250X.

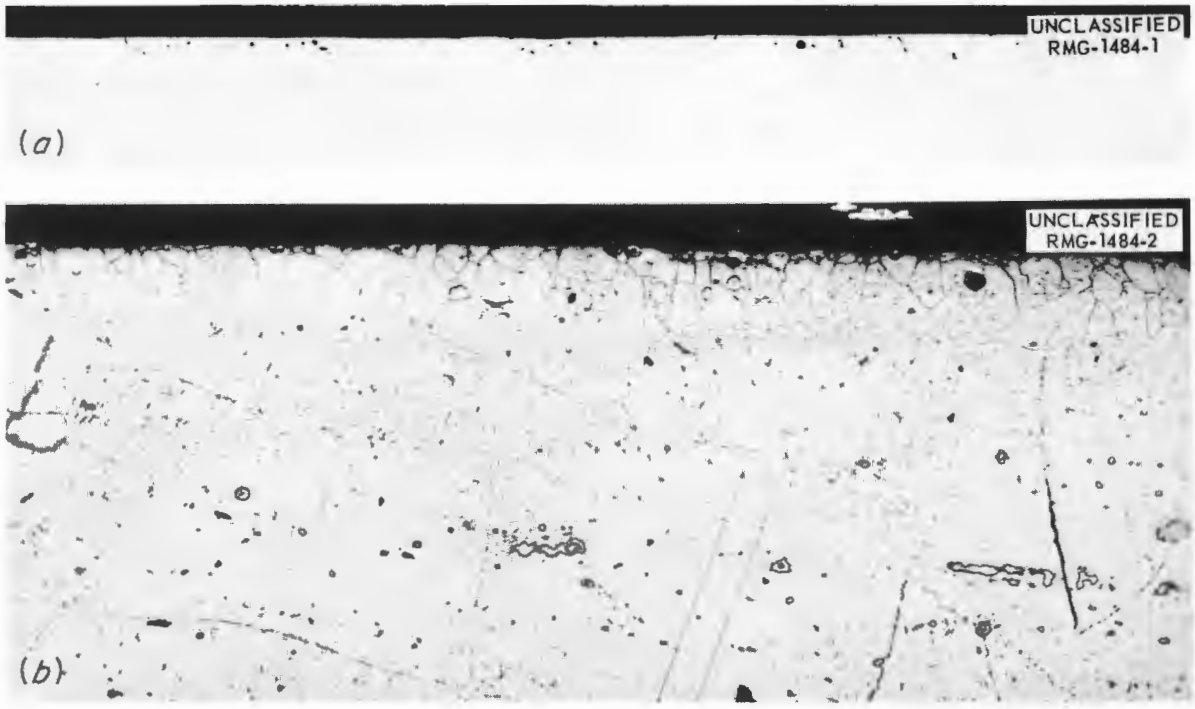

Fig. 4.2.21. Metallographic Sections of Unirradiated Inconel Capsule No. 5. (*a*) Unetched. (*b*) Etched. 250X.

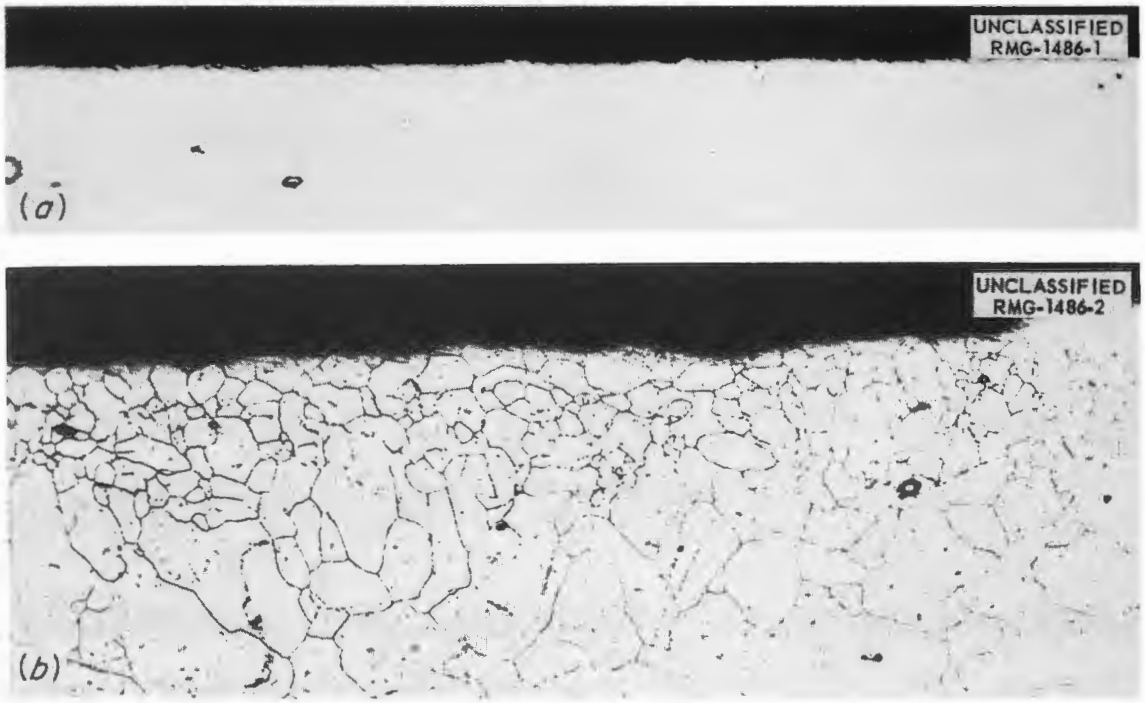

Fig. 4.2.22. Metallographic Sections of Unirradiated Inconel Capsule No. 6. (*a*) Unetched. (*b*) Etched. 250X.

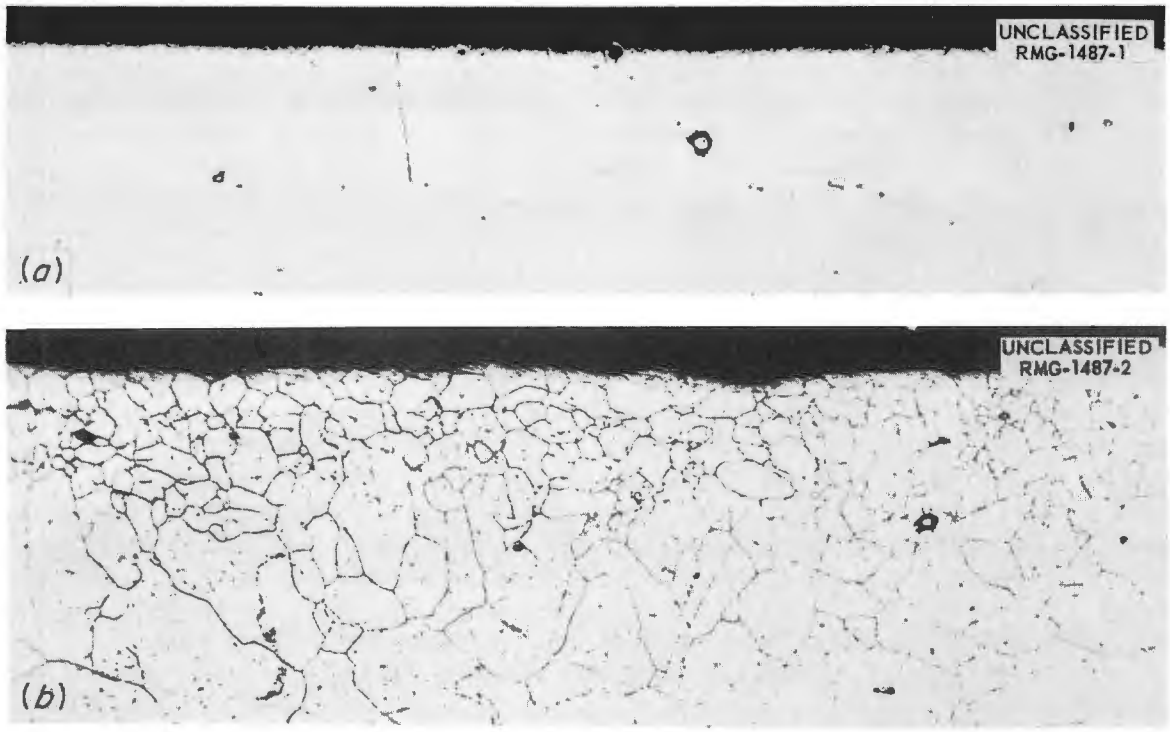

Fig. 4.2.23. Metallographic Sections of Unirradiated Inconel Capsule No. 7. (*a*) Unetched. (*b*) Etched. 250X.

Hastelloy B Capsules Containing $NaF\text{-}KF\text{-}LiF\text{-}UF_4$

Corrosion capsules made of Hastelloy B are being prepared for irradiation in the MTR. Hastelloy B corrodes in air at high temperatures,[10] and therefore the outer surfaces of the capsules must be protected during irradiation, since it is possible that the oxidation could become catastrophic and result in fission-product release.

Electroplating of the outer surfaces with nickel and then chromium provides a coating which forms a protective oxide that is permanent at all temperatures up to 1500°F. Specimens plated with 0.0001 in. of chromium over 0.001 in. of nickel and then heated to 1500°F showed no sign of spalling of the oxide coating after 255 hr. Other specimens plated in the same manner, heated in a static atmosphere to 1500°F, and thermally cycled to room temperature twice daily showed no signs of deep oxidation after 800 hr. Other plated specimens were electrically heated to 1500°F in a stream of air flowing through a 0.050-in. annulus at about 300 fps and thermally cycled to room temperature twice daily. These specimens showed no signs of breakdown of the oxide coating after 500 hr. This latter test simulated MTR capsule irradiation conditions. These data indicate that plated Hastelloy B capsules may be irradiated in the MTR without endangering reactor operations.

Two Hastelloy B capsules filled with the fuel mixture $NaF\text{-}KF\text{-}LiF\text{-}UF_4$ containing sufficient uranium to give a power density of 6000 w/cm^3 in the MTR are ready for irradiation. A glass-wool filter was placed in the off-gas line to provide extra protection by assuring that no loose radioactive oxide scale will enter the off-gas line.

INVESTIGATION OF REPRODUCIBILITY OF CHEMICAL ANALYSES OF LOOP AND CAPSULE FUELS

R. P. Shields R. E. Adams

Comparison of Analytical Results

An investigation is being made of the reproducibility which can be expected when many

[10] H. Inouye, M. D'Amore, and T. K. Roche, *Nickel Base Alloys for High Temperature Service*, ORNL CF-56-4-121 (April 16, 1956).

analyses of the same fuel mixture are made. The results obtained thus far have not been encouraging, and the poor reproducibility is thought to be partially attributable to the rather small samples submitted and to the difficulty encountered in dissolving the fuel. Because of the radioactivity of samples from in-pile loops and capsules the samples must remain small. In the case of the capsules, the size of the sample must remain small because the total available fuel is in the range of 300 to 400 mg. In order to evaluate the results of analyses, 17 samples of the same fuel were sent, one at a time, to three analytical facilities. The results are presented in Table 4.2.3. The methods used in analyzing for the various constituents of the fuel are outlined in Table 4.2.4.

Several steps are being considered for improving the analytical results. Each method used for the analyses is being reviewed in terms of reproducibility. Efforts will be made to submit for analysis as large a sample as can be handled both from standpoint of solubility and intensity of radiation. A sample of the original fuel will be submitted with each irradiated sample, and the two samples will be carried through the analytical procedure together. A further step that may be necessary will be the development of a technique whereby large amounts of dissolved fuel will be put onto a resin column so that the individual element of interest can be separated and concentrated before analysis.

Effect of Radiation on Analyses

Studies of the effect of radiation on analyses for iron, chromium, and nickel have been initiated. A series of experiments has been run in which the diphenylcarbazide method was used for the

TABLE 4.2.3. RESULTS OF INDEPENDENT ANALYSES AT THREE FACILITIES OF 17 SAMPLES OF ONE BATCH OF FUEL

Sample Code	Amount of Sample (mg)	Major Constituents (wt %)				Minor Constituents (ppm)		
		U	Na	Zr	F	Fe	Cr	Ni
			Facility No. 1					
A6-C-1a	287	17.55	13.81	25.34	33.29	82	30	10
-2a	269	17.98	12.73	26.05	29.42	370**	10	36
-3a	274	18.51*	14.90	24.70*	30.43	180	90	80
-4a	227	19.03	14.95	26.80	31.38	230	140	120
-5a	276	18.01**	13.99	24.33	31.34	25	78	10
-6a	233	18.07**	14.25	24.74*	32.41	45	120*	10
-8a	267	18.33	13.97	31.89	32.67	69	47	10
			Facility No. 2					
A6-C-1b	324	17.90	14.00	25.3	28.95	1200	800	500
-2b	257	18.55	13.99	32.64	27.13	25	1300	75
-3b	206	17.88	14.38	37.50	28.61	1400	0	380
-4b	270	16.9	12.50	35.00	26.00	3500	0	780
-5b	241	17.97	14.62	37.19	25.56	200	0	130
-8b	245	17.75	14.62	29.10	26.78	500	0	0
			Facility No. 3					
A6-C-1c	267	15.7	16.7	26.8	40.4	150	265	110
-2c		18.7	15.6	26.5	40.7	120	280	165
-3c		18.6	16.8	27.1	41.0	65	235	125
-4c		18.5	15.0	26.7	40.3	70	225	120

*Two identical answers received.

**Average of two answers.

TABLE 4.2.4. METHODS USED FOR ANALYZING FUEL MIXTURES

Constituent	Analytical Methods		
	At Facility No. 1	At Facility No. 2	At Facility No. 3
U	Potentiometry	Potentiometry	Jones reductor–ceric sulfate titration
Na	Flame photometry	Flame photometry	Ion exchange on Dowex-1 resin and subsequent titration of hydroxide released
Zr	Colorimetry; reagent, Thoron	Colorimetry; reagent, Thoron	Gravimetric, mandelic acid precipitate ignited to ZrO_2
Fe	Colorimetry; reagent, *o*-phenanthroline	Colorimetry; reagent, *o*-phenanthroline	Colorimetry; reagent, *o*-phenanthroline
Cr	Colorimetry; reagent, diphenylcorbazide	Coulometric titrimetry	Colorimetry; reagent, diphenylcarbazide
Ni	Colorimetry; reagent, dimethylglyoxime	Polarography	Colorimetry; reagent, dimethylglyoxime
F	Pyrohydrolysis	Pyrohydrolysis	Pyrohydrolysis

determination of chromium. The standard chromium solution was oxidized in the usual way with sodium bismuthate and centrifuged to remove excess bismuthate. The chromate was then complexed with diphenylcarbazide. Two samples were put into the absorption cells of a Beekman spectrophotometer, and a piece of irradiated palladium metal was hung on one side of one sample container. This source gave a 0.961-Mev beta ray from Pd^{109} and 1.04, 0.7, and 0.8-Mev beta rays from Ag^{111}. The instrument was set to zero absorption by using a blank with every reagent except the dye, and the absorption curves showed increasing divergence with time, as shown in Fig. 4.2.24. The effect of one source in the absorption cell is also compared in Fig. 4.2.24 with the effect of adding a second source of equal intensity in the same cell. The radiation does affect the analysis to a degree that depends on the amount of radiation absorbed. A ferrous sulfate actinometer was used to establish the amount of energy absorbed in the absorption cell, and the result showed that analyses made by the diphenylcarbazide method will be low by 4.9 atoms of chromium per 100 ev of radiation energy absorbed.

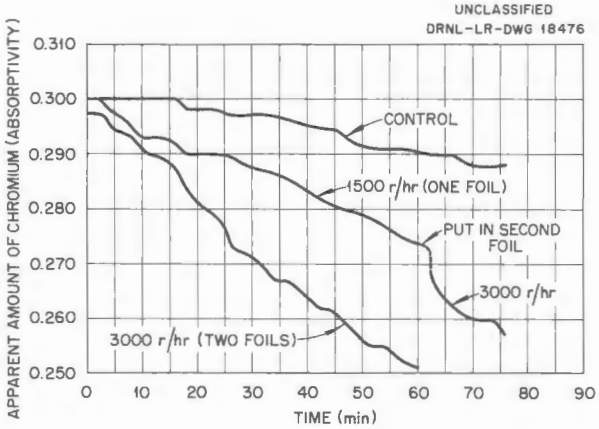

Fig. 4.2.24. Effect of Beta Radiation on Chromium Analysis by the Diphenylcarbazide Method.

The radiation effects on the diphenylcarbazide method, expressed in the terms more generally used, are summarized in Table 4.2.5, which gives the error that would be made if a sample containing 20 μg of chromium were analyzed under the conditions shown in Fig. 4.2.24.

Brief fluctuations in absorption, probably caused by circulation effects in the cell, make it difficult

TABLE 4.2.5. RADIATION EFFECTS ON DETERMINATION OF CHROMIUM BY DIPHENYLCARBAZIDE METHOD

Time After Adding Diphenylcarbazide (min)	Error in Chromium Analysis	
	μg	%
Beta-Ray Dose Rate of 1500 r/hr		
10	0.53	2.6
30	0.67	3.3
60	1.77	8.8
Beta-Ray Dose Rate of 3000 r/hr		
10	0.60	3
30	1.60	8
60	2.6	13

to compare the results of the two experiments at specific times. Further experiments will be run to obtain smoother curves with which to check the effect of concentrations and the effect of radiation on iron and nickel analyses.

FAST-NEUTRON DETECTORS

D. Binder J. F. Krause[5]

Neutron flux measurements in hole 51 of the ORNL graphite reactor were made with the fissionable isotopes Pu^{239}, Np^{237}, and U^{238} by using the method of Hurst *et al.*[11] The isotopes were enclosed in a shield containing 1.5 g of B^{10}/cm^2, which made the effective threshold for fission for Pu^{239} about 1 kev. The effective thresholds for Np^{237} and U^{238} are 0.6 and 1.5 Mev. The fission yields for Pu^{239}, Np^{237}, and U^{238} thus give a measure of the neutron fluxes at energies above 1 kev, 600 kev, and 1.5 Mev, respectively. The fission yield was measured by monitoring the fission-fragment gamma rays at energies above 1.2 Mev with a scintillation spectrometer. The counting rate at a fixed time (2 hr) after 10 min of irradiation in hole 51 was compared with the counting rate of a Pu^{239} foil irradiated in a known thermal flux. Since the relevant cross sections are known, the neutron flux in hole 51 could then be computed.

Hole 51 contains a "donut"-shaped enriched-uranium converter about 11 in. long. Measurements were made in the middle of the donut and 17 in. away from it where the effect of the donut is negligible. The measurement 17 in. from the donut is a measure of the normal reactor flux, while the measurement in the donut is a measure of the reactor flux plus a fission spectrum. The difference should give the known fission spectrum. Several measurements taken inside and outside the donut are summarized in Table 4.2.6.

The differences listed in Table 4.2.6 are in the ratio of 1:0.8:0.7, while the theoretical fission spectrum ratios are 1:0.84:0.52. The discrepancy for the last number is outside the error band, and thus it may be that the U^{238} detector (>1.5 Mev) has a large photofission component.

The reactor spectrum outside the donut contains a surprisingly small flux at energies above 1 kev compared with that at energies above 600 kev. The ratio is only 2:1, which is the ratio that would be expected if the effective threshold for Pu^{239} were much higher, say, between 10 and 100 kev. The ratio was checked by a measurement in a hole without a donut, hole 10, and was found to be the same, within the error band in Table 4.2.6. It is possible that the large B^{10} shield depresses the flux in the kev region. The test applied with the

[11] G. S. Hurst *et al.*, *Rev. Sci. Instr.* 27, 153 (1956).

TABLE 4.2.6. MEASUREMENTS OF NEUTRON FLUX IN HOLE 51 OF THE ORNL GRAPHITE REACTOR

Measurement	Neutron Flux ($nv \times 10^{-11}$)		
	Above 1 kev	Above 600 kev	Above 1.5 Mev
Inside donut	4.1 ± 0.2	2.7 ± 0.1	2.0 ± 0.2
Outside donut	1.8 ± 0.2	0.9 ± 0.1	0.42 ± 0.01
Difference	2.3 ± 0.3	1.8 ± 0.1	1.6 ± 0.2

donut is insensitive to the shield effect, since very little of the fission spectrum is in the 1- to 100-kev region.

Although the Pu^{239} threshold may have been higher than 1 kev, it is useful to have a comparison of the flux measurements with a solid-state reaction inside and outside the donut. The solid-state reaction chosen was the n to p transition in n-type germanium, which is probably 10 times as sensitive to 10-kev neutrons as 1-kev neutrons, and therefore the Pu^{239} detector was probably measuring the most important part of the flux. The flux at energies above 600 kev increased by a factor of 3 just inside the donut. The flux at energies above 1 kev increased by a factor of 2, but most of this increase was due to the flux at energies above 600 kev. In the 1-kev to 600-kev range the flux increased by only 30%. The germanium effect also increased by a factor of three, and thus the flux at energies above 600 kev is important in the study of radiation effects in germanium.

EFFECTS OF RADIATION ON ELECTRONIC COMPONENTS

J. C. Pigg

O. L. Curtis C. C. Robinson
O. E. Schow

Effect of Irradiation on Minority Carrier Lifetime

A circuit, Fig. 4.2.25, has been constructed with which to measure the lifetime of holes injected in p-type germanium. In the circuit an open delay line is charged to a selected voltage and then discharged across a variable resistor which can be set to adjust the output to the characteristic impedance of the line.

A constant current is supplied to the sample from a high-impedance-current source. When the injecting pulse is applied to the contact, a negative pulse from a power amplifier is applied to the high-voltage end of the sample. Thus the injecting contact is positive with respect to both ends of the sample during the injection pulse.

The measurements made with this circuit depend on the fact that the change of conductivity resulting from an injecting pulse decays with a time constant equal to the lifetime of the injected carriers.[12] The bridge type of circuit prevents the large amplitude injection pulse from overloading the oscilloscope. In this way, shorter lifetimes can be measured than could be measured with diode clipping circuits.

The minority-carrier lifetime can be determined in junction devices from the decay of the voltage at the barrier following a large amplitude injection pulse. In this case, the decay is linear, and the slope[13] is equal to $kT/q\tau$, where k is Boltzmann's constant, T is the absolute temperature, q is the electronic charge, and τ is the minority-carrier lifetime. It has been shown that this measuring technique can be applied to surface barriers, if the injection ratio is nearly unity.[14] Surface barriers may be prepared on bulk germanium samples by applying silver paste to a well-etched surface. Lifetimes determined by using the decay across the surface barriers agree with those determined by the first method described for measuring lifetime.

One high-resistivity (47 ohm-cm, n-type) germanium sample, from The Eagle-Picher Company, was tested for hole lifetime. It was not, however, used for irradiation experiments, because its hole lifetime was rather low (50 μsec). Some more suitable germanium was then obtained from Purdue University; the first sample (Sb-28A-1) showed a hole lifetime of 400 μsec. The sample was then irradiated at the center of the ORNL Graphite Reactor for 1 min, and the resistivity was found to have increased from 7 to about 40 ohm-cm.

The hole-injecting contact used for this sample was soldered, and it no longer injected after the irradiation. Upon removing the contact, etching the sample surface, and placing another soldered hole-injecting contact on the sample, the sample was found to have the same resistivity, within experimental error, as it had before irradiation. Therefore, it was concluded that no annealing had taken place. The hole lifetime was then measured as 3.0 μsec. (It is possible that the material was p-type and was annealed to n-type of about the same resistivity during the soldering process.)

The sample was again irradiated for 1 min in hole 51 of the ORNL Graphite Reactor. Following the irradiation, the sample had a resistivity of 33.6 ohm-cm, and it therefore was p-type. Again the contact would not inject after the irradiation,

[12] D. Navon, R. Bray, and H. Y. Fan, *Proc. I.R.E.* **40**, 1342–1347 (1952).

[13] B. R. Gossick, *J. Appl. Phys.* **26**, 1356–1365 (1955).

[14] B. R. Gossick, *J. Appl. Phys.* **27**, 905–911 (1956).

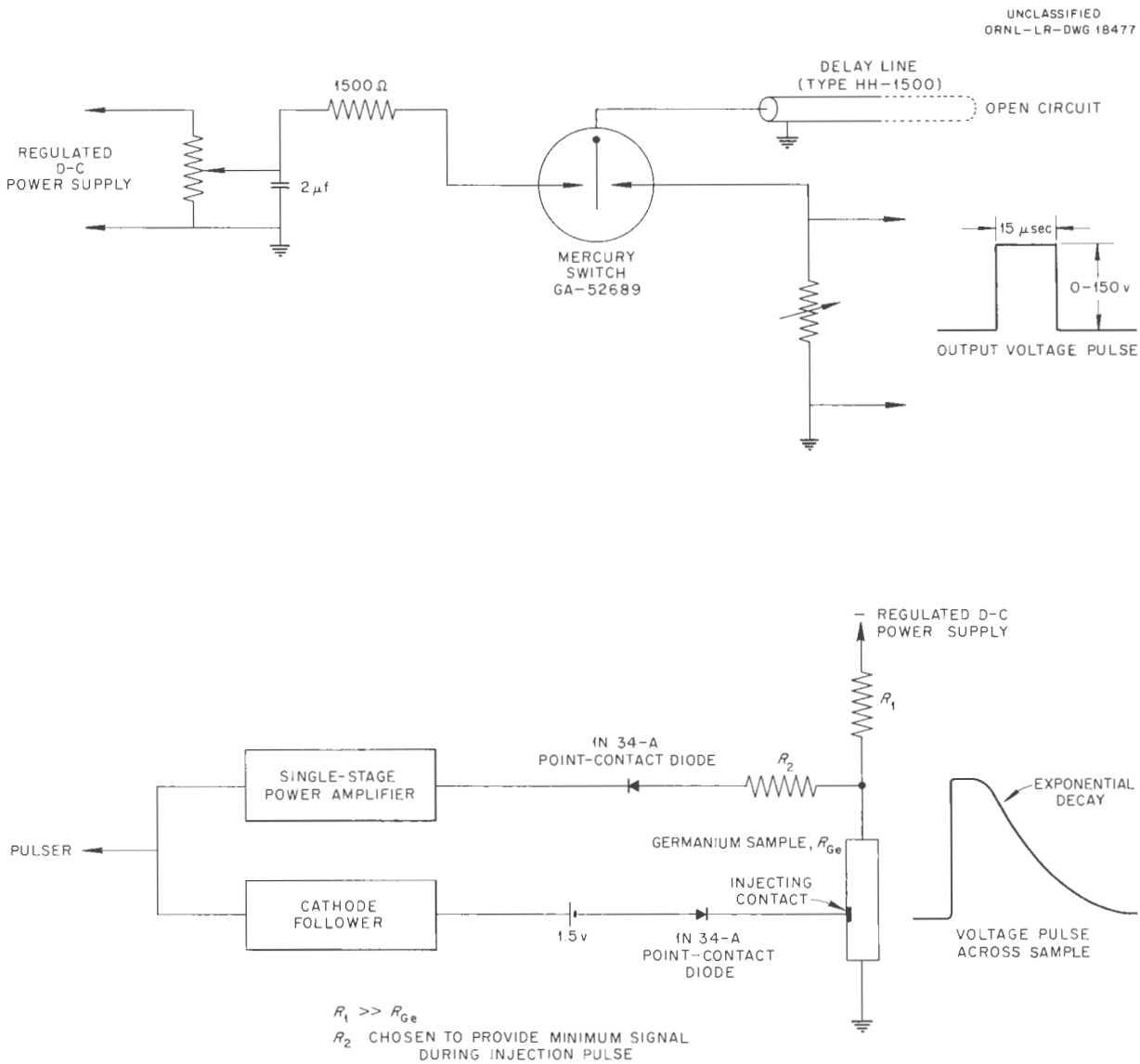

Fig. 4.2.25. Circuit for Measuring the Lifetime of Holes Injected in *p*-Type Germanium.

and therefore it was removed, without heat, the surface was etched, and a silver-paste contact was applied. The sample rectified as *p*-type material, and no success was achieved in measuring the electron lifetime.

The sample was then annealed at 96°C for 3 hr, and the resistivity was found to be 34.3 ohm-cm, which would seem to indicate very slight annealing. However, contacts made on the surface consistently indicated *n*-type, and the second method of measurement described above showed a hole lifetime of 3 μsec. Light etching did not change the properties of the contacts, but one of the 11 contacts indicated *p*-type material. It now seems possible that there was an *n*-type surface layer on the *p*-type material. The annealing was carried on in the presence of water vapor.

Twenty-five days later the sample was annealed at 115°C for 6.4 hr, and the resistivity was found to be 35.8 ohm-cm. At this time all contacts on the surface rectified as *p*-type, even after heavy etching. The annealing was done in the presence of air.

Another sample, Sb-28A-2, which was cut from the same portion of the Purdue ingot as sample Sb-28A-1 was cut, also gave a hole lifetime of about 400 μsec (412 μsec, in this case). This sample was irradiated to an integrated flux of 5×10^{13} nvt. As the result of this irradiation, the resistivity of the sample changed from 7.3 ohm-cm to 14.3 ohm-cm, and the hole lifetime dropped from 412 μsec to 3.5 μsec.

Sample Sb-28A-3, also from the same portion of the ingot, was then prepared, and especial care was taken to keep the surface recombination low. No leads were attached except to the ends of the sample, and a small hole-injecting contact was used. The increased lifetime of 1010 μsec measured for this sample showed the importance of surface preparation.

After irradiation to an integrated flux of about 10^{10} nvt, the hole lifetime dropped to 404 μsec. Since the original carrier concentration was about 3×10^{14} carriers/cm^3, it may be seen that with a change in carrier concentration of a factor of about 10^{-4}, the hole lifetime was changed by more than a factor of 2 on the basis of 3.2 carriers removed per incident neutron. A subsequent irradiation of the same magnitude also reduced the lifetime by a factor of 2.

Effect of Barrier Field on Annealing

Evidence which indicated the presence of an effect of the electric field created by the barrier in a semiconductor device on the annealing rate or radiation damage was discussed in a previous report,[15] and an experiment has been performed in an attempt to obtain more quantitative information on the observed effect. Three 1N 38-A germanium point-contact diodes were exposed for 5 min in hole 51N of the ORNL Graphite Reactor. The samples were chosen to have similar rectifier characteristics. After irradiation, it was noted that, in each case, the forward current at 0.7 v had decreased by about one order of magnitude. The samples were stored at room temperature, as in the previous case.

One sample was maintained at a 0.7-v forward bias; the second sample was open circuited; and the third sample was held at 1.5-v reverse bias. At 1-min intervals the current was read at a 0.7-v forward bias. The results are shown in Fig. 4.2.26 as annealing time vs forward current. Since only crude temperature control was provided by immersing the samples in a Dewar flask filled with Silicone oil, there were temperature variations of several degrees during the annealing period as a result of temperature variations. The exponential relationship between temperature and carrier concentration can account for the fluctuations in the observed currents.

All three samples behaved in the same manner. The only systematic change is attributable to radioactive decay of Ge^{70} to Ga^{70}. No annealing of any kind can be observed in Fig. 4.2.26. Therefore additional investigations will be necessary to determine the effect of the barrier field on the annealing rate.

It was noted after the experiment had been performed that the batch of units from which the samples had been chosen were covered with protective grease. Whether such grease was present in the units tested and, if it were, whether it was the same type of grease as that on the remaining units cannot now be determined. The charge-generation-center theory predicts that the saturation current will be sensitive to surface conditions. The surface condition is strongly dependent on the presence or absence of grease, as well as on the type of grease.

Effect of Radiation on Barrier Properties

A series of 1N 91 germanium junction diodes was exposed in the ORNL Graphite Reactor. The behavior of the forward-to-back current at a 0.5-v bias is shown in Fig. 4.2.27. The general shapes of the curves are similar to those observed for point-contact diodes, particularly in the case of the forward current. The reverse current shows the general destruction of the barrier, as observed in the point-contact units; however, the sample does not reach the condition of ohmic conduction after the minimum in the forward current is passed, as is the case for the point-contact unit. These units maintain a rectification ratio of 1.5:1 after passing the minimum in the forward current. This rectification is observed for exposures as high as 2×10^{17} nvt.

The humps in the reverse current curve are believed to be real. The current measurements are reliable to ±1%. The flux is not known to this degree of precision, but the relative value of the flux during the run is well calibrated. The

[15] J. C. Pigg and C. C. Robinson, *ANP Quar. Prog. Rep. Sept. 10, 1956*, ORNL-2157, p 254.

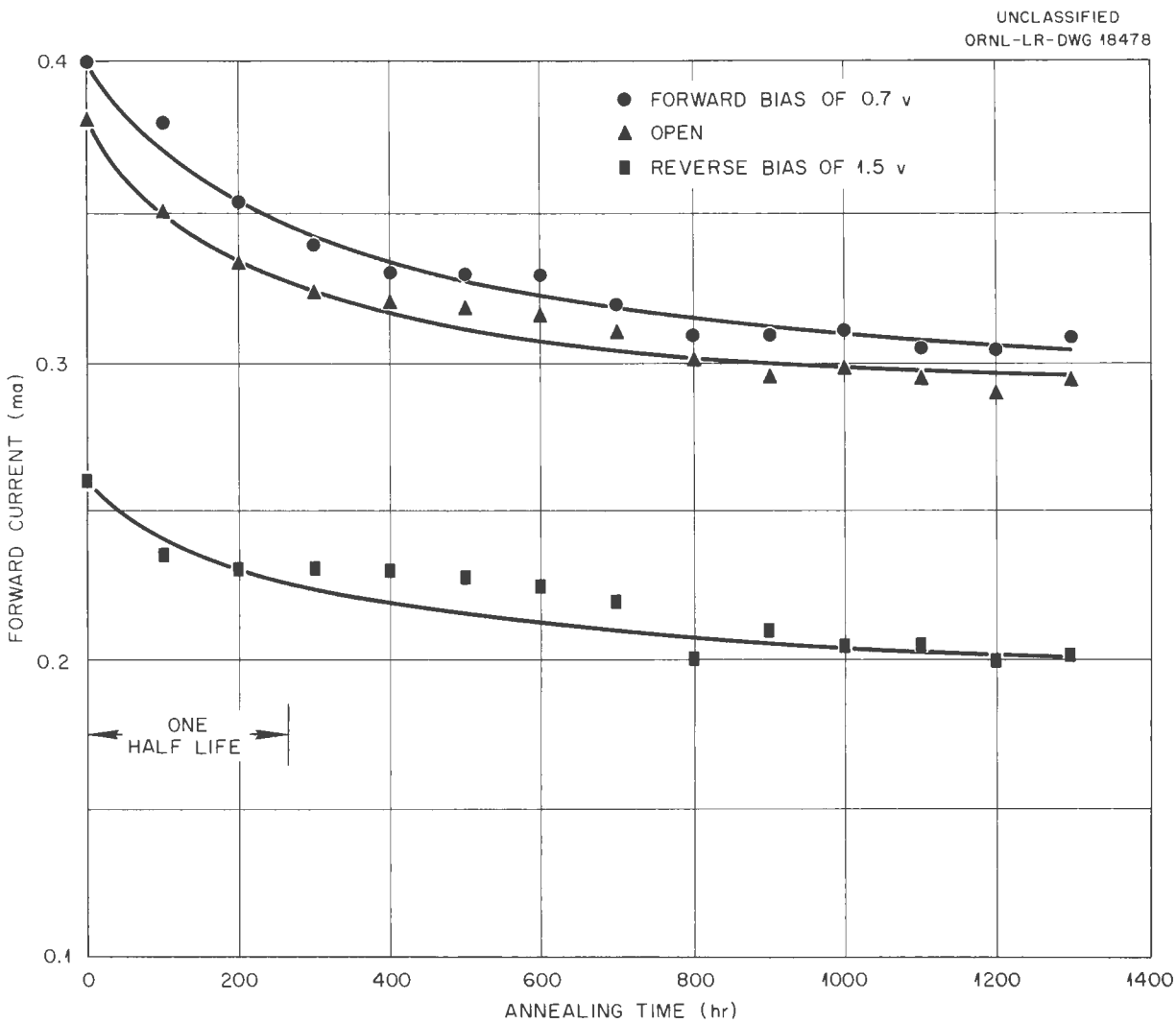

Fig. 4.2.26. Annealing of 1N 38-A Germanium Point-Contact Diodes as a Function of Bias-Voltage Current Read at a 0.7-v Forward Bias.

flux error in the readings would be primarily due to errors in timing. Since the time difference between readings is of the order of minutes, the relative value of nvt should also be good to a few per cent.

The initial change in current with irradiation was previously[16] found to be a function of the bias voltage at which the current reading is made. The rate of change of the current with respect to the reactor exposure as a function of bias voltage is shown in Fig. 4.2.28. These data are in agreement with the results reported previously.[15] Since the data in ref 15 were taken from a point-contact diode, Fig. 4.2.28 can be considered to be the behavior of the barrier under irradiation. There is an indication of a degree of symmetry in the region between +1.0 and −1.0 v. This region is probably primarily controlled by barrier properties. Values at larger reverse biases reflect the increase in surface leakage. The rate of change of current with exposure in the forward region shows a definite break where the effects of injection, lifetime, and

[16] J. C. Pigg, *Solid State Semiann. Feb. 28, 1954*, ORNL-1677, p 52.

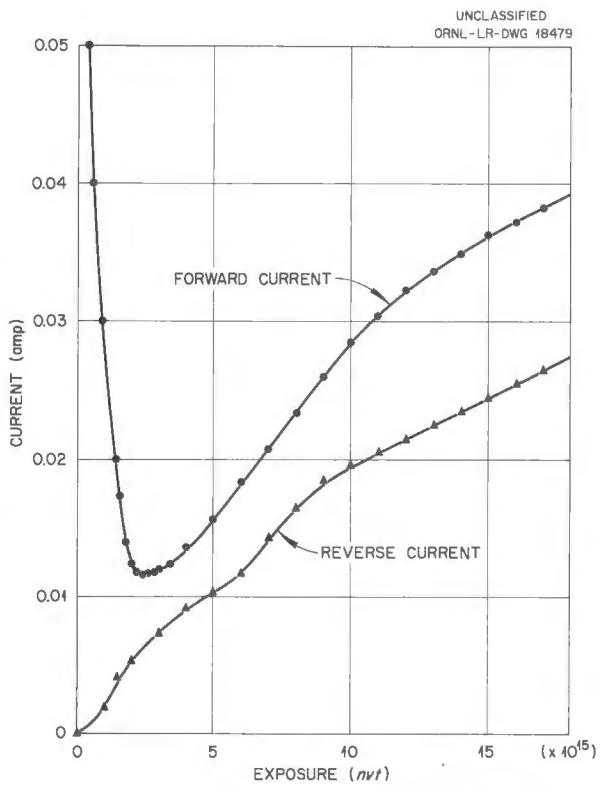

Fig. 4.2.27. Effect of Radiation on the 1N 91-2 Germanium Junction Diode Current Read at a 0.5-v Bias.

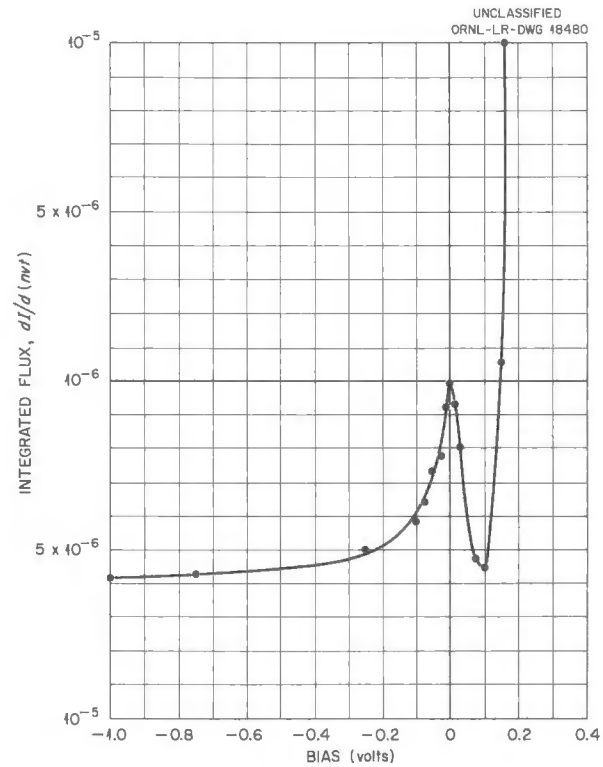

Fig. 4.2.28. Rate of Change of 1N 91-4 Germanium Junction Diode Current with Respect to Integrated Flux, *dI/d* (nvt), as a Function of Bias Voltage.

bulk resistance become more important than the barrier height. Since the injection ratio, lifetime, and bulk resistance all change in such a manner as to decrease the current, the large values for *dI/d* (nvt) were expected. The available data do not allow separation of the effects of injection, lifetime, and bulk resistance.

The change in surface leakage of the unit as a function of irradiation is shown in Fig. 4.2.29, and the change in saturation current as a function of exposure is shown in Fig. 4.2.30. For small exposures these changes are essentially linear.

EFFECTS OF RADIATION ON THERMAL-NEUTRON SHIELD MATERIALS

J. G. Morgan

R. M. Carroll M. T. Morgan
P. E. Reagan

Studies of metallographic sections[17] of irradiated samples of the stainless-steel-clad CaB_6-Fe and BN-Ni cermets being considered for use as thermal-neutron shielding materials were continued.[18] Examination of the CaB_6-Fe core matrix revealed significant amounts of a eutectic type of structure (Fig. 4.2.31) which is thought to have resulted from the reaction of the iron matrix material with CaB_6 to form Fe_2B. The occurrence of this reaction during the fabrication process was reported previously.[19] Comparison of the irradiated and unirradiated specimens revealed no evidence of an increase in the amount of Fe_2B which could be attributed to radiation exposure. Both specimens also showed a reaction zone between the type 304 stainless steel cladding and

[17] A. E. Richt and E. J. Manthos, *Metallographic Examination of Irradiated Ceramic Fuel Elements and Cermet Shielding Materials — Report No. 1*, ORNL CF-56-10-59 (Oct. 12, 1956).

[18] J. G. Morgan *et al.*, *ANP Quar. Prog. Rep. Sept. 10, 1956*, ORNL-2157, p 256.

[19] M. R. D'Amore and J. H. Coobs, *ANP Quar. Prog. Rep. June 10, 1956*, ORNL-2106, p 169.

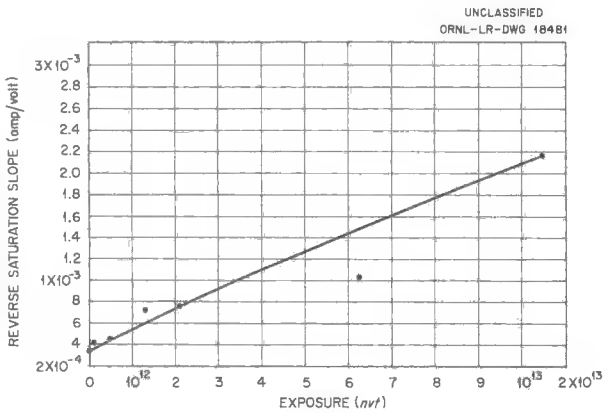

Fig. 4.2.29. Reverse Saturation Slope for a 1N 91-4 Germanium Junction Diode as a Function of Integrated Flux.

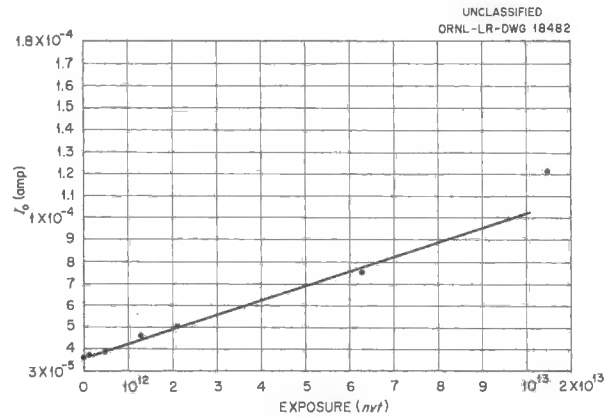

Fig. 4.2.30. Saturation Current of a 1N 91-4 Germanium Junction Diode as a Function of Integrated Flux.

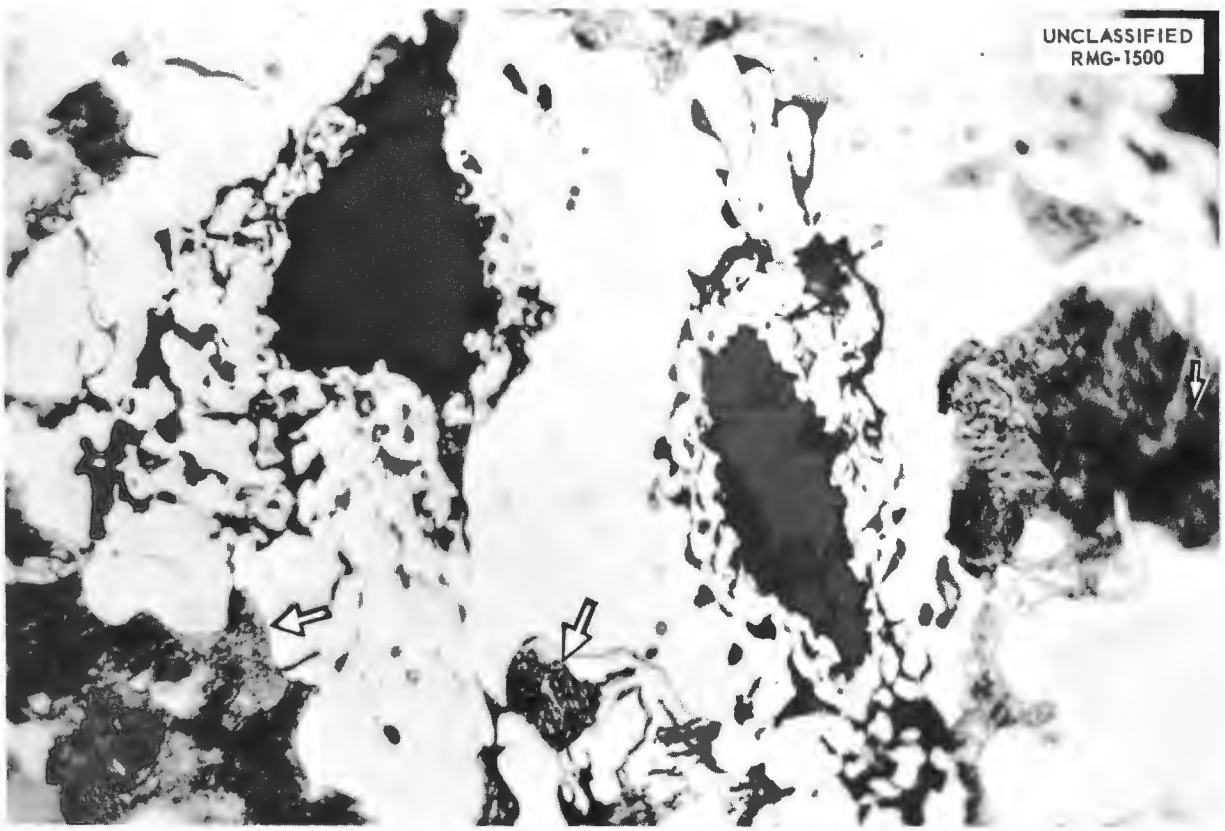

Fig. 4.2.31. Specimen from Cermet Core of Irradiated Stainless-Steel-Clad CaB_6-Fe Cermet. Arrows indicate reaction products thought to be Fe_2B. 1650X.

the core, as shown in Fig. 4.2.32. Hardness measurements showed the CaB_6-Fe core of the irradiated specimen to be slightly harder than the core of the unirradiated specimen. Since the cermet is relatively inhomogeneous it was necessary to utilize a large load in order to obtain a reproducible average value for the hardness. The results of the hardness measurements are presented in Table 4.2.7.

Samples of the BN-Ni cermet clad with type 304 stainless steel were examined after irradiation at reactor water temperature in the LITR to a dosage of 7.5×10^{19} nvt (thermal). The dimensions of the samples were unaffected by the exposure and the cladding retained continuity, as shown in Fig. 4.2.33. The core-to-cladding interfaces of irradiated and unirradiated specimens are shown at a higher magnification in Fig. 4.2.34. No separation at the interface or fracturing of the core was found, and there was no evidence of a reaction between the BN and the nickel matrix. Hardness measurements on the core and the cladding showed the irradiated specimens to be significantly harder than the unirradiated specimen. The hardness values are presented in Table 4.2.7.

Nine B_4C-Cu cermet somples were prepared for irradiation in the MTR, and three samples that were exposed for three weeks at 200°C are being returned to ORNL for examination. Three samples are now being irradiated at 485°C, and three more were shipped to NRTS for irradiation at 870°C.

EFFECTS OF RADIATION ON POLYMERS

O. Sisman

W. W. Parkinson R. F. Hornbeck[20]
W. C. Sears[21]

The investigation of the effects of radiation on polymeric materials is being conducted along two

[20]On assignment from The Glenn L. Martin Co.

[21]Summer participant from the University of Georgia.

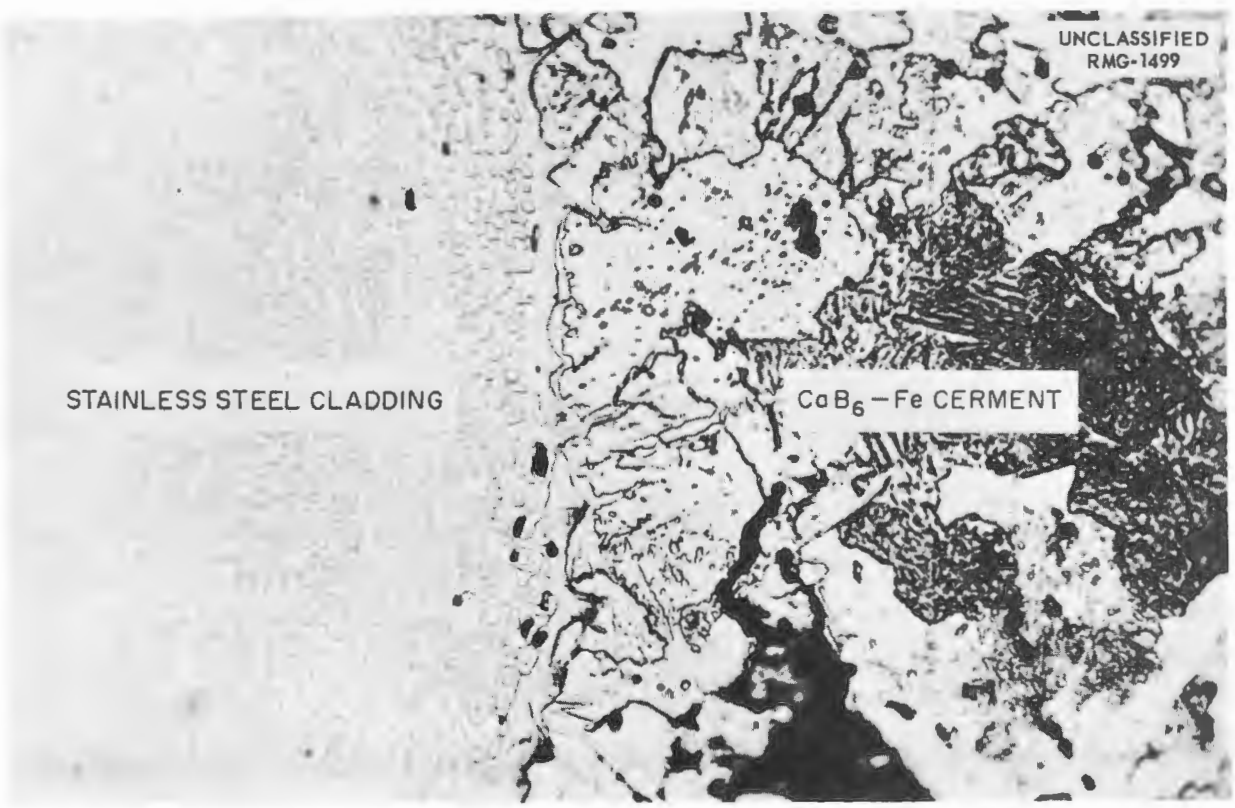

Fig. 4.2.32. Interface Between CaB_2-Fe Cermet and Stainless Steel Cladding Showing Reaction Zone. 1650X.

TABLE 4.2.7. RESULTS OF HARDNESS MEASUREMENTS ON IRRADIATED AND UNIRRADIATED CERMET SHIELDING MATERIALS

Specimen Condition	Hardness		
	CaB_6-Fe (DPH, 4-kg load)	BN-Ni (Knoop, 1-kg load)	Type 304 Stainless Steel Cladding (Knoop, 1-kg load)
Unirradiated			
Range	332–274	61–54	110–100
Average	299	58	105
Irradiated			
Range	344–305	121–94	142–124
Average	320	112	130

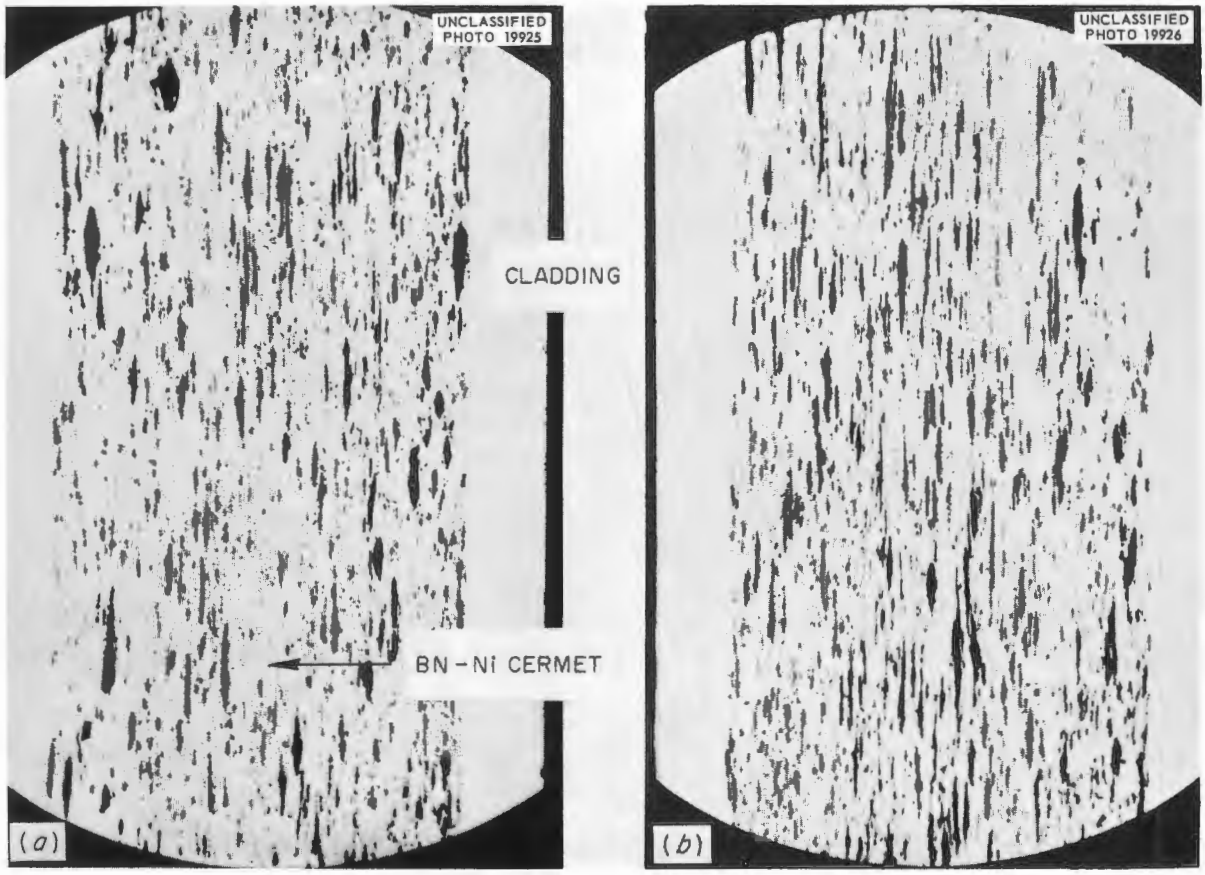

Fig. 4.2.33. Sections of (*a*) Unirradiated and (*b*) Irradiated BN-Ni Cermet Clad with Type 304 Stainless Steel.

major lines. The first is a study of the changes induced by radiation in the chemical and physical structure of polymers and the influence of the chemical and physical nature of the polymer on the rate and extent of the changes. The second approach is an evaluation by the common engineering tests of new materials for applications involving exposure to radiation. The analysis by infrared spectrometry of the chemical changes produced in several polymers by gamma and reactor radiation was discussed in a previous report.[22]

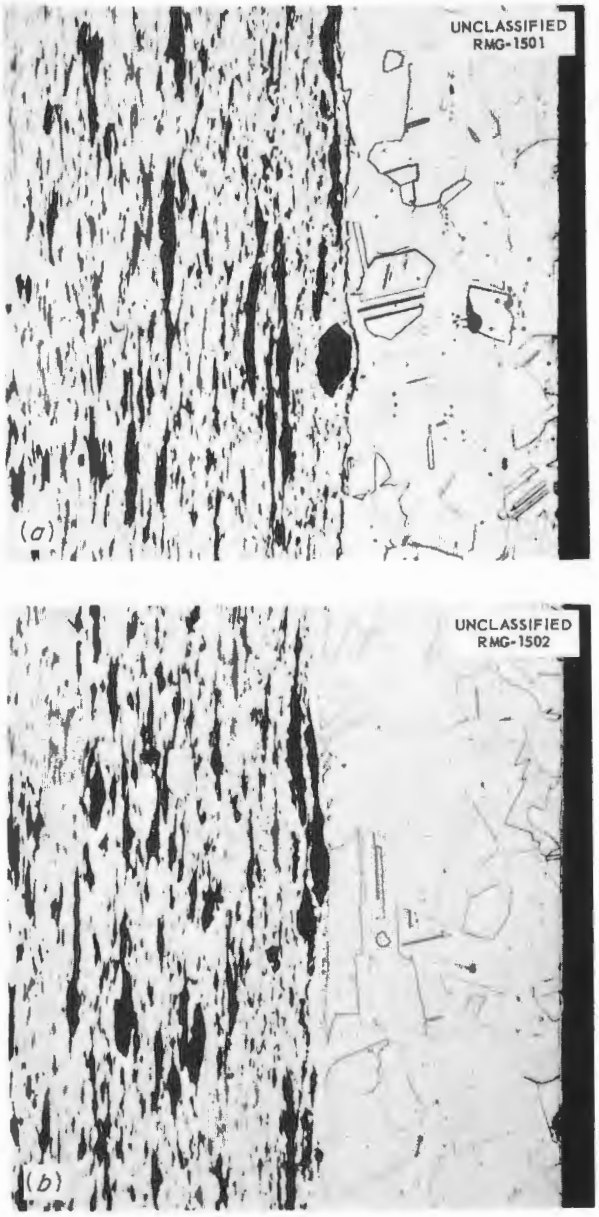

Fig. 4.2.34. Sections Showing Interface Between the BN-Ni Cermet and the Type 304 Stainless Steel Cladding of (*a*) an Unirradiated Specimen and (*b*) an Irradiated Specimen. The difference in cladding thickness of the two specimens is a function of fabrication rather than irradiation. 250X. Reduced 22%.

Infrared measurements of the formation of oxidation products in polymers during exposure to air following irradiation were continued. Storage of irradiated polystyrene specimens in various atmospheres proved that water was not involved to a large extent, if at all, in the oxidation reaction and that the reaction was dependent on the oxygen concentration in the atmosphere. The long duration of the susceptibility to oxidation was shown by the continued growth of O–H and C=O infrared bands after periods as long as 250 days. Measurements of unirradiated natural rubber specimens after storage for one year in air indicated that the rate of oxidation of a specimen irradiated to 2×10^9 rads is an order of magnitude greater. Measurements of polyvinyl chloride showed that it was only moderately susceptible to oxidation after irradiation and that it differed from the hydrocarbon polymers in that it formed very little hydroxy product but large amounts of carbonyl product.

For quantitative analysis of the spectra previously recorded it was necessary to determine the thickness and density of the specimens and the absorption coefficients of the chemical species observed. The densities have been determined by a flotation method. The thicknesses were measured by methods specifically adapted to each specimen because they varied in uniformity, hardness, and fragility. Absorption coefficients of infrared bands associated with three types of C=C groups have been measured on octene isomers.

An effort to obtain specimens suitable for measurement of radiation-induced changes was made by irradiating additional samples of alpha methyl styrene and polyethylene terephthalate (Mylar) in hole C-46 of the LITR. After less than one week in this location the methyl styrene specimens had deteriorated into shapeless masses, while the polyethylene terephthalate specimens

[22] O. Sisman, W. W. Parkinson, and W. C. Sears, *ANP Quar. Prog. Rep. June 10, 1956*, ORNL-2106, p 249.

split and broke to the extent that they were suitable only for qualitative measurement. Additional specimens of these materials will be irradiated to lower doses and with different mounting arrangements.

The cross-linking or scission of polymer chains can be determined most directly by molecular weight measurements, and therefore the average molecular weights of stocks of commercial polystyrene and polymethyl methacrylate have been determined by viscosity measurements on solutions. A preliminary irradiation of three samples of polystyrene was carried out to determine the doses suitable for viscometry specimens. One specimen was rendered insoluble by 6×10^7 rads, while another yielded a considerable insoluble fraction after about 10^7 rads. A third specimen which received about 10^6 rads showed a 6% increase in the viscosity of a dilute solution, which corresponds to a slightly larger increase in molecular weight.

Commercial polystyrene and polymethyl methacrylate have been separated into several molecular weight fractions to facilitate a study of the influence of polymer molecular weight on the radiation-induced change in molecular weight. This was accomplished with both materials by adding successive portions of a nonsolvent to solutions of the polymer. The change in molecular weight of these fractions will be compared after irradiation.

The differences which the molecular shape produced in radiation-induced changes were investigated by studying two types of polyethylene that had been irradiated in the ORNL Graphite Reactor. One type, Alathon 10 (made by Du Pont), contains a considerable number of side-chains that branch from the main polymer chains. The second type, Super Dylan 6200 (made by the Koppers Company), has very few side-chains and thus has greater regularity among the molecules and a higher degree of crystallinity. The results of tests of these materials are presented in Table 4.2.8.

The second part of the study of radiation effects on polymeric materials consisted of evaluation of miscellaneous materials. Samples of polyfluorobutyl acrylate rubber, prepared by using the normal methods for rubber compounding, were supplied by Wright Air Development Center. This elastomer is interesting as a solvent-resistant gasket material. The test results, as presented in Table 4.2.9, indicate that this material does not have radiation resistance superior to that of natural rubber.

Asbestos sheet impregnated with various polymers has applications as electrical insulation. The thickness of the available sample sheets ranged from 4 to 6 mils. The results of the applicable engineering tests of control and irradiated samples are presented in Table 4.2.10. The noteworthy radiation-induced change was the improvement in tensile strength of all the materials. Supposedly this improvement resulted from bonding of the asbestos fibers to reactive sites generated along the polymer chain by radiation or to sites activated in the asbestos. This improvement resulted at doses which would not have greatly affected the strength of polystyrene, although the strength of polyvinyl acetate probably would have begun to decrease. Typical tensile curves are shown for the three materials in Figs. 4.2.35, 4.2.36, and 4.2.37. The curves are shown only for the larger dose, but the curves for the smaller dose were almost identical. Additional irradiations to higher and lower doses are being carried out.

Di-isocyanate polyester elastomer has shown promise as a gasket material, and two small O-rings of this material were received for testing. Since many applications involve elevated temperatures the O-rings were irradiated at 135°C, along with natural rubber gaskets, for comparison. Gasket sections of these two materials were also

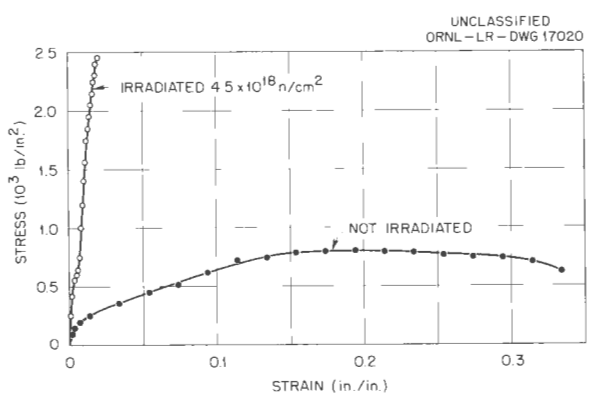

Fig. 4.2.35. Effect of Radiation on Tensile Properties of Polyvinyl-Acetate-Impregnated Asbestos Sheet.

held at this temperature for a period equal to the time of irradiation. The results of tests on gasket sections of the materials are given in Table 4.2.11. The di-isocyanate polyester showed less tendency to increase in weight and hardness and consequently demonstrates a definite superiority over natural rubber, although the compression set for all samples was 100%.

TABLE 4.2.8. RESULTS OF ENGINEERING TESTS OF CONTROL AND IRRADIATED SPECIMENS OF POLYETHYLENE

Properties	Control Sample	Irradiated Sample No. 1	Irradiated Sample No. 2
	Du Pont Alathon 10		
Dose			
Neutrons/cm^2	0	0.6×10^{18}	1.1×10^{18}
Rads	0	0.6×10^{9}	1.1×10^{9}
Tensile strength, psi	1938	1759	1825
Elongation, %	475	11	10.2
Density, g/cm^3	0.923	0.926	0.925
Volume resistivity, ohm-cm	1.2×10^{11}	1.3×10^{12}	4×10^{14}
Rockwell hardness,			
R scale	+1	46	76
α scale	−118	−74	−44
Shear strength, psi	1858	2386	2651
	Koppers Super Dylan 6200		
Dose			
Neutrons/cm^2	0	0.6×10^{18}	1.1×10^{18}
Rads	0	0.6×10^{9}	1.1×10^{9}
Tensile strength, psi	2996	4110	4177
Elongation, %	270	10	12
Density, g/cm^3	0.958	0.959	0.957
Volume resistivity, ohm-cm	9×10^{12}	1×10^{12}	3×10^{13}
Rockwell hardness			
R scale	52	82	88
α scale	+12	+46	+55
Shear strength, psi	2325	3696	4016

TABLE 4.2.9. RESULTS OF ENGINEERING TESTS OF CONTROL AND IRRADIATED SPECIMENS OF COMPOUND FLUOROBUTYL ACRYLATE RUBBER

Properties	Control Sample	Irradiated Samples		
		1	2	3
Dose				
Neutrons/cm^2	0	0.23×10^{18}	0.45×10^{18}	1.73×10^{18}
Rads	0	1.1×10^{8}	2.1×10^{8}	8.0×10^{8}
Tensile strength, psi	1069	837	658	563
Elongation, %	127	47	22	8
Shore durometer hardness	71	84	86	96
Specific gravity, g/cm^3	1.6349	1.6410	1.6421	1.6467
Dielectric strength, v/mm	126	125	120	114
Volume resistivity, ohm-cm	4×10^{10}	7×10^{6}	3×10^{5}*	5×10^{3}*
Weight loss, %	0	0.16	0.73	2.3

*These resistivity values were below the range of the available resistance bridge. They were taken with an ohmmeter and are subject to errors as large as ±25%.

TABLE 4.2.10. RESULTS OF ENGINEERING TESTS OF CONTROL AND IRRADIATED SPECIMENS OF POLYMER-IMPREGNATED ASBESTOS

Properties	Control Sample	Irradiated Sample No. 1	Irradiated Sample No. 2
Asbestos Impregnated with Polyvinyl Acetate			
Dose, neutrons/cm^2	0	2.3×10^{18}	4.5×10^{18}
Tensile strength, psi	800	2670	2570
Elongation, %	35.4	2.46	2.22
Asbestos Impregnated with Silicone			
Dose, neutrons/cm^2	0	2.3×10^{18}	4.5×10^{18}
Tensile strength, psi	1360	2070	2140
Elongation, %	4.6	2.41	2.11
Asbestos Impregnated with Polystyrene			
Dose, neutrons/cm^2	0	2.3×10^{18}	4.5×10^{18}
Tensile strength, psi	1260	2710	2820
Elongation, %	12.0	1.74	1.72

TABLE 4.2.11. EFFECTS OF HEAT TREATMENT AND RADIATION ON PROPERTIES OF DI-ISOCYANATE POLYESTER (DCP) ELASTOMERIC GASKETS AND NATURAL RUBBER GASKETS

Properties	Before Treatment	After Heat Treatment in Air at 135°C for 1.1×10^6 sec	After Irradiation to a Dose of 3.1×10^8 rads at 135°C
Weight change, %			
Natural rubber			
Large sample		±0.80%	±2.74%
Small sample		±1.55%	±2.61%
DCP			
Large sample		−1.16%	−0.93%
Small sample		−1.49%	−1.17%
Shore durometer hardness			
Natural rubber			
Large sample	68	90	95
Small sample	70	90	95
DCP			
Large sample	72	70	77
Small sample	72	71	76
Density, g/cm^3			
Natural rubber			
Large sample	1.226 ± 0.004	1.272	1.274
Small sample	1.223 ± 0.004	1.277	1.275
DCP			
Large sample	1.245 ± 0.004	1.236	1.248
Small sample	1.252 ± 0.004	1.249	1.249
Thickness, in.			
Natural rubber			
Large sample	0.255	0.227	0.230
Small sample	0.0685	0.060	0.060
DCP			
Large sample	0.0990	0.0820	0.0820
Small sample	0.0604	0.054	0.053

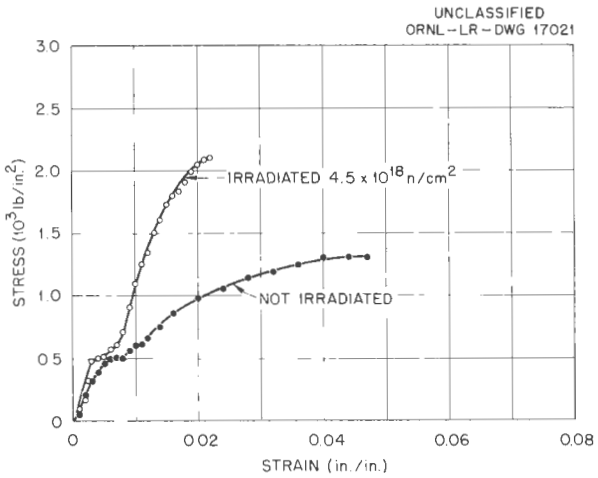

Fig. 4.2.36. Effect of Radiation on Tensile Properties of Silicone-Impregnated Asbestos Sheet.

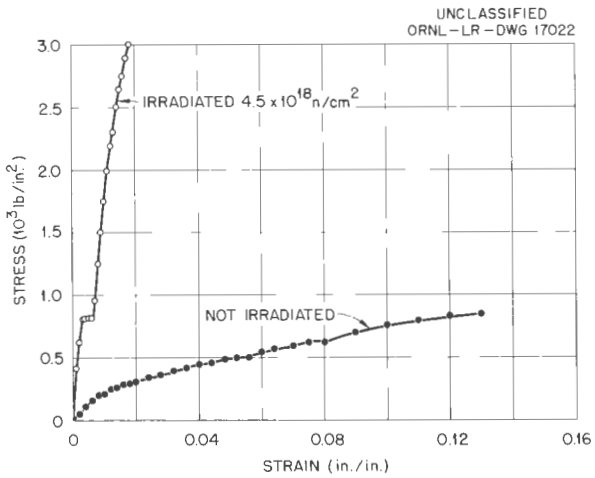

Fig. 4.2.37. Effect of Radiation on Tensile Properties of Polystyrene-Impregnated Asbestos Sheet.

4.3. FUEL RECOVERY AND REPROCESSING

R. B. Lindauer
D. E. Ferguson W. K. Eister H. E. Goeller

PILOT PLANT DESIGN AND CONSTRUCTION

W. H. Carr W. H. Lewis
J. E. Bigelow J. T. Long
F. N. Browder F. W. Miles
R. B. Keely S. H. Stainker
C. L. Whitmarsh

All major equipment for the fused salt–fluoride volatility pilot plant has been installed, except the facilities for handling the ARE dump tank (which will not be installed until runs have been made with nonirradiated material), the manipulator for introducing charge cans into the system, and the product receiver furnace and cooler. Auto-resistance heating of molten-salt transfer lines is being checked, but uniform temperature control has not yet been attained. Minor design modification and some remachining were necessary to eliminate leakage in remotely operated valves. Leak testing is now almost complete in the portion of the system which has been installed. Furnaces are being cured and other heating equipment is being checked.

Fluorine disposal studies are in progress. Flow rates of fluorine and of potassium hydroxide solution, concentration of fluorine (mixed with nitrogen) and of KOH, and temperatures are being varied to determine optimum operating conditions for the fluorine disposal system. The data obtained thus far show that at the flow rates expected during operation the fluorine can be satisfactorily scrubbed from the off-gas stream and can be disposed of at a rate of 2.8 scfm.

The high-density-graphite samplers, described previously,[1] filled satisfactorily. The samples were easy to remove from three samplers that had been degreased with acetone, methanol, or carbon tetrachloride, but difficulties were encountered in removing the samples from four of seven samplers that had not been degreased.

A 6 × 9 in. molten-salt freeze valve (Fig. 4.3.1) showed no leakage in 225 pressure tests in which the valve was held under a pressure of 20-psi N_2 for 20 min. This valve is of the same design as the 12 × 16 in. freeze valves incorporated in the pilot plant, but it provides less salt for the frozen seal. The pipe diameter showed little if any change in the course of the 225 cycles (Table 4.3.1). In 100 cycles the maximum valve temperature during thawing was not less than 675°C. The coldest point measured on the valve during the thawing cycle varied from 535 to 760°C.

PROCESS DEVELOPMENT

D. E. Ferguson G. I. Cathers
M. R. Bennett R. L. Jolley

In further laboratory-scale tests of the fused salt–fluoride volatility process in which the feed was of higher activity than that used in previous tests, Hanford-irradiated uranium was decontaminated from gross fission-product activity by a

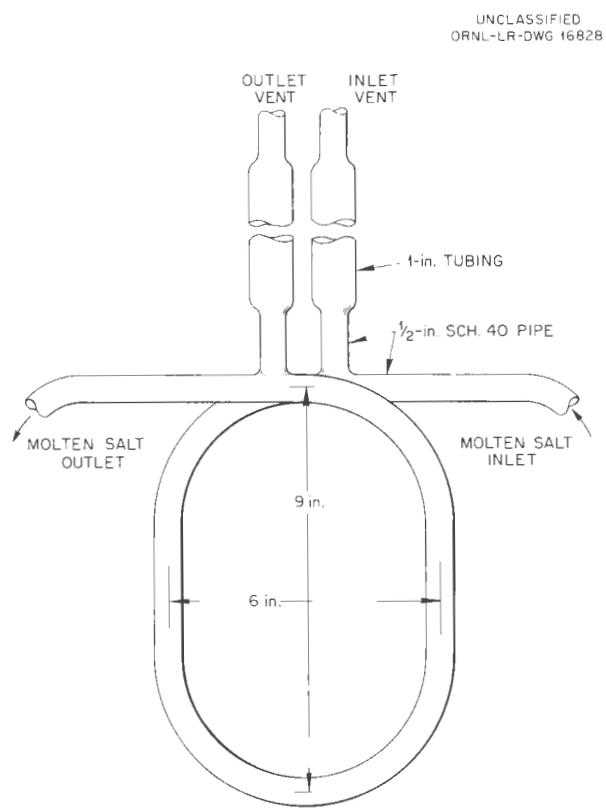

Fig. 4.3.1. Molten-Salt Freeze Valve.

[1] J. T. Long and S. H. Stainker, *ANP Quar. Prog. Rep. Sept. 10, 1956*, ORNL-2157, p 262, Fig. 4.3.1.

TABLE 4.3.1. DIAMETER MEASUREMENTS OF PIPE IN A MOLTEN-SALT FREEZE VALVE BEFORE AND AFTER PRESSURE TESTS

Tests carried out in elliptical loop, 9 in. high, 6 in. wide, made of ½-in. sched-40 Inconel pipe; 2 in. of high-temperature insulation around valve

Heating cycle: 200 to 650°C

Heating current through pipe: 250 amp

Molten salt: $NaF-ZrF_4-UF_4$ (50-46-4 mole %)

Point on Loop	Orientation of Measurement with Respect to Plane of Loop	Outside Diameter of Pipe (in.)*				
		Before Testing	After 70 Pressure Tests	After 99 Pressure Tests	After 192 Pressure Tests	After 225 Pressure Tests
"3 o'clock"	Parallel	0.850	0.850	0.850	0.850	0.848
	Transverse	0.840	0.840	0.840	0.840	0.840
"6 o'clock"	Parallel	0.780	0.780	0.780	0.780	0.775
	Transverse	0.880	0.884	0.888	0.880	0.892
"9 o'clock"	Parallel	0.840	0.842	0.845	0.846	0.850
	Transverse	0.840	0.840	0.835	0.836	0.836

* ±0.006 in. (95% confidence).

factor of $>10^6$. The work was carried out with natural uranium that had been irradiated to 600 Mwd/t. The material used in the first four tests had decayed for 420 days. At the end of three consecutive runs the over-all fission-product decontamination factor was $>10^6$ (Table 4.3.2, runs 1–3). However, owing to maloperation of the sodium fluoride step in the first run, only about 86% of the uranium volatilized during these three runs was recovered as product. The remaining 14%, which was sorbed as a U(V) complex, was recovered by heating the sodium fluoride beds to 500°C while passing fluorine through them (Table 4.3.2, run 3C). This procedure satisfactorily recovered the fixed uranium from the beds, but sufficient ruthenium activity was also removed to lower the gross fission-product decontamination factor to about 10^5, with a ruthenium decontamination factor of 2×10^3. This treatment apparently resulted in the diffusion of both niobium and ruthenium through the NaF beds, since the gross gamma decontamination factor in the following run was only 2×10^4, and detectable amounts of ruthenium and niobium activity broke through.

After the NaF beds had been cleaned up and filled with fresh NaF, two additional test runs were made with uranium irradiated to 600 Mwd/t that had been allowed to decay for only 120 days. In the first run the gross fission-product contamination factor was 3×10^6. However, in the second run a significant amount of activity, primarily ruthenium with some niobium, broke through and the over-all decontamination dropped by a factor of 10. This indicates that additional developmental work will be required to assure satisfactory re-use of the NaF beds. The zirconium and total-rare-earth decontamination factors indicate that even with higher irradiation levels no significant amount of these activities would be present in the UF_6 product.

In the first series of four runs the total uranium loss was 0.19%, with a material balance of 97%. In the second series the uranium loss was 0.20%, with a material balance of 88%. In both series the losses were >0.05% in the fluorination step; 0.04% and 0.12% of the uranium remained on the first NaF bed in the first and second series, respectively. In both series of runs the uranium that remained in the second NaF bed was neglected.

TABLE 4.3.2. DECONTAMINATION FACTORS AND URANIUM LOSSES OBTAINED IN LABORATORY TESTS OF THE FUSED SALT–FLUORIDE VOLATILITY PROCESS

Feed: Natural uranium irradiated to 600 Mwd/t

Run	Decontamination Factors						Uranium Losses* (%)				Uranium Material Balance* (%)
	Gross β**	Gross γ**	Ru	Zr	Nb	Total-Rare-Earth β	Waste Salt	First NaF Bed	Second NaF Bed	Fission-Product Cold Trap	
						Uranium Decay Time: 420 Days					
1	$>10^6$	$>10^6$	$>10^4$		$>10^5$	2×10^6	0.047				9
2	$>10^6$	$>10^6$	$>10^4$		$>10^5$	$>10^6$	0.018				33
3	$>10^6$	$>10^6$	$>10^4$		$>10^5$	$>10^6$	0.051				31
3C	3×10^5	9×10^4	2×10^3		$>10^5$	$>10^6$					12
4	7×10^4	2×10^4	4×10^2		4×10^4	$>10^6$	0.006				12
Total							0.122	0.04	0.01	0.02	97
						Uranium Decay Time: 120 Days					
5	3×10^6	3×10^6	9×10^3	$>10^7$	3×10^6	$>10^7$	0.034				47
6	4×10^5	2×10^5	3×10^2	$>10^7$	6×10^5	$>10^7$	0.028				41
Total							0.062	0.12	0.02	0.001	88

*Based on total uranium input of each series.

**Corrected by subtraction of $UX_1 + UX_2$ activity.

The UF_6 product from the feed that had decayed for 420 days was effectively decontaminated from Th^{234} (UX_1) and Pa^{234} (UX_2), the daughters of U^{238}. This $UX_1 + UX_2$ activity grows back with a half-period of 24 days. The calculated $UX_1 + UX_2$ activity present at specified periods after the separation time agreed closely with the experimental values (Table 4.3.3).

Volatile chromium fluorides formed in the fluorination step were removed in the NaF absorption step. The formation of either the tetra- or pentafluoride of chromium (estimated boiling points of 297 and 117°C, respectively), owing to the collection from the gas phase of reddish oily or solid material, has seemed probable in all fluorinations carried out in Inconel equipment. An analysis of some of this material showed a chromium content of 5.1%. About 82 mg of chromium was found in the first NaF absorption bed after a series of four fluorination runs. Substantially none was found in the second NaF bed, and thus it appears that the first bed effectively removed the chromium. The presence of chromium in the first bed was evident as a dark-red zone several millimeters deep where the fluorination gas stream entered. The amount of chromium found was calculated to be equivalent to corrosion attack on the Inconel vessel of 30 μ per fluorination. Although this is a point of interest in evaluating the corrosion behavior of Inconel, it is not probable that all volatile chromium fluorides formed in the process are transported to the absorption bed.

The high-activity-level tests were carried out under approximately normal process conditions. About 500 g of $NaF\text{-}ZrF_4$ (50-50 mole %) containing 20 to 50 g of uranium was fluorinated at 600°C in each run at an F_2/U mole ratio of 4/1. The UF_6 product was absorbed on a 150-g NaF bed (12-20 mesh) at 100°C and then desorbed through a second NaF bed by raising the temperature of both beds to 400°C. An F_2/U mole ratio of about 4/1 was also used in the desorption. A fluorine flow rate of 100 to 150 ml/min was used in both the fluorination and desorption runs.

The feasibility of operating process equipment on a small scale behind heavy shielding was demonstrated in these tests. A photograph of the equipment with the shielding removed is presented as Fig. 4.3.2. A uranium wafer was transferred

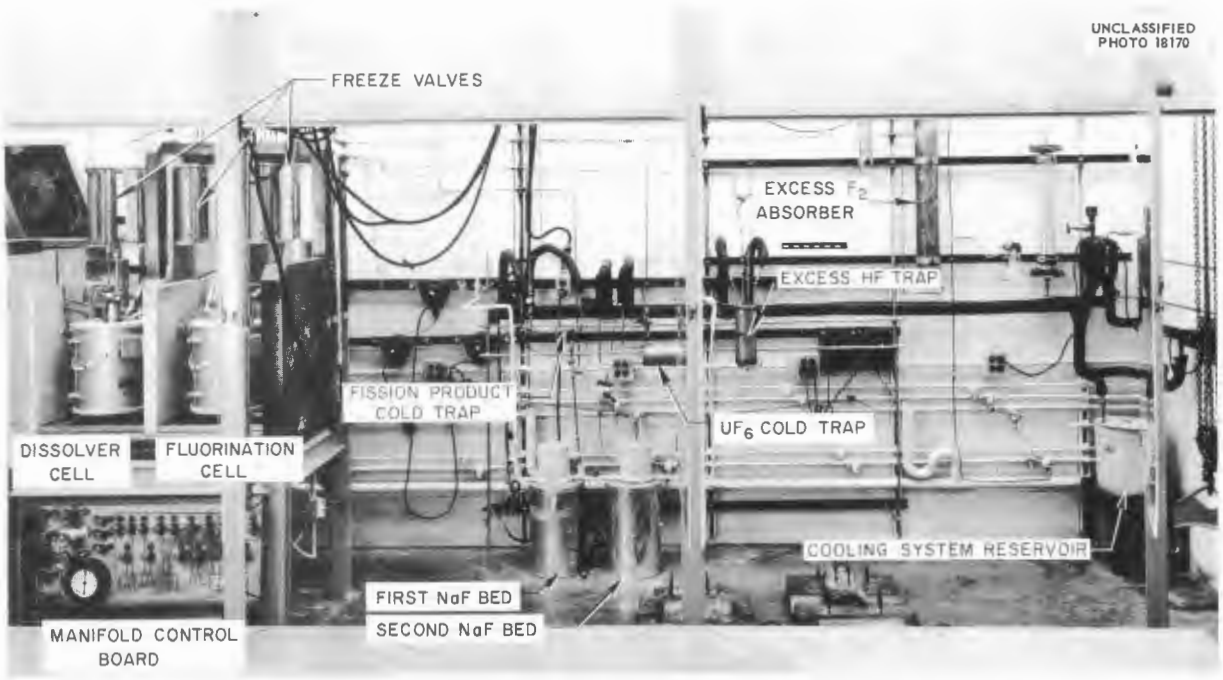

Fig. 4.3.2. Fused Salt–Fluoride Volatility Process Laboratory Test Assembly, with Shield Removed. ~~(Confidential with caption)~~

TABLE 4.3.3. PRODUCT AND FEED ACTIVITIES OBTAINED IN LABORATORY TESTS OF THE FUSED SALT–FLUORIDE VOLATILITY PROCESS

Feed: uranium irradiated to 600 Mwd/t

Sample	Remarks	Specific Activity (counts/min per mg of U)							
		Gross β*	Gross γ*	Ru	Zr	Nb	Total-Rare-Earth β	$UX_1 + UX_2, \beta$	
								Measured	Calculated
		Uranium Decay Time: 420 Days							
Feed	Total input, 140 g of U as $NaF\text{-}ZrF_4\text{-}UF_4$ (48-48-4 mole %)	7×10^6	2×10^6	3×10^4		5×10^4	4×10^6		
Product, run 1	Normal process conditions except for abnormal desorption run with yield of about 50%	0	0	0		0	2	38	38
Product, run 2	Normal process conditions	3	0	2		0	1	27	30
Product, run 3	Normal process conditions	3	<1	1		0	0	23	25
Product, run 3C	Special cleanup desorption run to remove U left in run 1	21	23	14		3	0	17	17
Product, run 4	Normal process conditions	105	83	73		14	1	10	10
		Uranium Decay Time: 120 Days (new NaF beds)							
Feed	Total input, 85 g of U	3.8×10^7	5×10^7	9×10^4	2.4×10^7	2×10^7	2.6×10^7		
Product, run 5	Normal process conditions	13	15	11	2	6	0	7	9
Product, run 6	Normal process conditions	108	280	270	1	35	1	5	4

*Corrected by subtraction of $UX_1 + UX_2$ and U^{237} activities.

from a radioactive cell to the dissolver through a chute, which is shown in Fig. 4.3.3. Molten salt was transferred from vessel to vessel through ¼-in. Inconel tubing heated by an electrical current of 100 to 200 amp. The freeze valves were positioned to allow good drainage of the salt from the transfer lines to prevent gas transfer between vessels. Drainage of the salt from transfer lines appears to be essential in repeated cycling if line breakage is to be avoided.

Fig. 4.3.3. Dissolver and Furnace of Fused Salt–Fluoride Volatility Process Laboratory Test Assembly. [redacted]

Part 5

REACTOR SHIELDING

E. P. Blizard

5.1 LID TANK SHIELDING FACILITY

R. W. Peelle

ATTENUATION BY WATER OF RADIATION FROM THE NEW LTSF FISSION SOURCE PLATE (SP-2)

J. R. Smolen[1] L. Jung
P. B. Hemmig[2] J. M. Miller
E. A. Warman[1]

Shielding studies have been performed at the LTSF since 1949, and, until recently, the source of radiation at the facility consisted of a plate containing U^{235} which absorbed thermal neutrons that issued from a hole in the ORNL Graphite Reactor shield and which, in turn, emitted a fission spectrum of neutrons and gamma rays. During the last few years it became apparent that a source plate of a different design would be an improvement in several respects, and, consequently, a new plate was installed. The plate, which has been described elsewhere,[3] was constructed so that its strength could be determined by three independent methods. The results from the three methods were averaged according to a system in which the result from each method was weighted with the inverse square of the absolute error. The resulting average source strength was 1.62×10^{11} fissions/sec $\pm 5\%$. This can be interpreted as 5.18 ± 0.26 w of power if an average reactor energy dissipation of 200 Mev/fission[4] is assumed.

Since the installation of the new source plate (designated as SP-2), measurements of the thermal-neutron flux and the gamma-ray and fast-neutron dose rates have been made in the water of the LTSF at various distances from the source plate along the source plate axis. The results are plotted in Fig. 5.1.1. These measurements cannot be considered as final because of the limited number and types of detectors used. Small corrections can be expected as measuring techniques are improved and new detection devices are employed to verify past measurements.

The detectors used for the measurements are listed in Table 5.1.1. For the fast-neutron detectors the integrator was biased at 10 v instead of the usual 6 v to eliminate the effect of gamma-ray sensitivity of the detectors. A 10-v bias discriminates against all neutrons below approximately 0.4 Mev.

The thermal-neutron fluxes, designated as "equivalent $1/v$" fluxes, are equivalent to the neutron density times 2200 m/sec. Measurements out to distances of 60 cm from the source plate surface were made with bare and cadmium-covered gold foils, and other measurements taken with fission chambers and BF_3 counters were normalized to the foil measurements. The magnitude of each of the possible errors shown at points in the thermal-neutron curve between 60 and 160 cm is a result of an estimate of the error involved in the extrapolation of foil measurements with the fission chambers and BF_3 counters.

For the conversion of the gamma-ray and fast-neutron dose rates to the tissue dose rates reported in Fig. 5.1.1. the energy absorption in tissues was taken to be 93 ergs/g·r or ergs/g·rep.

ATTENUATION OF FAST NEUTRONS FROM A FISSION SOURCE BY WATER: COMPARISON OF EXPERIMENT WITH THEORY

D. R. Otis[5]

Since the shielding problem in its simplest terms devolves into a calculation of the attenuation kernel, several computations have been performed to establish values of a kernel for various media. The first value for an attenuation kernel for the fast-neutron dose rate from a point, isotropic, fission source in water was determined by Blizard and Welton,[6] who based their calculation on some of the early experimental data obtained at the Lid Tank Shielding Facility (LTSF). At that time the LTSF fission source was the old source plate (SP-1), the power of which was estimated to be 6 w, with a neutron leakage factor of 0.6 (resulting in an effective power of 3.6 w). The

[1] On assignment from Pratt & Whitney Aircraft.

[2] On assignment from the U.S. Air Force.

[3] D. R. Otis, *Appl, Nuclear Phys. Ann. Rep. Sept. 10, 1956*, ORNL-2081, p 163.

[4] By comparison with the new source plate, the power of the old source plate (SP-1) has been established to be 1.7 w with an estimated error of $\pm 11\%$; see J. Smolen, *Appl. Nuclear Phys. Ann. Rep. Sept. 10, 1956*, ORNL-2081, p 164.

[5] On assignment from Convair, San Diego.

[6] E. P. Blizard and T. A. Welton, *The Shielding of Mobile Reactors—II*, ORNL-1133 (June 30, 1952).

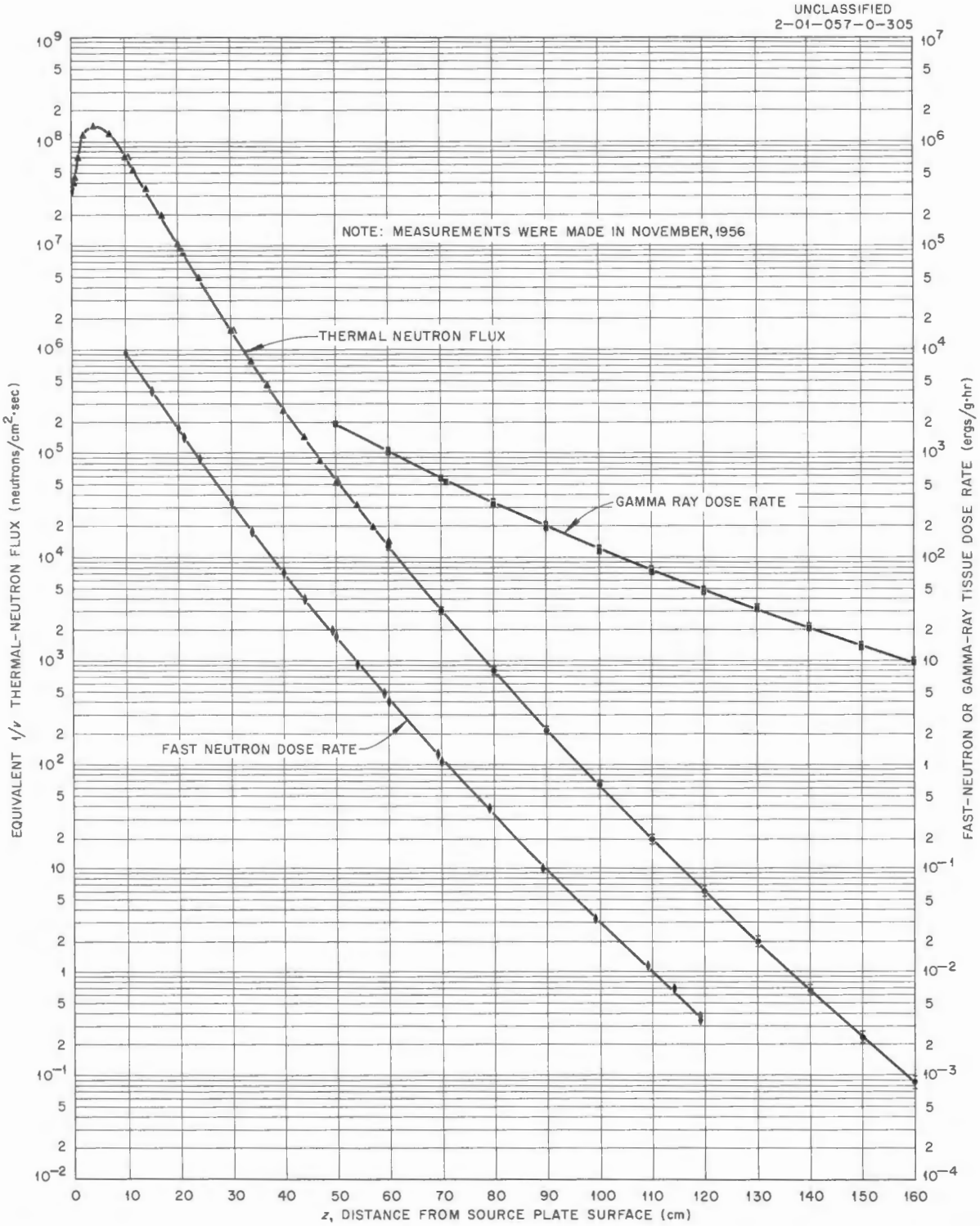

Fig. 5.1.1. Radiation Measurements in the Water of the LTSF as a Function of Distance from the New Fission Source Plate Having a Strength of 1.62×10^{11} fissions/sec.

TABLE 5.1.1. DETECTORS USED TO MEASURE RADIATIONS IN THE LTSF WATER

Radiation Measured	Detector	Useful Range	Calibration Standard
Gamma rays	Anthracene scintillation crystal	10^4–10^{-1} ergs/g·hr	Radium source (No. 234), strength = 3.92 ergs/g·hr at 1 m
	10^{10} ion chamber (900-cm^3)	10^3–10^1 ergs/g·hr	
Fast neutrons	"Phantom" Hurst proportional counter dosimeter	10^4–10^0 ergs/g·hr	Po-Be source (No. PN-237), strength (Sept. 14, 1956) = 30.44 curies, 7.64 × 10^7 neutrons/sec, 0.905 ergs/g·hr at 1 m (calculated)
	Hurst proportional counter dosimeter	10^1–10^{-2} ergs/g·hr	
Thermal neutrons	Bare and cadmium-covered gold foils	10^4 neutrons/cm^2·sec	Absolute measurement of foil activations
	½-in. fission chamber	10^9–10^5 neutrons/cm^2·sec	Normalized to bare and cadmium-covered gold foil measurements
	3-in. fission chamber	10^6–10^2 neutrons/cm^2·sec	
	8-in. BF_3 counter	10^4–10^0 neutrons/cm^2·sec	
	12½-in. BF_3 counter	10^3–10^{-1} neutrons/cm·sec	

results of this calculation were lower than those obtained in a similar calculation based on measurements with the Bulk Shielding Facility (BSF) reactor[6] (a factor of 2.5 to 1.7 at distances from the source ranging from 40 to 110 cm), but it was felt that the differences could be attributed to the difficulty in defining the leakage from the BSF reactor as well as the uncertainty in power calibration of the two sources. The subsequent BSF reactor calibration confirmed the assumed value, but the LTSF power calibration had to be deferred until a new source plate could be installed. The results based on the LTSF data were also lower by a factor of 4 than those obtained in a calculation performed later by Aronson *et al.*[7] with the use of the "moments" method. At the time, this discrepancy could not be resolved, but measurements with the new LTSF source plate (SP-2, see preceding paper and ref. 3) have allowed some of the differences to be explained. In addition, a new calculation based entirely on experimental data obtained with the new source plate has resulted in agreement with the moments-method calculation. A comparison of all the calculations is presented below.

[7] R. Aronson, *et al.*, *Penetration of Neutrons from a Point Isotropic Fission Source in Water*, NYO-6267 (Sept. 22, 1954).

Recalculation of Point Kernel for SP-1

The accurate source strength calibration for the new source plate[3] allowed a re-estimation of the old source plate power by a comparison of data taken with the old and new sources. A revised "effective power" of 1.7 w (where the "effective power" includes the neutron leakage factor) was thus obtained[4] in a calculation based upon the power for SP-2 and a comparison of the relative thermal-neutron flux levels for SP-1 and SP-2. (Thermal-neutron flux data were used rather than fast-neutron dose rate data because the former are, in general, more reliable.) In addition to the revision in power for SP-1, re-examination of the earlier dose rate measurements has resulted in different values from the preliminary data used by Blizard and Welton[6] (see Table 5.1.2). Since both these factors would have affected the calculation of the point kernel for SP-1, a new calculation was performed with the use of the revised values for the power and the dose rates. An analytical approximation for transforming from a disk to a point source was used.[8] The results are shown in Fig. 5.1.2 and seem to be in good agreement with the

[8] E. P. Blizard, "Nuclear Radiation Shielding," *Nuclear Engineering Handbook*, ed. by H. Etherington, McGraw-Hill, New York (in press).

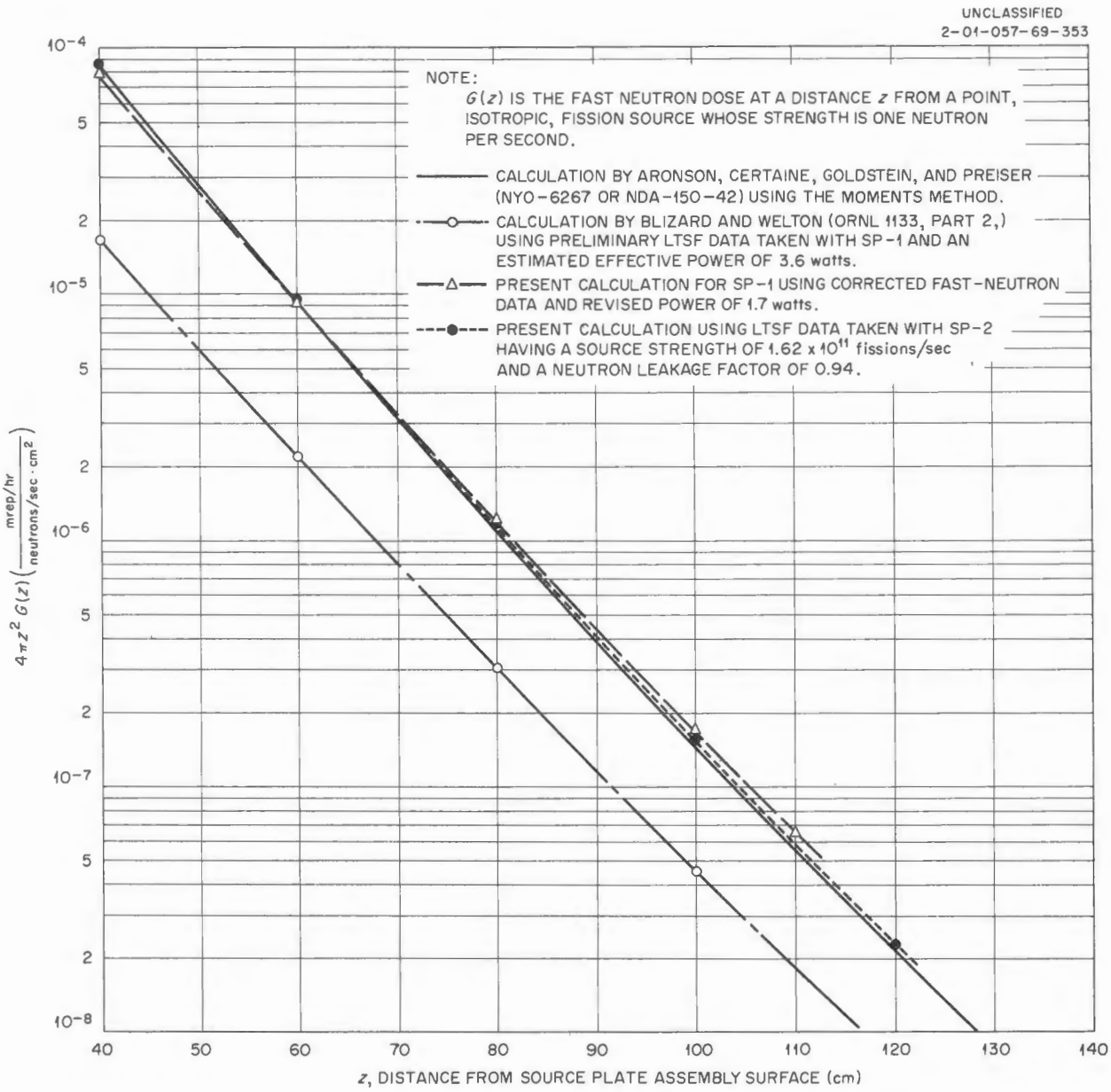

Fig. 5.1.2. Fast-Neutron Dose Rate Attenuation for a Fission Source in Water – Comparison of Kernel Theory with Experiment.

moments-method solution obtained by Aronson *et al.* The difference in slope can probably be ascribed to the old LTSF source plate being far from an ideal thin disk shape, as was assumed in the transformation to a point source.

Calculation of Point Kernel for SP-2

The calculation described above was repeated with the use of preliminary fast-neutron data (see Fig. 5.1.1) obtained with the new source plate (SP-2). The source strength was taken to be 1.62 $\times 10^{11}$ fissions/sec (uniformly distributed over the source plate) with a neutron leakage factor of 0.94 (ref 3). The results of this calculation (Fig. 5.1.2) show somewhat better agreement with the moments-method calculation than was the case for the calculation based on SP-1 data. This can be ascribed to the fact that the ideal thin disk shape was more nearly approached in the design of SP-2.

Comparison of Calculated and Experimental Dose Rate for SP-2

A calculation was also made of the fast-neutron dose rate in the LTSF water along the SP-2 axis with the use of the point kernel obtained by Aronson *et al.* This calculation involved no analytical approximations to the geometrical transformation but was simply a numerical integration over the source plate surface (assuming a uniform source strength). The results are compared with the experimental measurements in Table 5.1.3. Agreement between theory and experiment is within 12% in the 40- to 120-cm range.

TABLE 5.1.2. COMPARISON OF LTSF FAST-NEUTRON DOSE RATES USED IN CALCULATIONS FOR OLD SOURCE PLATE (SP-1)

z, Distance from SP-1 (cm)	Fast-Neutron Dose Rate (ergs/g·hr)	
	Used in Present Calculation	Used in Blizard-Welton Calculation
40	2.23×10^{1}	1.04×10^{1}
60	1.49×10^{0}	8.09×10^{-1}
80	1.23×10^{-1}	7.35×10^{-2}
100	1.21×10^{-2}	7.63×10^{-3}
110	3.91×10^{-3}	2.56×10^{-3}

STUDY OF ADVANCED SHIELDING MATERIALS

P. B. Hemmig[2]
E. A. Warman[1]
D. W. Cady[2]
D. R. Otis[5]
J. M. Miller
L. Jung

The current series of tests on advanced shielding materials[9,10] which are being performed to aid the GE-ANPD shield design effort is near completion. In the latest tests the materials used as the gamma-ray shields in the mockups have been stainless steel and tungsten. All the measurements for configurations using these two materials are presented here. In addition, the fast-neutron measurements for most of the configurations tested in the series are presented, since they were omitted in the earlier reports. All measurements are normalized by dividing the measured values by the standard source power of 5.18 ± 0.26 w.[3]

A summary of all the configurations is given in Table 5.1.4, and the physical properties of the materials used in configurations 69-4 and 69-5, the configurations containing stainless steel or tungsten, are listed in Table 5.1.5. (The physical properties of the materials used in all other configurations were presented previously.[9])

[9] R. W. Peelle *et al.*, *ANP Quar. Prog. Rep., June 10, 1956*, ORNL-2106, p 269.

[10] R. W. Peelle *et al.*, *ANP Quar. Prog. Rep. Sept. 10, 1956*, ORNL-2157, p 278.

TABLE 5.1.3. COMPARISON OF EXPERIMENTAL AND CALCULATED FAST-NEUTRON DOSE RATES FOR NEW SOURCE PLATE (SP-2)

z, Distance from SP-2 (cm)	Fast-Neutron Dose Rate (ergs/g·hr)		Ratio of Experimental to Calculated
	Calculated	Experimental	
5	2.47×10^{4}	1.95×10^{4}	0.79
20	1.16×10^{3}	1.70×10^{3}	1.46
40	5.79×10^{1}	6.10×10^{1}	1.05
60	3.79×10^{0}	4.25×10^{0}	1.12
80	3.19×10^{-1}	3.35×10^{-1}	1.05
100	2.83×10^{-2}	3.05×10^{-2}	1.08
120	3.11×10^{-3}	3.30×10^{-3}	1.06

TABLE 5.1.4. SUMMARY OF CONFIGURATIONS USED FOR LTSF MOCKUP TESTS OF ADVANCED SHIELDING MATERIALS

Configuration	Composition[a]
69-0B	Water only in configuration tank
0A	Oil only in configuration tank
69-1A′	1 ft of LiH in oil
1B′	2 ft of LiH in oil
69-2A′	4 in. of Zr + 1 ft of LiH in oil
2B′	4 in. of Zr + 2 ft of LiH in oil
2D′	4 in. of Zr in oil
69-3A′	4 in. of Be + 1 ft of LiH in oil
3B′	4 in. of Be + 2 ft of LiH in oil
3D′	4 in. of Be in oil
69-4A	4 in. of stainless steel + 1 ft of LiH in oil[b]
4B	4 in. of stoinless steel + 2 ft of LiH in oil
4D	4 in. of stoinless steel in oil
69-5AA	8 in. of W + 1 ft of LiH in oil[b]
5DD	8 in. of W in oil
69-6A′	3 in. of Pb + 1 ft of LiH in oil
6B′	3 in. of Pb + 2 ft of LiH in oil
6D′	3 in. of Pb in oil
69-12A	4 in. of Be + 3 in. of Pb + 1 ft of LiH in oil
12B′	4 in. of Be + 3 in. of Pb + 2 ft of LiH in oil
12D	4 in. of Be + 3 in. of Pb in oil
69-14A	4 in. of Be + 3 in. of U^{238} + 1 ft of LiH in oil[c]
14B	4 in. of Be + 3 in. of U^{238} + 2 ft of LiH in oil
14D	4 in. of Be + 3 in. of U^{238} in oil

[a]The materials are listed in order of increasing distance from the LTSF source; configurations are preceded by 2.2 cm of air and 1.0 cm of aluminum.

[b]See Table 5.1.5 for description of stainless steel and tungsten slabs.

[c]Depleted uranium, 0.24 wt % U^{235}.

The fast-neutron tissue dose rate measurements for all the configurations are presented in Figs. 5.1.3 through 5.1.10. In general, the fast-neutron measurements were made with Hurst-type proportional counters biased to discriminate against gamma rays and, consequently, against neutrons whose energies are less than approximately 0.5 Mev. The agreement between the three different instruments used was essentially within ±5% in the overlapping ranges. All the counters were routinely calibrated in air with a 30-curie polonium-beryllium source. One counter was constructed with an alpha source internally mounted for absolute calibrations. The absolute dose calibration from this counter agreed with the polonium-beryllium source calibration to within 10%. The source calibration depends on a measured intensity and on an assumed neutron spectrum.

In addition, some fast-neutron measurements were made with 2- and 5-in.-dia Hornyak buttons in an attempt to extend the dose rate measurements to lower fields. The usefulness of this approach is

TABLE 5.1.5. PHYSICAL PROPERTIES OF THE SHIELDING MATERIALS USED IN CONFIGURATIONS 69-4 AND 69-5

Material	Description
Transformer oil	Density, 0.87 g/cm^3 at 20°C; nominal composition, 86.7 wt % C and 12.7 wt % H
Lithium hydride	5 × 5 × 1 ft slabs encased in Al cans (1/4-in.-thick walls); density, about 0.75 g/cm^3; purity, about 95%
Type 347 stainless steel	5 ft × 5 ft × 1 in. slabs; density, 7.8 g/cm^3; composition: 68.35 wt % Fe, 18.0 wt % Cr, 10.5 wt % Ni, 2 wt % Mn, 1 wt % Si, 0.08 wt % C, 0.04 wt % P, 0.03 wt % S
Tungsten	Sintered-bar ends or clippings, approximately 7/8-in. cubes, encased in steel tank (1/4-in.-thick walls); inside dimensions of tank, 5 ft × 5 ft × 8 in.; approximately 62% of tank volume occupied by tungsten chunks; average density of chunks, 15.3 g/cm^3; impurities, negligible

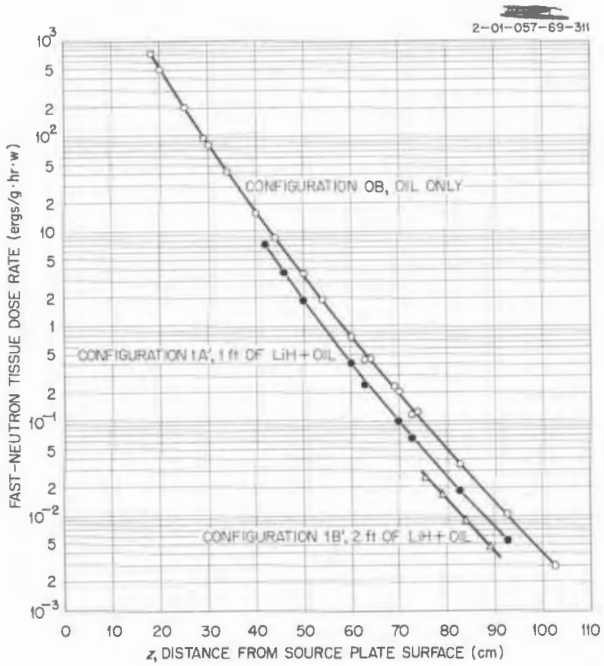

Fig. 5.1.3. Fast-Neutron Tissue Dose Rate Traverses Beyond Configurations 69-0B and 69-1A′ and B′.

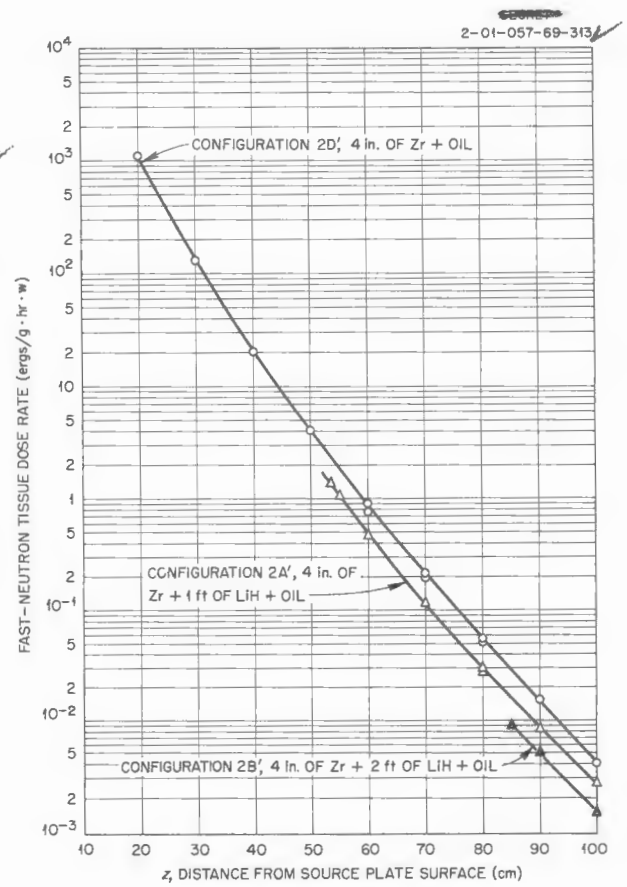

Fig. 5.1.4. Fast-Neutron Tissue Dose Rate Traverses Beyond Configurations 69-2A′, B′, and D′.

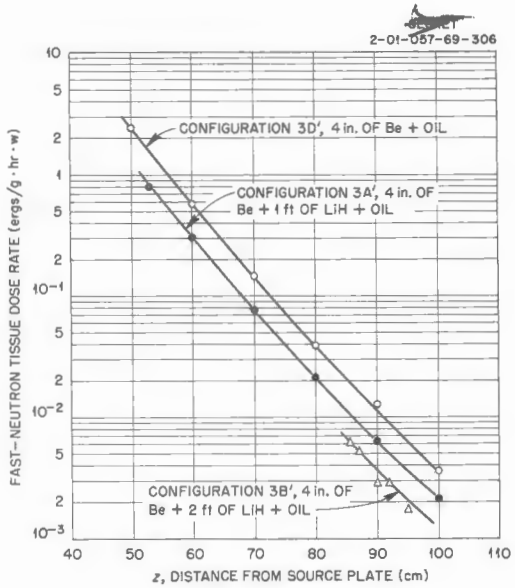

Fig. 5.1.5. Fast-Neutron Tissue Dose Rate Traverses Beyond Configurations 69-3A', B', and D'.

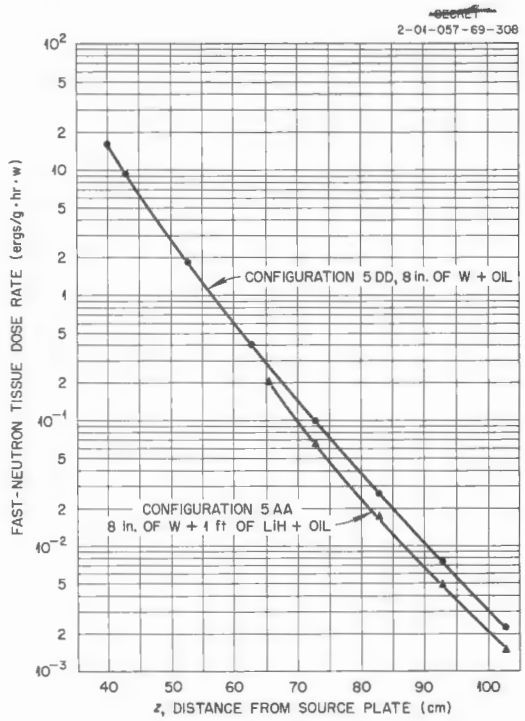

Fig. 5.1.7. Fast-Neutron Tissue Dose Rate Traverses Beyond Configurations 69-5AA and DD

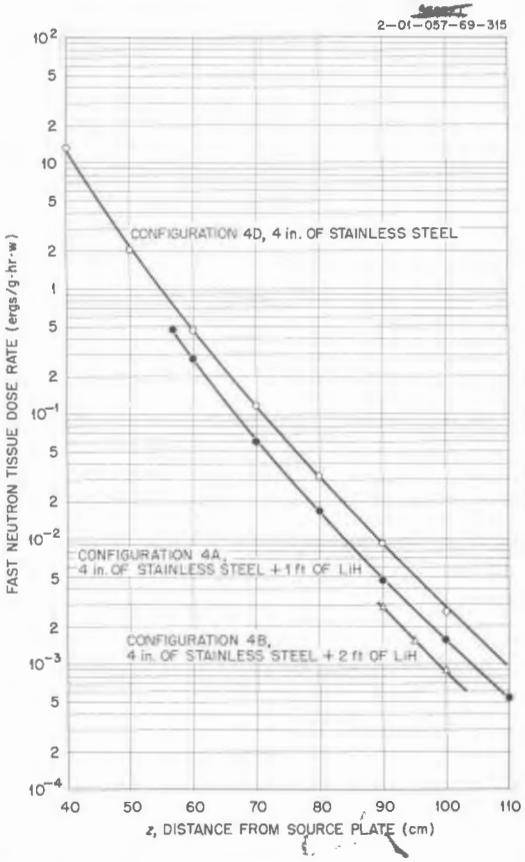

Fig. 5.1.6. Fast-Neutron Tissue Dose Rate Traverses Beyond Configurations 69-4A, B, and D.

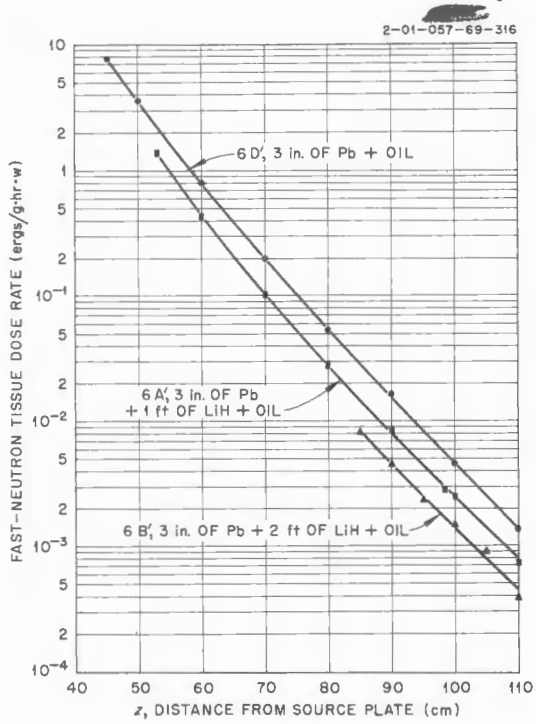

Fig. 5.1.8. Fast-Neutron Tissue Dose Rate Traverses Beyond Configurations 69-6A', B', and D'.

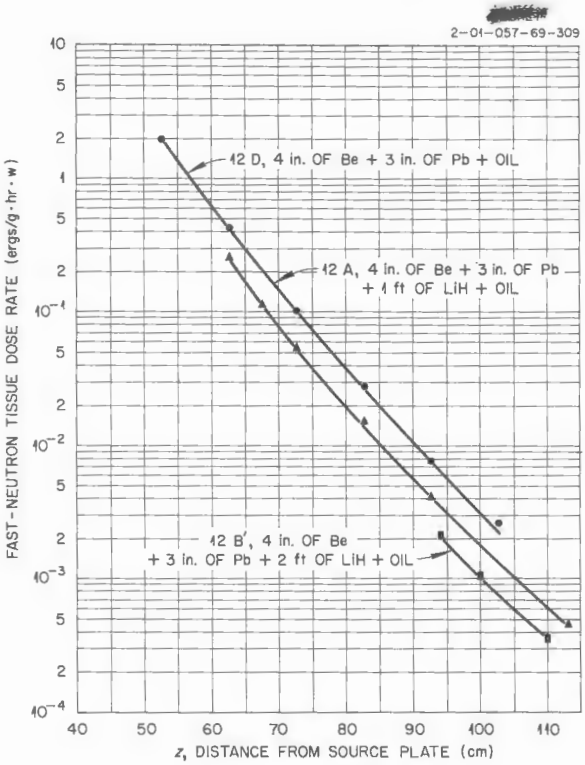

Fig. 5.1.9. Fast-Neutron Tissue Dose Rate Traverses Beyond Configurations 69-12A, B , and D.

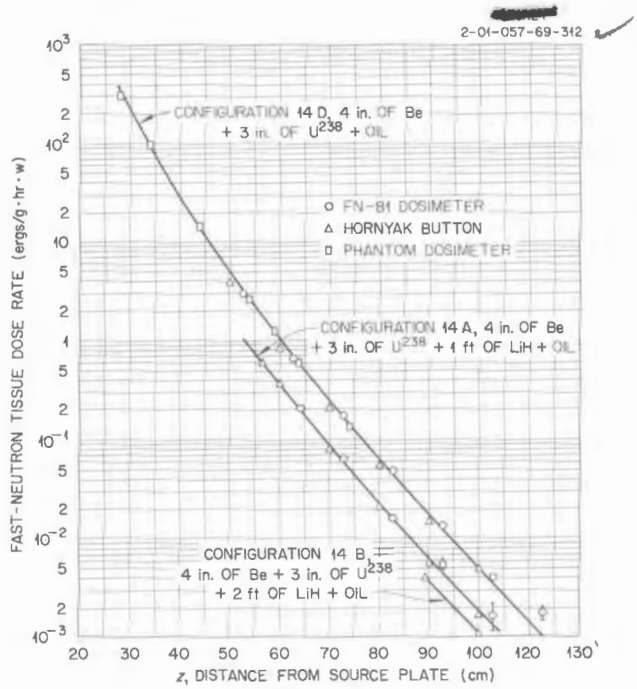

Fig. 5.1.10. Fast-Neutron Tissue Dose Rate Traverses Beyond Configurations 69-14A, B, and D.

not yet established; however, some Hornyak button data are shown in Fig. 5.1.10 for comparison.

Gamma-ray dose rate and "equivalent $1/v$" thermal-neutron flux measurements for the configurations containing tungsten and type 347 stainless steel are shown in Figs. 5.1.11 through 5.1.14. ("Equivalent $1/v$" thermal-neutron fluxes are equal to the neutron density times 2200 m/sec.) The shape of the thermal-neutron traverses at large distances from the source is attributed to photoneutrons produced in oil. Gold-foil measurements taken between the stainless steel slabs of configuration 69-4B yielded an average value of 6.7×10^6 neutrons/cm^2·sec for the equivalent $1/v$ thermal-neutron flux; in configuration 69-4D the value was 8.5×10^6 neutrons/cm^2·sec.

Two series of measurements that are not yet complete will provide additional information for the evaluation of stainless steel, as well as Hevimet,

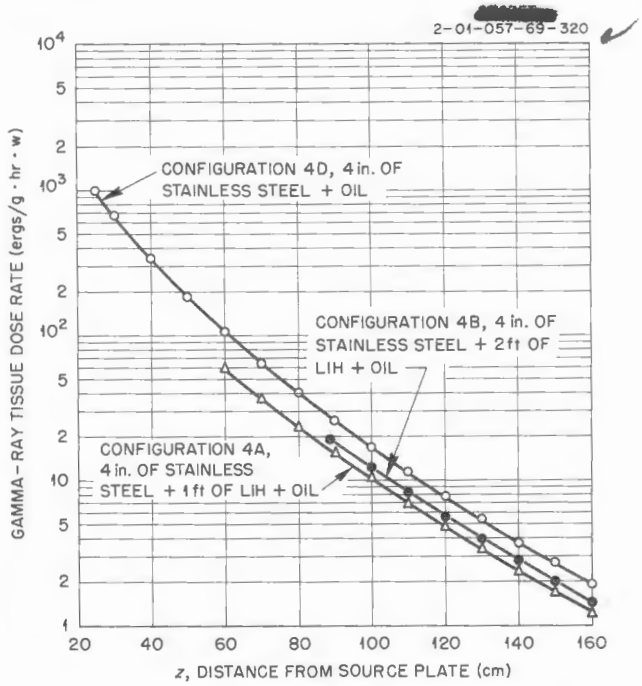

Fig. 5.1.11. Gamma-Ray Tissue Dose Rate Traverses Beyond Configurations 69-4A, B, and D.

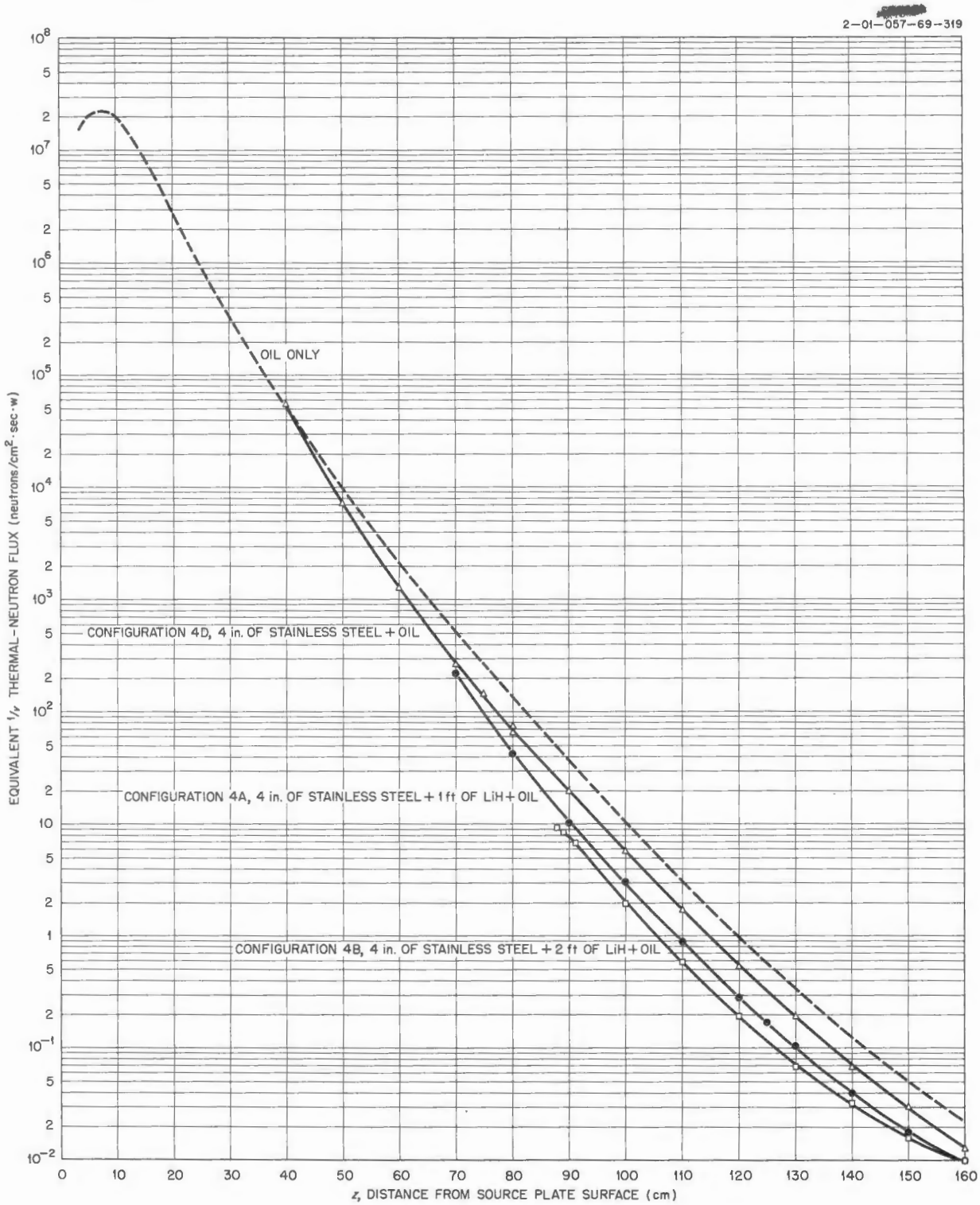

Fig. 5.1.12. Thermal-Neutron Flux Traverses Beyond Configurations 69-4A, B, and D.

a copper-nickel alloy of tungsten. One series differs from those reported above in that beryllium will be inserted between the source plate and the gamma-ray shielding material. In another series ½ in. of boral will be inserted between the gamma-ray shielding materials and the beryllium. These will be the final configurations for this group of tests.

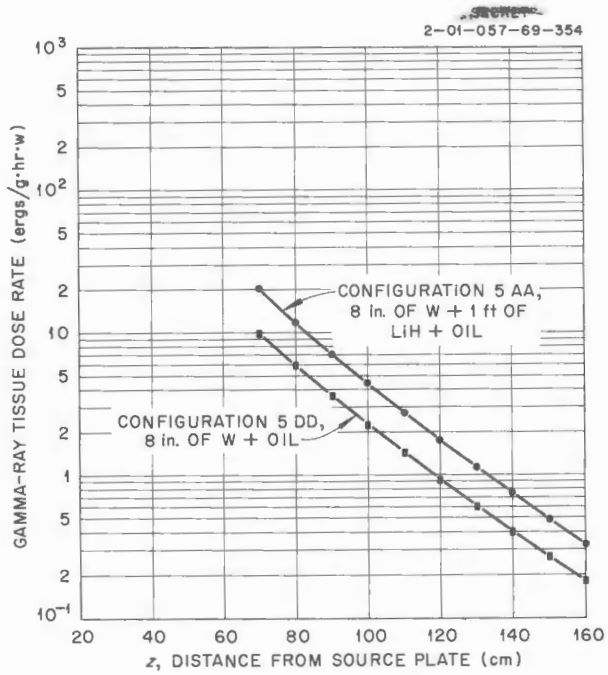

Fig. 5.1.13. Gamma-Ray Tissue Dose Rate Traverses Beyond Configurations 69-5AA and DD.

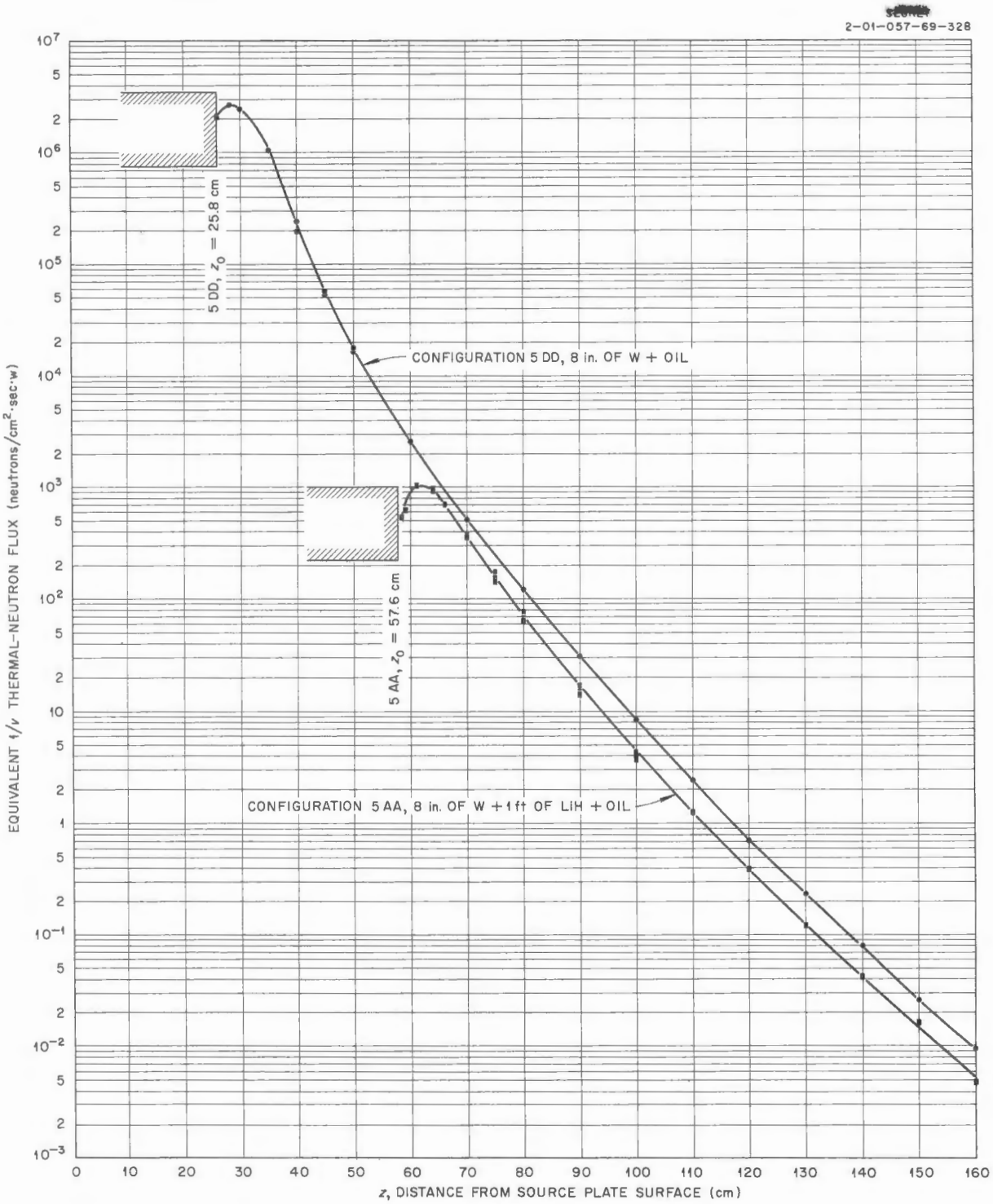

Fig. 5.1.14. Thermal-Neutron Flux Traverses Beyond Configurations 69-5AA and DD.

5.2. BULK SHIELDING FACILITY

F. C. Maienschein

CALCULATION OF THE GAMMA-RAY SPECTRUM AT THE SURFACE OF A BSF REACTOR CONTAINING UO_2–STAINLESS STEEL FUEL ELEMENTS

G. deSaussure

Some reactors currently being considered for the aircraft program contain a stainless steel component. Since the capture gamma-ray spectrum of stainless steel includes high-energy photons that are difficult to shield, it has therefore been proposed that the uranium-aluminum fuel elements in the BSF reactor be replaced with stainless steel–UO_2 fuel elements for future shielding tests.

In order to obtain some information as to how the substitution of stainless steel for aluminum in the BSF reactor will affect the gamma-ray flux spectrum at the surface of the core, a calculation of the gamma-ray flux at the surface of a reactor containing UO_2–stainless steel fuel elements was performed. As a check on the method, a parallel calculation was performed for the present BSF reactor containing uranium-aluminum fuel elements. This latter calculation has been compared with existing experimental measurements of the spectrum at the surface of the core.[1]

Method of Calculation

The determination of the gamma-ray spectrum at the surface of the core of a reactor was accomplished in two steps. First, the source spectrum of the gamma rays within the core was determined by dividing the energy spectrum into seven intervals and computing the number of photons per fission in each energy group. The resulting source spectrum was assumed to be uniformly distributed throughout the core, and the second step of the determination was undertaken, that is, the calculation of the energy spectrum of the gamma-ray flux at the surface of the core.

Determination of the Source Gamma-Ray Spectrum. – It was assumed that the sources which contribute to the gamma-ray source strength of the reactor are:

1. prompt gamma rays from fission,
2. capture gamma rays from U^{235},
3. gamma rays from fission products,
4. capture gamma rays from water and structural material (this includes short half-lived activation gamma rays),
5. gamma rays from inelastic scattering of fast neutrons.

Since it was assumed that the fuel elements were new, no long-lived activation or fission-product gamma rays were considered.

The spectra of these sources were designated $n_1(E)$, $n_2(E)$, etc.; the dimensions were photons per Mev. The contribution to the ith energy interval from each of these sources was designated as n_{1i}, n_{2i}, etc., and the photons in the energy group were weighted by their actual energy. The seven energy groups chosen and the energy assumed E_i for each group are given in Table 5.2.1.

TABLE 5.2.1. ASSUMED ENERGIES FOR SEVEN ENERGY GROUPS USED IN CALCULATION

Energy Group No.	E_a (Mev)	E_b (Mev)	E_i (Mev)
1	0	0.75	0.5
2	0.75	1.5	1.0
3	1.5	3.0	2.0
4	3.0	5.0	4.0
5	5.0	7.0	6.0
6	7.0	9.0	8.0
7	9.0	11.0	10.0

The contribution from the first source, the prompt gamma rays from fission, was calculated from the equation

$$n_{1i} = \frac{1}{E_i}\int_{E_a}^{E_b} n(E)\,E\,dE$$

$$= \frac{1}{E_i}\int_{E_a}^{E_b} 9.61E\,e^{-1.01E}\,dE\ ,$$

where

E_i = mean energy chosen for the ith group of width ΔE_i (Mev),

E_a, E_b = limits of the ith energy interval ($\Delta E_i = E_b - E_a$),

$n_i(E)$ = $7.6\,e^{-1.01E}$ (photons/Mev·fission).

[1] F. C. Maienschein, F. T. Bly, and T. A. Love, *Gamma Radiation in a Divided Aircraft Shield. Parts 1 and 2*, ORNL-1714 (Aug. 20, 1954).

This definition of $n_1(E)$ is a good approximation to the spectrum measured by Gamble.[2]

No data could be found on the spectrum resulting from radiative capture in U^{235} which could be used in the calculation of the contribution from the second source; however, it was assumed that this spectrum was identical in shape with the prompt fission gamma-ray spectrum. The spectrum was normalized by the ratio of the binding energy in U^{236} to the total prompt fission gamma-ray energy as reported by Gamble (E_B = binding energy = 6.43 Mev, E_p = total prompt gamma-ray energy per fission = 7.45 Mev/fission). The number of photons per fission in the ith interval emitted by this source was determined with the following equation:

$$n_{2i} = \frac{\sigma_c}{\sigma_f} \frac{1}{E_i} \int_{E_a}^{E_b} \frac{E_B}{E_p} n_1(E)\, E\, dE$$

$$= 0.118 \frac{1}{E_i} \int_{E_a}^{E_b} \frac{6.43}{7.45} 9.61E\, e^{-1.01E}\, dE \ ,$$

where σ_c/σ_f is the ratio of the microscopic capture cross section to the fission cross section for thermal neutrons in U^{235}. The value of σ_c/σ_f is 0.118 (ref 3), and its smallness prevents the rather crude assumption about the U^{235} capture gamma-ray spectrum from greatly affecting the calculation of the total gamma-ray source strength.

The contribution to the total source strength by the third source, the fission-product gamma rays, was determined from spectral measurements made by Peelle, Zobel, and Love.[4]

The data used in the calculation of the contribution by capture gamma rays from water and structural elements (source 4) were taken mainly from the article of Mittelman and Liedtke[5] and from the measurements of Kinsey, Bartholomew, and Walker[6] at Chalk River. Where the low-energy portion of the gamma-ray spectrum had not been measured, it was assumed that an equal number of photons were emitted at energies E and $E_B - E$, where E_B is the binding energy of the neutron in the element considered. The equation used for the calculation is as follows:

$$n_{4i} = \frac{1}{E_i} \frac{N\sigma_a}{N^{25}\sigma^{25}} \sum_{E=E_a}^{E_b} n_4(E)\, E \ ,$$

where

N = number of atoms per cubic centimeter of the contributing material,

σ_a = microscopic capture cross section of the contributing material, cm^2

N^{25}, σ^{25} = corresponding terms for U^{235}.

The inelastic scattering cross sections of the structural elements used in the calculation of the contribution from the fifth source were found in BNL-325 (ref 3) as measured at MIT. The fast-neutron flux per fission was assumed to be $\nu\lambda$, where ν is the number of neutrons per fission and λ is the mean free path in the core for fast neutrons. The energy of the fission neutrons was taken to be that measured by Watt[7] and Cranberg *et al.*[8] The equation used for the calculation was

$$n_{5i} = \frac{N}{E_i} \sum_{E_j > E_a}^{E_j < E_b} E_j \nu\lambda \int_0^\infty \sigma_{in}(E_n)\, n_f(E_n)\, dE_n$$

$$= \frac{N}{E_i} \sum E_j \nu\lambda \int_0^\infty \sigma_{in}(E_n) \times$$

$$\times \sqrt{\frac{2}{\pi e}} \sinh \sqrt{2E_n}\, e^{-E_n}\, dE_n \ ,$$

where $\sigma_{in}(E_n)$ is the inelastic scattering cross section for production of photons of energy E_j by neutrons of energy E_n, and $n_f(E_n)$ is the fission neutron spectrum.

The total number of photons per fission for each energy interval, n_{ti}, is then just the sum of contributions from the five sources.

Determination of the Gamma-Ray Flux at the Surface of the Reactor. – The measurement by Maienschein, Bly, and Love[1] of a gamma-ray spec-

[2] R. L. Gamble, *Prompt Fission Gamma Rays from Uranium-235*, (Dissertation presented to the faculty of the Graduate School of the University of Texas in partial fulfillment of the requirements for the Degree of Doctor of Philosophy).

[3] D. J. Hughes and J. A. Harvey, *Neutron Cross Sections*, BNL-325 (July 1, 1955).

[4] R. W. Peelle, W. Zobel, and T. A. Love, *Appl. Nuclear Phys. Ann. Rep. Sept. 10, 1956*, ORNL-2081, p 91.

[5] P. S. Mittelman and R. A. Liedtke, *Nucleonics* 13(5), 50 (1955).

[6] B. B. Kinsey, G. A. Bartholomew, and W. H. Walker, *Phys. Rev.* 82, 380 (1951); 83, 519 (1951).

[7] B. E. Watt, *Energy Spectrum of Neutrons from Thermal Fission of U235*, AECD-3359 (1952).

[8] L. Cranberg *et al.*, *Phys. Rev.* 103, 662 (1956).

trum for photons leaving the reactor in the nearly normal direction was available for comparison with a calculation of this quantity from the foregoing data. The number of uncollided photons escaping per fission was first calculated for the highest energy group (group 1) by the following integration:

$$J_1 = 2\pi n_1 \int_{\theta=0}^{\pi/2} \left(\cos\theta \sin\theta \times \int_0^{2R\cos\theta} \frac{e^{-\mu_1 r}}{4\pi r^2} r^2 \, dr \right) d\theta ,$$

$$\Gamma_i = \frac{a}{4\pi R^2} \left[n_{ti} + \sum_{j>i} n_{tj} \left(1 - \frac{3}{R} \frac{J_j}{n_{tj}} \right) \alpha_{ij} \right] \frac{3 J_i g_i}{R n_{ti} \Delta E_i}$$

$$= \frac{a}{(4/3)\pi R^3} \left[1 + \sum_{j>i} \left(\frac{n_{tj}}{n_{ti}} - \frac{3}{R} \frac{J_j}{n_{ti}} \right) \alpha_{ij} \right] \frac{J_i g_i}{\Delta E_i} ,$$

where

θ = angle between normal and trajectory,

R = radius of a sphere of volume equivalent to actual reactor volume,

r = distance from the point of escape to the differential volume within the sphere,

μ_1 = total gamma-ray attenuation coefficient for group 1 in the core, cm^{-1}.

Conservation of photons requires that those interacting within the sphere be equivalent to the difference between the total number of photons escaping and the total number of photons produced, that is,

$$\int_{surface} J \, dA = \int_{volume} p_1 \, dV - \int_{volume} q_1 \, dV ,$$

where q_1 is the density of scattered (or absorbed) photons from the first group. Of these, some remain in the first group, and the others are spread over the other groups according to the Klein-Nishina cross-section formula.

In order to obtain the outward-bound current in the region of $\theta \cong 0$, a separate similar calculation was performed to obtain a factor between the total and "nearly normal" current given by

$$g_1 = \frac{1}{2\pi} \frac{1 - e^{-2\mu R}}{\frac{1}{2} - \frac{1}{(2\mu R)^2} [1 - e^{-2\mu R}(1 + 2\mu R)]} \text{ per steradian .}$$

By successive calculations for each of the lower energy groups, it is thus possible to reconstruct an approximate spectrum for outward-directed escaping photons. The result of this process is given by the following expression:

where

a = total number of fissions per second per watt = 3.1×10^{10},

$R \cong 25$ cm,

α_{ij} = number of scattered photons of energy E_i per photon of energy E_j removed

$$= \frac{1}{\sigma_{total}(E_j)} \int_{E_a}^{E_b} \frac{d\sigma_{Compton}(E_j, E)}{dE} dE ,$$

$\sigma_{total}(E_j)$ = total cross section for interaction of gamma rays of energy E_j,

$\frac{d\sigma_{Compton}(E_j, E)}{dE} dE$ = differential cross section for scattering of gamma rays of energy E_j in energy interval dE at E.

Results of the Calculations

The calculated source spectrum is presented in Fig. 5.2.1 for the BSF reactor with aluminum fuel elements and in Fig. 5.2.2 for a reactor with stainless steel elements. For purposes of comparison, the gamma-ray spectrum of U^{235} is also given.

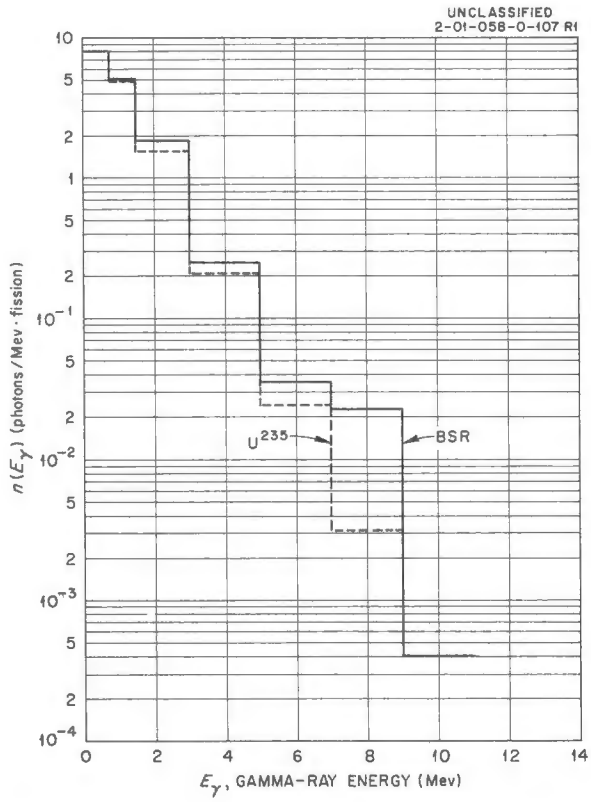

Fig. 5.2.1. Calculated Primary Gamma-Ray Spectrum of the BSF Reactor Containing Uranium Fuel Elements Compared with Spectrum of U^{235} Prompt Fission and Capture Gamma Rays.

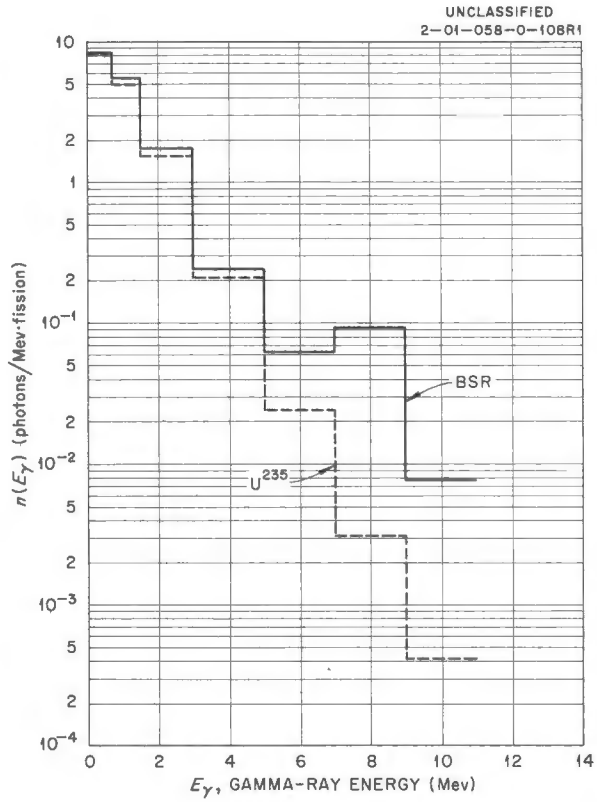

Fig. 5.2.2. Calculated Primary Gamma-Ray Spectrum of the BSF Reactor Containing UO_2–Stainless Steel Fuel Elements Compared with Spectrum of U^{235} Prompt Fission and Capture Gamma Rays.

This includes the prompt fission gamma rays (measured by Gamble[2]), the U^{235} capture gamma rays (assumed to have a spectrum similar to the prompt fission gamma rays), and the fission-product gamma rays (measured by Peelle, Zobel, and Love[4]). At energies above 2 Mev the capture gamma rays in the structural material constitute the main part of the source gamma-ray spectrum, and the stainless steel contributes more capture photons of higher energies than the aluminum.

The calculated gamma-ray flux in the forward direction at the surface of the BSF reactor with aluminum fuel elements is shown in Fig. 5.2.3, along with the actual flux measured by Maienschein, Bly, and Love.[1] There are two assumptions implicit in the above calculations that tend to underestimate the flux at the surface of the core. The first assumption is that the core is homogeneous: it is evident that for a core of the same composition but with the materials that have a high stopping power for gamma rays lumped together, the gamma-ray leakage would be larger, since some of the gamma rays would stream in between the slugs. The second assumption – that the Compton-scattered gamma rays have an isotropic angular distribution – tended to underestimate the gamma-ray flux at the surface of the core. It may be that a "straight-ahead approximation" (one that assumes that after a Compton collision gamma rays are degraded in energy but keep their original direction) would give a better estimate of the flux at the surface of the core. The latter approximation would tend to overestimate the flux. It is planned to repeat the calculations with this straight-ahead approximation.

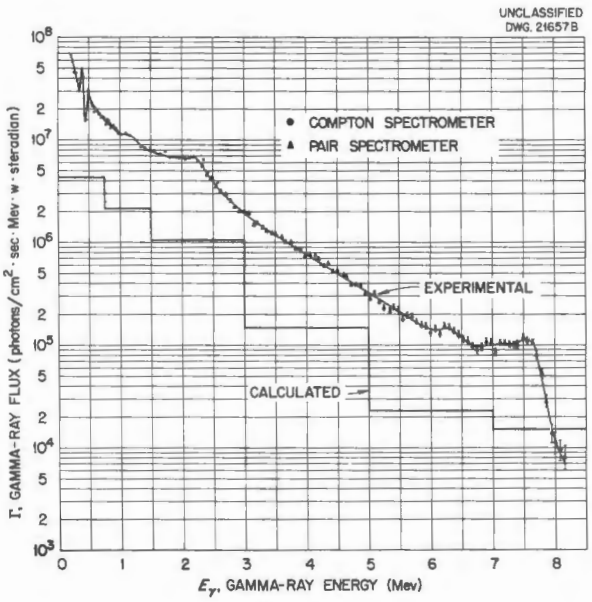

Fig. 5.2.3. Comparison of Calculated and Measured Gamma-Ray Spectra of the BSF Reactor Containing Uranium-Aluminum Fuel Elements.

The general shape of the calculated flux vs energy curve shown in Fig. 5.2.3 corresponds with that of the experimental curve. Thus it can be inferred that the calculations will at least predict correctly the way in which the surface gamma-ray spectrum will be affected by the substitution of stainless steel for the aluminum in the elements. This is shown in Fig. 5.2.4, where the calculated gamma-ray fluxes at the surface of the core of the two reactors are compared.

Conclusions

It is disappointing that the calculations of the magnitude of the flux at the surface of the reactor core are not in better agreement with the experimental results. Osborne and Montgomery[9] made a similar calculation of the spectrum at the surface of the core of the BSF reactor and obtained results in better agreement with the experimental measurements. It is not clear why the present calculations should give a different answer.

The calculations show that the substitution of stainless steel fuel elements for the aluminum fuel elements will increase the relative amount of the high-energy flux at the surface of the reactor.

[9]W. F. Osborne and D. W. Montgomery, Babcock and Wilcox, private communication.

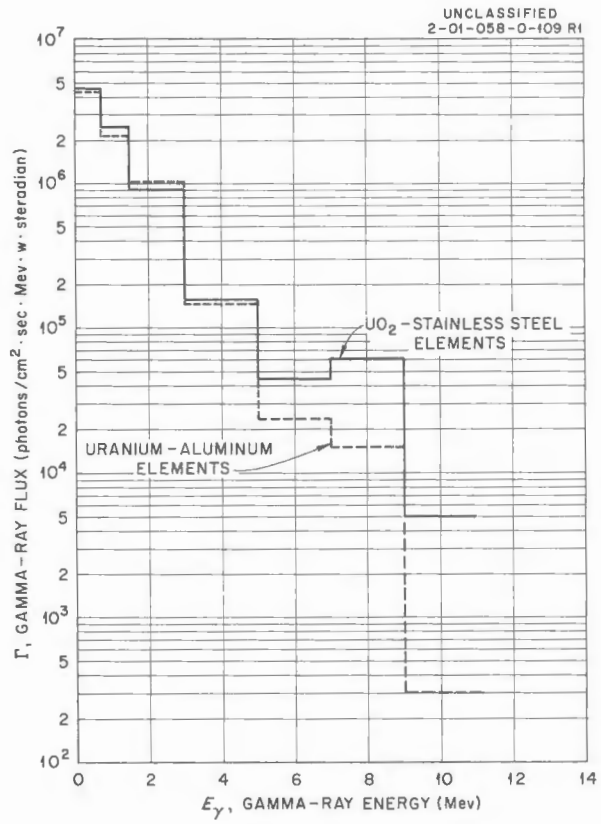

Fig. 5.2.4. Comparison of the Calculated Gamma-Ray Spectrum of the BSF Reactor Containing Uranium-Aluminum Fuel Elements with the Spectrum of the BSF Reactor Containing UO_2–Stainless Steel Fuel Elements.

THE ENERGY AND ANGULAR DISTRIBUTION OF GAMMA RADIATION FROM A Co^{60} SOURCE AFTER DIFFUSION THROUGH MANY MEAN FREE PATHS OF WATER

R. W. Peelle F. C. Maienschein
T. A. Love

The importance to shielding calculations of the "buildup factor" concept justified experiments designed to check gamma-ray attenuation calculations. Details of the penetration of gamma rays through many mean free paths have resulted from the "moments-method" calculations by the National

Bureau of Standards[10-12] and the Nuclear Development Corporation of America.[13] These calculations have provided the energy spectrum of the energy flux, integrated over all solid angles for an isotropic detector. Integrations have been carried out to provide dose buildup factors.

Various integral experiments have been performed which have been interpreted as substantiating the results of the moments-method calculations. As a result of these experiments, dose buildup factors as a function of detector separation distance from a Co^{60} point source have been measured in water,[14] in iron,[15,16] and in lead.[16] In addition, Hayward[17] measured the electron spectrum observed by an anthracene crystal in water as a function of distance from a Co^{60} source. The results of this experiment were compared with a special moments-method calculation designed to produce the electron spectrum.

In spite of the apparent agreement between these integral measurements and the calculations, it was considered important to check the differential spectra predicted by the calculations to provide a more stringent test. Therefore, an experiment designed to give these differential spectra was performed at ORNL. In this experiment the energy and angle spectra of the photon energy flux resulting from the diffusion in an infinite water medium of 1.17- and 1.33-Mev gamma rays from a point (Co^{60}) source were determined. Both a 100-curie and a 195-mc source were used, and the measurements were made with a Compton spectrometer having a peak-to-total ratio of 0.7 and a resolution of 14% (full width at half maximum) for 1.12-Mev photons. The spectra were measured at several angles between 0 and 90 deg for penetration distances corresponding to 6 to 9 mean free paths for the uncollided source photons.

It has been possible to provide an absolute normalization for the ORNL experiment. Considerable disagreement, about a factor of 2, appears to exist between the integrated experimental results and the calculated values, which is well outside the expected combined limits of error. Since this discrepancy may cast possible doubts on either the experiment or the calculated results, it is hoped that both may be repeated. Such a confirmatory experiment is planned at ORNL when suitable apparatus becomes available.

Since the ORNL experiment was performed, a similar experiment was carried out by Whyte[18] for a concrete medium which terminated at the point of detection for angles up to 60 deg. Whyte's results integrated over the solid angle appear to be in agreement with the calculated shapes. No absolute normalization was attempted in Whyte's experiment, however. The details of the ORNL experiment were published previously.[19]

PROGRAM FOR SHIELDING MEASUREMENTS AT THE ART

G. T. Chapman

It is apparent that the energy and angular distribution spectra of gamma rays and neutrons from circulating-fuel reactors must be known for accurate shielding calculations, and therefore provisions have been made at the ART facility for a limited number of measurements. The provisions include five collimator tubes which extend radially from the shield in its horizontal midplane (Fig. 5.2.5). Gamma-ray and neutron spectral and dose-rate measurements will be made within the tubes. In addition, dose-rate measurements will be made in a region at the north head of the reactor.

The design for the five 24-in.-dia collimator tubes[20] (Fig. 5.2.6) has been completed. In order to obtain the optimum collimator arrangement for both gamma-ray and neutron collimation, the reactor end of each tube was designed to contain a steel gamma-ray shield equivalent in thickness to 5 in. of lead. Neutron collimation will be obtained

[10] L. V. Spencer and U. Fano, *Phys. Rev.* 81, 464 (1951); see also L. V. Spencer and U. Fano, *J. Research Natl. Bur. Standards* 46, 446 (1951).

[11] L. V. Spencer and F. Stinson, *Phys. Rev.* 85, 662 (1952).

[12] U. Fano, *J. Research Natl. Bur. Standards* 51, 95 (1953).

[13] H. Goldstein and J. E. Wilkins, Jr., *Calculations of the Penetration of Gamma Rays. Final Report*, NYO-3075 (June 30, 1954).

[14] G. R. White, *Phys. Rev.* 80, 154 (1950).

[15] L. A. Beach, R. B. Theus, and W. R. Faust, *Phys. Rev.* 92, 355 (1953).

[16] C. Garrett and G. N. Whyte, *Phys. Rev.* 95, 889 (1954).

[17] E. Hayward, *Phys. Rev.* 86, 493 (1952).

[18] G. N. Whyte, *Can. J. Phys.* 33, 96 (1955).

[19] R. W. Peelle, F. C. Maienschein, and T. A. Love, *Appl. Nuclear Phys. Ann. Rep. Sept. 10, 1956*, ORNL-2081, p 170.

[20] A. P. Fraas, *ANP Quar. Prog. Rep. Sept. 10, 1955*, ORNL-1947, p 16, Fig. 1.1.

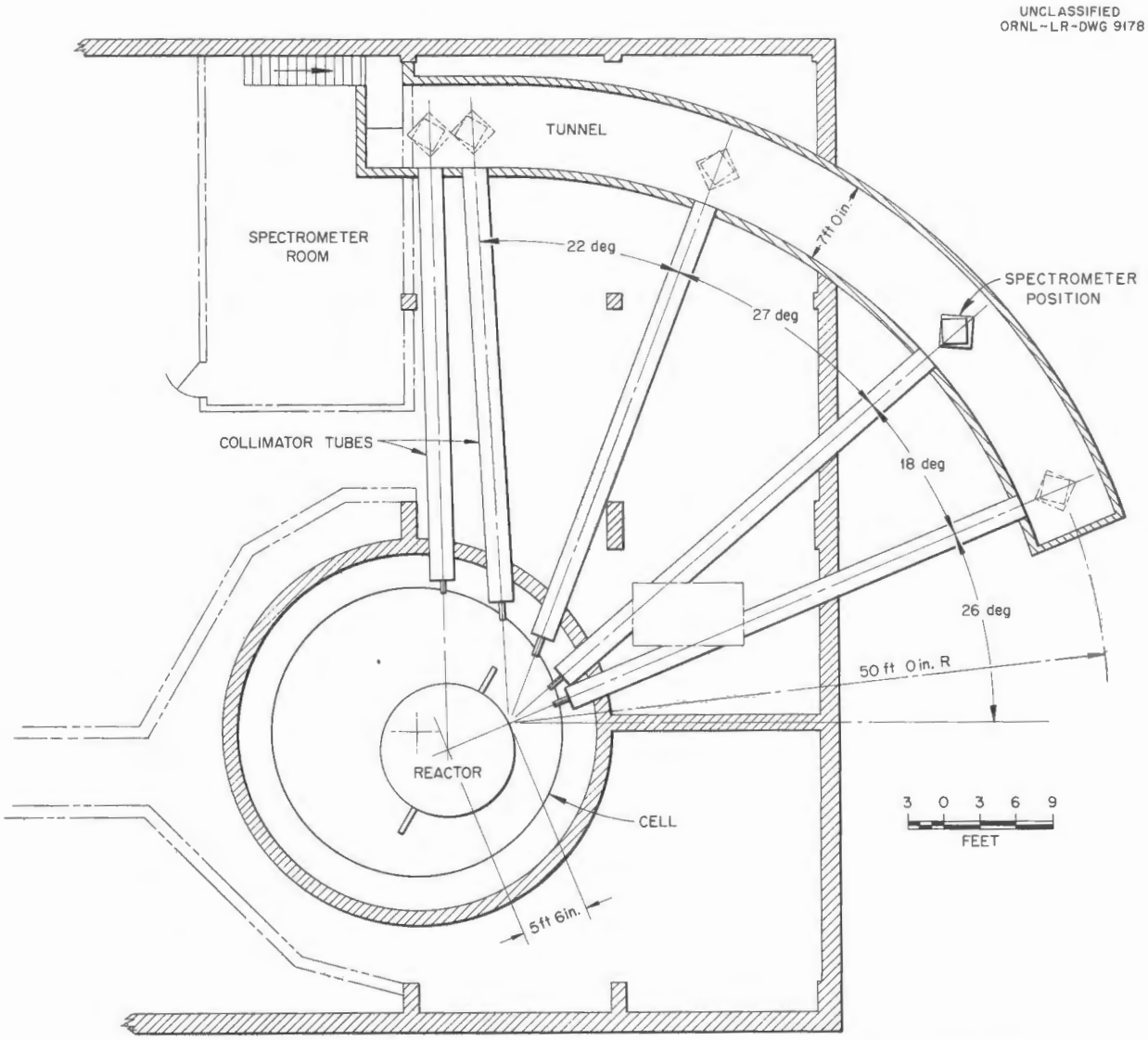

Fig. 5.2.5. Arrangement of Collimator Tubes for Shielding Measurements of the ART.

by inserting a 5-in.-dia cylinder of hydrogeneous material through and concentric with the gamma-ray shield. This cylinder will contain a central 1-in.-dia. collimating hole.

Gamma-ray collimation will be enhanced by the addition of a second lead disk immediately behind the gamma-ray shield. This disk, which will be 6 in. thick and 9 in. in diameter, will also contain a central 1-in.-dia hole for collimation. Each collimator tube will also contain two mobile "antiscattering" lead baffles to eliminate any gamma rays that might be scattered while traversing the tube. These baffles will be mobile so that they may be removed from the tubes when the tube is being used for neutron spectroscopy.

In order to see the effect of the outer water layers of the reactor shield proper, provisions have been made to drain the water from the shield in the quadrant of the shield seen by the spectrometers. The installation of partitioning walls makes it possible to remove the shield water in layers 6 in. thick while the reactor is operating. Approximately one-half the water thickness may be removed in this fashion.

UNCLASSIFIED
2-01-058-0-121

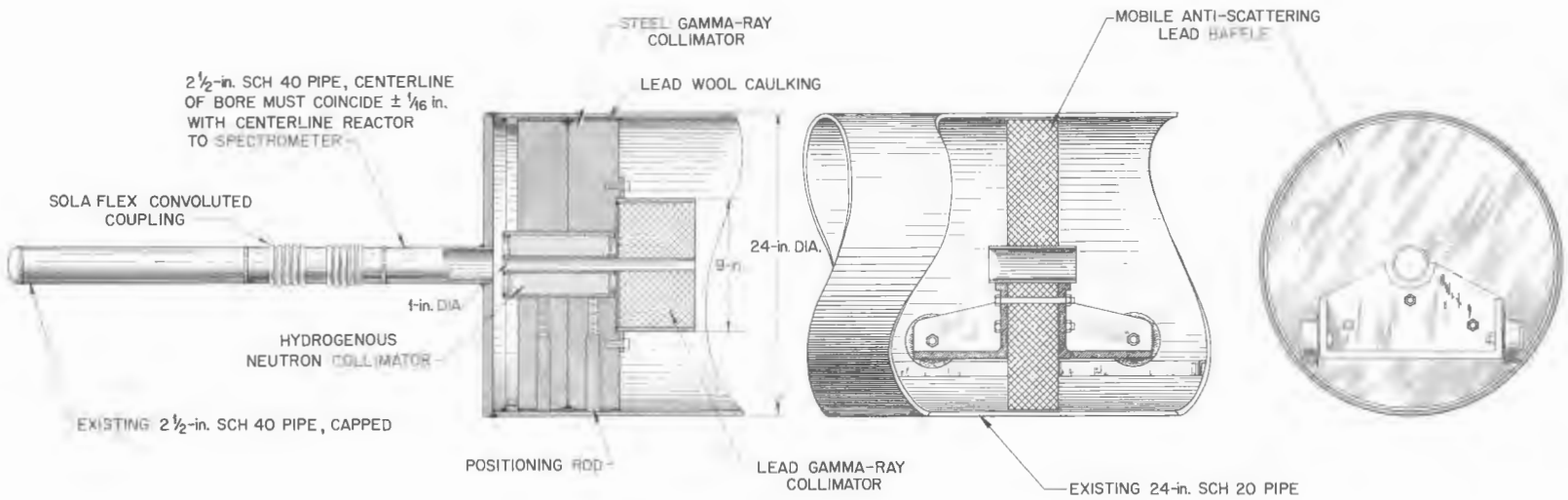

Fig. 5.2.6. Detail of a Collimator Tube.

The dose-rate measurements above the ART will be made at the end of a conical collimator which will extend through the water-filled reactor cell annulus (biological shield) above the ART (that is, it will extend from the outer tank to the inner tank, see Fig. 5.2.7). At this position the collimator will define a solid angle through the water which will include only the reactor. Thus it is hoped that gamma-ray and neutron dose-rate measurements will reflect radiations from the reactor only and will exclude, to a large extent, the radiations from NaK lines, etc., above the reactor.

[redacted]
2-01-058-0-122

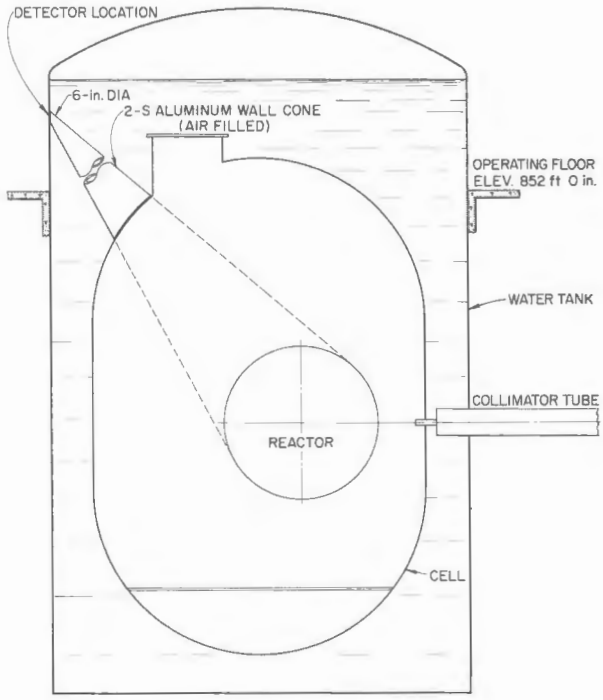

Fig. 5.2.7. Vertical Section Through the ART Showing Conical Collimator at North Head and One Collimator Tube at Horizontal Midplane.

5.3. THE TOWER SHIELDING REACTOR II

C. E. Clifford L. B. Holland

A change in the basic concept of the utility of the new reactor being designed for the Tower Shielding Facility (TSF) has brought about considerable revision of the design. The reactor, as originally conceived, was to mock up as closely as possible the reflector-moderated reactor then contemplated by Pratt & Whitney, and, as such, it was called the Shield Mockup Core (SMC).[1] Since a more general purpose radiation source is now desired, the new reactor will be called the Tower Shielding Reactor II (TSR-II). Its utility in the ANP program is intended to be sufficiently general to cover problems of importance to shields for any reactor cycle which might be undertaken.

Experience in shield calculations and design indicates that the following basic types of experiments should be performed.

Beam Differential Experiments. – Measurements should be made with a collimated source of radiation (neutrons or gamma rays). The direction of the beam, as well as the energy spectrum, should be variable (the spectrum would be changed by interposed absorbers), and the detector to be used should be equipped with a collimator and be able to measure spectra of air-, ground-, and structure-scattered radiation.

Differential Experiments. – Measurements should be made with the reactor or the detector covered, partially or wholly, by a section of a shield, for example, a lead shadow shield, which should then be varied in shape or size to determine its effectiveness.

Complete Mockup Experiments. – Measurements should be made with a complete shield configuration as a check on calculations which would be based on the differential tests.

In studying means for performing these experiments within a reasonable period and at the same time obtaining shielding data which would be amenable to analyses, several requirements for the new reactor became clear:

1. Its power would have to be significantly greater than the 400 kw at which the present TSF reactor can operate. A power of 5000 kw has been chosen as a compromise between need and cost.

2. Its shape should be such that its source could be calculated and the experimental data could be applied to most power reactors. A spherical configuration has been chosen, and the absorber plates for the reactor control will be inside the core to ensure a minimum perturbation on the leakage flux or spectrum.

3. Only the core should be built – adaptable to any shield. The spherical core would be held in a long pipe with a flange fitting for shields.

4. The direction and energy spectrum of the leakage radiation should be variable. This would be accomplished by external shields and collimators.

REACTOR MECHANICAL DESIGN[2]

A spherical arrangement of light-water-cooled and -moderated MTR-type fuel plates was chosen for the reactor (see Fig. 5.3.1). The core will be mounted in the bottom of a long cylindrical tank which will also enclose the control mechanism positioning rod and the control chambers. Connections to the inlet and exit water lines will be mounted at the top of the tank. The cooling water will flow downward through a central pipe, pass the central core region, turn at the bottom, and return through the outside core region and the annular space between the pipe and the tank.

A spherical region in the center of the core will be flooded with water but will be free of fuel plates. In this space umbrella-shaped boron-loaded grids will be located to serve as a control device for the reactor (see Fig. 5.3.2). By moving radially inward, away from the fuel, the plates will cause the reactivity to increase, and vice versa. Movement of the plates will be achieved by a combination of mechanical and hydraulic devices.

[1] In a few memoranda it has also been called the Shield Core II (SC-II).

[2] The mechanical design of the reactor is being performed by the following members of the ORNL Engineering Division: C. W. Angel (group leader), F. L. Hannon, L. Howell, R. K. Francis, P. E. Oliver, J. R. McIntosh, J. M. Skorski, and A. Daniels (on loan from Lockheed Aircraft).

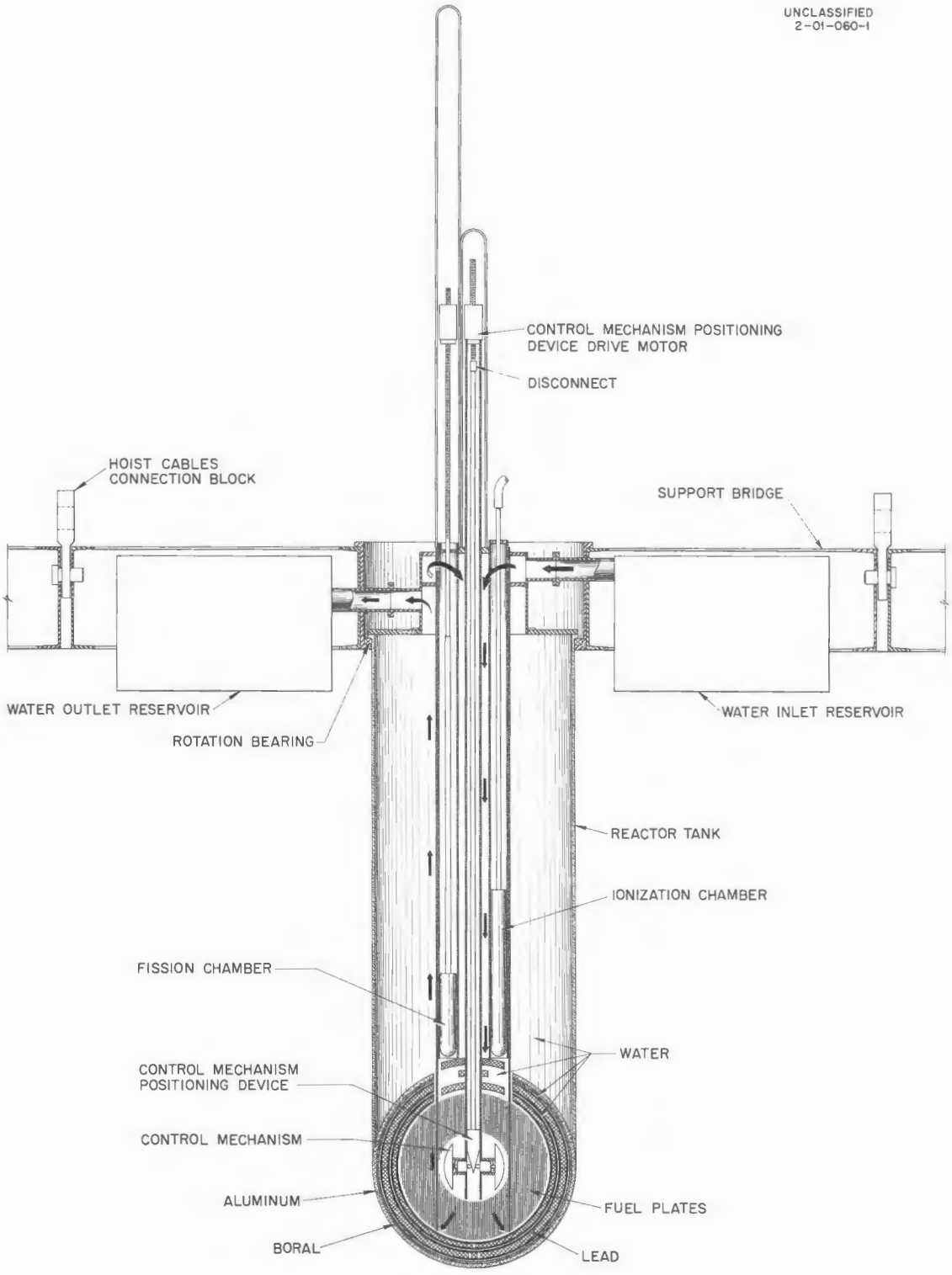

Fig. 5.3.1. Tower Shielding Reactor II (Vertical Section).

A lead-boral-water region adjacent to the core periphery will reduce the reactivity coupling between the reactor and close-fitting shields. Shields will be fastened to the cylindrical support tube by means of a flange so that the reactor and its shield will rotate as a unit.

EXPERIMENTAL SHIELD CONFIGURATIONS

Schematic shield designs for the basic experiments are shown in Fig. 5.3.3. A lead-water unit shield with a beam hole is proposed for the beam differential experiment. Differential partial shield

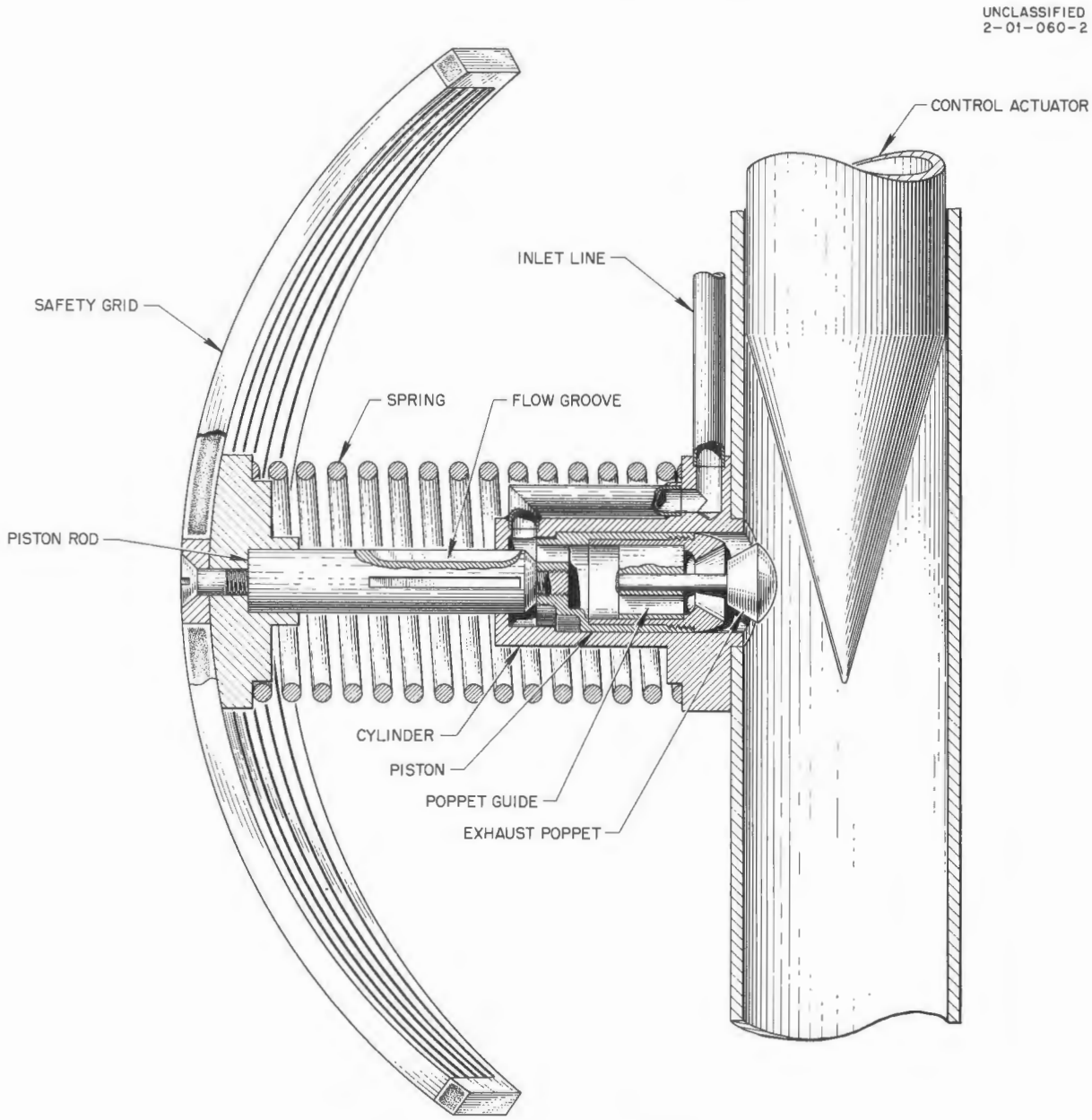

Fig. 5.3.2. TSR-II Control Mechanism.

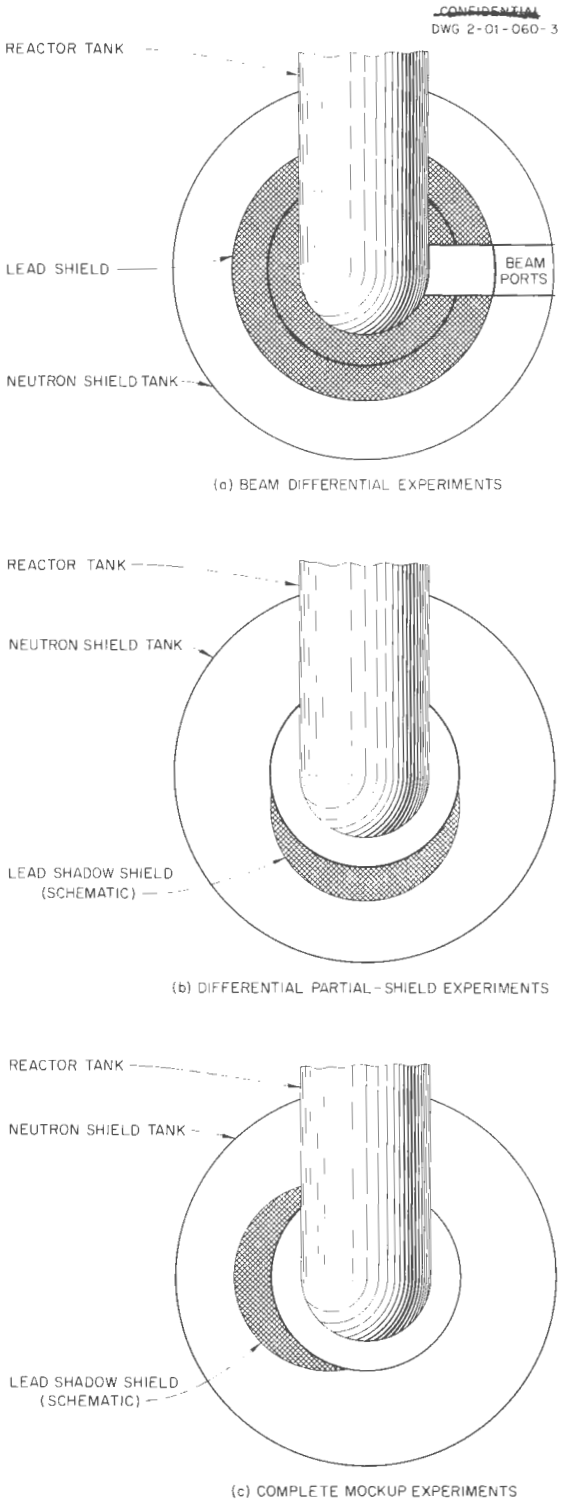

Fig. 5.3.3. Experimental Shield Configurations Planned for the TSR-II. *a.* Beam differential experiments. *b.* Differential partial shield experiments. *c.* Complete mockup experiments.

measurements can be facilitated by using the vertical geometry shown for a lead shadow shield (that is, the detector will be suspended below the reactor). Conventional horizontal TSF geometry would be employed for integral shield tests.

NUCLEAR CALCULATIONS

The multigroup nuclear calculations to date have been performed[3] with the Murine Code[4] on the UNIVAC and the COP II code on the Wright Air Development Center 1103 computer. Parameter studies have been carried out for several aluminum-to-water ratios and for different volumes of water in the center of the reactor. An aluminum-to-water ratio of 2:1 was chosen as a temporary design point, and the central water volume that would permit adequate control with boron control plates was established. The addition of 0.1% normal boron concentration to the ½-in.-thick water region adjacent to the inner edge of the core reduced the effective multiplication constant of the reactor (k) from 0.9937 to 0.9397; 1% boron reduced it to 0.8491.

DEVELOPMENT EXPERIMENTS

Two experiments of a preliminary nature were performed at the BSF[5] to determine the feasibility of the design features for the lead-water reflector immediately surrounding the core. In the first experiment the thickness of lead slabs adjacent to the reactor core that would be required to reduce the intensity of the core gamma rays below that of the water-capture gamma rays was determined. The experiment was performed by locking the reactor and a 50-cm^3 spherical ion chamber 3 ft apart with the lead slabs between them (see Fig. 5.3.4). The ion chamber current was noted while the distance from the reactor to the lead shield and the thickness of the lead shield were varied. As shown in Fig. 5.3.5, the gamma-ray dose rate for 4 in. of lead increases nearly a factor of 4 as the reactor-lead separation distance is reduced.

The second experiment utilized configuration No. 1 in Fig. 5.3.4, with thermocouples in the lead nearest

[3] These calculations have been performed by M. E. LaVerne.

[4] A variation of the ORNL Eyewash Code for the UNIVAC.

[5] These experiments were performed by K. M. Henry, E. B. Johnson, and J. D. Kington.

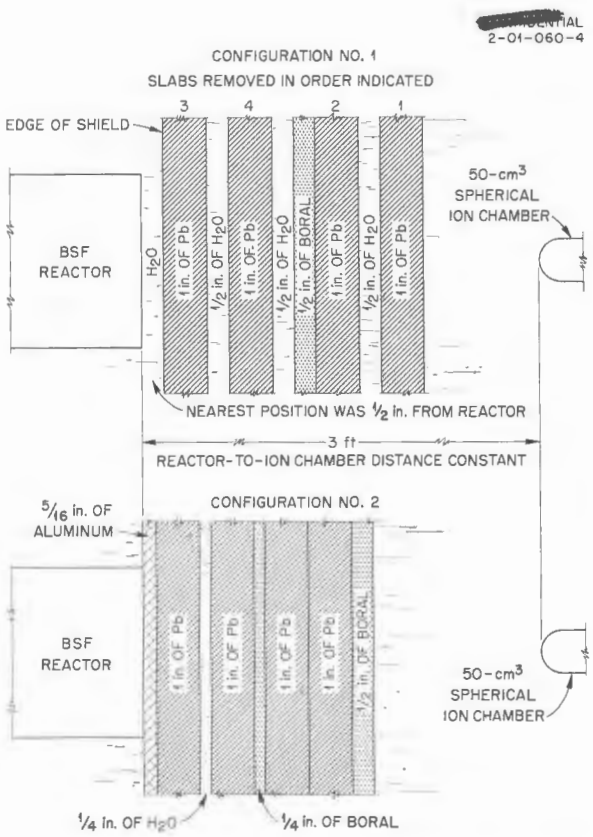

Fig. 5.3.4. Configurations Used for TSR-II Development Experiments at the BSF.

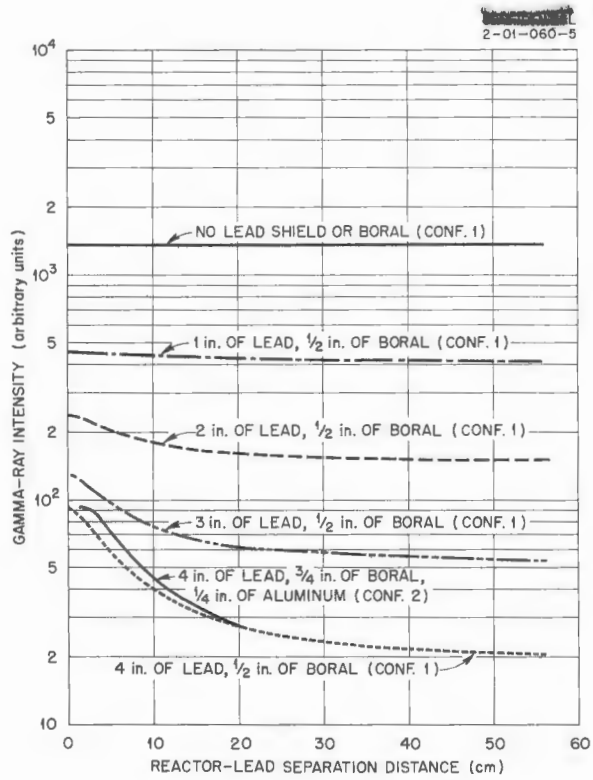

Fig. 5.3.5. Gamma-Ray Intensity 3 ft from the BSR as a Function of Reactor-Lead Separation Distance.

the reactor. The temperature rise of each point in the lead that was above the temperature of the pool water was noted for various reactor power levels (see Fig. 5.3.6). The slabs were convectively cooled by the pool water. While the results are not conclusive as regards the TSR-II, they give some idea of the problem of cooling large slabs of lead near the core.

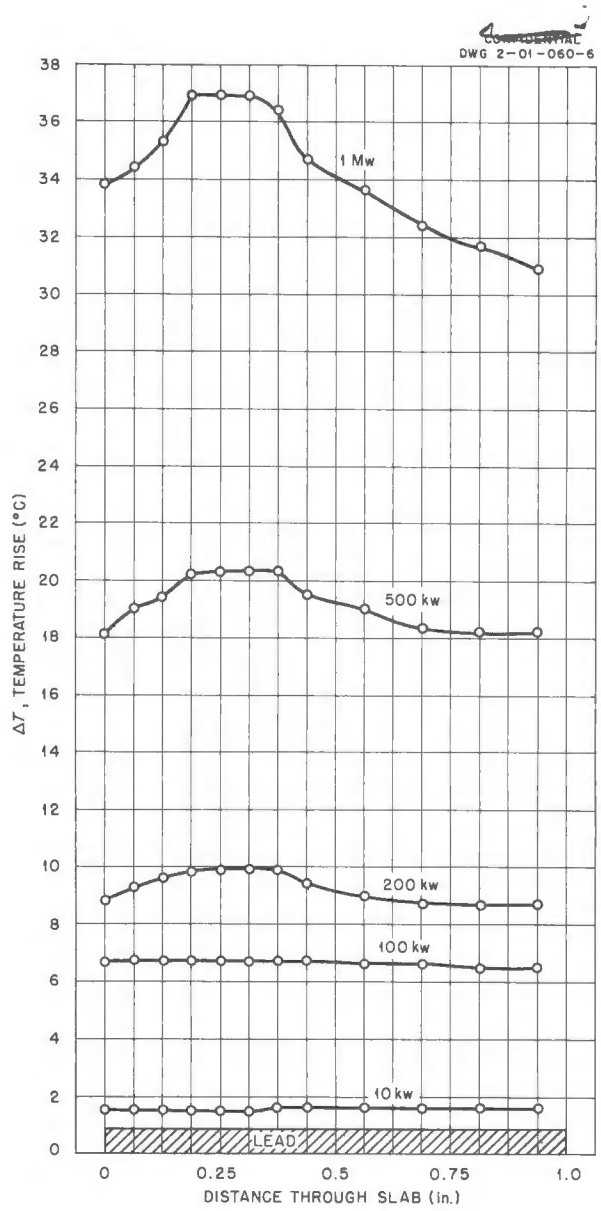

Fig. 5.3.6. Temperature Rise at Various Points in a Lead Slab Adjacent to the BSR.

[redacted]

THE AIRCRAFT NUCLEAR PROPULSION PROJECT
AT
THE OAK RIDGE NATIONAL LABORATORY

JANUARY 1, 1957

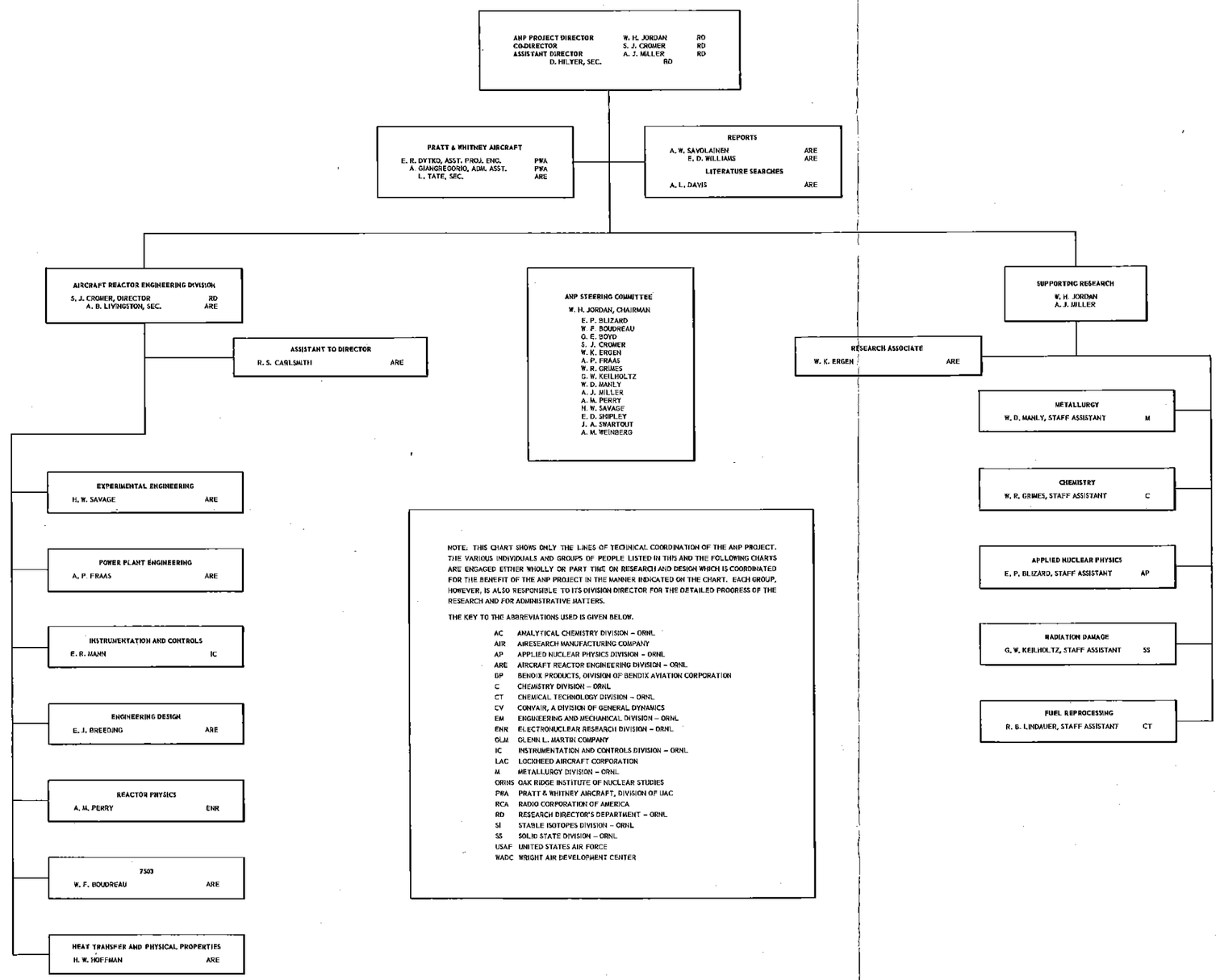

NOTE: THIS CHART SHOWS ONLY THE LINES OF TECHNICAL COORDINATION OF THE ANP PROJECT. THE VARIOUS INDIVIDUALS AND GROUPS OF PEOPLE LISTED IN THIS AND THE FOLLOWING CHARTS ARE ENGAGED EITHER WHOLLY OR PART TIME ON RESEARCH AND DESIGN WHICH IS COORDINATED FOR THE BENEFIT OF THE ANP PROJECT IN THE MANNER INDICATED ON THE CHART. EACH GROUP, HOWEVER, IS ALSO RESPONSIBLE TO ITS DIVISION DIRECTOR FOR THE DETAILED PROGRESS OF THE RESEARCH AND FOR ADMINISTRATIVE MATTERS.

THE KEY TO THE ABBREVIATIONS USED IS GIVEN BELOW.

AC	ANALYTICAL CHEMISTRY DIVISION – ORNL
AIR	AIRESEARCH MANUFACTURING COMPANY
AP	APPLIED NUCLEAR PHYSICS DIVISION – ORNL
ARE	AIRCRAFT REACTOR ENGINEERING DIVISION – ORNL
BP	BENDIX PRODUCTS, DIVISION OF BENDIX AVIATION CORPORATION
C	CHEMISTRY DIVISION – ORNL
CT	CHEMICAL TECHNOLOGY DIVISION – ORNL
CV	CONVAIR, A DIVISION OF GENERAL DYNAMICS
EM	ENGINEERING AND MECHANICAL DIVISION – ORNL
ENR	ELECTRONUCLEAR RESEARCH DIVISION – ORNL
GLM	GLENN L. MARTIN COMPANY
IC	INSTRUMENTATION AND CONTROLS DIVISION – ORNL
LAC	LOCKHEED AIRCRAFT CORPORATION
M	METALLURGY DIVISION – ORNL
ORINS	OAK RIDGE INSTITUTE OF NUCLEAR STUDIES
PWA	PRATT & WHITNEY AIRCRAFT, DIVISION OF UAC
RCA	RADIO CORPORATION OF AMERICA
RD	RESEARCH DIRECTOR'S DEPARTMENT – ORNL
SI	STABLE ISOTOPES DIVISION – ORNL
SS	SOLID STATE DIVISION – ORNL
USAF	UNITED STATES AIR FORCE
WADC	WRIGHT AIR DEVELOPMENT CENTER

~~OFFICIAL USE ONLY~~

THE AIRCRAFT NUCLEAR PROPULSION PROJECT
AT
THE OAK RIDGE NATIONAL LABORATORY

JANUARY 1, 1957

AIRCRAFT REACTOR ENGINEERING DIVISION
S. J. CROMER, DIRECTOR — RD
A. B. LIVINGSTON, SEC. — ARE

ASSISTANT TO DIRECTOR
R. S. CARLSMITH — ARE
R. E. THOMPSON — ARE

REACTOR PHYSICS
A. M. PERRY — ENR
M. WILSON, SEC. — ARE

H. W. BERTINI — ARE
C. M. COPENHAVER — ARE
M. TSAGARIS — ARE
D. C. DEAN, COMPUTER — ARE

HEAT TRANSFER AND PHYSICAL PROPERTIES
H. W. HOFFMAN — ARE
M. D. EDEN, SEC. — ARE

HEAT TRANSFER
N. D. GREENE — ARE
D. P. GREGORY — PWA
F. E. LYNCH — ARE
G. L. MULLER — PWA
L. D. PALMER — ARE
P. E. STOVER — ARE
J. L. WANTLAND — ARE
R. M. BURNETT — IC
J. M. COBURN — ARE
J. JONES — ARE
R. L. MILLER — ARE
G. M. WINN — ARE

PHYSICAL PROPERTIES
S. I. COHEN — ARE
W. R. GAMBILL — ARE
W. O. POWERS — ARE
G. C. BLALOCK — ARE
S. J. CLAIBORNE — ARE
T. N. JONES — ARE

POWER PLANT ENGINEERING
A. P. FRAAS — ARE
A. R. BENNETT, SEC. — ARE

ADMINISTRATION
W. L. SCOTT — ARE
W. R. LOCKHART, DRAFTSMAN — ARE

HYDRODYNAMICS AND THERMODYNAMICS
W. T. FURGERSON — ARE
J. A. BOPPART — AIR
L. G. EPEL — ARE
M. E. LACKEY — ARE
G. SAMUELS — ARE
B. H. FITZGERALD, COMPUTER — ARE
J. J. TUDOR, DRAFTSMAN — ARE

APPLIED MECHANICS AND STRESS ANALYSIS
R. V. MEGHREBLIAN — ARE
C. A. PROAPS, SEC. — ARE
B. L. GREENSTREET — ARE
H. LURIE — ARE
D. M. MILLER — PWA
S. E. MOORE — PWA
D. H. PLATUS — USAF
D. L. PLATUS — USAF
F. J. STANEK — ARE
J. R. TALLACKSON — IC

HEAT TRANSFER
R. D. SCHULTHEISS — ARE
F. C. ROBERTSON, SEC. — ARE
J. FOSTER — ARE
R. L. GRAY — PWA
M. M. YAROSH — ARE

7503
W. F. BOUDREAU — ARE
J. PARKER, SEC. — ARE

CONSTRUCTION
M. BENDER — ARE
M. C. OVERTON, SEC. — ARE

ETU AND ART ASSEMBLY
G. D. WHITMAN — ARE
S. J. HARRINGTON, SEC. — ARE
H. M. ABELE — ARE
P. A. GNADT — ARE
R. L. HEATHERLY — ARE
L. W. LOVE — PWA
C. K. MCGLOTHLAN — ARE
G. W. PEACH — ARE

ART OPERATIONAL AND DISASSEMBLY FACILITIES
F. R. MCQUILKIN — ARE
S. JANSCH, SEC. — ARE
J. H. DOUDY — CV
W. F. FERGUSON — ARE
V. J. KELLEGHAN — ARE
J. M. MILLS, JR. — ARE
G. C. ROBINSON — ARE
R. D. STULTING — ARE
C. F. WEST — ARE
T. E. CRABTREE — ARE

DISASSEMBLY TOOLS
A. A. ABBATIELLO — ARE
M. G. WILLEY — EM

EQUIPMENT CONTROL
B. B. BACHULIS — ARE
D. R. WESTFALL — ARE
B. L. HOUSER — ARE
J. J. PLATZ — ARE

OPERATIONS
D. B. TRAUGER — ARE
S. FURKEY, SEC. — ARE

REACTOR OPERATION AND DISASSEMBLY
W. B. COTTRELL — ARE
W. E. BROWNING* — SS
C. W. CUNNINGHAM — ARE
S. M. DECAMP — ARE
R. A. DREISBACH — PWA
R. P. SHIELDS* — SS

IN-PILE LOOP OPERATION
J. A. CONLIN — ARE
C. C. BOLTA — PWA
D. M. HAINES — PWA

SPECIAL ENGINEERING
J. ZASLER — ARE
M. AUBUCHON, SEC. — ARE
R. B. CLARKE — ARE
W. S. HARRIS — ARE
H. W. HOOVER — ARE
E. A. JAGGERS — ARE
R. G. JENNESS — ARE
T. A. KING — ARE
J. W. TEAGUE — ARE
W. E. THOMAS — ARE
G. B. TYLER — ARE
T. K. WALTERS — ARE

*ON PART-TIME LOAN

EXPERIMENTAL ENGINEERING
H. W. SAVAGE — ARE
D. ALEXANDER, SEC. — ARE

TEST OPERATION
W. B. MCDONALD — ARE
D. P. HARRIS, SEC. — ARE
A. MONTGOMERY, SEC. — ARE

TEST FACILITIES ASSEMBLY COORDINATION
E. STORTO — ARE
E. A. ALMGREN — ARE
J. L. CROWLEY — ARE
W. J. MUENZER — ARE
H. C. SANDERSON — PWA

CORROSION LOOPS
W. H. KELLEY — ARE
J. W. KINGSLEY — ARE
A. S. OLSON — ARE

ELECTRICAL SERVICES
E. M. LEES — ARE
D. L. CLARK — ARE
C. E. MURPHY — ARE

TECHNICIAN GROUP
R. HELTON — ARE
T. ARNEINE — ARE
B. R. CHILCOAT — ARE
G. S. CHILTON — ARE
E. D. CLEMMER — ARE
J. M. CUNNINGHAM — ARE
S. J. DAVIS — ARE
R. E. DIAL — ARE
J. R. DUCKWORTH — ARE
W. H. DUCKWORTH — ARE
J. D. EACH — ARE
R. H. FRANKLIN — ARE
H. FOUST — ARE
W. D. GROMLEY — ARE
C. J. GREEN — ARE
T. L. GREGORY — ARE
R. A. HAMRICK — ARE
P. P. HAYDON — ARE
C. G. HENLEY — ARE
B. L. JOHNSON — ARE
S. G. KENT — ARE
J. R. LOVE — ARE
G. E. MILLS — ARE
B. H. MONTGOMERY — ARE
C. C. NANCE — ARE
D. G. PEACH — ARE
H. W. PENLAND — ARE
R. REID — ARE
F. J. SCHAFER — ARE
J. R. SHUGART — ARE
D. E. TIDWELL — ARE
G. A. TOMS — ARE
C. A. WALLACE — ARE
B. C. WILLIAMS — ARE
G. W. WILSON — ARE
L. H. WRIGHT — ARE

DEVELOPMENT
E. R. DYTKO — PWA
K. LANE, SEC. — ARE

PUMPS
A. G. GRINDELL — ARE
J. W. COOKE — PWA
R. CURRY — PWA
J. J. SIMON — PWA
J. N. SIMPSON — PWA
P. G. SMITH — ARE
W. L. SNAPP — PWA
H. YOUNG — PWA

HEAT EXCHANGERS AND SPECIAL DEVELOPMENT
R. E. MACPHERSON — ARE
J. C. AMOS — ARE
M. H. COOPER — PWA
L. H. DEVLIN — PWA
I. T. DUDLEY — ARE
R. L. SENN — ARE
D. R. WARD — ARE

SPECIAL COMPONENTS TESTING
J. J. KEYES — ARE
A. I. KRAKOVIAK — ARE
S. KRESS — PWA
J. E. MOTT — PWA
R. D. PEAK — PWA
A. G. SMITH — PWA
W. J. STELZMAN — ARE

PROCUREMENT
W. R. OSBORN — ARE
D. STOREY, SEC. — ARE
F. LEWIS, SEC. — ARE
S. ASHTON — ARE
W. O. CHANDLER — ARE
J. EVANS — ARE
D. L. GRAY — ARE
G. JENKINS — ARE
E. MAEYENS — ARE
T. MAYES — ARE

OFFICE SERVICES
J. P. LANE — ARE

ENGINEERING DESIGN
E. J. BREEDING — ARE
L. E. FERGUSON, SEC. — ARE
F. I. TAYLOR, SEC. — ARE

REACTOR DESIGN
N. J. GEBERT — PWA
J. Y. ESTABROOK — ARE
R. E. HELMS — ARE
F. L. MAGLEY — ARE
W. A. SYLVESTER — PWA
G. R. HICKS — ARE
J. R. LARRABEE — PWA

PUMP AND PIPING DESIGN
W. G. COBB — ARE
W. C. GEORGE — ARE
A. D. JARRATT — PWA
L. R. KOFFMAN — ARE
W. I. NELSON — PWA
L. V. WILSON — ARE

ELECTRICAL DESIGN
T. L. HUDSON — ARE
A. H. ANDERSON — ARE
B. C. GARRETT — ARE
J. KERR — ARE
S. F. HOWELL — ARE
R. H. JONES — ARE
J. O. NICHOLSON — ARE

GENERAL DESIGN
R. C. DANIELS — ARE
J. T. MEADOR — ARE
A. P. MARQUARDT — ARE
J. C. CABLE — ARE
W. I. GALYON — ARE
G. G. MICHELSON — ARE
C. A. MILLS — ARE
C. F. SALES — ARE

RECORDS AND PRINTING
E. E. CHAMBERS — ARE
S. J. FOSTER — ARE

INSTRUMENTATION AND CONTROLS
E. R. MANN — IC
C. S. WALKER — IC
V. CUMMINS, SEC — IC

SYSTEM DESIGN
E. VINCENS — IC
M. C. BECKER — IC
C. F. HOLLOWAY — IC
G. C. GUERRANT — IC
T. A. HERRELL — IC

INSTRUMENTATION
R. G. AFFEL — IC
R. E. ANDERSON — USAF
A. E. G. BATES — IC
G. H. BURGER — IC
C. M. BURTON — IC
J. T. DELORENZO — IC
F. C. HAZZARD — GLM
R. F. HYLAND — IC
J. W. KRENSON — IC
A. M. LEPPERT — IC
H. J. METZ — IC
W. R. MILLER — IC
R. E. PIDGEON, JR. — RCA
C. L. PEARCE, JR. — RCA
A. L. SOUTHERN — IC
J. S. ADDISON — IC
R. S. HENSLEY — IC
J. R. JONES — IC
B. R. ROSS — IC
H. P. SMITH — IC
J. W. STARKEN — IC
C. E. STEVENSON — IC
C. W. WRIGHT — IC
K. M. YOUNG — IC

NUCLEAR AND SPECIAL DEVICES
C. S. WALKER — IC
S. C. SHUFORD — PWA
W. E. WERTS — BP

SIMULATOR
F. P. GREEN — IC

CONSULTANTS
F. A. ANDERSON, UNIVERSITY OF MISSISSIPPI
J. F. BAILEY, UNIVERSITY OF TENNESSEE
A. H. FOX, UNION COLLEGE
J. FRENCH, UNIVERSITY OF TENNESSEE
W. LOWEN, UNION COLLEGE
R. L. MAXWELL, UNIVERSITY OF TENNESSEE
P. H. PITKANEN, UNIVERSITY OF SOUTH CAROLINA
J. M. TRUMMELL, STATE UNIVERSITY OF IOWA
W. K. STAIR, UNIVERSITY OF TENNESSEE
J. B. WEST, OKLAHOMA A&M COLLEGE
G. F. WISLICENUS, PENNSYLVANIA STATE COLLEGE

[redacted]

THE AIRCRAFT NUCLEAR PROPULSION PROJECT
AT
THE OAK RIDGE NATIONAL LABORATORY

JANUARY 1, 1957

SUPPORTING RESEARCH
W. H. JORDAN
A. J. MILLER

RESEARCH ASSOCIATE
W. K. ERGEN — ARE

STAFF ASSISTANT
E. P. BLIZARD — AP

APPLIED NUCLEAR PHYSICS
E. P. BLIZARD* — AP
R. RICKMAN,* SEC. — AP
L. S. ABBOTT* — AP

SHIELDING THEORY
A. SIMON* — AP
V. GLIDEWELL,* SEC. — AP
H. B. MORAN — PWA
C. D. ZERBY — AP

SHIELD DESIGN
C. E. CLIFFORD** — AP
F. L. KELLER — AP
E. McBEE, SEC. — AP
L. DOWMAN — WADC
A. T. FUTTERER — PWA
C. A. GOETZ — PWA
J. HILGEMAN — WADC
S. K. PENNY — AP
D. K. TRUBEY — AP

LID TANK SHIELDING FACILITY
R. W. PEELLE — AP
J. LUTTRELL, SEC. — AP
D. CADY — USAF
P. HEMMIG — USAF
L. JUNG — AP
J. M. MILLER — AP
E. A. WARMAN — PWA
L. BECKHAM — AP
O. R. HENDRIX — AP
H. JARVIS — IC
T. B. MILLICAN — AP
J. R. TAYLOR — AP

BULK SHIELDING FACILITY
F. C. MAIENSCHEIN* — AP
C. BOUNDS,* SEC. — AP
T. V. BLOSSER — AP
C. T. CHAPMAN — AP
G. deSAUSSURE* — AP
G. ESTABROOK* — AP
K. M. HENRY* — AP
E. B. JOHNSON* — AP
J. D. KINGTON* — AP
J. LEWIN — GLM
T. A. LOVE* — AP
E. G. SILVER* — AP
W. ZOBEL* — AP
O. W. CHRISTIAN* — AP
D. K. KIRBY* — AP
C. E. McNEW* — IC
F. E. RICHARDSON* — AP
J. SELLERS* — IC
R. M. SIMMONS* — AP
D. SMIDDIE* — IC
G. G. STOUT* — IC
H. WEAVER* — AP

TOWER SHIELDING FACILITY
C. E. CLIFFORD** — AP
W. G. BLESSING — CV
V. R. CAIN — AP
C. R. FINK — GLM
F. N. GREEN — GLM
J. L. HULL — AP
W. J. McCOOL — PWA
F. J. MUCKENTHALER — AP
W. E. PRICE — PWA
M. G. WELCH — AP
G. M. ARGO — AP
C. C. BARRINGER — AP
W. A. BIRD — IC
E. D. CARROLL — IC
I. D. CONNER — AP
J. N. MONEY — AP
G. G. UNDERWOOD — IC
R. E. WRIGHT — AP

SHIELD CORE II
C. E. CLIFFORD** — AP
L. B. HOLLAND — AP
A. DANIEL — LAC
F. MAGLEY — ARE

REACTOR PHYSICS
A. SIMON* — AP
R. R. COVEYOU* — AP
L. DRESNER* — AP
W. E. KINNEY* — AP
M. E. LAVERNE* — AP
J. H. MARABLE* — AP
J. G. SULLIVAN* — AP

CRITICAL EXPERIMENTS
A. D. CALLIHAN* — AP
M. L. RUEFF,* SEC. — AP
E. DEWSKI — PWA
J. F. ELLIS* — AP
W. J. FADER — PWA
Y. G. HARNESS* — AP
D. A. HARVEY — PWA
J. J. LYNN — AP
R. E. MALENFANT — AP
E. R. ROHRER* — AP
E. V. SANDIN — PWA
D. SCOTT, JR. — ARE
W. C. TUNNELL,* — AP
M. K. ALBRIGHT* — AP
D. E. McCARTY — AP

CONSULTANTS
H. A. BETHE, CORNELL UNIVERSITY
J. A. NOHEL, GEORGIA INSTITUTE OF TECHNOLOGY

CONTRACTORS
METAL HYDRIDES, INC.
NUCLEAR DEVELOPMENT CORPORATION OF AMERICA
TECHNICAL RESEARCH GROUP

STAFF ASSISTANT
W. R. GRIMES — C

CHEMISTRY
W. R. GRIMES — C
D. E. CALDWELL, SEC. — C
D. R. CUNEO — C
A. L. ATCHLEY, SEC. — C

SPECIAL PROBLEMS
R. F. NEWTON — RD
C. C. BEAUSMAN — ORINS
R. E. MINTURN — USAF

PHASE STUDIES
C. J. BARTON — C
R. J. SHEIL — C
R. E. THOMA — C
H. A. FRIEDMAN — C
B. S. LANDAU — C
B. C. THOMAS — C
R. E. MOORE — C
R. E. MEADOWS — C
R. P. METCALF — C
R. K. BAGWELL — C

FUEL PREPARATION RESEARCH
G. M. WATSON — C
C. M. BLOOD — C
R. A. GILBERT — C
J. H. SHAFFER — C
N. V. SMITH — C
R. A. STREHLOW — C
W. T. WARD — C
G. A. PALMER — C

CHEMICAL EQUILIBRIA
L. G. OVERHOLSER — C
E. E. KETCHEN — C
J. D. REDMAN — C
B. J. STURM — C

CORROSION STUDIES
F. KERTESZ — C
H. J. BUTTRAM — C
F. A. KNOX — C
D. ZUCKER — C
J. M. DIDLAKE — C

MATERIALS PRODUCTION
G. J. NESSLE — C
M. R. SWAN, SEC. — C
C. R. CROFT — C
F. A. DOSS — C
J. E. BORGAN — C
J. TRUITT — C
D. C. WOOD — C
C. N. ADKINS — C
R. T. ATKINS — C
D. H. DOWMAN — C
J. P. EUBANKS — C
W. K. R. FINNELL — C
B. F. HITCH — C
E. HOLT — C
W. JENNINGS — C
W. M. JOHNSON — C
L. MASSENGILL — C
B. WEAVER — C
R. G. WILEY — C

THERMODYNAMICS
F. F. BLANKENSHIP — C
M. BLANDER — C
S. CANTOR — C
S. LANGER — C
M. D. PANISH — C
L. E. TOPOL — C

SUPPORTING STUDIES
P. A. AGRON — C
J. E. SUTHERLAND — C
M. D. DANFORD — C

CONSULTANTS
H. INSLEY
T. N. McVAY

CONTRACTORS
BATTELLE MEMORIAL INSTITUTE
CARTER LABORATORIES

ANALYTICAL CHEMISTRY
J. C. WHITE — AC
E. M. ZARZECKI, SEC. — AC

RESEARCH AND DEVELOPMENT
A. S. MEYER, JR. — AC
J. P. YOUNG — AC
R. E. FEATHERS, JR. — AC
J. R. FRENCH — AC
T. W. GILBERT, JR. — AC
G. GOLDBERG — AC
B. L. McDOWELL — AC
W. J. ROSS — AC

SERVICE
W. F. VAUGHAN — AC
R. F. APPLE — AC
D. E. CARPENTER — AC
H. L. HOLSOPPLE, JR. — AC
R. C. BRYANT — AC
L. R. HALL — AC
L. E. IDOM — AC
A. H. MATTHEWS — AC
A. D. WILSON — AC
C. M. WILSON — AC

SPECTROGRAPHIC ANALYSIS
J. R. McNALLY* — SI
J. A. NORRIS* AND OTHERS — SI

MASS SPECTROMETRY
J. R. SITES — SI

*PART TIME
**DUAL CAPACITY

STAFF ASSISTANT
W. D. MANLY — M

METALLURGY
W. D. MANLY — M
T. HIKIDO — USAF
M. R. HILL* — M
J. MORRISON, SEC. — M

GENERAL CORROSION
E. E. HOFFMAN — M
R. CARLANDER — PWA
W. H. COOK — M
D. H. JANSEN — M
J. L. GRIFFITH — M
J. W. HENDRICKS — M
J. E. POPE — M
L. R. TROTTER — M

DYNAMIC CORROSION
J. H. DEVAN — M
E. A. KOVACEVICH — M
G. D. BRADY — M
E. J. LAWRENCE — M
M. A. REDDON — M

FABRICATION
J. H. COOBS — M
M. R. D'AMORE — PWA
H. INOUYE — M
Y. KOLBA — GLM
R. E. McDONALD — PWA
J. P. PAGE — M
T. K. ROCHE — M
R. W. JOHNSON — M
J. F. NEWSOME — M

WELDING AND BRAZING
P. PATRIARCA — M
R. E. CLAUSING — M
E. A. FRANCO-FERREIRA — M
G. M. SLAUGHTER — M
E. J. WILSON — M
B. McDOWELL — M
C. E. SHUBERT — M
R. G. SHOOSTER — M
L. C. WILLIAMS — M

MECHANICAL PROPERTIES
D. A. DOUGLAS — M
C. W. DOLLINS — M
C. R. KENNEDY — PWA
J. R. WEIR, JR. — M
J. W. WOODS — M
F. L. BEELER — M
K. W. BOLING — M
E. BOLLING — M
J. T. EAST — M
J. D. HUDSON — M
V. G. LANE — M
B. McNABB, JR. — M
E. D. PATTON, JR. — M
C. K. THOMAS — M
C. W. WALKER — M

MASS TRANSFER STUDY
J. L. SCOTT — M
H. W. LEAVENWORTH — PWA

NONDESTRUCTIVE TESTING
R. B. OLIVER — M
J. W. ALLEN — M
R. W. McCLUNG — M
R. A. NANCE — M
O. E. CONNER — M
R. A. CUNNINGHAM — M
W. J. MASON — M

INSPECTION
A. TABOADA — M
A. E. GOLDMAN — M
R. L. HEESTAND — PWA
G. M. TOLSON — M
R. M. EVANS — M
J. B. PHILLIPS — M

METALLOGRAPHY
R. J. GRAY — M
R. S. CROUSE — M
J. R. RIDDLE — M
D. F. STONEBURNER — M
J. E. VANCLEVE — M
M. D. ALLEN — M
L. M. AMBURN — M
H. M. ATCHLEY — M
E. R. BOYD — M
R. L. FITZGERALD — M
E. P. GRIGGS — M
T. J. HENSON — M
E. H. LEE — M
G. C. LESLIE — M
B. J. REECE — M
L. G. SCHRADER — M
C. E. ZACHARY — M

CERAMICS RESEARCH
L. M. DONEY — M
A. HOBBS, SEC. — M
C. E. CURTIS — M
S. D. FULKERSON — M
R. L. HAMNER — M
L. A. HARRIS — M
R. A. POTTER — M
A. J. TAYLOR — M
G. D. WHITE — M
J. A. GRIFFIN — M

CONSULTANTS
GRAPHITE SPECIALTIES CORPORATION
H. INSLEY
T. N. McVAY
T. S. SHEVLIN, OHIO STATE EXPERIMENT STATION

METALLURGY CONSULTANTS
N. CABRERA, UNIVERSITY OF VIRGINIA
N. J. GRANT, MASSACHUSETTS INSTITUTE OF TECHNOLOGY
J. L. GREGG, CORNELL UNIVERSITY
W. D. JORDAN, UNIVERSITY OF ALABAMA
E. F. NIPPES, RENSSELAER POLYTECHNIC INSTITUTE
W. F. SAVAGE, RENSSELAER POLYTECHNIC INSTITUTE

METALLURGY CONTRACTORS
BATTELLE MEMORIAL INSTITUTE
BRUSH BERYLLIUM COMPANY
GLENN L. MARTIN COMPANY
METAL HYDRIDES, INC.
NEW ENGLAND MATERIALS TESTING LABORATORY
RENSSELAER POLYTECHNIC INSTITUTE
SUPERIOR TUBE COMPANY
UNIVERSITY OF ALABAMA
UNIVERSITY OF FLORIDA
UNIVERSITY OF TENNESSEE

STAFF ASSISTANT
G. W. KEILHOLTZ — SS

RADIATION DAMAGE
G. W. KEILHOLTZ — SS

MTR LIAISON
H. V. KLAUS — SS

HOT LAB FACILITY
S. E. DISMUKE — SS
A. E. RICHT — SS
C. ELLIS — SS
E. J. MANTHOS — SS
W. B. PARSLEY — SS
R. N. RAMSEY — SS
E. S. SCHWARTZ — SS
E. D. SIMS — SS
J. O. STIEGLER — SS
R. M. WALLACE — SS

RADIATION METALLURGY
J. C. WILSON — SS
C. D. BAUMANN — SS
W. E. BRUNDAGE — SS
W. W. DAVIS — SS
N. E. HINKLE — SS
T. C. PRICE — PWA

REACTOR EXPERIMENTS
W. E. BROWNING — SS
R. E. ADAMS — SS
D. E. GUSS — USAF
H. L. HEMPHILL — SS
M. F. OSBORNE — SS
H. E. ROBERTSON — SS
R. B. SHIELDS — SS

CHEMICAL EFFECTS OF NUCLEAR REACTIONS
R. J. CARTER — SS
L. H. JENKINS — SS
M. T. ROBINSON — SS

FLUX MEASUREMENTS
D. BINDER — SS
J. E. KRAUSE — PWA

ELECTRICAL COMPONENTS
J. C. PIGG — SS
O. L. CURTIS — SS
C. C. ROBINSON — SS
O. E. SCHOW — SS

ENGINEERING PROPERTIES
O. SISMAN — SS
J. C. MORGAN — SS
R. M. CARROLL — SS
P. E. REAGAN — SS

STAFF ASSISTANT
R. B. LINDAUER — CT

FUEL REPROCESSING
R. B. LINDAUER* — CT

CHEMICAL DEVELOPMENT
D. E. FERGUSON* — CT
G. I. CATHERS — CT
M. R. BENNETT — CT
R. L. JOLLEY — CT
C. J. SHIPMAN — CT

UNIT OPERATIONS
J. C. BRESEE* — CT
J. T. LONG — CT
S. H. STANKER — CT
C. L. WHITMARSH — CT
G. JONES, JR. — CT

DESIGN
H. E. GOELLER* — CT
R. P. MILFORD — CT

PILOT PLANT
R. B. LINDAUER* — CT
W. H. LEWIS* — CT
W. H. CARR — CT
F. N. BRONDER — CT
J. E. BIGELOW — CT
R. B. KEELY — CT
F. W. MILES — CT

[redacted]

[redacted]

[redacted]
Energy Act of 1954. Its transmittal or the disclosure of its contents [redacted]
in any manner to an unauthorized person is pro[redacted]d.

[redacted]